Formulation and Characterization of New Innovative Colloidal Systems Involving Ionic Liquids for the Application at High Temperatures

Dissertation

zur Erlangung des Grades

Doktor der Naturwissenschaften (Dr. rer. nat.)

Naturwissenschaftliche Fakultät IV

Chemie und Pharmazie

Universität Regensburg

vorgelegt von

Dipl.-Chem.

Stefan Thomaier

Regensburg 2009

Promotionsgesuch eingereicht am : 08.04.2009

Tag des Kolloquiums: 13.05.2009

Die Arbeit wurde angeleitet von: Prof. Dr. Werner Kunz

Prüfungsausschuß:

Prüfungsvorsitzender: Prof. em. Dr. Dr. h. c. Josef Barthel

1. Gutachter: Prof. Dr. Werner Kunz

2. Gutachter: Prof. em. Dr. Georg Schmeer

3. Prüfer: Prof. em. Dr. Jörg Daub

For my family and Susanne

Acknowledgements

Table of Contents

I. Introduction

During the last decades, the field of nanotechnology has become more and more important, because of the upcoming miniaturization according to which the size of microelectronics, for example, shrinks drastically year by year. In general, the term nanotechnology (or nanoscience) is employed to describe the fabrication and the research of materials that have structural features in the submicron range, i.e. between 1 nm and 1 μm. Many different materials, which achieve this criterion, are reported in the literature [1]. One area of research focuses nanocrystals composed of periodic groups of II-VI or III-V semiconductors, e.g. CdS, CdSe or CdTe, with almost spherical geometry of sizes from 2 - 10 nm in diameter. These materials show characteristic luminescence phenomena (with quantum yields exceeding 50%) which do not occur in the corresponding bulk semiconductors. The latter is the direct consequence of the nanometer size leading to the so-called quantum confinement. Electrons in bulk semiconductor materials have energy levels that are so close together that they behave as if the levels were the same. This characteristic sets the band gap energy at a fixed amount. Quantum dots behave differently. An exciton is defined as an excited electron–hole pair. The average distance between an excited electron and a hole is called the Exciton Bohr Radius. In bulk material, this radius is much smaller than the semiconductor crystal. However, nanocrystal diameters are smaller than this Bohr radius and therefore, the "continuous band" of electron energy levels no longer can be viewed as continuous. The energy levels become discrete meaning that there is a small and finite separation between the energy levels. This situation of discrete energy levels is denoted as quantum confinement that causes the special material properties. Because quantum dots' electron energy levels are discrete rather than continuous, the addition or subtraction of just a few atoms to the quantum dot has the effect of altering the boundaries of the bandgap. Changing the geometry of the surface of the quantum dot also changes the bandgap energy, owing again to the small size of the dot, and the effects of quantum confinement. Therefore, it is clear that the size of the bandgap is simply controlled by adjusting the size and the

shape of the dot. Since the emission frequency of a dot is dependent on the bandgap, it is possible to control the output wavelength of a dot with extreme precision. In effect, it is possible to tune the bandgap of a dot, and therefore specify its "colour" output depending on the needs of the application. Because of the tuneable optical features, it is not surprising that these kind of nanomaterials were found to be well suited for the usage in security applications (e.g. security inks), life science (e.g. diagnostics, biological sensors), and electronics (data storage, LEDs, photo voltaics, flat panel displays) [1-3].

Beside the quantum dots a lot of other nanoscale functional materials, including colour pigments ($CoAl_2O_4$, Cr_2O_3, α-Fe_2O_3, TiO_2), transparent conducting oxides (In_2O_3:Sn), and catalytically active oxides (CeO_2, Mn_3O_4, V_2O_5) are of great interest for various applications [4-12]

In the early 1990s, the study of porous silica with very high surfaces and well-defined monodisperse pores in the nanometer scale have attracted much attention of chemists and nanomaterial scientists caused by the fact that these materials are very interesting in their applications, e.g. chemical separations, heterogeneous catalysis, chemical sensing, or electronic and optoelectronic technologies [13, 14]. However, not only silica with unimodal pore distributions are of great interest, but also hierarchical bi- or trimodal mesoporous silica materials are in the focus of many workgroups [15-20]. Ideally, such multimodal materials should possess adjustable and well-defined macropores and tuneable, interconnected mesopore types of different size (between 2 to 50 nm) in the macropore walls. On all length scales, the larger pores should be connected through the smaller pores [18]. First, introduction of hierarchy in the pore system leads to a higher surface area, facilitating an enhanced interaction with adsorbents, and second hierarchical pore structures allow a better macroscopic transport within the matrix [19].

Another type of porous crystalline solids with nanoscale cavities are zeolites, which are extremely useful catalysts for many industrial chemical reactions. The main difference to the previous presented mesoporous materials is that the structural features of zeolites are significantly smaller ($\leq$ 1 nm). In general, the building blocks of these types of solids are tetrahedral of oxygen atoms, with a cation at the centre of each tetra-

hedron. By corner sharing of the tetrahedra, three-dimensional networks are formed. One example is the aluminophosphate zeolite constructed from combinations of aluminium-based tetrahedra (AlO_4) and phosphorous-based tetrahedra (PO_4) [21].

In order to synthesize nanoparticles (quantum dots or colour pigments), mesoporous materials, and zeolites, respectively, different innovative strategies were developed over time. Since the properties of nanomaterials is directly connected to their dimension and thus to their applications, the most crucial point in synthesis is the size control of their structural features, i.e. the particle sizes in the case of nanoparticles and the pore sizes in the case of porous materials, respectively. It has been shown for nanoparticles that the size control can be very well established by using surfactant systems. Droplet microemulsions composed of water, surfactant, co-surfactant, and hydrocarbon, for example, contain spherical aggregates with dimensions on the nanometer-scale. These aggregates have to be turned out to be very versatile in controlling the primary size of nanoparticles when they act as nano-reactors in which the nano-material is synthesized by the reaction of suitable precursors. Beside the droplet phases of microemulsions, also other microemulsion phases, e.g. the bicontinuous phase, are suited as structural templates for the preparation of nanometer structured materials [22-26]. A big advantage of such multicomponent templates is that the droplets and structures present in the microemulsion phase can be systematically altered by the composition. Consequently, the variety of the as-prepared nanomaterials is very wide [11, 27-29]. For the preparation of ordered porous silica, the microemulsion approach is not suitable. The synthesis of such materials is normally established by sol-gel templating utilizing amphiphilic surfactants in aqueous phase as templates [30]. Fundamentally, sol-gel templating can be classified into two strategies. In the so-called nanocasting technique, a concentrated lyotropic surfactant mesophase is converted into its mesoporous replica in a 1:1 copy process. At the end, the observed silica replica is calcinated between 500 and 600°C. Here, the tuning of the mesopores is mainly enabled by the appropriate choice of the surfactant (chain-length, head group nature). Contrarily, the second strategy denoted as hydrothermal approach is based on recipes starting from dilute surfactant containing aqueous solutions. In this connection, the desired structure of the mesoporous material

is usually obtained during the reaction by the cooperative interaction of the surfactant (as well as of the eventually formed surfactant aggregates) with the applied siliceous precursors. In the hydrothermal synthesis, the reaction is completed in an autoclave working at 100°C under autogeneous pressure of water normally used as solvent [13, 30, 32]. Zeolites are also prepared from the hydrothermal approach [33].

It is noteworthy that a good quality of nanomaterials is quite often restricted to high material crystallinity. For instance, specific material properties such as the bright colour of pigments, as well as the electrical conductivity of transparent conductive oxides or the luminescence of quantum dots can be excluded or drastically reduced in quality, if these materials are amorphous. However, high temperatures are often a precondition for the crystallization of inorganic compounds in crystal lattices. Since colloidal systems incorporating water as polar solvent are limited to ambient or near ambient application, because of the thermal stability of the micelles, which leads to phase separation at temperatures higher than about 80°C (especially when non-ionic surfactants are used), crystalline materials are usually obtained after an additional thermal post-treatment of the as-prepared amorphous powder samples. Such a treatment, however, is generally accompanied by extensive agglomeration and particle growth [11]. In addition, the evaporation of water at higher temperatures continuously changes the colloidal architecture of the template, which finally disturbs the templating process. Sometimes, the difficulty of water evaporation at elevated temperature is overcome by the usage of an autoclave, e.g. in the case of the hydrothermal synthesis.

Recently, it has been shown that ionic liquids (ILs) (cp. Chapter II.1) are predestined for the preparation of nanomaterials including nanoparticles, mesoporous silica, and zeolites. Up to now, the preparation of these nanomaterials utilizing ILs can be divided into two general approaches. First, a pure ionic liquid, in which the appropriate precursors are solubilised (sometimes together with a small amount of co-solvent) acts as template solvent and therefore directs the formation of the nanomaterials. For this strategy, ILs with short alkyl chains (so-called solvent-like ILs) were recommended which are liquid at room-temperature and are based on the imidazolium cation, e.g.

1-ethyl-3-methylimidazolium bis(trifluoromethylsulfonyl)imide (emimTf$_2$N), 1-ethyl-3-methylimidazolium tetrafluoroborate (emimBF$_4$), or 1-butyl-3-methylimidazolium tetrafluoroborate (bmimBF$_4$). By using ILs of the previous type, the preparation of TiO$_2$ nanoparticles, gold nanosheets, nanoscale transparent conductive oxides, and other nanomaterials have been reported in the open literature [34-38]. Further, the synthesis of already known and novel type zeolites was impressively demonstrated using ILs as solvent and simultaneously as "structure-directing agent" [33]. The main advantages of this IL-templating strategy results from the unique properties of these ionic solvents (cp. Chapter II.1.4). Mainly the negligible vapour pressure, the extraordinary high thermal stability, the polar properties, and in some cases the favourable interactions of the imidazolium cation with the precursors can be denoted to be the relevant features provided by these substance class. For example, the very good thermal stability in combination with the negligible vapour pressure enables the application of ILs also for templating at elevated temperatures leading to highly crystalline materials with low defect concentrations, since thermal post-treatment of the as-prepared nanopowders or the employment of autoclaves can be avoided [33, 37-40]. However, it must be noted that there is also one disadvantage, especially for the preparation of nanoparticles in pure ILs, which arises mainly from the fact that the size/structure tuning of the nanomaterials is limited to only a few parameters including for example reaction time, temperature, or precursor concentrations. A fine-tuning of the template, which can be performed by default in colloidal formulations, e.g. microemulsions or micellar solutions, is often not possible in this case.

In contrast to the previous templating approach utilizing liquid short-chain imidazolium ionic liquids, the second strategy features imidazolium based ionic liquids with long alkyl-chains, e.g. 1-hexadecyl-3-methylimidazolium chloride (C$_{16}$mimCl), which exhibit surfactant properties, for the synthesis of mesoporous highly structured silica materials. It was reported that such amphiphilic ionic liquids are very suitable for the nanocasting technique. In the latter, a three-dimensional self-assembled nanostructure, e.g. a lamellar phase, of a concentrated aqueous surfactant solution is transformed into hollow inorganic replicas with preservation of the fine structural details by hy-

drolysis and condensation of inorganic precursors in the aqueous domain of the micro-phase-separated medium (derived from the self-assembled phase of the used surfactant template) [13, 17, 41]. Further, the generation of mesoporous silica was realized via the hydrothermal synthesis using the surfactant-like ionic liquid $C_{16}mimCl$ in aqueous solution, but at significantly lower IL concentrations compared to nanocasting templating. Particularly the workgroups at the Max-Planck-Institute of Colloids and Interfaces in Golm, Germany, showed that the application of long-chain surfactant ionic liquids in sol-gel templating chemistry of mesoporous materials offers superior advantages in comparison to the conventional cationic surfactants, e.g. 1-hexadecyltrimethyl-ammonium chloride (CTACl), which were used in the standard sol-gel approaches [30, 31]. The unique templating features of the $C_{16}mimCl$ compared to traditional surfactants are (i) the unusual high degree of order of the resulting nanocasted silica, (ii) the need of lower amphiphile concentrations in the hydrothermal synthesis, and finally (iii) the generation of hierarchical mesoporous systems using $C_{16}mimCl$ together with a copolymer or polystyrene beads as templates which is not possible with common CTACl [13, 17, 41-44]. In addition, Antonietti et al. reported that the employment of imidazolium chloride amphiphiles in sol-gel templating provides also benefits for the post-calcination of nano-structured silica. They showed that $C_{16}mimCl$ has significant higher thermal stability than the conventional CTACl. This fact is responsible for the conservation of the $C_{16}mimCl$-template also at increased temperatures giving the silica framework longer time for the process of condensation and densification during calcination than CTACl does [13].

Although, the aqueous sol-gel approach for the preparation of mesoporous silica is well established using an amphiphilic imidazolium ionic liquid template, the reasons for the very good templating abilities of these kind of surfactants are not fully under-stood up to now. Today the question arises, whether there is a relationship between the molecular structure, the aggregation/phase behaviour in water and the sol-gel templating features of the ionic liquid $C_{16}mimCl$ in comparison to CTACl (denoted as reference in sol-gel chemistry) [45]. This problem mainly results from the fact that there is nearly no

information concerning the aggregation behaviour of IL-surfactants in the open literature. Only a handful reports are known [46-57].

Based on the information given above as well as in the previous chapter, the objective of the present study was threefold: First, the aggregation behaviour of three IL-amphiphile homologous ($C_n$mimCl), namely 1-dodecyl-3-methylimidazolium chloride (C_{12}mimCl), 1-tetradecyl-3-methylimidazolium chloride (C_{14}mimCl), and 1-hexadecyl-3-methylimidazolium chloride (C_{16}mimCl) in dilute aqueous solution was systematically investigated and the results were compared to literature data of the common well-investigated 1-alkyl-trimethylammonium chlorides (C_nTACl), 1-dodecyl-trimethylammonium chloride (DTACl), 1-tetradecyl-trimethylammonium chloride (TTACl), and 1-hexadecyl-trimethylammonium chloride (CTACl), respectively. Thereby, it was possible to highlight the main differences between the two types of surfactants. Since the only disparity between these two surfactant analogues is the head group, the one of C_nTACl being a substituted ammonium head group with a localized positive charge and the one of $C_n$mimCl being an imidazolium head group with a delocalized positive charge, a fundamental understanding of the peculiarity of the imidazolium head in comparison to the ammonium head could be achieved. This basic research was of great interest, since it should bridge the gap in the open literature concerning imidazolium chloride surfactants.

Second, this study is concerned with the question of whether it is possible to formulate new colloidal systems consisting of micellar aggregates by mixing an imidazolium based surfactant-like ionic liquid (SLIL) acting as surfactant and a room-temperature molten salt (RTMS) acting as solvent. As amphiphilic ILs C_{12}mimCl, C_{14}mimCl, and C_{16}mimCl were used and as solvent IL ethylammonium nitrate (EAN) as well as 1-butyl-3-methyl-imidazolium tetrafluoroborate (bmimBF$_4$) were applied. Beside the fundamental investigation of aggregation in SLIL/RTMS-mixtures at room-temperature, additional efforts have been made to screen the thermal stability of such systems (until 150°C). As noted previously, high-temperature (HT) stable colloidal systems composed of ingredients with negligible vapour pressure and high thermal resis-

tance could be very interesting for the high-temperature synthesis of already known and perhaps of new nanomaterials with good crystallinity without using an autoclave or post-calcination. At this point, it must be remarked that common ionic as well as non-ionic surfactant/RTMS mixtures incorporating self-assembled surfactant aggregates are already known in the open literature [58-68]. In addition, also lyotropic phases of such systems are reported [69-71]. However, only one study published by Warr et al. deals with surfactant/RTMS solutions at elevated temperatures. The authors present binary phase diagrams of various non-ionic surfactants of the C_nE_m-type in solution of EAN (up to 100% of surfactant amount) in a temperature range up to 150°C. Interestingly, all reported systems demix into two phases at higher temperatures (the most stable at about 130°C) making a high-temperature application impossible. Such behaviour is highly reminiscent of the well-known cloud-point phenomenon of non-ionic surfactants in aqueous solutions [71]. In contrast, the usage of ionic surfactants, in particular imidazolium based ones, which show better thermal stability than the conventional ammonium surfactants, appears more suitable for the formulation of HT-stable colloidal RTMS-systems, since the phase behaviour of ionic amphiphiles is extensively less vulnerable to temperature [72-77].

The third and final part of this work addresses the formulation of non-aqueous microemulsions consisting of SLIL as surfactant, a long-chain alcohol as co-surfactant, oil as the apolar phase, and a RTMS as the polar phase. Microemulsions incorporating a RTMS as polar phase are reported in the open literature, but up to now only systems containing non-ionic surfactants acting as amphiphile were investigated [78-97]. With regard to the fact that the recently investigated RTMS-based microemulsions feature non-ionic amphiphiles, these systems were only examined near room-temperature (at elevated temperature demixing occurs as illustrated graphically in the paper of Estoe et al. because of the desolvation of the ethoxylene groups of the surfactant) [85]. The underlying work focuses, for the first time, on the formulation of RTMS-microemulsions formed by the aid of an ionic liquid surfactant (together with a co-surfactant) as surface-active compound. In addition to the fundamental aspects, as previously for the SLIL/RTMS-colloids, the additional aim of the third study is to demonstrate that the prepared RTMS-

microemulsions are stable also at temperatures higher than 130°C. All ingredients for the formulations (C_{16}mimCl/1-decanol/dodecane/RTMS; where RTMS is either EAN or bmimBF$_4$) were chosen in order to provide good thermal stabilities and low or negligible vapour pressures. Especially for the microemulsion templating of nanoparticles at elevated temperatures, e.g. metaloxides or quantum dots with good crystallinity, the regions where reverse microemulsions are formed are of particular interest, since the most precursors used for the synthesis of these types of materials are readily soluble in polar solvents. Therefore, the characterization of the formulated systems was limited to the areas of the phase-diagrams in which reverse RTMS nanodroplets may be assumed.

1.1 Bibliography

[1]   C. N. R. Rao, A. Mueller and A. Cheetham; The Chemistry of Nanomaterials: Synthesis, Properties and Applications. Wiley-VCH (2004)**.**

[2]   C. Feldmann and C. Metzmacher; Polyol mediated synthesis of nanoscale MS particles (M = Zn, Cd, Hg). *Journal of Materials Chemistry* **11**, 10, 2603-2606 (2001).

[3]   J. Park, J. Joo, S. G. Kwon, Y. Jang and T. Hyeon; Synthesis of monodisperse spherical nanocrystals. *Angewandte Chemie, (Int.Ed.)* **46**, 25, 4630-4660 (2007).

[4]   H. O. Jungk and C. Feldmann; Nonagglomerated, submicron α-Fe$_2$O$_3$ particles: preparation and application. *Journal of Materials Research* **15**, 10, 2244-2248 (2000).

[5]   J. Merikhi, H. O. Jungk and C. Feldmann; Sub-micrometer CoAl$_2$O$_4$ pigment particles - synthesis and preparation of coatings. *Journal of Materials Chemistry* **10**, 6, 1311-1314 (2000).

[6]   C. Feldmann and H. O. Jungk; Polyol-mediated preparation of nanoscale oxide particles. *Angewandte Chemie, (Int. Ed.)* **40**, 2, 359-362 (2001).

[7]   C. Feldmann; Preparation of nanoscale pigment particles. *Advanced Materials* **13**, 17, 1301-1303 (2001).

[8]   C. Feldmann; Polyol mediated synthesis of oxide particle suspensions and their application. *Scripta Materialia* **44**, 8/9, 2193-2196 (2001).

[9]   C. Feldmann; Polyol-mediated synthesis of nanoscale functional materials. *Advanced Functional Materials* **13**, 2, 101-107 (2003).

[10]   G. Buehler, D. Thoelmann and C. Feldmann; One-pot synthesis of highly conductive indium tin oxide nanocrystals. *Advanced Materials* **19**, 17, 2224-2227 (2007).

[11]   D. H. M. Buchold and C. Feldmann; Microemulsion approach to non-agglomerated and crystalline nanomaterials. *Advanced Functional Materials* **18**, 7, 1002-1011 (2008).

[12]   E. Hammarberg, A. Prodi-Schwab and C. Feldmann; Microwave-assisted synthesis of indium tin oxide nanocrystals in polyol media and transparent, conductive layers thereof. *Thin Solid Films* **516**, 21, 7437-7442 (2008).

[13]   Y. Zhou and M. Antonietti; A Series of Highly Ordered, Super-Microporous, Lamellar Silicas Prepared by Nanocasting with Ionic Liquids. *Chemistry of Materials* **16**, 3, 544-550 (2004).

[14]   L. Yang, W. Meijia, L. I. Zhiying, L. Hongtao, H. E. Ping and L. I. Jinghong; Preparation of porous aminopropylsilsesquioxane by a nonhydrolytic sol-gel method in ionic liquid solvent. *Langmuir* **21**, 4, 1618-1622 (2005).

[15]   C. J. Adams, A. E. Bradley and K. R. Seddon; The synthesis of mesoporous materials using novel ionic liquid templates in water. *Australian Journal of Chemistry* **54**, 11, 679-681 (2001).

[16]   Y. Zhou and M. Antonietti; A novel tailored bimodal porous silica with well-defined inverse opal microstructure and super-microporous lamellar nanostructure. *Chemical Communications* **20**, 2564-2565 (2003).

[17]   Y. Zhou and M. Antonietti; Preparation of highly ordered monolithic super-microporous lamellar silica with a room-temperature ionic liquid as template via the nanocasting technique. *Advanced Materials* **15**, 17, 1452-1455 (2003).

[18]   D. Kuang, T. Brezesinski and B. Smarsly; Hierarchical porous silica materials with a trimodal pore system using surfactant templates. *Journal of the American Chemical Society* **126**, 34, 10534-10535 (2004).

[19]   T. Brezesinski, C. Erpen, K. Iimura and B. Smarsly; Mesostructured Crystalline Ceria with a Bimodal Pore System Using Block Copolymers and Ionic Liquids as Rational Templates. *Chemistry of Materials* **17**, 7, 1683-1690 (2005).

[20]   O. Sel, D. Kuang, M. Thommes and B. Smarsly; Principles of Hierarchical Meso- and Macropore Architectures by Liquid Crystalline and Polymer Colloid Templating. *Langmuir* **22**, 5, 2311-2322 (2006).

[21]   R. A. van Santen; Physical chemistry: Porous solids get organized. *Nature* **444**, 7115, 46-47 (2006).

[22]   M. P. Pileni; Reverse micelles as microreactors. *Journal of Physical Chemistry* **97**, 27, 6961-6973 (1993).

[23]   M. P. Pileni; Water in oil colloidal droplets used as microreactors. *Advances in Colloid and Interface Science* **46**, 139-163 (1993).

[24]   J. Casado, C. Izquierdo, S. Fuentes and M. L. Moya; Microemulsions as a new working medium in physical chemistry: an integrated practical approach. *Journal of Chemical Education* **71**, 5, 446-450 (1994).

[25]   N. Garti and K. Holmberg; Reactions in microheterogeneous media. *Current Opinion in Colloid & Interface Science* **8**, 2, 135-136 (2003).

[26]   K. Holmberg; Organic reactions in microemulsions. *Current Opinion in Colloid & Interface Science* **8**, 2, 187-196 (2003).

[27]   W. F. C. Sager; Microemulsion templating. *Schriften des Forschungszentrums Juelich, Materie und Material* **10**, Soft Matter: Complex, A6/1-A6/37 (2002).

[28]   D. H. M. Buchold and C. Feldmann; Synthesis of Nanoscale $Co_3[Co(CN)_6]_2$ in Reverse Microemulsions. *Chemistry of Materials* **19**, 14, 3376-3380 (2007).

[29]   C. Zimmermann, C. Feldmann, M. Wanner and D. Gerthsen; Nanoscale gold hollow spheres through a microemulsion approach. *Small* **3**, 8, 1347-1349 (2007).

[30]   J. S. Beck, J. C. Vartuli, W. J. Roth, M. E. Leonowicz, C. T. Kresge, K. D. Schmitt, C. T. W. Chu, D. H. Olson and E. W. Sheppard; A new family of mesoporous molecular sieves prepared with liquid crystal templates. *Journal of the American Chemical Society* **114**, 27, 10834-10843 (1992).

[31]   G. S. Attard, J. C. Glyde and C. G. Goltner; Liquid-crystalline phases as templates for the synthesis of mesoporous silica. *Nature* **378**, 6555, 366-368 (1995).

[32]   T. Wang, H. Kaper, M. Antonietti and B. Smarsly; Templating Behavior of a Long-Chain Ionic Liquid in the Hydrothermal Synthesis of Mesoporous Silica. *Langmuir* **23**, 3, 1489-1495 (2007).

[33]   E. Cooper, I., C. Andrews, P. Wheatley, P. Webb, P. Wormald and R. E. Morris; Ionic liquids and eutectic mixtures as solvent and template in synthesis of zeolite analogues. *Nature* **430**, 7003, 1012-1016 (2004).

[34]   Y. Liu, J. Li, M. Wang, Z. Li, H. Liu, P. He, X. Yang and J. Li; Preparation and Properties of Nanostructure Anatase TiO_2 Monoliths Using 1-Butyl-3-methyl-imidazolium Tetrafluoroborate Room-Temperature Ionic Liquids as Template Solvents. *Crystal Growth & Design* **5**, 4, 1643-1649 (2005).

[35]   L. I. Zhonghao, L. Zhimin, Z. Jianling, H. Buxing, D. U. Jimin, G. Yanan and J. Tao; Synthesis of single-crystal gold nanosheets of large size in ionic liquids. *The Journal of Physical Chemistry. B* **109**, 30, 14445-14448 (2005).

[36]   H. Kaper, F. Endres, I. Djerdj, M. Antonietti, B. Smarsly, J. Maier and Y.-S. Hu; Direct low-temperature synthesis of rutile nanostructures in ionic liquids. *Small* **3**, 10, 1753-1763 (2007).

[37]   G. Buehler, A. Zharkouskaya and C. Feldmann; Ionic liquid based approach to nanoscale functional materials. *Solid State Sciences* **10**, 4, 461-465 (2008).

[38]   A. Zharkouskaya, C. Feldmann, K. Trampert, W. Heering and U. Lemmer; Ionic liquid based approach to luminescent $LaPO_4$:Ce,Tb nanocrystals. Synthesis,

characterization and application. *European Journal of Inorganic Chemistry* **6**, 873-877 (2008).

[39]   G. Buehler and C. Feldmann; Microwave-assisted synthesis of luminescent LaPO$_4$:Ce,Tb nanocrystals in ionic liquids. *Angewandte Chemie, (Int. Ed.)* **45**, 29, 4864-4867 (2006).

[40]   C. Feldmann, G. Buehler and D. Thoelmann; Microwave syntheses of crystal-line metal oxide particles in ionic liquids. Degussa G.m.b.H., Germany, (2007). **DE 102006011754**

[41]   Y. Zhou, J. H. Schattka and M. Antonietti; Room-Temperature Ionic Liquids as Template to Monolithic Mesoporous Silica with Wormlike Pores via a Sol-Gel Nanocasting Technique. *Nano Letters* **4**, 3, 477-481 (2004).

[42]   Y. Zhou and M. Antonietti; A novel tailored bimodal porous silica with well-defined inverse opal microstructure and super-microporous lamellar nanostructure. *Chemical Communications* **20**, 2564-2565 (2003).

[43]   O. Sel, D. Kuang, M. Thommes and B. Smarsly; Principles of Hierarchical Meso- and Macropore Architectures by Liquid Crystalline and Polymer Colloid Templating. *Langmuir* **22**, 5, 2311-2322 (2006).

[44]   H. Kaper, D. Franke, B. Smarsly and C. F. J. Faul; A Pyrrole-Containing Surfactant as a Tecton for Nanocomposite SiO$_2$ Films. *Langmuir* **23**, 22, 11273-11280 (2007).

[45]   H. Kaper and B. Smarsly; Templating and phase behavior of the long chain ionic liquid C$_{16}$mimCl. *Zeitschrift fuer Physikalische Chemie* **220**, 10-11, 1455-1471 (2006).

[46]   S. Thomaier; Strukturcharakterisierung von Mischungen ionischer Flüssigkeiten. *Diploma Thesis, University of Regensburg, Germany* (2003).

[47]   J. Bowers, C. P. Butts, P. J. Martin, M. C. Vergara-Gutierrez and R. K. Heenan; Aggregation Behavior of Aqueous Solutions of Ionic Liquids. *Langmuir* **20**, 6, 2191-2198 (2004).

[48]   L. Gaillon, J. Sirieix-Plenet and P. Letellier; Volumetric Study of Binary Solvent Mixtures Constituted by Amphiphilic Ionic Liquids at Room Temperature (1-Alkyl-3-Methylimidazolium Bromide) and Water. *Journal of Solution Chemistry* **33**, 11, 1333-1347 (2004).

[49]   Z. Miskolczy, K. Sebok-Nagy, L. Biczok and S. Goektuerk; Aggregation and micelle formation of ionic liquids in aqueous solution. *Chemical Physics Letters* **400**, 4-6, 296-300 (2004).

[50]   B. Dong, N. a. Li, L. Zheng, L. i. Yu and T. Inoue; Surface Adsorption and Micelle Formation of Surface Active Ionic Liquids in Aqueous Solution. *Langmuir* **23**, 8, 4178-4182 (2007).

[51]   O. A. El Seoud, P. A. R. Pires, T. Abdel-Moghny and E. L. Bastos; Synthesis and micellar properties of surface-active ionic liquids: 1-Alkyl-3-methylimidazolium chlorides. *Journal of Colloid and Interface Science* **313**, 1, 296-304 (2007).

[52]   I. Goodchild, L. Collier, a. Millar, L., I. Prokes, J. Lord, C., D., C. P. Butts, J. Bowers, J. Webster, R., P. and R. Heenan, K.; Structural studies of the phase, aggregation and surface behaviour of 1-alkyl-3-methylimidazolium halide + water mixtures. *Journal of colloid and interface science* **307**, 2, 455-468 (2007).

[53]   T. Inoue, B. Dong and L.-Q. Zheng; Phase behavior of binary mixture of 1-dodecyl-3-methylimidazolium bromide and water revealed by differential scanning calorimetry and polarized optical microscopy. *Journal of Colloid and Interface Science* **307**, 2, 578-581 (2007).

[54]   T. Inoue, H. Ebina, B. Dong and L. Zheng; Electrical conductivity study on micelle formation of long-chain imidazolium ionic liquids in aqueous solution. *Journal of Colloid and Interface Science* **314**, 1, 236-241 (2007).

[55]   R. Vanyur, L. Biczok and Z. Miskolczy; Micelle formation of 1-alkyl-3-methylimidazolium bromide ionic liquids in aqueous solution. *Colloids and Surfaces, A: Physicochemical and Engineering Aspects* **299**, 1-3, 256-261 (2007).

[56] J. Wang, H. Wang, S. Zhang, H. Zhang and Y. Zhao; Conductivities, Volumes, Fluorescence, and Aggregation Behavior of Ionic Liquids [C$_4$mim][BF$_4$] and [C$_n$mim]Br (n = 4, 6, 8, 10, 12) in Aqueous Solutions. *Journal of Physical Chemistry B* **111**, 22, 6181-6188 (2007).

[57] S. Thomaier and W. Kunz; Aggregates in mixtures of ionic liquids. *Journal of Molecular Liquids* **130**, 1-3, 104-107 (2007).

[58] D. F. Evans, A. Yamauchi, R. Roman and E. Z. Casassa; Micelle formation in ethylammonium nitrate, a low-melting fused salt. *Journal of Colloid and Interface Science* **88**, 1, 89-96 (1982).

[59] D. F. Evans, A. Yamauchi, G. J. Wei and V. A. Bloomfield; Micelle size in ethylammonium nitrate as determined by classical and quasi-elastic light scattering. *Journal of Physical Chemistry* **87**, 18, 3537-3541 (1983).

[60] J. L. Anderson, V. Pino, E. C. Hagberg, V. V. Sheares and D. W. Armstrong; Surfactant solvation effects and micelle formation in ionic liquids. *Chemical Communications* **19**, 2444-2445 (2003).

[61] K. A. Fletcher and S. Pandey; Surfactant Aggregation within Room-Temperature Ionic Liquid 1-Ethyl-3-methylimidazolium Bis(trifluoromethylsulfonyl)imide. *Langmuir* **20**, 1, 33-36 (2004).

[62] H. Jingcheng, S. Aixin, W. Jingzheng, C. Xiao, Z. Wenchang, S. Feng, Z. Feng and L. Weimin; Self-assembled structure in room-temperature ionic liquids. *Chemistry* **11**, 13, 3936-3940 (2005).

[63] C. D. Tran and S. Yu; Near-infrared spectroscopic method for the sensitive and direct determination of aggregations of surfactants in various media. *Journal of Colloid and Interface Science* **283**, 2, 613-618 (2005).

[64] S. Bordel Velasco, M. Turmine, D. Di Caprio and P. Letellier; Micelle formation in ethyl-ammonium nitrate (an ionic liquid). *Colloids and Surfaces, A: Physicochemical and Engineering Aspects* **275**, 1-3, 50-54 (2006).

[65]   C. Patrascu, F. Gauffre, F. Nallet, R. Bordes, J. Oberdisse, N. de Lauth-Viguerie and C. Mingotaud; Micelles in ionic liquids: Aggregation behavior of alkyl poly(ethyleneglycol)-ethers in 1-butyl-3-methyl-imidazolium type ionic liquids. *ChemPhysChem* **7**, 1, 99-101 (2006).

[66]   J. Tang, D. i. Li, C. Sun, L. Zheng and J. Li; Temperature dependent self-assembly of surfactant Brij 76 in room temperature ionic liquid. *Colloids and Surfaces, A: Physicochemical and Engineering Aspects* **273**, 1-3, 24-28 (2006).

[67]   T. L. Greaves, A. Weerawardena, C. Fong and C. J. Drummond; Many Protic Ionic Liquids Mediate Hydrocarbon-Solvent Interactions and Promote Amphiphile Self-Assembly. *Langmuir* **23**, 2, 402-404 (2007).

[68]   T. L. Greaves, A. Weerawardena, C. Fong and C. J. Drummond; Formation of Amphiphile Self-Assembly Phases in Protic Ionic Liquids. *Journal of Physical Chemistry B* **111**, 16, 4082-4088 (2007).

[69]   D. F. Evans, E. W. Kaler and W. J. Benton; Liquid crystals in a fused salt: b,g-distearoylphosphatidylcholine in N-ethylammonium nitrate. *Journal of Physical Chemistry* **87**, 4, 533-535 (1983).

[70]   W. Tamura-Lis, L. J. Lis and P. J. Quinn; Thermodynamic characterization of phospholipids dispersed in ethylammonium nitrate (a fused salt). *Journal of Colloid and Interface Science* **150**, 1, 200-207 (1992).

[71]   M. U. Araos and G. G. Warr; Self-Assembly of Nonionic Surfactants into Lyotropic Liquid Crystals in Ethylammonium Nitrate, a Room-Temperature Ionic Liquid. *Journal of Physical Chemistry B* **109**, 30, 14275-14277 (2005).

[72]   C. Tanford; *The Hydrophobic Effect: Formation of Micelles and Biological Membranes. 2nd Edition*. Wiley, (1980).

[73]   D. F. Evans; *The Colloidal Domain: Where Physics, Chemistry, Biology, and Technology Meet, 2nd Edition*. Wiley-VCH, (1998).

[74]   K. Holmberg; *Handbook of Applied Surface and Colloid Chemistry, Volume 1*. John Wiley & Sons, (2002).

[75]   K. Holmberg, D. O. Shah and M. J. Schwuger; *Handbook of Applied Surface and Colloid Chemistry, Volume 2*. John Wiley & Sons, (2002).

[76]   M. J. Rosen; *Surfactants and Interfacial Phenomena, 3rd Edition*. Wiley & Sons, (2004).

[77]   D. Myers; *Surfactant Science and Technology, 3rd Edition*. John Wiley & Sons, (2005).

[78]   S. E. Friberg, Q. I. Yin, F. Pavel, R. A. Mackay, J. D. Holbrey, K. R. Seddon and P. A. Aikens; Solubilization of an ionic liquid, 1-butyl-3-methylimidazolium hexafluorophosphate, in a surfactant-water system. *Journal of Dispersion Science and Technology* **21**, 2, 185-197 (2000).

[79]   H. Gao, J. Li, B. Han, W. Chen, J. Zhang, R. Zhang and D. Yan; Microemulsions with ionic liquid polar domains. *Physical Chemistry Chemical Physics* **6**, 11, 2914-2916 (2004).

[80]   D. Chakrabarty, D. Seth, A. Chakraborty and N. Sarkar; Dynamics of Solvation and Rotational Relaxation of Coumarin 153 in Ionic Liquid Confined Nanometer-Sized Microemulsions. *Journal of Physical Chemistry B* **109**, 12, 5753-5758 (2005).

[81]   Y. Gao, S. Han, B. Han, G. Li, D. Shen, Z. Li, J. Du, W. Hou and G. Zhang; TX-100/Water/1-Butyl-3-methylimidazolium Hexafluorophosphate Microemulsions. *Langmuir* **21**, 13, 5681-5684 (2005).

[82]   E. Julian, G. Sarah, R. S. E, P. Alison, W. Tom, H. R. K and G. Isabelle; Ionic liquid-in-oil microemulsions. *Journal of the American Chemical Society* **127**, 20, 7302-7303 (2005).

[83]   J. Li, J. Zhang, H. Gao, B. Han and L. Gao; Nonaqueous microemulsion-containing ionic liquid [bmim][PF$_6$] as polar microenvironment. *Colloid and Polymer Science* **283**, 12, 1371-1375 (2005).

[84]   Y. Feng and T. John; Surfactant ionic liquid-based microemulsions for polymerization. *Chemical communications* **25**, 2696-2698 (2006).

[85]   Y. Gao, J. Zhang, H. Xu, X. Zhao, L. Zheng, X. Li and L. I. Yu; Structural stud-
       ies of 1-butyl-3-methylimidazolium tetrafluoroborate/TX-100/p-xylene ionic
       liquid microemulsions. *ChemPhysChem* **7**, 7, 1554-1561 (2006).

[86]   D. Seth, A. Chakraborty, P. Setua and N. Sarkar; Interaction of Ionic Liquid
       with Water in Ternary Microemulsions (Triton X-100/Water/1-Butyl-3-methyl-
       imidazolium Hexafluorophosphate) Probed by Solvent and Rotational Relaxa-
       tion of Coumarin 153 and Coumarin 151. *Langmuir* **22**, 18, 7768-7775 (2006).

[87]   G. Yanan, W. Suqing, Z. Liqiang, H. Shuaibing, Z. Xuan, L. U. Deming, L. I.
       Yu, J. I. Yongqiang and Z. Gaoyong; Microregion detection of ionic liquid mi-
       croemulsions. *Journal of Colloid and Interface Science* **301**, 2, 612-616 (2006).

[88]   R. Atkin and G. G. Warr; Phase Behavior and Microstructure of Microemulsions
       with a Room-Temperature Ionic Liquid as the Polar Phase. *Journal of Physical
       Chemistry B* **111**, 31, 9309-9316 (2007).

[89]   S. Cheng, X. Fu, J. Liu, J. Zhang, Z. Zhang, Y. Wei and B. Han; Study of ethyl-
       ene glycol/TX-100/ionic liquid microemulsions. *Colloids and Surfaces, A: Phys-
       icochemical and Engineering Aspects* **302**, 1-3, 211-215 (2007).

[90]   S. Cheng, J. Zhang, Z. Zhang and B. Han; Novel microemulsions: ionic liquid-
       in-ionic liquid. *Chemical Communications* **24**, 2497-2499 (2007).

[91]   Y. Gao, N. A. Li, L. Zheng, X. Zhao, J. Zhang, Q. Cao, M. Zhao, Z. Li and G.
       Zhang; The effect of water on the microstructure of 1-butyl-3-methyl-
       imidazolium tetrafluoroborate/TX-100/benzene ionic liquid microemulsions.
       Chemistry-A European Journal **13**, 9, 2661-2670 (2007).

[92]   N. A. Li, C. Quan, G. Yanan, Z. Jin, Z. Liqiang, B. Xiangtao, D. Bin, L. I. Zhen,
       Z. Mingwei and L. I. Yu; States of water located in the continuous organic phase
       of 1-butyl-3-methylimidazolium tetrafluoroborate/Triton X-100/triethylamine
       reverse microemulsions. *Chemphyschem : A European journal of chemical
       physics and physical chemistry* **8**, 15, 2211-2217 (2007).

[93]   N. A. Li, G. Yan'an, Z. Liqiang, Z. Jin, L. I. Yu and L. I. Xinwei; Studies on the micropolarities of bmimBF4/TX-100/toluene ionic liquid microemulsions and their behaviors characterized by UV-visible spectroscopy. *Langmuir* **23**, 3, 1091-1097 (2007).

[94]   Z. Qiu and J. Texter; Ionic liquids in microemulsions. *Current Opinion in Colloid & Interface Science* (2007).

[95]   D. Seth, A. Chakraborty, P. Setua and N. Sarkar; Dynamics of Solvent and Rotational Relaxation of Coumarin-153 in Room-Temperature Ionic Liquid 1-Butyl-3-methyl Imidazolium Tetrafluoroborate Confined in Poly(oxyethylene glycol) Ethers Containing Micelles. *Journal of Physical Chemistry B* **111**, 18, 4781-4787 (2007).

[96]   G. Yan'an, N. A. Li, Z. Liqiang, B. Xiangtao, L. I. Yu, Z. Xueyan, Z. Jin, Z. Mingwei and L. I. Zhen; Role of solubilized water in the reverse ionic liquid microemulsion of 1-butyl-3-methylimidazolium tetrafluoroborate/TX-100/benzene. *The Journal of Physical Chemistry. B* **111**, 10, 2506-2513 (2007).

[97]   N. A. Li, S. Zhang, L. Zheng, Y. Gao and L. I. Yu; Second Virial Coefficient of bmimBF4/Triton X-100/ Cyclohexane Ionic Liquid Microemulsion as Investigated by Microcalorimetry. *Langmuir* **24**, 7, 2973-2976 (2008).

II. Fundamentals

1 Ionic liquids

During the last years the interest in ionic liquids (ILs) increased rapidly by a growing number of scientists and engineers as demonstrated by the increasing number of papers published in recent years. This fact could be mostly attributed to the very interesting properties of this substance class resulting mainly from the fact that these materials consist only of cations and anions. Especially, the usage as new innovative solvents for industrial processes is partially responsible for this interest [1, 2].

1.1 General aspects

In general, ionic liquids are salts having a melting point (*mp.*) below 100°C. In special cases, these substances are free-flowing liquids already at room temperature (*mp.* ≤ 25°C). In this case, they are called room temperature molten salts (RTMS). The number of ILs is increasing daily, but the cations are generally bulky, asymmetric ammonium, sulfonium or phosphonium salts, or heteroatomics, with very low symmetry, weak intermolecular interactions and low charge densities [2-7].

The very low melting point of a room temperature molten salt is a synergistic effect of both, the used cation and the used anion both influencing the lattice energy E within the crystals (II-1).

$$E = M \frac{Q^+ Q^-}{d_{ion}} \qquad \text{(II-1)}$$

In Eq. (II-1), M is the Madelung constant reflecting the packing efficiency, Q^+ and Q^- are the charges of the ions, and d_{ion} is the interionic separation. With larger ions d_{ion} is effectively larger resulting in a smaller lattice energy and therefore in a lower melting point. For this reason, low melting salts can be obtained when charges of the

involved ions are ±1. In addition, charge delocalization reduces overall charge density further [8].

Figure II-1 : Schematic comparison between the NaCl-crystal packing and the IL-crystal packing.

Due to these reasons, the lowering of the symmetry of the cation lowers the melting point of an IL, since the crystallisation in an ideal closely packed (*cp*) crystal lattice is hindered and d_{ion} becomes larger. In contrast, sodium chloride, a well known salt, with symmetric ions (spheres) forms a cubic closely packed crystal structure in the solid state and has therefore a very high lattice energy and a high melting-point of about 800°C (cp. Figure II-1) [1, 4]. As Table II-1 illustrates, the alkyl-chain of the 1-alkyl-3-methyl-imidazolium chloride controls the symmetry and d_{ion}. Thus, it has a great influence on the temperature of the solid-liquid phase transitions of these salts (cp. Table II-1).

Salt		**Symmetry**	*mp.* / [°C]	**Ref.**
NaCl		high	803	[9]
KCl			772	[9]
	R = Me		125	10]
	R = Et		87	10]
	R = nBu	low	65	10]

Table II-1 : Melting points of chloride salts in dependence of cation symmetry.

However, if the alkyl-chain becomes longer (n ≥10) van der Waal interactions between the hydrocarbons gain more and more in importance. The melting point starts to raise with increasing alkyl chain length while the symmetry is decreasing, because the long hydrocarbon chains contribute to local structure by induction of microphase separation between the covalent, hydrophobic alkyl chains and the charged ionic re-

gions of the molecules. In fact, this is the reason for the higher melting point of ionic liquids with long alkyl-chains [1].

As already considered above, the anion further alters the melting point: The larger the size of the anion, the lower is the melting point of the ionic liquid reflecting the weaker Coulombic interactions in the crystal lattice. In combination with a good charge delocalization, low solid-liquid phase transition temperatures can be achieved (cp. Table II-2).

Salt		Anion size	*mp.* / [°C]	Ref.
	Cl^-	small	87	10]
	NO_2^-		55	[11]
	NO_3^-		38	[11]
	$AlCl_4^-$		7	[12]
	BF_4^-		6	[13]
	$CF_3SO_2^-$		-9	[14]
	$CF_3CO_2^-$	large	-14	[14]

Table II-2 : Influence of the anion size on the melting points of ILs.
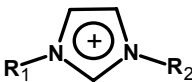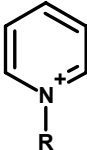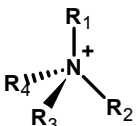
Cations	Anions
	Cl^- / $AlCl_3^-$
	Cl^-, Br^-, I^-, $(CN)_2N^-$
	NO_3^-, CO_3^{2-}, SO_4^{2-}
	CF_3COO^-, $CF_3SO_3^-$
	BF_4^-, PF_6^-
	$EtSO_4^-$
	$(CF_3SO_2)_2N^-$

Table II-3 : Survey of the mostly used cation-anion combinations in IL research.

Since ionic liquids are composed of two parts, the cation and the anion, a big synthetic flexibility arises which is not available for single component molecules. Therefore, it is not surprising that until now a variety of possible cation-anion combina-

tions were synthesized and investigated. Table II-3 gives a survey of mostly common cations and anions used in recent ionic liquid research [1, 2, 15].

1.2   Evolution of ionic liquid development

The development of ionic liquids started in 1914 with the synthesis of ethyl ammonium nitrate, which was obtained by the reaction of nitric acid and ethylamine in aqueous solution. This salt has a melting point of about 12°C and was the first protic ionic liquid (*PIL*) [16]. Twenty years later Hurley and Wier reported on mixtures of 1-ethylpyridinium halogenides and $AlCl_3$, which had a very low melting point and good properties as bath solutions for electroplating of aluminium [17, 18]. However, systems composed of organic chloride salts and $AlCl_3$ were not studied further until 1968 when Osteryoung and Wilkes rediscovered them and prepared, for the first time, room-temperature liquid chloroaluminate melts [10, 12, 19-23]. At this time, the IL research was mainly focused on electrochemical applications. In the early 1980s, the workgroups of Seddon and Hussey began to use chloroaluminate melts as non-aqueous, polar solvents for transition metal complexes [24, 25]. During this time, ionic liquids became more familiar to a broad public. However, a big problem persists, the high reactivity of this type of molten salts towards water. This confinement was solved by Wilkes et al. in 1992 when they described the synthesis of ILs, incorporating the 1,3-dialkyl imidazolium cation and the tetrafluoroborate anion with significantly reduced instability against hydrolysis [26]. This was a break through, because these systems also offered a higher tolerance versus functionalized groups within the cation compared to the chloroaluminate melts and therefore they opened a much larger range of applications, especially in the field of new high polar solvents. Today, many different anions with good stability against water are known [2].

In recent years, many researchers deal with the synthesis of new ionic liquids and with the finding of applications in industrial processes. Now, it is also possible to source ionic liquids commercially from a number of suppliers in a range of different qualities, which was not possible some years ago [1].

1.3 Concepts of ionic liquid synthesis

Before the synthesis of ionic liquids will be presented in detail, it should be noted that in order to obtain ionic liquids with high purity, it is essential to use purified starting materials. Any trace impurities introduced during the synthesis are hardly to remove, especially when the synthesized salt is a room temperature molten salt with a low melting point where recrystallization is not possible at all. An extensive analysis (e.g. NMR, mass analysis, elementary analysis and water determination) of the used reactants, solvents and the achieved ILs is a crucial point for the detection of unintentional impurities diverted during the synthesis.

Principally, the synthesis of ionic liquids includes 1-2 steps. The initial step is the quaternization, of an amine for example, in order to form the cation (Figure II-2, step I). If it is not possible to introduce the desired anion during the quaternization reaction, an additional step follows: the anion metathesis (Figure II-2, step IIa and IIb) [4, 27]. The construction of the cation either can be carried out by the protonation with a Brønsted acid or by the above mentioned quaternization reaction with an alkylating agent. For protonation normally a strong acid, such as HNO_3, is used which reacts with an appropriate amine or phosphane (Figure II-3, top). The so formed ionic liquids are known as protic ILs (*PILs*), since a Brønsted acid and base formed them [28-31].
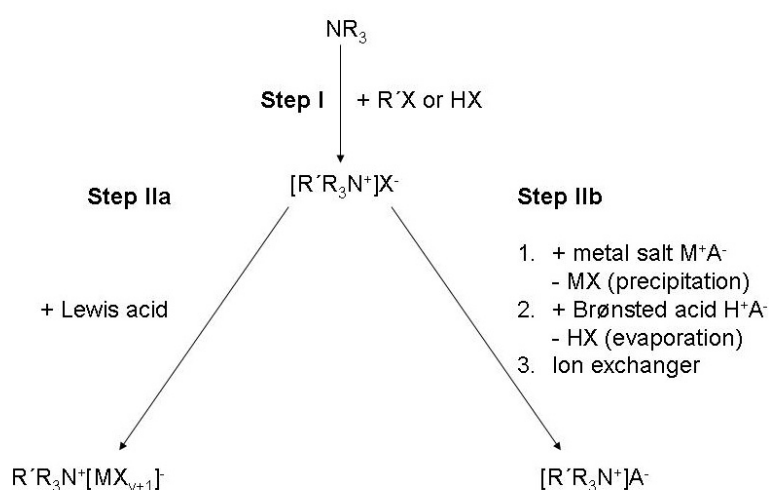
Figure II-2 : Synthesis path for the preparation of an ammonium ionic liquid. Represented from Refs. [4, 27].
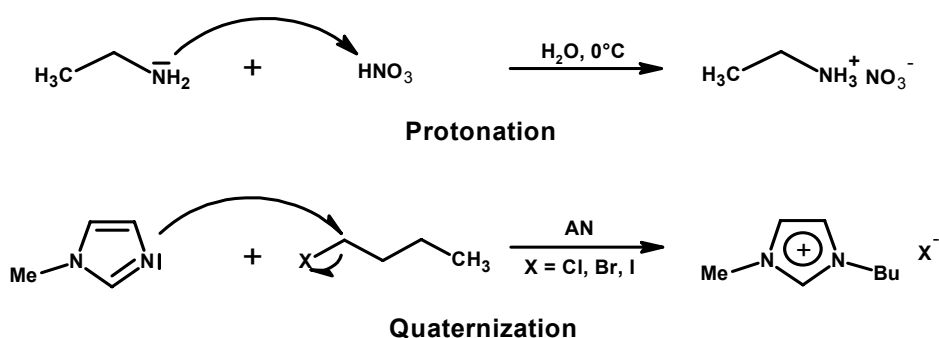
Figure II-3 : Example of a protonation reaction (top) and a quaternization reaction (bottom).

Typical alkylating agents used in quaternization are alkane halogenides. They react according to a substitution reaction with the amine (Figure II-3, bottom) forming so-called aprotic ILs (AILs) [30]. Consequently, an ammonium cation can be obtained with an anion depending on the used acid and the alkylating agent, respectively. Table II-4 shows an overview of ionic liquids, which can be achieved in this manner.

Ionic liquid	Reactant		Mp. / [°C]	Ref.
EtNH$_3$NO$_3$	HNO$_3$	Acid	10-14	[16]
[EMIM]CF$_3$SO$_3$	Methyltriflat		-9	[14]
[BMIM]CF$_3$SO$_3$	Methyltriflat		16	[14]
[Ph$_3$POc]OTs	OcOTs	Alkylating agent	70-71	[32]
[Bu$_3$NMe]OTs	MeOTs		62	[33]
[BMIM]Cl	Chlorbutan		65-69	[10]

Table II-4 : Ionic liquids obtained by direct synthesis (one step synthesis).

In cases where it is impossible to form the desired anion directly within the first step, two different pathways to vary the anion are possible. The anion-exchange can be realized via Lewis-acid-base reaction or via anion-metathesis. Both types of reactions are carried out from the halogenide salts of ionic liquids. With the reaction of a Lewis acid MX_y with an IL of the type [cation]$^+$X$^-$, salts of the formula [cation]$^+$MX$^-_{y+1}$ can be obtained (R.III-1).

$$[R'R_3N]^+ Cl \quad + \quad AlCl_3 \quad \rightleftharpoons \quad [R'R_3N]^+ AlCl_4^- \qquad (R.III-1)$$
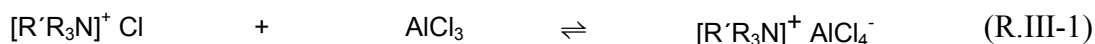
Typical Lewis acids in this context are $AlCl_3$, BCl_3, or $CuCl_2$. Depending on the molar ratio between the used halogenide salt and the Lewis acid, different anion species are present in equilibrium (R. III-2 / ratio 1:1, R. III-3 / ratio 1:2, R. III-4 / ratio 1:3).

$$[R'R_3N]^+ Cl \quad + \quad AlCl_3 \quad \rightleftharpoons \quad [R'R_3N]^+ AlCl_4^- \qquad (R.III-2)$$

$$[R'R_3N]^+ AlCl_4^- \quad + \quad AlCl_3 \quad \rightleftharpoons \quad [R'R_3N]^+ Al_2Cl_7^- \qquad (R.III-3)$$

$$[R'R_3N]^+ Al_2Cl_7^- \quad + \quad AlCl_3 \quad \rightleftharpoons \quad [R'R_3N]^+ Al_3Cl_{10}^- \qquad (R.III-4)$$
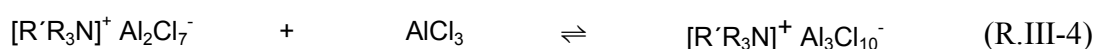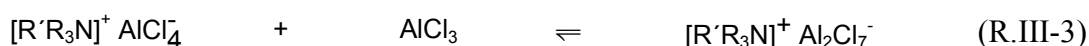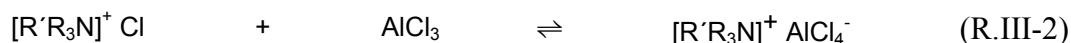
Chloroaluminate ionic liquids are the best known, but not the only ionic liquids that can be prepared by the reaction of a chloride salt with a Lewis acid. Further examples and the corresponding equilibria are shown in Table II-5.

Ionic liquid	Established anions	Ref.
[Cation]Cl/AlCl$_3$	**Cl$^-$, AlCl$_4^-$, Al$_2$Cl$_7^-$, Al$_3$Cl$_{10}^-$**	**[20, 34]**
[Cation]Cl/AlEtCl$_2$	**AlEtCl$_3^-$, AlEt$_2$Cl$_5^-$**	**[35, 36]**
[Cation]Cl/BCl$_3$	**Cl$^-$, BCl$_4^-$**	**[37]**
[Cation]Cl/CuCl	**CuCl$_2^-$, Cu$_2$Cl$_3^-$, Cu3Cl$_4^-$**	**[38]**
[Cation]Cl/SnCl$_2$	**SnCl$_3^-$, Sn$_2$Cl$_5^-$**	**[39, 40, 41]**

Table II-5 : Examples of ILs, which can be prepared by the reaction of a halide with a Lewis acid.

In contrast to the Lewis acid/Lewis base reactions presented above, during the anion metathesis the halogenide X^- is replaced completely by the desired anion A^-. Hence, the salt of the type $[cation]^+A^-$ is formed containing only one anion species when the exchange reaction has proceeded to completion. Normally, this procedure is carried out by the addition of a metal salt M^+A^- or by a strong Brønsted acid H^+A^- under release of H^+X^- (R.III-6). In the case of anion metathesis by means of a metal salt, solvents such as acetonitrile or acetone are used in which the formed salt M^+X^- has a very low solubility product and therefore precipitates. Thus, the equilibrium is largely on the right side

of the reaction path and a complete anion exchange can be achieved (R.III-5). A further possibility to change the anion is an appropriate ion exchanger (R.III.7). A summary of anions, which can be introduced in such ways, are given in Table II-6.

$$[R'R_3N]^+ X^- \quad + \quad Li^+BF_4^- \quad \rightleftharpoons \quad [R'R_3N]^+ BF_4^- \quad + \quad Li^+X^-\uparrow \quad (R.III-5)$$

$$[R'R_3N]^+ X^- \quad + \quad H^+BF_4^- \quad \rightleftharpoons \quad [R'R_3N]^+ BF_4^- \quad + \quad H^+X^-\uparrow \quad (R.III-6)$$

$$[R'R_3N]^+ X^- \quad + \quad -NH_3^+OH^- \quad \rightleftharpoons \quad [R'R_3N]^+ OH^- \quad + \quad -NH_3^+X^- \quad (R.III-7)$$
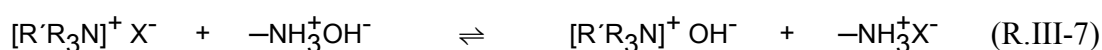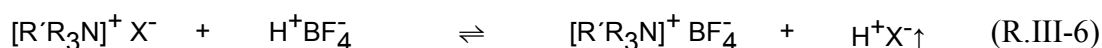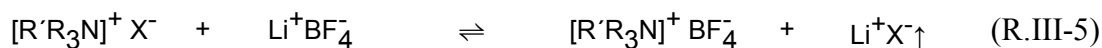
As already remarked at the beginning of this chapter, ILs are readily prepared from commercially available sources by following comparatively easy synthesis routes. Nevertheless, special demands on the preparative work must be made because every impurity highly alters not only the physical but also the chemical properties of these substances.

Ionic liquid	Anion sources	Ref.
[Cation]PF_6	HPF_6	42-45]
[Cation]BF_4	HBF_4, NH_4BF_4, $NaBF_4$	[11, 13, 44, 45]
[Cation]$(CF_3SO_2)_2N$	$Li(CF_3SO_2)_2N$	[14, 45]
[Cation]CF_3S_3	$CF_3SO_3CH_3$, $NH_4(CF_3SO_2)$	[14, 45]
[Cation]CH_3CO_2	$Ag(CH_3CO_2)$	[11]
[Cation]CF_3CO_2	$Ag(CF_3CO_2)$	[11]
[Cation]$CF_3(CF_2)_3CO_2$	$K(CF_3(CF_2)_3CO_2$	[14]
[Cation]NO_3	$AgNO_3$, $NaNO_3$	[14, 45, 46]
[Cation]$N(CN)_2$	$AgN(CN)_2$	[47]
[Cation]$CB_{11}H_{12}$	$Ag(CB_{11}H_{12})$	[48]
[Cation]$AuCl_4$	$HAuCl_4$	[49]

Table II-6 : ILs, which can be synthesized by anion metathesis from the halogenides in a solvent in which the resulting metal halogenides are insoluble, e.g. acetone or acetonitrile, respectively.

Usual impurities are non reacting educts, not completely removed side products, remaining solvents or absorbed water due to the hygroscopicity of most ionic liquids [46]. Since purification by a distillation process is not possible considering the negligible vapour pressure of salts and a recrystallization is also not possible in many cases due to the very low melting points, the best way to obtain high qualities is the usage of purified and dried educts and solvents. Another popular problem is the decontamination of the ionic liquids with anions and cations from the metathesis reaction. New reaction paths favour anion metathesis in aqueous solution followed by an extraction of the prepared ionic liquid with dichloromethane (CH_2Cl_2). The side product M^+X^- remains in the aqueous phase because of its high solubility in water. For this reason, anion sources with sodium or lithium as cation, $(Na, Li)^+A^-$, have to be chosen, since their halogenides are very soluble in water. It is noteworthy that this strategy only works fine for the synthesis of ILs, which are hydrophobic enough because of their structure, e.g. long alkyl chains and/or hydrophobic anions such as BF_4^- or PF_6^-, and therefore are very soluble in apolar solvents [13]. Beside the metal halogenides, water is another main impurity. Some ILs can absorb water up to 2 wt. %. Normally, it can be easily removed *in vacuo* at about 70°C. However, it must be taken into account that some ILs, especially protic ILs, can decompose very easily *in vacuo*, in particular at elevated temperatures.

1.4 Bulk physical and chemical properties

The physical and chemical properties of ionic liquids are altered by the cations and the anions in the same degree. This results in the ability to vary the properties of these salts in a wide range selectively. For instance, the solvent properties (e.g. polarity, solvation strength, acidity, and coordination behaviour) can be adjusted and thus a customized solvent is available even for special applications [50]. Hence, ionic liquids are often called "designer solvents" or "task-specific ionic liquids" [51].

1.4.1 Phase transition (melting point, glass point, thermotropy)

The melting point of ionic liquids represents the lower limit of the liquid gap. Together with the thermal stability, it defines the range of temperature within it is pos-

sible to use the salt in the liquid state. Many attempts have been made to correlate the structures of these substances with their melting points. The exact melting point determination of ILs, unfortunately, is a big problem, since they undergo considerable supercooling. For this reason, the temperature of the phase-transition can differ a lot depending on whether the sample is heated or cooled [14, 42, 52, 53]. Beside the already discussed asymmetry [52], size [12] and charge delocalization [1] of the cation and anion, another important feature influencing the melting point is the occurrence of hydrogen bonding between the present ions. Normally, this effect takes place between the anion and the protons of the cation, in particular with that in the C-2 position relative to the heteroatom. Hydrogen bonding is observed, especially in the case of imidazolium-ILs, when basic anions such as halides, polyhalogenated metals, fluorinated organic anions, NO_3^-, BF_4^- or PF_6^- are present. Especially, imidazolium chlorides exhibit high melting points (between 40 and 80°C) and form 3-D networks, in the case of 1-ethyl-3-methyl imidazolium chloride (emimCl) [54], or layered structures, in the case of 1-butyl-3-methyl imidazolium chloride (bmimCl) [55, 56]. This observation is attributed to the chloride anion which possesses a high charge density and for this reason forms very strong C-H···Cl hydrogen-bonds. In contrast, intermolecular H···F interactions in BF_4^-- or PF_6^--ILs are considered to be very weak because of the lower charge-densities of these types of anions. Consequently, the melting point of imidazolium salts with fluoro-counterions is generally lower compared to the corresponding halide analogues [57].

Glass formation, sometimes in addition or instead of crystal formation respectively, is a common characteristic associated with many, but not all, of the ionic liquid salts. It is the result of the extreme unfavourable packing-efficiency of some ILs in the solid state. Normally, the glass transition temperature (T_g) is found to be lower than -50°C [14, 29].

Interestingly, long-chain IL salts (n≥10) have attracted some interest due to their liquid crystalline (*LC*) state occurring on average below 100°C. The origin for this characteristic can be explained by the formation of domains where the ionic head-groups interact with the counterions by means of Coulombic forces and layers built from

(anti)parallel stacking of the long alkyl-chains through van-der-Waals attraction. The melting to isotropic liquids occur at rather high temperatures (>>100°C) [13, 42].

1.4.2   Vapour pressure & thermal stability

Generally, ionic liquids are often described as substances having a negligible vapour pressure due to their salt character. However, this is not completely true. Some ILs undergo a boiling point (T_b) before they decompose (T_d) upon heating. Well-known examples, in this context, are the already presented PILs. Consequently, these salts are distillable, so long as they do not decompose before boiling. The mechanism involves the simple proton transfer from the cation back to the anion reforming the original acid and base neutral species. During condensing, the PIL is rebuilt. PILs with low proton-transfer energies are suitable for distillation, whereas protic ionic liquids with high proton-transfer energies undergo decomposition before they reach their boiling points [29, 58, 59]. Very recently, it was shown that certain AILs are also distillable [60], but there are a number of key differences between the distillation of PILs and AILs. Usually, protic ionic liquids just require moderate heating, whereas AILs need heating to high temperatures in combination with very low pressures to prevent decomposition. In principle, the volatilization of AILs base on cluster formation of the ionic species rather than including neutral species, which occur during PIL distillation [60, 61]. As, only a small moiety of aprotic ionic liquids are distillable under extreme conditions, the declaration that these substances are non-volatile still persists in the literature. The negligible vapour pressure of most AILs is a great advantage from a process-engineering viewpoint, since separation by distillation of a reaction mixture becomes more effective as a method of product isolation because solvent-product azeotropic formation cannot occur [50].

The thermal stability of ionic liquids is higher than 300°C on average. The crucial point of the IL stability are the heteroatom-proton bonds (PILs) and the heteroatom-carbon bonds (AILs), respectively. Usually, T_d of PILs is much lower than that of AILs, because of the tendency of *PIL*s to deprotonate at elevated temperatures (between 200°C and 300°C) [62-64]. It should be noted that PILs having carboxylate anions easily form amides through condensation reaction (R.III-8), especially at higher temperatures,

but sometimes already at room temperature. Therefore, salts with these anions exhibit only low thermal stabilities [28].

$$R\text{-}NH_3^+ \ ^-OOCH\text{-}R' \qquad\rightarrow\qquad R\text{-}NH\text{-}OCH\text{-}R' \ + \ H_2O \qquad (RIII\text{-}8)$$

In contrast, the AILs whose cations were obtained by quaternization reaction using an alkylating agent provide high decomposition temperatures, in special cases up to 450°C. These salts mainly decompose by chemical reversal of the alkylating step (through elimination reaction, E2) [50, 65] Especially, AILs with long alkyl-chains in the cations are vulnerable to elimination and therefore show lower T_ds (between 150 to 300°C) [1]. The thermal stability of AILs is also affected by the present anions. Relative anion stabilities have been suggested as $PF_6^- > (CF_3SO_2)N^- (= Tf_2N^-) \sim BF_4^- >$ halides. In general, the temperature stability is higher when weak coordinating anions are used [13, 14, 52, 66, 67].

1.4.3   Viscosity

Ionic liquid viscosities are always higher than those values of water and conventional organic solvents, respectively. On average quantities similar to those of oils are found [9]. This characteristic represents one of the largest barriers to the application of ILs. A high viscosity may produce a reduction in the rate of many organic reactions or in the diffusion of redox species. Shear-rate dependent measurements of the viscosity show that ILs can be classified in terms of being Newtonian fluids whose viscosities remain constant with increasing shear rate, or thixotropic fluids whose viscosities decrease as the shear rate increases [46]. The viscosity of ionic liquids is essentially determined by their tendency to form hydrogen bonds and by the strength of their van-der-Waals interactions [14]. The ability of hydrogen bonding is mostly influenced by the present anions. Low viscosities are obtained using large fluorinated asymmetric anions with good charge delocalization by weakening of the hydrogen bonds. Therefore, the viscosity decreases in the order $Cl^- > PF_6^- > BF_4^- > Tf_2N^-$. Another factor considered to affect the viscosity is the structure of the cation: Cations substituted by long alkyl-

chains show higher viscosities by means of stronger van-der-Waal interactions [14, 68]. The temperature dependence of the viscosity is often expressed by the empiric Vogel-Fulcher-Tammann equation (Eq. (II-2) which describes the viscosity decrease of a liquid (fundamentally, of a glass forming liquid) with increasing temperature [69].

$$\eta = \eta_0 \exp\left(\frac{B}{T - T_0}\right) \qquad \text{(II-2)}$$

In Eq. (II-2), η is the viscosity at a given absolute temperature T. η_0, B and T_0 are fitting parameters depending on the investigated system. It should be noted that present impurities remaining from the synthesis, e.g. solvents or halides from the metathesis reaction, influence the viscosity drastically. A viscosity reduction in the case of remaining solvents is observed, whereas a viscosity increase in the case of halide impurities by 30 to 600% depending on the concentration is found [46, 70].

1.4.4   Density & molar volume

The density d of ILs is a very important material parameter, because nearly every application requires knowledge of it. The density of an ionic material depends on the packing efficiency of ions respectively and, hence, on the size and shape of the ions and ion-ion interactions. Generally, ionic liquids are denser than water and their densities are not strongly affected by temperature or impurities. A water content of about 20 wt.% in bmimBF$_4$, for example, decreases the density only by 4% [71]. Usually, the density of ILs decreases slowly as the bulkiness of the cation increases. Thus, ionic liquids with planar cations such as imidazolium show higher densities as the corresponding tetraalkylammonium salts. Ionic liquids having long alkyl substituents within the cation exhibit lower densities than those with short chains. In addition, the counter ions significantly influence the overall density of ILs. This observation can be easily explained by means of cation-anion size match. So, the density of ionic liquids increases as the packing may become more compact since the alternating positive and negative species become more even in size [28, 66, 72, 73].

The molar volume V_m has to be considered as a representation of the ion-ion spacing for ideal ionic liquids, where there is little association between the ions [74]. For these substances, the ion-ion attractive force insist of Coulombic and van-der-Waal interactions, whereby the repulsive force is due to Pauli repulsions from filled electron shells. Ideal ionic liquids are in this context the most AILs, whereas PILs show non-ideal behaviour, which probably results from charge neutralization by some association of the ions and possibly from some weak proton transfer back from the acid to the base. In this case, V_m is only indicative of the ion-ion-spacing resulting in low molar volumes [28, 74].

1.4.5   Surface tension

Surface tension may be an important property in multiphase processes. In general, liquid/gas surface tensions of ILs are slightly higher than those quantities of conventional solvents, but not as high as that of water. The surface tension is a measure of the cohesion of liquids, and is dependent upon the liquid structure and orientation. Changes to either the cation or the anion structures show a similar effect on the surface tension [28, 75-77]. This is attributed to the fact that both ions are present at the surface and affect the surface tension [78, 79]. A model has been proposed in which the basis is the assumption that the charged groups of the cation and the anion are always located toward the bulk of the liquid, while the hydrocarbon chain is exposed to the gas phase [28]. Cations with long-alkyl chains increase the amount of hydrocarbons situated at the surface, and therefore decrease the surface tension by means of higher cohesive energy. An incorporation of large anions causes high surface tension values, which suggests that as the anion radius is increased, the cations are pushed further apart, and the surface tension increases due to the reduction in the amount of hydrocarbon present at the liquid/gas interface. The surface tension decreases for the same cation in the order $I^- > Cl^- > PF_6^- > BF_4^-$ [77]. Hence, the surface tension of ILs is strongly connected to length and the packing efficiency of the hydrocarbons of the ILs at the surface [28]. With increasing temperature, the surface tension decreases quite linearly [78].

1.4.6 Refractive index & polarizability

Normally, ionic liquids have a refractive index n_D between 1.42 and 1.58 comparable to those of organic solvents [28, 66]. This is due to similar densities and atomic compositions (C, H, N). n_D is related to the electron polarizability α_E of a medium through the molar refraction R_{mol} (cp. Eq. (II-3).

$$R_{mol} = \frac{n_D^2 - 1}{n_D^2 + 2} \frac{M_w}{d} = \frac{1}{3} \frac{N_A}{\varepsilon_0} \alpha_E \qquad (II\text{-}3)$$

R_{mol} can be considered as the sum of contributions either from units within a non-ionic molecular liquid or from both non-ionic and ionic units within an ionic liquid. Since Eq. (II-3) is only entirely valid for non-polar molecules, it is only an approximation for fused salts.

1.4.7 Polarity & solubility strength

In general, ionic liquids can be described as dipolar, protic (PILs) or aprotic (AILs) solvents respectively [1]. Usually, the polarity of molecular solvents (solvent polarity) is often quantitatively characterized by their dielectric constant ε_r. As this polarity classification is not entirely useful in the case of ILs, another polarity scale has to be chosen. Therefore, empirical solvent polarity scales mostly based on solvatochromic or fluorescent dyes are utilized to classify ionic liquids. Established dyes in this context are Nile red (neutral dye) and Reichardt´s dye (betaine dye) [80, 81]. Investigations of solute-solvent interactions by means of solvatochromic dyes are easy to perform, and they are convenient, if the interpretation is carefully considered. Generally, each dye is sensitive to a certain kind of interaction, e.g. hydrogen bonding or dipolarity/polarizability. Nevertheless, solvent polarity arises from the sum of all possible intermolecular interactions, and therefore different probes can result in different polarities of the investigated IL. Nile red (cp. Figure II-4, left) is sensitive to solvent dipolarity/polarizability, whereas the Reichardt´s dye (cp. Figure II-4, right) reflects the solvents hydrogen-

bonding ability. For Nile red, polarity values of ionic liquids similar to short-chain alcohols were found. The range of the values is narrow.

Nile red   **Reichhardt´s dye**
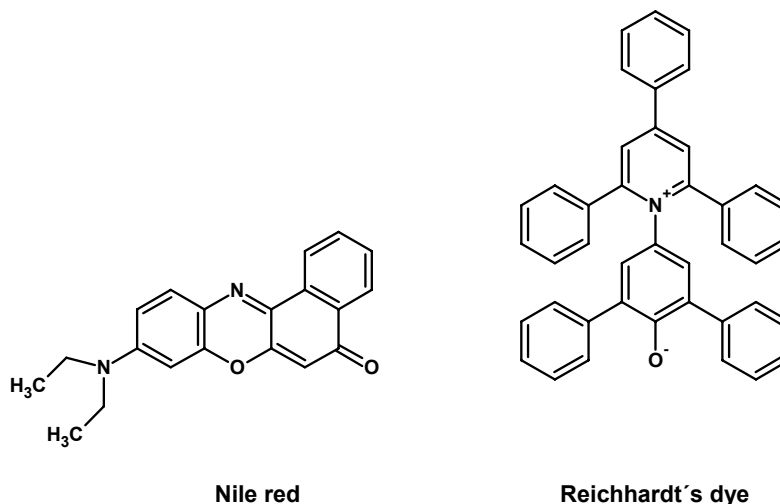
Figure II-4 : Solvatochromic dyes: Nile red (left) and Reichardt´s dye (right).

In the case of ILs with short 1-alkyl chains within the cation, the polarity is dominated by the present anion, whereas the polarity of cations containing long 1-alkyl chains are less influenced by the present anion. The polarity decreases through the series $NO_2^- >$ $NO_3^- > BF_4^- > Tf_2N^- > PF_6^-$ and therefore the decrease correlates with anion size, i.e. with the effective charge density of the anion [80]. The most popular polarity scale is based on $E_{T(30)}$ values utilizing the solvatochromic shift of the lowest energy π-π^* absorption band of the Reichardt´s betaine dye. The $E_{T(30)}$ values of 1-alkyl-3-methyl imidazolium salts are similar to that of ethanol and are not hardly affected by long 1-alkyl-chains. Noteworthy, is the influence of a present methyl group instead of a proton in the C-2 position in the case of imidazolium-ILs. It reduces the polarity obtained by Reichardt´s dye considerably. This is in agreement with the often proposed ability of the proton at C-2 to form hydrogen bonds with the anion and with the presumption that changes in the $E_{T(30)}$ values are dominated by the hydrogen bonding acidity of the solvent. Cations synthesized from protonation (*PIL*s) have in general higher polarities compared to *AIL*s,

sometimes similar to water. Alteration of the anion (PF_6^-, BF_4^-, TfO$^-$) has only little effect on the $E_{T(30)}$ values of these substances [81].

As mentioned above, the polarities and thus the solvent properties of ionic liquids can be tuned by the cation-anion combination. A stepwise variation from hydrophilic to hydrophobic is possible which enables the solubilisation of either polar or nonpolar substances [50].

1.4.8   Acidity & coordination ability

The acidity and the coordination ability of ILs are dominated by the anions. Between strong basic/strong coordinating and strong acidic/non-coordinating, many intermediate levels can be obtained (cp. Table II-7) [50].

Acidity/coordination ability		
Basic	**Neutral**	**Acidic**
Strong coordinating	**Weak coordinating**	**Non coordinating**
Cl^-	$AlCl_4^-$	$Al_2Cl_7^-$
$CH_3CO_2^-$	$CuCl_2^-$	$Al_3Cl_{10}^-$
NO_3^-	SbF_6^-	
SO_4^{2-}	BF_4^-	$Cu_2Cl_3^-$
	PF_6^-	$Cu_3Cl_4^-$

Table II-7 : Coordinative characteristics of various anions. Represented from Ref. [50].

1.5   Toxicity & biological activity

The popularity of ionic liquids is not only based on their unique tuneable properties leading to quite a lot of different applications (cp. Chapter II.1.6). In addition, they have also widely been promoted as "green solvents". The rational for calling them green mainly consists of three arguments [82]:

(i)   Their vapour pressure is generally negligible, and thus inhalative exposure of workers is reduced as compared to conventional molecular solvents.

(ii)   They have been shown to be non-flammable, and therefore the risk of fast exo-
thermic oxidations in the case of an accident is strongly reduced.

(iii)   They are claimed to be relatively non-toxic.

Since the large majority of ionic liquids are still in a very early phase concerning their
usage in industrial processes in large scale, it is clear that there is not a lot of risk data
available up to now. Therefore, point (iii) has to be dealt carefully. During the last three
years more and more toxicity investigations of ILs are reported in the literature, includ-
ing comparisons to commonly utilized molecular solvents such as tert-butyl ether
(MTBE), tetrahydrofuran (THF), dichlormethane (CH_2Cl_2) and acetonitrile (AN). An-
other set of reference substances that are not always functionally analogous to ILs, but
have structural analogies, are ionic surfactants including mostly cationic but also ani-
onic ones. In summary, ionic liquids are often compared to organic solvents and ionic
surfactants regarding five risk indicators: (i) release, (ii) spatiotemporal range, (iii) bio-
accumulation, (iv) biological activity and (v) uncertainty. Giving a résumé, the struc-
tural variability of ionic liquids provides substances that have a low risk regarding each
of the five risk indicators. However, the ionic liquids commonly used to date in applica-
tions (especially the imidazolium-ILs) are toxic in nature, which has been proven by
various toxicological data collections aimed at a wide range of organisms [83]. For this
reason, the term "green solvents" is a varnished sight often given by chemists and engi-
neers who work in the field of ionic liquids as these substances indeed are not com-
pletely harmless for the environment. Nevertheless, the adjustable nature of ionic liq-
uids once again embodies the omnipotence of designer solvents, i.e. ionic liquids can be
designed to be less and nontoxic, respectively. With the close collaboration of toxico-
logical and synthetic chemists, evermore genuinely green and efficient ionic liquids
may make an appearance [83].

1.6   Applications

Ionic liquids are predominately considered as alternatives of common organic
solvents for industrial applications. It could be shown that ILs are not only interesting
substitutes by means of their non-volatile characteristic. In fact, at the current level of

development, ionic liquids can nicely complement, and even sometimes work better than conventional solvents in a number of different applications [2]. Table II-8 shows the key differences of ionic liquids in comparison to organic solvents.

Property	Organic solvents	Ionic liquids
Number of solvents	> 1000	> 1,000,000
Applicability	Single function	Multifunction
Catalytic ability	Rare	Common and tuneable
Chirality	Rare	Common and tuneable
Vapour pressure	Obeys the Clausius-Clapeyron equation	Negligible vapour pressure under normal conditions
Flammability	Usually flammable	Usually non-flammable
Solvation	Weakly solvating	Strongly solvating
Polarity	Conventional polarity concepts apply	Polarity concept questionable
Tune ability	Limited range of solvents available	Virtually unlimited / "designer solvents"
Cost	Normally cheap	Typically 2 to 100 times the cost of organic solvents
Recyclability	Green imperative	Economic imperative
Viscosity / cP	0.2 - 100	22 - 40,000
Density / g cm^{-3}	0.6 - 1.7	0.8 - 3.3
Refractive index	1.3 - 1.6	1.5 - 2.2

Table II-8 : Comparisons of organic solvents with ionic liquids. Represented from Ref. [2].

Currently, the most popular and well established example of an industrial process involving an ionic liquid is the BASIL^{TM} (Biphasic Acid Scavenging utilizing Ionic Liquids) process which was introduced by BASF AG in 2002 (cp. Figure II-5). This process is used for the production of alkoxyphenylphospines. In the original process chart, triethylamine was used to scavenge the acid formed during the reaction. However, this made the obtained reaction mixture difficult to handle, since the trimethylammonium chloride formed an insoluble paste. Replacing triethylamine by 1-methylimidazole

results in the formation of 1-methyimidazolium chloride, an ionic liquid, which sepa-rates out of the reaction mixture as a discrete phase at process temperature. This made the process more effective in consideration of scale and yield [2].
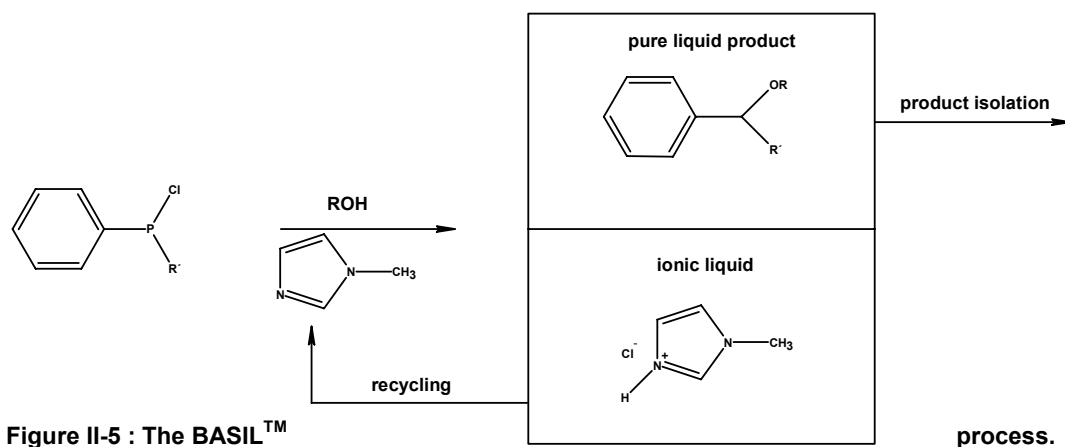
Figure II-5 : The BASIL^{TM} process.

Another development of BASF AG demonstrates that hydrogen chloride solubilised in ionic liquids could act as phosgene substitute. A reaction mixture of 1,4-dihydroxybutane and HCl/IL results in an almost pure 1,4-dichlorobutane (98% selec-tivity) product. In contrast, the direct reaction of 1,4-dihydroxybutane with HCl instead of phosgene produces a reaction mixture of four products and the desired 1,4-dichlorobutane is only a minor by-product [84].

Great efforts have also been made utilizing ionic liquids as solvents for bio-polymers. Especially, cellulose, the most important bio-renewable resource (about 7.5×10^{10} t/a), can be dissolved up to high concentrations (25 wt.%) which is not possible in conventional solvents [85].

Beside the usage of ILs as solvents for organic reactions, the application as elec-trolytes in lithium batteries [86-89], in electroplating processes [90-93], and solar cells [94-98] reflects the applicability in electrochemistry.

Noteworthy are also the investigations of ionic liquids with regard to their ad-vantages in formulation technology, in colloid science and in tribology during the last years leading to their usage e.g. as additives in paintings [99], templates in nano-

technology [100-121] or as innovative lubricants for steel on aluminium applications [122, 123]. An overview of the diversity of IL employments gives Figure II-6.
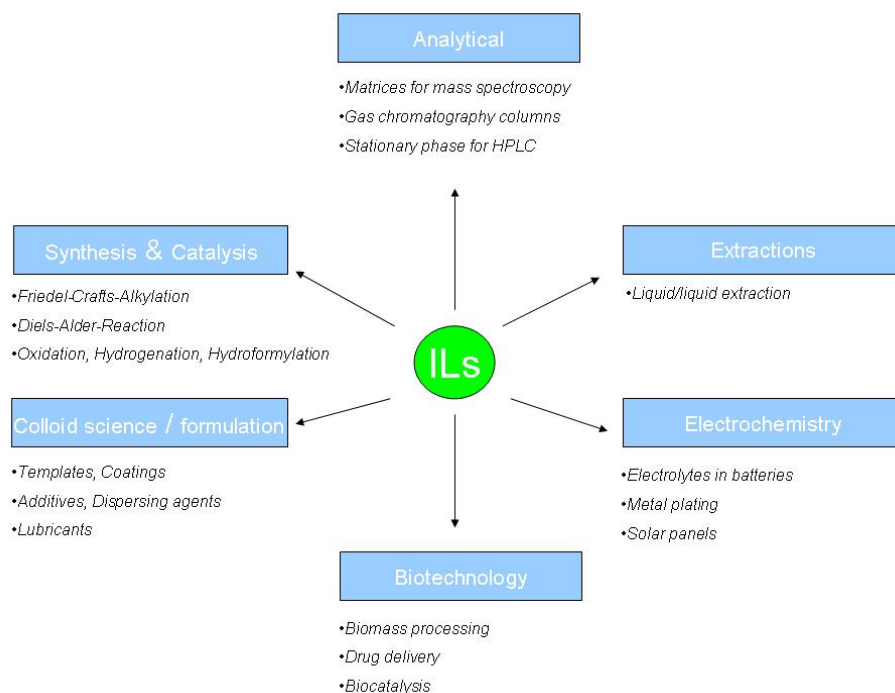
Figure II-6 : Survey of recent applications of ionic liquids.

1.7   Bibliography

[1]   P. Wasserscheid, T. Welton; *Ionic Liquids in Synthesis. 1st Edition*. Wiley-VCH (2003)**.**

[2]   N. V. Plechkova and K. R. Seddon; Applications of ionic liquids in the chemical industry. *Chemical Society Reviews* **37**, 1, 123-150 (2007).

[3]   T. Welton; Room-Temperature Ionic Liquids. Solvents for Synthesis and Catalysis. *Chemical Reviews* **99**, 8, 2071-2083 (1999).

[4]   P. Wasserscheid and W. Keim; Ionic liquids - new "solutions" for transition metal catalysis. *Angewandte Chemie (Int. ed.)* **39**, 21, 3772-3789 (2000).

[5]   P. Wasserscheid; Ionische Flüssigkeiten. *Chemie in unserer Zeit* **37**, 1, 52-63 (2003).

[6]   J. S. Wilkes; *Introduction [to ionic liquids in synthesis]*. in: *Ionic Liquids in Synthesis, 1st Edition.* Wiley-VCH, (2003).

[7]   J. S. Wilkes; Properties of ionic liquid solvents for catalysis. *Journal of Molecular Catalysis A: Chemical* **214**, 1, 11-17 (2004).

[8]   A. Hamnett, C. H. Hamann and W. Vielstich; *Electrochemistry, 3rd Edition.* Wiley-VCH, (1997).

[9]   D. R. Lide; *CRC Handbook of Chemistry and Physics, 83rd Edition.* CRC Press, (2002).

[10]   J. S. Wilkes, J. A. Levisky, R. A. Wilson and C. L. Hussey; Dialkylimidazolium chloroaluminate melts: a new class of room-temperature ionic liquids for electrochemistry, spectroscopy and synthesis. *Inorganic Chemistry* **21**, 3, 1263-1264 (1982).

[11]   J. S. Wilkes and M. J. Zaworotko; Air and water stable 1-ethyl-3-methylimidazolium based ionic liquids. *Chemical Communications* **13**, 965-967 (1992).

[12]   A. A. Fannin, Jr., D. A. Floreani, L. A. King, J. S. Landers, B. J. Piersma, D. J. Stech, R. L. Vaughn, J. S. Wilkes and W. J. L; Properties of 1,3-dialkyl-imidazolium chloride-aluminum chloride ionic liquids. 2. Phase transitions, densities, electrical conductivities, and viscosities. *Journal of Physical Chemistry* **88**, 12, 2614-2621 (1984).

[13]   J. D. Holbrey and K. R. Seddon; The phase behaviour of 1-alkyl-3-methylimidazolium tetrafluoroborates; ionic liquids and ionic liquid crystals. *Journal of the Chemical Society, Dalton Transactions: Inorganic Chemistry* **13**, 2133-2140 (1999).

[14]   P. Bonhote, A.-P. Dias, N. Papageorgiou, K. Kalyanasundaram and M. Graetzel; Hydrophobic, Highly Conductive Ambient-Temperature Molten Salts. *Inorganic Chemistry* **35**, 5, 1168-1178 (1996).

[15] C. Chiappe and D. Pieraccini; Ionic liquids: solvent properties and organic reactivity. *Journal of Physical Organic Chemistry* **18**, 4, 275-297 (2005).

[16] P. Walden; *Bull. Acad. Imper. Sci. (St. Petersburg)* 1800 (1914).

[17] F. H. Hurley; Electrodeposition of aluminum. Rice Institute. **US 2446331** (1948).

[18] T. P. Wier, Jr. and F. H. Hurley; Electrodeposition of aluminum. Rice Institute. **US 2446349** (1948).

[19] R. J. Gale, B. Gilbert and R. A. Osteryoung; Raman spectra of molten aluminum chloride: 1-butylpyridinium chloride systems at ambient temperatures. *Inorganic Chemistry* **17**, 10, 2728-2729 (1978).

[20] Z. J. Karpinski and R. A. Osteryoung; Determination of equilibrium constants for the tetrachloroaluminate ion dissociation in ambient-temperature ionic liquids. *Inorganic Chemistry* **23**, 10, 1491-1494 (1984).

[21] S. Tait and R. A. Osteryoung; Infrared study of ambient-temperature chloroaluminates as a function of melt acidity. *Inorganic Chemistry* **23**, 25, 4352-4360 (1984).

[22] T. A. Zawodzinski, Jr. and R. A. Osteryoung; Oxide and hydroxide species formed on addition of water in ambient-temperature chloroaluminate melts: an oxygen-17 NMR study. *Inorganic Chemistry* **29**, 15, 2842-2847 (1990).

[23] R. A. Mantz, P. C. Trulove, R. T. Carlin and R. A. Osteryoung; ROESY NMR of Basic Ambient-Temperature Chloroaluminate Ionic Liquids. *Inorganic Chemistry* **34**, 14, 3846-3847 (1995).

[24] C. L. Hussey; Room temperature haloaluminate ionic liquids. Novel solvents for transition metal solution chemistry. *Pure and Applied Chemistry* **60**, 12, 1763-1772 (1988).

[25] A. J. Dent, K. R. Seddon and T. Welton; The structure of halometallate complexes dissolved in both basic and acidic room-temperature haloaluminate(III)

ionic liquids, as determined by EXAFS. *Chemical Communications* **4**, 315-316 (1990).

[26] J. S. Wilkes and M. J. Zaworotko; Air and water stable 1-ethyl-3-methylimidazolium based ionic liquids. *Chemical Communications* **13**, 965-967 (1992).

[27] P. Wasserscheid and T. Welton; *Ionic Liquids in Synthesis*. Wiley-VCH, (2003).

[28] T. L. Greaves, A. Weerawardena, C. Fong, I. Krodkiewska and C. J. Drummond; Protic Ionic Liquids: Solvents with Tunable Phase Behavior and Physico-chemical Properties. *Journal of Physical Chemistry B* **110**, 45, 22479-22487 (2006).

[29] J.-P. Belieres and C. A. Angell; Protic ionic liquids: preparation, characterization, and proton free energy level representation. *Journal of Physical Chemistry B* **111**, 18, 4926-4937 (2007).

[30] C. A. Angell, N. Byrne and J.-P. Belieres; Parallel Developments in Aprotic and Protic Ionic Liquids: Physical Chemistry and Applications. *Accounts of Chemical Research* **40**, 11, 1228-1236 (2007).

[31] T. L. Greaves and C. J. Drummond; Protic Ionic Liquids: Properties and Applications. *Chemical Reviews* **108**, 1, 206-237 (2008).

[32] H. Waffenschmidt; PhD Thesis. University of Erlangen, (2000).

[33] N. Karodia, S. Guise, C. Newlands and J.-A. Andersen; Clean catalysis with ionic solvents-phosphonium tosylates for hydroformylation. *Chemical Communications* **21**, 2341-2342 (1998).

[34] A. K. Abdul-Sada, A. M. Greenway, K. R. Seddon and T. Welton; A fast atom bombardment mass spectrometric study of room-temperature 1-ethyl-3-methylimidazolium chloroaluminate(III) ionic liquids. Evidence for the existence of the decachlorotrialuminate(III) anion. *Organic Mass Spectrometry* **28**, 7, 759-765 (1993).

[35]   Y. Chauvin, S. Einloft and H. Olivier; Catalytic Dimerization of Propene by Nickel-Phosphine Complexes in 1-Butyl-3-methylimidazolium Chloride / AlEt$_x$Cl$_{3-x}$ (x = 0, 1) Ionic Liquids. *Industrial & Engineering Chemistry Research* **34**, 4, 1149-1155 (1995).

[36]   B. Gilbert, Y. Chauvin, H. Olivier and F. Di Marco-Van Tiggelen; *Journal of the Chemical Society, Dalton Transactions* **25**, 3867-3871 (1995).

[37]   S. D. Williams, J. P. Schoebrechts, J. C. Selkirk and G. Mamantov; A new room temperature molten salt solvent system: organic cation tetrachloroborates. *Journal of the American Chemical Society* **109**, 7, 2218-2219 (1987).

[38]   Y. Chauvin and H. Olivier-Bourbigou; Nonaqueous ionic liquids as reaction solvents. *CHEMTECH* **25**, 9, 26-30 (1995).

[39]   G. W. Parshall; Catalysis in molten salt media. *Journal of the American Chemical Society* **94**, 25, 8716-8719 (1972).

[40]   G. Ling and N. Koura; Electrodeposition of Nb-Sn alloy from ambient-temperature molten salt electrolytes by pulse electrolysis. *Hyomen Gijutsu* **48**, 4, 454-459 (1997).

[41]   P. Wasserscheid and H. Waffenschmidt; Ionic liquids in regioselective platinum-catalyzed hydroformylation. *Journal of Molecular Catalysis A: Chemical* **164**, 1-2, 61-67 (2000).

[42]   C. M. Gordon, J. D. Holbrey, A. R. Kennedy and K. R. Seddon; Ionic liquid crystals: hexafluorophosphate salts. *Journal of Materials Chemistry* **8**, 12, 2627-2636 (1998).

[43]   J. G. Huddleston and R. D. Rogers; Room temperature ionic liquids as novel media for 'clean' liquid-liquid extraction. *Chemical Communications* **16**, 1765-1766 (1998).

[44]   J. Fuller, R. T. Carlin, H. C. De Long and D. Haworth; Structure of 1-ethyl-3-methylimidazolium hexafluorophosphate: model for room temperature molten salts. *Chemical Communications* **3**, 299-300 (1994).

[45] L. Cammarata, S. G. Kazarian, P. A. Salter and T. Welton; Molecular states of water in room temperature ionic liquids. *Physical Chemistry Chemical Physics* **3**, 23, 5192-5200 (2001).

[46] K. R. Seddon, A. Stark and M.-J. Torres; Influence of chloride, water, and organic solvents on the physical properties of ionic liquids. *Pure and Applied Chemistry* **72**, 12, 2275-2287 (2000).

[47] D. R. MacFarlane, J. Golding, S. Forsyth, M. Forsyth and G. B. Deacon; Low viscosity ionic liquids based on organic salts of the dicyanamide anion. *Chemical Communications* **16**, 1430-1431 (2001).

[48] A. S. Larsen, J. D. Holbrey, F. S. Tham and C. A. Reed; Designing Ionic Liquids: Imidazolium Melts with Inert Carborane Anions. *Journal of the American Chemical Society* **122**, 30, 7264-7272 (2000).

[49] M. Hasan, I. V. Kozhevnikov, M. R. H. Siddiqui, A. Steiner and N. Winterton; Gold Compounds as Ionic Liquids. Synthesis, Structures, and Thermal Properties of N,N'-Dialkylimidazolium Tetrachloroaurate Salts. *Inorganic Chemistry* **38**, 25, 5637-5641 (1999).

[50] P. Wasserscheid and W. Keim; Ionische Flüssigkeiten - neue "Lösungen" für die Übergangsmetallkatalyse. *Angewandte Chemie* **112**, 3926-3945 (2000).

[51] M. Freemantle; *Chem. Eng. News* **76**, 32-37 (1998).

[52] H. L. Ngo, K. LeCompte, L. Hargens and A. B. McEwen; Thermal properties of imidazolium ionic liquids. *Thermochimica Acta* **357-358**, 97-102 (2000).

[53] R. Hagiwara and Y. Ito; Room temperature ionic liquids of alkylimidazolium cations and fluoroanions. *Journal of Fluorine Chemistry* **105**, 2, 221-227 (2000).

[54] A. Elaiwi, P. B. Hitchcock, K. R. Seddon, N. Srinivasan, Y.-M. Tan, T. Welton and J. A. Zora; Hydrogen bonding in imidazolium salts and its implications for ambient-temperature halogenoaluminate(III) ionic liquids. *Journal of the Chemical Society, Dalton Transactions: Inorganic Chemistry* **21**, 3467-3472 (1995).

[55] S. Saha, S. Hayashi, A. Kobayashi and H. O. Hamaguchi; Crystal structure of 1-butyl-3-methylimidazolium chloride. A clue to the elucidation of the ionic liquid structure. *Chemistry Letters* **32**, 8, 740-741 (2003).

[56] J. D. Holbrey, W. M. Reichert, M. Nieuwenhuyzen, S. Johnson, K. R. Seddon and R. D. Rogers; Crystal polymorphism in 1-butyl-3-methylimidazolium halides: supporting ionic liquid formation by inhibition of crystallization. *Chemical Communications* **14**, 1636-1637 (2003).

[57] P. Koelle and R. Dronskowski; Hydrogen Bonding in the Crystal Structures of the Ionic Liquid Compounds Butyldimethylimidazolium Hydrogen Sulfate, Chloride, and Chloroferrate(II,III). *Inorganic Chemistry* **43**, 9, 2803-2809 (2004).

[58] M. Yoshizawa, W. U. Xu and C. A. Angell; Ionic Liquids by Proton Transfer: Vapor Pressure, Conductivity, and the Relevance of ΔpK_a from Aqueous Solutions. *Journal of the American Chemical Society* **125**, 50, 15411-15419 (2003).

[59] D. R. MacFarlane, J. M. Pringle, K. M. Johansson, S. A. Forsyth and M. Forsyth; Lewis base ionic liquids. *Chemical Communications* **18**, 1905-1917 (2006).

[60] M. J. Earle, J. M. S. S. Esperanca, M. A. Gilea, J. N. Canongia Lopes, L. P. N. Rebelo, J. W. Magee, K. R. Seddon and J. A. Widegren; The distillation and volatility of ionic liquids. *Nature* **439**, 7078, 831-834 (2006).

[61] B. A. DaSilveira Neto, L. S. Santos, F. M. Nachtigall, M. N. Eberlin and J. Dupont; On the species involved in the vaporization of imidazolium ionic liquids in a steam-distillation-like process. *Angewandte Chemie (Int. ed.)* **45**, 43, 7251-7254 (2006).

[62] M. A. B. H. Susan, A. Noda, S. Mitsushima and M. Watanabe; Bronsted acid-base ionic liquids and their use as new materials for anhydrous proton conductors. *Chemical Communications* **8**, 938-939 (2003).

[63] H. Ohno and M. Yoshizawa; Ion conductive characteristics of ionic liquids prepared by neutralization of alkylimidazoles. *Solid State Ionics* **154-155**, 303-309 (2002).

[64] A. Noda, M. A. B. H. Susan, K. Kudo, S. Mitsushima, K. Hayamizu and M. Watanabe; Bronsted Acid-Base Ionic Liquids as Proton-Conducting Nonaqueous Electrolytes. *Journal of Physical Chemistry B* **107**, 17, 4024-4033 (2003).

[65] J. L. Anthony, J. F. Brennecke, J. D. Holbrey, E. J. Maginn, R. A. Mantz, R. D. Rogers, P. C. Trulove, A. E. Visser and T. Welton; *Physicochemical properties of ionic liquids: melting points and phase diagrams*. in: *Ionic Liquids in Synthesis*. Wiley-VCH, (2003).

[66] J. G. Huddleston, A. E. Visser, W. M. Reichert, H. D. Willauer, G. A. Broker and R. D. Rogers; Characterization and comparison of hydrophilic and hydrophobic room temperature ionic liquids incorporating the imidazolium cation. *Green Chemistry* **3**, 4, 156-164 (2001).

[67] S. Takahashi, N. Koura, S. Kohara, M. L. Saboungi and L. A. Curtiss; Technological and scientific issues of room-temperature molten salts. *Plasmas & Ions* **2**, 3/4, 91-105 (1999).

[68] E. Cooper, I. and E. O´Sullivan, J., M.; Proceedings of the Eighth International Symposium on Molten Salts. *The Electrochemical Society* **92-16**, 386-396 (2000).

[69] K. R. Harris, M. Kanakubo and L. A. Woolf; Temperature and Pressure Dependence of the Viscosity of the Ionic Liquids 1-Hexyl-3-methylimidazolium Hexafluorophosphate and 1-Butyl-3-methylimidazolium Bis(trifluoromethylsulfonyl)imide. *Journal of Chemical & Engineering Data* **52**, 3, 1080-1085 (2007).

[70] Q. Liao and C. L. Hussey; Densities, Viscosities, and Conductivities of Mixtures of Benzene with the Lewis Acidic Aluminum Chloride + 1-Methyl-3-ethyl-

imidazolium Chloride Molten Salt. *Journal of Chemical and Engineering Data* **41**, 5, 1126-1130 (1996).

[71]   R. L. Perry, K. M. Jones, W. D. Scott, Q. Liao and C. L. Hussey; Densities, Viscosities, and Conductivities of Mixtures of Selected Organic Cosolvents with the Lewis Basic Aluminum Chloride + 1-Methyl-3-ethylimidazolium Chloride Molten Salt. *Journal of Chemical and Engineering Data* **40**, 3, 615-619 (1995).

[72]   S. V. Dzyuba and R. A. Bartsch; Influence of structural variations in 1-alkyl(aralkyl)-3-methylimidazolium hexafluorophosphates and bis(trifluoromethylsulfonyl)imides on physical properties of the ionic liquids. *Chemphyschem* **3**, 2, 161-166 (2002).

[73]   S. Carda-Broch, A. Berthod and D. W. Armstrong; Solvent properties of the 1-butyl-3-methylimidazolium hexafluorophosphate ionic liquid. *Analytical and Bioanalytical Chemistry* **375**, 2, 191-199 (2003).

[74]   W. U. Xu, L.-M. Wang, R. A. Nieman and C. A. Angell; Ionic Liquids of Chelated Orthoborates as Model Ionic Glassformers. *Journal of Physical Chemistry B* **107**, 42, 11749-11756 (2003).

[75]   B. Alessandro, B. Craig, C. Cinzia, D. Fabio, L. J. C. D, P. Daniela and R. Federico; The effect of the anion on the physical properties of trihalide-based N,N-dialkylimidazolium ionic liquids. *Organic & biomolecular chemistry* **3**, 9, 1624-1630 (2005).

[76]   G. F. Mara, C. J, P. J., A. M. Fernandes, M. I. M., Q. A. J. and J. A. P. Coutinho; Surface tensions of imidazolium based ionic liquids: anion, cation, temperature and water effect. *Journal of colloid and interface science* **314**, 2, 621-630 (2007).

[77]   M. H. Ghatee and A. R. Zolghadr; Surface tension measurements of imidazolium-based ionic liquids at liquid-vapor equilibrium. *Fluid Phase Equilibria* **263**, 2, 168-175 (2008).

[78] G. Law and P. R. Watson; Surface Tension Measurements of N-Alkylimidazolium Ionic Liquids. *Langmuir* **17**, 20, 6138-6141 (2001).

[79] G. Law and P. R. Watson; Surface orientation in ionic liquids. *Chemical Physics Letters* **345**, 1,2, 1-4 (2001).

[80] A. J. Carmichael and K. R. Seddon; Polarity study of some 1-alkyl-3-methylimidazolium ambient-temperature ionic liquids with the solvatochromic dye, Nile Red. *Journal of Physical Organic Chemistry* **13**, 10, 591-595 (2000).

[81] M. J. Muldoon, C. M. Gordon and I. R. Dunkin; Investigations of solvent-solute interactions in room temperature ionic liquids using solvatochromic dyes. *Journal of the Chemical Society, Perkin Transactions 2* **4**, 433-435 (2001).

[82] J. Ranke, S. Stolte, R. Stormann, J. Arning and B. Jastorff; Design of sustainable chemical products - the example of ionic liquids. *Chemical reviews* **107**, 6, 2183-2206 (2007).

[83] D. Zhao, Y. Liao and Z. Zhang; Toxicity of ionic liquids. *Clean: Soil, Air, Water* **35**, 1, 42-48 (2007).

[84] V. Stegmann and K. Massonne; Method for producing haloalkanes from alcohols. BASF Aktiengesellschaft, Germany, (2005). **WO 2005026089**

[85] R. P. Swatloski, S. K. Spear, J. D. Holbrey and R. D. Rogers; Dissolution of cellulose with ionic liquids. *Journal of the American Chemical Society* **124**, 18, 4974-4975 (2002).

[86] N. Byrne, P. C. Howlett, D. R. MacFarlane and M. Forsyth; The zwitterion effect in ionic liquids: Towards practical rechargeable lithium-metal batteries. *Advanced Materials* **17**, 20, 2497-2501 (2005).

[87] H. Matsumoto and Z.-B. Zhou; Ionic liquid, its manufacture, and secondary lithium battery and double layer capacitor comprising the liquid. National Institute of Advanced Industrial Science and Technology, Japan, (2005). **WO 2005063773**

[88]   S. Seki, Y. o. Kobayashi, H. Miyashiro, Y. Ohno, A. Usami, Y. Mita, M. Wata-
         nabe and N. Terada; Highly reversible lithium metal secondary battery using a
         room temperature ionic liquid/lithium salt mixture and a surface-coated cathode
         active material. *Chemical Communications* **5**, 544-545 (2006).

[89]   H. Sakaebe, H. Matsumoto and K. Tatsumi; Application of room temperature
         ionic liquids to Li batteries. *Electrochimica Acta* **53**, 3, 1048-1054 (2007).

[90]   R. Bomparola, S. Caporali, A. Lavacchi and U. Bardi; Silver electrodeposition
         from air and water-stable ionic liquid: An environmentally friendly alternative to
         cyanide baths. *Surface and Coatings Technology* **201**, 24, 9485-9490 (2007).

[91]   F. Endres; Ionic liquids for metal deposition. *Nachrichten aus der Chemie* **55**, 5,
         507-511 (2007).

[92]   B. Kuzmanovic, C. J. G. Van Strien, C. E. Bartel and M. Zeitler; Method to
         electrodeposit metals using ionic liquids. Akzo Nobel N.V., Netherland, (2007).
         WO 2007093574

[93]   W. Yang, H. Cang, Y. Tang, J. Wang and Y. Shi; Electrodeposition of tin and
         antimony in 1-ethyl- 3-methylimidazolium tetrafluoroborate ionic liquid. *Jour-
         nal of Applied Electrochemistry* **38**, 4, 537-542 (2008).

[94]   D. Kuang, C. Klein, Z. Zhang, S. Ito, J. E. Moser, S. M. Zakeeruddin and M.
         Gratzel; Stable, high-efficiency ionic-liquid-based mesoscopic dye-sensitized
         solar cells. *Small* **3**, 12, 2094-2102 (2007).

[95]   M. Berginc, U. Opara Krasovec, M. Hocevar and M. Topic; Performance of
         dye-sensitized solar cells based on Ionic liquids: Effect of temperature and io-
         dine concentration. *Thin Solid Films* **516**, 20, 7155-7159 (2008).

[96]   Y. Cao, J. Zhang, Y. U. Bai, R. Li, S. M. Zakeeruddin, M. Gratzel and P. Wang;
         Dye-Sensitized Solar Cells with Solvent-Free Ionic Liquid Electrolytes. *Journal
         of Physical Chemistry C* **112**, 35, 13775-13781 (2008).

[97]   M. Gorlov and L. Kloo; Ionic liquid electrolytes for dye-sensitized solar cells.
         Dalton Transactions 20, 2655-2666 (2008).

[98]   D. Kuang, S. Uchida, R. Humphry-Baker, S. M. Zakeeruddin and M. Graetzel; Organic dye-sensitized ionic liquid based solar cells: remarkable enhancement in performance through molecular design of indoline sensitizers. *Angewandte Chemie (Int. Ed.)* **47**, 10, 1923-1927 (2008).

[99]   T. Nagano, T. Takahashi and H. Sugai; Paint compositions containing polyole-fins and an ionic liquid. Japan, (2006). **US 2006052493**

[100]   G. Buehler and C. Feldmann; Microwave-assisted synthesis of luminescent LaPO$_4$:Ce,Tb nanocrystals in ionic liquids. *Angewandte Chemie (Int. Ed.)* **45**, 29, 4864-4867 (2006).

[101]   G. Buehler, M. Stay and C. Feldmann; Ionic liquid-based approach to doped nanoscale oxides: LaPO$_4$:RE (RE = Ce, Tb, Eu) and In$_2$O$_3$:Sn (ITO). *Green Chemistry* **9**, 9, 924-926 (2007).

[102]   C. Feldmann, G. Buehler and D. Thoelmann; Microwave syntheses of crystal-line metal oxide particles in ionic liquids. Degussa G.m.b.H., Germany, (2007). **DE 102006011754**

[103]   G. Buehler, A. Zharkouskaya and C. Feldmann; Ionic liquid based approach to nanoscale functional materials. *Solid State Sciences* **10**, 4, 461-465 (2008).

[104]   A. Zharkouskaya, C. Feldmann, K. Trampert, W. Heering and U. Lemmer; Ionic liquid based approach to luminescent LaPO$_4$:Ce,Tb nanocrystals. Synthesis, characterization and application. *European Journal of Inorganic Chemistry* **6**, 873-877 (2008).

[105]   C. J. Adams, A. E. Bradley and K. R. Seddon; The synthesis of mesoporous ma-terials using novel ionic liquid templates in water. *Australian Journal of Chem-istry* **54**, 11, 679-681 (2001).

[106]   Y. Zhou and M. Antonietti; Preparation of highly ordered monolithic super-microporous lamellar silica with a room-temperature ionic liquid as template via the nanocasting technique. *Advanced Materials* **15**, 17, 1452-1455 (2003).

[107] B. G. Trewyn, C. M. Whitman and V. S. Y. Lin; Morphological control of room-temperature ionic liquid templated mesoporous silica nanoparticles for controlled release of antibacterial agents. *Nano Letters* **4**, 11, 2139-2143 (2004).

[108] Y. Zhou and M. Antonietti; A Series of Highly Ordered, Super-Microporous, Lamellar Silicas Prepared by Nanocasting with Ionic Liquids. *Chemistry of Materials* **16**, 3, 544-550 (2004).

[109] Y. Zhou, J. H. Schattka and M. Antonietti; Room-Temperature Ionic Liquids as Template to Monolithic Mesoporous Silica with Wormlike Pores via a Sol-Gel Nanocasting Technique. *Nano Letters* **4**, 3, 477-481 (2004).

[110] T. Brezesinski, C. Erpen, K. Iimura and B. Smarsly; Mesostructured Crystalline Ceria with a Bimodal Pore System Using Block Copolymers and Ionic Liquids as Rational Templates. *Chemistry of Materials* **17**, 7, 1683-1690 (2005).

[111] J. Jiang, S.-H. Yu, W.-T. Yao, H. Ge and G.-Z. Zhang; Morphogenesis and Crystallization of Bi_2S_3 Nanostructures by an Ionic Liquid-Assisted Templating Route: Synthesis, Formation Mechanism, and Properties. *Chemistry of Materials* **17**, 24, 6094-6100 (2005).

[112] Y. Liu, J. Li, M. Wang, Z. Li, H. Liu, P. He, X. Yang and J. Li; Preparation and Properties of Nanostructure Anatase TiO_2 Monoliths Using 1-Butyl-3-methyl-imidazolium Tetrafluoroborate Room-Temperature Ionic Liquids as Template Solvents. *Crystal Growth & Design* **5**, 4, 1643-1649 (2005).

[113] L. Yang, W. Meijia, L. I. Zhiying, L. Hongtao, H. E. Ping and L. I. Jinghong; Preparation of porous aminopropylsilsesquioxane by a nonhydrolytic sol-gel method in ionic liquid solvent. *Langmuir* **21**, 4, 1618-1622 (2005).

[114] L. I. Zhonghao, L. Zhimin, Z. Jianling, H. Buxing, D. U. Jimin, G. Yanan and J. Tao; Synthesis of single-crystal gold nanosheets of large size in ionic liquids. *The Journal of Physical Chemistry. B* **109**, 30, 14445-14448 (2005).

[115] H. Kaper and B. Smarsly; Templating and phase behavior of the long chain ionic liquid C_{16}mimCl. *Zeitschrift fuer Physikalische Chemie* **220**, 10-11, 1455-1471 (2006).

[116] K. Zhu, F. Pozgan, L. D'Souza and R. M. Richards; Ionic liquid templated high surface area mesoporous silica and Ru-SiO$_2$. *Microporous and Mesoporous Materials* **91**, 1-3, 40-46 (2006).

[117] H. Kaper, F. Endres, I. Djerdj, M. Antonietti, B. Smarsly, J. Maier and Y.-S. Hu; Direct low-temperature synthesis of rutile nanostructures in ionic liquids. *Small* **3**, 10, 1753-1763 (2007).

[118] T. Wang, H. Kaper, M. Antonietti and B. Smarsly; Templating Behavior of a Long-Chain Ionic Liquid in the Hydrothermal Synthesis of Mesoporous Silica. *Langmuir* **23**, 3, 1489-1495 (2007).

[119] N. Yu, L. Gong, H. Song, Y. Liu and D. Yin; Ionic liquid of [Bmim]$^+$Cl$^-$ for the preparation of hierarchical nanostructured rutile titania. *Journal of Solid State Chemistry* **180**, 2, 799-803 (2007).

[120] Z. Li, L. I. Yu, L. Zheng, N. A. Li, S. Han and G. Li; Characterization Studies on the Ionic Liquid-Templated Mesoporous Silica with Wormlike Pores. *Journal of Dispersion Science and Technology* **29**, 7, 1029-1034 (2008).

[121] E. Cooper, I., C. Andrews, P. Wheatley, P. Webb, P. Wormald and R. E. Morris; Ionic liquids and eutectic mixtures as solvent and template in synthesis of zeolite analogues. *Nature* **430**, 7003, 1012-1016 (2004).

[122] N. Doerr, E. Kenesey, C. Oetsch, A. Ecker, A. Pauschitz and F. Franek; Evaluation of ionic liquids for the application as lubricants. *Tribology and Interface Engineering Series* **48**, Life Cycle Tribology, 123-129 (2005).

[123] N. Canter; Using dicationic liquids as high temperature lubricants. *Tribology & Lubrication Technology* **63**, 5, 12-13 (2007).

2 Colloidal systems

2.1 Amphiphiles - surfactants

Surfactants or amphiphiles are terms used to described molecules formed by to distinctive parts, one that is soluble in water (hydrophilic) and one part that is not (hydrophobic). The hydrophilic part of the surfactant is usually called the head and the hydrophobic part the tail (cp. Figure II-7).

Hydrophilic headgroup   Hydrophobic alkyl chain

Counterion
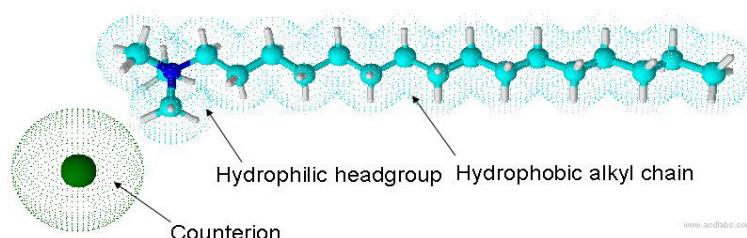
Figure II-7 : Schematic presentation of a single surfactant molecule; hexadecyltrimethylammonium bromide in this case.

Surfactants can be classified depending on the charge of their head group (*HG*). The ones that have a charged *HG* are called ionic surfactants, while those with uncharged head groups are called non-ionic surfactants.

Classification	Head group (*HG*)	Name
Anionic		**Alkylsulfate**
Cationic		**Alkyltrimethylammonium**
Zwitterionic		**N-Alkylbetaine**
Non-ionic		**Polyethylenoxidalkylether**

Table II-9: Classification of surfactants in dependence on the nature of their head groups.

Ionic surfactants can be classified depending on the charge of their *HG* as anionic (negatively charged), cationic (positively charged) or zwitterionic (two charged groups of different sign) (cp. Table II-9) [1-5].

2.2   Adsorption of surfactants at the liquid-gas interface

An elementary feature of surfactants (adsorbate) is their tendency to adsorb at interfaces in an oriented fashion due to their amphiphilic character. The adsorption of amphiphilic molecules at the interface, liquid-gas (*l/g*) interface for example[a], helps them to lower their free energy in order to satisfy their hydrophilic/hydrophobic affinities. In the case of a surfactant solubilised in a polar solvent, the latter is accomplished by orientation of the hydrophobic alkyl-chains away from the polar solvent into the gaseous phase [1-5]. The energy change *ΔG* (and consequently, the change of enthalpy *ΔH* and entropy *ΔS*) in the system occurring from the adsorption process delivers an insight into the interface behaviour of surfactants, since these magnitudes provide information about the efficiency and effectiveness of a surface-active substance.

For the purpose of comparing the performance of surfactants in changing interfaces, as in adsorption, it is necessary to distinguish between the efficiency of the surfactant, i.e. the bulk phase concentration of surfactant required to change the interface properties by some significant mount, and its effectiveness, the maximum change of the interface property that can be observed, regardless of bulk phase concentration of the adsorbate. These two parameters do not necessarily run parallel to each other and sometimes even run counter to each other. In dilute surfactant solutions, the magnitude of change in any interfacial phenomenon related to the adsorption of a surfactant molecule to the surface is a function of concentration of the adsorbate. Thus, efficiency is determined by the ratio between the surfactant concentrations at the interface and in the bulk phase [1, 2].

---

[a] In this work the interface between gas (air or inert gas) and liquid (polar solvent, water and solvent-IL, respectively) is the most important situation. Therefore, the upcoming discussion is only addressed to this interface. In this context, the phrase surface denotes the surfaces of the liquid phase.

2.2.1   Gibbs adsorption theory

In the discussion of adsorption processes, two aspects have to be taken into account: (i) the effect of the adsorbed species on the final equilibrium interfacial energy of the system and (ii) the kinetics of the adsorption process. The consideration to follow is concerned only with equilibrium conditions and dynamic processes are not addressed. In general, exchange of surfactant molecules between the surface and the bulk phase is very fast and therefore such a restriction does not result in significant limitations to the validity of the concept involved. Obvious exceptions would be those processes, which are kinetically "slow", coating operations at the liquid-solid or gas-solid interface for example [2].

The presence of amphiphilic molecules at the interface results in a reduction of the free energy of the interface, i.e. the surface (interfacial) tension σ of the system decreases. The adsorption of a solute can be considered as the existence at the interface of the adsorbed material, n_i^s, that differs from its concentration, n_i^b, in the bulk phase, where s denotes the surface and b the bulk. The amount of component i at the surface in excess of the amount of the same species in the bulk referred to the dividing plane $S - S$ to which each phase is spatially extended is the so-called surface excess concentration Γ_i. Formally, it is defined as by

$$\Gamma_i = \frac{n_i^s}{A} \tag{II-4}$$

In principle, Γ_i may be either positive or negative, and its value is determined by the arbitrary choice of the location of the dividing surface $S - S$ [1, 2, 4-6].

The concept of Gibbs relates the change of the interfacial energy σ_i of a system to the degree of adsorption of a species to the interface and the compositions of the bulk phase, polar solvent in the present case. Under conditions of constant temperature T and pressure p the basic equation is written as

$$d\sigma_i = -\Gamma_1 d\mu_1 - \Gamma_2 d\mu_2 - \Gamma_3 d\mu_3 - ... \tag{II-5}$$

where σ_i is the surface tension (interfacial energy), Γ_i is the surface excess of component i at the surface and interface, respectively, and μ_i is its chemical potential in each bulk phase (liquid or gas). The change in the free energy dG of a system may be given by

$$dG = -SdT + Vdp + \sigma dA + \sum \mu_i dn_i \tag{II-6}$$

where S is the entropy, p is the pressure, V is the volume, A the interface, n_i is the amount of substance i in each bulk phase, and T is the absolute temperature. At equilibrium and under constant conditions of T, p and n_i, Eq. (II-6) is reduced to

$$dG = \sigma dA \tag{II-7}$$

If the surface excess of component i is allowed to vary during adsorption, then

$$d\sigma = -\sum \Gamma_i d\mu_i \tag{II-8}$$

As already mentioned, Γ_i is defined by the choice of the location of the dividing surface. For simplification, it is convenient to define $S - S$ so that the surface excess of one component, normally the bulk solvent phase, is zero ($\Gamma_1 = 0$). For a simple two-component system (e.g. 2 dissolved in 1) Eq. (II-8) is reduced to

$$d\sigma = -\Gamma_2 d\mu_2 \tag{II-9}$$

The chemical potential of a species is correlated to the species activity a_2 by

$$\mu_2 = \mu_2^0 + RT \ln a_2 \tag{II-10}$$

so that

$$d\mu_2 = RTd \ln a_2 \tag{II-11}$$

$$d\sigma = -\Gamma_2 RT d \ln a_2 \qquad \text{(II-12)}$$

For dilute solutions where the activity coefficient of the solute is approximately 1, the concentration c_2 can be substituted for a_2. This leads to the final form of the Gibbs equation:

$$\Gamma_2 = -\frac{1}{RT}\frac{d\sigma}{d \ln c_2} \qquad \text{(II-13)}$$

The form of Eq. (II-13) holds true for the adsorption of a non-dissociated species, e.g. non-ionic surfactants to the interface. In the case of ionic surfactants, however, consisting of cations and anions, dissociation of these species in a polar solvent has to be taken into account. Assuming a monovalent completely dissociated ionic surfactant, Eq. (II-13) must be modified by consideration of the dissociation reaction of the ionic surfactant in equilibrium. For a monovalent ionic surfactant the dissociation reaction in equilibrium is described by

$$\Delta G_R = \mu^+ + \mu^- - \mu_2 = 0 \qquad \text{(II-14)}$$

and

$$d\mu_2 = d\mu^+ + d\mu^- \qquad \text{(II-15)}$$

where μ^+ and μ^- are the chemical potential of the cation and the anion, respectively. At the surfactant concentration c_2 and with the dissociation degree α representing the degree of dissociated surfactant molecules (Eq. (II-16)), one obtains

$$c^+ = c^- = (\alpha c_2) \qquad \text{(II-16)}$$

$$d\mu^+ = d\mu^- = RT d \ln(\alpha a_2) \qquad \text{(II-17)}$$

$$d\mu_2 = 2RTd\,ln(\alpha a_2)$$ (II-18)

Applying Eq. (II-18) in Eq. (II-13) at infinite dilution, the final form of the Gibbs equation for monovalent completely dissociated ionic surfactants is written as

$$\Gamma_2 = -\frac{1}{2RT}\frac{d\sigma}{d\,ln\,c_2}$$ (II-19)

Eq. (II-19) can be used for the determination of the surface excess concentration of the adsorbed substance and, in principle, to relate that quantity to the structure of the molecule, especially, when the interfacial energy can be directly determined (e.g. for liquid-liquid or liquid-gas systems). The surface excess concentration at surface saturation Γ_{max} is, given as

$$\Gamma_{max} = \frac{1}{2RT}\frac{d\sigma}{d\,ln\,c_2}$$ (II-20)

It is the maximum value that adsorption can attain and is a useful measure of the effectiveness of adsorption of the surfactant at the interface. The Γ_{max} value is directly correlated to the minimum area per molecule at surface saturation A_{min} via

$$A_{min} = \frac{1}{N_A\Gamma_{max}}$$ (II-21)

The minimum area per molecule at the interface/surface provides information on the degree of packing and orientation of the adsorbed surfactant molecule when compared with the dimensions of the present molecule as obtained by use of molecular models [1,2].

2.2.2 Efficiency & effectiveness of surface tension reduction

For comparing the performance of surfactants at l/g and l/l interfaces, it is very useful to have a parameter that measures the concentration of surfactant in the one phase needed to produce a given amount of adsorption at the interface. This is directly related to the efficiency of surface tension reduction of the surfactant. A commonly used concept in this context is the negative logarithm of the concentration of surfactant in the bulk phase required to produce an interfacial or surface tension reduction $\Delta\sigma = 20$ mN/m (or surface pressure Π of 20 mN/m) of the interface:

$$-log\, C_{(\Delta\sigma=20)} \equiv pC_{20} \qquad \text{(II-22)}$$

This concept is based on the following considerations:

(i)   The ideal measure of the efficiency of a surfactant at the interface is a function of the minimum concentration of amphiphile in the bulk phase necessary to produce maximum surface tension reduction.

(ii) From investigations of the σ-$log\,c$ plots in the literature it was concluded that when the interfacial or surface tension of the pure solvent has been decreased about 20 mN/m, the surface excess concentration Γ_2 of the surfactant reached nearly its maximum value Γ_{max} (saturation). At this point, the surface is nearly completely saturated (85.0 – 99.9%) and thus it can be a reference point for the comparison of surfactants concerning their efficiency.

Since surface or interfacial tension reduction depends on the replacement of solvent molecules at the interface by surfactant molecules, the efficiency of a surfactant in reducing surface tension should reflect the concentration of the surfactant at the interface relative to that in the bulk liquid phase. For surfactants in aqueous solution, the efficiency increases with increase in the hydrophobic character of the surfactant, e.g. with increasing alkyl-chain length of a homologous surfactant series [1, 7].

The effectiveness of a surfactant in reducing surface tension can be measured by the amount of reduction (or surface pressure, Π), attained at maximal surface saturation. As will be discussed later, the surface tension of a solution of an individual surfactant decreases steadily as the bulk concentration of surfactant is increased until the concentration reaches a nearly constant value known as the critical micelle concentration *cmc* above which the tension remains virtually unchanged. The surface tension at the *cmc* is therefore very close to the minimum tension (or maximum surface pressure, Π_{cmc}) that the system can achieve. Consequently, the surface pressure at this point is a suitable measure of the ''effectiveness'' of a surfactant in reducing surface tension [1, 7].

2.2.3   Efficiency of Adsorption: Free Energy of adsorption

The standard free energy change upon adsorption ΔG_{ads}^{0} tells one whether the adsorption is spontaneous (negative values of ΔG_{ads}^{0}) and the magnitude of the driving force. Normally, ΔG_{ads}^{0} is calculated from surface tension measurement data by the following equation [1, 7]

$$\Delta G_{ads}^{0} = 2.303RT \left[log\left(\frac{C_{20}}{\omega} \right) + log\, f_{\pm} \right] - \left[6.023 \cdot 20 \cdot A_{min} \right] \qquad \text{(II-23)}$$

where C_{20} is the concentration of the surfactant in the bulk phase at Π_{cmc} = 20 mN/m, ω is the number of moles per liter of the solvent (water or solvent-IL for the present work), A_{min} is the area of the surfactant monomer at the surface, and $log\, f_{\pm}$ is the amphiphile activity coefficient, which can be considered as 1 at low amphiphile concentrations. The ΔG_{ads}^{0} values of amphiphiles are usually negative indicating that adsorption of these molecules at the interface is a spontaneous process. In this context, it is important to note that the major contribution to the negative values of the free energy change and thus the driving force for adsorption at the interface of these compounds is the positive entropy change upon adsorption ΔS_{ads}^{0}, as the entropy is related to ΔG_{ads}^{0} by

$$\Delta G_{ads}^{0} = \Delta H_{ads}^{0} - T\Delta S_{ads}^{0} \qquad \text{(II-24)}$$

where ΔH^0_{ads} is the enthalpy change upon adsorption. In addition, the negative loga-rithm of the bulk phase concentration of surfactant necessary to reduce the surface ten-sion about 20 mN/m is related to the standard free energy change involved in the trans-fer of the surfactant molecule from the interior of the bulk phase to the interface near surface saturation. This feature is very important concerning the fact that the total stan-dard energy change on adsorption ΔG^0_{ads} can be broken into the individual standard free energy changes related to the influence of the different structural groupings in the sur-factant molecule. Thus, the efficiency with which the surfactant is adsorbed at a surface or interface enables correlations between the various structural groupings in the surfac-tant and its interfacial properties. For a single-chain surfactant of the structure $CH_3(CH_2)_nHG$, where HG is the hydrophilic head group of the molecule, the standard free energy on adsorption ΔG^0_{ads} can be broken into the following portions:

(i)   Standard free energy change associated with the transfer of the terminal methyl group from the interior of the liquid phase to the interface at $\Delta\sigma = 20$ mN/m.

(ii)   Standard free energy change associated with the transfer of the $-CH_2-$ groups of the hydrocarbon chain from the interior of the liquid phase to the interface at $\Delta\sigma = 20$ mN/m.

(iii)   Standard free energy change associated with the transfer of the head group from the interior of the liquid phase to the interface at $\Delta\sigma = 20$ mN/m.

Thus, the transfer of the discrete surfactant segments (including the methylene groups, the methyl group, and the head group) from bulk water to the interface contrib-utes to ΔG^0_{ads} as given by the following equation

$$\Delta G^0_{ads} = m\Delta G^0_{ads}(-CH_2-) + \Delta G^0_{ads}(HG) + \Delta G^0_{ads}(-CH_3) \qquad (II-25)$$

where m is the number of the methylene groups, $G^0_{ads}(-CH_2-)$ is the contribution of one methylene group of the alkyl chain, $G^0_{ads}(-CH_2-)$ is the contribution of the termi-nal methyl group, and $G^0_{ads}(HG)$ is the contribution of the head-group. Eq. (II–25) pre-

dicts a linear correlation between ΔG^0_{ads} and m, where the intercept includes contributions from the terminal methyl group and the head group. Since $G^0_{ads}(HG)$ and $G^0_{ads}(-CH_3)$ are independent of the chain length of the surfactant, its contribution is constant in a homologous series and the relation of pC_{20} and $\Delta G^0_{ads}(-CH_2-)$ becomes [1, 2]:

$$pC_{20} = \left(-\frac{\Delta G^0_{ads}(-CH_2-)}{2.303RT} \right) m + const. \tag{II-26}$$

Eq. (II-26) impresses that pC_{20} is a linear function of the number of carbon atoms in a straight-chain hydrophobic group, increasing as m increases. The larger the value of pC_{20}, the more efficiently the surfactant is adsorbed at the interface and the more efficiently it reduces the interfacial or surface tension. The efficiency of surfactants normally increases linearly with an increasing number of carbon atoms in the hydrophilic chain, reflecting the negative free energy on adsorption of a methylene group at the interface. An addition of two methylene groups to the hydrophobic chain results in an increase of the pC_{20} value by about 0.6, which corresponds to a concentration decrease of the surfactant in the bulk phase of 30% compared to the concentration previously required [1, 2]. The value of $-\Delta G^0_{ads}$ per $-CH_2-$ group is about 3 to 3.5 kJ/mol at 25°C. Therefore, an increase in the length of the alkyl chain increases the tendency of the compound to adsorb at the interface.

2.3   Self-assembly of surfactants in solution: micelles

Beside the ability of surfactants to adsorb at interfaces, another important feature dominates these compounds in aqueous solution. As it has been mentioned previously, materials that contain a hydrophilic as well as a hydrophobic group solubilised in a polar solvent minimize their free energy by adsorption at interfaces orienting their hydrophobic part away from the polar solvent. However, there is another possibility of minimizing the free energy of the system and therefore decrease the distortion of the solvent structure. The free energy of a surfactant system can also be decreased by aggregation

of the surface-active molecule into clusters (micelles) with their hydrophobic groups directed toward the interior of the cluster and their hydrophilic groups directed toward the polar solvent [1, 2, 4-6, 8].

The formation of micelles is often explained by the "hydrophobic effect" [9-12]. The hydrophobic effect is the result of two contributions, (i) the structuring of water molecules around the solute and (ii) the energy needed to create a cavity in the solvent large enough for incorporating the non-polar solute. The first point is the result of fewer conformations available for the vicinal water molecules around the polar head group compared to free water molecules, causing negative entropy. The second opposite contribution can be correlated to the large energy required to form a cavity for the incorporation of the hydrophobic part leading to an unfavourable arrangement, due to both, the high cohesion in water arising from the hydrogen-bonding, and the small size of the water molecules compared to, e.g. alkanes. These facts impress a balance between the forces, hindering micellization and those promoting it. An important consequence of this mechanism is that the magnitude of the hydrophobic effect is proportional to the area of the hydrophobic contact between water and the apolar part of the solute [11-13].

As the formed micellar structures are in the nano scale, these aggregates are investigated by means of colloid science. However, differing from "hard matter" such as inorganic nanomaterials and polymers (also situated in the nano meter range), aggregates consisting of surfactant molecules are easily deformable and rearranged by physical and chemical factors leading to pronounced differences and are more precisely described as "soft matter".

Surfactant self-assembly leads to a variety of different structures (Figure II-8). The major types of structures appear to be (i, ii) relatively small, spherical structures, (iii) elongated cylindrical, rod-like micelles with hemispherical ends, (iii) large flat, lamellar phases, (v) vesicles - spherical structures consisting of bilayer lamellar micelles arranged in one or more concentric spheres, and (vi) bicontinuous structures with surfactant molecules aggregated into connected films [4].

(i) Micelle   **(ii) Reverse micelle**   **(iii) Cylindrical micelles**

(iv) Lamellar phase   **(v) Vesicle**   **(vi) Bicontinuous structure**
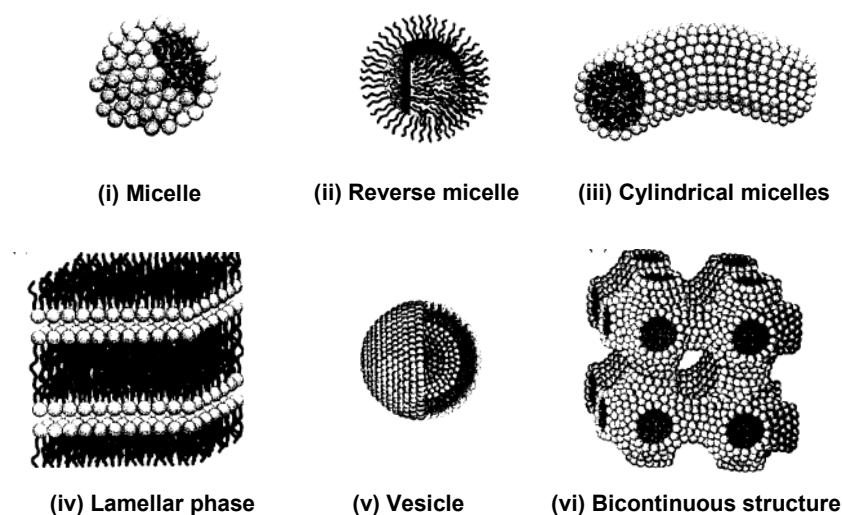
Figure II-8 : Amphiphilic aggregate structures formed by surfactants in aqueous solution. Taken from Ref. [4].

2.3.1   Critical micelle concentration (*cmc*)

At low concentrations, surfactants exist as monomers (ionic surfactants are dissociated), but as the concentration of the surfactant in aqueous solution increases, aggregates, i.e. micelles, are formed. This happens at a well defined concentration denoted as the critical micelle concentration (*cmc*). Another convenient expression is critical aggregation concentration (*cac*) which is often used, especially, when the formed aggregates are not well investigated. This behaviour of surfactants is well monitored by measuring physical parameters of the solution as a function of amphiphile concentration. An abrupt change of the physical property indicates the *cmc* and the *cac*, respectively, as illustrated by Figure II-9.

When surfactants are dissolved in water at low concentrations, they exist as monomers or dissociated monomers in the case of ionic surfactants, respectively. Dilute ionic amphiphile solutions below the *cmc* are similar to those of simple electrolytes. At some higher concentration, which is different for different surfactants, abrupt unusual changes of the physical properties of the bulk are recorded.
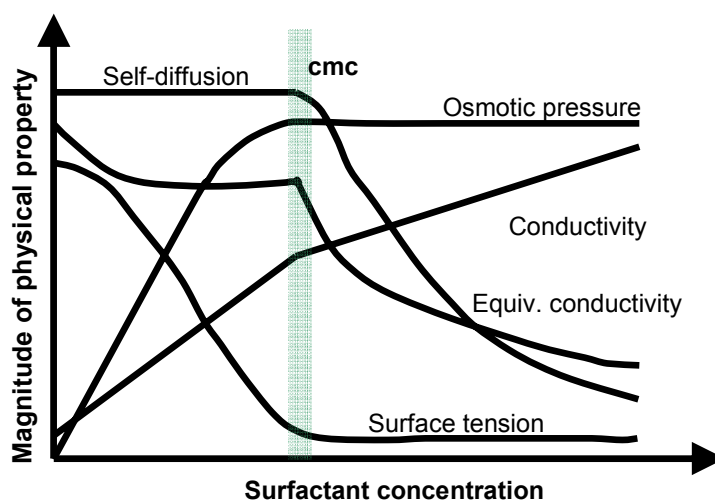
Figure II-9: Schematic presentation of the concentration dependence of some physical properties for solutions of a micelle forming amphiphile.

For example, the surface tension, and also the osmotic pressure, takes on a nearly constant value, while the self-diffusion coefficient starts to decrease. In the case of ionic surfactants, a monitoring via conductivity measurements is also possible and often preferred as this technique is very precise and easy to perform. All these observations are consistent with a change from a solution containing single monomer surfactant molecules or ions, to a situation where the amphiphile exists in a self-assembled state.

2.3.2   Influence of surfactant structure on the *cmc*

The value of the cmc strongly depends on the present surfactant. During the last years a lot of work has been done on elucidating the various factors that determine the cmc, especially in aqueous solution [14]. From these investigations, several general conclusions can be drawn about the influence of the chemical structure of the surfactant on the *cmc* [5, 15, 16]:

(i)   The *cmc* decreases with increasing hydrocarbon chain length of the amphiphile. The *cmc* decreases by a factor of approximately 2 for ionics and by a factor of 3 for nonionics on adding one $-CH_2-$ group to the alkyl chain.

(ii)   The *cmc*s of a non-ionic surfactant is generally lower than those of ionics with the same alkyl-chain length.

(iii)   Cationic surfactants have slightly higher *cmc*s than anionics.

(iv)   In the case of ionic amphiphiles the valency of the counter ion has a great influence. Simple monovalent inorganic counterions give nearly the same *cmc*, while a higher valency to 2 results in a reduction of the cmc by a factor of about 4.

 (v)   Perfluorinated alkyl chains lower dramatically lower the *cmc*, whereas partial fluorinated increase the *cmc*.

Especially, the relationship between the length of the chain of a hydrocarbon amphiphile and the critical micelle concentration is a crucial factor in surfactant science. It is known that the *cmc* decreases logarithmically as the number of carbons in the chain of a homologous series *n* increases. Mathematically, this relation is expressed by the Klevens equation [17]:

$$log(cmc) = A - Bn$$ (II-27)

where *A* and *B* are constants specific to the homologous series under the same micro-environmental conditions (i.e. temperature, pressure…) [18]. Generally, the value of *A* is approximately constant for a particular head group, whereas *B* is constant and approximately equal to 0.30 (log 2) for all paraffin chain surfactants solubilised in water having a single charged ionic head group. For a non-ionic amphiphiles *B* becomes 0.5. The basis for the rule mentioned earlier that the *cmc* being halved for each increase in the hydrophobic chain by one carbon atom is apparent from this relation.

2.3.3   Temperature dependence of surfactant solubility

The solubility of ionic surfactants in water shows strong temperature dependence. Figure II-10 schematically illustrates the amphiphile solubility as a function of temperature. The solubility may be very low at low temperatures and it increase rapidly in a narrow temperature range. This phenomenon is generally denoted as the "Krafft phenomenon" [1, 2, 4-6, 8]. In fact, the Krafft point is defined as the intersection of the solubility curve and the *cmc* curve. Additionally, the so-called Krafft temperature is defined in literature. The latter is the denoted as the temperature of the Krafft boundary at an arbi-

trarily selected composition, often 1 wt.% of ionic amphiphile in the polar solvent [19]. The Krafft point and the Krafft temperature, respectively, vary extremely with changes in the chemical structures of ionic surfactants [20-22]:

(i) The Krafft point/temperature decreases as the alkyl chain length increases.

(ii) The head group and the present counterion influence the Krafft temperature dramatically. For example, the Krafft point/temperature of cationic surfactants is higher for bromide than for chloride, and still higher for iodide. With divalent counterions, the increase of the Krafft point/temperature is typically more dramatic. Salt addition raises or decreases the Krafft point/temperature depending on the added salt.

The Krafft phenomenon is often described as interplay between the temperature dependence of the amphiphile monomer solubility and the temperature dependence of the *cmc*. The temperature dependence of the latter can be considered, in a good approximation, as very weak. If the surfactant concentration is below the *cmc* the total solubility is limited by the monomer solubility, but if the monomer solubility reaches the *cmc*, micelles are formed, which are highly soluble compared to the monomers. This indicates why a small increase in monomer solubility, which results, in the concept of the Krafft phenomenon, from a temperature increase, leads to a dramatic raise of the overall amphiphile solubility. More general, the Krafft point/temperature is determined by the energetic relationship between the solid crystalline state (melting point) and the heat of hydration of the system [21]. Lower Krafft points/temperatures are generally obtained by making the packing of the surfactant in the solid state unfavourable and by using highly hydrated polar head groups [2, 4, 5]. An unfavourable crystal packing can be achieved in the following ways [23, 24]:

(i) Branching of the hydrophobic alkyl chain

(ii) Introduction of a double bond in the alkyl chain

(iii) Introduction of polar segments in the alkyl chain

In contrast, non-ionic surfactants do not exhibit a Krafft temperature, because of their different mechanism of solubilization (hydrogen bonds between the EO units and water in contrast to hydration of the ionic head group). Nevertheless, they also have a characteristic temperature–solubility relationship in water that causes them to become less soluble as the temperature increases. In some cases, phase separation occurs, producing a cloudy suspension of surfactant. The temperature (usually a range of temperature) at which the phases separate is referred to as the ''cloud point'' for that non-ionic surfactant [1, 2, 4].
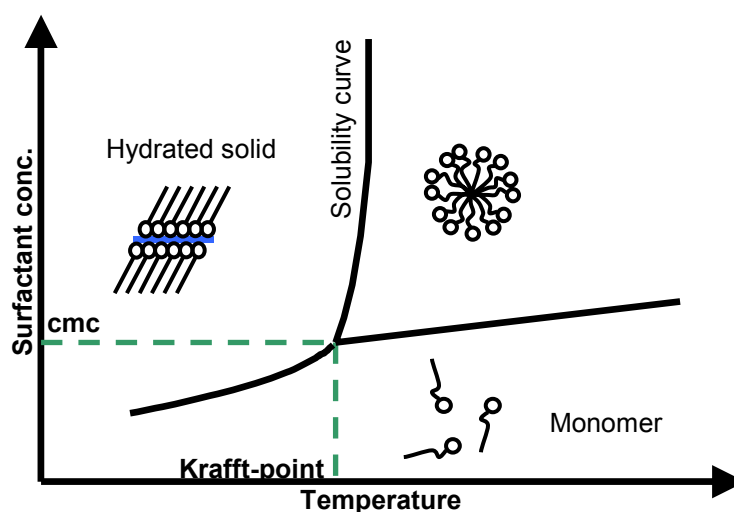
Figure II-10 : Solubility of an amphiphile as a function of temperature in the region of the Krafft point.

2.3.4   Structure & shape of micelles: packing parameter

Surfactant self-assembly in water leads to variety of different structures, as already discussed previously (Figure II-8). In fact, the most common structure is the spherical micelle with an interior composed of the hydrocarbon chains and a surface of polar head groups towards the bulk water phase. The hydrocarbon core has a radius nearly equal to the length of the extended alkyl chain. In contrast, the cross-section of elongated cylindrical micelles is similar to that of spherical aggregates, but the length is highly variable resulting in polydisperse solutions. Another possibility of surfactant self-assembly is the formation of bilayers, which build up lamellar phases or vesicles.

The latter is characterized by two distinct water compartments, with one forming the core and one the external medium. The reverse micelle is a special case of the spherical micelle having a water core surrounded by the amphiphile head groups. The hydrophobic alkyl chains form the continuous medium [1, 2, 4-6, 8].

The formation of this type of assemblies strongly depends on the geometry of the single surfactant molecule, which is well presented by the critical packing parameter P as was shown by Israelachvilli et al. [25, 26]. P is defined as

$$P = \frac{v}{al} \tag{II-28}$$

where v is the volume of a single surfactant hydrocarbon chain, a is the cross-sectional area of one surfactant molecule in the aggregate, and l is the length of the fully extended hydrocarbon chain. The packing parameter can be evaluated by the aggregation number N_{agg}, which represents the number of surfactant molecules forming the assembled aggregate. The latter is defined as the ratio of the core volume of the micelle V_{mic} to the volume of one single surfactant alkyl chain v:

$$N_{agg} = \frac{V_{mic}}{v} = \frac{4}{3}\pi \frac{R_{mic}^{3}}{v} \tag{II-29}$$

The aggregation number is also given by the ration of the area of the micelle (assuming the surface is completely covered with surfactant head groups) to the cross-sectional area per surfactant molecule:

$$N = \frac{A_{mic}}{a} = 4\pi \frac{R_{mic}^{2}}{a} \tag{II-30}$$

Combining Eq. (II-30) and Eq. (II-31) yields:

$$\frac{v}{aR_{mic}} = \frac{1}{3} \tag{II-31}$$

Spherical micelle, ellipsoids

$P < \frac{1}{3}$

Cylindrical micelle

$\frac{1}{3} \leq P \leq \frac{1}{2}$

Planar bilayer

$P \approx 1$

Vesicle, flexible bilayers

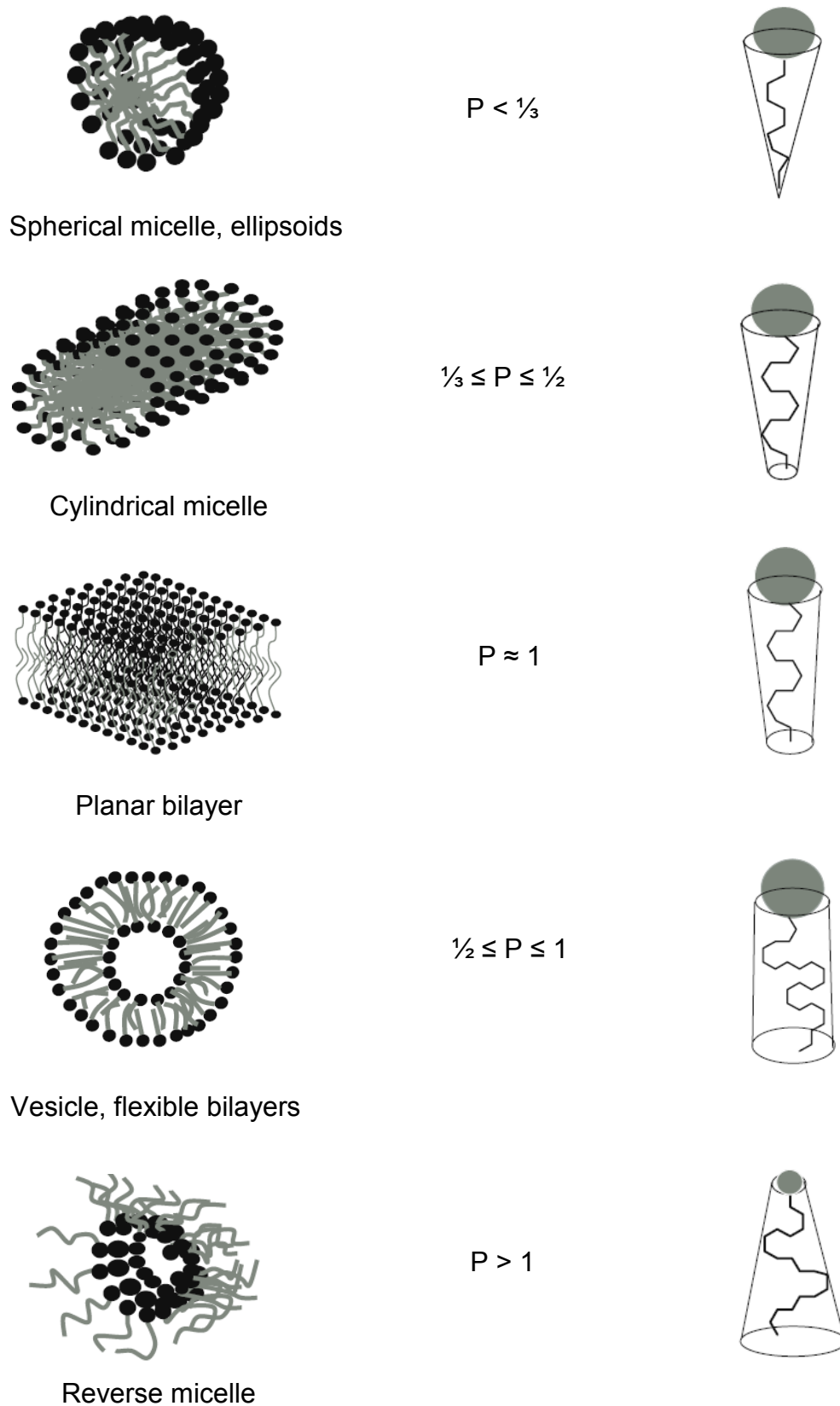$\frac{1}{2} \leq P \leq 1$

Reverse micelle

$P > 1$

Figure II-11 : Packing parameters for different self-assembled structures.

The radius of the micelle R_{mic} cannot exceed the length of the fully extended chain l, so Eq. (II-31) can be written as

$$P = \frac{v}{al} \leq \frac{1}{3}$$ (II-32)

The values of v and l can be estimated by the two formulae of Tanford [27]:

$$v = 27.4 + 26.9 n_c \ \text{Å}^3$$ (II-33)

and

$$l = 1.5 + 1.265 n_c \ \text{Å}$$ (II-34)

The aggregates, which do not exhibit spherical shapes, are characterized by packing parameters larger than ⅓. The surfactant packing parameter range and the various surfactants aggregate shapes are compared in Figure II-11. The spherical micelles can be considered to be built from the packing of cones, corresponding to effective molecular volumes (large difference between the cross-sectional area of the head group and tail group). Other aggregate of types, e.g. cylindrical micelles, are preferably formed by surfactants with truncated cones (with packing parameters ⅓ < P < ½). The flexible bilayers and vesicles result from a packing of surfactants with almost equal cross sectional areas of head group and tail group (½ < P ≤ 1). For P ≈ 1, planar extended bilayered structures can be expected. When P exceeds 1 (P > 1), reversed micelles are the favoured aggregate.

Apart from these aggregate shapes, it was shown that the surfactant molecules can also pack into prolate and oblate spheroids [27, 28]. Figure II-12 gives the schematic view of the prolate and oblate spheroids. (i) The semi-major axis 'a' (rotational axis) is larger than the semi-minor axis 'b' in case of prolate spheroids and (ii) In case of oblate spheroids the rotational axis 'a' is smaller than the semi axis 'b'.

(i) Prolate ellipsoid   (ii) Oblate ellipsoid
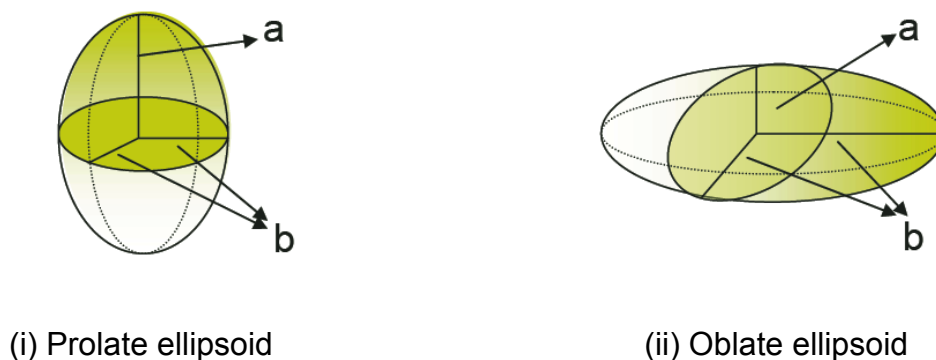
Figure II-12: Schematic representation of the models of prolate (i) and oblate (ii) spheroids (*a*, the major semi-axis and *b*, the minor semi-axis).

2.3.5   Models of surfactant aggregation

Two well-known models generally discuss micelle formation: (i) the pseudo-phase separation model and the (ii) mass action law model [4, 29]. The first model treats the surfactant solution as a two-phase system, where the micelles are considered as a separate phase. In this case, the Gibbs phase rule would apply and micelles are in thermodynamic equilibrium with the surfactant monomers in solution. Within the framework of the pseudo-phase model, solubilization is considered as equilibrium of the solute between the micellar phase and the bulk,

$$\mu_{mono} = \mu_{mic} \tag{II-35}$$

where μ_i is the chemical potential of the solute in the aqueous bulk phase (monomeric surfactant) or in the micellar phase (aggregated surfactant) [8].

An alternative approach to describe micellization is the mass action model. This model is further able to consider a fraction of counterions bound to the micelles and thus is better suited for modelling ionic surfactants. At equilibrium, the micelle formation of an ionic surfactant, is written as

$$nS + mC \rightleftharpoons S_nC_m^z \equiv M^z \tag{R.III-9}$$

where S represents the surfactant ions, C the surfactant counter ions, and S_n the formed aggregate with the bound counterions C_m, abbreviated as M^z. z is the micellar charge, m is the number of counterions bound to the micelle, and n is the aggregation number (N_{agg})[30]. The equilibrium constant K of the reaction (R.III-9) can then be formulated as

$$K = \frac{a_{M^z}}{a_S{}^n a_C{}^m} \qquad\qquad\qquad \text{(II-36)}$$

where a_i is the activity of the species i. If one assumes that the activity coefficient is 1, which is a good approximation for dilute solutions, Eq. (II-36) becomes

$$K = \frac{X_{M^z}}{X_S{}^n X_C{}^m} \qquad\qquad\qquad \text{(II-37)}$$

where X_i is the mol fraction of species i. In terms of the present equilibrium, it follows that

$$\Delta G^0 = -RT(\ln X_{M^z} - n \ln X_S - m \ln X_C) \qquad\qquad \text{(II-38)}$$

where R and T have their usual meaning. ΔG^0 is the free energy of micellization. The latter can be further expressed by

$$\Delta G^o = \mu^o_{M^z} - n\mu^o_S - m\mu^o_C \qquad\qquad\qquad \text{(II-39)}$$

in which μ^o_i is the standard chemical potential of species i. If one defines ΔG^0_{mic} as the standard Gibbs free energy change of micellization per mole of amphiphile, $\Delta G^0_{mic} = \Delta G_{mic} / n$, then

$$\Delta G_{mic}^{0} = \frac{1}{n} \mu_{M^z}^o - \mu_S^o - \frac{m}{n} \mu_C^o \qquad \text{(II-40)}$$

and

$$\Delta_{mic} G^o = -\frac{RT}{n} \ln K = -RT(\frac{1}{n} \ln X_{M^z} - \ln X_S - \frac{m}{n} \ln X_C) \qquad \text{(II-41)}$$

Introducing the ratio $X_\sigma = X_{M^z} / X_{cmc}$ as Tanford did and recognizing that, at the *cmc*, $X_S = X_{cmc} - X_{M^z}$, and that $X_C \approx X_S$ (X_{cmc}) when the ionic surfactant $S_{\nu_S} S_{\nu_C}$ is like a symmetric electrolyte, i.e. $\nu_S = \nu_C$, one obtains [9]

$$\frac{\Delta G_{mic}^{0}}{RT} = (1 + \frac{m}{n} - \frac{1}{n}) \ln X_{cmc} - \frac{1}{n} \ln X_\sigma + \ln(1 - X_\sigma) \qquad \text{(II-42)}$$

For large n (for example, $n \geq 50$) the $1/n$ terms and the last term in the right-hand side are negligible. Hence in this case, Eq. (II-42) is reduced to

$$\Delta G_{mic}^{0} = (1 + \alpha_{mic}) RT \ln X_{cmc} \qquad \text{(II-43)}$$

where

$$\alpha_{mic} = \frac{m}{n} \qquad \text{(II-44)}$$

is the degree of counterion binding. Instead of the degree of counterion binding, the degree of ionization of micelles, β, is often taken into account as $\beta = 1 - \alpha_{mic}$ which results in the expression

$$\Delta G_{mic}^{0} = (2 - \beta) RT \ln X_{cmc} \qquad \text{(II-45)}$$

The enthalpy of micellization, ΔH^0_{mic}, is obtained from ΔG^0_{mic} using the Gibbs-Helmholtz relation:

$$\left(\frac{\partial\left(\dfrac{\Delta G^0_{mic}}{T}\right)}{\partial T}\right)_p = -\frac{\Delta H^0_{mic}}{T^2} \qquad (\text{II-46})$$

Taking into account the dependence of ΔG^0_{mic} on n and β, which may vary with the temperature, one obtains

$$\Delta H^0_{mic} = -RT^2(2-\beta)\left(\frac{\partial \ln X_{cmc}}{\partial T}\right)_p + \frac{\partial f(n;\beta)}{\partial n}\frac{\partial n}{\partial T} \qquad (\text{II-47})$$

where the quantity $f(n,\beta)$ is, in principle, a function of n and β. ΔH^0_{mic} is usually been determined by this (indirect) method using Eq. (II-47) but neglecting the contribution of the second term:

$$\Delta H^0_{mic} = -RT^2(2-\beta)\left(\frac{\partial \ln X_{cmc}}{\partial T}\right)_p \qquad (\text{II-48})$$

In many cases, comparison of ΔH^0_{mic} values obtained from Eq. (II-47) with those determined directly by calorimetry suggests that the temperature dependence of the terms containing n and β compensate in such a way that ΔH^0_{mic} can be given by the simplified relation, Eq. (II-48). Other authors have suggested this too, so Eq. (II-48) was used in the thermodynamic analysis presented in this work [31, 32].

The standard entropies of micellization ΔS^0_{mic} can be obtained from the relation

$$\Delta S^0_{mic} = \frac{\Delta H^0_{mic} - \Delta G^0_{mic}}{T} \qquad (\text{II-49})$$

Therefore, from the temperature dependence of the *cmc* one can determine the values of ΔG^0_{mic}, enthalpy ΔH^0_{mic}, and entropy ΔS^0_{mic} with the help of the following previously presented equations [1].

Generally, the value of ΔH^0_{mic} decreases with the increase in temperature and with increase of the hydrocarbon chain of the surfactant. The Gibbs free energy of micellization is negative as expected for spontaneous micellization near the *cmc*. Its value becomes more negative as the temperature and the alkyl chain length increase. Fundamentally, micellization is entropy-driven, i.e. the contribution of ΔH^0_{mic} to the Gibbs free energy is less than that of $T\Delta S^0_{mic}$. The entropy decreases with increasing in temperature and increases with longer alkyl chains [1, 8, 15].

The contribution of the discrete surfactant segments (including the methylene groups, the methyl group, and the head group) from bulk water to the interface contributes to ΔG^0_{mic} as already discussed above for adsorption. ΔG^0_{mic} is written analogously to Eq. (II–50):

$$\Delta G^0_{mic} = m\Delta G^0_{mic}(-CH_2-) + \Delta G^0_{mic}(HG) + \Delta G^0_{mic}(-CH_3) \qquad \text{(II–50)}$$

where *m* is the number of the methylene groups, $G^0_{mic}(-CH_2-)$ is the contribution of one methylene group of the alkyl chain, $G^0_{mic}(-CH_2-)$ is the contribution of the terminal methyl group, and $G^0_{mic}(HG)$ is the contribution of the head-group. Eq. (II–50) postulates a linear correlation between ΔG^0_{mic} and *m*, where the intercept includes contributions from the terminal methyl group and the head group. Since $G^0_{mic}(HG)$ and $G^0_{mic}(-CH_3)$ are independent of the chain length of the surfactant, its contribution is constant in a homologous series [1, 2].

2.3.6   Non-aqueous solvents: Solvophobic effect, Gordon parameter, cohesion energy density, internal pressure

The most common solvent, as already mentioned, in surfactant science is water, as it is considered to be a unique liquid promoting amphiphilic self-aggregation due to

its high cohesive energy, its high relative dielectric constant ε_r, and its considerable hydrogen bonding ability [33, 34]. Evans et al. suggested that especially the hydrogen bonding ability is a prerequisite for micellization to happen [4, 35]. The low solubility of the surfactant hydrocarbon chain forces aggregation in polar solvents like water to occur (solvophobic effect) [33]. It arises because of the introduction of a weakly interacting species into a liquid of high cohesive energy. Evans et al. correlated the self-assembly promotion of solvents with the Gordon parameter G_P, which is a useful parameter for characterizing the cohesiveness of a solvent. The Gordon parameter is defined as

$$G_P = \frac{\sigma}{V_m^{1/3}} \tag{II-51}$$

where σ is the surface tension and V_m is the molar volume of the solvent. Evans et al. postulated that a sufficient high Gordon parameter (≥ 1.3 J/m^3) is a crucial factor for solvents to support self-aggregation of amphiphilic molecules in solution [4]. Table II-10 summarizes Gordon parameters and related values of ε_r and σ of various polar solvents as published by Evans et al [36].

Polar solvent	ε_r	σ (mN/m)	G_P (J/m^3)
Water	78.4[a,b]	72.0 [a,b]	2.75[a, b], 2.8[c], 2.743[d]
Hydrazine	51.7[a,b]	66.4 [a,b]	2.10[a, b]
EAN	∞[a,b]	46.0 [a,b]	1.060[e], 1.40[b], 1.30[a, b]
Formamide	109.0[a,b]	58.2 [a,b]	1.50[a, b]
Ethylene glycol	37.7[a,b]	47.0 [a,b]	1.20[a, b]
3-Methylsydnone	144.0[a,b]	57.0 [a,b]	1.40[a, b]

Table II-10 : Properties of polar solvents at 25°C except for 3-methylsydnone, which is at 40°C. [a]Ref. [4]. [b]Ref. [36]. [c]Ref. [10]. [d]Ref. [73]. [e]Ref. [74].

Beside the investigations of Evans et al. concerning self-assembly of amphiphilic molecules in non-aqueous solvents, Rico and Lattes also examined micelle for-

mation in alternative media. They supposed that a water replacement should have the following properties in order to enable surfactant aggegation: (i) High polarity, (ii) high solvating power, and (iii) highly structured. In this connection, they recommended two physical solvent properties, the cohesive pressure (cohesive energy density) *ced* and the internal pressure P_i, from which the structuredness of a solvent can be evaluated [75]. The cohesive pressure is a measure of the total molecular cohesion per unit volume, given by Eq. (II-52)

$$ced = \frac{\Delta U_{vap}}{V_m} = \frac{\Delta H_{vap} - RT}{V_m}$$
(II-52)

where ΔU_{vap} and ΔH_{vap} are respectively the energy and enthalpy (heat) of vapourization of the solvent to a gas of zero pressure, V_m is the molar volume of the solvent, R is the gas constant, and T is the absolute temperature. During vapourization of a solvent to a non-interacting vapour, all intermolecular solvent-solvent interactions will be broken. Consequently, *ced* stands for the total strength of the intermolecular solvent structure. High *ced* values can be found for solvents of high polarities and are further increased due to the presence of hydrogen bonds. In addition, this parameter is related to the energy required to create cavities in a liquid in order to accommodate solute molecules during the process of dissolution [76].

On the other hand, the internal pressure P_i is defined as the change in internal energy of a solvent as it undergoes a very small isothermal expansion, as seen in Eq. (II-55)

$$P_i = \left(\frac{\partial U}{\partial V_m}\right)_T = T\left(\frac{\partial p}{\partial T}\right)_{V_m} \approx T\left(\frac{\alpha_p}{\beta_T}\right)$$
(II-53)

where U, V_m, p and T are the molar internal energy, the molar volume, the applied pressure and the absolute temperature, respectively. This small expansion does not necessarily disrupt all the intermolecular solvent-solvent interactions. Thus, the internal pressure

results from the forces of attraction between solvent molecules exceeding the forces of repulsion, i.e. mainly dispersion forces and dipole-dipole interactions [76]. P_i can be equated to the ratio of the thermal expansion coefficient α_p and the isothermal compressibility β_T, as shown by Wilson et al. (cp. Eq. (II-53)) [77]. The values obtained from the latter relation are extremely useful, but errors in the individual properties are compounded in the ratio. Therefore, direct measurement of $\left(\partial p / \partial T\right)_{V_m}$ is essential for accurate determinations of P_i, especially when differences in P_i between the solvent and very dilute solutions are being examined.

Although there is obviously a close connection between cohesive pressure and internal pressure, they are not equivalent, as indicated by the compilation of *ced* and P_i values for some selected solvents given in Table II-11.

Solvent	*ced* (J/cm^3)	P_i (J/cm^3)	*ced* $-$ P_i (J/cm^3)	$n = P_i / ced$
Water	2303	151	2152	0.07
MeOH	875	285	590	0.33
Formamide	1574	544	1030	0.35
EtOH	674	293	381	0.43
Ethane-1,2-diol	1050	502	548	0.48
Ethylene glycol	892	502	390	0.56
DMF	582	477	105	0.82

Table II-11: Cohesive pressures, *ced*, internal pressures, P_i, and their ratio *n* for some solvents, arranged in order of decreasing *n*, that is, in order of increasing "structuredness". Further, the difference between *ced* and P_i is given. All values of *ced* and P_i were taken from Ref [78], in which the internal pressure was calculated from $T\alpha/\beta$.

It has been assumed that P_i is mainly a reflection of temporary dispersion forces and permanent dipole-dipole interactions within the solvent, whereas *ced* additionally includes specific solvent-solvent interactions such as hydrogen bonding. Hydrogen bonding in a solvent increases the cohesive pressure, while the internal pressure is compara-

ble to that of solvents without hydrogen bonding. Therefore, the hydrogen-bonding pressure or energy density contribution can be measured by the difference *ced–P_i*. Values of P_i approach those of *ced* only for weakly polar solvents without specific solvent/solvent interactions. The ratio *$n=ced/P_i$* approaches a value of unity for nonpolar solvents (e.g. hydrocarbons), but it can be less than or greater than unity for other solvents. High values of *n* are obtained for the noninteracting fluorohydrocarbons, while for highly interacting solvents, e.g. for water, very low values of *n* are found [78, 79].

2.4   Colloidal forces

Colloidal assemblies are stabilized or destabilized by numerous interactions, which can be classified into two interaction forces, *repulsion* and *attraction*. Basically, interaction between colloidal particles is determined in terms of the balance of van-der-Waals force (attractive potential energy) and electrostatic force (repulsive potential energy). This is well-know as *Derjaguin-Landau-Verwey-Overbeek (DLVO)*-theory [37-39]. *DLVO*-theory, in general, applies for considerably low surfactant concentration, especially, for ionic surfactants which have the strong electric hindrance on coagulation. For high concentration solutions, micelles are obliged to approach each other because of the decrease in bulk phase volume. This is energetically disadvantageous. However, if a micellar structure is reconstructed into a long cylindrical micelle, for example, the assemblies can be apart more far from each other.

2.4.1   Van-der-Waal forces

The van-der-Waals force contains several contributions resulting in long-range attractive forces. One is the quantum mechanical dispersion interaction (London dispersion force). The second term arises from the thermally averaged dipole-dipole interaction (*Keesom term*) and the third contribution comes from dipole-induced-dipole interactions (*Debye term*). The van-der-Waals force operates between both apolar and polar molecules and varies rather little between different materials, i.e. compared to the double-layer force, which can change by orders of magnitude upon addition of small amounts of salt [40]. The most straightforward way to calculate the van-der-Waals force is

by assuming that the total potential is given by the sum of potentials between pairs of molecules, i.e. the potential is said to be pair wise additive. This is usually called the Hamaker approach [4, 6, 41]. The resulting potential depends on the shapes of the colloidal particles and on their separation. In the case of two spheres (cp. Figure II-13) separated in vacuum by a distance d having a volume V_1 and V_2, respectively, the non-retarded potential energy E_{vdW} is

$$E_{vdW} = -\iint \frac{\rho_1 \rho_2 C_{12}}{r^6} dV_1 dV_2 \qquad (\text{II-54})$$

and after integration using spherical geometry with r_1 and r_2 are the radii of the sphere 1 and 2, respectively, E_{vdW} becomes

$$E_{vdW} = -\frac{A_{12}}{6d} \frac{r_1 r_2}{(r_1 + r_2)} \qquad (\text{II-55})$$

where A_{12} is the Hamaker constant which is given by the following equation:

$$A_{12} = \pi^2 C_{12} \rho_1 \rho_2 \qquad (\text{II-56})$$

C_{12} is the coefficient concerning in the inter-atom pair potential (London constant), ρ_1 and ρ_2 are the number densities of particle 1 and 2 in unit volume. The Hamaker constant is normally found in the range of 10^{-20} J [4, 6].

In this context, another theory has been presented by Lifshitz et al. [42]. The mathematical formalism of the Lifshitz-theory is rather sophisticated and in order to fully utilize the approach, the knowledge of the frequency-dependent dielectric permittivity of all frequencies is needed. This method assumes that the interacting particles and the dispersion medium are all continuous. The basic idea of the theory is that the interaction between the bodies is considered to take place through a fluctuating electromagnetic field. This leads to another definition of the Hamaker constant. Although the

Lifshitz theory and the Hamaker theory use very different approaches, the net results are similar [4].
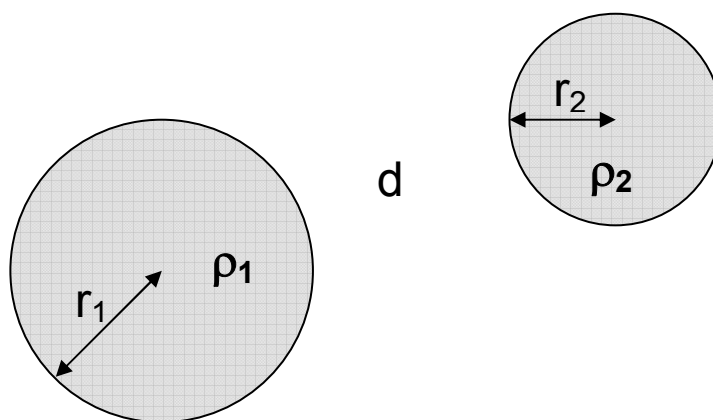
Figure II-13 : Sketch of two dispersed spheres of different radii (r_1, r_2) and different number densities (ρ_1, ρ_2), respectively, in distance d.

2.4.2   Electric double-layer forces

We now consider the electrical potential around a charged colloidal particle in solution. A particle, e.g. an micelle formed by an ionic surfactant that is charged at the surface attracts counterions, i.e. an ionic atmosphere is formed around it. These tend to segregate into a layer adjacent to the layer of surface charges in the colloid particle. Since van-der-Waals forces between identical species of particles are always attractive, it would have seemed that the dissolved particles coagulate one another and precipitate as solid mass out of the solution, if van der Waals force alone were operative. However, it does not necessarily occur, because the particles dispersed in solution with large permittivity such as water are charged commonly, resulting in hindrance of coalescence by electrostatic repulsion. Surface charge originates from two processes: (i) ionization or dissociation of a functional group on the surface, (ii) ionic adsorption (bond) onto the non-charged surface from solution. Thus, an electric double layer is created [4, 6]. In the diffuse double layer model, the ionic atmosphere is supposed to consist of two regions. Close to the colloid particle, counterions tend to predominate due to strong electrostatic forces. Ions further away from the particles are assumed to be organized more diffusely,

according to a balance of electrical forces and those resulting from random thermal motion. In this outer region, the concentration of counterions thus decreases gradually away from the surface. For the Stern model, another single layer is formed over the surface. This layer and the inner layer are termed Stern and Helmholtz layer, respectively (Figure II-14).
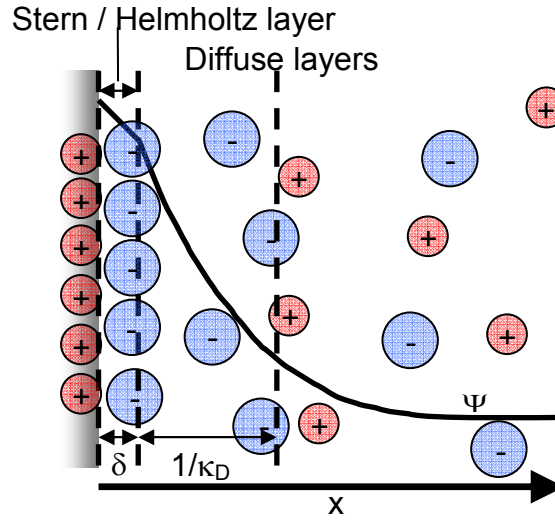

Figure II-14 : Stern double-layer model

Inside the Stern layer, the potential Ψ decreases linearly. The diffuse double layer or the outer diffuse region away from the inner layer can be described by the Gouy-Chapman equation Eq. (II-57), which is a solution of the Poisson-Boltzmann equation for a planar diffuse double layer.

$$\Psi = -\frac{4k_BT}{e}\tanh\left(\frac{e\Psi_0}{4k_BT}\right)\exp\left(-\kappa_D x\right) \qquad (II\text{-}57)$$

where x is the distance from the middle of the two planes, e the electron charge, k_B the Boltzmann constant, and κ_D is defined as follows

$$\kappa_D = \left(\frac{e^2\sum_i c_i z_i}{\varepsilon k_BT}\right)^{\frac{1}{2}} \qquad (II\text{-}58)$$

The quantity $1/\kappa_D$ has dimensions of length and it is called the Debye screening length. In the case of $ze\Psi_0/(k_BT) < 1$, i.e. for a system where the thermal diffusion energy k_BT is dominant rather than the surface potential Ψ_0 and/or the electrolyte is weakly charged, then the potential simplifies to

$$\Psi = \Psi_0 \exp(-\kappa_D x) \qquad\qquad \text{(II-59)}$$

This equation is known as Debye-Hückel equation [4, 43].

2.4.3 DLVO theory

The DLVO-theory consists of the above presented forces. The total interaction energy is formulated by sum of the two contributions. Differing from the electric double layer force, the van-der-Waals potential is not much sensitive to the concentration of electrolyte and pH, whereby it can be considered to be constant. The van-der-Waals attraction would be greater than the double layer repulsion whenever the distance between two particles or planes is enough small, because the attraction increases exponentially with decreasing distance, while the repulsion increases rather slowly. The relationship of both the forces exhibits as a function of distance d in Figure II-15.
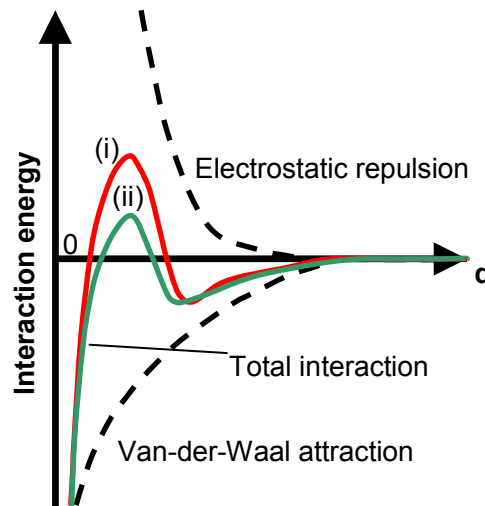

Figure II-15 : DLVO interaction vs. distance: (i) → (ii), decreasing surface potential (e.g. due to salt addition)

In the case of strongly charged particles, the repulsion over long range causes, as a consequence, an energy barrier that appears commonly in the distance from 1 to 4 nm. The energy barrier does not allow the particles to approach each other. Then the colloid particles settle down at the minimum, i.e. keep a constant distance away from one another. Reduction of the charge density or potential suppresses the energy barrier (Figure 2.5 (a)→(b)), resulting in flocculation. The colloidal system therefore becomes unstable [4].

2.4.4   Hydration forces

The hydration force between the amphiphilic surfaces is proposed firstly by Langmuir [44]. A charged or zwitterionic surface immersed in aqueous solution results in one or several well-defined layers of water molecules hydrating the surface in the same way as a dissolved ion has a hydration shell. Pushing two such surfaces together results in a dehydration and could be anticipated to be accompanied by a repulsive hydration force. The hydration force often exceeds the *DLVO* force in the short range and prevents from coalescence of bilayer, vesicle, and bio membrane. This is the background to the notation of repulsive hydration forces. Very strong short-ranged repulsive forces have been found to act between lipid bilayers [45]. The range is somewhere between 10 and 30 Å and the repulsion is found to decay exponentially with separation [46, 47]. Similarly, repulsive forces between solid mica surfaces are reported from experiments using surface apparatus. Repulsive hydration forces seem to exist both between neutral and charged surfaces. Despite the fact that the mica surfaces in the force apparatus are rigid and the bilayer systems studied have certain flexibility, there is surprisingly good agreement between the two techniques. The repulsive forces between mica surfaces have also been seen in other solvent. These experiments have given rise to a wide range of theoretical explanations. Structural or H-bonding polarization at the surface has been suggested as the cause for the repulsion. Bilayer undulations and image charge interactions have also been put forward as possible mechanisms. Recently, it has been suggested that the lipids protrude out into the solvent and this protrusion is limited when two surfaces approach and a repulsive force appears. The mechanism is akin to the idea

of undulation forces. The difference lies mainly in the range of the fluctuations. The original undulations model invoked long wavelength undulation, while in the protrusion model the 'undulations' are molecular in range [4].

2.5   Microemulsions

As the previous chapters demonstrate, binary water-surfactant and oil-surfactant systems form colloidal systems driven by the self-association feature of the amphiphilic ingredient. However, ternary systems are also well-known resulting from self-assembly of non-ionic or ionic double-chain surfactants. In general, these systems, commonly known as microemulsions, are equilibrium solutions containing substantial amount of both a polar component (usually water) and an apolar component, such as a medium- or long chain alkane (oil) that are stabilized by an amphiphilic additive. The phrase "microemulsion" was introduced by Schulman in 1959, who defined them as optically isotropic transparent oil and water dispersions which are thermodynamically stable and are spontaneously formed by mixing the appropriate amount of ingredients [48].

If a small amount of a non-polar component is added to micelles in water, this third component is solubilised in the interior of the micelle. This is the basic mechanism of microemulsion formation. In the case of regular micelles, first swollen micelles and then oil in water (O/W) microemulsions are formed upon the addition of oil, while water in oil (O/W) microemulsions form from reversed micelles upon addition of water. By the incorporation of larger amount of the third component, a number of different, sometimes coexisting, phases may form and the phase diagram can become rather complex, especially at high surfactant content (compared to binary surfactant solutions with water and oil, respectively) [49].

Microemulsions are structurally well-defined self-organizing mixtures where the interfacial tension between water and oil is strongly decreased by the surfactant ($\approx 10^{-2}$ mN/m). They comprise droplet phases, which consist of more or less spherical nano-droplets (radii between 1 to 100 nm) of oil in water (L_1-phases) and water in oil (L_2-phases), as well as bicontinuous (L_3) phases. Bicontinuous structures are interwoven

networks of water and oil tunnels separated by a surfactant film. The phase behaviour of such ternary systems shows a great variety influenced by, i.e., composition, temperature, and/or ionic strength. Noteworthy is that microemulsion phases can coexist with water and/or oil excess phases as well as liquid crystalline phases forming two or three-phase equilibria [4, 50].

The formulation of microemulsions utilizing single chain ionic surfactants is also possible but not without the usage of additional added compounds. Suitable additives in this context are aliphatic alcohols and/or electrolytes (e.g. NaCl). The basic necessity of these additives is a consequence of the charged head group of ionic surfactants which is responsible for the relative low solubility of them in oils and it also destabilizes the surfactant film through repulsive forces. These effects can be lowered by addition of a suitable alcohol, which is incorporated in the surfactant film resulting in an alternation of surfactant and alcohol in this film. This increases the distance between the charged head groups of the amphiphiles, therefore reduces the repulsive forces, and consequently stabilizes the film. Additionally, the compatibility of the amphiphile towards the used oil is also enhanced as an appropriate alcohol increases the polarity of the apolar component. With other words, ionic surfactants are not hydrophobic enough to solubilise the oil phase. The added alcohol balances this disadvantage. Salt addition, in contrast, lowers the repulsive forces between the ionic head groups directly by ion condensation of the added electrolyte onto the charged surface of the ionic surfactant film making it more hydrophobic ("non-ionic"). Again, the solubilisation of the oil is enhanced. Because of the large number of components, the phase diagrams of single chain ionic surfactants are generally very complex (multidimensional) [51-54].

### 2.5.1   Phase diagrams and phase evolution of microemulsions

The different phases and coexisting regions of more component systems is generally represented in microemulsion science in a triangular phase diagram (Gibbs-triangle). At each point in the diagram, the concentration of each species is determined by drawing a line parallel to the corresponding axis lying along one edge of the triangle. Figure II-16 shows a Gibbs-triangle of a non-ionic surfactant used as surface-active

compound displaying a wide range of structural different phases, which can principally form in a ternary or pseudo-ternary (for ionic surfactant with constant surfactant/additive ratio) system of a strong amphiphile.
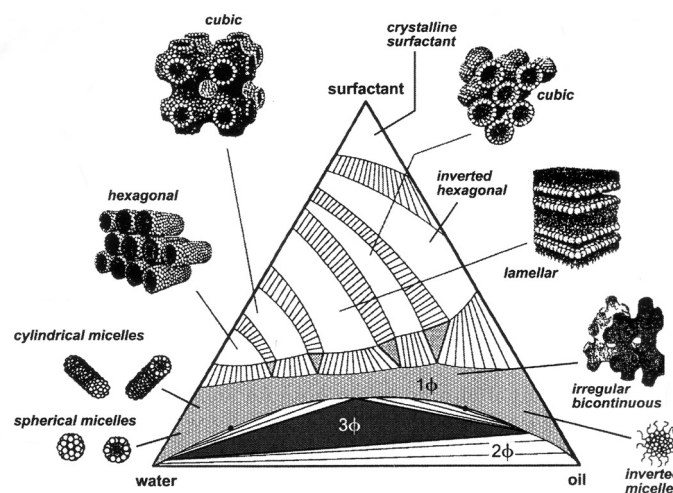
Figure II-16 : Schematic representation of a Gibbs triangle of a non-ionic surfactant used as surface-active compound. Represented from Ref. [49].

In the upper part of the phase diagram, at high surfactant concentrations, the different liquid crystalline phases reach from the water-surfactant and oil-surfactant (reverse structures) sides into the triangle. These phases form two and three phase equilibria at intermediate surfactant concentration with the microemulsion phases at lower surfactant concentrations. In the central part of the phase diagram bicontinuous microemulsions, and bilayer as well as bicontinuous crystalline phases at high surfactant concentration normally occur. Isotropic bicontinuous microemulsions only can be found over a small surfactant concentration range at comparable amounts of water and oil. At low amphiphile concentration (bottom region within the phase diagram), there is not enough surfactant present to form a bicontinuous structure over the whole sample. In this case, the sample is split into three phases, a bicontinuous middle phase and almost pure water and oil phases (Winsor III phase). Depending on the temperature or the added alcohol and/or salt amount also a Winsor I (O/W microemulsion in equilibrium with an excess oil phase) and a Winsor II phase (W/O microemulsion in equilibrium with an excess water phase) can be observed [50, 51]. This is schematically illustrated in Figure II-17.
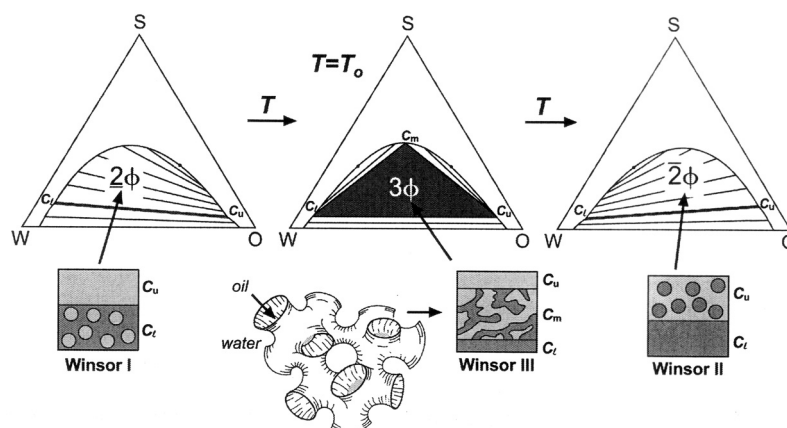
Figure II-17: Phase evolution resulting in Winsor I-III-II microemulsion equilibria for a non-ionic surfactant as a function of temperature (also possible for ionic microemulsions with increasing amount of added salt for example). Represented from Ref. [49].

2.5.2 Curvature energy model - Understanding the phase behaviour of microemulsions

During the last twenty years it has been shown that the structure and phase behaviour of microemulsion systems results, beside the composition, from the elastic property of the surfactant film separating the water and oil domains. This effect can be described successfully by a geometrical concept based on the statistical mechanics of curved interfaces, which was introduced by Helfrich et al. [55]. The Helfrich free energy E_H defines the bending energy of a shaped surface in terms of the spontaneous curvature H_0, the rigidity constant κ_b connected with bending, and the rigidity constant κ_g connected with Gaussian curvature. E_H is defined as

$$E_H = \int \left[f_0 + 2\kappa_b (H - H_0)^2 + \kappa_g K \right] dA \tag{II-60}$$

where H is the mean curvature, K the Gaussian curvature, and A the whole surface area. Using the definition of H and K with R_1 and R_2, the principle radii of curvature at a certain point on the surface A (the sign of the radii is taken as positive when the film curves toward oil and negative when it is curved toward water.),

$$H = \frac{1}{2}\left(\frac{1}{R_1} + \frac{1}{R_2}\right) \qquad\qquad\qquad \text{(II-61)}$$

$$K = \left(\frac{1}{R_1 R_2}\right) \qquad\qquad\qquad \text{(II-62)}$$

the Helfrich free energy becomes

$$E_H = \int\left[\sigma_H - \frac{2\kappa_b}{R_0}\left(\frac{1}{R_1}+\frac{1}{R_2}\right) + \frac{\kappa_b}{2}\left(\frac{1}{R_1}+\frac{1}{R_2}\right)^2 + \frac{\kappa_g}{R_1 R_2}\right]dA \qquad \text{(II-63)}$$

where the parameters R_0 is the radius of spontaneous curvature and σ_H the surface tension of the planar surface.

$$R_0 = \frac{1}{H_0} \qquad\qquad\qquad \text{(II-64)}$$

f_0 is defined such that σ_H includes all the contributions which are independent of curvature

$$\sigma_H = f_0 + 2\kappa_b H_0^2 \qquad\qquad\qquad \text{(II-65)}$$

The model of Helfrich et al. is quite difficult to use quantitatively, as the present parameters cannot be obtained directly by a molecular model, for example. However, they are accessible experimentally. Nevertheless, the curvature energy concept allows a basic qualitative understanding of the formed type of microemulsion in the single phase and in multiphase equilibria in dependence of the spontaneous curvature H_0.

The spontaneous curvature H_0 is defined as the curvature H an amphiphile film has when the film is totally unconstrained. In this situation, the film has its lowest obtainable energy state and so

$$\frac{\partial E_H}{\partial H} = 0 \qquad\qquad\qquad \text{(II-66)}$$

for $H = H_0$. Therefore, H_0 is the most favourable packing configuration of the amphiphile molecules in the surface. Positive and negative values of H_0 result in the formation of droplets with spherical and cylindrical geometry, respectively. Depending on the sign, regular or reversed structures are obtained. When H_0 is zero (balanced state), the film is generally flat and form planar bilayers or bicontinuous structures ($R_1 = -R_2$). This is illustrated in Figure II-18.
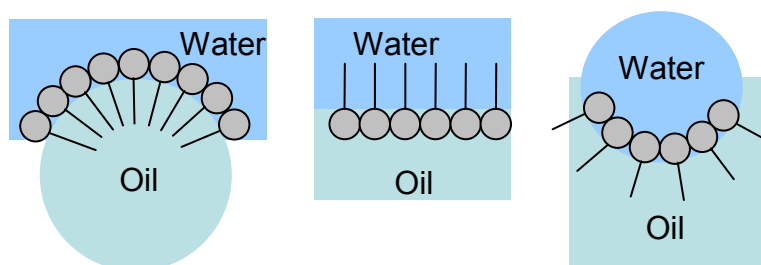
Spontaneous curvature	$H_0 > 0$	$H_0 \approx 0$	$H_0 < 0$
Interfacial film curved towards	oil	balanced state	water
Microemulsion type	O/W (L_1)	Bicontinuous (L_3)	W/O (L_2)
Multiphase equilibria	Winsor I ($\underline{2}\,\Phi$)	Winsor III ($3\,\Phi$)	Winsor II ($\overline{2}\,\Phi$)

Figure II-18 : Curved surfactant monolayers at the water/oil interface, with the corresponding values for the spontaneous curvature H_0 and the type of microemulsion formed in the single phase and in the multiphase. Represented from Ref. [49].

For a given surfactant, H_0 can be adjusted by the common formulation variables (T, additives). In the case of non-ionic surfactants, e.g. C_iE_j, the temperature has a major influence on H_0. With increasing temperature the hydrogen bonds between the hydrating water and the ether groups of the ethylene oxide part E_j break and therefore the surfactant becomes less soluble in the aqueous phase. Consequently, H_0 is tuned via its

balanced state ($H_0 = 0$) toward negative values and thus the curvature turns from oil toward water. For ionic surfactants, the strongest influence is the salt concentration. Trough salt addition to an ionic microemulsion the effective charge of the head group is screened resulting in lower repulsion energy between the heads. This can lead to a H_0 change in the following order: $H_0 > 0 \rightarrow H_0 < 0$. The temperature dependence of H_0 for an ionic surfactant film is opposite ($H_0 < 0 \rightarrow H_0 > 0$) to the salt dependence and also opposite to the temperature dependence in the case of non-ionic microemulsions, since the Debye length screening length includes the ratio of T and the salt concentration I (ionic strength of the aqueous phase) (Eq. (II-58)). The addition of alcohol has the same effect for non-ionic as for ionic microemulsions. It stabilizes structures, which are curved toward water [49, 54]. The bending rigidity constant κ_b describes how easily an interfacial film can be bent and therefore influences the static and dynamic properties of microemulsions. This parameter is given in a unit of energy and values typically between 1-20 $k_B T$ are obtained. The rigid constant κ_g associated with the Gaussian curvature, in contrast, is connected with the topology of the surface, whereas κ_b is not affected in this way. Typically, κ_g is negative and its magnitude is usually lower than that of κ_b. In ionic surfactant films, both parameters depend strongly on the salt concentration of the aqueous phase. Generally, the surfactant films are stiffer when no screening occurs [49].

2.5.3   Electrical conductivity of microemulsions: The Microstructure

An easy way to obtain fundamental insights into the microstructure change of isotropic microemulsions, depending of composition or temperature respectively, can be achieved by conductivity measurements. Unfortunately, this technique is limited to ionic microemulsions (or non-ionic with added salt) as charged species have to be present to get reliable results. Nevertheless, this is of special interest, especially when the phase transitions cannot be obtained visually, i.e. if W/O $\rightarrow$ bicontinuous $\rightarrow$ O/W phase evolution has to be expected [56, 57]. Considering an ionic microemulsion (ionic surfactant/co-surfactant/water/oil) with a constant surfactant/co-surfactant mass ratio w_s ($w_s = m_{surf.}/m_{co\text{-}surf.}$), the electrical conductivity κ changes characteristically depending

on the followed experimental path P. Figure II-19 shows the variation of the electrical conductivity with Φ_w, the volume fraction of water, of three different experimental paths P_1, P_2, and P_3. At this, Φ_w is defined as

$$\Phi_w = \frac{V_w}{V_{total}} \qquad\qquad\text{(II-67)}$$

where V_w is the present volume of water and V_{total} is the total volume of the microemulsion.
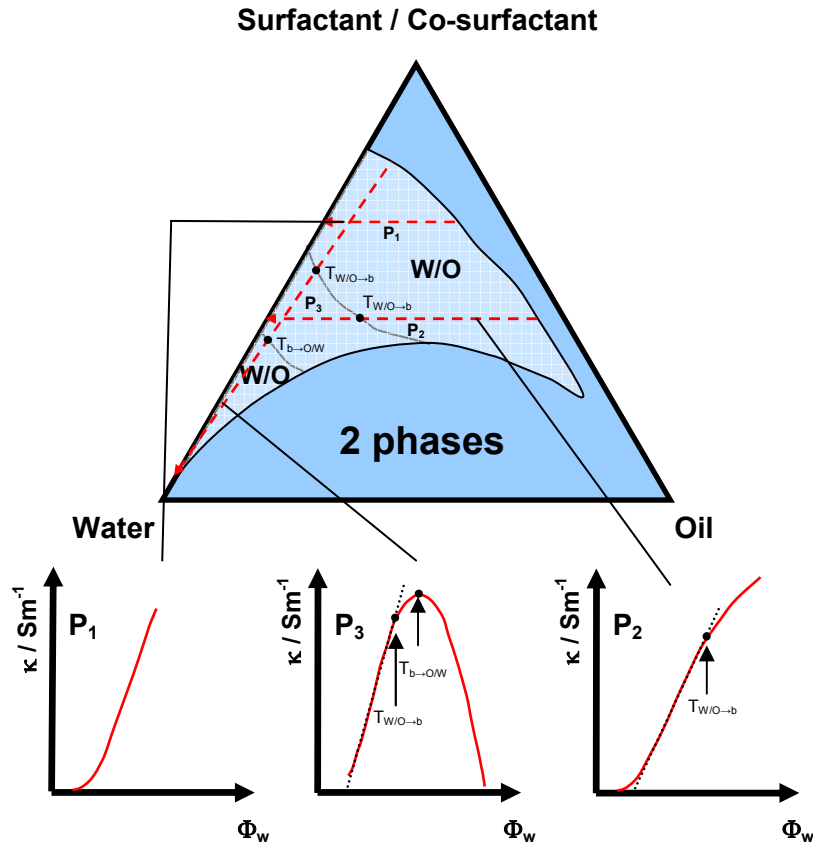

Figure II-19 : Schematic phase diagram and the corresponding κ-Φ_w-plots obtained from different experimental paths (P$_1$, P$_2$, P$_3$). The surfactant/co-surfactant mass ratio is constant.

In the case of P_1 and P_2, the molar ratio of surfactant/co-surfactant w_s remains constant and the water/oil mass ratio $w_{w/o}$ ($w_{w/o} = m_w/m_o$) varies through a stepwise addition of water (alpha-path), whereas the surfactant/co-surfactant to oil mass ratio

$w_{surf.co\text{-}surf./o}$ ($w_{surf.co\text{-}surf./o} = m_{surf.co\text{-}surf.}/m_o$) remains constant by following P_3 (beta-path). The conductivity behaviour described in Figure II-19 (left, P_1) represents a percolation phenomenon which results from a progressive droplet interlinking and clustering process, as the water content is raised [58]. At certain water content, Φ_w^p, κ increases drastically indicating the interlinking of the droplets. Below Φ_w^p, non-aggregated water droplets dominate which do not contribute to the conductivity as they are isolated by a non-conducting medium (oil). The same phenomenon is monitored for the second alpha-path but with a marked curvature in the upper part of the κ - Φ_w -plot (Figure II-19, right, P_2). This observation cannot be described by the percolation theory, as we will see later, but can be attributed to a new conduction mechanism reflecting structural alterations undergone by the microemulsion system at higher water content. Therefore, $T_{w/o \to b}$ marks an internal phase boundary of the mono-phasic region. The conductivity evolution along the beta-path (Figure II-19, middle, P_3), in contrast, comprises two distinctive features associated with two internal phase boundaries. The features of the conductivity plot are similar to those of P_1 and P_2, the toe at the bottom and the medium linear part, which is again characteristic for a percolation phenomenon. In the upper region of the κ -plot, when the water content is further increased, the conductivity deviates, as in P_2, from a straight line, reaches a maximum and then decreases down to the value of bulk water conductivity. It has been shown by Clausse et al. that the descending branch of κ is typical for O/W microemulsions whose global conductivity decreases because of the progressive dilution of their continuous aqueous phase with water. Consequently, the κ - Φ_w -plot indicates the presence of a special conduction mechanism reflecting an intermediary physical state of the system between the points $T'_{w/o \to b}$ and $T_{b \to o/w}$. With these results, it is possible to divide the phase diagram in Figure II-19 into three sub-regions: W/O, bicont. (b), and O/W, whereby the topology of the mono-phase is completely described [59-61].

2.5.3.1 The dynamic percolation model

The model of dynamic percolation can describe the phenomenon of percolation in reverse water droplet microemulsions occurring at higher water content. This model

assumes spherical independently moving droplets, which is the case in dilute W/O mi-croemulsions. At low concentrations of the dispersed water phase, the electrical conduc-tivity is very low and approximately constant as long as the water volume fraction is smaller than a critical value Φ_w^p called the percolation threshold. When Φ_w is increased beyond Φ_w^p, the conductivity suddenly changes toward higher values of κ. The dy-namic percolation model can give an explanation of this observation: At low concentra-tions below the percolation threshold conductivity is given by the Brownian motion of charged droplets or by charge hopping from one micelle to another. Near the percola-tion threshold, the droplets grow together and finally, at Φ_w^p, the first charge conducting cluster stretches from one electrode to the other forming a more bicontinuous-like me-dium.

For a three-dimensional system composed of identical droplets in a continuum (acting as isolator), which is a good approximation for a microemulsion, the theoretical percolation threshold Φ^p expressed in droplet volume fraction Φ is around 0.31 ($\Phi^p \approx$ 0.29) [58]. Here, Φ denotes the volume fraction of all components, which form the drop-let phase (droplet volume fraction), i.e. in the case of microemulsions formed by ionic surfactant, co-surfactant, oil, and water (surfactant/co-surfactant mass ratio is constant), Φ is calculated by:

$$\Phi = \frac{V_w + V_{surf.co\text{-}surf.}}{V_{total}} \qquad (\text{II-68})$$

where V_w is the present volume of water, $V_{surf.co-surf.}$ is the volume of the droplet form-ing phase, and V_{total} is the total volume of the microemulsion.

For spheres with an infinitely conductivity dispersed in an isolator the conduc-tivity, for $\Phi < \Phi^p$, is related to

$$\kappa \sim (\Phi^p - \Phi)^{-s} \qquad (\text{II-69})$$

whereas for not to high $\Phi > \Phi^p$

$$\kappa \sim (\Phi - \Phi^p)^t \tag{II-70}$$

is valid. The parameters s and t are called the critical exponents and they define the modality of the present percolation (static or dynamic). Because of the appearing droplet Brownian motion and the attractive droplet-droplet interactions, microemulsions normally show dynamic percolation. Theoretical values of s and t in the case of dynamic percolation were calculated from Monte-Carlo-simulations by Grest et al. [62], who found: $t = 1.9$ and $s = 1.2$. In contrast, the experimental values are in the range of $1.1 \leq s \leq 1.6$ and $1.6 \leq t \leq 2.2$ [63].

Above the percolation threshold, as already pointed out, the droplets are highly connected and form clusters, which get more and more branched. In this region, the conductivity is mostly related to the cluster volume fraction. A theoretical approach for the description of this is the "Theory of the effective medium" which is given as

$$\kappa \sim (\Phi - \Phi^c) \tag{II-71}$$

The critical volume fraction Φ^c, at which this model is valid, is $\Phi^c \geq 1/3$ [64-66].

2.5.3.2 Charge fluctuation model

Beside the model of dynamic percolation, there exist further models that describe the κ-Φ-plot of microemulsions, but they are only valid at very low Φ-values. The charge fluctuation model of Eicke et al. also bases on the assumption of spherical microemulsion droplets with a defined identical radius r_d, which move independently through Brownian motion. In thermal equilibrium, they possess no net charge, but they show a mean charge fluctuation $<z^2>$ due to instantaneous charge transfer between the droplets [67, 68]. The mean charge fluctuation can be described in two ways: By (i) the correlation with the electrical conductivity κ via Ohm´s and Stoke´s law, and by (ii) the consideration of only electrostatic interactions for the excess term of the chemical potential. The two expressions for $<z^2>$ are:

$$\kappa = \frac{\rho e_0^2}{6\pi\eta r_d}\left\langle z^2 \right\rangle \tag{II-72}$$

$$\left\langle z^2 \right\rangle = \frac{4\pi k_B T \varepsilon_0 \varepsilon_r r_d}{e_0^2} \tag{II-73}$$

where ρ is the particle density of the droplets, η the viscosity of the medium, ε_0 the electric field constant, ε_r the relative permittivity of the continuous phase, and e_0 the elementary charge. By using Eq. (II-72) and Eq. (II-73) and after conversion of ρ to the volume fraction Φ, the conductivity is finally given by

$$\kappa = \frac{\varepsilon_0 \varepsilon_r k_B T}{2\pi\eta} \frac{\Phi}{r_d^3} \tag{II-74}$$

At constant temperature T and pressure p, the parameters ε_r and η are constant and therefore, the charge fluctuation model is limited to the range of linear dependence of κ on Φ.

The droplet radii obtained by the model of Eicke et al. tend to be too large, which results from the assumption of purely electrostatic interactions, which is only valid for highly charged droplets and hence for droplet radii larger than 7 nm [67, 69, 70].

The model of Kallay et al. fixes this problem by the introduction of two different radii r_d and r_c. These are radii are defined as the droplet radius and the effective radius of charge separation within the droplet [69, 70]. They are related by the thickness l of the surfactant layer according to

$$r_d = r_c + l \tag{II-75}$$

Insertion of the respective radii yields:

$$\kappa = \frac{\varepsilon_0 \varepsilon_r k_B T}{2\pi\eta} \frac{r_d - l}{r_d^4} \Phi \tag{II-76}$$

This equation provides generally better results than that of Eicke et. al, but the value of l has to be known.

Hall and Halle & Boerling introduced other improved charge fluctuation models that are more complex. Hall assumes an equilibrium charge separation between two droplets and arbitrary charge z given by a Poisson-Boltzmann distribution with electrostatic energy [71]. Halle & Bjoerling describe the microemulsion media as polyelectrolytes with permanent or also fluctuating charges with the help of the MSA theory [72].

2.6   Bibliography

[1]   M. J. Rosen; *Surfactants and Interfacial Phenomena, 3rd Edition*. Wiley & Sons, (2004).

[2]   D. Myers; *Surfactant Science and Technology, 3rd Edition*. John Wiley & Sons, (2005).

[3]   J. Desnoyers, E., R. DeLisi and G. Perron; Thermochemistry of aqueous micellar systems. *Pure & Appl. Chem.* **52**, 433-444 (1980).

[4]   D. F. Evans; *The Colloidal Domain: Where Physics, Chemistry, Biology, and Technology Meet, 2nd Edition*. Wiley-VCH, (1998).

[5]   K. Holmberg; *Handbook of Applied Surface and Colloid Chemistry, Volume 1*. John Wiley & Sons, (2002).

[6]   H. Mollet and A. Grubenmann; *Formulation Technology: Emulsions, Suspensions, Solid Forms, 1st Edition*. (2000).

[7]   M. J. Rosen; The relation of structure to properties in surfactants. IV. Effectiveness in surface or interfacial tension reduction. *Journal of Colloid and Interface Science* **56**, 2, 320-327 (1976).

[8]   K. Holmberg, D. O. Shah and M. J. Schwuger; *Handbook of Applied Surface and Colloid Chemistry, Volume 2*. John Wiley & Sons, (2002).

[9]   C. Tanford; *The Hydrophobic Effect: Formation of Micelles and Biological Membranes. 2nd Edition*. Wiley, (1980).

[10]   D. F. Evans; Self-organization of amphiphiles. *Langmuir* **4**, 1, 3-12 (1988).

[11]   M. Costas, B. Kronberg and R. Silveston; General thermodynamic analysis of the dissolution of non-polar molecules into water. Origin of hydrophobicity. *Journal of the Chemical Society, Faraday Transactions* **90**, 11, 1513-1522 (1994).

[12]   B. Kronberg, M. Costas and R. Silveston; Understanding the hydrophobic effect. *Journal of Dispersion Science and Technology* **15**, 3, 333-351 (1994).

[13]   B. Kronberg, M. Costas and R. Silveston; Thermodynamics of the hydrophobic effect in surfactant solutions - micellization and adsorption. *Pure and Applied Chemistry* **67**, 6, 897-902 (1995).

[14]   P. Mukerjee and K. J. Mysels; Critical Micelle Concentrations of Aqueous Surfactant Systems (**NSRDS-NBS 36**). 222 (1971).

[15]   B. Lindman and H. Wennerstroem; Micelles. Amphiphile aggregation in aqueous solution. *Topics in Current Chemistry* **87**, 1-83 (1980).

[16]   V. Degiorgio; Physics of amphiphiles, micelles and microemulsions. *Europhysics News* **16**, 6, 9-12 (1985).

[17]   H. B. Klevens; Structure and aggregation in dilute solutions of surface-active agents. *Journal of the American Oil Chemists' Society* **30**, 74-80 (1953).

[18]   K. Shinoda and T. Nakagawa; *Colloidal Surfactants* (1963).

[19]   R. G. Laughlin; Aqueous phase science of cationic surfactant salts. *Surfactant Science Series* **37**, Cationic Surfactants, 1-40 (1991).

[20]   Z. Yu, X. Zhang, G. Xu and G. Zhao; Physicochemical properties of aqueous mixtures of tetrabutylammonium bromide and anionic surfactants. 3. Effects of surfactant chain length and salinity. *Journal of Physical Chemistry* **94**, 9, 3675-3681 (1990).

[21]   K. Shinoda, M. Hato and T. Hayashi; Physicochemical properties of aqueous solutions of fluorinated surfactants. *Journal of Physical Chemistry* **76**, 6, 909-914 (1972).

[22]   H. V. Tartar and R. D. Cadle; Studies of sulfonates. VI. Effect of sodium chloride on the solubility of sodium dodecyl sulfonate and sodium tetradecyl sulfonate. The solubility at 50°C of calcium dodecyl sulfonate and calcium dodecyl sulfate in aqueous solution of the correspon. *Journal of Physical Chemistry* **43**, 1173-1179 (1939).

[23]   F. Nilsson, O. Soederman and I. Johansson; Physical-Chemical Properties of Some Branched Alkyl Glucosides. *Langmuir* **13**, 13, 3349-3354 (1997).

[24]   H. Kunieda, K. Shigeta, K. Ozawa and M. Suzuki; Self-organizing structures in poly(oxyethylene) oleyl ether-water system. *Journal of Physical Chemistry B* **101**, 40, 7952-7957 (1997).

[25]   J. N. Israelachvilli, D. J. Mitchell and B. W. Ninham; Theory of self-assembly of hydrocarbon amphiphiles into micelles and bilayers. *Journal of the Chemical Society, Faraday Transactions 2: Molecular and Chemical Physics* **72**, 9, 1525-1568 (1976).

[26]   J. N. Israelachvili; *Intermolecular and Surface Forces: With Applications to Colloidal and Biological Systems.* Academic Press, (1985).

[27]   C. Tanford; Micelle shape and size. *Journal of Physical Chemistry* **76**, 21, 3020-3024 (1972).

[28]   H. V. Tartar; A theory of the structure of the micelles of normal paraffin-chain salts in aqueous solution. *Journal of Physical Chemistry* **59**, 1195-1199 (1955).

[29]   M. J. Blandamer, P. M. Cullis, L. G. Soldi, J. B. F. N. Engberts, A. Kacperska, N. M. Van Os and M. C. S. Subha; Thermodynamics of micellar systems: Comparison of mass action and phase equilibrium models for the calculation of standard Gibbs energies of micelle formation. *Advances in Colloid and Interface Science* **58**, 2/3, 171-209 (1995).

[30]   H. U. Kim and K.-H. Lim; A model on the temperature dependence of critical micelle concentration. *Colloids and Surfaces, A: Physicochemical and Engineering Aspects* **235**, 1-3, 121-128 (2004).

[31]   Z. Kiraly and I. Dekany; A Thermometric Titration Study on the Micelle Formation of Sodium Decyl Sulfate in Water. *Journal of Colloid and Interface Science* **242**, 1, 214-219 (2001).

[32]   G. C. Kresheck and W. A. Hargraves; Thermometric titration studies of the effect of head group, chain length, solvent, and temperature on the thermodynamics of micelle formation. *Journal of Colloid and Interface Science* **48**, 3, 481-493 (1974).

[33]   R. Palepu, H. Gharibi, D. M. Bloor and E. Wyn-Jones; Electrochemical studies associated with the micellization of cationic surfactants in aqueous mixtures of ethylene glycol and glycerol. *Langmuir* **9**, 1, 110-112 (1993).

[34]   M. Sjoeberg, U. Henriksson and T. Waernheim; Deuteron nuclear magnetic relaxation of [1,1-2H] hexadecyltrimethylammonium bromide in micellar solutions of nonaqueous polar solvents and their mixtures with water. *Langmuir* **6**, 7, 1205-1211 (1990).

[35]   D. F. Evans, S.-H. Chen, G. W. Schriver and E. M. Arnett; Thermodynamics of solution of nonpolar gases in a fused salt. Hydrophobic bonding behavior in a nonaqueous system. *Journal of the American Chemical Society* **103**, 2, 481-482 (1981).

[36]   A. H. Beesley, D. F. Evans and R. G. Laughlin; Evidence for the essential role of hydrogen bonding in promoting amphiphilic self-assembly: measurements in 3-methylsydnone. *Journal of Physical Chemistry* **92**, 3, 791-793 (1988).

[37]   E. J. W. Verwey; The forces between particles in lyophobic colloidal systems. *Kolloid-Zeitschrift* **136**, 46-52 (1954).

[38]   B. Deryagin and L. Landau; Theory of the stability of strongly charged lyopho-bic sols and of the adhesion of strongly charged particles in solutions of electro-lytes. *Acta Physicochimica URSS* **14**, 633-662 (1941).

[39]   E. J. W. Verwey and J. T. G. Overbeek; Long-distance forces acting between colloidal particles. *Transactions of the Faraday Society* **42B**, 117-123 (1946).

[40]   J. N. Israelachvili and G. E. Adams; Measurement of forces between two mica surfaces in aqueous electrolyte solutions in the range 0-100 nm. *Journal of the Chemical Society, Faraday Transactions 1: Physical Chemistry in Condensed Phases* **74**, 4, 975-1001 (1978).

[41]   H. C. Hamaker; The London-van der Waals attraction between spherical parti-cles. *Physica (The Hague)* **4**, 1058-1072 (1937).

[42]   J. N. Israelachvili; *Intermolecular and Surface Forces*. Academic Press, (1991).

[43]   A. Hamnett, C. H. Hamann and W. Vielstich; *Electrochemistry, 3rd Edition*. Wiley-VCH, (1997).

[44]   I. Langmuir; The role of attractive and repulsive forces in the formation of tac-toids, thixotropic gels, protein crystals and coacervates. *Journal of Chemical Physics* **6**, 873-896 (1938).

[45]   J. S. Clunie, J. F. Goodman and P. C. Symons; Solvation forces in soap films. *Nature (London, United Kingdom)* **216**, 5121, 1203-1204 (1967).

[46]   D. Marsh; Water adsorption isotherms and hydration forces for lysolipids and diacyl phospholipids. *Biophysical journal* **55**, 6, 1093-1100 (1989).

[47]   R. P. Rand and V. A. Parsegian; Hydration forces between phospholipid bilay-ers. *Biochimica et Biophysica Acta, Reviews on Biomembranes* **988**, 3, 351-376 (1989).

[48]   J. H. Schulman, W. Stoeckenius and L. M. Price; Mechanism of formation and structure of micro emulsions by electron microscopy. *Journal of Physical Chem-istry* **63**, 1677-1680 (1959).

[49]   W. F. C. Sager; Microemulsion templating. *Schriften des Forschungszentrums Juelich, Materie und Material* **10**, Soft Matter: Complex, A6/1-A6/37 (2002).

[50]   H. N. W. Lekkerkerker, W. K. Kegel and J. T. G. Overbeck; Phase behavior of ionic microemulsions. *Berichte der Bunsen-Gesellschaft* **100**, 3, 206-217 (1996).

[51]   K. V. Schubert and E. W. Kaler; Nonionic microemulsions. *Berichte der Bunsen-Gesellschaft* **100**, 3, 190-205 (1996).

[52]   Y. Chevalier and T. Zemb; The structure of micelles and microemulsions. *Reports on Progress in Physics* **53**, 3, 279-371 (1990).

[53]   M. Kahlweit, R. Strey and G. Busse; Weakly to strongly structured mixtures. *Physical Review E: Statistical Physics, Plasmas, Fluids, and Related Interdisciplinary Topics* **47**, 6, 4197-4209 (1993).

[54]   D. Langevin; Recent advances in the physics of microemulsions. *Physica Scripta* **T13**, Proc. Gen. Conf. Con, 252-258 (1986).

[55]   W. Helfrich; Elastic properties of lipid bilayers. Theory and possible experiments. *Zeitschrift fuer Naturforschung, Teil C: Biochemie, Biophysik, Biologie, Virologie* **28**, 11-12, 693-703 (1973).

[56]   M. Clausse, A. Zradba, L. Nicolas-Morgantini and D. Tourand; *Microemulsion Systems*, Marcell Dekker, (1987) .

[57]   M. Clausse, A. Zradba and L. Nicolas-Morgantini; *Microemulsion Systems*, Marcell Dekker, (1987).

[58]   B. Lagourette, J. Peyrelasse, C. Boned and M. Clausse; Percolative conduction in microemulsion type systems. *Nature* **281**, 60-62 (1979).

[59]   M. Clausse, J. Heil, J. Peyrelasse and C. Boned; Phase diagram features and electrical conductive behavior of Winsor IV systems as correlated to alkyl chain-length compatibility. *Journal of Colloid and Interface Science* **87**, 2, 600-602 (1982).

[60]   C. Boned, M. Clausse, B. Lagourette, V. E. R. McClean, V. E. R. Mc Clean and R. J. Sheppard; Detection of structural transitions in water-in-oil microemulsion-type systems through conductivity and permittivity studies. *Journal of Physical Chemistry* **84**, 12, 1520-1525 (1980).

[61]   D. O. Shah, A. Tamjeedi, J. W. Falco and R. D. Walker, Jr; Interfacial instability and spontaneous formation of microemulsions. *AIChE Journal* **18**, 6, 1116-1120 (1972).

[62]   G. S. Grest, I. Webman, S. A. Safran and A. L. P. Bug; Dynamic percolation in microemulsions. *Physical Review A: Atomic, Molecular, and Optical Physics* **33**, 4, 2842-2845 (1986).

[63]   Y. Feldman, N. Kozlovich, I. Nir and N. Garti; Dielectric relaxation in sodium bis(2-ethylhexyl)sulfosuccinate-water-decane microemulsions near the percolation temperature threshold. *Physical Review E: Statistical Physics, Plasmas, Fluids, and Related Interdisciplinary Topics* **51**, 1, 478-491 (1995).

[64]   D. A. G. Bruggeman; The calculation of various physical constants of heterogeneous substances. I. The dielectric constants and conductivities of mixtures composed of isotropic substances. *Annalen der Physik* **24**, 665-679 (1935).

[65]   C. J. F. Bottcher; The dielectric constant of crystalline powders. *Recueil des Travaux Chimiques des Pays-Bas et de la Belgique* **64**, 47-51 (1945).

[66]   R. Landauer; The electrical resistance of binary metallic mixtures. *Journal of Applied Physics* **23**, 779-784 (1952).

[67]   H. F. Eicke, M. Borkovec and B. Das-Gupta; Conductivity of water-in-oil microemulsions: a quantitative charge fluctuation model. *Journal of Physical Chemistry* **93**, 1, 314-317 (1989).

[68]   H. F. Eicke, H. Hammerich and G. Vasta; A thermodynamic analysis of the molar conductivity of the ternary system: water-aerosol OT-isooctane. *Journal of Colloid and Interface Science* **93**, 2, 593-595 (1983).

[69]   N. Kallay and A. Chittofrati; Conductivity of microemulsions: refinement of charge fluctuation model. *Journal of Physical Chemistry* **94**, 11, 4755-4756 (1990).

[70]   N. Kallay, M. Tomic and A. Chittofrati; Conductivity of water-in-oil microemulsions: comparison of the Boltzmann statistics and the charge fluctuation model. *Colloid and Polymer Science* **270**, 2, 194-196 (1992).

[71]   D. G. Hall; Conductivity of microemulsions: an improved charge fluctuation model. *Journal of Physical Chemistry* **94**, 1, 429-430 (1990).

[72]   B. Halle and M. Bjoerling; Microemulsions as macroelectrolytes. *Journal of Chemical Physics* **103**, 4, 1655-1668 (1995).

[73]   T. L. Greaves, A. Weerawardena, C. Fong and C. J. Drummond; Formation of Amphiphile Self-Assembly Phases in Protic Ionic Liquids. *Journal of Physical Chemistry B* **111**, 16, 4082-4088 (2007).

[74]   T. L. Greaves, A. Weerawardena, C. Fong and C. J. Drummond; Many Protic Ionic Liquids Mediate Hydrocarbon-Solvent Interactions and Promote Amphiphile Self-Assembly. *Langmuir* **23**, 2, 402-404 (2007).

[75]   A. Lattes and I. Rico; Aggregation in formamide solution: Reactivity and structure of non-aqueous microemulsions. *Colloids and Surfaces* **35**, 2-4, 221-235 (1989).

[76]   M. R. J. Dack; Importance of solvent internal pressure and cohesion to solution phenomena. *Chemical Society Reviews* **4**, 2, 211-229 (1975).

[77]   G. Allen, G. Gee and G. J. Wilson; Intermolecular forces and chain flexibilities in polymers. I. Internal pressures and cohesive energy densities of simple liquids. *Polymer* **1**, 456-466 (1960).

[78]   M. R. J. Dack; Solvent structure. Use of internal pressure and cohesive energy density to examine contributions to solvent-solvent interactions. *Australian Journal of Chemistry* **28**, 8, 1643-1648 (1975).

[79]   A. F. M. Barton; *CRC Handbook of Solubility Parameters and Other Cohesion Parameters*. CRC Press, (1983).

III. Synthesis

The following chapters present the syntheses of the applied 1-alkyl-3-methylimidazolium chloride ionic liquids (C_{12}mimCl, C_{14}mimCl, C_{16}mimCl) as well as of the used room-temperature molten salts, ethylammonium nitrate (EAN) and 1-butyl-3-methyl-imidazolium tetrafluoroborate (bmimBF$_4$), respectively. It should be noted, that in order to obtain reliable results, chemicals of high purity are crucial for the fundamental investigation of surfactant systems. Any impurities (especially when they are surface active) remaining from the synthesis can drastically alter the aggregation/phase behaviour of colloidal systems [1]. For this purpose, analyses were carefully performed including for example NMR, mass analysis, and water determination of the achieved SLILs and RTMS, respectively, in order to exclude the presence of unintentional impurities. In general, the purities of the synthesized salts were always $\geq$ 99% as determined from NMR. In the case of the used surfactant-like ionic liquids, the high purity was further confirmed from the surface tension measurements of these ILs in water (cp. Chapter V.2.2)

1 Chemicals

1-chlorohexadecane (Merck, for synthesis), 1-chlorotetradecane (Fluka, for synthesis), 1-chlorododecane (Fluka, for synthesis), 1-chlorobutane (Merck, for synthesis), 1-methylimidazole (Merck, for synthesis), ethylamine (Fluka, 70% (w/w) in water, for synthesis), KOH (Merck, p.a.), NaBF$_4$ (Fluka, p.a.), conc. HNO$_3$ (Merck, 65% (w/w), p.a.), MgSO$_4$ (Riedel-de Haën, p.a.), ethyl acetate (Merck, p.a.), dichloromethane (Acros, p.a.) as well as acetonitrile (Baker, analyzed) and tetrahydrofurane (Baker, analyzed) used in this study were purchased from the companies given in brackets. Water was taken from a Millipore-Q-installation (Millipore Corporation, conductivity $< 10^{-7}$ S cm^{-1}). For the formulation of the SLIL/RTMS microemulsions, additionally, dodecane (Aldrich, ReagentPlus) and 1-decanol (Merck, for synthesis) were used. The purification of 1-methylimidazole was accomplished by fractionated distillation from KOH un-

der reduced pressure, followed by drying above a molecular sieve (Roth, 3 Å) for 1 week in N_2-atmosphere. Then, it was distilled again under reduced pressure and stored in dry nitrogen. Acetonitrile was dried by refluxing it over CaH_2 for 1 h followed by distillation into a nitrogen flushed solvent-Schlenk flask in which it was stored until use. All other products were used as received.

2   Analytics

^{1}H- and ^{13}C-NMR spectra were recorded on a Bruker Avance 300 spectrometer operating at 300.13 MHz. The ^{11}B- and ^{19}F-NMR were obtained on a Bruker Avance 400 spectrometer working at 400.13 MHz. The preparation of the NMR-samples was carried out in a glovebox to avoid moisture contamination. As solvent d-chloroform (99.8%, deutero, Germany) and d_3-acetonitrile (99.8%, deutero, Germany) was used, respectively. (+/-)-ESI-MS were recorded on a Varian Mat 311A. All presented melting points were determined via differential scanning calorimetry (DSC). The measurements were performed on a Perkin Elmer DSC 7 in a nitrogen flow with hermetically sealed Al pans, which were prepared before the measurement in the glovebox. The measurements were recorded at a heating rate of 10°C/min. All melting points T_m were received from the DSC thermograms during the heating steps via onset analysis by determining the intersection point between the baseline and the tangent defined by the reflection point of the peak onset (cp. Chapter IV.8) [2, 3]. The decomposition temperature T_{dec} of each synthesized ionic liquid was determined via TGA measurements. Like in the case of the DSC measurements, the data evaluation was achieved by onset analysis (cp. Chapter IV.9) [2]. The water content was determined on a Mitsubishi Moisturemeter CA-20.

3 Synthesis of the used ionic liquids

3.1 1-alkyl-3-methylimidazolium chlorides

The surface-active 1-alkyl-3-methylimidazolium chlorides were obtained by the reaction of 1-methylimidazole with the appropriate 1-chloroalkane giving the desired chloride salt [4]. The representative reaction scheme is given in Figure III-1.
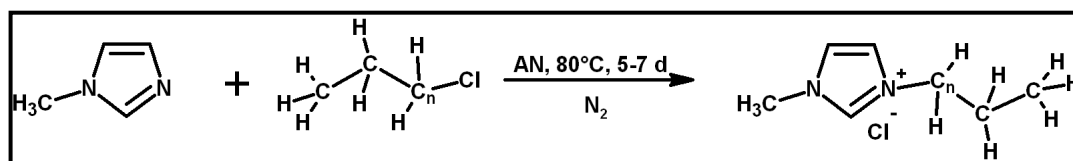
Figure III-1 : Representative reaction scheme for the synthesis of the 1-alkyl-3-methyl-imidazolium chlorides. *n* denotes 10, 12, and 14, respectively.

3.1.1 1-dodecyl-3-methylimidazolium chloride (C_{12}mimCl)

1-dodedecyl-3-methylimidazolium chloride was obtained from the reaction of 1-methylimidazole with an equimolar amount of 1-chlorododedecane in acetonitrile at 80°C in nitrogen atmosphere. The reaction progress was monitored via NMR and after 5-7 days, nearly no remaining reactants were found. After slow cooling to room-temperature, the C_{12}mimCl salt crystallizes as long white needles. After decanting the organic layer and removing the remaining AN *in vacuo* ($\approx 1 \times 10^{-3}$ mbar), purification was further conducted by recrystallization of the salt three times using tetrahydrofurane (THF). Between each recrystallization step, the salt solution was placed in a cool box overnight at -30°C in order to assist crystallization. Each time when crystallization was completely finished, the organic phase was decanted from the remaining crystal product. The crystals were washed three times with cooled THF. At the end, the salt was dried *in vacuo* ($\leq 1 \times 10^{-5}$ mbar) at *RT* for one week yielding small white crystalline solids, which were stored in a nitrogen flushed glovebox.

Analytics:

δ_H *(300MHz; d-chloroform):* 10.54 (1 H, s), 7.59 (1 H, t, J 1.78 Hz), 7.38 (1 H, t, J 1.78 Hz), 4.25 (2 H, t, J 7.55 Hz), 4.07 (3 H, s), 1.84 (2 H, quint, J 7.32 Hz), 1.32 (18 H, m), 0.81 (3 H, t, J 7.14); δ_C *(300MHz; d-chloroform):* 137.95, 123.64, 121.77, 50.05, 36.54, 31.84, 29.33, 28.97, 26.23, 22.63, 14.09; *m/z (+ESI):* 251.2 (100%, C$^+$), 537.6 (9%, 2CA$^+$-Cluster); *water content:* < 100 ppm; *melting point:* T_m = 41.1°C (DSC-onset); *decomposition temperature:* T_{dec} = 273°C;

3.1.2   1-tetradecyl-3-methylimidazolium chloride (C$_{14}$mimCl)

1-tetradecyl-3-methylimidazolium chloride was obtained by refluxing of 1-methylimidazole with an equimolar amount of 1-chlorotetradecane in acetonitrile at 80°C under a nitrogen atmosphere. The reaction progress was monitored via NMR and after 5-7 days, nearly no remaining reactants were found. Purification was conducted by addition of AN to the reaction mixture from which the first recrystallization was performed. The AN diluted reaction mixture was placed in a cool box overnight at -30°C to assist crystallization of the C$_{14}$mimCl. The organic phase was decanted from the remaining crystal product. After drying *in vacuo* ($\approx$ 1 × 10^{-3} mbar), the salt was further recrystallized three times in tetrahydrofurane in order to obtain high purity of the ionic liquid. Crystallization was assisted by cooling the salt solution in a cool box at -30°C overnight. After filtering off the THF, the remaining solid was washed with fresh cooled THF. At the end, the IL was dried *in vacuo* ($\leq$ 1 × 10^{-5} mbar) at *RT* for one week yielding small white crystalline solids, which were stored under nitrogen.

Analytics:

δ_H *(300MHz; d-chloroform):* 10.50 (1 H, s), 7.61 (1 H, t, J 1.78 Hz), 7.39 (1 H, t, J 1.78 Hz), 4.23 (2 H, t, J 7.41 Hz), 4.05 (3 H, s), 1.82 (2 H, quint, J 7.14 Hz), 1.16 (22 H, m), 0.79 (3 H, t, J 7.00); δ_C *(300MHz; d-chloroform):* 137.85, 123.70, 121.81, 50.02, 36.52, 31.85, 29.61, 26.21, 22.62, 14.07; *m/z (+ESI):* 279.2 (100%, C$^+$), 593.5 (2%, 2CA$^+$-Cluster); *water content:* < 100 ppm; *melting point:* T_m = 53.1°C (DSC-onset); *decomposition temperature:* T_{dec} = 280°C;

3.1.3   1-hexadecyl-3-methylimidazolium chloride (C$_{16}$mimCl)

1-hexadecyl-3-methylimidazolium chloride was obtained from the reaction of 1-methylimidazole with an equimolar amount of 1-chlorohexadecane in acetonitrile at 80°C under a dry nitrogen atmosphere. The reaction progress was monitored via NMR and after 5-7 days, nearly no remaining reactants were found. After cooling to room-temperature a paste-like often amorphous material was obtained. After removing the remaining AN *in vacuo* ($\approx 1 \times 10^{-3}$ mbar), the first purification was conducted recrystallization of the raw C$_{16}$mimCl in ethyl acetate assisted by storage of the salt solution in a cool box at -30°C overnight. Then, the organic phase was decanted from the remaining crystal product followed by washing the crystals with fresh cooled ethyl acetate. After drying *in vacuo* ($\approx 1 \times 10^{-3}$ mbar), the product was further recrystallized three times in tetrahydrofurane in order to obtain high purity of the ionic liquid. During each purification step, crystallization was assisted by cooling the salt solution in a cool box at -30°C overnight. After filtering off the THF, the remaining solid was always washed with fresh cooled THF. At the end, the C$_{16}$mimCl was dried at RT *in high vacuo* ($\leq 1 \times 10^{-5}$ mbar) for one week yielding small white crystalline solids, which were stored under nitrogen.

Analytics:

δ_H *(300MHz; d-chloroform):* 10.79 (1 H, s), 7.43 (1 H, t, J 1.78 Hz), 7.28 (1 H, t, J 1.78 Hz), 4.29 (2 H, t, J 7.25 Hz), 4.11 (3 H, s), 1.88 (2 H, quint., J 6.68 Hz), 1.23 (26 H, m), 0.86 (3 H, t, J 6.45); δ_C *(300MHz; d-chloroform):* 137.82, 123.22, 121.47, 50.18, 36.64, 31.92, 29.69, 26.28, 22.69, 14.13; *m/z (+ESI):* 307.2 (100%, C$^+$), 649.6 (0.19%, 2CA$^+$-Cluster); *water content:* < 100 ppm; *melting point:* T_m = 63.8°C (DSC-onset); *decomposition temperature:* T_{dec} = 274°C;

3.2   1-butyl-3-methylimidazolium tetrafluoroborate (bmimBF$_4$)

3.2.1   1-butyl-3-methylimidazolium chloride (bmimCl)

1-butyl-3-methylimidazolium chloride was synthesized according to standard reaction given in Figure III-2 [4].
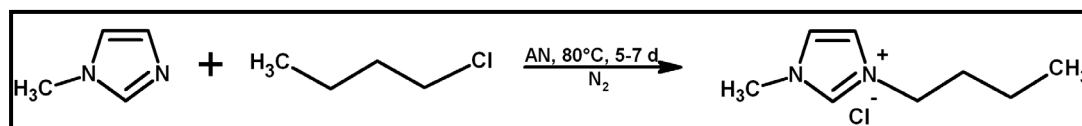
Figure III-2 : Reaction scheme of the synthesis of bmimCl.

1-butyl-3-methylimidazolium chloride was synthesized by the reaction of equi-molar amounts of 1-methylimidazole and 1-chlorobutane in acetonitrile under N$_2$-atmosphere. The reaction, which was monitored via NMR, was normally completed after 4 days. At this time, nearly no remaining reactants were observed within the NMR-spectrum. After further addition of a small amount of AN to the reaction mixture, crystallization of the bmimCl was obtained by cooling the reaction mixture to about 0°C followed by the addition of a seed crystal. Then, the crystallization process was completed in a cool box at -30°C overnight. After entire crystallization, the supernatant acetonitrile was decanted and fresh solvent was added. Because of the hygroscopicity, all work was performed in a N$_2$-atmosphere using Schlenk-technique. This procedure was repeated at least three times until a colourless crystalline product of high purity was obtained. The latter was dried *in vacuo* ($\approx 1 \times 10^{-3}$ mbar) for 2 days at *RT*. It was stored within a glove box.

Analytics:

δ_H (300MHz; d$_3$-acetonitrile): 10.09 (1 H, s), 7.70 (1 H, t, J = 1.78 Hz), 7.65 (1 H, t, J = 1.65 Hz), 4.23 (2 H, t, J = 7.27 Hz), 3.90 (3 H, s), 1.79 (2 H, quint., J = 7.34 Hz), 1.31 (2 H, sext., J = 7.41), 0.87 (3 H, t, J = 7.27); *δ_C (300MHz; d$_3$-acetonitrile):* 136.96, 122.99, 121.73, 48.40, 35.17, 31.20, 18.45, 12.26; *m/z (+ESI):* 138.9 (100%, C$^+$), 313.0

(1.14%, 2CA$^+$-Cluster), (0.04%, 3C2A$^+$-Cluster); *water content:* < 100 ppm; *melting point:* T_m = 63.8°C (DSC-onset);

3.2.2   1-butyl-3-methylimidazolium tetrafluoroborate (bmimBF$_4$)

The 1-butyl-3-methylimidazolium tetrafluoroborate salt was synthesized following the general procedure of Holbrey et al. [5]. The reaction scheme is presented in Figure III-3.
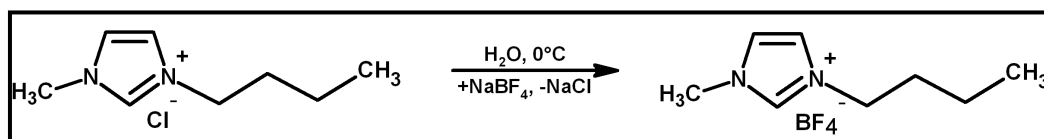
Figure III-3 : Reaction scheme of the synthesis of bmimBF$_4$.

An equimolar amount of NaBF$_4$ was added slowly to an ice cooled, rapidly stirred aqueous solution of 1-butyl-3-methylimidazolium chloride. The product was extracted from the aqueous phase by dichloromethane and washed three times with Millipore-Q water. The organic layer was dried over MgSO$_4$, filtered and then the solvent was removed *in vacuo* ($\approx 1 \times 10^{-3}$ mbar) to yield the tetrafluoroborate RTMS. The obtained colourless liquid was dried *in high vacuo* ($< 1 \times 10^{-5}$ mbar) for 4 days at elevated temperature (about 60°C) and stored in a nitrogen glovebox.

Analytics:

δ_H (300MHz; d$_3$-acetonitrile): 8.48 (1 H, s), 7.39 (2 H, t, J = 1.78 Hz), 7.36 (2 H, t, J = 1.78 Hz), 4.13 (2 H, t, J = 7.27 Hz), 3.82 (3 H, s), 1.80 (2 H, quint., J = 7.48 Hz), 1.31 (2 H, sext., J = 7.55), 0.92 (3 H, t, J = 7.27); *δ_C (300MHz; d$_3$-acetonitrile):* 135.77, 123.36, 121.98, 48.94, 35.47, 31.28, 18.65, 12.38; *δ_B (400 MHz; d$_3$-acetonitrile):* -0.96 (quint., J 1.15 Hz); *δ_F (400 MHz; d$_3$-acetonitrile):* -147.89 (quart., J 1.15), -147.84 (quart., J 1.15 Hz); *m/z (+ESI):* 138.9 (100.00%, C$^+$), 365.1 (1.02%, 2CA$^+$-Cluster); (0.02%, 3C2A$^+$-Cluster); *m/z (-ESI):* 86.9 (100.00%, A$^-$), 312.9 (0.19%, C2A$^-$-Cluster), 539.2 (4.00%, 2C3A$^-$-Cluster); *water content:* < 100 ppm; *decomposition temperature:* T_{dec} = 393°C;

3.3   Ethylammonium nitrate (EAN)

Ethylammonium nitrate was prepared according to a modified procedure originally reported by Evans et al. [6]. The reaction scheme is given in Figure III-4.
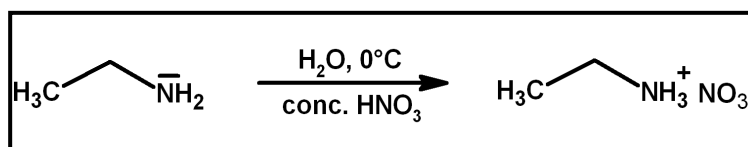
Figure III-4 : Reaction scheme for the synthesis of EAN.

To an ice-cooled stirred solution of 70% (w/w) ethylamine in water a concentrated nitric acid was slowly added so that a slight excess of amine remained. The solution was stirred over night at RT and then concentrated with a rotary evaporator (55°C, ≈ 10 mbar). The residual amounts of water were removed with a lyophilizer. The obtained liquid ethylammonium nitrate was recrystallized three times from acetonitrile. After the removal of the solvent using *vacuo* (≈ 1×10^{-3} mbar), the ethylammonium nitrate was dried *in high vacuo* (< 1×10^{-5} mbar) at *RT* for 4 days. The molten salt was stored under nitrogen in a glovebox.

Analytics:

δ_H *(400MHz; d_3-acetonitrile):* 7.37 (3 H, s), 3.03 (2 H, quart., J 7.32 Hz), 1.23 (3 H, t, J 7.00 Hz); δ_C *(400MHz; d_3-AN):* 35.28, 11.59; ***water content:*** < 100 ppm; ***melting point:*** T_m = 12.2°C (DSC-onset); ***decomposition temperature:*** T_{dec} = 260°C;

3.4   Bibliography

[1]   K. Lunkenheimer, G. Wienskol and A. J. Prosser; Automated High-Performance Purification of Surfactant Solutions: Study of Convective-Enhanced Adsorption. *Langmuir* **20**, 14, 5738-5744 (2004).

[2]   W. F. Hemminger and H. K. Cammenga; *Methoden der Thermischen Analyse, 1st Edition*. Springer, (1989).

[3]   G. Hohne, W. Hemminger and H. J. Flammersheim; *Differential Scanning Calo-rimetry: An Introduction for Practitioners*, *1st Edition.* Springer, (1995).

[4]   K. R. Seddon, A. Stark and M.-J. Torres; Influence of chloride, water, and or-ganic solvents on the physical properties of ionic liquids. *Pure and Applied Chemistry* **72**, 12, 2275-2287 (2000).

[5]   J. D. Holbrey and K. R. Seddon; The phase behaviour of 1-alkyl-3-methylimidazolium tetrafluoroborates; ionic liquids and ionic liquid crystals. *Journal of the Chemical Society, Dalton Transactions: Inorganic Chemistry* **13**, 2133-2140 (1999).

[6]   D. F. Evans, A. Yamauchi, R. Roman and E. Z. Casassa; Micelle formation in ethylammonium nitrate, a low-melting fused salt. *Journal of Colloid and Inter-face Science* **88**, 1, 89-96 (1982).

IV. Experimental

1 Density

1.1 General aspects

During this work density measurements of the investigated systems were carried out in order enable the conversion of different concentration dimensions between each other, e.g. mass ratio into molarity. Additionally, it is possible to extract the molar volume V_m of a component in solution from density measurements, which is a crucial factor in surfactant science, since it can be used to estimate the volume of a monomer molecule in a solvent or the volume of a surfactant aggregated in a micelle, respectively. This has an important meaning, especially for the analysis of scattering data, since it enables the assessment of the particle volume fraction in solution. Densities were determined for all investigated systems presented in this work (SLIL/water-, SILS/IL-, and SLIL/IL/microemulsion-systems) at the interesting temperatures.

1.2 Principle

A very precise method for the evaluation of solution densities is the U-tube method. The oscillating U-tube density meter is based on the principle of a U-tube which has a resonant frequency that is inversely proportional to the square root of its mass. The volume of the tube is given and the density of the liquid sample filled into the U-tube is calculated from its resonant frequency. The relation between periodic time T_{per} and density ρ is given by

$$\rho = \left(A T_{per}^2 \right) - B \qquad \text{(IV-1)}$$

where *A* and *B* are instrument constants. Generally, they are determined from two calibration measurements of two substances with exactly known densities, e.g. water and nitrogen [1].

1.2.1   Apparent Molar Volumes of Surfactants

The apparent molar volumes of an amphiphile can be calculated from density data by the equation

$$V_\phi = \frac{M}{\rho} + \frac{10^3 (\rho_0 - \rho)}{\tilde{m} \rho \rho_0} \qquad\qquad \text{(IV-2)}$$

where *M* and $\tilde{m}$ are the molar mass of the amphiphile and the molality of the surfactant solution. ρ and ρ_0 are the densities of the solutions and pure solvent, respectively [2, 3].

In general, the plot of the apparent molar volume against the molality (or the reciprocal of molality) of a surfactant in aqueous solution shows two linear portions. The intercept of the line at concentrations above the *cac* with the *y*-axis gives the value of V_ϕ^{mic}, and that at concentrations below the *cac* represents the value of V_ϕ^0. The concentration and the apparent molar volume at which the two linear portions intersect correspond to the *cac* of the surfactant and to the corresponding apparent molar volume of the surfactant at the *cac* V_ϕ^{cac} [4].

1.3   Instrumentation

All solution densities were determined by an Anton Paar DMA60/601 HT vibrating-tube density meter connected to a PC with a resolution of 1×10^{-5} g cm^{-1}. The temperature around the density meter cell was controlled by circulating oil from a constant-temperature bath (Thermostat: M. Braun, Thermomix 1400; Cooling source: MGW Lauda RK 20). The temperature was monitored by an ASL F-250 high-precision thermometer connected to a Pt100 probe. The sensor/instrument combination was previously calibrated against a triple point water cell. The temperature uncertainty in all experiments was ± 0.005 K. In order to enable density measurements in nitrogen atmos-

phere, the inlet of the density meter was connected with the gas-tight sample syringe and the nitrogen feed line via a two-way stopcock. The outlet was connected to the wastage reservoir, which acted also as a back-diffusion barrier of air moisture. All connections were made of PTFE-tubes (Figure IV-1).
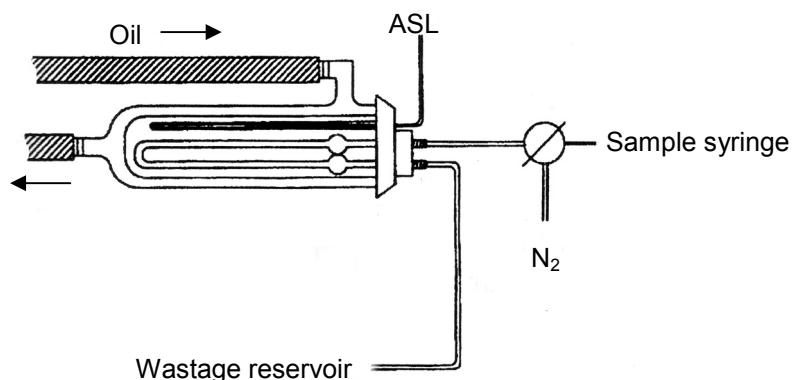
Figure IV-1 : Schematic representation of the instrument setup for the density measurements; indicating the connections of inlet and outlet for measurements in nitrogen atmosphere.

1.4   Sample preparation & measurement procedure

The sample preparation of all solutions was performed one day before the density determination in order to ensure the equilibration of the samples. In the case of the hygroscopic SLIL/RTMS-mixtures and SLIL/RTMS-microemulsion, all samples were prepared in a glovebox filled with dry nitrogen. The investigated aqueous samples were prepared in ambient atmosphere. The sample preparation was performed by weighting the appropriate amount of the components into a glass vessel, which was sealed immediately. For the hygroscopic samples, special glass vessels were used which could be tightly closed in the glovebox by a septum and used at ambient conditions.

Before each measurement series, the instrument constants were estimated with the known densities of pure freshly degassed Millipore-water and dry nitrogen before each measurement series. The literature values of water and nitrogen used for the calibration were taken from Ref. [5].

Every solution was injected slowly to the density meter inlet with a syringe, avoiding bubbles, which would drastically fudge the density result. The density value was taken after 10 minutes of thermal equilibration. Between each measurement, the instrument was comprehensively cleaned with pure Millipore-Q-water, ethanol (technical grade), and finally with acetone (Merck, p.a.) in order to avoid the diversion of impurities from the previous sample solution. After that, the U-tube was dried completely in a flush of dry nitrogen for 15 minutes. The Data evaluation was done with a home-made software package, which directly transferred the obtained periodic time into absolute density values. The uncertainty of the density was estimated to be $\pm\ 5\times10^{-5}$ g cm^{-1} for all performed measurements.

2 Surface tension

2.1 General aspects

Beside conductivity measurements, surface tension measurements as a function of amphiphile concentration are probably the most popular technique to investigate surface-active substances in solution. Consequently, this technique was used to estimate the critical aggregation concentrations (*cac*) and the free energy of adsorption ΔG_{ads}^0 of different long-chain ionic liquids at the liquid-gas interface in aqueous and non-aqueous media. As already pointed out, the non-aqueous media in this context, means RTMS.

2.2 Principle

The cohesive forces between molecules down into a liquid are shared with all neighboring atoms. Those on the surface have no neighboring atoms above and exhibit stronger attractive forces upon their nearest neighbors on the surface (Figure IV-2). This enhancement of the intermolecular attractive forces at the surface is called surface tension.
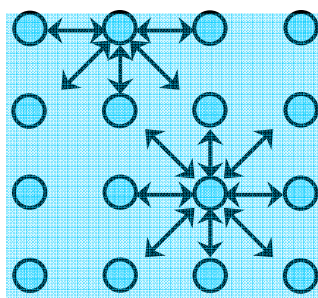
Figure IV-2 : Cohesive forces in liquids.

The enhancement of the intermolecular attractive forces at the surface is called surface tension. It is defined as

$$\sigma = \frac{dW}{dA} \tag{IV-3}$$

where σ is the surface tension, dW is the work of extension which is required to increase the surface A about dA.
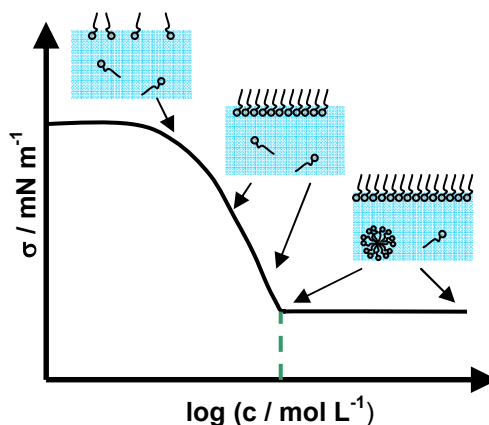
Figure IV-3 : Surface tension evolution as a function of amphiphile concentration.

The presence of amphiphilic molecules at the (l/g)-interface results in a reduction of the surface tension σ as the surface concentration of the surface-active compound increases. At a certain concentration, the solvent surface is densely packed with surfactant monomers. Therefore, σ reaches a constant value and simultaneously mi-

celles are formed and the critical aggregate concentration can be directly determined by the measurement of σ as a function of surfactant concentration. Additionally, information about the surface excess concentration, the area per molecule at surface saturation, and the free energy of adsorption is obtained by analysing the decreasing part σ-$log(c)$-plot, which is related to surfactant adsorption at the interface (cp. Chapter II.2.2). Figure IV-3 illustrates the surface tension evolution as a function of amphiphile concentration.

2.2.1 Surface tension determination: The Du-Noüy-Ring method

The surface tension determination according to Du Noüy utilizes an optimally wettable platinum-iridium ring suspended from a precision balance. A height-adjustable sample carrier is used to bring the liquid to be measured into contact with the probe. The sample is then lowered again so that the liquid film produced beneath the ring is stretched. As the film is stretched a maximum force is experienced; this is recorded by the measurement.

The force F and the resulting work dW, which is required to pull out the wetted platinum-iridium ring by a certain distance is related to the surface tension. The work, which is accomplished during the measurement, is given by

$$dW = F \cdot dx \qquad\qquad \text{(IV-4)}$$

where F is the force needed to pull out the ring from the solution by the distance dx. Hence, this results in an infinitesimal increase of the surface dA:

$$dA = U_{ring} \cdot dx \qquad\qquad \text{(IV-5)}$$

where U_{ring} is defined as the circumference of the platinum ring ($U_{ring} = 4\pi R_{ring}$). By using Eq. (IV-4) and Eq. (IV-5)

$$\frac{dW}{dA} = \frac{F}{U_{ring}}$$ (IV-6)

and with Eq. (IV-3) σ can be finally expressed as

$$\sigma = \frac{F}{U_{ring}}$$ (IV-7)

It is recommended to correct the surface tension values obtained by the weight of the solvent volume below the platinum ring in order to get absolute quantities of σ [6].

2.3 Instrumentation

The surface tension measurements were carried out on a Krüss processor tensiometer K100MK2 connected to a PC. The big advantage of this tensiometer is its ability to measure surface tensions of small volume samples, down to about 1 mL. The instrument setup included a double dosing system (Methrom Liquino 711) with which an automated surface tension determination as a function of amphiphile concentration was possible. In order to achieve an optimal sample thermostatisation, the gadget was connected to circulating oil from a constant-temperature bath (thermostat: Lauda C 6; cooling source: Lauda RC 6 CP). Figure IV-4 illustrates the instrument setup of the K100MK2 used in this work.
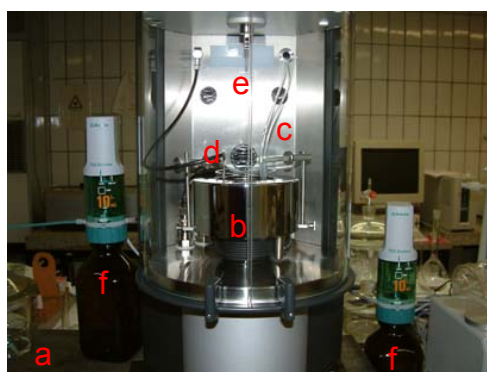
Figure IV-4 : Krüss K100MK2 instrument setup. (a) buffered table, (b) thermostatisation block, (c) PTFE dosing tubes, (d) temperature sensor, (e) ring, (f) double dosing sytem.

The uncertainty of the temperature within the sample was monitored online during each measurement using an external temperature sensor connected to the K100MK2 tensiometer. In each measurement, the temperature was kept constant with an uncertainty lower than ± 0.1 °C. All functions of the Krüss tensiometer was controlled by the Laboratory Desktop Software shipped with the instrument.

2.3.1   Measurement modes

As already mentioned above, the K100MK2 measures a series of different amphiphile concentrations automatically using a double dosing system, which persists of two automatic dispensers. The latter are fully controlled by the tensiometer software. When using the automated measurement feature two procedures can be chosen: (i) direct concentration measurement or (ii) reversed concentration measurement. In the case of a direct measurement, the sample vessel is filled with pure solvent and a stock solution is dosed to the sample, whereas in the case of a reversed measurement the parent solution is first put into the sample vessel and then gradually diluted with the solvent.

In addition to the automated procedures, manual measurements, as in common tensiometer systems, are possible, and sometimes preferable, especially if measurements in nitrogen atmosphere have to be carried out, since measurements in inert-gas are not possible when the automated configuration is used.

2.3.2   Wettable probe: The ring

Although the plate method is also available for the Krüss tensiometer, the ring method based on Du-Noüy was used for all investigated methods because of the following reasons [7]:

(i)   Many values found in the literature were obtained using the ring method. Therefore, the ring method should be preferred for comparison purposes.

(ii)   The wetting length of the ring exceeds that of the plate by a factor of three. This fact leads to a higher force on the balance and accordingly to a better accuracy.

(iii)   Some substances, i.e. cationic surfactants, show poor wetting properties on platinum. In such cases, the line between ring and the solution is more even in the case of the ring than in the case of the plate.

The K100MK2 tensiometer measure samples with a volume down to 1 mL with high accuracy. Depending on the sample volume two different platinum-iridium rings had to be used. For volumes greater or equal than 50 mL a "big ring" (Figure IV-5, right) had to be used, whereas for volumes lower than 50 mL a "small ring" (Figure IV-5, left) had to be applied.
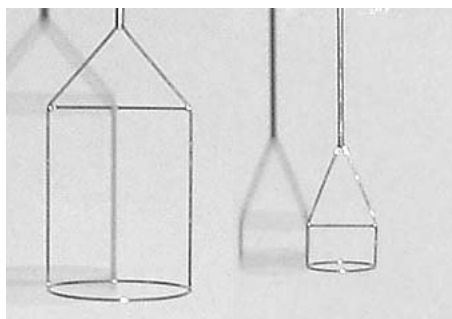
Figure IV-5 : Two different platinum-iridium-rings for big (left) and small sample volumes (right).

2.3.3   Sample cells

As in the case of the wettable probes, two different sample cells, for large and small sample volumes, were supplied with the tensiometer. For volumes $\geq$ 50 mL a standard glass vessel with a maximum volume of 120 mL is recommended by the supplier, whereas in the case of smaller volumes, i.e. 1.5 mL, Krüss delivers two special small volume sample cells, one made of Teflon and one made of metal. Interestingly, both standard small volume sample cells showed no good accuracy during test measurements of pure water. The tensiometer generally measured too high surface tension values for water (1.5 mL) when the metal cell was used and too low surface tensions when the Teflon cell acted as solvent vessel. Further, a good thermostatisation of the two cells was not possible, since the contact between the gadget and the cell was not factory-provided. Therefore, a homemade sample cell construction was applied utilizing

a copper block, which fits into the tensiometer cell holder for thermostatisation purposes and a watchglass used as sample cell. Extensive test measurements of water at 25 °C showed very good accuracy using the new cell design. The optimal sample volume was determined to be between 1.5 and 2 mL. The time to reach the thermal equilibrium within the samples was 1 h for the large volume and 15 minutes for the small volume cells. An overview of the sample cells used in this work is given in Figure IV-6.

Figure IV-6 : Homemade sample cell construction for small sample volumes (right) utilizing a copper block, which fits into the tensiometer cell holder for thermostatisation purposes, and a watchglass acted as sample vessel. Standard sample container for big sample volumes (left).

Principally, investigations of surface tensions in inert atmosphere are possible with the K100MK2 tensiometer, but only in the manual measurement mode. Therefore, all measured hygroscopic solutions (SLIL/RTMS-mixtures) had to be prepared and measured separately. When measurements were performed in inert atmosphere, the sample cell was enhanced by a top cover (Figure IV-7), which separates it from air moisture. The closed assembly was purged with the inert gas for 20 minutes until all air was exchanged by it. Then, the sample was filled into the cell during gas flow. As inert atmosphere, argon from a pressure bottle was chosen, because of its high molecular weight, supporting the cell filling.
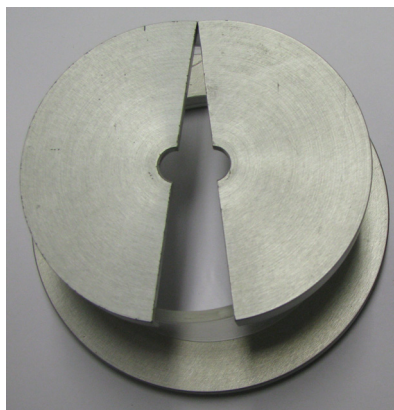
Figure IV-7: Top cover used for surface tension measurements in argon atmosphere.

2.3.4 Calibration & corrections

The Krüss K100MK2 tensiometer measures the surface tension on absolute scale; no specific calibrations had to be taken into account. However, the high precision balance, which measures the force, necessary for the σ calculation, had to be calibrated. This procedure was done automatically by the tensiometer using an internal weight standard, as in common modern balances. Calibration of the balance was performed before each measurement series [8]. Additionally, the surface tension had to be corrected by the weight of the solvent volume below the platinum ring. Three different correction methods were available and recommended by the supplier:

    (i)   Corrections of Harkins & Jordan

   (ii)   Corrections of Zuidema & Waters

  (iii)   Corrections of Huh & Mason

The most popular method to correct surface tensions is that of Harkins and Jordan, therefore, this method is the most suitable for comparison purposes. The other two methods are not well established in the literature, thus they are of low interest in scientific investigations. For all investigations, the correction of Harkins & Jordan was applied [9]. The Krüss software calculated the corrected surface tension values automatically.

2.4   Cleaning, sample preparation & measurement procedure

Estimating surface tension data with high accuracy, all measurements were carried out carefully including extensively cleaning of the used glassware and the wettable probe. Additionally, many test measurements were performed in order to determine the optimal sample preparation and the optimal input parameters for the control software, especially in the case of the investigated SLIL/IL-mixtures measured in inert atmosphere. At the end, a reliable procedure was obtained resulting in surface tension data with high accuracy and reproducibility.

2.4.1   Cleaning

Surface tension measurements require a large operating expense by the scientist, because every impurity influences the value of σ drastically [10, 11]. Contaminant pollutes normally result from impure substances, cruddy sample cells, and dirty wettable probes. Therefore, great efforts have been made during this thesis to avoid this problem by using only compounds with very high purity and by cleaning all needed glassware (sample cells, ect.) extensively before use.

The general procedure of cleaning was carried out as follows: First, the glassware was rinsed with Millipore-Q-water. Then, it was stored over night in a special cleaning bath, a mixture of KOH (technical grade), isopropanol (technical grade), and water (bi.dest). After that, the glassware was washed with Millipore-Q-water and aqueous HCl (Merck, p.a.). Finally, it was rinsed with Millipore-Q-water and then with acetone (Merck, p.a.). Drying was performed over night in a drying oven working at 100°C. The wettable probes were cleaned between each measurement as it is recommended by Krüss [12]: First, the ring was carefully burned out using a gas torch and afterwards, it was rinsed with ethanol p.a (Baker, analyzed) and acetone (Merck, p.a.), respectively.

2.4.2   Sample preparation

The aqueous long-chain ionic liquid systems were measured using the automated reverse measurement feature of the K100MK2. Therefore, a stock solution of each sur-

factant ionic liquid in water with a concentration of 0.1 mol/L was prepared one day before the investigation. On the next day, 100 mL of the parent solution was carefully transferred into the sample cell for large volumes. After 1 h of thermostatisation at 25°C, the measurement was started. Then, the tensiometer began to record the surface tension as a function of surfactant-IL concentration by diluting the stock solution gradually with pure Millipore-Q-water. After each dilution, the solution was stirred automatically by the tensiometer for 3 minutes, establishing temperature and concentration equilibrium.

The hygroscopic SLIL/IL-mixtures were prepared one day before the measurement in a glovebox filled with dry nitrogen. The sample preparation was done by weighting the appropriate amount of components into special glass vessels, which could be tightly closed with a septum. Each compounded concentration was measured consecutively in the manual mode of the tensiometer in argon atmosphere. A sample volume of 1.7 mL and the small ring as wettable probe was used. As sample cell, the homemade construction was applied and filled with a syringe in a flow of argon. Between each sample, the watchglass was displaced by a clean one. The SLIL/EAN-systems were investigated at 25°C, whereas the SLIL/BmimBF$_4$-systems were measured at 40°C. The thermal equilibrium was reached within 15 minutes in all cases.

2.4.3   Input parameters

The supplied Laboratory Desktop Software tensiometer software package controls the whole measurement and it calculates the absolute surface tensions. For this purpose, the program needs several input parameters. Table IV-1 summarizes the basic input parameters for large and small sample volumes used in this work. For the automatic dosing measurements additional input parameters had to be given, which are mainly used to calculate the current solution concentrations and to define the covered concentration range. The additional parameters used for the three aqueous SILS-systems are summarized in Table IV-2.

Parameters	Inputs: Large volume measurements (100 mL)	Inputs: Small volume measurements (1.7 mL)	
Wettable probe	Large ring	Small ring	
Radius / mm	9.545	4.85	
Wire diameter / mm	0.37	0.3	
Liquid phase	Water	EAN	bmimBF$_4$
Density / g cm^{-3}	0.9970 (25°C)[a]	1.2110 (25°C)[b]	1.1960 (40°C)[b]
Gas	Air	Argon	
Density / g cm^{-3}	1.2929	1.7837	
Procedure control	automatic	manual	
Detection / mm min^{-1}	6	6	
Measuring / mm min^{-1}	4	3	
Immersion depth / mm	3	2.5	

Table IV-1 : Parameters used for the Krüss K100MK2. [a]From Ref. [5]. [b]Obtained from density measurement.

Parameters	Inputs		
Solvent	Water		
Molarity / mol L^{-1}	55.409		
Surfactant	C$_{12}$mimCl	C$_{14}$mimCl	C$_{16}$mimCl
Molar mass / g mol^{-1}	286.88	314.94	342.99
Base solution	SLIL / water		
Concentration / mg L^{-1}	28688	31494	34299
Density / g cm^{-3}	0.996	0.996	0.996
Add solution	Water		
Concentration[a] / mg L^{-1}	0		
Density / g cm^{-3}	0.9970		
Dosing control	Automatic		
Stirring time / s	300		
Stirring speed / %	50		
Dosing volume / mL	10		
Dosing steps	60		

Table IV-2 : Additional parameters used for automated measurements of the C$_n$mimCl amphiphiles in water. [a]Concentration of the respective amphiphile in the stock solution. [b]From Ref. [5].

3   Conductivity

3.1   General aspects

With electrical conductivity investigations, it is possible to further characterize colloidal systems. Today, conductivity measurements of aqueous surfactant solutions are conducted by default in order to obtain the critical micellar concentration and the degree of counterion dissociation (or ionization degree) α_{mic} of the surfactant monomers within the micelle [13-15]. Additionally, conductivity measurements can be used for the determination of the degree of counterion binding and the determination of the aggregation number by applying the mixed electrolyte mass action model of 1:1 electrolytes [16-19].

In the case of microemulsion science, conductance measurements are also a very convenient technique to obtain information about these interesting systems. The conductivity data of microemulsions can be discussed by applying different theories, which were already pointed out in Chapter II.2.5.3, because of their importance in understanding microemulsion evolution.

3.2   Principle

In this work, conductivity measurements were carried out for the aqueous SLIL-systems as well as for the SLIL/RTMS-microemulsions. Conductance data can be expressed in two ways, (i) as specific conductance, κ,

$$\kappa = \frac{C}{R}$$

(IV-8)

where C is the cell constant and R the measured resistance; or as (ii) equivalent conductance, Λ,

$$\Lambda = \frac{10^3 \kappa}{c}$$

(IV-9)

which gives the conductance per mole electrolyte [20].

3.2.1 Determination of *cmc* & α_{mic} in aqueous surfactant systems

Conductivity measurement as a function of surfactant concentration c is a very powerful method to determine the *cmc* and α_{mic} of aqueous surfactant systems, since this method supplies high sensitivity. Figure IV-8 shows a typical $\kappa - c$ –plot of an aqueous amphiphile system. The κ value increases linearly with increasing surfactant concentration and the slope changes suddenly at a certain concentration. This steep change of the $\kappa - c$ –plot indicates the formation of molecular aggregates. The *cmc* is determined from the break point of the $\kappa - c$ –plot. The ionization degree, in the case of ionic surfactants, can be obtained form the plot using the following equation:

$$\alpha_{mic} = \frac{S_2}{S_1}$$
                              (IV-10)

where S_1 and S_2 denote the pre-micellar slope (below the bend) and the post-micellar slope (above the bend) of the conductivity plot, respectively [21].
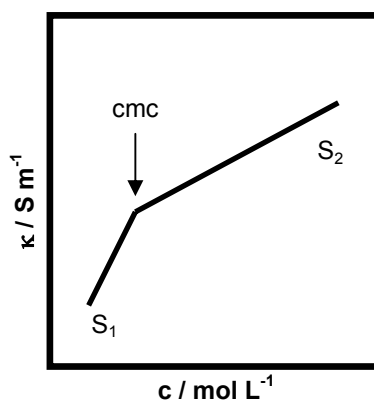
Figure IV-8 : $\kappa - c$ –**plot of an aqueous surfactant solution below and above the *cmc*.**

However, the above mentioned procedure encloses two problems: (i) At very dilute concentrations, the Kohlrausch´s law of the square root of concentration predicts a

non-linear relation between conductivity and concentration [20] and (ii) at higher concentrations (much higher than the *cmc*), one can observe a lack of linearity in the $\kappa - c$ –plot. An additional problem arises, when the conductivity plot exhibits only a weak curvature. In this case, the width of the transition, which indicates how abrupt or gradual the micellization process is, complicates the exact determination of the *cmc*, and therefore the determination of α_{mic}. Consequently, the value reported as the *cmc* depends, in some measure, on the good judgement of the researcher, especially, when weak amphiphiles are investigated. It has been shown by Carpena et al. that by fitting the $\kappa - c$ –plot of surfactants with Eq. (IV-11), more reliable and more accurate values of the *cmc* as well as of the degree of counterion dissociation can be obtained.

$$\kappa = \kappa_0 + S_1 c + dx \left(S_2 - S_1 \right) ln \left(\frac{1 + exp\left(\frac{(c - cmc)}{dx} \right)}{1 + exp\left(\frac{-cmc}{dx} \right)} \right) \tag{IV-11}$$

where S_1 and S_2 represents the asymptotic value for small and large values of *c*, respectively. The parameter dx deals with the width of the transition [22]. For the estimation of α_{mic} two different references are given in literature. It is possible to calculate α_{mic} by Frahm's method by dividing the slopes of the straight lines above and below the cac (Eq. (IV-10)) [21]. This method is simple, but is only a useful approximation when the aggregation number of the micelle is not available. The reason is that the conductivity of the macroion is not taken into account leading to relatively high values for α_{mic}. Another possibility for the determination of the latter is to use the Evans equation, which additionally considers N_{agg} [14]:

$$1000 S_2 = \frac{\left(N_{agg} - m_{coion} \right)^2}{\left(N_{agg} \right)^{4/3}} \left(1000 S_1 - \Lambda_{coion} \right) + \left(\frac{N_{agg} - m_{coion}}{N_{agg}} \right) \Lambda_{coion} \tag{IV-12}$$

where m_{coion} is the number of associated counterions, Λ_{coion} is the equivalent conductance of the surfactant counterion at infinite dilution, and S_2 and S_1 are the same slopes as defined before.

3.2.2 The mixed electrolyte mass action model for aqueous surfactant systems

A further method to analyse conductivity-concentration data of aqueous surfactant solutions was originally developed by Shanks & Franses, and has been frequently applied to estimate the micellization parameters, i.e. *cmc*, the aggregation number N_{agg}, and the degree of counterion binding β [16, 18, 19]. In contrast to the analysis presented previously, the method of Shanks et al. describes the equivalent conductivity-square root concentration plot ($\Lambda - \sqrt{c}$ –plot) of aqueous surfactant solutions. An example of a Λ –plot as a function of the square root of surfactant concentration in aqueous solution is schematically shown in Figure IV-9.
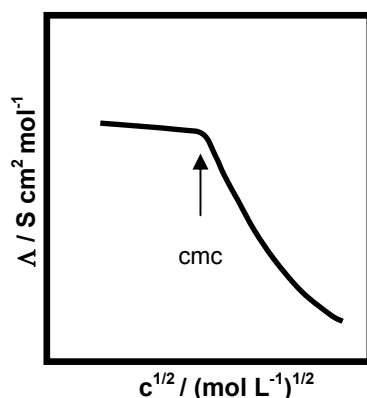
Figure IV-9 : $\Lambda - \sqrt{c}$ –plot of an aqueous surfactant solution below and above the *cmc*.

The so-called mixed electrolyte mass action model makes use of an effective combination of (i) the monodisperse mass action model and (ii) the Debye-Hückel-Onsager conductivity equations, to calculate the equivalent conductivities of the monomeric surfactant and micelle, respectively.

The mass action model, as already explained (cp. Chapter II.2.3.5), describes the self-assembly of a cationic surfactant into micelles as follows:

$$nS^+ \quad + \quad n\beta X^- \quad \rightleftharpoons \quad S_nX_{n\beta}{}^{n(1-\beta)} \qquad (R.V\text{-}1)$$
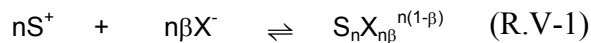
where S^+ is the monodispersed surfactant ion, X^- is the counterion, n the micellar aggregation number (also denoted N_{agg}) and β the degree of counterion binding on the micelle. According to this model, the molar conductance Λ of micellar solution is expressed by the sum of the two contributions resulting from the monomeric species and the micellar species as

$$\Lambda = \Lambda_{1eq} \cdot \frac{cmc}{c} + \Lambda_{meq} \cdot \left(1 - \beta\right) \cdot \frac{c - cmc}{c} \qquad (IV\text{-}13)$$

where Λ_{1eq} and Λ_{meq} represent the equivalent conductance of the monomeric surfactant and the micelle, respectively. c is the total surfactant concentration, and the monomeric surfactant concentration is approximated by the *cmc*.

Using the Onsager theory for the electrical conductance, Λ_{1eq} and Λ_{meq} are given by the following equations

$$\Lambda_{1eq} = \Lambda_1^0 - A_1 \frac{\sqrt{I}}{1 + B_0 a_1} \qquad (IV\text{-}14)$$

$$\Lambda_{meq} = \Lambda_m^0 - A_m \frac{\sqrt{I}}{1 + B_0 a_m} \qquad (IV\text{-}15)$$

where Λ_1^0 and Λ_m^0 are the equivalent conductance at infinite dilution for monomeric surfactant and micelle, respectively. A_1 and A_m are constants expressed by

$$A_i = \frac{2.801 \times 10^6 |z_+ z_-| q \Lambda_i^0}{\left(\varepsilon_r^w T\right)^{3/2} \left(1 + \sqrt{q}\right)} + \frac{41.25\left(|z_+| + |z_-|\right)}{\eta \sqrt{\varepsilon_r^w T}}$$

(IV-16)

where ε_r^w is the dielectric constant of water, z_+ and z_- are the valences of the electric charge of cationic and anionic species, respectively; for a cationic 1:1 surfactant: $z_+ = +1$, and $z_- = -1$ for the surfactant monomer; $z_+ = n(1-\beta)$ and $z_- = -1$ for the micelle. q in Eq. (IV-16) is a constant presented by

$$q = \frac{|z_+ z_-|\left(\lambda_+^0 + \lambda_-^0\right)}{\left(|z_+| + |z_-|\right)\left(|z_+ \lambda_-^0| + |z_- \lambda_+^0|\right)}$$

(IV-17)

where λ_+^0 and λ_-^0 are the limiting equivalent ionic conductance of cationic and anionic species, respectively; for a cationic 1:1 surfactant: $\lambda_+^0 = \lambda_{S^+}^0$ for the surfactant mono-mer; $\lambda_+^0 = \lambda_m^0$ for the micelle, and $\lambda_-^0 = \lambda_{Cl^-}^0$. In Eq. (IV-14) and in Eq. (IV-15), I is the ionic strength, which is defined as

$$I = \frac{1}{2} \sum_i z_i^2 c_i$$

(IV-18)

and B_0 is a constant given by

$$B_0 = \sqrt{\frac{8\pi N_A e_0^2}{10^3 \varepsilon k_B T}} \cdot \sqrt{I}$$

(IV-19)

where N_A is the Avogadro number, e_0 is the electronic charge and k_B is the Boltz-mann constant. The parameters a_1 and a_m in Eq. (IV-14) and Eq. (IV-15), respectively, are effective diameters of ions. For the present case (1:1 cationic surfactant)

$$a_1 = r_1 + r_{Cl^-}$$

(IV-20)

$$a_l = r_m + r_{Cl^-} \tag{IV-21}$$

where r_1, r_m, r_{Cl^-} are the radius of surfactant monomer, micelle, and chloride ion, respectively.

If the values of *cmc*, N_{agg}, and β are given, Λ can be calculated from the above introduced equations because the values of parameters and constants appearing in these formulas can be estimated. In other words, these parameter values can be determined by comparing the calculated Λ with experimental Λ. Their true values must reproduce the experimental $\Lambda - \sqrt{c}$ –profile. In the three parameters, the *cmc* can be determined from the $\kappa - c$ –plot, and the other two can be obtained so as to provide the best-fit curve to the experimental data. The remaining unknown parameters, which are necessary for the calculation of Λ, can be estimated as follows: The value of Λ_l^0 is determined experimentally by extrapolating the linear part of the $\Lambda - \sqrt{c}$ –plot to zero concentration. Λ_l^0 is composed of two terms as

$$\Lambda_l^0 = \lambda_{S^+}^0 + \lambda_{Cl^-}^0 \tag{IV-22}$$

The value of $\lambda_{Cl^-}^0$ can be taken from literature, and the value of $\lambda_{S^+}^0$ was estimated from Λ_l^0 and $\lambda_{Cl^-}^0$. The equivalent conductance is expressed by

$$\Lambda_{meq}^0 = \lambda_m^0 + \lambda_{Cl^-}^0 \tag{IV-23}$$

The value of λ_m^0 was estimated from the Stokes-Einstein relation with the knowledge of the radius of the micelle:

$$\lambda_m^0 = \frac{e_0 F}{6\pi \eta r_m} \tag{IV-24}$$

where F is the Faraday constant, η is the viscosity of the solution, and r_m is the radius of the micelle. The value of r_m was estimated by the use of the radius of surfactant

monomer, r_1, and the micellar aggregation number, N_{agg}, assuming the following relation

$$\frac{4}{3}\pi r_m^3 = N_{agg} \cdot \frac{4}{3}\pi r_l^3 \qquad\qquad (IV\text{-}25)$$

which leads to

$$r_m = N_{agg}^{1/3} \cdot r_l \qquad\qquad (IV\text{-}26)$$

The radius of the surfactant monomer, r_1, is estimated using the Stokes-Einstein relation,

$$r_l = \frac{e_0 F}{6\pi\eta\lambda_{S^+}^0} \qquad\qquad (IV\text{-}27)$$

where a spherical shape is assumed for the monomeric surfactant molecule in solution. Using r_m thus obtained from r_1 according to Eq. (IV-26), the value of λ_m^0 is estimated from Eq. (IV-24), and then, Λ_{meq}^0 from Eq. (IV-23). The value of r_{Cl^-} needed in Eq. (IV-20) and in Eq. (IV-21) was estimated from $\lambda_{Cl^-}^0$ using the Stokes-Einstein relation again.

It has been reported that the estimation of ionic strength of micellar solution is a major problem in the application of this model to analyze the experimental conductivity data [16, 18, 19]. Several expressions were proposed for the ionic strength of micellar solutions [16, 18]. The results have demonstrated that the contribution of micelles to effective ionic strength is negligible in most cases. Therefore, the ionic strength given by $I = c_t$ for $c_t < cmc$ and $I = cmc$ for $c_t > cmc$ is satisfactory for estimation of micellization parameters by applying the mixed electrolyte model [18]. The latter assumption was also applied in the underlying study.

3.2.3   Low concentration chemical model: lcCM

The analysis of conductivity data below the *cmc*, where ionic surfactants behave as classical binary electrolytes, can be carried out in the framework of the low concentration chemical model (lcCM). This model represents the ions as spherical particles of a certain charge in a homogeneous and isotropic solvent of relative permittivity. It further considers the possibility of ion pair configurations of oppositely charged ions in solution. For example, electrically neutral ion pairs of the types $[C^{z+}A^{z-}]^0$, $[C^{z+}SA^{z-}]^0$, and $[C^{z+}SSA^{z-}]^0$ are taken into account by the lcCM, where C denotes the cation, A the anion, and S the solvent molecule. $z+$ and $z-$ are the charges of the ions, positive and negative, respectively. For a detailed description of the lcCM model and its theory, the reader is referred to Ref. [23]. The basic equations of the lcCM are

$$\frac{\Lambda}{\alpha} = \Lambda^\infty - S\sqrt{\alpha c_s} + E\alpha c_s \, ln(c_s) + J_1 \alpha c_s + J_2(\alpha c_s)^{2/3} \qquad \text{(IV-28)}$$

$$K_A = \frac{1-\alpha}{c_s \alpha^2 \gamma'^2_\pm} \qquad \text{(IV-29)}$$

$$\gamma^2_\pm = exp\left(-\frac{\kappa q}{1+\kappa R}\right) \qquad \text{(IV-30)}$$

$$\kappa^2 = 16\pi N_A q\alpha c_s \qquad \text{(IV-31)}$$

$$q = \frac{e_0^2}{8\pi\varepsilon_r\varepsilon_0 kT} \qquad \text{(IV-32)}$$

$$K_A = 4\pi N_A \int_a^R r^2 \, exp\left[\frac{2q}{r} - \frac{W^*}{kT}\right] dr \qquad \text{(IV-33)}$$

where Λ and Λ^∞ are the molar conductivities at molarity c and infinite dilution, $(1-\alpha)$ is the fraction of oppositely charged ions acting as ion pairs, and K_A is the equilibrium constant of the lcCM with an upper association limit R; $\gamma'_\pm$ is the corresponding activity coefficient of the free ions ($(\gamma'_\pm)^2 = \gamma'_+\gamma'_-$), k is the Debye parameter, e_0 is the proton charge, ε_r is the relative permittivity of the solvent, ε_0 is the permittivity of vacuum and T the absolute temperature. The other symbols have their usual

meaning. W^* is a step function for the potential of mean force between cation and anion due to non-Coulombic interactions.

The coefficients of Eq. (IV-28) are given in Ref. [23]. The limiting slope S and the parameter E are evaluable when the solvent data is available. The coefficients J_1 and J_2 are functions of the distance parameter R, representing the distance to which oppositely charged ions can approach as freely moving particles in solution.

Analysis of the conductivity data of associated electrolytes are carried out by setting the coefficients S, E and J_1 of Eq. (IV-28) to their calculated values and then usually using three-parameter fits to obtain the limiting values of molar conductivity Λ^∞, the association K_A and the coefficient J_2 by non-linear least squares iterations [23]. The input data for the calculation of the coefficients are the known solvent properties given in literature and the distance parameter R (upper limit of the association integral). R can be expressed by the following formula:

$$R = a + n \cdot s \qquad\qquad \text{(IV-34)}$$

where s is the length of an oriented solvent molecule, n is an integer, n = 0, 1, 2,..., and a is the lower limit of the association integral. The lower limit of the association integral is the distance of closest approach of cation and anion (contact distance, $a = a_+ + a_-$) calculated from the ionic radii of the cations [23, 24].

3.2.4 Dynamic percolation & charge fluctuation model

Conductivity investigations are also very useful for the investigation of microemulsions. Several methods like the percolation model or charge fluctuation models have been applied by colloid chemists for the characterization of microemulsion systems. The information, which can be obtained by these models, was already described in detail in Chapter (II.2.5.3). Therefore, no further information concerning these theories is given here.

3.3   Instrumentation

The temperature and concentration dependence of electrolytes and polyelectrolytes in solution has been proved as one of the most appropriate methods for studying ion-ion interactions. Evaluating the conductivity within the framework of present electrolyte theories mentioned above, requires data with high accuracy, which is difficult to achieve over a sufficiently large temperature range.

For the recent investigations of the aqueous SLIL systems and for the microstructure characterization of the SLIL/IL-based microemulsions, a homemade conductivity equipment, which has been applied by the Institute of Physical and Theoretical Chemistry, University of Regensburg, Germany for more than 30 years, was used. The evidence of its excellence is represented in more than 100 papers on high precision conductance data[b]. This equipment has been accomplished by using an electrode assembly in the arm of an a.c. bridge built on the classical lines of Jones [25] and Shedlovsky [26, 27]. Using the precise conductance bridge, the electrolyte conductance at every measured temperature could be obtained with accuracy better than 0.01%.

Detailed information of the equipment including temperature control and measuring method is given in literature [28, 29]. Nevertheless, a short overview of the gadget will be presented in the following chapters.

3.3.1   Thermostatisation

The thermostatisation of the conductivity cells is established with the help of a circulating silicon oil bath. The temperature of the oil is controlled by a main- and pre-thermostat (Figure IV-10). The pre-thermostat has a mean of constant cooling source. Thereto, its temperature is adjusted 10°C below the temperature of the main-thermostat. The cooling medium is permanently circulated through the main-thermostat. The flow rate and the cooing rate, respectively, can be controlled by a needle valve (NV). The temperature of the main thermostat is adjusted via a platinum-resistance-thermometer (PT) connected to a Wheatstone-bridge. In order to control the temperature, the calibra-

---

[b] *Reference: SciFinder*

tion value of the platinum-resistance-thermometer for the required temperature has to be set at the Wheatstone-bridge. The latter, was calibrated at the beginning of this work with an ASL F-250 high precision thermometer utilizing a Pt100 temperature sensor calibrated prior with a triple-water-cell.

The temperature is a linear function of the resistance. It can be described using the following formula

$$\theta = 0.53449 \frac{°C}{\Omega} \cdot R - 251.25815°C \qquad \text{(IV-35)}$$

The difference between this set point and the actual value of the platinum-resistance-thermometer within the thermostat is transferred via a PID-controller into a control signal which actuates the heater (H). The temperature uncertainty is ± 0.001 K. Additionally, the main-thermostat is equipped with a high-performance heater (AH), which can be used for fast heating of the oil bath. The conductivity cells are directly attached into the thermostat by mounting the cells into the cell holder (CH).
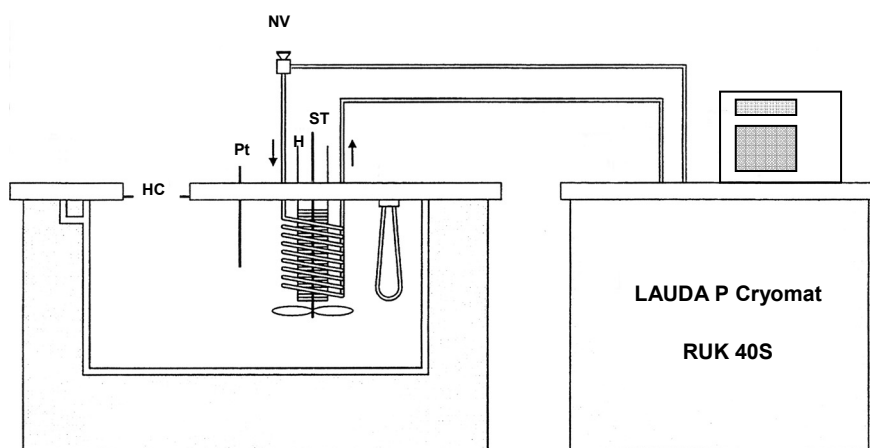
Figure IV-10 : Thermostatisation construction: (CH) cell holder, (PT) platinum resistance thermometer, (NV) needle valve, (H) heater, (AH) additional heater, (ST) stirrer.

3.3.2   Conductivity cells

Two types of conductivity cells were used for the measurements, cells for small sample volumes (3 - 10 mL), which had to be readily filled with the sample, and cells with a volume of about 400 mL, named mixture cells. The latter were filled with pure solvent and a stock solution was dosed step by step to the sample. Between each dosing step, the conductivity was measured. Normally, mixture cells are used for very dilute concentration ranges, as they are equipped with three electrode cavities with different cell constants allowing the selection of the optimal resistance range during the measurement. Figure IV-11 shows a schematic representation of a small sample conductivity cell. These types of cells are made up of only one electrode cavity, which is very small. The platinum electrodes are based upon the three-electrode-arrangement (E_1, E_2, E_3) which eliminates disturbing earth impedances.
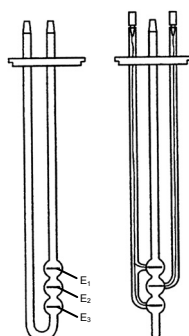
Figure IV-11 : Small sample conductivity cell with a three-electrode-arrangement (E_1, E_2, E_3).

Six different conductivity cells of the above type were used in this work differing by the cell constants.

The mixture cells presented in Figure IV-12 consisted of a big mixing vessel (MV) which was stirred by a magnetic stir bar. The stirrer (ST) was placed below. Around the mixing vessel, the three different electrode cavities were arranged. The elec-

trodes provided also a three-electrode arrangement (E_1, E_2, E_3). The electrode cavities and the corresponding electrodes are given in more detail in Figure IV-13.

In the case of the mixture cell, a parent solution was dosed stepwise to the pure solvent using a syringe. The actual concentration in the cell was obtained from the weight and density of the injected stock solution using Eq. (IV-39) and Eq. (IV-40). An additional advantage of the mixture cell was the possibility to completely run measurements in inert gas atmosphere, which resulted in very accurate and reproducible data.
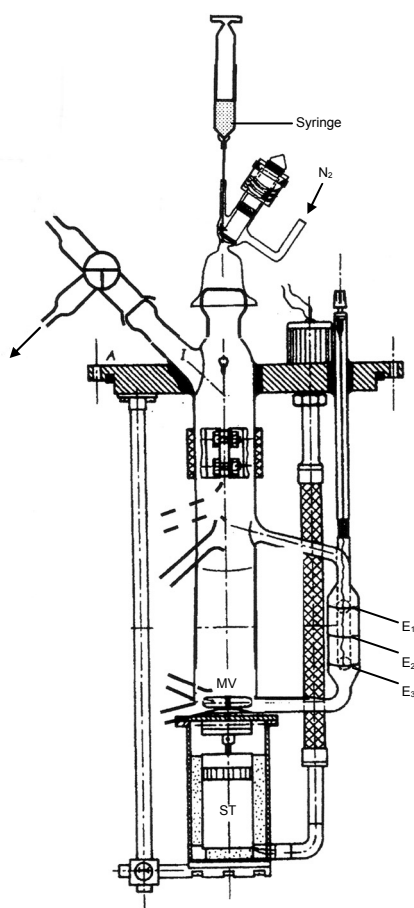
Figure IV-12 : Schematic representation of the mixture cell with one electrode cavity, the other two are not given for clarity purposes.
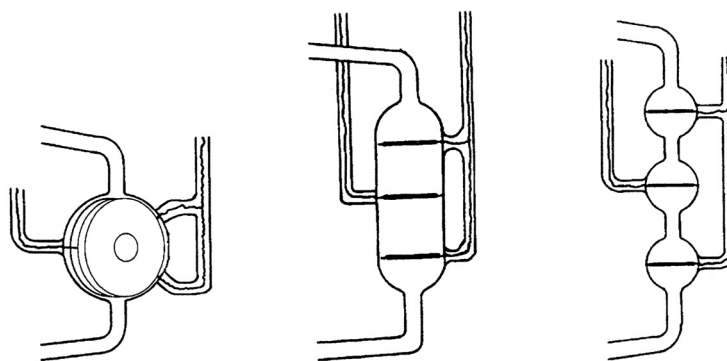
Figure IV-13 : The three electrode cavities of the mixture conductivity cell.

In contrast to the mixture cell, the small sample conductivity cells could be used only in semi-inert gas atmosphere, i.e. during the filling procedure, no argon or nitrogen purge was available, because of the cell layout. In general, the results obtained by the small sample cells were excellent at very dilute concentrations, but far from the accuracy of the mixture cells.

3.3.3   Calibration: Cell constants

The exact determination of the conductivity cell constants is a very crucial factor in order to obtain reliable data. All the presented conductivity cells used in this work were calibrated by the use of aqueous KCl solutions at different concentrations c. The equivalent conductivity of KCl at 25°C is given by

$$\Lambda = 149.873 - 95.01\sqrt{c} + 38.48 c \log c + 183.1c - 176.4\sqrt[3]{c} \qquad \text{(IV-36)}$$

where Λ is obtained in cgs-units [30]. The conversion in SI-units was performed by the following relation:

$$\Lambda / cm^2 \Omega^{-1} mol^{-1} = \Lambda / 10^4 m^2 \Omega^{-1} mol^{-1} \qquad \text{(IV-37)}$$

The cell constant C can then be calculated by

$$C = \Lambda \cdot \left(10^3 \, dm^3 m^{-3}\right) c \left(\frac{1}{R_e} - \frac{1}{R_{solv}}\right) \qquad \text{(IV-38)}$$

where R_e is the resistance of the electrolyte solution at infinite frequency, whereas R_{solv} is the resistance of the pure solvent at 120 Hz.

The obtained cell constants used for the calculation of the whole conductivities, which are presented in this work are summarized in Table IV-3. The calibration measurements were performed with KCl of highest purity available (Merck, selectipur) which was dried in high-vacuo ($\leq 10^{-5}$ Torr) for 5 days. The stock solution for the mixture cells was prepared using Millipore-Q-water ($\Lambda_{Milli} = 10^{-7}$ S m^{-1}) which was degassed previously *in vacuo* for 20 minutes. The molonity of the parent solution was 0.355 mol/kg.

Cell constants	
Small volume cells	*C / 10² m⁻¹*
Cell 1	0.020842
Cell 2	0.24611
Cell 3	0.53638
Cell 4	2.2398
Cell 5	4.6980
Cell 6	11.607
Mixture cell^c	*C / 10² m⁻¹*
Cell cavity 1	0.872
Cell cavity 2	11.614
Cell cavity 3	212.750

Table IV-3 : Cell constants of the used conductivity cells as determined from KCl-calibration.

The density of the stock solution was determined before starting the calibration measurement. For calibration, the mixture cell was filled with a weighted amount of

---

^{c} *The mixture cell was calibrated by Dipl.-Chem. Bernhard Ramsauer.*

degassed water under an atmosphere of nitrogen and thermostated at 25°C for 1 h. After measurement of the solvent conductivity, a weighted amount of KCl stock solution was added using a gas-tight syringe in nitrogen purge. The temperature equilibrium after dosing was reached within 1 minute. Then, the conductance of the solution was measured for all three electrode cavities at a constant frequency of 10 kHz. This procedure was repeated several times in order to ensure good statistics. From the weight and density of the added stock solutions, the corresponding solution molonities were calculated. The conversion into molarities was established using the following formulas

$$c = \tilde{m} \cdot d \qquad\qquad \text{(IV-39)}$$

and

$$d = d_{\text{solv}} + D\tilde{m} \qquad\qquad \text{(IV-40)}$$

where c is the concentration of the solution in mol/L, $\tilde{m}$ is the molonity of the solution, d is the density of the solution, d_{solv} is the density of the solvent, and D is the density gradient. For aqueous KCl solutions at 25°C, d_{solv} is 977.0480 kg m^{-3} and D is 0.047 kg^2 mol^{-1} m^{-3} [5, 30]. Now, the cell constant C of the conductance cell is accessible.

The same stock solution was used for the calibration of the small volume cells by directly filling it into them. The same principle as described above yield the corresponding cell constants.

3.4   Cell preparation, sample preparation & measurement procedure

In order to obtain conductance data with high accuracy, all measurements were carefully performed including extensively cleaning of the cells and a particular sample preparation. Another crucial factor was a good thermostatisation of the solution, because the conductivity is highly influenced by this parameter.

3.4.1 Cell preparation

The conductivity cells were cleaned one day before the measurement with iso-propanol (Merck, p.a.), Millipore-Q-water and acetone (Merck, p.a). Then, the cell was purged with dry nitrogen for 12 h in order to remove residual solvent and to exchange the air by nitrogen. This procedure was carried out for the small volume cells as well as for the mixture cell.

3.4.2 Sample preparation

The aqueous long-chain ionic liquid systems were measured in both types of conductivity cells. When the small volume cells were used, a concentration row of the investigated SLIL in water was prepared by diluting an appropriate stock solution. Generally, Millipore-Q-water was used as solvent. This work was done one day before the measurement in order to assure equilibrium. For the investigations of the SLIL/water-systems, which were carried out in the mixture cell, only a stock solution with certain molonity was needed. The prepared stock solutions had a molonity of 1.01 mol/kg, 0.63 mol/kg, and 0.1 mol/kg for C_{12}mimCl, C_{14}mimCl, and C_{16}mimCl, respectively. The stock solutions were prepared one day before the measurement by weighting the appropriate amount of SLIL and Millipore-Q-water into a glass flask, which was closed subsequently.

The SLIL/IL-based microemulsions were measured just in the small conductivity cells, since only small volumes of these mixtures were available for investigation. The microemulsions were generally prepared within the glovebox filled with dry nitrogen by weighting the appropriate amounts of the components into special glass vessels, which were subsequently sealed with a septum. Then, the samples were stirred for one night in order to obtain isotropic solutions.

3.4.3 Measurement procedure

When the measurements were carried out in the small volume cells, the sample solutions were directly filled into the cells, which were then sealed by gas-tight caps. Now, the cells were thermostated for 30 minutes to achieve thermal equilibrium. Resis-

tance measurements were made at constant frequency (10 kHz). No solvent correction was applied for the SLIL/water-system, since it was not possible to attain a reasonable value of the Millipore-Q-water conductance in the case of the small volume cells. Also, no solvent correction was done for the SLIL-microemulsions because there was no basic necessity to do that for the analysis of the data.

The preparation of conductivity measurements, which were applied in the mixture cell, is more extensive compared to those performed in the small volume cells. At the beginning of every measurement cycle, the cell was filled with a weighted amount of water under an atmosphere of nitrogen. Then, the cell was thermostated for 1 h. After measurement of the solvent conductivity, a weighted amount of stock solution was added using a gas-tight syringe. From the weights and density gradient D, which was obtained from density measurements of the different SLIL/water-systems, the molar concentrations c were determined by using Eq. (IV-39) and Eq. (IV-40). The resistance of each concentration was measured for the three electrode cavities at a constant frequency of 10 kHz. All conductions were corrected by the water conductivity, which was estimated at 120 Hz.

Taking into account the sources of error (calibration, weighting, measurements, impurities, …), the specific conductivity were accurate to within 0.5 % for the small volume cells and within 0.1% for the mixture cells.

4 Rheology

4.1 General aspects

The term "Rheology" is defined as the study of deformation and flow of matter. Specifically, it is concerned with the description of mechanical properties under various deformation conditions. Dilute solutions of surfactant and microemulsion systems usually behave as Newtonian liquids. The viscosities of these solutions can be based on the size and shape of present aggregates, besides on the second binding force such as van-der- Waals, electrostatic, and hydration forces. At higher concentration, colloidal solu-

tions can show a complicated rheological behavior. They can come to be elastic and their viscosities depend on the shear time or the shear rate. Generally, the viscosity increases with the surfactant (for aqueous systems) or droplet (for microemulsion systems) concentration, however, there are systems which are of low viscosity even at high concentrations and there are other systems which show the opposite behavior [31, 32].

In the present work, rheological investigations were exclusively performed for the characterization of the reversed SLIL/IL/-microemulsions. The rheological behavior and the viscosity of these systems were of special interest to achieve fundamental information about the change of the microstructure within the reverse microemulsions as a function of added polar component. In certain cases, also the percolation behavior of reversed microemulsions can be monitored by viscosity measurements [33, 34].

4.2   Principle

One can consider a coordinate system, with the x direction perpendicular to the shearing planes (Figure IV-14). A shear stress, τ, is applied to an upper plate, forcing it to move with a velocity v relatively to an infinite distance from the upper plate, $v = dx / dt$. If the displacement of a given element located at arbitrary dy is dx, the shear strain γ and shear rate $\dot{\gamma}$ are defined as
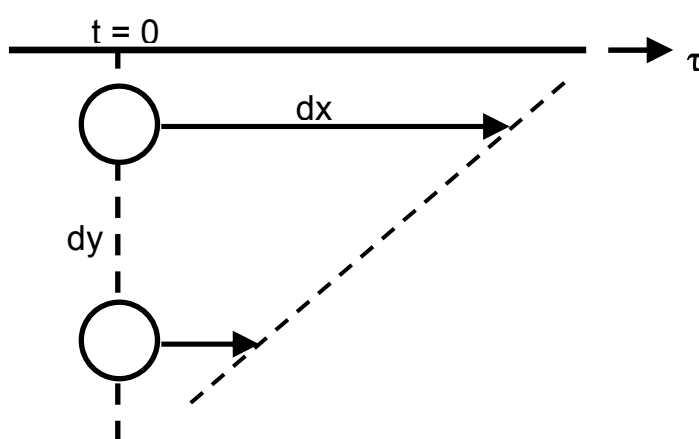
Figure IV-14 : Kinematics of simple shear.

$$\gamma = \frac{dx}{dy} \qquad\qquad \text{(IV-41)}$$

$$\dot{\gamma} = \frac{d\gamma}{dt} = \frac{d}{dt}\left(\frac{dx}{dy}\right) \qquad\qquad \text{(IV-42)}$$

A Newtonian fluid is defined as the relation that the applied stress is proportional to the resulting rate of deformation or simply the resulting velocity of flow.

$$\tau = \eta\dot{\gamma} = \left(\eta\frac{d\gamma}{dt}\right) = \eta v = \left(\eta\frac{dx}{dt}\right) \qquad\qquad \text{(IV-43)}$$

The proportional coefficient is the viscosity η obtained from a single measurement of the shear stress τ and the shear rate $\dot{\gamma}$ [31].

The value of η depends on the shear stress or shear rate for a non-Newtonian liquid. The relationship between shear rate and shear stress is different for different systems. The flow properties of Newtonian and Non-Newtonian behavior are shown in Figure IV-15 [35].
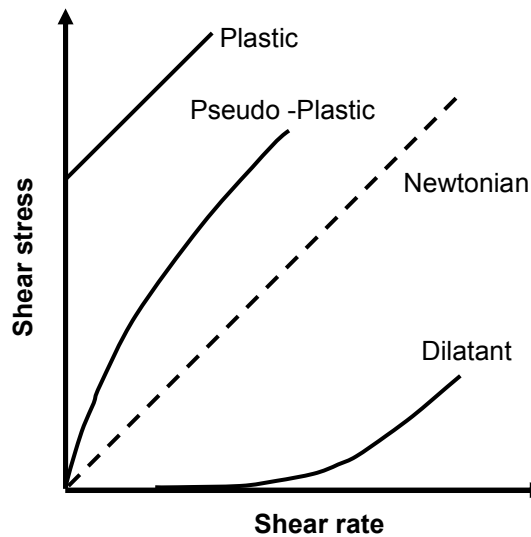
Figure IV-15 : Different relationships between shear stress and shear rate at constant conditions.

Non-Newtonian behavior can arise from many different mechanisms, some of them are illustrated in Figure IV-16. For dilute systems, shear-thinning can be due to flow orientation of the particles or the change in conformation of the polymer molecules or elongated micelles. Thus, when the shear rate is larger than the rate of thermal reorientation of the particles, they will be aligned in the flow direction. Shear-thinning appears for concentrated systems when the shear rate is larger than the rate of build-up of the equilibrium supra-particulate structures. For a shear-thinning or pseudo-plastic system, η decreases with increasing shear rate; plastic liquids are characterized by a finite yield value, i.e. a minimal yield stress needed before they start to flow [31, 32, 35].
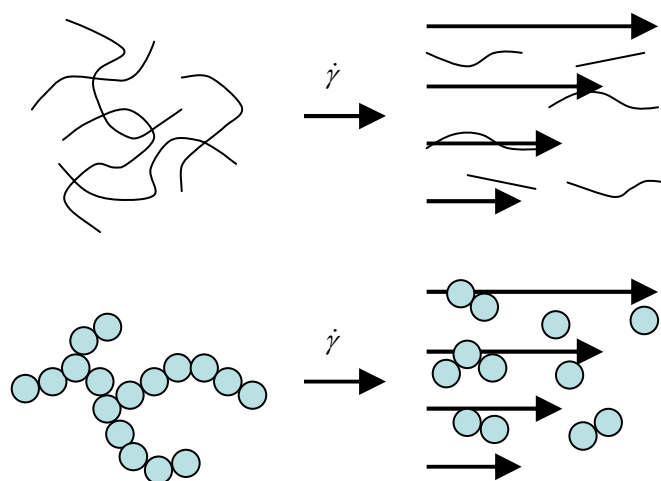
Figure IV-16 : Examples of shear-thinning.

4.3   Instrumentation

The rheological measurements were performed on a Bohlin Instruments Rheometer, CVO 120 High Resolution, with a cone-plate sensor. The cone-plate geometry is described in Table IV-4 and Figure IV-17. The sensor systems could be used properly according to the viscosity of ≥ 2 cP, as determined from test measurements. Temperature in the measuring system could be controlled to an accuracy of $\pm$ 0.2 °C by a thermo-controller supplied with the rheometer. The measurements were operated by the software shipped with the instrument. The data on the measurements were also analyzed by the supplier's software, automatically.
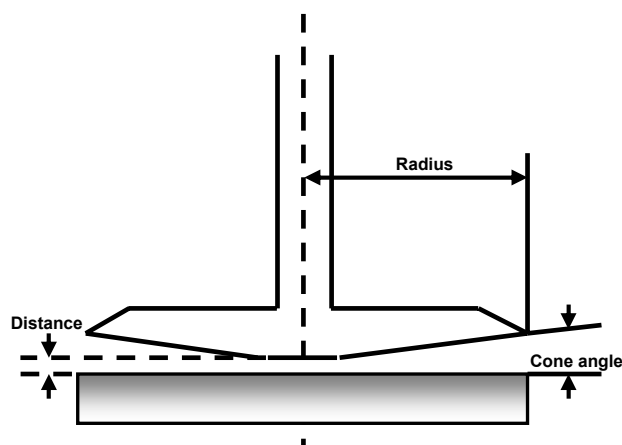
Figure IV-17: Sensor system: cone-plate geometry.

In order to enable measurements in inert gas atmosphere, the rheometer was upgraded by a self-made sample cell which insulates the samples from air moisture by purging argon through it during the measurement. Figure IV-18 shows the constructed cell and the corresponding cell cover.
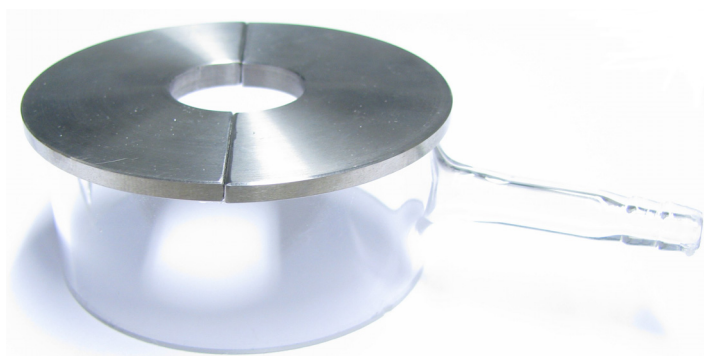
Figure IV-18: Homemade sample cell used for the rheological measurements in argon atmosphere.

4.3.1 Cone parameters

One type of cone was used for all performed measurements. The optimal sample volume for the used geometry was estimated to be 2 mL. The parameters of the cone are summarized in Table IV-4.

Parameters: CP-40/4	
Radius / mm	20
Cone angle / deg.	4
Distance / μm	150
Range / cP	1.31 - 32700

Table IV-4: Geometrical information of the cone-plate sensor.

4.4 Sample preparation & measurement procedure

In order to obtain reliable rheological data, all measurements were carried out carefully including good thermostatisation of the solution, since the viscosity is a function of temperature. Additionally, all measurements of the reverse SLIL/RTMS-based microemulsions were carried out in an argon flow minimizing moisture adsorption to the samples.

4.4.1 Sample preparation

The reversed microemulsion samples were prepared within the nitrogen glovebox by weighting the appropriate amounts of compounds into glass vessels, which were sealed by a septum afterwards. Then, the samples were stirred until use. The preparation was performed one day before the measurement in order to equilibrate the samples.

4.4.2 Measurement procedure

First, the sample cell was purged with dry argon (Linde, 5.0) for 15 minutes in order to exchange the air by argon. Then, 2 mL of sample solution was slowly filled into the cell with a gas-tight syringe in a flow of argon. The thermostatisation of the samples was established within 5 minutes. Now, the measurement was started. The viscosity was measured in the shear rate mode from 10 to 400 s^{-1} including an up- and down-scan. Between each measurement, cone and plate were extensively cleaned with a wipe using ethanol (technical grade), Millipore-Q-water, and acetone (Merck, p.a.).

5 Spectrophotometry: UV/Vis & Fluorescence

5.1 General aspects

Spectrophotometry is the quantitative study of electromagnetic spectra. The term electromagnetic deals, e.g. with visible light, near-ultraviolet, and near-infrared. This technique is very useful to investigate colloidal systems, such as aqueous surfactant systems or microemulsions [36-50]. Therefore, spectrophotometry was used in the present work to characterize the aqueous SLIL solutions and the SLIL/RTMS-based microemulsions as well. The SLIL/water-systems were investigated by fluorescence spectroscopy using the pyrene-quencher technique based on the work of Turro et al in order to determine the critical aggregation concentrations and the aggregation numbers of the formed aggregates [38]. The SLIL/IL-microemulsions were characterized by fluorescence spectroscopy in order to obtain information about their microviscosity, and consequently, about their microstructure [49] and, additionally, by UV/Vis-spectroscopy in order to investigate the solubilisation behaviour of different coloured metal salts within the reverse microemulsions.

5.2 Principle

Many compounds adsorb visible or ultraviolet light leading to an excitation of an electron of the outer shell of the molecule and atom, respectively. For instance, all visible colours are the consequence of electron transfer between different energetic states. Observing colours results from the absorption of definite wavelengths by the material, whereas our eyes recognize the reflected waves only which means the complementary to the absorbed one. Figure IV-19 illustrates the transfer of an electron from the ground state to an excited state by the absorption of a photon (1). There are several possible pathways, which are also included in Figure IV-19, for de-excitation. Following radiation less transitions (3), the transfer of the electron back to the ground state is connected to heat development, because of the released energy leading to intramolecular vibrations (internal conversion). External conversion, in contrast, is a radiation less transition to a lower state by collision-deactivation.
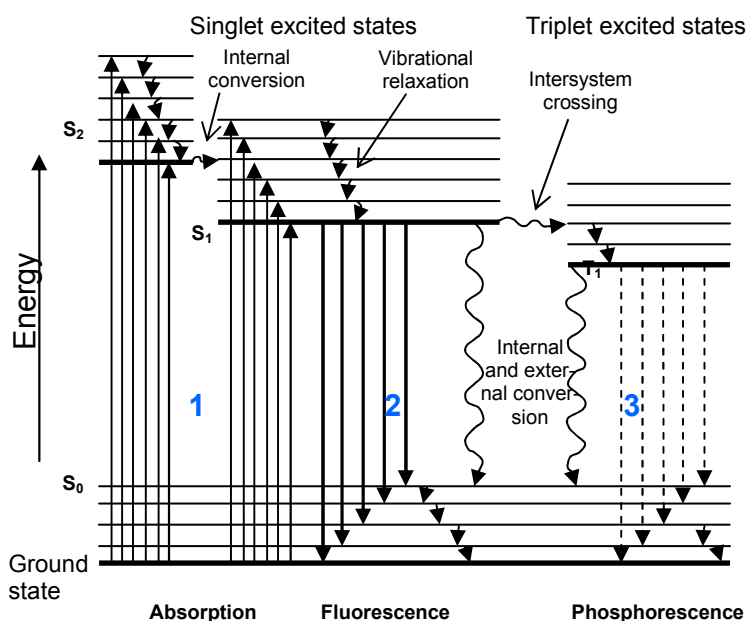
Figure IV-19 : Energy level diagram: adsorption, fluorescence, phosphorescence.

The transition involving a spin change of the elctrons (S → T) is called intersystem crossing. A further de-excitation of an electron is light emission. Here, a photon is generated and radiated. Two types of such deactivations are well-known, (i) the phosphorescence (4), which is an emission of photons involving a spin change (T_1 → S_0), and (ii) fluorescence which means an emission of photons not involving spin change such as S_1 → S_0. The lifetime of the excited states S_1 is between 10^{-19} and 10^{-7} s, whereas the lifetime of the excited states T_1 lies between 10^{-5} and 1 s. Therefore, fluorescence is a much faster process than phosphorescence [51].

5.2.1   Lambert-Beer-Law: Concentration determination

UV/Vis-spectroscopy is widely used to determine the concentration of an absorbing solute in solution, using the Lambert-Beer-law:

$$A = -\log\left(\frac{I}{I_0}\right) = \varepsilon^* \cdot c \cdot L \qquad (IV-44)$$

where A, is the absorbance, I_0 is the intensity of the incident at a given wavelength, I is the transmitted intensity, L is the path length through the sample, and c is the concentration of the absorbing species. For each species and wavelength ε^* is a constant known as the molar absorptivity or extinction coefficient [51].

5.2.2 Fluorescence quenching: Aggregation number determination

The fluorescence quantum yield Φ_f is the ratio of the fluorescence intensity I_f to the intensity of adsorption I_a

$$\Phi_f = \frac{number\ of\ photons\ emitted}{number\ of\ photons\ absorbed} = \frac{I_f}{I_a} \tag{IV-45}$$

Fluorescence molecules are often cyclic substance with several π-bonds. Suitable molecules possess certain Φ_f with values between 0.2 and 1.0. The difference between I_0 and the emitted intensity I_f is related to the intensity of adsorption:

$$I_a = I_0 - I_f \tag{IV-46}$$

with Eq. (IV-46) and the definition of the absorbance A, I_f can be described by

$$I_f = \Phi_f \left(I_0 - I_f \right) = \Phi_f I_0 \left(1 - \frac{I_f}{I_0} \right) = \Phi_f I_0 \left(1 - 10^{-A} \right) \tag{IV-47}$$

Using a series expansion, which is stopped after the second element, I_f is finally written as

$$I_f = 2.3 \cdot \Phi_f \cdot I_0 \cdot A = 2.3 \cdot \Phi_f \cdot I_0 \cdot \varepsilon^* \cdot c \cdot L \tag{IV-48}$$

which is the equivalent of the Lambert-Beer-law for fluorescence.

The fluorescence quantum yield can be affected by the presence of a quencher molecule Q. After the excitation of a fluorescence molecule M by a photon, the excited state population M^* decreases more rapidly in the presence of a quencher molecule. This loss of fluorescence intensity is named fluorescence quenching. Different pathways for de-excitation of an excited fluorescent molecule M^* [52]:

(i)   Collision of M^* with a heavy atom or a paramagnetic species. As this pathway is a diffusion controlled process, especially species with a long fluorescence lifetime (pyrene, naphthalene) are vulnerable for this deactivation process.

(ii)   Photoinduced electron transfer which is often involved in many organic photochemical reactions.

(iii)   Collision between an excited molecule and an identical unexcited molecule leading to a so-called excimer formation (diffusion controlled).

(iv)   Collision of an excited molecule (electron donor or acceptor) with an unexcited molecule (electron donor or acceptor). The latter is named exciplex formation (diffusion controlled).

(v)   Proton transfer results from the fact that the acid or basic properties are not the same in the ground state and in the excited state.

(vi)   Excitation energy transfer is observed between an excited molecule (donor) and an unexcited molecule. If the donor and the acceptor are identically, it is called homotransfer, if the acceptor is structurally different from the donor, it is named heterotransfer.

For the determination of the aggregation number of a surfactant in aqueous solution, point (vi) is of special interest. In principle, the micelles of the investigated amphiphile are labelled with a fluorescent probe P and a quencher molecule Q. The relation of the steady-state fluorescence before and after the quencher labelling exhibits N_{agg} [38]. As fluorescence probe often pyrene (Figure IV-20) combined with cetylpyridinium halogenide as quencher (Figure IV-21) is used [38].
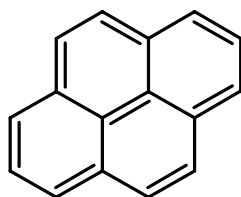
Figure IV-20 : Molecular structure of pyrene fluorescence probe.
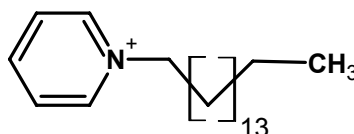
Figure IV-21 : Molecular structure of the quencher: hexadecylpyridinium cation.

Both, the pyrene and the quencher are soluble within the hydrophobic part of the micelles because of the apolar nature of the guest molecules. The probe, pyrene, is deactivated by a transfer of the excited electron to the amino group of the quencher [53]. A single pyridinium molecule, which is present in a micelle deactivates all probe molecules within. This is an important feature in order to get a relation between N_{agg} and the fluorescence before and after addition of the quencher [38].

The probe and the quencher are randomly distributed within the micelle which can be described by a Poisson statistics. Therefore, the mean number of quencher molecules per micelles $\langle Q \rangle$ is given by

$$\langle Q \rangle = \frac{[Q]}{[M]} \qquad \text{(IV-49)}$$

where $[M]$ is the concentration of micelles and $[Q]$ is the bulk concentration of quencher. The statistical probability P_n of a micelle having n quencher molecules is given by

$$P_n = \frac{\langle Q \rangle^n}{n!} \exp\left(-\langle Q \rangle\right) \qquad \text{(IV-50)}$$

whereas the probability of a micelle having no quencher incorporated is represented by

$$P_0 = \exp\left(-\langle Q \rangle\right) \qquad \text{(IV-51)}$$

Therefore, the probability that a probe molecule will be in a micelle allowing fluorescence, is the ratio between the number of probe molecules emitting fluorescence and the total number of probe molecules. The ratio of luminescence intensities I^Q / I_0^Q, where I^Q is the intensity of fluorescence in the presence of quencher, and I_0^Q is the intensity in absence of quencher is therefore given by

$$\frac{I^Q}{I_0^Q} = \exp\left(-\langle Q \rangle\right) = \exp\left(\frac{[Q]}{[M]}\right) \qquad \text{(IV-52)}$$

The surfactant concentration in solution is expressed by the concentration of the monomers $\left[S_{free}\right]$ and the surfactant molecules within the micelle $\left[S_{mic}\right]$:

$$[S] = \left[S_{free}\right] + \left[S_{mic}\right] \qquad \text{(IV-53)}$$

With the definition that the surfactant concentration in the micelle is the product of N_{agg} and the micelle concentration, and with the assumption that the free monomer concentration is almost equal to the *cmc*, $[M]$ can be witten as

$$[M] = \frac{[S] - [cac]}{N_{agg}} \qquad \text{(IV-54)}$$

Finally, the combination of Eq. (II-48) and Eq. (II-49) leads to

$$\ln\left[\frac{I_0^Q}{I^Q}\right] = \frac{[Q]\cdot N_{agg}}{[S]-[cac]} \qquad\qquad \text{(IV-55)}$$

Two different procedures to determine the aggregation number are possible using Eq. (IV-55): (i) by working at constant surfactant concentration $[S]$ and constant probe concentration, but varying the quencher concentration $[Q]$, or (ii) by varying the surfactant concentration $[S]$ and keeping $[P]$ and $[Q]$ constant. If procedure (i) is used, the aggregation number can be determined from the slope of the straight line plotting $\ln\left(I_0^Q / I^Q\right)$ versus $[Q]$, if the second procedure is used, N_{agg}, and additionally the *cmc*, can be calculated from the slope of the straight line plotting $\left(\ln\left(I_0^Q / I^Q\right)\right)^{-1}$ and from the intersection with the y-axis, respectively. In the case (i), the *cmc* has to be known for the analysis.

It is recommended that the final pyrene concentration within the investigated surfactant solutions must be less than 10^{-6} mol/L in order to avoid excimer formation and further, that the cetylpyridinium salt concentration must be below its *cmc* [53].

5.2.3   Microviscosity

Empirical solvent polarity scales mostly based on solvatochromic or fluorescent dyes are utilized to classify solvents. Beside these investigations concerning polarity, also the spectrophotometric study of the microviscosity of solvents (or solvent-mixtures) is possible by means of a suitable dye [46]. It has been shown by Moore et al. that the examination of microviscosity change within aggregates formed in colloidal systems yields very useful information about aggregate evolutions, e.g. the transition from reverse micelles towards reverse microemulsion droplets with increasing amount of polar phase [49]. The basic principle of such investigations is based on the complete incorporation of a suitable dye within the droplet in the microemulsion. In the case of a reverse microemulsion, a polar dye probe has to be used, since it is soluble within the polar droplet core of such a system, but not soluble in the continuous oil phase. Additionally, the used dye must provide spectrophotometric properties manipulable by the surrounding environment, fluidity in the present case. The change of the fluorescence

behaviour, e.g. red-shift, blue-shift, and intensity change of the emission spectra of such dyes, is characteristic for an increase or decrease of microviscosity. Therefore, information about the droplet core evolution at different polar-apolar solvent ratios (at constant surfactant concentration) can be obtained by analysing the change of the fluorescence characteristics.

In the present work, information about the microenvironment of the reverse microemulsions was obtained by using a cationic fluorescence dye with a chloride counterion. The reason for this choice was to minimize the interaction, i.e. counterion metathesis, between the present surfactant-like ionic liquid and the fluorescence dye. Figure IV-22 shows the chemical structure of the used dye auramine-O (N,N,N',N'-tetramethyldiaminodiphenylketoimine hydrochloride) (Au.O.).
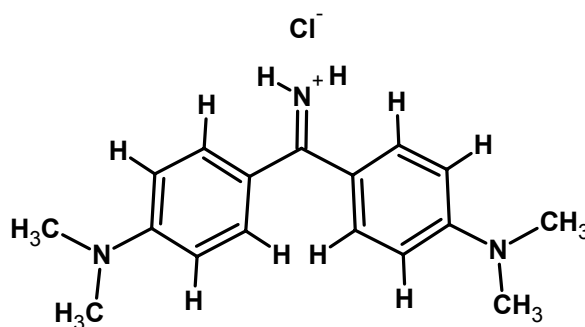
Figure IV-22 : Chemical structure of the Auramine-O (N,N,N',N'-tetramethyldiaminodiphenylketoimine hydrochloride) fluorescence dye.

It is well known that the microviscosity of its environment affects this dye. Both, its fluorescence intensity as well as the position of the maximum value of its emission wavelength λ_{max}^{em} are considerably altered (e.g. λ_{max}^{em} increases as the microviscosity decreases). Consequently, it has been used already for the investigation of the polar pool of microemulsions [49] and micelles [46]. Another reason for the choice of auramine-O in the framework of this thesis is the fact that this dye will be localized in the polar pool owing to the electrostatic repulsion of the imidazolium cationic head-groups of the surfactant-like ionic liquid forming the outer layer of the aggregates and with further addition of the polar solvent RTMS [49].

5.3   Instrumentation

Two different photometers were used for the spectrophotometric investigations presented here. The adsorption measurements (solubilization of metal salts in the SLIL/RTMS-microemulsions) were carried out on a Cary 3E UV/Visible spectrophotometer connected to a PC. The complete measurement was controlled by the Carey software package. The apparatus was located in a thermostated room (about 30°C). Before a measurement series was carried out, the Cary spectrophotometer was turned on at least one hour before in order to ensure constant lamp intensities.

In the case of the emission measurements, an Aminco Bowman luminescence spectrometer of the series 2 was used, which was thermostated by an external thermostat[d] adjusted to 25°C and 30°C for the emission investigations of the aqueous SLIL systems and the SLIL/RTMS-microemulsions, respectively. As done for the Cary instrument, the Aminco Bowman spectrophotometer was turned on at least one hour before the measurements in order to provide for constant lamp intensities. The luminescence spectrometer was controlled by the standard software package of the supplier.

5.4   Sample preparation & measurement procedure

The solubilization behaviour of transition metal salts within the droplets of the SLIL/RTMS/decanol/dodecane-systems was investigated by UV/Vis-spectroscopy. Therefore, two different metal salts with intensive colours were used as probe. The blue cobalt dichloride (Merck, p.a.) and the green nickel dinitrate (Merck, p.a.) were used as received, but dried *in vacuo* for 2 days at 100°C prior use in order to remove residual crystal water. Two saturated stock solutions of the transition metal salts in EAN and bmimBF$_4$ were prepared, respectively. The solutions were filtered through a 0.2 μm syringe filter removing residual salt crystals. Then, using the metal-RTMS stock solutions and the other components, the reversed microemulsions were weighted into glass vessels, which were sealed by a septum afterwards. All these work was performed in the

---

[d] *This equipment was gratefully provided by the Institute of Analytical Chemistry, Chemo- and Biosensors, University of Regensburg, Germany.*

glovebox. The spectra were recorded between 400 and 800 nm using 1 cm quartz cuvette (Hellma QS). Before the measurement, the each sample was thermostated for 5 minutes.

The aggregation numbers and the *cac*s were determined by the steady-state fluorescence quenching technique [38]. A combination of pyrene (Aldrich, for synthesis) and cetylpyridinium chloride (Aldrich, for Synthesis) as fluorescence probe and quencher, respectively, was utilized for these measurements. Prior use, the pyrene was excused from fluorescence active impurities disturbing the measurements by repeated recrystallization from ethanol (Baker analyzed) followed by column chromatography. For the latter, eluent ethyl acetate (Merck, p. a.) as eluent was used. The adsorption material was silica (Merck, 60). After chromatography, the eluent was removed using a rotary evaporator. Then, the pyrene was dried *in vacuo* for one night removing residual solvent. The quencher was recrystallized from ethanol (Baker, analyzed) three times and dried *in vacuo* for one night. Two solutions, a 4×10^{-4} M pyrene- and a 1.95×10^{-2} M quencher-stock solution in methanol (Merck, p.a.), were prepared for the measurements. From an aqueous stock solution of the SLIL (0.1 M), a concentration line was prepared by dilution. In each case, 5 mL of the made SLIL-solutions were added to 3.2 μg of pyrene. The latter results from 40 μL of pyrene-stock solution, whereof the methanol was evaporated in a flow of nitrogen. After 24 h of agitation at 25°C, the samples were taped, temperature controlled, and measured using 1 cm plastic cells (VWR Collection). The probes were excited at 337 nm and the fluorescence spectra were recorded between 350 and 400 nm. Both bandwidths, excitation and emission, were adjusted to 4 nm. After that, 8 μL of the quencher-stock solution was filled in a vessel and 2.5 mL of the already measured, pyrene containing, solution was added, agitated for 1 h, temperature controlled and measured again with the same instrument parameters.

First, a stock solution of Au.O. in methanol (Merck, p.a.) with a concentration of 2.65×10^{-3} M was prepared for the microenvironment investigations. The reverse SLIL/RTMS-microemulsions were prepared by weighing the needed compounds into glass vessels, which were sealed by a septum afterwards. This was performed in the

glovebox one day before the measurement. Then, 2.5 mL of the particular sample were added to 8.05 µg Au.O., which came from 10 µL of the stock solution, whereof the solvent was evaporated using a flow of nitrogen. The excitation wavelength was adjusted to 440 nm, the bandwidth to 3 nm, and a range between 450 and 550 nm was recorded. The excitation and emission bandwidths were 3 nm and 5 nm, respectively. Each sample was measured three times in a 1 cm quartz cell (Hellma QS) sealed with a Teflon stopper. A minimal interval of 0.2 nm and a scan rate of 3 nm per second were used for the measurements.

6   Dynamic light scattering (DLS)

6.1   General aspects

Dynamic light scattering (DLS) measurements were exclusively performed with the C_{16}mimCl/EAN-based microemulsion systems, because the scattering contrast was found to be good enough to obtain analyzable autocorrelation functions resulting in reliable information. Contrary, all other systems (SLIL/RTMS- as well as the C_{16}mimCl/1-decanol/dodecane/bmimBF$_4$-mixtures) presented in this work showed a too weak scattering intensity that made a reliable analysis impossible. With DLS, it was possible to investigate the diffusional characteristics of the superstructures within the SLIL/EAN-microemulsions and the corresponding hydrodynamic radii (when meaningful), using the Stokes-Einstein expression.

6.2   Principle

By using dynamic light scattering, it is possible to determine diffusion coefficients on the basis of the Doppler-effect. The latter causes a frequency shift Δf between a source of radiation and an observer located at a scattering angle q (Eq. (IV-56)), if the distance between the two changes temporally. Here, q is defined as

$$q = \frac{4\pi}{\lambda} \cdot n_D \cdot sin\left(\frac{\varphi}{2}\right)$$

(IV-56)

where n_D is the refractive index of the medium, φ is the scattering angle (in degrees), and λ is the wavelength of the radiation *in vacuo* (cp. also Chapter IV.7.2.1).

The resulting frequency increases compared to the irradiation frequency, if the radiator moves towards the observer, and it decreases, if the radiator departs from the observer, respectively. The frequency displacement depends on the ratio between the relative speed and the propagation of the wave. Therefore, a change of photon energy is observed, although the thrusts are elastic [54].

Particles dispersed in a continuous phase are moving non-directionally because of molecular Brownian motion relative to an observer and detector, respectively. If light is scattered by such particles, this results in a frequency shift of the scattered light. The detection of the scattered light in comparison to the radiated one provides the Doppler-shift spectrum, scattering intensity $I(t)$ as a function of time t (Figure IV-23), which includes the basic information about the particle movement in solution [54-56].
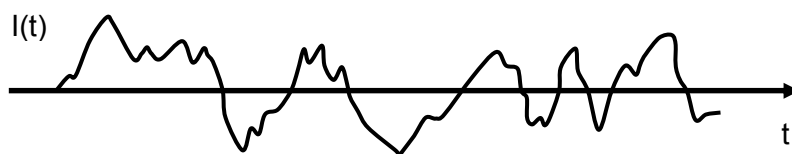
Figure IV-23 : Doppler-shift spectrum (power spectrum). Represented from Ref. [35].

The fluctuations of the stray field at a given scattering angle (vector) shown in the Doppler-shift-spectrum $J(q,\omega)$ is transformed into a normalized time-correlation function $G_1(t)$ using the Wiener-Khintschin-theorem, which is defined as [57, 58]

$$J(q,\omega) = \int_0^\infty G_1(t)\,exp(-i\omega t)\,dt \qquad (IV\text{-}57)$$

where and ω denotes the angular frequency. $G_1(t)$ at constant q is further defined by

$$G_1(t) = \frac{\langle E_S(0) \cdot E_S(t) \rangle}{\langle |E_S|^2 \rangle} \qquad \text{(IV-58)}$$

where $E_S(0)$ is the electric field of the scattered light at zero time ($t = 0$), $E_S(t)$ is the electric field at time t, and E_S is the overall scattered electric field.

In praxis, the temporal fluctuating intensity is detected during the DLS-experiment, which is converted into the normalized intensity time-correlation function by correlation. The intensity normalized intensity time-correlation function $G_2(t)$ is accessible at a given scattering vector q by

$$G_2(t) = \frac{\langle I(0) \cdot I(t) \rangle}{\langle |I|^2 \rangle} \qquad \text{(IV-59)}$$

where $I(0)$ is the intensity at $t = 0$, $I(t)$ is the intensity at t, and I is the overall intensity. The normalized intensity time-correlation function $G_2(t)$ and the normalized electric time-correlation function $G_1(t)$ transformed to the amplitude time-correlation function $G_1(t)$, via the following equation are related by the Siegert-relation:

$$G_2(t) = 1 + |G_1(t)|^2 \qquad \text{(IV-60)}$$

For non-interacting monodisperse particles in Brownian motion $G_1(t)$ decays like a single exponential curve to zero

$$G_1(t) = B \exp(-\Gamma t) \qquad \text{(IV-61)}$$

Where Γ is the average reciprocal relaxation time of the exponential function. Contrary, the intensity $G_2(t)$ decays exponentially in time towards a baseline A. Therefore, by combination of Eq. (IV-60) and Eq. (IV-61), $G_2(t)$ can be expressed as

$$G_2(t) - 1 = A + \left[B\,exp\left(-\Gamma t\right) \right]^2 \qquad \text{(IV-62)}$$

D_{app}, the apparent diffusion coefficient of the scattering particles, is related to Γ by

$$\Gamma = D_{app} \cdot q^2 \qquad \text{(IV-63)}$$

As described previously, $G_1(t)$ is a single decaying exponential function for monodisperse and interaction free systems consisting of spherical particles. If polydisperse, interacting or non-spherical particles are present, the exponential function does not single-decay anymore. Actually, $G_1(t)$ must be modified to a distribution of several exponential functions and Eq. (IV-61) becomes

$$G_1(t) = \int_0^\infty G(\Gamma) \cdot exp\left(-\Gamma t\right) d\Gamma \qquad \text{(IV-64)}$$

where $G(\Gamma)$ is the distribution function of the relaxation rates ($\int_0^\infty G(\Gamma) d\Gamma = 1$) [54, 55, 59, 60].

Another possibility to characterize $G_1(t)$ is the so-called cumulant-analysis originally introduced by Koppel, which works very well for systems with low or moderate polydispersities [61]. For monodisperse non-interacting particles in solution $ln\,G_1(t)$ is a straight line, which drops down with a slope equal to $-\Gamma$. In the case of polydispersity or the occurrence of interactions, $ln\,G_1(t)$ deviates from linearity, but the initial slope is still given by Eq. (IV-63). This deviation can be considered by a series expansion of the exponential function $G_1(t)$ [54, 59, 60]:

$$ln\,G_1(t) = \Gamma_0 - \Gamma_1 t + \frac{\Gamma_2 t^2}{2!} - \frac{\Gamma_3 t^3}{3!} + \dots \qquad \text{(IV-65)}$$

where Γ_0 is the amplitude. The first cumulant Γ_1 is related to the averaged diffusion coefficient by Eq. (IV-63), whereas the ratio between the second, Γ_2, and the first cumulant is related to the degree of deviation of $G_1(t)$ from linearity:

$$PDI. = \frac{\Gamma_2}{\Gamma_1^2} \qquad \text{(IV-66)}$$

where *PDI.* is the polydispersity index. Consequently, a high value of the *PD.I.* denotes a strong departure of $G_1(t)$ from linearity and therefore a high polydispersity or significant interactions within the investigated system. A fit of Eq. (IV-65) to the plot of $ln\sqrt{G_2(t)-1}$ vs. *t* obtained from the measurement, gives D_{app} as well as the *PDI.* by using Eq. (IV-63) and Eq. (IV-66).

The dimension of the aggregates in solution is calculated from the Stokes-Einstein-relation, which relates the hydrodynamic radius R_h^{app} of spherical aggregates to the achieved D_{app}. The Stokes-Einstein-relation is

$$R_h^{app} = \frac{k_B T}{6\pi\eta D_{app}} \qquad \text{(IV-67)}$$

where η is the solvent viscosity, and the other parameters have their usual meaning [59, 60].

Beside the above-mentioned cumulant-analysis, the CONTIN-analysis is another possibility to analyze DLS data. This method estimates the distribution of relaxation rates (Eq. (IV-64)) by means of an inverse Laplace-transformation. In reality, the program CONTIN developed by Provencher can be applied to get the distribution function $G(\Gamma)$ of the relaxation rates and consequently, the size distribution of the present aggregates in solution. Therefore, the evaluation of DLS data using the CONTIN procedure is of special interest for complex colloidal systems, which show multi-exponentially decaying autocorrelation functions due to high degree of polydispersity or other multi-diffusional processes [62, 63].

6.3   Instrumentation

An ALV Goniometer CGS II was employed for the light scattering experiments. A 22 mW He-Ne laser working at 632.8 nm stabilized by a voltage regulator served as light source. The temperature was kept at the measurement temperature with an equipped water-circulator (LAUDA RS 6) resulting in a maximal temperature uncertainty of $\pm$ 0.1°C within the sample cell. The data acquisition of the DLS-experiment took place with an ALV-5000/E/WIN-correlator card installed in a PC from which the instrument was controlled by the ALV software. The correlator simultaneously calculates the temporal averaged intensities and the intensity time-correlation function from the input signals of the detector.

6.3.1   Test measurements

Since the goniometer is a very complex machine including very sensitive optics, a lot of standard measurements were performed using a different Latex standards (varying in size) suspended in Millipore-Q-water in order to guarantee a trustworthy working of the CGS II. The obtained R_h of the Latex particles always reproduced the specifications of the supplier with an error of about 5%.

6.4   Cell cleaning, sample preparation & measurement procedure

In order to obtain reliable DLS-data, which is not influenced by residual dust within the samples, all measurements were carried out carefully including extensively cleaning of the used cells and filtering of the samples. Additionally, the optimal measurement procedure, i.e. measurement time and sample preparation, had to be optimized.

6.4.1   Cell cleaning

Reliable DLS-experiments require laborious preparatory work, as residual contaminants, especially dust, strongly affect the DLS results. Therefore, the used cylindrical quartz cells (Hellma, Suprasil) were extensively cleaned by the following procedure: First, the cells were rinsed with Millipore-water. Then, they were consecutively deposited in a KOH (technical grade)/Isopropanol (technical grade)/water-bath and afterwards

in a HCl-bath. The exposure time was at least 1 h for each bath. After that, the cells were rinsed with filtered Millipore-water (pore size 0.2 μm). The last cleaning step was performed within a vapour cleaning instrument, where the inside and the outside of the cells were wept with freshly distilled acetone (Merck, p.a.). This was done at least for one hour. Now, the quartz cylinders were lightly closed with Teflon caps, transferred to a desiccator, and completely dried *in vacuo*. Until use, the cells were stored in the closed desiccator avoiding dust contamination.

6.4.2 Sample preparation

The SLIL/IL-microemulsions were prepared in the glovebox by weighting the components into glass vessels equipped with a magnetic stir bar. Then, the vessels were sealed with a septum and the samples were stirred for one night to assure equilibrium. The sample solutions were directly filtered through a syringe filter (Nagelene, SFCA) with a pore size of 0.2 μm into the cleaned quartz cells, which were immediately sealed with the Teflon caps, afterwards. As this procedure caused many bubbles within the sample, they were equilibrated again for at least 24 h.

6.4.3 Measurement procedure

In order to assure a constant laser power of the goniometer, the latter was switched on at least 24 h before the measurements. The sample cell was transferred to the cell holder of the instrument, where it was thermostated for at least 30 minutes in order to obtain thermal equilibrium within the sample. Ten measurements was carried out and then averaged. The duration of each measurement was set to 45 s using a laser power of 100%. The detector angle was always set to 90°.

7 Small angle scattering: SAXS, SANS

7.1 General aspects

Neutron small angle scattering (SANS) experiments were carried out at room-temperature (RT) for the structure analysis of the formed aggregates within SLIL/water-

and within SLIL/RTMS-systems, respectively. In the case of the SLIL/RTMS-based microemulsions, neutron as well as x-ray small angle scattering (SAXS) was also performed at RT to get an insight into the formed superstructures. Further, the C_{16}mimCl/RTMS-systems were measured at high-temperature (up to 150°C) using SANS and SAXS. In addition, the SLIL/RTMS-based microemulsions were examined as a function of temperature up to 150°C.

7.2   Principle

Small angle scattering experiments, with neutrons (SANS) as well as with x-rays (SAXS), are very powerful techniques to reveal the size, shape and internal structure of colloidal particles in homogeneous solution. The investigated particles can be colloids or macromolecules like polymers or micelles with size ranges from one nanometer to several micrometers. In order to get information about the structure and size distribution of such particles, the wave length of the radiation, λ, used in the scattering experiment should match the size range of interest [64-66].

In principal, all small angle scattering methods bear on the interference phenomenon. In the case of X-ray scattering, the X-ray radiation excites all electrons present within the trans-illuminated volume. This results in an emission of scattered radiation, which can be described as waves. These waves interfere with each other causing different intensities of the scattered radiation at different locations in space, depending on constructive and destructive interference. The interference contains structural information, as, if two centres of distance d scattering the waves, one of the two scattered waves has to run a little bit further until it is parallel to the second wave again. This results in a way difference λ at different scattering angles φ which depends on the distance between the scatterers (Figure IV-24, left). If λ is the wavelength of the used radiation, the angle at which constructive interference is obtained depends on d between the scatterers. This means that the pattern of constructive and destructive interference can be observed at different angles depending on the distance between the scattering centres. In this connection, the reciprocal principle applies: Information of larger distances can be obtained at small scattering angles. Therefore, each scattering experiment

can be described by a Fourier-transformation relating the real space information of the scattering object to the q-space (reciprocal space) scattering intensity (cp. Figure IV-24) [65, 66].
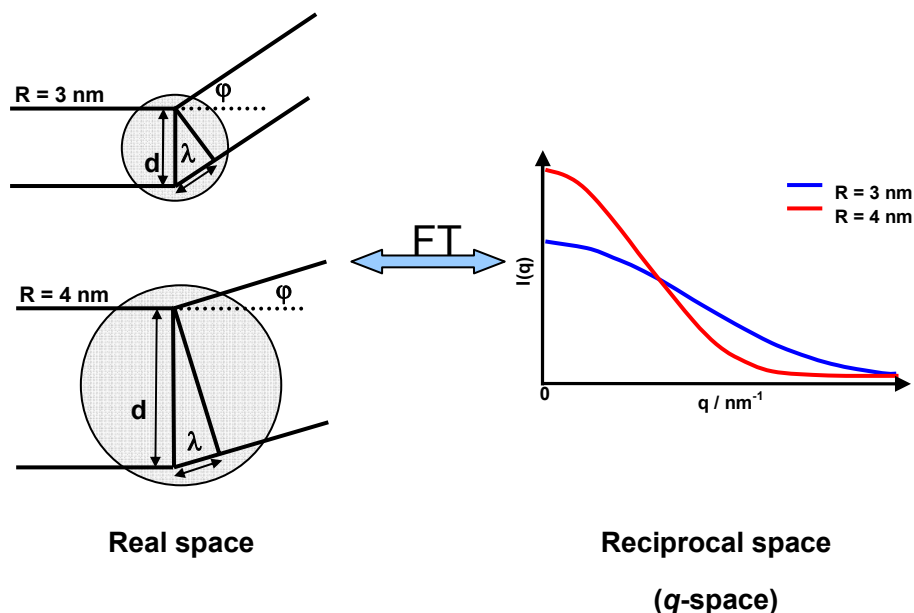
Figure IV-24 : Constructive interference between two scattering centers with different distances.

So far, the discussion was only related to X-rays, however neutrons can also be described as waves because of the wave-particle-dualism, and therefore the same principles as for X-rays apply [58]. Usually, the chosen wavelengths of neutrons are situated in the same range as those of the x-ray radiation.

7.2.1 Scattering wave vector

The scattering angle is defined by the used radiation wavelength. In order to compare scattering for different wavelength, the fundamental variable in a scattering experiment is the Bragg wave vector q. The incident and the scattered wave vectors of the radiation in the medium, k_i and k_s respectively, define the latter. Figure IV-25 illustrates the geometrical situation of the wave vectors, when a neutron or X-ray beam passes through the sample that contains particles or aggregates in solution [64-66].
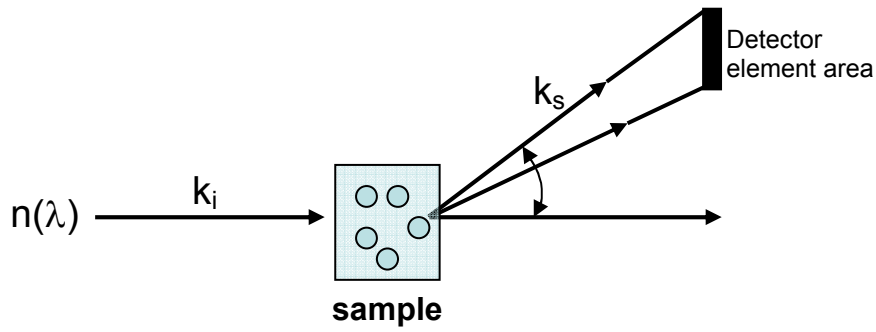
Figure IV-25 : Schematic representation of the small angle scattering geometry.

In a small angle scattering experiment from an isotropic medium containing particles, one measures predominately the elastic and quasi-elastic scatterings for which the two wave vectors can be defined as

$$|k_i| = |k_s| = \frac{2\pi}{\lambda} \cdot n_D \qquad (IV-68)$$

Consequently, the q vector has the magnitude

$$q = \frac{4\pi}{\lambda} n_D \cdot \sin\left(\frac{\varphi}{2}\right) \qquad (IV-69)$$

where φ is the scattering angle, λ is the wavelength of the incident radiation, and n_D is the refraction of the medium. n_D is close to 1 for neutrons and X-ray. Typical q-values in small angle experiments are between 0.06 and 5 nm^{-1}.

7.2.2   Contrast - Scattering length density

A very important aspect of scattering measurements is that of the scattering contrast between the particles and the environment. As already pointed out, X-rays interact with electrons of a scatterer (electromagnetic interaction) leading to scattering. This interaction is strong, and the beam penetrates through matter not very deeply. Contrary, neutrons interact with the atomic nuclei (nuclear interaction) via the very short-range strong nuclear force and thus penetrate matter much more deeply than X-rays. If there

are unpaired electrons in the material, neutrons may also interact by a second mechanism: a dipole-dipole interaction between the magnetic moment of the neutron and the magnetic moment of the unpaired electron [67].

The scattering contrast of a particle in solution is defined as

$$\Delta\rho = \rho_p - \rho_{solv} \qquad \text{(IV-70)}$$

where ρ_p and ρ_{solv} are the contrast contributions of the particle and the solvent, respectively [64, 65, 68]. As the nature of used radiation (X-rays or neutrons) results in different interaction mechanisms, the two contrast contributions have different meanings. In the case of SAXS, the important quantity is the X-ray scattering amplitude in the forward direction $f_x(0)$ (also known as the electron density ρ^x), whereas for neutron scattering, the scattering length density ρ^n (*sld*) is the corresponding quantity. The two quantities, $f_x(0)$ and ρ^n, are defined as:

$$f_x(0) = \frac{\sum_{i=1}^{n} Z_i \cdot f_T}{V} \qquad \text{(IV-71)}$$

where Z_i are the electrons of the ith atom in the volume V, f_T is the Thomson-factor, and V is the volume containing n atoms.

$$\rho^n = \frac{\sum_{i=1}^{n} b_i}{V} \qquad \text{(IV-72)}$$

where b_i is the scattering length of the ith atom in the volume V, and V is the volume containing n atoms. Table IV-5 summarizes scattering properties of some elements [65]. As one can see from Table IV-5, b_i is more or less in the same order for all nuclei except for deuterium, which has a negative b_i. However, $f_x(0)$ is always positive, and its magnitude increases linearly with the atomic number of the element.

Element	b_i (10^{-12} cm)	$f_x(0)$ (10^{-12} cm)
Hydrogen	-0.3742	0.28
Deuterium	0.6674	0.28
Carbon	0.6648	1.69
Nitrogen	0.9360	1.97
Oxygen	0.5805	2.25
Fluorine	0.5654	2.67
Chlorine	0.9579	4.80

Table IV-5: Scattering properties of some elements. Represented from Ref. [65].

Consequently, the scattering powers of hydrocarbons and water are not significantly different for X-rays, but for neutrons, the scattering power of the hydrogen containing molecules can be made to vary greatly by substitution of the protons by deuterons. This aspect is very useful to study the structure of surfactant aggregation as the contrast can be fine tuned.
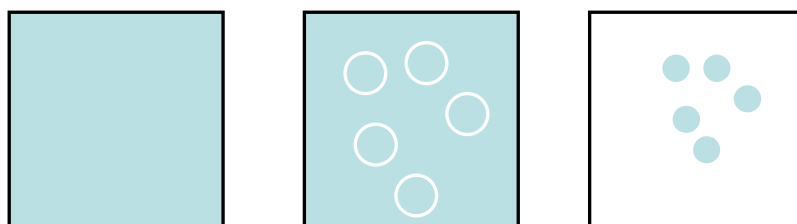
Figure IV-26 : Schematic illustration of the isotopic effect in SANS study.

The scattering length densities of light water (H_2O) and heavy water (D_2O) are -0.56 × 10^{10} cm^{-2} and 6.38 × 10^{10} cm^{-2}, respectively. For the sample and the solvent of the same atoms, for example H rich atoms in surfactant and the H_2O as solvent there is no difference in scattering length densities and therefore no or less structural information, as shown in Figure IV-26 (left). Figure IV-26 also illustrates the situations where only the head group of the surfactant is deuterated and H_2O is the solvent (middle) and a non-deuterated surfactant in solution of D_2O (right), respectively [65, 68].

In general, SAXS is rather difficult to apply to the determination of the structure of association colloids, e.g. micelles in water, because there is only little contrast be-

tween the solvent and the hydrocarbon part of the aggregates. In aqueous medium X-rays are primarily scattered by the polar part of the aggregated amphiphilic molecule. Therefore, SAXS provide mainly information about the structure of the head-group region and of the counterion distribution and hydration [65].

From a scattering experiment, no information about the present contrast between the particle and the solvent can be obtained, since only an intensity detection of the scattered radiation is possible, but no estimation of the amplitude. From this fact, the so called phase problem arises: From the scattering pattern it is not possible to distinguish whether the electron density (or scattering length density of the dispersed objects) is above or below the electron density (or scattering length density) of the surrounding medium. However, the absolute value of the electron density difference (or the scattering length density difference) can be obtained [69].

7.2.3   Scattering cross section

The scattering cross section of a scattering experiment, which is also called the differential scattering cross section, is given by

$$\frac{d\Sigma}{d\Omega}(q) = \frac{1}{V}\frac{d\sigma}{d\Omega} \qquad\qquad (IV\text{-}73)$$

where $d\sigma / d\Omega$ is the scattering cross section of one electron (SAXS) and of one nuclei (SANS), respectively. V is the probe volume. The scattering cross section $d\Sigma / d\Omega$ is also denoted as the normalized scattering intensity $I(q)$.

The following relation describes the normalized scattering intensity, for an isotropic monodisperse micellar solution:

$$I(Q) = n_P \cdot P(Q) \cdot S(Q) \qquad\qquad (IV\text{-}74)$$

where n_p is the particle density, $P(q)$ is the contribution of particle form factor, and $S(q)$ is the contribution of interparticle structure factor of the particles in solution [65, 68].

7.2.4 Form factor

The particle form factor depends on the size, form, electron density difference (or scattering length density difference), and orientation of the particles in solution. For easy geometries and constant contrast between particle and solvent, the form factor can be calculated [57]:

(i) Spheres

For spherical particles with a radius R the form factor is defined as

$$F(q) = \Delta\rho \cdot V_{sph} \cdot \frac{3(\sin X - X \cdot \cos(X))}{(X)^3} \qquad \text{(IV-75)}$$

where V_{sph} is the volume of the sphere and $X = q \cdot R$. $F(q)$ is related to $P(q)$ by:

$$P(q) = |F(q)|^2 \qquad \text{(IV-76)}$$

(ii) Ellipsoid (prolate or oblate)

For an ellipsoid with two axis ($a = b \neq c$), the form factor is defined with the help of an orientation angle ω between the scattering vector $\vec{q}$ and the ellipsoid axis as

$$F(q,\omega) = \Delta\rho \cdot V_{elli} \cdot \frac{3(\sin X - X \cdot \cos(X))}{(X)^3} \qquad \text{(IV-77)}$$

where V_{elli} is the volume of the ellipsoid, and

$$X = q \cdot \sqrt{a^2 \cdot \sin^2 \omega + c^2 \cdot \cos^2 \omega} \qquad \text{(IV-78)}$$

(iii)   *Cylinder*

A cylindrical form factor with the radius R, the length L and the volume V_{cyl} is expressed by

$$F(q,\omega) = \Delta\rho \cdot V_{cyl} \cdot \frac{\sin\left(q \cdot \dfrac{L}{2} \cdot \cos(\omega)\right)}{q \cdot \dfrac{L}{2} \cos(\omega)} \cdot \frac{2 \cdot J_1\left(q \cdot R \cdot \sin(\omega)\right)}{q \cdot R \cdot \sin(\omega)} \qquad \text{(IV-79)}$$

Where ω is the orientation angle between the scattering vector $\vec{q}$ and the cylinder axis. The first ratio describes the length of the cylinder, whereas the second ratio defines the spherical cross section of the cylinder. J_1 is the Bessel function of the first order.

Figure IV-27 shows the different scattering patters of a sphere, an ellipsoid, and a cylinder. The particle dimensions are defined so that the smallest extent of the different geometries is always the same.
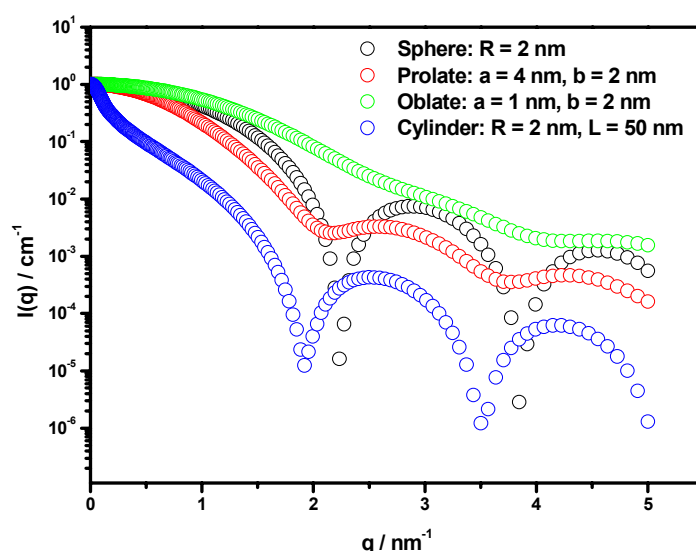
Figure IV-27 : Scattering pattern of different particle shapes using the presented form factors: Sphere, ellipsoid (prolate and oblate), and cylinder (calculated with SASFit).

7.2.5   Core-shell model

Until now, the scattering contrast, which mainly defines $P(q)$, was considered for homogeneous particles surrounded by a homogenous medium (solvent). For the interpretation of micelle (and microemulsion) scattering patterns, a more convenient model has to be used. The core-shell model defines a micelle as an object consisting of two different electron densities (or scattering length densities), which are associated to the micelle hydrocarbon core and to a shell where the head-group, the counterions, and H_2O molecules (or D_2O molecules) are located (Figure IV-28).
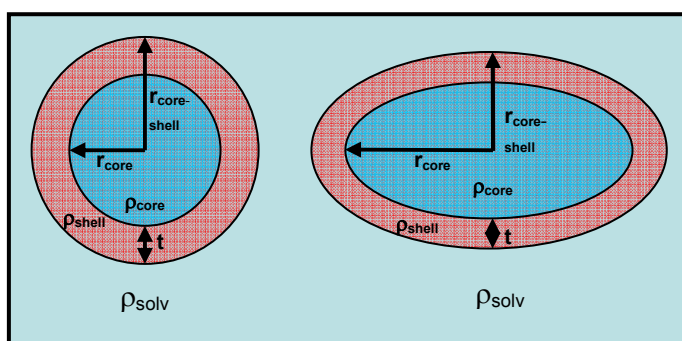
Figure IV-28 : Core-shell model for a sphere and an ellipsoid. The scattering contributions of core and shell are indicated by the different scattering densities ρ.

7.2.6   Structure factor

The structure factor describes the interparticle interactions of particles or aggregates in solution. It is based on the Ornstein-Zernike equation

$$h(r) = c(r) + n \int c(r-r') \cdot h(r')dr'$$
(IV-80)

and a radial interparticle distribution function $g(r)$

$$g(r) = h(r) - 1$$
(IV-81)

where the total correlation $h(r)$ is related to the direct correlation function between the particles $c(r)$ and the indirect contributions, which are represented by the integral [70].

The $g(r)$ function gives the probability for a particle to find another particle in the volume dV at a distance r. For distances smaller than the particle diameter D ($r < D$), the probability is equal to zero ($g(r) = 0$), because of the impenetrability of the particles, whereas at long distances ($r > D$) the $g(r)$ function has the value one ($g(r) = 1$).

However, the direct correlation function is unknown and therefore an easy analytical expression for the structure factor does not exist. Most of the available expressions have been obtained from liquid state theory for particles with spherical symmetry interacting with a spherically symmetric potential. By combination of the Ornstein-Zernike-equation with approximate relations, denoted as closure relations, it is possible to obtain reasonable expressions for the structure factor. Many different models for the structure factor are known including different appendages and relations [57, 68]:

(i) ***Mean spherical approximation (MSA) & rescaled mean spherical approximation (RMSA)***

Hayter and Penfold have developed an analytical method to determine the structure factor of charged monodisperse macroions in solution (*MSA*) [71, 72]. It takes into account the mutual (screened) Coulomb interactions (repulsion) between the particles in solution and assumes that the particles are monodisperse impenetrable spheres (hard spheres). The closure-relations are given by [71]

$$c(r) = -\beta \cdot U(r) \qquad for \qquad r > d \qquad (IV\text{-}82)$$

and

$$h(r) = -1 \qquad for \qquad r < d \qquad (IV\text{-}83)$$

where β is an energy term ($\beta = 1/k_B T$), $U(r)$ is the introduced potential, and d is the diameter of the hard sphere. The *MSA* combined with a Coulomb potential, leads to good results for medium and high particle concentrations, but the results become unphysical for low concentrations [57]. This problem was solved

by an iterative rescaling procedure of the *MSA*, which increases the apparent radius of the particles until a reasonable solution is obtained. The rescaled mean spherical approximation (*RMSA*) is an enhancement of the *MSA* model [73]. For not too high concentrations and not too big axis ratios, this model is also useful for ellipsoidal objects, as the potentials of ellipsoids, which are far away from each other, are similar to those of spheres.

Based on this closure relation the hard-sphere structure factor as well as the attractive sticky-hard-sphere structure factor was calculated [57].

(ii) Hypernetted-chain approximation (HNC)

The closure relation of the hypernetted-chain approximation (*HNC*) is given by [74]

$$g(r) = \exp\left(-\beta \cdot U(r) + h(r) - c(r)\right) \qquad \text{(IV-84)}$$

The *HNC* approximation is less accurate for hard-sphere repulsions, but it is very well applicable for Coulombic systems with long-range interactions. Strong attractions and repulsions are correctly represented [68].

(iii) Percus-Yevick approximation (PY)

The Percus-Yevick (*PY*) equation gives good results in cases where short-range potentials are present. However, this approximation fails for long range Coulombic potentials. The closure relation is obtained by a linear evolution of the *HNC*-relation. Therefore, it is given by

$$g(r) = \exp\left(-\beta \cdot U(r)\right) \cdot \left(1 + h(r) - c(r)\right) \qquad \text{(IV-85)}$$

with the pair distribution function $g(r) = h(r) + 1$ [60, 75].

(iv) Rogers-Young approximation (RY)

By mixing the *HNC* and the *PY* approximations, the Rogers-Young (*RY*) equation is related to the following closure relation

$$g(r) = \exp(-\beta \cdot U(r)) \cdot \left\{ \left(1 + \frac{1}{f(r)} \left[\exp(f(r)h(r) - c(r)) - 1 \right] \right) \right\} \qquad \text{(IV-86)}$$

which depends on the mixing function

$$f(r) = 1 - \exp(-\varsigma r) \qquad \text{(IV-87)}$$

The mixing parameter ς has to be adjusted by checking the obtained thermodynamic parameters, which result from the structure factor [60].

The contribution of the structure factor $S(q)$ (green) to the form factor $P(q)$ (red) and the resulting scattering pattern $I(q)$ (black) are presented in Figure IV-29.
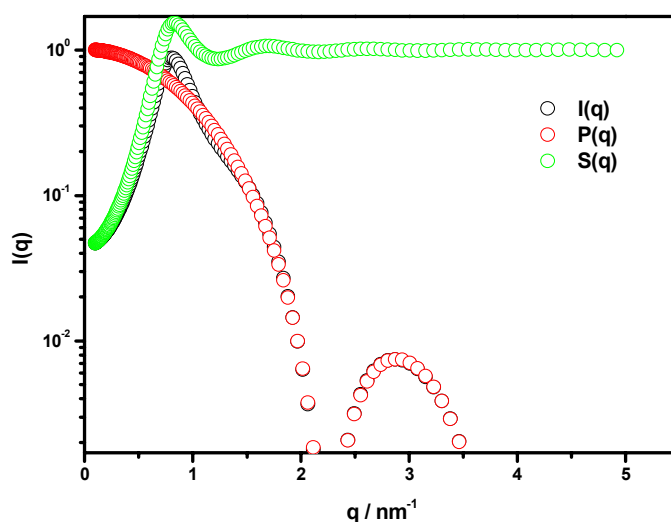
Figure IV-29 : The scattering function *I(q)* (black) as a product of the form factor *P(q)* (red) and the structure factor *S(q)* (green) for a charged sphere. Calculated by the program SASFit.

7.2.7 Scaling laws

Since data on scattering measurements is dealt within the reciprocal space, the structural information is reflected in the opposite q-range. The scattering at large q value gives information in terms of the relatively microscopic structure, and small q refers to the large structure. For small-angle scattering, three regions can be classified ordinarily into, as shown in Figure IV-30. In the small q-range, the dimension of an aggregate or a particle can be evaluated by the Guinier law, if particle interactions are negligible and the scattering experiment was performed on absolute scale [76]. The size of a particle, irrespective of whether it is geometrically well defined or irregular in shape, can be conveniently characterized by its radius of gyration R_g according to the Guinier law. For spherical particles, the Guinier law is given by

$$I(q) = I(0) \, exp\left(\frac{q^2 \langle R_g^2 \rangle}{3}\right) \tag{IV-88}$$

where $I(0)$ is the scattering intensity at zero scattering angle. Therefore, a plot of $\ln I(q)$ vs. q^2 (Guinier plot) shows a negative slope within the Guinier-regime ($qR_g \ll 1$). From the slope, R_g can be calculated according to Eq. (IV-88) [64, 76]. For spherical particles, the radius of the sphere can be estimated from R_g by

$$R_g^{\,2} = \frac{3}{5} R^2 \tag{IV-89}$$

Following Hayter and Penfold, the Guinier law is still valid for higher particle concentrations, where interactions have to be considered, but it is no longer possible to extract the exact R_g from the slope due to the influence of $S(q)$ at low q [77].

For many of the particles having well-defined, simple geometric shapes, it is possible to calculate the intensity curve without any approximation. Simply the power law of intensity decay in the intermediate q-range can identify these different shapes

$$I(q) \sim q^{-s} \tag{IV-90}$$

The exponent s is equal to 4 for spheres (three dimensional), 2 for thin disks (two dimensional), and 1 for thin rods (one dimensional), and is thus seen to reflect the dimensionality of the object [68].
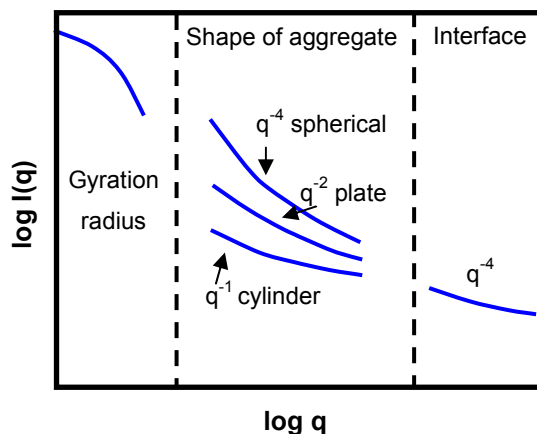
Figure IV-30 : Different scattering ranges and the corresponding structural information, which can be obtained by power laws.

At further large q, the scattering intensity is reflected by a surface fractal of aggregates. Porod et al. proposed for the ideal two-phase model that the scattering intensity should decrease as $\sim q^{-4}$ in the large q range, and moreover, that the proportionality constant should be related to the total area S of the boundaries between two phases in the scattering volume [78]. This means, as $q \rightarrow \infty$,

$$I(q) \rightarrow \frac{2\pi(\Delta\rho)^2 S}{q^4} \qquad\qquad \text{(IV-91)}$$

and therefore,

$$\lim q^4 I(q) = 2\pi(\Delta\rho)^2 S/V \qquad\qquad \text{(IV-92)}$$

where $\Delta\rho$ is the electron density difference (or scattering length density difference). With other words, it is possible to measure the quantity of particle/solvent interfaces per

unit volume of solution (S/V) by SAS experiments, if the two media have different scattering densities, the intensity scale is in absolute units, and the background is subtracted [64, 68]. Consequently, a plot of $I(q)q^4$ vs. q will level off at a constant value in the region where the Porod limit is applicable. If there is a constant background attached to the scattering data, then this curve does not reach a constant value, but will rapidly increase at high q-values due to the q^4 dependence. This is a very sensitive way to determine if there is even a small background superimposed on the scattering data. In addition, this power law indicates that the surface of aggregate is smooth, and if the decay is more than -4, it is likely that the boundaries between the two phases would be indistinct [79]. Further, an estimate of the aggregate size is accessible from the quantity of S/V by

$$l_p = 4(V/S)\Phi(1-\Phi) \qquad \text{(IV-93)}$$

where l_p is the Porod length and Φ is the volume fraction of the scattering particles. If the aggregates are spheres of equal radius R_p (Porod radius) [80],

$$R_p = \frac{3}{4}l_p \qquad \text{(IV-94)}$$

7.2.8   Model-dependent analysis

There are essentially two different approaches to analyse small angle scattering data. In free form method, also denoted as model-independent analysis, assumptions are made about the structure of the present particles, which are the basis for a geometrical model. The scattering pattern, which is related to the form factor of the particle, is then calculated and the remaining unknown parameters are fitted using the least-square technique. A powerful software package for such an analysis is SASFit, which also takes many different structure factors into account [81]. If the so defined model of a form factor and a structure factor is not able to fit the data appropriately, it is further modified and this trial-and-error procedure continuous until a satisfactory interpretation of the scattering pattern is obtained. However, this technique needs reasonable form- and structure

factor models and parameters, respectively, as the scattering data is often accurately represented by several different models, which can lead to a false data interpretation [82].

7.2.9   Model-independent analysis

The second possibility of small angle data evaluation is the free-form model approach, which is based on the model-free transformation of the measured scattering pattern (reciprocal space) to real space by the indirect Fourier transformation (IFT). This technique was introduced by Glatter in 1977 [69, 69, 83]. The conventional Fourier transformation of $I(q)$ involves the integral

$$p(r) = \frac{1}{2\pi^2} \int_0^\infty I(q)(qr)\sin(qr)dq \qquad\qquad \text{(IV-95)}$$

which provides the pair distance distribution function $p(r)$ (*PDDF*). The usage of Eq. (IV-95) requires scattering data in the full q-range, $0 \leq q \leq \infty$, and a desmearing (cp. Chapter IV.7.3.3) of the data. The limited q-range available from the experimental setup would lead to strong oscillations (termination effects) in such a direct Fourier transformation. This disadvantage is minimized in the ITF. The latter can simultaneously perform the three steps of least-squares fitting (smoothing), desmearing, and at the end the Fourier transformation assuming a limitation in the *PDDF*, i.e. $p(r) = 0$ for $r > D_{max}$, where D_{max} is the maximum dimension of the particle.

The *PDDF* contains the same information as the original scattering pattern, however it is more useful as it is easier to interpret the scattering pattern in real space, where real distances within the particles are presented. Therefore, it is often possible to make a qualitative statement about the particle shape directly. Additionally, the PDDF provides information of the electron density (or scattering length density) distribution of the particles and also about their maximal dimensions [83-85]. For homogeneous particles with constant electron density (or scattering length density), this function has an exact geometrical definition. Such a particle consists of a very large number of identical small volume elements. Considering this fact, the *PDDF* function is proportional to the num-

ber of lines with a length between r and $r + dr$ which are found in the combination of any volume element i with any other volume element k of the particle (Figure IV-31).
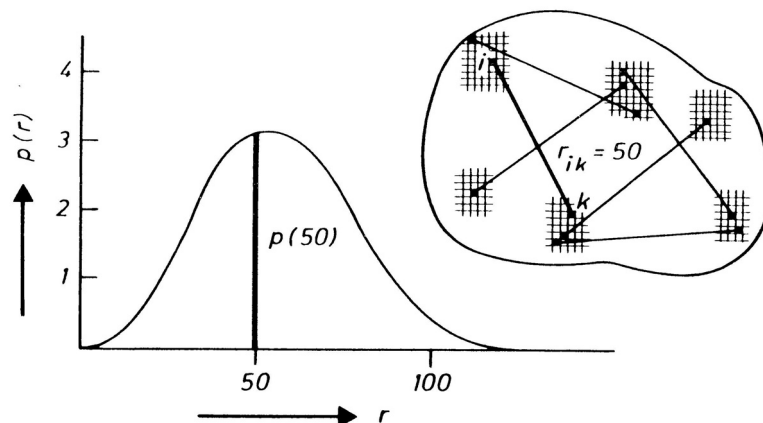
Figure IV-31 : The PDDF can be understood as a distance histogram for homogeneous particle. The height of the $p(r)$-function is proportional to the number of all lines, with a length within the interval r and $r + dr$. Represented from [86].

For $r = 0$, there is no other volume element, so $p(r)$ must be zero. For $r > 0$, $p(r)$ increases initially with r^2 as the number of possible neighbouring volume elements is proportional to the surface of a sphere with radius r. Starting from an arbitrary point in the particle, there is a certain probability to reach the surface within the distance r. The latter forces the $p(r)$ function to drop below the r^2 parabola and finally it becomes zero for all $r > D_{max}$. Consequently, the *PDDF* is a distance histogram of the particle. However, there is no information about the orientation of these lines in p(r) because of the spatial averaging. If inhomogeneous particles, such as micelles or microemulsions, are investigated, the lines have to be weighted by the scattering contrast of the volume elements. For this reason, also negative contributions to the *PDDF* can arise.

In the context of the model-independent analysis, the phrase "free form" means that a large set of basis functions are used to describe $p(r)$, so that no specific form factor (form and shape) is assumed. Figure IV-32 shows the *PDDF*"s of different particle shapes for comparison. From the pair distribution functions the geometric properties

of the particle can be easily obtained, whether it is globular, elongated, flat or rod-like [84]. The occurrence of a minimum in the PDDF can be caused by a small number of distances, or by the addition of positive and negative contributions, as the $p(r)$ function is weighted by the electron density (or scattering length density) distribution of the particles. Further information about the features of the $p(r)$ function and its interpretation is given in literature [66, 84, 86, 87].
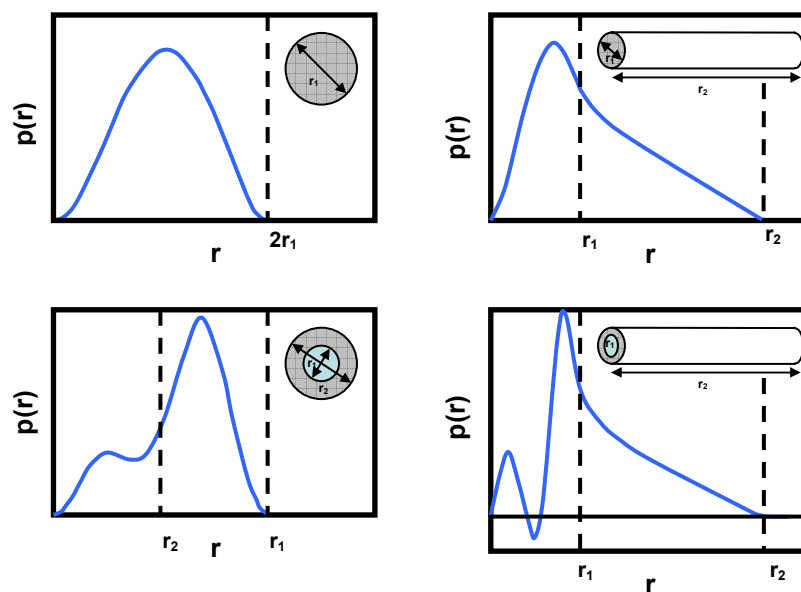
Figure IV-32 : *p(r)* **functions of a (i) homogeneous sphere, (ii) a core-shell sphere, (iii) a homogeneous cylinder, and a (iv) core-shell cylinder. Represented from Refs. [66, 84, 86, 87].**

The $p(r)$ function is directly related to the contrast of the particle (excess electron or scattering length density) by the square-root deconvolution [69, 85]:

$$p(r) = r^2 \Delta \widetilde{\rho}^2(r) \qquad (IV\text{-}96)$$

where $\Delta \widetilde{\rho}^2(r)$ is the convolution square (spatial correlation function) of $\Delta\rho(r)$.

One limitation of the IFT method is that it is based on the assumption that no correlations of the particles occur, which is not valid especially for charged micelles where strong interactions take place and for systems where high volume fractions of

dispersed phase have to be taken into account. This problem was solved by Glatter who improved the IFT-technique to the generalized form (GIFT-technique) in which also interparticle correlations are taken into account by using a structure factor model [88-90].

In a concentrated system containing a monodisperse, homogeneous, and iso-tropic dispersion of interacting particles, the scattering intensity is no longer propor-tional only to the form factor and therefore $I(q)$ has to be expressed by

$$I(q) = nP(q)S(q) \qquad \text{(IV-97)}$$

where n is the particle number density, $P(q)$ is the form factor, and $S(q)$ is the struc-ture factor which takes particle interaction into account. In this case, the GIFT method is able to extract the form factor, represented by the $p(r)$-function in a model free way, and simultaneously the parameters of the structure factor model.

Eq. (IV-97) is correct only for the monodisperse case of interacting particles, but it is also possible to factorise $I(q)$ similar to the previous equation, as

$$I(q) = n\overline{P}(q)S_{eff}(q) \qquad \text{(IV-98)}$$

with

$$\overline{P}(q) = \sum_k x_k f_k^2 B_k^2(q) \qquad \text{(IV-99)}$$

the mean form factor, averaged over all of the particle dimensions, and

$$S_{eff}(q) = \frac{1}{\overline{P}(q)} \sum_{k,l} f_k f_l B_k(q) B_l(q) S_{kl}(q) \qquad \text{(IV-100)}$$

the effective structure factor of interacting spheres [88-91]. x_k is the mole fraction of spe-cies k. f_k denotes the form amplitude at $q = 0$ of species k, $B_k(q)$ is the normalised form amplitude of species k, and the cross term $S_{kl}(q)$ the partial structure factor,

which takes the hard-sphere interaction between species k and l into account. It is clear from Eq. (IV-100) that $S_{eff}(q)$ is not longer independent of the form factor, i.e. $S_{eff}(q)$ also includes particle properties. Often, the different sizes of particles in Eq. (IV-99) and (IV-100) are assumed as Schulz distributed [90, 91].

Therefore, within the GIFT-technique, $\bar{P}(q)$ of a model system of Schulz-distributed homogeneous spheres is calculated for the evaluation of $S_{eff}(q)$. Based on Eq. (IV-98) the form factor respectively the corresponding $p(r)$-function, is again extracted in a model free way, and simultaneously the parameters of the effective structure factor $S_{eff}(q)$ concerning hard-sphere interaction, namely the effective interaction radius R_{eff}, the volume fraction of the particles Φ and the polydispersity $PDI.$, respectively the width of the Schulz distribution.

For practical use, Glatter et al. developed a software bundle for the scattering data analysis based on the former presented model-free analysis. They use a robust Boltzmann simplex simulated annealing algorithm to solve the highly non-linear system of equations resulting from the product of form and structure factor [92]. For a further detailed description of the GIFT-method, the reader is referred to the literature [88-95].

7.2.10   Small angle scattering of microemulsions

During the last decades, a number of scattering experiments were also performed on ternary (or pseudo-ternary) aqueous microemulsion systems. It was shown that small angle scattering spectra of such systems exhibit a single broad peak. The position of this peak varies systematically with the amphiphile concentration and the water to oil ratio, respectively. The scattering amplitude is highest at comparable amounts of oil and water [96-100]. Additionally, a characteristic q^{-4} dependence of the intensity distribution at large wave vectors, q, is observed that is attributed to the existence of a well-defined internal interface formed by a monolayer of amphiphile molecules [64, 78, 96, 97].

7.2.10.1   Teubner-Strey-model

The simplest model is to describe microemulsions as a collection of droplets consisting either of water and surfactant or of oil and surfactant defined as water in oil

(W/O) and oil in water (O/W) microemulsions, respectively. Here, the scattering peak is attributed to the first maximum of the structure factor [64, 66]. For some scattering experiments on microemulsions, this description is sufficient to explain the scattering behaviour. However, there are cases where another explanation is needed, especially when comparable amounts of oil and polar component are present and the structure is known to be bicontinuous [97].

A widely used model to analyze scattering patterns of droplet microemulsions as well as of bicontinuous microemulsions is the parametric Teubner-Strey-model (TS-model) which bases on Debye´s prediction of the scattering spectrum of a two component porous media [101, 102]. Their system consists of a continuous matrix with embedded "particles". The fundamental point of their theory is that these scattering regimes are completely independent in their position and shape. The correlation function of this model is

$$\gamma(r) = \exp\left(-\frac{r}{a}\right) \tag{IV-101}$$

with a is the typical length of the system. The corresponding scattering intensity function $I(q)$ obtained from Fourier transformation of Eq. (IV-101) shows no correlation peak, rather, a monotonous decay. Teubner and Strey supposed a fluid multi-component system in which a flexible film consisting of surfactant microscopically separates two phases, i.e. water and oil, from each other [97, 98, 103], which finally results in a similar situation as for porous materials. In their model, however, the structures of the oil and water regimes are not independent anymore; they are connected via the film. This coupling results in a single broad peak in terms of scattering. Contrary to Debye et al., the correlation function of Teubner and Strey

$$\gamma(r) = \exp\left(-\frac{r}{\xi_{TS}}\right) \sin\left(-\frac{2\pi r}{d}\right) \frac{d}{2\pi r} \tag{IV-102}$$

introduces two length scales, (i) the typical size of the system d_{TS} (periodicity), and (ii) a persistence length ξ_{TS} (correlation length) [97, 98, 103, 104]. Following the T-S-model, the scattering pattern of a microemulsion can be fitted by

$$I(q) = \frac{1}{a^2 - c_1 q^2 + c_2 q^4} + BG \qquad (IV\text{-}103)$$

where the parameters a_2, c_1, c_2 (with a_2, $c_1 < 0$, and $c_2 > 0$) stem from the coefficients of an order parameter expansion of the free energy density and BG is an incoherent background [97, 98, 103-106]. The periodicity and the correlation length expressed in terms of the order parameter coefficients are of the following form

$$d_{TS} = 2\pi \left[\frac{1}{2}\left(\frac{a_2}{c_2}\right)^{1/2} - \frac{1}{4}\frac{c_1}{c_2} \right]^{-1/2} \quad \text{and} \quad \xi_{TS} = \left[\frac{1}{2}\left(\frac{a_2}{c_2}\right)^{1/2} + \frac{1}{4}\frac{c_1}{c_2} \right]^{-1/2} \qquad (IV\text{-}104)$$

The length scale d_{TS} represents a quasi-periodic repeat distance between polar solvent-polar solvent and oil-oil regions within the solution, respectively, whereas the correlation length ξ_{TS} corresponds to a characteristic length for positional correlation (decay of the order by the amphiphilic layers). While there is no clear physical interpretation of ξ_{TS} in the open literature, the half of d_{TS} is often connected to the average diameter, ξ, of a water or oil domain [96, 99, 107, 108]:

$$\xi = \frac{d_{TS}}{2} \qquad (IV\text{-}105)$$

The maximum of the scattering peak, q_{max}, is related to the correlation length and the periodicity by [97, 98, 105]

$$q_{max} = \left[\left(\frac{2\pi}{d_{TS}}\right)^2 - \frac{1}{\xi_{TS}^2} \right]^{1/2} \qquad (IV\text{-}106)$$

Another possibility to obtain q_{max} and additionally the corresponding intensity $I(q_{max})$ can be also estimated by [97]

$$I(q) = \frac{I(0)}{\left(1 - \dfrac{I(0)}{I(q_{max})}\right)\left(\dfrac{q^2}{q_{max}^2} - 1\right)^2 + \dfrac{I(0)}{I(q_{max})}} - BG \qquad \text{(IV-107)}$$

where $I(0)$ is the scattering intensity at $q = 0$ and $I(q_{max})$ is the scattering intensity at $q = q_{max}$, respectively.

The ratio d_{TS}/ξ_{TS} can be interpreted as a measure of the polydispersity of the disordered water and oil domains. The smaller this ratio, the more ordered the system. An argument has been given for aqueous microemulsions setting limits on the ratio d_{TS}/ξ_{TS} in the bicontinuous microemulsion regime. In this regime, the characteristic average size of water and oil domains is $d_{TS}/2$ (Equ. (IV-105)). The exponential damping of the T-S correlation function means that the domain fluctuations are correlated over distances of the order of ζ_{TS}. Therefore d_{TS}/ξ_{TS} is a measure of the dispersion in the domain sizes. The region that can be identified as a bicontinuous microemulsion is confined by the critical end points where the microemulsion breaks up and the lamellar phase, which sets bounds on d_{TS}/ξ_{TS}. If the dispersion in the domain sizes is too small, $d_{TS}/\xi_{TS} < 2$, the entropy of folding the amphiphilic film is no longer sufficiently large to stabilize a disordered phase and a first order transition to a lamellar phase, with zero d_{TS}/ξ_{TS}, occurs. Larger values of d_{TS}/ξ_{TS} imply a large dispersion and more fluctuating amphiphilic film. Again there is a natural limit to this dispersion corresponding to $d_{TS}/\xi_{TS} \approx 2\pi$, for then the fluctuations of the amphiphilic film are so large that the bicontinuous microemulsion breaks up [106].

The fact that the ratio d_{TS}/ξ_{TS} of bicontinuous aqueous microemulsions is limited to a narrow range is also reflected by the amphiphilicity factor f_a that is a measure of the surfactant strength within the mixture of microemulsions. It is defined in terms of the expansion coefficients as [106, 109]

$$f_a = \frac{c_1}{\sqrt{4a_2c_2}} \tag{IV-108}$$

Thereby, the amphiphilicity factor amounts to -1 for the liquid crystalline lamellar phase. f_a amounts to 1 for the disorder line where the solution loses its quasiperiodical order. For well-structured bicontinuous microemulsions, f_a ranges between -0.9 and -0.7 [108, 109].

One problem, which arises from the fact that the TS-model is able to describe both, droplet microemulsions as well as bicontinuous microemulsions, is to distinguish between these two types of microstructures. Beside f_a, which takes a value near -1 (lamellar phase) in the highly structured bicontinuous regime and higher values in the case of droplet microemulsions, another dimensionless quantity, in the original paper denoted as C_3, was introduced by Chen et al. [104]. It is related to the internal interfacial behaviour and is seen at the high q-limit. The C_3-parameter is defined as

$$C_3 = 2\pi \frac{\left(k^2\xi_{TS}^2 - 1\right)^{3/2}}{k^2\xi_{TS}^2} \tag{IV-109}$$

where k is

$$k = \frac{2\pi}{d_{TS}} \tag{IV-110}$$

Chen et al. recommended C_3 in order to judge, whether the microemulsion is bicontinuous or not. The interesting phenomenological observation made for aqueous microemulsions using C_3 is that when the peak width is large and there is strong scattering at high q, then C_3 becomes less than 10 ("rule of ten"). It is asserted that this is a condition for bicontinuity, which is independent of such measurements as conductivity for example.

7.2.10.2   Model-independent analysis: GIFT-evaluation, Percus-Yevick- $S_{eff}(q)$

Beside the parametric TS-model, the small-angle scattering data of microemulsion is often evaluated in the open literature by the application of a model-dependent analysis. However, the interpretation of microemulsion scattering patterns is difficult, since they form concentrated colloidal dispersions in which there can be a simultaneous variation, with the volume fraction of the microemulsion-droplet cores, of both particle size and the strength of the interaction between the particles. The fact that the interactions are important in this type of system is immediately clear from the small-angle scattering data. At the high volume fractions, marked peaks are often observed indicating that, because of the interactions, considerable short-range order exists in the spatial arrangements of the droplets. For the detailed analysis of such scattering data, often a core-shell form factor in combination with a hard-sphere interaction model based on the Perkus-Yevick structure factor, which is very suitable for the interpretation of short-range interactions, is used (cp. also Chapter IV.7.2.6) [60, 75, 110]. It is clear that the successful application of a model requires the knowledge of the compositions of the polar and organic phases within the microemulsion, which are required to calculate scattering contrast used in the core-shell form factor. However, the exact compositions are often unknown. This is a recurrent problem for the modelling of microemulsion systems. One possibility to solve this problem in spite of the unknown scattering contrast is the model-independent interpretation of the microemulsion scattering data by applying the GIFT method. The latter enables the extraction of $P(q)$ from the scattering data in a model free way with a minimum of *a priori* information, and simultaneously the determination of the effective structure factor $S_{eff}(q)$ (cp. Chapter IV.7.2.9) [90, 91, 111-113]. The $S_{eff}(q)$ in terms of hard-sphere interaction and Percus–Yevick closure relation, gives a correlation peak similar to that of the TS-model (Eq. (IV-103)). However, contrary to the TS-model, which features both characteristics, droplets and bicontinuous microemulsions, the GIFT-technique bases on the particle picture of microemulsions. Interestingly, it was shown recently by Glatter et al. that the GIFT-method is also applicable to the bicontinuous phase [113]. Indeed, good fits were obtained and the extracted $p(r)$-functions as well as the parameters observed from $S_{eff}(q)$ were physically meaningful,

but no clear indication was achieved to judge whether a microemulsion is a particulate system or a bicontinuous microemulsion. Nevertheless, the work of Glatter et al. clearly demonstrates that the fact that the scattering pattern of a microemulsion can be interpreted in terms of a particulate model does not necessarily proof that the microstructure is really particulate. Therefore, a successful application of the GIFT-evaluation to a droplet microemulsion phase seems more obvious.

7.3   Instrumentation

In the underlying work, small angle scattering experiments with both radiation types, X-rays and neutrons, were carried out to investigate the formed colloidal aggregates. The aqueous SLIL-systems were investigated only at room-temperature, whereas the other systems (the SLIL/RTMS-systems and the SLIL/RTMS-based microemulsions) were also investigated at higher temperatures (up to 150°C) in order to proof the high-temperature stability of these systems. The SAXS experiments were obtained at the Max-Planck Institute of Colloids and Interfaces (Golm, Germany) and at the Laboratoire Léon Brillouin (LLB, CEA Saclay, France)[e]. The performed SANS experiments were carried out at the Berlin Neutron Scattering Center (Hahn-Meitner-Institute Berlin, HMI, Germany) and at the Institute Laue-Langevin (ILL, Grenoble, France).

7.3.1   Small-angle X-ray scattering

The small angle X-ray scattering data, which will be presented in this work, was obtained at two different instruments:

(i)   Kratky apparatus (MPI, Golm)

By using a classical Kratky compact small-angle camera (Figure IV-33), the spectra of the SLIL/RTMS-systems were measured [64].

---

[e] *Dr. Pierre Bauduin (LSRM Bat 391, CEA de Saclay) carried out these scattering experiments.*
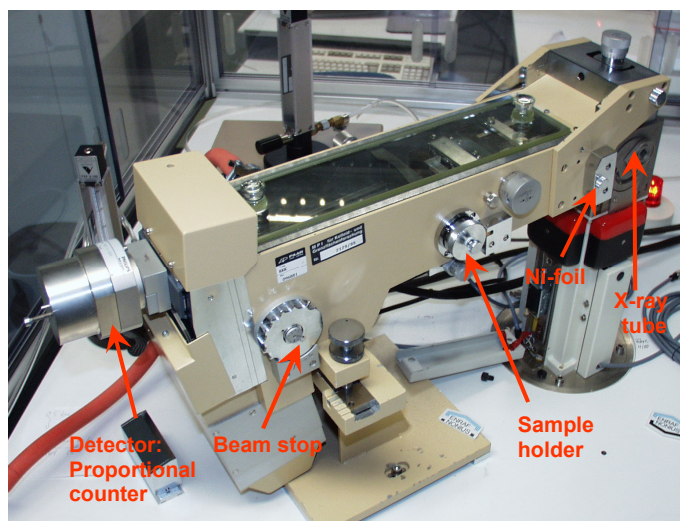
Figure IV-33 : The Kratky instrument (Anton Paar KG, Graz, Austria) used for the measurements of the C$_{16}$mimCl/ RTMS-systems at the MPI Golm.

The instrument is composed of an X-ray generator containing a copper anode (Bruker AXS, Karlsruhe, Germany) that mainly produces a radiation with a wavelength of $\lambda = 0.154$ nm (CuK$_\alpha$). The disturbing CuK$_\beta$ radiation was reduced by a Ni-monochromator (Ni-foil). During running time, the generator is cooled by circulating water of constant temperature. The latter worked at 40 kV and 20 mA. The 1D-detector was a gas detector (M. Braun, Garching, Germany). The sample holder is temperature-controlled within a range of 25°C to 300°C. In order to provide a high flux at the sample resulting in a higher scattering intensity, the instrument principle of the Kratky-camera is based on the long-slit geometry. For a detailed description of this collimation system, the reader is referred to Ref. [64]. The main part of the instrument (collimation system, sample cell, flight path after the sample) can be evacuated or purged with helium, which minimizes air adsorption and air scattering. The covered q-range of this apparatus was 0.20 nm to 5.39 nm^{-1}.

(ii) Rotating anode (CEA, Saclay)

SAXS experiments at 30°C were performed in flat cells of 0.1 and 0.2 mm thicknesses with Kapton windows on the Huxley-Holms High-Flux camera [114, 115]. The X-ray source is a copper rotating anode operating at 15 kW with a pinhole collimation system. The CuK$_\alpha$ radiation ($\lambda = 0.154$ nm) is selected by a Xenocs monochromator mirror. Spectra are recorded with a two-dimensional gas detector of 0.3 m in diameter giving an effective q-range of 0.2 to 3.5 nm^{-1}.

7.3.2   Small-angle neutron scattering

Small-angle neutron scattering of the SLIL/water-systems, the SLIL/RTMS-systems, and the SLIL/IL-based microemulsions was measured at two different spectrometers localized at the HMI and the ILL, respectively:

(i) Instrument V4 (HMI, Berlin)

The pin-hole small-angle scattering instrument V4 is installed at the BER II reactor of the Hahn-Meitner-Institute with a power of 10 MW. A mechanical velocity selector (Dornier Deutsche Aerospace GmbH, Germany) monochromes incoming cold neutrons resulting in a variable wavelength range of 0.38 to 3 nm. The wavelength resolution lies between 8 and 18 %.
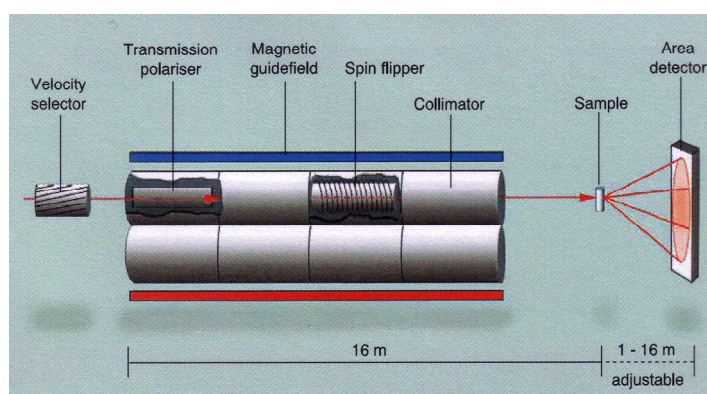
Figure IV-34 : The V4 small-angle neutron scattering spectrometer localized at the 10 MW BER II reactor, HMI Berlin. Represented from Ref. [117].

The two-dimensional position sensitive detector can be positioned at any distance between 1 to 16 m. Therefore, a q-range $0.01 \leq q \leq 8.5$ nm^{-1} can be covered. The ^{3}He-detector of 64×64 cm^2 has a pixel size of 5×5 mm^2 and is equipped with readout electronics for 128×128 cells. A sample holder with a working temperature between $-20 \leq \vartheta \leq 80°C$ and 16 sample slots allows operating the instrument in an automatic measurement mode. Figure IV-34 shows the technical layout of the V4 device [116].

(ii)   *Instrument D22 (ILL, Grenoble)*

Amongst all classical pin-hole small-angle neutron scattering instrument, the D22 (Figure IV-35) is the one with the highest flux at the sample. A 58.3 MW high–flux reactor supplies it. The wavelength of the cold neutrons is chosen by a Dornier (Deutsche Aerospace GmbH, Germany) velocity selector in the range $0.45 \leq \lambda \leq 4$ nm. The wavelength band is relatively narrow for each λ (normally 10 %). D22 possesses a large ^{3}He area multidetector (active area 1 m^2), with a pixel size of 8×8 mm^2. The sample-to-detector distance can be varied between 1.1 to 17.6 m. Thus, the instrument covers a total q-range of 4×10^{-4} to 4.4 nm^{-1} (with detector offset 8.5 nm^{-1}). The apparatus provides a temperature-controlled ($-20 \leq \vartheta \leq 80°C$) sample changer with 20 slots. Additionally, a furnace with 4 sample slots is available for high-temperature measurements (up to 300°C) [118].
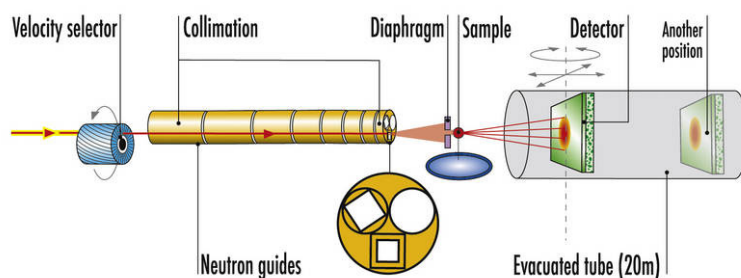
Figure IV-35 : The schematic instrument layout of the D22 localized at the 58.3 MW reactor, ILL Grenoble. Represented from Ref. [119].

7.3.3   Instrument broadening: Smearing effects of small-angle scattering instruments

Traditionally, many small-angle scattering experiments have been performed on instruments using the Kratky-camera system with long-slit geometry [64]. In contrast, SANS instruments and actual SAXS devices are usually carried out using pinhole geometry and area sensitive detectors. Depending on the geometry, the instrument layout has an influence on the recorded scattering data leading to the so-called smearing effects. In general, the smearing effects are much smaller for pinhole geometry than for long-slit geometry as long as the wavelength spread of the incident beam is small. Figure IV-36 illustrates the resulting q-distributions for two different values of the scattering vector q of a long-slit geometry and of pinhole geometry.
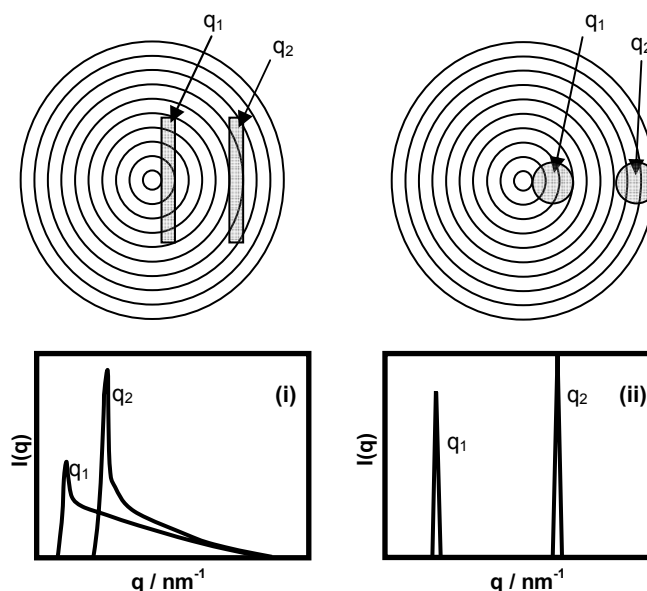
Figure IV-36 : Representation of the q-distribution for two different values of the scattering vector q of (i) long-slit geometry and (ii) pinhole geometry. The origin of the *q*-scale is located at the centre of the concentric shells.

The q-distributions of the long-slit geometry have a sharp maximum that is close to the centre at low q and a broad tail towards high q. By contrast, the distributions of the pinhole geometry are nearly identical sharp peaks.

The present smearing effects of the long-slit geometry can be divided into three components, a wavelength effect and two geometrical contributions. The latter consists

of two one-dimensional, effects, one parallel to q and one perpendicular to q, which are called the slit-length smearing effect ($\parallel$ to q) and the slit-width smearing effect ($\perp$ to q). Figure IV-37 shows the resulting q-distributions resulting from the three different smearing effects in the case of a Kratky-apparatus.
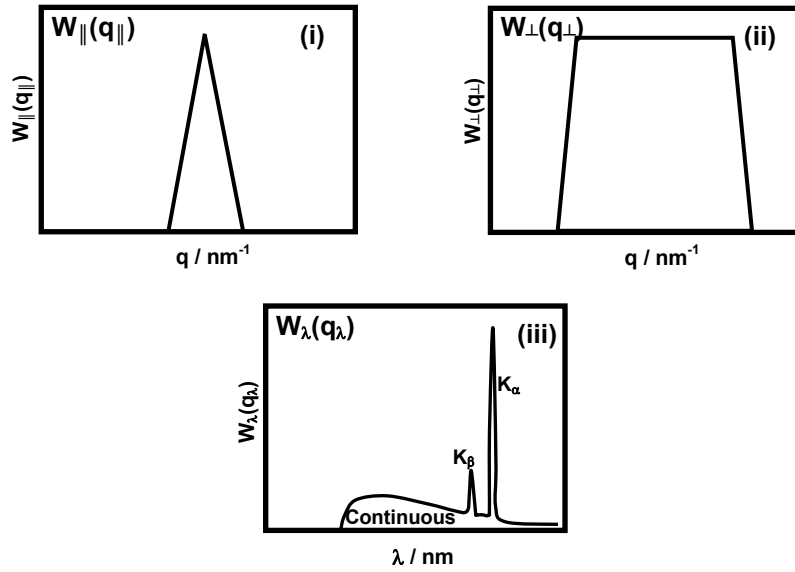
Figure IV-37 : Smearing effects of a slit-length Kratky camera with their corresponding distributions, (i) slit-length smearing, (ii) slit-width smearing, and (iii) wavelength distribution.

For SAXS-instruments with a copper anode, the wavelength distribution can be neglected, as the CuK_α radiation is normally very well monochromed by an appropriate monochromator (e.g. Ni-foil) installed in the device. Therefore, only the geometrical smearing effects must be taken into account during the data analysis. The two-dimensional intensity of the primary beam $I_0(t,x)$ that reaches the sample is described by the product

$$I_0(t,x) = C_\parallel(t) \cdot C_\perp(x) \tag{IV-111}$$

where $C_\parallel(t)$ is the contribution of the slit-length and $C_\perp(x)$ is the contribution of the slit-width. By knowing both contributions, the slit-length profile and the slit-width pro-

file, the scattering pattern can be desmeared [64]. The profiles are usually obtained by the so-called moving-slit method, as described by Kratky et al. [120]. Generally, the smearing effects influence the shape of the scattering curve by means of smoothing out the pronounced maxima and minima of the form factor and the slope of the curve is changed. A detailed explanation of the smearing effects occurring in Kratky based small angle compact cameras and their considering is available elsewhere [64].

In the case of pinhole SANS- or SAXS-systems using a 2D area detector, the smearing effect is also caused by three different contributions, the finite size of the incident beam, the wavelength resolution and the pixel size on the detector. For pinhole SAXS devices, the corresponding scattering patterns are less smeared compared to the scattering patterns of SANS-experiments since there is nearly no wavelength distribution of the radiation and also the influence of the pixel size has a negligible effect. Therefore, such scattering data is often treated without considering any smearing effects. However, the wavelength distribution $\Delta\lambda/\lambda$ and the shape of the direct beam have a major effect on scattering patterns derived from SANS measurements. $\Delta\lambda/\lambda$ is related to the FWHM (full width at half maximum) value of a triangular function describing the wavelength distribution by FWHM $= \lambda_0(\Delta\lambda/\lambda)$ [121-123].
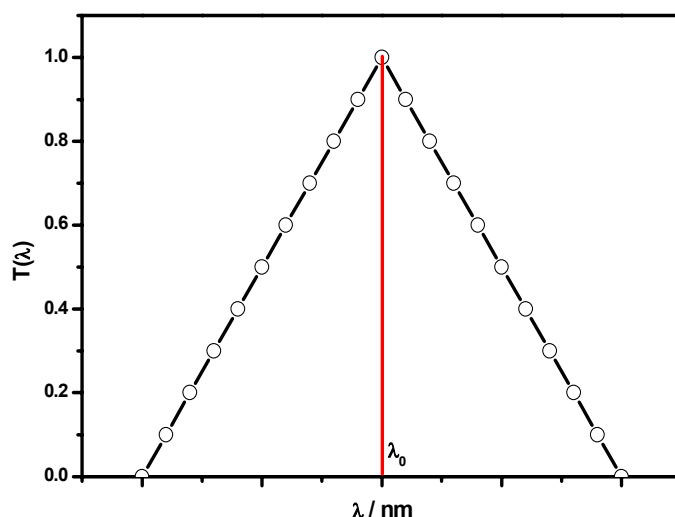
Figure IV-38 : A typical triangular wavelength distribution ($\Delta\lambda/\lambda$ = 10 %) resulting from a mechanical wavelength selector of a SANS-spectrometer. Represented from Ref. [122].

An example of the triangular wavelength distribution ($\Delta\lambda/\lambda$ = 10 %) of a SANS spectrometer resulting from a mechanical velocity selector shows Figure IV-38.

Additionally, the beam size and its shape on the detector influence the obtained neutron scattering curve. The latter depends on the configuration of the spectrometer, i.e. collimation distance C, detector distance D, and size of the collimation guide [122].

As already mentioned above, smearing effects lower the resolution of a SAS-spectrometer, mainly by smoothing of the form factor oscillations and by broadening of Bragg peaks (Figure IV-39) [121-123].
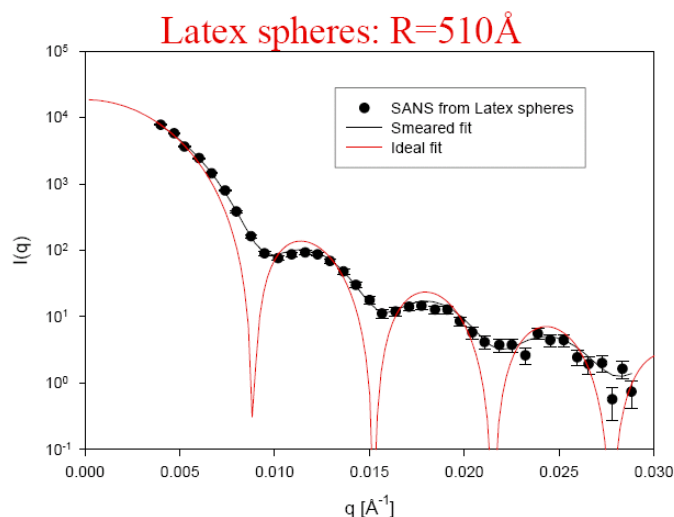
Figure IV-39 : Simulation of a scattering curve of a homogeneous sphere (red) and the corresponding real smeared scattering pattern (circle) that was fitted with a resolution term in addition to the spherical form factor (black). Represented from Ref. [123].

Especially for investigations of polydisperse samples, the resolution effects of the SAS-instruments must be considered carefully, since polydispersity and smearing on the experimental scattering curve are very similar [121, 122].

7.4   Sample preparation, measurement setup & data reduction

In the following chapter, the preparation of the investigated samples will be presented. Additionally, the measurement conditions as well as the instrument configura-

tions of the used SANS-devices will be given, which were applied for considering the resolution effects. Finally, the data reduction of the raw data will be described for each performed SAXS- and SANS-measurement.

7.4.1   Sample preparation

For the SAXS measurements, the samples of the SLIL/RTMS-systems and of the SLIL/RTMS-based microemulsions were completely prepared within the glovebox by weighting the appropriate amount of components into glass tubes equipped with a magnetic stir bar. The vessels were sealed with a septum afterwards. Then, the samples were homogenized over night by stirring at 40°C.

For the SANS investigations of the aqueous SLIL-systems, the water was replaced by D_2O (99.8 %, deutero, Germany) in order to improve the scattering contrast. In the case of the SLIL/RTMS-based microemulsions, the dodecane was also substituted by its deuterated analogon (d_{26}-dodecane, 99.8 %, euro-isotope, France) for the SANS investigations, because of the same reason. The preparation of the microemulsions was completely performed within the glovebox by weighting the exact amount of the components into sealable septum vessels equipped with a magnetic stir bar. After stirring over night at 40°C, isotropic solutions were obtained. Unfortunately, no substitution of one species for the binary SLIL/RTMS-systems was possible, since the SLILs as well as the RTMS were synthesized in the laboratory using non-deuterated reactants. Nevertheless, the contrast was good enough to achieve analysable scattering patterns for these systems. The samples were prepared according to the preparation route of the SLIL/RTMS-based microemulsions.

7.4.2   Measurement setup

The SAXS investigations on the Kratky-camera were performed using glass capillaries with a diameter of 1 mm (distributed by W. Müller, Berlin). Each measured sample was filled into a capillary with a syringe. Afterwards, the capillary was tipped-off by a Bunsen burner. The measurement time was set to 90 minutes. Before starting the measurement, the sample was thermostated for 15 minutes in order to reach thermal

equilibrium. The complete q-range was measured without changing the instrument configuration.

For the SANS, in contrast, two instrument setups had to be programmed in order to obtain the desired q-ranges. Table IV-1 summarizes the measurement conditions of the spectrometers used at the HMI and the ILL, respectively.

HMI Berlin	Configuration	
	1	2
q-range	$0.1428 \leq q / nm^{-1} \leq 0.9447$	$0.6912 \leq q / nm^{-1} \leq 3.7000$
Neutron guide width / mm	30	30
Sample aperture / mm	1	1
Collimation length / m	4.000	2.000
Sample det. distance / m	4.000	0.975
λ_0 / nm	0.605	0.605
$\Delta\lambda/\lambda$ (FWHM) / %	10	10
Detector pixel size / mm	5	5
Measurement time / s	600	120

ILL Grenoble	Configuration	
	1	2
q-range	$0.0168 \leq q / nm^{-1} \leq 1.510$	$0.0524 \leq q / nm^{-1} \leq 4.400$
Neutron guide width / mm	40	40
Sample aperture / mm	1	1
Collimation length / m	8	8
Sample det. distance / m	5.000	1.600
λ_0 / nm	0.600	0.600
$\Delta\lambda/\lambda$ (FWHM) / %	10	10
Detector pixel size / mm	8	8
Measurement time / s[a]	300 or 800	120 or 300

Table IV-6: SANS instrument configurations at the V4 and the D22, respectively. [a]Low measurement time for the SLIL/IL-based microemulsions, high measurement time for the binary SLIL/IL-systems.

At both instruments, the samples were measured using 1 mm quartz cuvettes (Hellma, suprasil). Each sample was thermostated for 15 minutes in order to reach thermal equilibrium conditions.

7.4.3 Data processing

Normally, the raw data obtained by the scattering experiment has to be corrected and then converted to absolute intensities by the usage of a standard, i.e. water. Unfortunately, no correction of the SAXS data that was achieved at the MPI was possible, as this institute usually work without absolute intensities and therefore the instruments were not equipped for the standard measurements (sample transmission, primary beam profile, primary beam intensity, …) needed for the conversion procedure. In addition, no high-precise quartz sample cuvettes were available which also made quantitative measurements impossible, as the sample thickness varied from measurement to measurement due to changing capillary quality. Consequently, the SAXS data obtained at the MPI will be presented on relative intensity scale and it will be analyzed qualitatively. The raw data of the Kratky-camera with the 1D gas detector was converted to the corresponding scattering pattern by an in-house computer program of the MPI. The SAXS data obtained from Dr. Pierre Bauduin (CEA, Saclay) were available on absolute scale. For this purpose, the raw data was treated using routine procedures including data correction, radial averaging, and absolute scaling [124].

The raw SANS scattering data obtained from the experiment at the HMI and at the ILL was converted to absolute scale by the following steps (primary data handling):

(i) *Correction of the detector inhomogeneity*

The inhomogeneous detection probability of the detector was corrected by a standardization file that contained the different sensibilities of each detector elements.

(ii)   *Masking of the data files*

In order to remove artefacts of the detector, which fudge the scattering pattern, a masking file was multiplied with the raw data. Additionally, the beam stop in the middle of the two-dimensional scattering pattern was removed by the masking procedure.

(iii)   *Radial averaging & normalization*

By radial averaging, the three-dimensional scattering patterns gained from the 2D detectors were reduced into two dimensions giving a higher statistical accuracy. Therefore, the scattering intensities have to be isotropic which means that they only depend on the absolute value of the scattering vector (Figure IV-40).
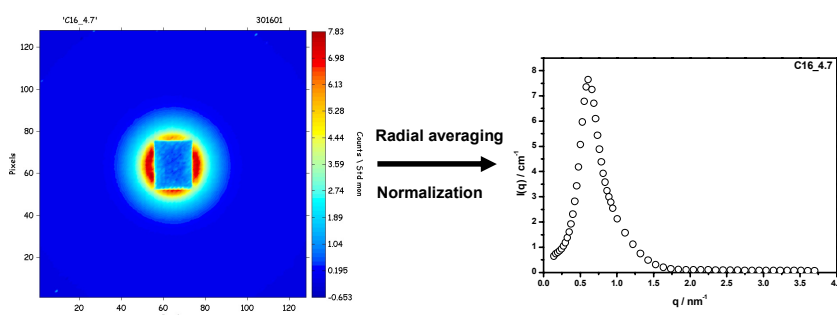
Figure IV-40 : Three-dimensional scattering intensity (left) and the corresponding two-dimensional scattering curve (right) after the radial averaging and normalization shown for an aqueous C$_{16}$mimCl sample (4.7 wt.%). The rectangle in the middle of the three-dimensional pattern represents the beam stop that is removed by the masking procedure.

In order to obtain normalized (absolute) scattering intensities, the raw data has to be corrected for a constant background scattering I_{back} resulting from the geometry of the SAS-spectrometer, and for the scattering of the quartz cuvette I_{cuv}. Consequently, an empty cell was measured and the corresponding scattering intensity was subtracted from each sample scattering intensity I_{sample}. Additionally, the transmission of each sample, T_{sample}, and the empty cell, T_{cuv}, has to be taken into account:

$$I^x_{sample} = \frac{\left(I_{sample} - I_{back}\right)}{T_{sample}} - \frac{\left(I_{cuv} - I_{back}\right)}{T_{cuv}} \qquad \text{(IV-112)}$$

where I^x_{sample} is the corrected sample intensity. The normalization to absolute intensity was performed using water as external standard:

$$I^{nor}_{sample} = \frac{I^x_{sample}}{I^x_{H_2O}} \qquad \text{(IV-113)}$$

where I^{nor}_{sample} is the absolute intensity (noted as $I(q)$).

The primary data handling including the steps presented previously was performed at the respective institutes by applying their own data reduction software packages [125-127].

8   Differential scanning calorimetry (DSC)

8.1   General aspects

The different scanning calorimetry (DSC) is often used to determine phase transitions, i.e. melting, and freezing of substances. However, Krafft-temperatures of surfactant solutions and stability temperatures can be also obtained by this technique, if the corresponding transition energies have a magnitude within the sensitivity of the used instrument [128].

In the framework of this thesis, DSC measurements of the pure synthesized ionic liquids were carried out in order to obtain their melting points, which indicate their purity by comparing their phase transition temperatures with the literature. In addition, the Krafft-temperature of the $C_{16}mimCl/bmimBF_4$-systems was achieved via DSC. Further, the high-temperature stability of the SLIL/RTMS-based microemulsions was checked.

8.2   Principle

The differential scanning calorimeter measures the amount of energy (heat) absorbed or released by a sample as it is heated, cooled, or held at a constant temperature. Typical applications include determination of the melting point, the corresponding heat of melting; measurement of the glass transition temperature, curing examinations, crystallization studies, and identification of phase transformations. The measurement of thermal effects in a Tian-Calvet type microcalorimeter is done by two fluxmeters (one on the measurement side and one on the reference side), each of them measures the thermal power exchanged constantly between the experimental vessels (probe vessel and reference vessel) and the calorimetric unit. The main difference, in comparison to the DSC technique with a flat plate probe, is that the Tian-Calvet type fluxmetric probe envelopes the sample and is therefore capable of measuring almost all the exchanges between the vessel and the unit, a characteristic that gives this device a clear advantage in terms of both, the quantity of the measured sample and the sensitivity (capacity to measure very weak effects) [128]. When two fluxmeters start to be heated, a computer plots the difference in heat flow against temperature. That is to say, the heat absorbed by the object is plotted against temperature. The heat flow (*HF*) at a given temperature is shown in units of heat, h, supplied per unit time, t. The heating rate (sweep rate) is the temperature increase ΔT per unit time, t.

$$\frac{heat}{time} = \frac{h}{t} = heat\,flow \qquad\qquad\qquad (\text{IV-114})$$

$$\frac{temperatur\,increase}{time} = \frac{\Delta T}{t} = sweep\,rate \qquad\qquad (\text{IV-115})$$

For many systems, the phase transition would be of the first-order. This means that when it reaches a specific transition temperature, the temperature would not rise until all the material have been transformed. This also means that the furnace is going to have to put additional heat into the object in order to transform into another structure and keep the temperature rising at the same rate as that of the reference probe [128]. This extra heat

flow during transformation shows up as a more or less dip in the DSC plot as the material absorbs heat. The heat required during transition can be calculated by integrating the area of this dip (Figure IV-42). Consequently, the transition enthalpy, ΔH, is given by

$$\Delta H = \int\limits_{t}^{t+\Delta t} \frac{h}{t} dt \qquad \text{(IV-116)}$$
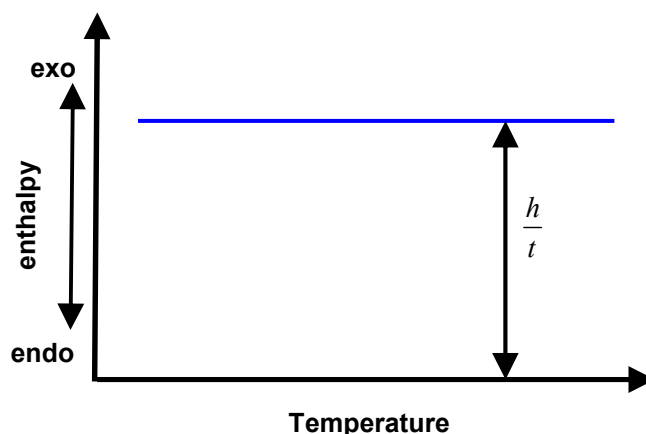
Figure IV-41 : Schematic DSC-plot against temperature.
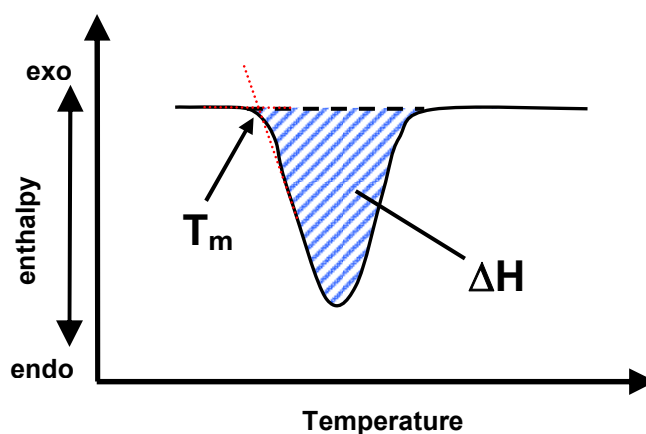
Figure IV-42 : Endothermic peak of DSC curve.

The melting point T_m can be received from the DSC thermograms via onset analysis by determining the intersection point between the baseline and the tangent defined by the reflection point of the peak onset (Figure IV-42). The heating mode is more recommendable for the determination of T_m than the cooling mode, because many organic

substances have a tendency to supercool considerably (especially ionic liquids, cp. Chapter II.1.4.1) [128].

8.3   Instrumentation

The DSC measurements of the SLIL/IL-systems were carried out on a micro-DSC III+ (SETARAM, France), a Tian-Calvet microcalorimeter, because of the expected low transition energies of Krafft-phase-transitions. The instrument was connected to a cooling thermostat working at 5°C. To avoid steam condensation in the calorimetric wall, especially at low temperatures, a constant purge of dry nitrogen was circulated through the sample holders during the measurements. The available temperature range is -20 to approximately 90 °C. A standard batch vessel, made of Hastelloy C276 steel, was used throughout the present experiments. The vessel is composed of a cylinder of 8 mm of internal diameter and useful height equivalent to 19.5 mm for the sample. The useful volume for the sample is equal to about 1 cm^3. The sample is filled in the vessel and closed with a stopper and a rubber o-ring (Kalrez). The reference depends on the aim of the measurement. It can be a blank cell or a cell filled with an appropriate solvent. The temperature sweep rate can be fixed between 0.1 and 1 °C/min. Before each measurement, the starting temperature has to be kept for more than 30 minutes in order to stabilize the temperature of the cells. The results were monitored and analyzed on the connected computer using the supplied SETARAM software package.

In the case of the pure synthesized ionic liquids, a Perkin-Elmer DSC 7 was used for all measurements. This machine is a flat plate probe differential scanning calorimeter, which is not as sensitive as the micro-DSC and provides only a sample volume of about 50 µL. Nevertheless, the accuracy of this machine was by far enough for the determination of T_m, because of the high energy changes normally occurring during melting. The DSC was connected to a cryostat (Lauda RL 6) operating as cooling source (-70°C). The operating temperature of the cryostate defined the low temperature limit of the DSC to approximately -35°C. The sample cells were made of aluminium consisting of a bottom part and an applicable cover part. The application of aluminium cells limited the upper temperature boundary of the instrument to 400°C. A molding press sealed

the two cell parts before the calorimeter was loaded. The volume of the cell was always 50 μL. The reference can be a blank cell or a cell filled with an appropriate solvent. The cell holders were purged by a flow of dry nitrogen avoiding moisture condensation. Different scan rates can be chosen between 0.1 to 10 °C/min. The measurement was controlled and monitored by the Pyris software package.

The thermal stability of two SLIL/RTMS-microemulsion compositions were investigated externally by Dr. Didier Dalmazzone (ENSTA/UCP[f]) using a DSC111 (SETARAM) differential scanning calorimeter with tight high-pressure resistant security vessels.

8.3.1 Calibration

During this work, the two differential scanning calorimeters, the DSCIII+ as well as the DSC 7, were calibrated several times. For this purpose, the standard procedures described in the manuals of each DSC were applied [129, 130]. The SETARAM DSC III+ was calibrated with gallium (T_m = 32.79 °C) performing a one point calibration, whereas in the case of the Perkin Elmer DSC 7 a three point calibration was accomplished using gallium (T_m = 32.79 °C), indium (T_m = 160.27 °C), and tin (T_m = 236.04 °C).

8.4   Sample preparation & measurement procedure

The SLIL/RTMS-systems were prepared in the glovebox stirred over night at 40°C to reach equilibrium. The SETARAM cells were filled and sealed in the glovebox, too. After transfer of the cells into the calorimeter, the probes were equilibrated at the starting temperature for more than 30 minutes. Then, the measurement was performed using a temperature sweep rate of 1 °C/min including an up- and down-scan.

Using the Perkin Elmer DSC 7, the melting points of EAN, C_{12}mimCl, C_{14}mimCl and C_{16}mimCl were investigated. The aluminium pan was filled with the IL in the glovebox, and sealed. After the cell assembly, the cells were equilibrated for 30

---

[f] *Ecole Nationale Supérieure de Techniques Avancées*

minutes at the starting temperature. The measurements were carried out performing an up- and down-scan with a temperature sweep rate of 10°C/min.

For the external measurements performed at the Ecole Nationale Supérieure de Techniques Avancées, the microemulsions were prepared by weighting the appropriate amounts of the components into glass vessels, which were sealed with a septum. Then, the samples were equilibrated one night. After that, the samples were provided to Dr. Didier Dalmazzone (ENSTA/UCP). The measurements were carried out as follows: 30 to 60 mg samples were precisely weighted into the DSC111 sample cells before tightening the vessels. For each sample, two runs were performed, the first one using aluminium seals to tighten the vessel, with a temperature limits of 400 °C and the second one using nickel seals, up to 500 °C. A heating rate of 4 °C/min was used in each experiment.

9   Thermal gravimetric analysis (TGA)

9.1   General aspects

The thermal stability of the used pure ionic liquids as well as of the formulated SLIL/RTMS-systems was determined within this work by thermalgravimetric analysis. This was an important measurement, since the new formulated systems should provide high-thermal stability.

9.2   Principle

Thermal gravimetric analysis (TGA) is performed on samples to determine changes in weight in relation to change in temperature. This needs a high degree of precision in three measurements: weight, temperature, and temperature change [130]. The TGA is a common technique to obtain characteristics of materials, i.e. the degradation and decomposition temperature (T_{dec}) or adsorbed moisture content. A typical weight temperature curve is given in Figure IV-43.
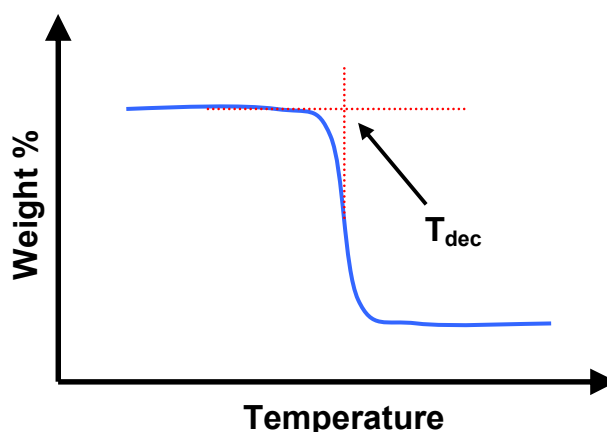
Figure IV-43 : Typical TGA curve.

9.3 Instrumentation

In this thesis, a Perkin Elmer TGA-analyzer TGA 7 connected to a PC was used. It consisted of a high-precision balance with a pan loaded with the sample. The pan, which was made of platinum, was placed in a small electrically heated oven with a thermocouple to accurately measure the temperature. The atmosphere was purged with an inert gas to prevent oxidation or other undesired reactions. The analysis was carried out by raising the temperature linearly and measuring the associated weight.

9.3.1 Calibration

During this work, the thermal gravimetric analyzer was calibrated using the standard procedures described in the manual. The procedure included a weight calibration of the balance, a furnace calibration, and the calibration of the thermocouple. For the thermocouple, a four point calibration was performed with calibration standards (Perkin Elmer) based on their curie temperatures T_c (alumel, $T_c = 163°C$; nickel, $T_c = 354°C$; perkalloy, $T_c = 596°C$; iron, $T_c = 596°C$;) covering a temperature range between room-temperature and 770°C. The calibration procedure was done according to the description given in the instrument manual [131].

9.4 Sample preparation & measurement procedure

The SLIL/IL-systems were prepared in the glovebox by weighting into a septum vessel and stirred over night at 40°C to reach equilibrium. Then, about 15 mg sample were filled into the platinum pan of the analyzer. After the sample cavity was closed, the furnace was purged with nitrogen for 15 minutes in order to reach thermal equilibrium. Now, the measurement was started with a heating rate of 10°C/min.

The thermal stability of the pure ionic liquids was measured in the same way.

10 Bibliography

[1]   O. Kratky, H. Leopold and H. Stabinger; Density determination of liquids and gases to an accuracy of 10^{-6}g/cm^3, with a sample volume of only 0.6 cm^3. *Zeitschrift fuer Angewandte Physik* **27**, 4, 273-277 (1969).

[2]   H. Hoiland and E. Vinkingstad; Partial molal volumes and volumes of ionization of hydroxycarboxylic acids in aqueous solution at 25, 30, and 35°C. *Journal of the Chemical Society, Faraday Transactions 1: Physical Chemistry in Condensed Phases* **71**, 10, 2007-2016 (1975).

[3]   H. Hoiland and E. Vikingstad; Partial molal volumes and additivity of group partial molal volumes of alcohols in aqueous solution at 25°C and 35 °C. *Acta Chemica Scandinavica, Series A: Physical and Inorganic Chemistry* **A30**, 3, 182-186 (1976).

[4]   J. E. Desnoyers, R. De Lisi, C. Ostiguy and G. Perron; *Direct measurements of the thermodynamic properties of surfactants*. in: *Solution Chem. Surfactants, [Proc. Sect. 52nd Colloid Surf. Sci. Symp.]*, (1979).

[5]   D. R. Lide; *CRC Handbook of Chemistry and Physics, 83rd Edition*. CRC Press, (2002).

[6]   Kruess;

http://www.kruss.info/index.php?content=http%3A//www.kruss.info/techniques/
surface_tension_e.html

[7]   T. Skrivanek; *Kruess Wissenschaftliche Laborgeraete GmbH.*

[8]   Kruess; Tensiometer K100MK2; Users manual (2006).

[9]   W. D. Harkins and H. F. Jordan; A method for the determination of surface tension from the maximum pull on a ring. *Journal of the American Chemical Society* **52**, 1751-1772 (1930).

[10]   N. D. Weiner and G. L. Flynn; Explanation of the minima in surface tension-log concentration profiles. *Chemical & Pharmaceutical Bulletin* **22**, 10, 2480-2483 (1974).

[11]   K. Lunkenheimer, G. Wienskol and A. J. Prosser; Automated High-Performance Purification of Surfactant Solutions: Study of Convective-Enhanced Adsorption. *Langmuir* **20**, 14, 5738-5744 (2004).

[12]   Kruess; *http://www.kruss.de.*

[13]   S. Yiv and R. Zana; Chemical relaxation and equilibrium studies of association in aqueous solutions of bolaform detergents. 2. Hexadecane-1,16-bis(trimethyl-ammonium bromide) and dodecane-1,12-bis(tributylammonium bromide). *Journal of Colloid and Interface Science* **77**, 2, 449-455 (1980).

[14]   H. C. Evans; Alkyl sulfates. I. Critical micelle concentrations of the sodium salts. *Journal of the Chemical Society* 579-586 (1956).

[15]   N. Nishikido; Estimation of micellar charge or aggregation number from conductivity and counterion-activity measurements. *Journal of Colloid and Interface Science* **92**, 2, 588-591 (1983).

[16]   P. C. Shanks and E. I. Franses; Estimation of micellization parameters of aqueous sodium dodecyl sulfate from conductivity data. *Journal of Physical Chemistry* **96**, 4, 1794-1805 (1992).

[17]   A. A. Dar, M. A. Bhat and G. M. Rather; Application of mixed electrolyte mass-action model to the micellization of 1-dodecylpyridinium chloride in aqueous medium. *Colloids and Surfaces, A: Physicochemical and Engineering Aspects* **248**, 1-3, 67-74 (2004).

[18]   B. C. Paul, S. S. Islam and K. Ismail; Effect of acetate and propionate co-ions on the micellization of sodium dodecyl sulfate in water. *Journal of Physical Chemistry B* **102**, 40, 7807-7812 (1998).

[19]   S. Dev, K. Gunaseelan and K. Ismail; Micellization of Surfactants in Acetamide Melt. *Langmuir* **16**, 15, 6110-6113 (2000).

[20]   A. Hamnett, C. H. Hamann and W. Vielstich; *Electrochemistry, 3rd Edition*. Wiley-VCH, (1997).

[21]   J. Frahm, S. Diekmann and A. Haase; Electrostatic properties of ionic micelles in aqueous solutions. *Berichte der Bunsen-Gesellschaft* **84**, 6, 566-571 (1980).

[22]   P. Carpena, J. Aguiar, P. Bernaola-Galvan and C. C. Ruiz; Problems Associated with the Treatment of Conductivity-Concentration Data in Surfactant Solutions: Simulations and Experiments. *Langmuir* **18**, 16, 6054-6058 (2002).

[23]   J. M. G. Barthel, H. Krienke and W. Kunz; *Physical Chemistry of Electrolyte Solutions - Modern Aspects*. Springer, (1998).

[24]   M. Bester-Rogac, R. Neueder and J. Barthel; Conductivity of sodium chloride in water + 1,4-dioxane mixtures at temperatures from 5°C to 35 °C. Part 1. Dilute solutions. *Journal of Solution Chemistry* **28**, 9, 1071-1086 (1999).

[25]   G. Jones and R. C. Josephs; The measurement of the conductance of electrolytes. I. An experimental and theoretical study of principles of design of the

Wheatstone bridge for use with alternating currents and an improved form of direct-reading alternating-current bridge. *Journal of the American Chemical Society* **50**, 1049-1092 (1928).

[26]   T. Shedlovsky; A screened bridge for the measurement of electrolytic conductance. I. Theory of capacity errors. II. Description of the bridge. *Journal of the American Chemical Society* **52**, 1793-1805 (1930).

[27]   T. Shedlovsky; A conductivity cell for eliminating electrode effects in measurements of electrolytic conductance. *Journal of the American Chemical Society* **52**, 1806-1811 (1930).

[28]   R. Wachter and J. Barthel; Studies on the temperature dependence of properties of electrolyte solutions. Part II. Conductivity determination over a large temperature range. *Berichte der Bunsen-Gesellschaft* **83**, 6, 634-642 (1979).

[29]   J. Barthel, R. Wachter and H. J. Gores; Temperature dependence of conductance of electrolytes in nonaqueous solutions. *Modern Aspects of Electrochemistry* **13**, 1-79 (1979).

[30]   J. Barthel, F. Feuerlein, R. Neueder and R. Wachter; Calibration of conductance cells at various temperatures. *Journal of Solution Chemistry* **9**, 3, 209-219 (1980).

[31]   D. F. Evans; *The Colloidal Domain: Where Physics, Chemistry, Biology, and Technology Meet, 2nd Edition*. Wiley-VCH, (1998).

[32]   G. T. Barnes and I. R. Gentle; *Interfacial Science - An Introduction*. Oxford University Press, (2005).

[33]   J. Peyrelasse, M. Moha-Ouchane and C. Boned; Viscosity and the phenomenon of percolation in microemulsions. *Physical Review A: Atomic, Molecular, and Optical Physics* **38**, 8, 4155-4161 (1988).

[34]   C. Mathew, Z. Saidi, J. Peyrelasse and C. Boned; Viscosity, conductivity, and dielectric relaxation of waterless glycerol-sodium bis(2-ethylhexyl)sulfo-succinate-isooctane microemulsions: the percolation effect. *Physical Review A: Atomic, Molecular, and Optical Physics* **43**, 2, 873-882 (1991).

[35]   H. J. Gores; *Physikalisch-chemisches Praktikum für Studierende der Chemie vor dem Vordiplom*. University of Regensburg, (2002).

[36]   M. Almgren, K. E. Wang and T. Asakawa; Fluorescence Quenching Studies of Micellization and Solubilization in Fluorocarbon-Hydrocarbon Surfactant Mixtures. *Langmuir* **13**, 17, 4535-4544 (1997).

[37]   Y. Moroi, R. Humphry-Baker and M. Gratzel; Determination of micellar aggregation number of alkylsulfonic acids by fluorescence quenching method. *Journal of Colloid and Interface Science* **119**, 2, 588-591 (1987).

[38]   N. J. Turro and A. Yekta; Luminescent probes for detergent solutions. A simple procedure for determination of the mean aggregation number of micelles. *Journal of the American Chemical Society* **100**, 18, 5951-5952 (1978).

[39]   N. Baden, O. Kajimoto and K. Hara; High-Pressure Studies on Aggregation Number of Surfactant Micelles Using the Fluorescence Quenching Method. *Journal of Physical Chemistry B* **106**, 34, 8621-8624 (2002).

[40]   S. Reekmans, D. Bernik, M. Gehlen, J. van Stam, M. Van der Auweraer and F. C. De Schryver; Change in the micellar aggregation number or in the size distribution? A dynamic fluorescence quenching study of aqueous cetyltrimethyl-ammonium chloride. *Langmuir* **9**, 9, 2289-2296 (1993).

[41]   M. Swanson-Vethamuthu, M. Almgren, G. Karlsson and P. Bahadur; Effect of Sodium Chloride and Varied Alkyl Chain Length on Aqueous Cationic Surfactant-Bile Salt Systems. Cryo-TEM and Fluorescence Quenching Studies. *Langmuir* **12**, 9, 2173-2185 (1996).

[42]   R. T. Buwalda, J. M. Jonker and J. B. F. N. Engberts; Aggregation of azo dyes with cationic amphiphiles at low concentrations in aqueous solution. *Langmuir* **15**, 4, 1083-1089 (1999).

[43]   L. P. Novaki and O. A. El Seoud; Solvatochromism in aqueous micellar solutions: effects of the molecular structures of solvatochromic probes and cationic surfactants. *Physical Chemistry Chemical Physics* **1**, 8, 1957-1964 (1999).

[44]   L. T. Okano, F. H. Quina and O. A. El Seoud; Fluorescence and Light-Scattering Studies of the Aggregation of Cationic Surfactants in Aqueous Solution: Effects of Headgroup Structure. *Langmuir* **16**, 7, 3119-3123 (2000).

[45]   T. Asakawa, H. Kitano, A. Ohta and S. Miyagishi; Convenient Estimation for Counterion Dissociation of Cationic Micelles Using Chloride-Sensitive Fluorescence Probe. *Journal of Colloid and Interface Science* **242**, 2, 284-287 (2001).

[46]   S. Miyagishi, T. Asakawa and M. Nishida; Influence of external environment on microviscosity in micelles. *Journal of Colloid and Interface Science* **115**, 1, 199-205 (1987).

[47]   R. D. Falcone, N. M. Correa, M. A. Biasutti and J. J. Silber; Properties of AOT aqueous and nonaqueous microemulsions sensed by optical molecular probes. *Langmuir* **16**, 7, 3070-3076 (2000).

[48]   N. O. Mchedlov-Petrossyan, Y. V. Isaenko and S. T. Goga; Reichardt betaines as combined solvatochromic and acid-base indicators in microemulsions. *Russian Journal of General Chemistry* **74**, 11, 1741-1747 (2004).

[49]   S. A. Moore and R. M. Palepu; Fluorometric investigations on the transition from reverse micelles to microemulsions in non-aqueous microemulsions. *Journal of Molecular Liquids* **135**, 1-3, 123-127 (2007).

[50]   M. Almgren, P. Hansson and K. Wang; Distribution of Surfactants in a Nonideal Mixed Micellar System. Effect of a Surfactant Quencher on the Fluorescence Decay of Solubilized Pyrene. *Langmuir* **12**, 16, 3855-3858 (1996).

[51]   G. Wedler; *Lehrbuch der Physikalischen Chemie, 4th Edition.* Wiley-VCH, (1997).

[52]   O. Zech; Thermosensitive metal-chelating surfactants and their use in separation processes. University of Regensburg / Université de Versailles Saint-Quentin-en-Yvelines, (2006).

[53]   S. S. Atik and J. K. Thomas; Photochemistry in polymerized microemulsion systems. *Journal of the American Chemical Society* **104**, 22, 5868-5874 (1982).

[54]   B. J. Berne and R. Pecora; *Dynamic Light Scattering: with Applications to Chemistry, Biology, and Physics.* Dover Pubn, (2000).

[55]   B. Chu; *Laser Light Scattering: Basic Principles and Practice.* Academic Press, (1974).

[56]   C. S. Johnson, Jr. and D. A. Gabriel; *Laser light scattering.* CRC Press, (1981).

[57]   J. S. Pedersen; Analysis of small-angle scattering data from colloids and polymer solutions: modeling and least-squares fitting. *Advances in Colloid and Interface Science* **70**, 171-210 (1997).

[58]   L. de Broglie; Waves and quanta. *Compt. rend.* **177**, 507-510 (1923).

[59]   W. Brown; *Dynamic Light Scattering: The Method and Some Applications.* Oxford University Press, (1993).

[60]   W. Brown; *Light Scattering: Principles and Development.* Oxford University Press, (1996).

[61]   M. B. Huglin; Determination of molecular weights by light scattering. *Topics in Current Chemistry* **77**, Inorg. Phys. Chem., 141-232 (1978).

[62]   S. W. Provencher; Inverse problems in polymer characterization: direct analysis of polydispersity with photon correlation spectroscopy. *Makromolekulare Chemie* **180**, 1, 201-209 (1979).

[63]   S. W. Provencher and V. G. Dovi; Direct analysis of continuous relaxation spectra. *Journal of Biochemical and Biophysical Methods* **1**, 6, 313-318 (1979).

[64]   O. Glatter and O. Kratky; *Small Angle X-ray Scattering*. Academic Press, (1982).

[65]   S. H. Chen; Small angle neutron scattering studies of the structure and interaction in micellar and microemulsion systems. *Annual Review of Physical Chemistry* **37**, 351-399 (1986).

[66]   P. Lindner and T. Zemb; *Neutrons, X-Rays and Light: Scattering Methods Applied to Soft Condensed Matter*. North-Holland Elsevier Science Publishers B.V., (1991).

[67]   A. Heinemann, A. Hoell, A. Wiedenmann and L. M. Pop; Small-angle scattering of orientated magnetic structures and applications to magnetic colloids. *Physica B: Condensed Matter* **385-386**, Pt. 1, 461-464 (2006).

[68]   P. Lindner and T. Zemb; *Neutron, X-Ray and Light Scattering: Introduction to an Investigative Tool for Colloidal and Polymeric Systems*. (1991).

[69]   O. Glatter; Data Evaluation in Small-Angle Scattering: Calculation of the Radial Electron Density Distribution by Means of Indirect Fourier Transformation. *Acta Phys. Austriaca* **47**, 83-102 (1977).

[70]   L. S. Ornstein and F. Zernike; *Proc. Sect. Sci. K. Ned. Akad. Wet.* **17**, 793 (1914).

[71]   J. B. Hayter and J. Penfold; An analytic structure factor for macroion solutions. *Molecular Physics* **42**, 1, 109-118 (1981).

[72]   J. B. Hayter and J. Penfold; Self-consistent structural and dynamic study of concentrated micelle solutions. *Journal of the Chemical Society, Faraday Transactions 1: Physical Chemistry in Condensed Phases* **77**, 8, 1851-1863 (1981).

[73]   J. P. Hansen and J. B. Hayter; A rescaled MSA structure factor for dilute charged colloidal dispersions. *Molecular Physics* **46**, 3, 651-656 (1982).

[74]   J. Chihara; A series of integral equations for liquids varying from the Percus-Yevick to hypernetted chain. *Progress of Theoretical Physics* **58**, 3, 1061-1063 (1977).

[75]   J. K. Percus and G. J. Yevick; Analysis of classical statistical mechanics by means of collective co.ovrddot.ordinates. *Physical Review* **110**, 1-13 (1958).

[76]   A. Guinier and G. Fournet; Small-Angle Scattering of X-rays. (1955).

[77]   J. B. Hayter and J. Penfold; Determination of micelle structure and charge by neutron small-angle scattering. *Colloid and Polymer Science* **261**, 12, 1022-1030 (1983).

[78]   R. Kirste and G. Porod; Small-angle scattering of x-rays by colloidal systems. Asymptotic behavior of the scattering curves. *Kolloid-Zeitschrift* **184**, No. 1, 1-7 (1962).

[79]   T. Hashimoto, M. Fujimura and H. Kawai; Domain-boundary structure of styrene-isoprene block copolymer films cast from solutions. 5. Molecular-weight dependence of spherical microdomains. *Macromolecules* **13**, 6, 1660-1669 (1980).

[80]   T. Perche, X. Auvray, C. Petipas, R. Anthore, E. Perez, I. Rico-Lattes and A. Lattes; Micellization of N-Alkylpyridinium Halides in Formamide Tensiometric and Small Angle Neutron Scattering Study. *Langmuir* **12**, 4, 863-871 (1996).

[81]   J. Kohlbrecher; Software package SASfit for fitting small-angle scattering curves. *Paul Scherrer Institute* (2008).

[82]   J. S. Pedersen; Analysis of small-angle scattering data from micelles and microemulsions: free-form approaches and model fitting. *Current Opinion in Colloid & Interface Science* **4**, 3, 190-196 (1999).

[83]   O. Glatter; Determination of particle-size distribution functions from small-angle scattering data by means of the indirect transformation method. *Journal of Applied Crystallography* **13**, 1, 7-11 (1980).

[84]   O. Glatter; The interpretation of real-space information from small-angle scattering experiments. *Journal of Applied Crystallography* **12**, 2, 166-175 (1979).

[85]   O. Glatter and B. Hainisch; Improvements in real-space deconvolution of small-angle scattering data. *Journal of Applied Crystallography* **17**, 6, 435-441 (1984).

[86]   O. Glatter; *Lecture: Streumethoden; Department of Physical Chemistry, University of Graz, Austria*. (1993).

[87]   G. Fritz and A. Bergmann; Interpretation of small-angle scattering data of inhomogeneous ellipsoids. *Journal of Applied Crystallography* **37**, 5, 815-822 (2004).

[88]   J. Brunner-Popela and O. Glatter; Small-angle scattering of interacting particles. I. Basic principles of a global evaluation technique. *Journal of Applied Crystallography* **30**, 4, 431-442 (1997).

[89]   B. Weyerich, J. Brunner-Popela and O. Glatter; Small-angle scattering of interacting particles. II. Generalized indirect Fourier transformation under consideration of the effective structure factor for polydisperse systems. *Journal of Applied Crystallography* **32**, 2, 197-209 (1999).

[90]   J. Brunner-Popela, R. Mittelbach, R. Strey, K. V. Schubert, E. W. Kaler and O. Glatter; Small-angle scattering of interacting particles. III. D_2O-$C_{12}E_5$ mixtures and microemulsions with n-octane. *Journal of Chemical Physics* **110**, 21, 10623-10632 (1999).

[91]   R. Strey, O. Glatter, K. V. Schubert and E. W. Kaler; Small-angle neutron scattering of D_2O-$C_{12}E_5$ mixtures and microemulsions with n-octane: direct analysis by Fourier transformation. *Journal of Chemical Physics* **105**, 3, 1175-1188 (1996).

[92]   A. Bergmann, G. Fritz and O. Glatter; Solving the generalized indirect Fourier transformation (GIFT) by Boltzmann simplex simulated annealing (BSSA). *Journal of Applied Crystallography* **33**, 5, 1212-1216 (2000).

[93]   D. J. Iampietro, L. L. Brasher, E. W. Kaler, A. Stradner and O. Glatter; Direct Analysis of SANS and SAXS Measurements of Catanionic Surfactant Mixtures by Fourier Transformation. *Journal of Physical Chemistry B* **102**, 17, 3105-3113 (1998).

[94]   R. Mittelbach and O. Glatter; Direct structure analysis of small-angle scattering data from polydisperse colloidal particles. *Journal of Applied Crystallography* **31**, 4, 600-608 (1998).

[95]   G. Fritz, A. Bergmann and O. Glatter; Evaluation of small-angle scattering data of charged particles using the generalized indirect Fourier transformation technique. *Journal of Chemical Physics* **113**, 21, 9733-9740 (2000).

[96]   F. Lichterfeld, T. Schmeling and R. Strey; Microstructure of microemulsions of the system water-n-tetradecane-alkyl polyglycol ether (C12E5). *Journal of Physical Chemistry* **90**, 22, 5762-5766 (1986).

[97]   M. Teubner and R. Strey; Origin of the scattering peak in microemulsions. *Journal of Chemical Physics* **87**, 5, 3195-3200 (1987).

[98]   S. H. Chen, S. L. Chang and R. Strey; Structural evolution within the one-phase region of a three-component microemulsion system: water-n-decane-sodium bisethylhexylsulfosuccinate (AOT). *Journal of Chemical Physics* **93**, 3, 1907-1918 (1990).

[99]   T. Sottmann, R. Strey and S. H. Chen; A small-angle neutron scattering study of nonionic surfactant molecules at the water-oil interface: area per molecule, microemulsion domain size, and rigidity. *Journal of Chemical Physics* **106**, 15, 6483-6491 (1997).

[100] S. M. Choi, S. H. Chen, T. Sottmann and R. Strey; The existence of three length scales and their relation to the interfacial curvatures in bicontinuous microemulsions. *Physica A: Statistical Mechanics and Its Applications (Amsterdam, Netherlands)* **304**, 1-2, 85-92 (2002).

[101] P. Debye and A. M. Bueche; Scattering by an inhomogeneous solid. *Journal of Applied Physics* **20**, 518-525 (1949).

[102] P. Debye, H. R. Anderson, Jr. and H. Brumberger; Scattering by an inhomogeneous solid. II. The correlation function and its application. *J. Appl. Phys.* **28**, 679-683 (1957).

[103] S. H. Chen, S. L. Chang, R. Strey, J. Samseth and K. Mortensen; Structural evolution of bicontinuous microemulsions. *Journal of Physical Chemistry* **95**, 19, 7427-7432 (1991).

[104] S. H. Chen, S. L. Chang and R. Strey; On the interpretation of scattering peaks from bicontinuous microemulsions. *Progress in Colloid & Polymer Science* **81**, Trends Colloid Inter, 30-35 (1990).

[105] M. Gradzielski, D. Langevin, T. Sottmann and R. Strey; Small angle neutron scattering near the wetting transition: discrimination of microemulsions from weakly structured mixtures. *Journal of Chemical Physics* **104**, 10, 3782-3787 (1996).

[106] H. Leitao, M. M. Telo da Gama and R. Strey; Scaling of the interfacial tension of microemulsions: A Landau theory approach. *Journal of Chemical Physics* **108**, 10, 4189-4198 (1998).

[107] S. H. Chen, S. L. Chang and R. Strey; Simulation of bicontinuous microemulsions: comparison of simulated real-space microstructures with scattering experiments. *Journal of Applied Crystallography* **24**, 5, 721-731 (1991).

[108] S. Engelskirchen, N. Elsner, T. Sottmann and R. Strey; Triacylglycerol microemulsions stabilized by alkyl ethoxylate surfactants-A basic study; Phase behav-

ior, interfacial tension and microstructure. *Journal of Colloid and Interface Science* **312**, 1, 114-121 (2007).

[109] K. V. Schubert, R. Strey, S. R. Kline and E. W. Kaler; Small angle neutron scattering near Lifshitz lines: transition from weakly structured mixtures to microemulsions. *Journal of Chemical Physics* **101**, 6, 5343-5355 (1994).

[110] D. J. Cebula, R. H. Ottewill, J. Ralston and P. N. Pusey; Investigations of microemulsions by light scattering and neutron scattering. *Journal of the Chemical Society, Faraday Transactions 1: Physical Chemistry in Condensed Phases* **77**, 11, 2585-2612 (1981).

[111] D. C. Liliana, Y. Anan, G. Nissim, L. M. E, F. Britta and G. Otto; Five-component food-grade microemulsions: structural characterization by SANS. *Journal of colloid and interface science* **274**, 1, 251-67 (2004).

[112] A. Yaghmur, L. de Campo, A. Aserin, N. Garti and O. Glatter; Structural characterization of five-component food grade oil-in-water nonionic microemulsions. *Physical Chemistry Chemical Physics* **6**, 7, 1524-1533 (2004).

[113] N. Freiberger, C. Moitzi, L. de Campo and O. Glatter; An attempt to detect bicontinuity from SANS data. *Journal of Colloid and Interface Science* **312**, 1, 59-67 (2007).

[114] T. Zemb, O. Tache, F. Ne and O. Spalla; Improving sensitivity of a small angle x-ray scattering camera with pinhole collimation using separated optical elements. *Review of Scientific Instruments* **74**, 4, 2456-2462 (2003).

[115] T. Zemb, O. Tache, F. Ne and O. Spalla; A high sensitivity pinhole camera for soft condensed matter. *Journal of Applied Crystallography* **36**, 3, Pt. 1, 800-805 (2003).

[116] U. Keiderling and A. Wiedenmann; New SANS instrument at the BER II reactor in Berlin, Germany. *Physica B: Condensed Matter* **213&214**, 1-4, 895-897 (1995).

[117]   Hahn-Meitner-Institute; *www.hmi.de*.

[118]   Institute-Laue-Langevin; *http://www.ill.fr/YellowBook/D22/ and http://www.ill.fr/YellowBook/D22/D22_info/*

[119]   Institute-Laue-Langevin; *http://www.ill.fr*

[120]   H. Stabinger and O. Kratky; A new technique for the measurement of the absolute intensity of x-ray small angle scattering. The moving slit method. *Makromolekulare Chemie* **179**, 6, 1655-1659 (1978).

[121]   J. S. Pedersen, D. Posselt and K. Mortensen; Analytical treatment of the resolution function for small-angle scattering. *J. Appl. Cryst.* **23**, 321-333 (1990).

[122]   I. Grillo; Effect of instrumential resolution and polydispersity on ideal form factor in Small-angle Neutron Scattering. *ILL Technical Report* **ILL01GR08T**, 1-20 (2001).

[123]   J. S. Pedersen; Instrumentation for Small-Angle X-ray and Neutron Scattering and Instrumental Smearing Effects. *Presentation* (2006).

[124]   F. Ne, A. Gabriel, M. Kocsis and T. Zemb; Smearing effects introduced by the response function of position-sensitive gas detectors in SAXS experiments. *Journal of Applied Crystallography* **30**, 3, 306-311 (1997).

[125]   U. Keiderling; A new software package for SANS data processing at the Hahn-Meitner-Institut in Berlin, Germany. *Physica B: Condensed Matter* **234-236**, 1111-1113 (1997).

[126]   U. Keiderling; The new "BerSANS-PC" software for reduction and treatment of small angle neutron scattering data. *Applied Physics A: Materials Science & Processing* **74**, Suppl., Pt. 2, S1455-S1457 (2002).

[127]   Institute-Laue-Langevin; *http://www.ill.eu/computing-for-science/cs-software/all-software/sans/#c5452*.

[128] G. Hohne, W. Hemminger and H. J. Flammersheim; *Differential Scanning Calorimetry: An Introduction for Practitioners*. Springer, (1995).

[129] SETARAM; *Users Manual, DSC III+*. (2000).

[130] Perkin Elmer; *Users Manual, 7 Series, DSC 7*. (1996).

[131] Perkin Elmer; *Users Manual, 7 Series, Thermal Gravimetric Analyzer 7*. (1996).

V.   Results & Discussion

1   Aggregation of surfactant-like ionic liquids in aqueous solution

The investigation of new amphiphiles concerning their properties in solution is always a very important topic in colloid science, both scientifically, and from the application point of view. Especially, the understanding of surfactant structure, i.e. the head group nature and the head group-counterion interactions, respectively, in relation to the out coming phase behaviour of the amphiphile in solution is essential for the product design of new innovative formulations [1-6].

Interestingly, beside the studies concerning ILs in traditional applications such as solvents in organic reactions or catalysis, as medium in extraction processes, and as electrolytes in electrochemical devices (batteries, double layer capacitors, solar cells) (cp. Chapter II.1.6), recent investigations deal also with the phase behaviour of ionic liquids, mainly based on the 1-alkyl-3-methylimidazolim cation ($C_n mim^+$) with different anions, in aqueous solution. It was found that ILs of the imidazolium type with short and medium-length alkyl-chains aggregate, as cationic surfactants do, in polar solvents, which is not surprising due to their structure [7]. During the last years, critical aggregation concentrations (*cacs*) of ionic liquids like $bmimBF_4$, $bmimC_8SO_4$, $C_{8,10}mimCl$ and $C_{2,6,8,10}mimBr$ in aqueous media determined via standard techniques were reported by different workgroups [8-16]. Further, the micellar aggregates of $bmimBF_4$, C_8mimCl, C_8mimBr, $C_{10}mimBr$, and C_8mimI formed above the *cac* were characterized with regard to the mean radius, aggregation number and polydispersity by small angle neutron scattering (SANS) [8, 15]. The obtained values were in the same order of magnitude as for aggregates formed by common short-chain ionic surfactants.

By contrast, the self-assembly of long-chain imidazolium ILs chlorides and bromides ($C_n mimCl$, Br; n ≥ 12) in aqueous solution was proofed just recently by our

workgroup and others [12-19]. These studies demonstrate the structural resemblance of imidazolium ILs in relation to the corresponding conventional well-known alkyltrimethylammonium surfactant analogues (C_nTACl, Br; $n \geq 12$). Consequently, fundamental surfactant parameters of these two surfactant types like the critical aggregation concentration, the adsorption behaviour of the amphiphile at the liquid/gas interface, the thermodynamic parameters of micelle formation, the counterion binding at the micelle surface, and the aggregation number of the formed aggregates were compared and interpreted. In the public literature, most studies concern surfactant-like ionic liquids (SLILs) incorporating the bromide anion, whereas the self-assembly of the chloride salts in water is only poorly investigated, although the $C_n$mimCl/water systems already play an outstanding role in material science as surfactant templates for the synthesis of various types of mesoporous metal oxides via nanocasting sol-gel (liquid crystalline templating) and hydrothermal approach, respectively (cp. Chapter I) [20-26].

Very recently, different templating features of C_{16}mimCl have been obtained in comparison to the well-known C_{16}TACl by the workgroup of Smarsly et al. In the framework of their study, the following conclusions were drawn [19]:

(i) C_{16}mimCl/water mixtures can be used for the preparation of ordered silica with an unusually high degree of order and very low defects compared to C_{16}TACl.

(ii)   Additionally, C_{16}mimCl enables the reproducible preparation of mesoporous hexagonal and cubic silica (which is not possible with C_{16}TACl).

(iii) Hierarchical mesoporous systems using C_{16}mimCl and block copolymer as template can be achieved. This is not possible with the respective conventional alkyltrimethylammonium chloride surfactant.

The exceptional templating properties of SLIL must be attributed to the molecular structure of the imidazolium head group, which affects the formed superstructures of this SLIL in solution and therefore, the templated metal oxides. Kaper et al. showed the different phase behaviour of C_{16}mimCl in water determined via SAXS measurements compared to C_{16}TACl. The C_{16}mimCl/water mixtures show a large micellar L_1 region extending up to 55 wt.%, whereas the phase diagram of C_{16}TACl/water shows a much

smaller micellar region. Here already at ca. 32 wt.% a hexagonal H_1-phase is formed. For C_{16}mimCl the H_1-phase appears at about 55 wt.%, followed by a hexagonal-lamellar and a pure lamellar phase region at ca. 80 wt.%. A gel phase that is found in the phase diagram of C_{16}TACl is absent in the C_{16}mimCl system. From the analysis of the SAXS data of the lyotropic phases with 60 wt.%, 67wt.% and 70 wt.%, radii of the elongated micelles R_{fit} were obtained. Interestingly, the theoretical radii, R_{calc}, of the hexagonal phase which could be calculated from the volume fraction based on the weight percentage is much smaller than the fitted radius, and also its change with increasing C_{16}mimCl concentration, is much smaller compared to the SAXS results (Table V-1).

C_{16}mimCl wt. %	R_{fit} / nm	d_{10} / nm	N	a	R_{calc} / nm
60	2.1 ± 0.03	4.4 ± 0.05	8 ± 4	3.8	1.55
67	2.5 ± 0.03	4.4 ± 0.05	8 ± 1	3.9	1.65
70	3.3 ± 0.03	4.4 ± 0.05	8 ± 2	3.8	1.66

Table V-1: Parameters obtained from SAXS fitting. R_{fit} radius, d_{10} d-spacing, N stack height, a lattice parameter, R_{calc} calculated radius from the volume fraction. Represented from Ref. [19].

Kaper et al. supposed that this pronounced increase of the micellar radius with concentration is unusual for common cationic surfactants and can be attributed to strong interactions of the imidazolium head groups between each other that leads to a high tendency to reduce the curvature of the formed micelles at higher concentrations in water [19].

Based on this fact that the surfactant properties of the surfactant-like imidazolium chlorides (resulting in considerable differences of phase behaviour compared to the C_nTACl/water mixtures) are nearly unknown, the following chapters will deal with the study of the formed superstructures of the $C_n$mimCl (n = 12, 14, 16) surfactants in aqueous solution. Thus, more information about the amphiphilic character of the imidazolium based SLILs should be achieved. The obtained results will be compared to the

conventional 1-alkyltrimethylammonium halogenides, to the 1-alkylpyridinium halogenides, and, when meaningful, to the 1-alkyl-3-methylimidazolium bromide analogues in order to get a basic understanding of the influence of the imidazolium head group in aqueous media. These fundamental investigations can be the initial basis for the usage of SLILs in more complex formulations. The achieved surfactant parameters will be related to the recently published values of El Seoud et al., who investigated the same systems, but in less detail [16].

Many different techniques were used to characterize the binary SLIL/water systems including (i) solubility measurements of the SLILs, (ii) surface tension, (iii) conductivity, (iv) fluorescence quenching, and finally (v) small-angle neutron scattering experiments. The data thus obtained were employed in order to obtain the Krafft-temperature, maximal areas/surfactants at the liquid/gas interface, the critical aggregation concentrations, the degrees of counterion dissociation (and therefore the degree of counterion binding), aggregation numbers, and finally micellar properties, e.g. aggregate size and shape. In addition, thermodynamic parameters including the Gibbs free energies of adsorption and micellization, were calculated for C_{12}mimCl, C_{14}mimCl, and C_{16}mimCl, respectively. From Gibbs free energies of micellization, the contributions of enthalpies and entropies of micellization were extracted.

1.1   Krafft temperature

The Krafft temperature T_m (and solubility behaviour) of surfactants is a crucial property. It limits the temperature range, in which these substances can be successfully utilized in formulation technology, since Krafft temperature is the lowest temperature where the solution is fully transparent. Further, the solubility behaviour allows an estimation of the free energy of the crystal state present in the surfactant crystal and further on the hydration of the head group (cp. Chapter II.2.3.3).

In the framework of this study, the solubility behaviour of the respective $C_n$mimCl salts was investigated by visual determination of the clarification of the SLIL/water mixtures during heating. For this purpose, several aqueous solutions of the

SLILs were prepared, homogenized at elevated temperature (40°C), and then cooled to 0°C using a KCl/water/ice mixture. During cooling, the turbidity was visually monitored. For the C_{12}mimCl and the C_{14}mimCl, all prepared solutions remained clear down to 0°C, but the C_{16}mimCl samples became turbid at 0°C. The exact solubility temperature of each aqueous C_{16}mimCl solution was obtained by heating the turbid samples using a constant heating rate and notation of the clarification temperature (reproducibility with the used thermometer was about 0.2°C). The whole solubility curve of the C_{16}mimCl, also denoted as Krafft boundary, is shown in Figure V-1. At a concentration of 1 wt.% (w/w), the Krafft temperature was obtained giving a value of 13.1°C ($\pm$ 0.2°C) for C_{16}mimCl.
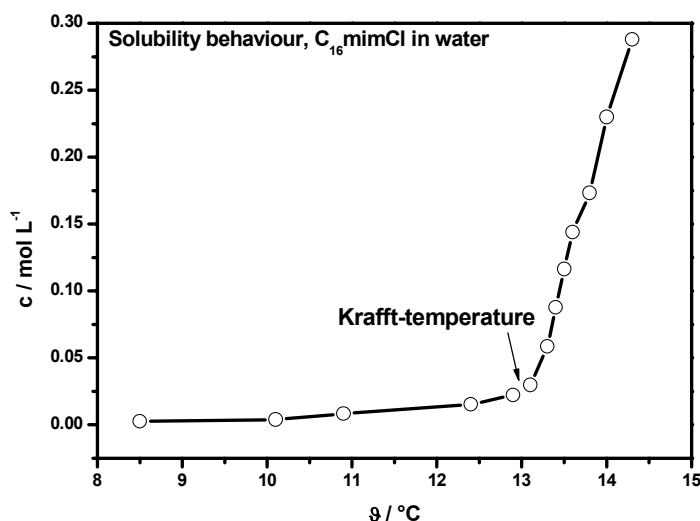
Figure V-1: Solubility curve (Krafft boundary) of the C_{16}mimCl ionic liquid in water observed visually by heating of the respective solutions. The location of the Krafft temperature estimated for the 1 wt.% (w/w) solution is indicated by the arrow.

Since the Krafft phenomenon is a consequence of the interplay of the hydrophilicity, which tends to favour hydrated phases (isotropic solutions), and of the free energy of the crystal phase, which defines the thermodynamic tendency of crystal formation, the low Krafft temperatures of the $C_n$mimCl salts are generally attributed to the high free energies of their crystal states caused by an unfavourable packing of the

asymmetric ionic liquid molecules in the solid state [27]. However, the higher Krafft temperature of the C_{16}mimCl indicates a lower free energy of its crystal state opposing the formation of an isotropic phase. Considering the long alkyl-chain with 16 carbon atoms, the main contribution of hydrated crystal formation below the Krafft temperature are the van-der-Waal interactions between the hydrophobic chains, which become fairly strong and oppose the solubilization of C_{16}mimCl at low temperature.

The Krafft temperature of a surfactant is often related to its melting point [27]. The difference between melting point T_m and Krafft temperature T_{Krafft} has been recognized as a phase parameter whose magnitude reflects the intrinsic hydrophilicity of the hydrophilic head group: The higher the difference between the observed Krafft temperature and the measured melting point, the higher is the hydrophilicity of the present head group [28]. Therefore, the Krafft temperatures of the $C_n$mimCl ionic liquids as well as their melting points are compared in Table V-2. Additionally, available values of the respective C_nTACl analogues obtained from literature are presented.

Surfactant	T_{Krafft} / °C	T_m / °C	ΔT / °C	Ref. T_{Krafft}	Ref. T_m
C_{12}mimCl	< 0	41.1	-	This work	This work[b]
C_{14}mimCl	< 0	53.1	-	This work	This work[b]
C_{16}mimCl	13.1[a]	63.8	50.7	This work	This work[b]
C_{12}TACl	< 0	70.5	-	[29]	This work[b]
C_{14}TACl	< 0	81.2	-	[28]	This work[b]
C_{16}TACl	8	92.3	84.3	[28]	This work[b]

Table V-2: Summary of the Krafft temperatures and melting points of the $C_n$mim$^+$ and the C_nTA$^+$ chlorides. [a]Obtained visually. [b]Via DSC.

None of the presented chloride surfactants with dodecyl- and tetradecyl-chain showed Krafft temperatures down to 0°C, but the Krafft temperatures for all substances with a carbon chain of 16 atoms are generally above 0°C reflecting lower free energies in their crystal states. Since the imidazolium salts possess a lower symmetry of the cation scaffold, they show lower melting points than the C_nTACl surfactants. According

to the theory, a lower melting point reflects a lower stability of the solid state, which should lead to a lower Krafft temperature in aqueous solution. Interestingly, T_{Krafft} reported for 1-hexadecyl-3-methyl-imidazolium chloride is higher compared to the value observed for 1-hexadecyl-trimethylammonium chloride. Since the length of the carbon chain is equal for $C_{16}mimCl$ and $C_{16}TACl$ resulting in equal or at least comparable van-der-Waal interactions, the gap between the Krafft temperatures must be attributed to the different head groups. Consequently, it seems that surfactants with a delocalized charge within the head group show slightly higher Krafft temperatures as comparable amphiphiles with a fixed charge. This is not astonishing, because the charge density of a delocalized head group is generally lower resulting in a lower hydrophilicity of the latter. In other words, it seems that the alkyltrimethylammonium head group is better solubilised by water molecules than that of its delocalized counterpart. This observation is also manifested in the larger difference of T_{Krafft} and T_m in the case of the alkyltrimethylammonium surfactants. Consequently, the effect of hydrophilicity contribution of the head groups seems to be superior to the crystal state stability for the appointment of T_{Krafft} (in the present case).

1.2   Surface tension: *cac*, *pC_{20}*, *Γ_{max}*, *A_{min}*, *ΔG^0_{ads}*

The surface tension isotherms at 25°C were measured in order to get an impression about the surface activity of the SLIL chlorides and to determine their critical aggregation concentrations in water. Figure V-2 shows the surface tension σ versus the logarithm of concentration $log(c)$ for the three systems studied. There are several features to note. First, all three systems display a pronounced decrease of the surface tension to a plateau region with increasing SLIL concentration. The sharp break-points in the $\sigma - log(c)$-plots indicate the SLIL aggregation concentrations. The absence of minima, which are often caused by the presence of highly surface-active impurities altering the surface tension data near the inflection points, confirms the high purity of the synthesized SLILs [30]. *cac* values were estimated at the intersection of the two almost linear portions of the surface isotherms.
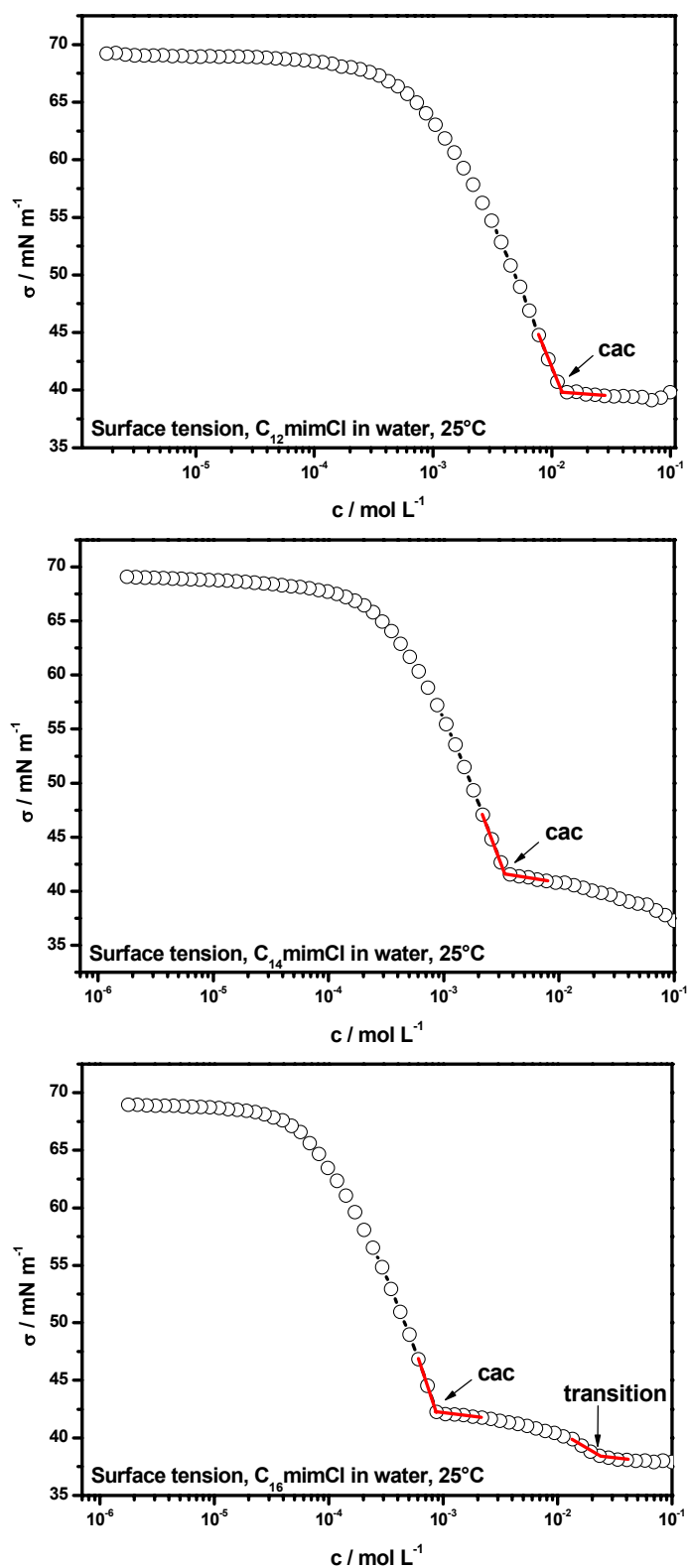
Figure V-2 : Surface tensions isotherms of the three SLILs measured at 25°C. The *cac*s are indicated by two red lines. The C_{16}mimCl system shows a further inflection point, which is also marked.

The red lines in Figure V-3 are guides for locating the *cac*s, which are presented in Table V-3. They decrease by a factor of about 4 with increasing chain-length (from 12 to 16 carbons), since the hydrophobicity raises due to elongation of the hydrocarbon chain. This observation is in line with a factor of 2 per methylene group usually expected for an ionic surfactant [31]. Interestingly, the $C_{16}mimCl$ plot shows another pronounced reproducible break-point at about 2.3×10^{-2} mol/L. This second minimum may arise from a further reorientation process of the surfactant monomers at the surface. No additional inflection points were found in the case of the other two SLILs within the investigated concentration range (up to 0.1 mol L^{-1}). The *cac*s are in the same order of magnitude as for common ionic surfactants with comparable carbon chains (cp. Table V-3). However, they are slightly smaller as the critical aggregation concentrations of the corresponding alkyltrimethylammonium and 1-alkylpyridinium chloride surfactants indicating a slightly higher aggregation tendency of the imidazolium surfactants in water. Normally, this reflects a smaller repulsion of the head groups compared to the analogues with ammonium and pyridinium head groups, which makes self-aggregation more favourable for the C_nmimCl salts [5].
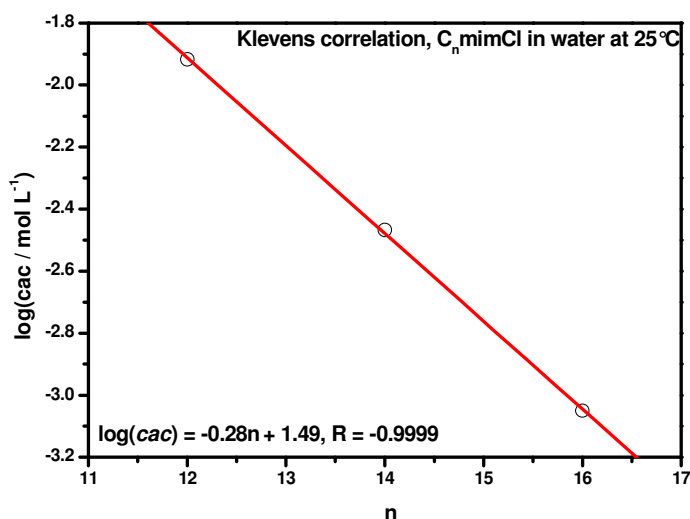
Figure V-3 : Logarithmic plot of the *cac*s obtained from surface tension measurements at 25°C as a function of the carbon number *n* in the C_nmimCl series.

As already pointed out, the experimentally achieved *cac*s decrease with increasing number of carbon atoms *n* in the hydrophobic alkyl-chain of the SLILs. This obser-

vation is illustrated in Figure V-3, in which the logarithm of the *cac*s is presented as a function of the carbon number in the alkyl-chain. The linear dependence (R = -0.999) can be described by the Klevens-equation giving two parameters, *A* and *B*, respectively [32]. For the present $C_n$mimCl homologous series, the parameters equal 1.49 (*A*) and 0.28 (*B*). These values are consistent with those of cationic surfactants, for which the Klevens constants are normally found to be $1.2 \leq A \leq 2.0$ and $B \approx 0.3$ (for a given head group and thermodynamic conditions) [5, 33].

For comparison, Table V-3 summarizes the critical aggregation concentrations for the 1-alkyl-3-methylimidazolium chloride series recently published by El Seoud et al. Their *cac*s are in good agreement with the values obtained in the framework of these investigations [16]. For the sake of completeness, it should be mentioned that the *cac* value for C_{12}mimBr was reported by Dong et al. and estimated to 1.09×10^{-2} mol L^{-1} by surface tension measurement [13]. The latter is similar, but a little smaller than the value of 1.21×10^{-2} mol L^{-1} for C_{12}mimCl reported here. This is reasonable, because the counterion influences the aggregation tendency of the surfactant cation. In fact, cationic amphiphiles containing Br$^-$ show higher aggregation power, and therefore a lower *cac*, than their chloride analogues, since the bromide more effectively screens the electrostatic repulsion among the polar head groups resulting from its smaller degree of hydration [1, 5, 31, 34, 35].

The effectiveness and efficiency of surfactant adsorption at the liquid/gas interface are given by the surface pressure at the *cac* (Π_{cac}) and by the surfactant concentration required for the reduction of the solvent surface tension, in this case water, by 20 mN/m (pC_{20}). Normally, both parameters increase with lengthening the carbon-chain and by increasing the binding ability of the counterion [5, 36]. Table V-3 lists the obtained quantities of Π_{cac}, pC_{20}, and additionally, the cac / C_{20} ratio that is a measure of the tendency of the amphiphile to adsorb at the liquid/gas interface relative to its tendency to form aggregates. The surface tensions at the *cac* for the imidazolium homologues become slightly higher as the chain-length increases. At first, this tendency is unexpected, since a surfactant with a longer carbon-chain should decrease the surface tension

more than homologues with a shorter one. Nevertheless, this observation is in agreement with the cac / C_{20} ratio, which decreases from 2.91 for C_{12}mimCl to 2.24 for the C_{16}mimCl SLIL. This indicates a stronger tendency of C_{12}mimCl to adsorb at the planar liquid/gas interface relative to its tendency to form micelles. Therefore, C_{12}mimCl is preferably located at the interface lowering the surface tension more effectively (greater cac / C_{20} ratio). El Seoud et al. reported the same trend (cp. Table V-3), although their cac / C_{20} ratio for C_{14}mimCl seems to be significantly too high compared to their results for C_{12}mimCl and C_{16}mimCl, respectively. Additionally, another inconsistency was found within the paper of El Seoud et al. during recalculation of their cac / C_{20} ratio. With the presented cac and C_{20} parameter, it is not possible to obtain the reported cac / C_{20} ratio. The recalculated ratio is also shown in brackets in Table V-3. Interestingly, the corrected values agree very well with those observed within the underlying work. The efficiency of adsorption pC_{20} of the SLIL chlorides increases nearly linearly (R = 0.998) by lengthening the alkyl-chain. This corresponds to a value of about 0.6 per two methylene groups, which is in excellent agreement to the expected value for amphiphilic molecules of a given homologous series [37].

Unfortunately, a detailed comparison of the imidazolium chlorides with common chloride surfactants in consideration of the adsorption parameters is difficult, since only few data exist in the open literature. Nevertheless, it was possible to complete the found literature values by extraction of some quantities by using the reported raw data. For this reason, not all literature values reported in Table V-3 (calculated quantities are marked by a star) can be understood as exact values, however, they enable at least a qualitative comparison to the here presented data leading to some general conclusions. It is evident that the pC_{20} values for the $C_n$mimCl series are quite high compared to the average values of common cationic surfactants.

Surfactant	cac mmol/L	σ_{cac} mN/m	Π_{cac} mN/m	$\Gamma_{max} \times 10^{-6}$ mol/m^2	A_{min} nm^2	$-\Delta G^0_{ads}$ kJ/mol	C_{20} mmol/L	$\dfrac{cmc}{C_{20}}$	pC_{20}
C$_{12}$mimCl	12.10	39.8	32.2	2.13	0.78	32.9	4.14	2.92	2.38
	13.17[a]	42.3[a]	29.7[a]	2.31[a]	0.72[a]	32.0[a]	4.46[a]	2.44 (2.95)[a]	2.35[a]
C$_{14}$mimCl	3.41	41.4	30.6	2.32	0.71	34.8	1.46	2.34	2.84
	2.98[a]	38.2[a]	33.8[a]	2.96[a]	0.56[a]	33.8[a]	1.00[a]	2.98[a]	3.00[a]
C$_{16}$mimCl	0.89	42.1	29.9	2.55	0.65	37.3	0.39	2.28	3.41
	0.87[a]	40.9[a]	31.1[a]	3.39[a]	0.49[a]	35.2[a]	0.40[a]	2.05 (2.18)[a]	3.40[a]
C$_{12}$TACl	22.4[b]	45.7[b*]	27.6[b*]	2.30[b*]	0.72[b*]	21.03[b*]	11.91[b*]	1.88[b*]	1.92[b*]
C$_{14}$TACl	5.40[c]	-	-	-	-	-	-	-	-
C$_{16}$TACl	1.57[d]	42.5[d*]	29.5[d*]	2.18[d*]	0.75[d]	28.04[d*]	0.71[d*]	2.23[d*]	3.15[d*]
C$_{12}$PyCl	16.20[e]	43.7[e]	28.3[e]	2.68[e]	0.62[e]	31.6[e]	8.10[e]	2.0[e]	2.10[e]
C$_{14}$PyCl	3.50[f]	-	-	1.49[g]	1.11[g]	-	-	-	-
C$_{16}$PyCl	0.89[g], 0.91[h]	42.0[h]	30.0[h]	3.39[g], 3.95[h*]	0.49[g], 0.42[h]	28.85[h*]	0.50[h]	1.82[h*]	3.30[h*]

ΔG^0_{ads}	$\Delta G^0_{ads}(-CH_2-)$ kJ/mol		$\Delta G^0_{ads}(HG) + \Delta G^0_{ads}(-CH_3)$ kJ/mol	
C$_n$mimCl	-0.80		-24.60	
	-0.85[a]		-22.60[a]	
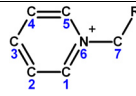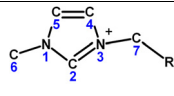
Table V-3: Relationship between SLIL structures and the *cacs*, minimum areas of the surfactant monomer at the liquid/gas interface A_{min}, Gibbs free energies of adsorption ΔG^0_{ads}, and the effectiveness- & efficiency-parameters Π_{cac} and pC_{20}. Available literature data of meaningful surfactants are also given for comparison. As far as possible, all literature data presented here were obtained from surface tension measurements at 25°C. [a]Ref. [16]. [b]Ref. [38]; extracted from graph and calculated. [c]Ref. [39]; *cac* / mmol kg^{-1}. [d]Ref. [40]; data was extracted from graphs. [e]Ref. [37]. [f]Ref. [41]; *cac* was obtained from conductivity; no *cac* from surface tension measurement was available in literature. [g]Ref. [42]. [h]Ref. [33], presented parameters were obtained at 30°C, no values at 25°C were available. [*]Note: Missing quantities were calculated from the available literature data (sometimes obtained from the graphs) using formulas presented in Chapter II.2.2.

For example, the pC_{20} value of C_{16}mimCl was found to be 3.40, which is actually in the order of magnitude as values estimated for non-ionic surfactants. Generally, non-ionic amphiphiles show higher efficiency of adsorption, since no head group repulsion hinders the adsorption process [5]. One possible explanation for the quite high pC_{20} of the $C_n$mimCl series may be a lower charge density of the imidazolium head group caused by the charge delocalization, which is not the case for the alkyltrimethylammonium salts for example. Additionally, a better screening of the head group charge by the anion compared to pyridinium surfactants and/or a different charge distribution within the surfactant molecule could be further reasons. El Seoud et al., who reported values that differ only slightly from those obtained during this work, also confirmed such high pC_{20} values for $C_n$mimCl SLILs (cp. Table V-3). The better performance of the imidazolium SLILs concerning their surface activity is also proved by Π_{cac}, which is always lower than the quantities of the respective common surfactant analogues. Therefore, they are more prone to form micelles and are more efficient and more effective at reducing the surface tension of water than the compared conventional cationic amphiphiles.

In order to clearify whether there exists a significant difference in charge configuration within the molecules of alkyl trimethylammonium, alkyl pyridinium and 1-alkyl-3-methylimidazolium cations, respectively, which could lead to the different adsorption/aggregation power of these cationic surfactants compared to the conventional amphiphiles, theoretically calculated charge distributions of the respective surfactant types were taken from the literature and compared. Table V-4 summarizes the distributions of charge for the three amphiphile classes separated into the different surfactant segments HG, α-methylene and hydrophobic alkyl tail R, respectively. Additionally, the atomic partial charges (of the backbone atoms with attached hydrogens included) are presented, if they were available from literature. It becomes immediately clear from an examination of these charge groupings that not all charge is present in the head group, but a significant fraction of charge is distributed into the α-methylene and remaining alkyl chain. The large partial charge for the α-methylene supports its classification as a part of the head group, as already supposed by Tanford and Huibers [75, 112, 113]. For all three amphiphiles, a significant portion (about 10 %) of the positive charge resides on

the alkyl tail. The small partial charge on the alkyl chain has only little effect on the solubility of the surfactant molecule, since a charge of only few percent is not sufficient to enhance the ordering of water around the tail, with the resulting increase in solubility. A greater effect, e.g. on the *cac*, is apparent from the change in charge of the head group due to the fact that the magnitude of electrostatic repulsion between ionic head groups strongly influences the monomer solubility and the adsorption/aggregation tendency, respectively [112, 113].

Charge on	q / e	q / e	q / e
C1	-	0.205^b	-
N1	-	-	0.133^c
C2	-	0.064^b	0.233^c
N2	-	-	-
C3	-	0.184^b	-
N3	-	-	0.111^c
C4	-	0.064^b	0.040^c
C5	0.132^a	0.206^b	-0.010^c
C6	-	-	0.183^c
N6	-	-0.032^b	-
C7	-	0.202^b	0.195^c
HG	0.755^a	0.700^a, 0.691^b	0.690^c
α-CH$_2$-	0.132^a	0.187^a, 0.202^b	0.195^c
R (alkyl tail)	0.113^a	0.113^a, 0.107^b	0.115^c
HG+α-CH$_2$	0.887^a	0.887^a, 0.893^b	0.885^c

Table V-4: Comparison of segmental charge distributions for alkyl trimethylammonium, alkyl pyridinium and 1-alkyl-3-methylimidazolium cations. Additionally, the atomic partial charges (of the backbone atoms with hydrogen included), if available from the literature. ^aRef. [112]. ^bRef. [113]. ^cRef. [114].

A comparison of the segmental charge distributions given in Table V-4 leads to the following conclusions: (i) The highest *HG* charge is reported for the trimethylammonium surfactant, whereas charges on the the pyridinium and imidazolium *HG* are somewhat lower, but on average equal to each other. (ii) Contrary, the α-methylene charge of the

trimethylammonium cation is significantly lower than the corresponding values of the pyridinium and the imidazolium molecules, respectively. However, nearly no difference exists between the charges of the α-methylenes of the pyridinium und imidazolium surfactants. (iii) The charges on the alkyl tails are on average equal for the three types of surfactants. It has been shown by Huibers that the most convenient way for comparing different cationic surfactants using charge distributions is to compare the overall head group charges (*HG* plus α-methylene) [112, 113]. The latter are equal for all cationic surfactant types compared leading to the assumption that the higher adsorption/aggregation tendency of the imidazolium surfactants cannot be the direct consequence of different head group charges existing within the imidazolium amphiphiles. For this reason, the theory that the charge of the imidazolium head group is more effectively screened compared to the trimethylammonium and pyridinium cations resulting in higher surface-activity seems more likely. This thesis is further supported by the fact that the proton (H2) at the C2 position of the imidazolium ring is more acidic than the corresponding ones of the pyridinium ring, due to the presence of two heteroatoms in the former [76, 77, 78]. Consequently, the electrostatic attraction of the H2 and the chloride counterion should be higher leading to very efficient charge screening, and thus, to a higher surface-activity of the imidazolium amphiphile. Such a favourable contribution of hydrogen-bonding between an acidic proton of the surfactant head group and the counterion to amphiphile aggregation/adsorption was already reported in the literature [115]. Additionally, this explanation is in agreement to the assumption given by El Seoud et al. for imidazolium surfactants [16].

Surface excess concentrations, Γ_{max}, and minimum areas per surfactant molecule at the solution/air interface, A_{min}, were calculated according to the Gibbs adsorption theory (Chapter II.2.2.1)[g]. The obtained values are shown in Table V-3. Γ_{max} is a useful measure of the effectiveness of adsorption of the surfactant liquid/air interface, since it is the maximum value that adsorption can attain. The values of Γ_{max} observed

---

[g] *The activity coefficients have not been applied for the calculations. Nevertheless, at low concentrations, $c \leq 10^{-2}$ mol L^{-1}, activity coefficients can be considered to be one as a good approximation [5].*

for the SLILs increase linearly (R = 0.998) from 2.13×10^{-6} mol/m^2 to 2.55×10^{-6} mol/m^2 with increasing chain-length. This corresponds to a lowering of the area per molecule at the interface from 0.78 nm^2 to 0.65 nm^2. Such a decrease can be related to a closer packing of the amphiphile molecules at the interface as the alkyl-chain increases [5]. Interestingly, all A_{min} values presented here are higher than the corresponding values published by El Seoud et al. It is assumed that the values obtained in the framework of this thesis are more accurate, because the underlying surface tension isotherms consist of much more data points in the vicinity of the *cac* compared to the isotherms presented by El Seoud et al. The determination of the exact slope of the surface tension isotherm near the *cac* is an important feature for the successful extraction of A_{min} by the Gibbs equation. A comparison between A_{min} of the C$_n$mimCls with A_{min} of conventional sur-factants incorporating ammonium and pyridinium head groups is not easy because of inconsistent data extracted from the literature (cp. Table V-3). However, one gets the impression that the imidazolium SLILs under consideration occupy on average some-what more space at the liquid/gas interface than the respective conventional amphi-philes. Probably, this observation is the consequence of a more unfavourable packing of the SLILs at the interface induced by the bulky asymmetric imidazolium head group [1, 3, 5].

The transfer of a surfactant from the bulk solution to the interface contributes to the free energy change upon adsorption ΔG^0_{ads}, which can be split into three different contributions resulting from the structural segments of an ionic surfactant. These contri-butions arise from the terminal –CH$_3$ group of the hydrophobic chain $\Delta G^0_{ads}(-CH_3)$, the methylene groups of the carbon chain $m \times \Delta G^0_{ads}(-CH_2-)$, and the head group $\Delta G^0_{ads}(HG)$. The free energy changes of the different contributions as well as of the overall free energy change upon adsorption are presented in Table V-3. ΔG^0_{ads} decreases linearly (R = -0.997) from -32.9 kJ/mol to -37.3 kJ/mol with elongation of the hydro-phobic alkyl-chain of the C$_n$mimCls, which is in line with the increasing hydrophobic-ity. The calculated values are slightly higher than those achieved by El Seoud et al. All achieved ΔG^0_{ads} quantities are significantly lower than those values of the alkyl-trimethylammonium and alkylpyridinium chlorides, respectively. Therefore, the adsorp-

tion tendency of the $C_n$mimCl surfactants at the liquid/gas interface is the highest one among these three amphiphile classes.

1.3 Conductivity

1.3.1 Small volume cells: *cac, α_{mic}, ΔG^0_{mic} , ΔH^0_{mic} , ΔS^0_{mic}*

The estimated molar dependence of specific conductivity for C_{12}mimCl, C_{14}mimCl and C_{16}mimCl solutions at four temperatures (15°C, 20°C, 25°C, and 35°C) are given in Table V-5 and are graphically displayed in Figure V-4. It can be observed that for all SLILs sharp break points at each measured temperature appear in the κ-c-plot. The conductance isotherms are well described by two linear portions with two different slopes, which occur when the nature of the charge carrier changes, e.g. from surfactant monomers to self-assembled aggregates. For this reason, the break-points are associated to the *cac*s of each system. Additionally, a second distinct break at higher concentrations was found for the C_{16}mimCl/water-system at all investigated temperatures, possibly, a further change of the aggregate nature with increasing SLIL concentration (cp. Figure V-4, C_{16}mimCl, inset). The *cac*s were located by fitting Eq. (IV-11) to the experimental data following the procedure of Carpena et al. [43]. All obtained critical aggregation concentrations are summarized in Table V-5. The transition concentrations of the C_{16}mimCl were determined from the concentrations where the fits deviate from the experimental curve. The transition concentrations were achieved at 2.08×10^{-2} mol L^{-1}, 2.08×10^{-2} mol L^{-1}, 2.17×10^{-2} mol L^{-1}, and 2.31×10^{-2} mol/L for the temperatures 15°C, 20°C, 25°C, and 35°C, respectively. The *cac* results at 25°C agree nicely with the corresponding values obtained from the already presented surface tension measurements (cp. Table V-3). The small differences can be attributed to the dependence of the *cac* on the technique employed for its determination [51]. It is obvious that the *cac* values of each SLIL reach a minimum at about room-temperature. This is the same trend as already reported in literature for conventional ionic surfactants [5].
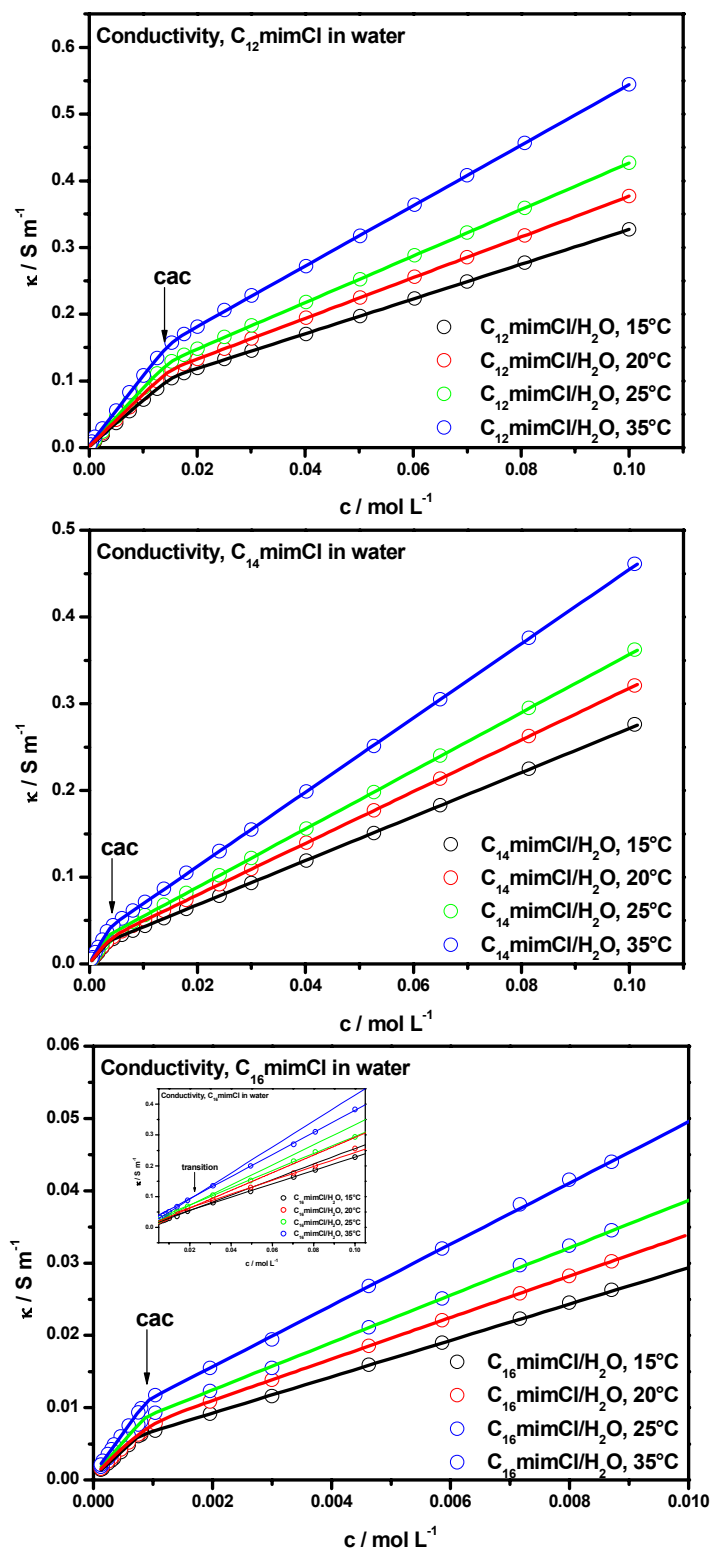
Figure V-4 : Conductivity isotherms for $C_n$mimCl SILSs (n = 12, 14, 16) at 15°C, 20°C, 25°C, and 35°C, respectively. The *cacs* are indicated for each system by an arrow. The solid lines represent fits to the data using the expression of Carpena et al. [43]. For C_{16}mimCl, the inset shows an additional break of the κ-c-plot indicating a further transition.

Surfactant	cac				α_{mic}				$-\Delta G^0_{mic}$ / kJ mol^{-1}				ΔH^0_{mic} / kJ mol^{-1}				ΔS^0_{mic} / kJ mol^{-1} K^{-1}			
	15°C	20°C	25°C	35°C	15°C	20°C	25°C	35°C	15°C	20°C	25°C	35°C	15°C	20°C	25°C	35°C	15°C	20°C	25°C	35°C
C$_{12}$mimCl	14.94[a]	14.61[a]	14.46[a]	14.76[a]	0.374[a]	0.390[a]	0.399[a]	0.433[a]	32.01[a]	32.34[a]	31.65[a]	30.90[a]	5.22[a]	2.86[a]	0.52[a]	-5.09[a]	0.129[a]	0.120[a]	0.108[a]	0.084[a]
	-	-	13.47[b]	-	-	-	0.230[b]	-	-	-	36.51[b]	-	-	-	-	-	-	-	-	-
C$_{14}$mimCl	3.58[a]	3.54[a]	3.54[a]	3.61[a]	0.347[a]	0.359[a]	0.368[a]	0.382[a]	38.20[a]	37.97[a]	37.77[a]	37.38[a]	2.32[a]	1.43[a]	-0.51[a]	-3.82[a]	0.141[a]	0.134[a]	0.125[a]	0.109[a]
	-	-	3.68[b]	-	-	-	0.200[a]	-	-	-	42.91[b]	-	-	-	-	-	-	-	-	-
C$_{16}$mimCl	0.88[a]	0.87[a]	0.87[a]	0.89[a]	0.338[a]	0.345[a]	0.350[a]	0.370[a]	44.01[a]	43.86[a]	43.73[a]	43.13[a]	1.78[a]	0.01[a]	-0.60[a]	-3.38[a]	0.160[a]	0.150[a]	0.145[a]	0.129[a]
	-	-	0.86[b]	-	-	-	0.190[b]	-	-	-	49.68[b]	-	-	-	-	-	-	-	-	-
C$_{12}$mimBr	10.10[c]	9.60[c]	9.53[c]	10.40[c]	0.230[c]	0.230[c]	0.240[c]	0.260[c]	36.85[c]	37.36	37.87[c]	38.38[c]	7.50[c]	-4.37[c]	-15.03[c]	-35.84[c]	0.152[c]	0.112[c]	0.076[c]	0.008[c]
	-	-	9.80[d]	-	-	-	0.270[d]	-	-	-	-	-	-	-	-	-	-	-	-	-
C$_{14}$mimBr	2.65[c]	2.63[c]	2.61[c]	2.80[c]	0.210[c]	0.220[c]	0.220[c]	0.240[c]	42.44[c]	43.45[c]	43.96[c]	44.47[c]	0.71[c]	-6.90[c]	-14.52[c]	-28.22[c]	0.151[c]	0.124	0.100[c]	0.054[c]
	-	-	2.50[d]	-	-	-	0.240[d]	-	-	-	-	-	-	-	-	-	-	-	-	-
C$_{16}$mimBr	-	0.65[c]	0.65[c]	0.72[c]	-	0.220[c]	0.230[c]	0.240[c]	-	49.04[c]	49.54[c]	50.56[c]	-	11.88[c]	-7.92[c]	-45.99[c]	-	0.209[c]	0.139[c]	0.013[c]
	-	-	0.61[d]	-	-	-	0.300[d]	-	-	-	-	-	-	-	-	-	-	-	-	-
C$_{12}$TACl	23.60[e]	22.60[e]	22.20[e]	21.90[e]	0.398[e]	0.417[e]	0.424[e]	0.451[e]	25.99[e]	26.93[e]	27.64[e]	29.14[e]	8.22[e]	6.17[e]	3.86[e]	-1.36[e]	0.119[e]	0.113[e]	0.106[e]	0.090[e]
C$_{14}$TACl	5.80[e]	5.68[e]	5.63[e]	5.66[e]	0.352[e]	0.362[e]	0.377[e]	0.410[e]	36.19[e]	36.66[e]	37.01[e]	37.43[e]	7.54[e]	4.83[e]	1.95[e]	-4.24[e]	0.152[e]	0.142[e]	0.131[e]	0.108[e]
C$_{16}$TACl	-	-	1.45[f]	-	-	-	0.350[f]	-	-	-	26.50[f]	-	-	-	-	-	-	-	-	-
C$_{12}$PyCl	-	17.41[g]	16.96[g]	17.36[g]	-	0.395[h]	0.491[i]	-	19.46[g]	19.78[g]	19.94[g]	20.58[g]	4.89[g]	3.77[g]	2.65[g]	-1.36[g]	0.084[g]	0.080[g]	0.076[g]	0.063[g]
C$_{14}$PyCl	4.52[j]	4.37[j]	4.34[j]	4.56[j]	0.343[j]	0.359[j]	0.378[j]	0.410[j]	37.38[j]	37.76[j]	38.04[j]	38.35[j]	-13.95[j]	-18.71[j]	-23.69[j]	-34.11[j]	0.081[j]	0.064[j]	0.048[j]	0.014[j]
C$_{16}$PyCl	-	-	0.99[k]	-	-	-	0.380[k]	-	-	-	27.08[k]	-	-	-	-	-	-	-	-	-

Table V-5 : Conductivity results for the investigated C$_n$mimCl SLILs including *cac*, degree of dissociation α_{mic}, and the thermodynamic parameters (ΔG^0_{mic}, ΔH^0_{mic}, ΔS^0_{mic}) for various temperatures. Available literature data of conventional surfactants and the recently published data of El Seoud et al (C$_n$mimCl), Inoue et al. (C$_n$mimBr), and Vanyúr et al. (C$_n$mimBr) are presented for comparison. [a]This work; *cac* / mmol L^{-1}; α_{mic} was estimated by Frahms method. [b]Ref. [16]; *cac* / mol L^{-1}; α_{mic} was estimated by Evans method. [c]Ref. [18]; α_{mic} was estimated by the mixed electrolyte model; thermodynamic parameters were extracted from plots. [d]Ref. [12]; *cac* /mmol L^{-1}; α_{mic} was estimated by Frahms method. [e]Ref. [44]; *cac* / mmol kg^{-1}; α_{mic} was estimated by Frahms method. [f]Ref. [45], *cac* / mmol L^{-1}. [g]Ref. [46], *cac* / mmol kg^{-1}; thermodynamic parameters were extracted from graphs; no α_{mic} was taken into account for the calculation of the thermodynamic parameters. [h]Ref. [47], *cac* / mmol L^{-1}. [i]Ref. [48]. [j]Ref. [49]; *cac* / mmol L^{-1}; α_{mic} was estimated by Frahms method; thermodynamic parameters were extracted from graphs. [k]Ref. [50], *cac* / mmol L^{-1}.

Further, the transition concentration of C_{16}mimCl at 25°C nearly equals the value of 2.3×10^{-2} mol L^{-1}, which was previously determined from the second minimum observed in the surface tension isotherm and was associated to a further reorientation process of the surfactant monomers at the surface. The latter seems to involve also a structural change of the charge carriers in solution, e.g. growth and/or shape change of the formed micellar aggregates at higher C_{16}mimCl concentration. This is consistent with the results of other investigators, who showed by conductivity measurements that aggregates of cationic surfactants undergo a substantial growth at higher amphiphile concentrations or salt addition [48, 52, 53]. The transition interval dx obtained from Eq. (IV-11) describes the width of the transition of an amphiphile from its monomeric form to the aggregated form. It increases slightly for each SLIL with raising temperature, e.g. for the C_{12}mimCl from 1.13 mmol L^{-1} at 15°C to 1.14 mmol L^{-1} at 35°C. Additionally, dx decreases at a constant temperature as the alkyl-chain of the SLILs becomes longer, which is the consequence of increasing hydrophilicity of the systems. At 25°C, dx was calculated as 1.14 mmol L^{-1}, 2.80×10^{-1} mmol L^{-1}, and 4.11×10^{-2} mmol L^{-1} for C_{12}mimCl, C_{14}mimCl, and C_{16}mimCl, respectively. All dx compared to the respective *cac*s indicate small size distributions of the micellar aggregates.

At each temperature, the observed *cac*s of the imidazolium homologues decrease linearly (R = 0.999) according to the Klevens rule. The Klevens constants do not change considerably as the temperature increases. Average values of 1.85 and 0.31 were estimated for A and B, respectively. These quantities are slightly higher than the parameters calculated from the surface tension isotherms, but in the dimension expected for cationic surfactants [32].

From the slopes below and above the *cac*, the degrees of counterion dissociation of the micellar aggregates α_{mic} were determined according to Frahm et al. for each SLIL and temperature (cp. Table V-5) [54]. The change of specific conductance with molarity near the *cac* changes less at higher temperatures in the case of all SLILs which indicates that aggregates with a higher surface charge and/or a lower aggregation number are formed at higher concentrations. Whereas α_{mic} increases with temperature for all sys-

tem measured, it decreases considerably with increasing alkyl-chain length (cp. Figure V-5).
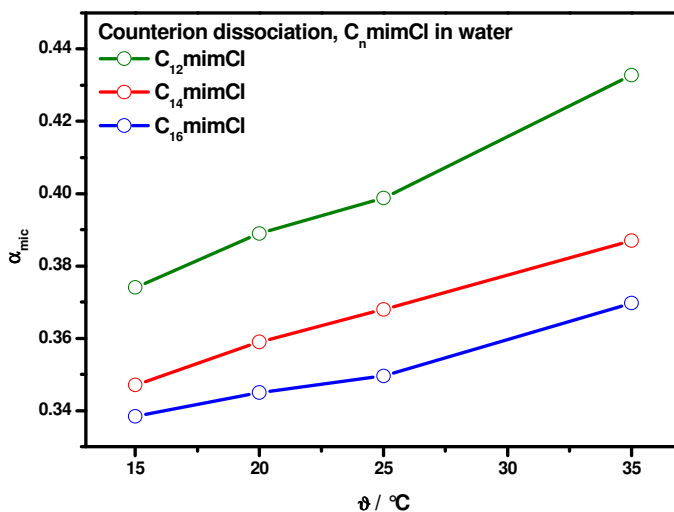
Figure V-5 : Temperature dependence of the degree of counterion dissociation α_{mic} of the micellar aggregates for the investigated aqueous $C_n$mimCl-systems.

For example, values of $\alpha_{mic}^{25°C} = 0.399$, $\alpha_{mic}^{25°C} = 0.368$, and $\alpha_{mic}^{25°C} = 0.350$ for C_{12}mimCl, C_{14}mimCl, and C_{16}mimCl, respectively, were found at 25°C. This means that the counterion is easier to bind with the aggregates as the alkyl-chain of the SLIL homologues becomes longer and/or the temperature decreases. This observation is in accordance to conclusions drawn for conventional cationic surfactants [5, 55].

The *cac* of an amphiphile is connected to the stability of its aggregated form relative to its monomeric form and therefore it is a measure of its tendency, to form self-assembled structures in solution. The latter is related according to the mass-action model to the standard Gibbs free energy of micellization ΔG_{mic}^{0}. With the knowledge of the temperature dependence of the *cac* and α_{mic} it is accessorily possible to calculate the standard enthalpies of micelle formation ΔH_{mic}^{0} and the standard entropies of micelle formation ΔS_{mic}^{0}. In Figure V-6 the temperature dependence of the critical aggregation concentration is shown for the investigated SLILs, where $ln\,X_{cac}$ represents the *cac* in the mole fraction scale, which is given by the ratio of the *cac* and the concentration of the solvent, water in this case (55.403 mol L^{-1}).
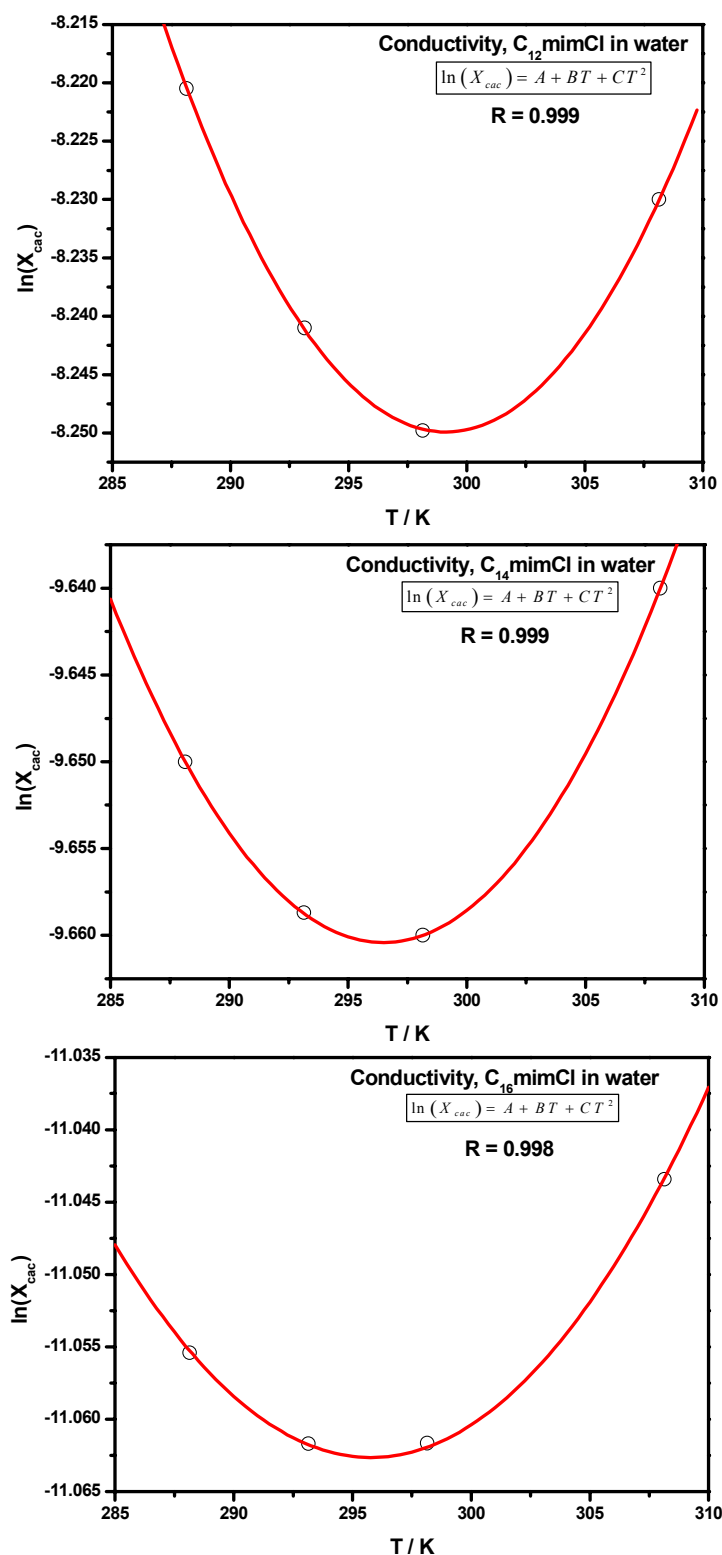
Figure V-6 : Temperature dependence of the *cac*s expressed in mole fractions X_{cac} scale for the $C_n$mimCl homologues. The red curves indicate a second-degree polynomial function fitted to the data.

The classical U-shaped curve, characteristic of the dependence of *cac* with temperature, can be observed in this representation. The increase of the alkyl-chin length shifts the minimum towards lower temperature because of the enhancement of the hydrophobicity of the system [46, 56-58].

The effect of temperature on the *cac* of amphiphiles in aqueous solution can be analyzed in terms of two opposing forces. As the temperature increases, the hydration of the hydrophilic head group decreases favouring monomer self-assembly. However, an increasing temperature also results in disruption of the water structure around the hydrophobic part of the surfactant molecule, which is unfavourable to self-assembly. Consequently, the *cac* decreases as the head group is dehydrated and then increases as the water structure breaks around the hydrophobic portion if the amphiphile [58]. It is evident from the results that in the case of the SLILs under investigation, the first effect seems to dominate at low temperatures, whereas at higher temperature the second effect begins to control the aggregation.

Values of ΔG^0_{mic}, ΔH^0_{mic} and ΔS^0_{mic} for all $C_n$mimCl-systems have been estimated by Eq. (II-43), Eq. (II-48), and Eq. (II-49), respectively. For the calculation of ΔH^0_{mic}, additionally the value of $(\partial ln\, X_{cac} / \partial T)$ has to be known. This parameter was obtained by fitting a second order polynomial function to the temperature dependence of the *cac* followed by the calculation of the slope at each *cac* by the first derivative. The calculated quantities are given in Table V-5 and are graphically presented in Figure V-7. As can be seen, the standard free energy of micellization shows moderate temperature dependence for all SLILs, whereas longer alkyl-chains result in considerably more negative values of ΔG^0_{mic}, -31.65 kJ/mol, -37.77 kJ/mol, and -43.74 kJ/mol for C_{12}mimCl, C_{14}mimCl, and C_{16}mimCl at 25°C, respectively. In contrast, ΔH^0_{mic} and ΔS^0_{mic} show stronger temperature dependence for all systems investigated. The parameter ΔS^0_{mic} is always positive, increases with the SLIL chain-length and strongly decreases with increasing temperature leading to a decrease of the entropic term $(-T\Delta S^0_{mic})$ with raising temperature. On the other hand, ΔH^0_{mic} decreases with increase in temperature, and changes its sign from positive to negative near room-temperature.
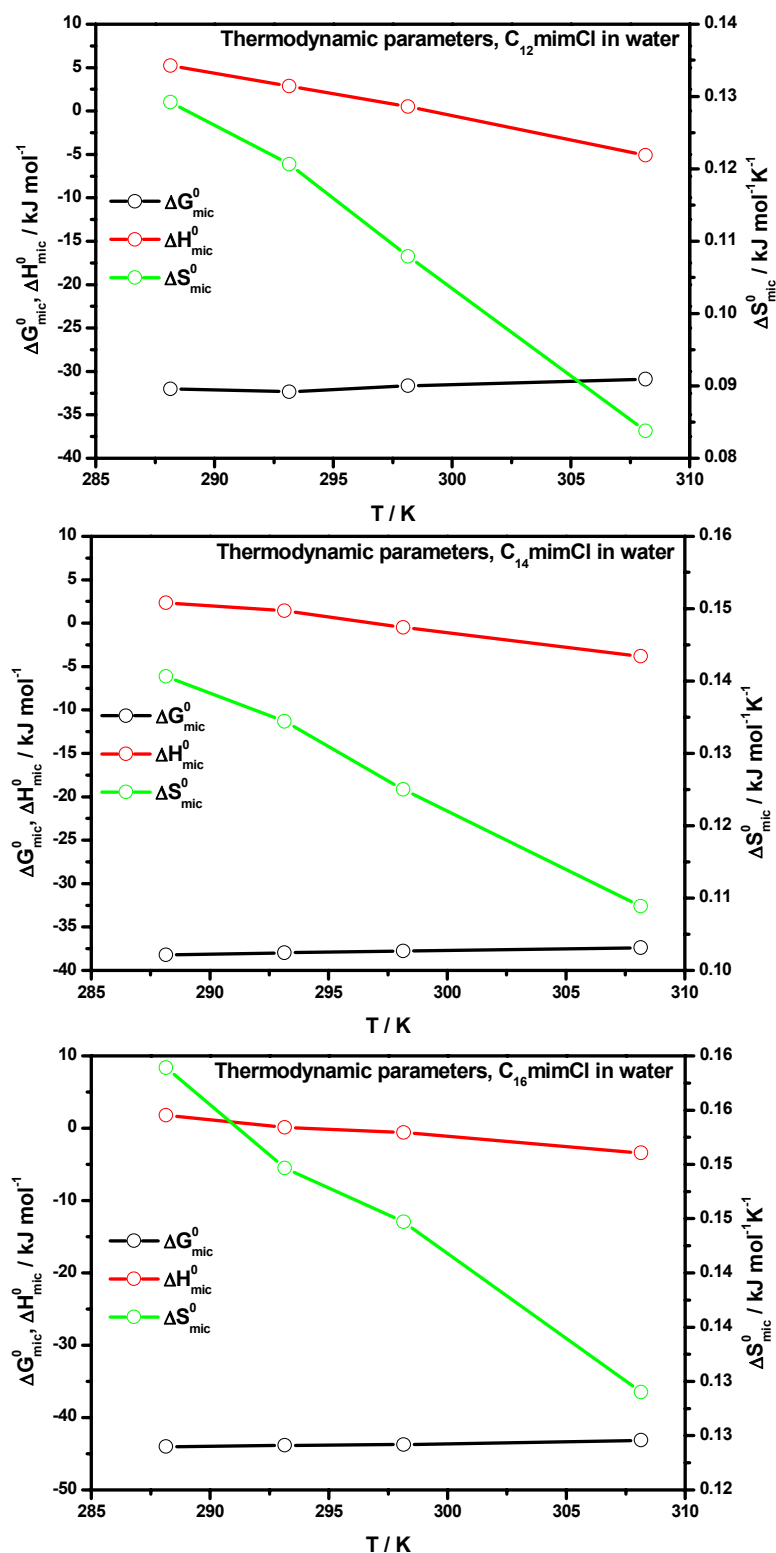
Figure V-7 : Thermodynamic parameters of aqueous $C_n$mimCl solutions including ΔG_{mic}^0, ΔH_{mic}^0, and ΔS_{mic}^0 obtained from temperature dependent conductivity measurements.

Consequently, the micelle formation of the $C_n$mimCl series is an endothermic entropy-driven process at low temperature and an exothermic enthalpy-driven process at high temperature. Such behaviour is well known for conventional surfactants [1, 5]. The enthalpy-entropy relation of surfactant aggregation can be quantified in the so-called enthalpy-entropy compensation plot. Figure V-8 gives the compensation plots for the measured $C_n$mimCl homologues. The plots are linear, almost parallel, and shifted towards higher entropy values for the homologous SLILs (within the investigated temperature range). The same behaviour has already been reported for conventional ionic surfactants [58-61].
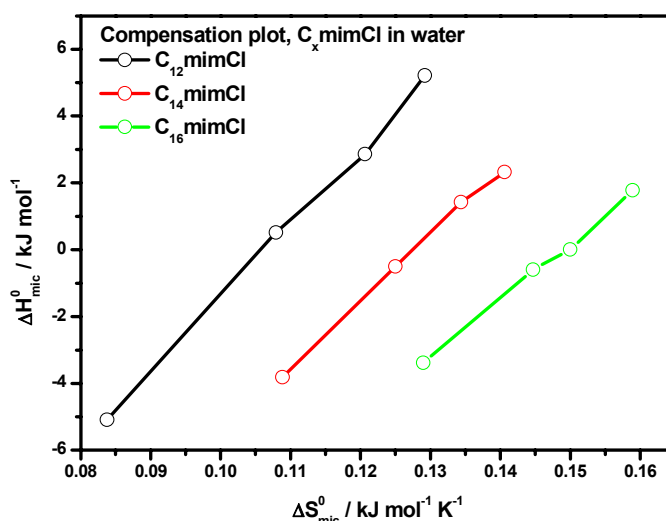
Figure V-8 : Enthalpy-entropy compensation plot of the $C_n$mimCl SLIL homologues.

For the $C_n$mimCl series, the transfers of a –CH_2– group from water to the micelles were calculated to -3.00 kJ mol^{-1} (R=0.999), -2.88 kJ mol^{-1} (R=0.998), -3.02kJ mol^{-1} (R=0.999), and -3.06 kJ mol^{-1} (R=0.999) for 15°C, 20°C, 25°C, and 35°C, respectively. These results are in good agreement to -3.10 kJ mol^{-1} reported by El Seoud et al. at 25°C and also similar to that of ΔG_{trans}^{0} of –CH_2– groups of alkanes from water to bulk hydrocarbons, -0.56 kJ mol^{-1} [16].

The comparison of the *cac*, α_{mic}, and the thermodynamic parameters of the $C_n$mimCl series with literature values of conventional cationic surfactants leads to the

following conclusions (cp. Table V-5). As already confirmed in the surface tension measurements, the *cac*s of the surface-active imidazolium chloride homologues are significantly lower than those values of the respective alkyltrimethylammonium and alkylpyridinium chlorides. As for the *cac*s, the values obtained for ΔG^0_{mic} differ noteworthy from the corresponding quantities of common cationic surfactants. They were found to be more negative indicating that micellization is somewhat more favourable for the surfactants with an imidazolium head group than for surfactants with ammonium and pyridinium head groups, respectively. The same trend can be found for ΔH^0_{mic}. Even though the presented values of ΔH^0_{mic} have some uncertainty because of the low number of data points available for the temperature dependence of the *cac,* the available data at least allow relative comparisons of the SLILs in regard to their micellization enthalpies, and it seems that ΔH^0_{mic} is considerably smaller for the imidazolium surfactants. Since the process of aggregate formation results mainly from the destruction of the water structure around the hydrocarbon tail of surfactant molecules, and, additionally, from the dehydration of the polar part and its electrostatic interaction due to aggregation, the lower ΔH^0_{mic} is a consequence of the lower heat required to pass the electrostatic repulsion between the head groups. Therefore, a lower value of ΔH^0_{mic} of an amphiphile in comparison to another with the same anion reflects a lower electrostatic repulsion between the head groups, the energy required to overpass the repulsion is lower, and the process is more exothermic. The latter is also confirmed by the degree of counter ion dissociations found for the $C_n$mimCl homologues that are lower compared to the respective ammonium and pyridinium salts. The self-assembly of ionic amphiphile consisting of weakly hydrated ions is generally more favourable, since the charge repulsion between the head groups is decreased more than in the case of heavily hydrated ions. In total, the chloride anions are highly hydrated species leading to a partially screening of their charge by the surrounding tightly bound water molecules and thus chloride is less effective in reducing the charge repulsion of surfactant head groups. Nevertheless, lower α_{mic} values observed for chloride surfactants incorporating the imidazolium head group with respect to their conventional analogues support the idea of basically low electrostatic repulsion between the imidazolium heads as a consequence of effective *HG*

charge screening, resulting in a stronger aggregation tendency of the SLILs in aqueous solution. The latter result is also in very good agreement to the assumption already presented in the previous Chapter that hydrogen-bonding between the imidazolium *HG* and the chloride counterion, which is not actually happening in the case of the trimethyl-ammonium based surfactants and to a lesser extent occurring in the case of pyridinium surfactants, supports charge screening by the counterions and favours self-assembly due to the reduction of hindering electrostatic repulsions between the *HG*s.

Basically, the same conclusions were drawn in the recently published papers of Inoue et al. and Vanyúr et al., who performed conductance studies on $C_n$mimBr homologues in aqueous solution and proposed also a somewhat more superior aggregation tendency for the $C_n$mimBr SLILs compared to their conventional counterparts [12, 18, 62]. Their results are also included to Table V-5 for comparison and complement well the conclusions of the underlying work. As can be seen, the *cac* and α_{mic} values of the two workgroups are always lower than the data presented here for the chloride salts. This is expected, since the bromide, a weaker hydrated counterion than the chloride, screens the head group charge more effectively resulting in a higher aggregation tendency of the $C_n$mimBr series reflected by the lower *cac* and α_{mic}, respectively. The values of ΔG^0_{mic} and ΔH^0_{mic} given by Inoue et al. for the SLIL bromides are lower than those of the $C_n$mimCl analogues, which is again in agreement with the theory considering the lower hydration of the bromide ion [1, 3, 5].

Interestingly, the values of ΔG^0_{mic} reported by El Seoud et al. (cp. Table V-5) for C_{12}mimCl, C_{14}mimCl, and C_{16}mimCl at 25°C are remarkably lower (between 12 and 15 %) than the achieved values within the framework of this study. Since the *cac*s of the two works are in the same order of magnitude, the reason for this discrepancy is that El Seoud et al. did not estimate α_{mic} by Frahm's method using the S_2/S_1 ratio for the calculation of ΔG^0_{mic}. The authors obtained α_{mic} by the method of Evans et al. taking also the aggregation number of the micellar aggregates above the *cac* into account. N_{agg} has been achieved previously from fluorescence measurements by his workgroup. It has been reported that α_{mic} calculated by Evans method is generally a little bit lower [63].

Therefore, the observed values of ΔG^0_{mic} will be higher. Noteworthy is the fact that El Seoud et al. reported lower α_{mic} values than Inoue et al., who estimated the degree of counter ion binding β_{mic} ($\equiv 1 - \alpha_{mic}$) for the respective $C_n$mimBr series at 25°C by conductivity measurements and application of the mixed electrolyte model (MEM) for micellar solutions which also considers N_{agg} (cp. Chapter IV.3.2.2). Further it has been pointed out that β_{mic} values (and thus α_{mic}) derived from the MEM method are consistent with those obtained by other methods such as electrophoretic mobilities [64]. Consequently, the quantities of β_{mic} or rather α_{mic} estimated by the two workgroups should be consistent with each other, which is actually not the case. Normally, as already pointed out, an amphiphile with bromide a counterion shows a lower α_{mic} value than its corresponding chloride analogue, because of the different screening properties of the two types of counterions [3, 5, 6, 45, 49, 65, 66]. Additionally, the α_{mic} results for C_{12}mimBr, C_{14}mimBr, and C_{16}mimBr of Inoue et al. at 25°C was confirmed by the paper of Vanyúr et al. [12]. Therefore, it must be assumed that the counterion dissociation parameters published by El Seoud et al. are too low. In contrast, the here presented degrees of counterion dissociation seem more consistent with the work of Inoue et al. and Vanyúr et al., respectively. This assumption is also confirmed by the recent paper of Bales and Zana who have collected values of α_{mic} of dodecyltrimethylammonium bromide and chloride from the literature along with their own results [66].

1.3.2   Dilution cells: MEM & IcCM

In order to proof the consistency of the obtained results and to get further information about the aggregation behaviour, additional conductivity measurements of the three $C_n$mimCl salts were performed at 25°C with the intension to apply the mixed electrolyte model (MEM). As already pointed out previously, the application of the MEM to the conductance data of an amphiphile gives information about the micellization parameters, such as aggregation number N_{agg} and the degree of counterion binding β_{mic} [64]. Additionally, electrochemical results, e.g. limiting equivalent conductivities of the surfactant monomers, counterions and micelles can be obtained (cp. Chapter IV.3.2.2).
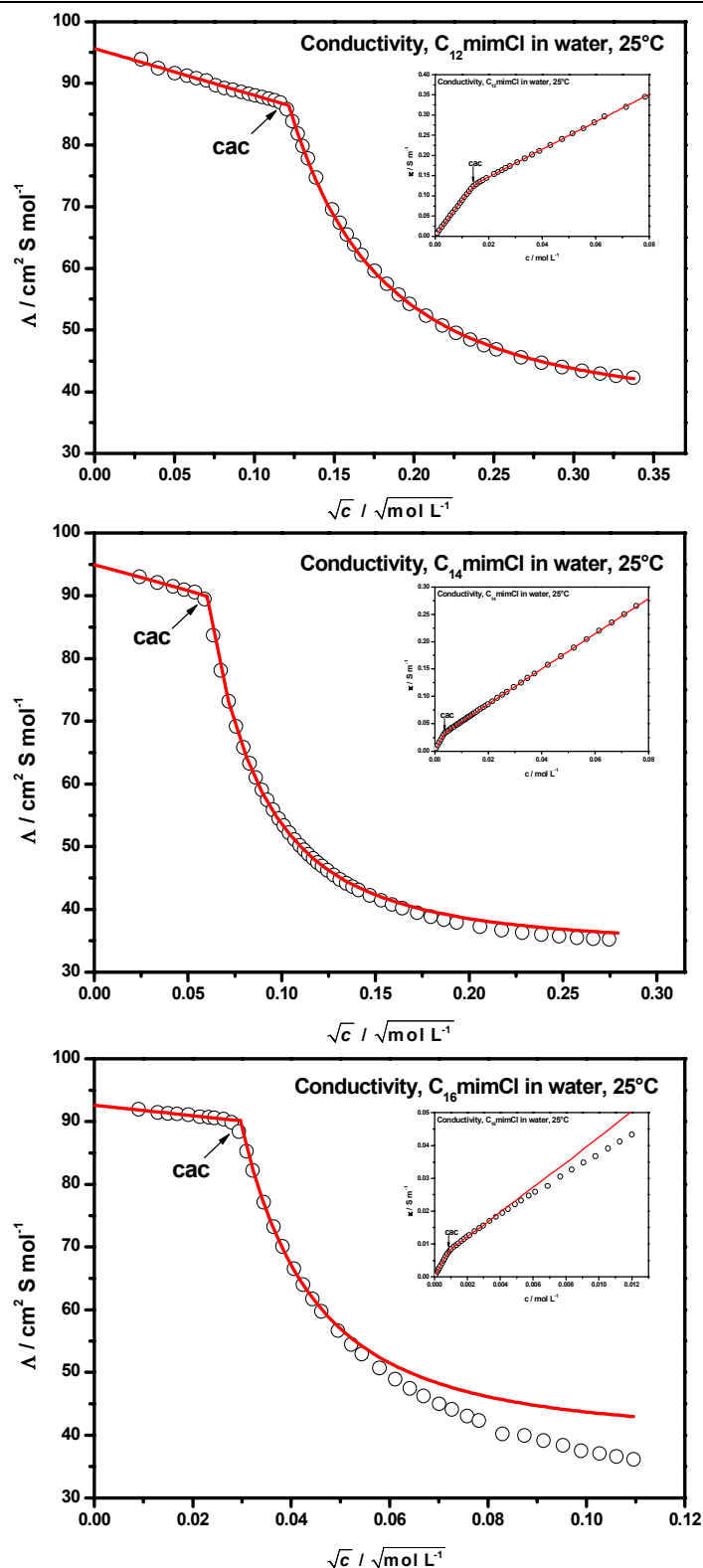
Figure V-9 : The conductivity isotherms for the C$_n$mimCl homologues measured at 25°C with the modelled MEM curves according to the mixed electrolyte model (red lines). The insets represent the plots of the *cac* determination according to Carpena et al.

However, the successful application of this model, which is based on the Onsager theory for electrical conductance, requires very accurate conductance data below the *cac*, since it assumes that the knowledge of the equivalent conductivity of the amphiphile in its monomeric form at infinite dilution is known. As the small volume cells, which were used for the former conductance investigations, were not able to provide this accuracy at very low concentrations, a dilution conductance cell was applied that allows precise conductivity measurements also at very low concentrations [67, 68]. The $\kappa - c$ –plots measured for the $C_n$mimCl homologues in the dilution cells at 25°C are presented in Figure V-9 (insets). The *cac*s were estimated for each system according to the procedure of Carpena et al., which gave values of 14.54 mol L^{-1}, 3.55 mol L^{-1}, and 0.89 mol L^{-1} for C_{12}mimCl, C_{14}mimCl, and C_{16}mimCl, respectively (Figure V-9, insets) [43]. These quantities are in very good agreement to the previous experiments (cp. Table V-3 for surface tension and Table V-5 for conductivity). The ratio of the post-micellar region to that in the pre-micellar region (S_2/S_1) was related to the degree of counterion dissociation according to Frahm et al. [54]. All α_{mic} agree satisfactorily with those extracted from the previous conductivity measurements at 25°C using the small volume cells. The *cac* and α_{mic} are given in Table V-6. N_{agg} and β_{mic} were obtained to provide a best model curve to the experimental equivalent conductivity by minimizing the deviation from the calculated Λ from the experimental ones. With other words, the model parameters N_{agg} and β_{mic} were varied until the value of χ^2 reached a minimum value [69]. As basis for the modelling, the already determined *cac*s, α_{mic} (β_{mic}), and the equivalent conductivity of the surfactant at infinite solution Λ_1^0, which was determined previously from the $\Lambda - \sqrt{c}$ –plot by extrapolation to zero concentration, were used following the procedure presented in Chapter IV.3.2.2. All calculated quantities of the investigated systems are summarized in Table V-6. For the C_{12}mimCl, the modelled curve agree very well with the experimental data over the whole concentration range measured, as can be seen in Figure V-9 (top). The value of β_{mic} (and thus α_{mic}) nearly equals that obtained previously from Frahm's method. As the MEM takes the contribution of micellar aggregates to the conductivity into account, whereas Frahm's method does not, one may assume that in the present case, the macroions do not contribute a lot to the

conductivity and consequently, the S_2/S_1 ratio obtained from $\kappa - c$ –plot describes the counterion ion dissociation satisfactorily for C_{12}mimCl in the studied concentration range. This is also confirmed by the very low values for the equivalent conductivity of the formed aggregates λ_m^0. Further, one can infer that counterion binding (or counterion dissociation) does not change with C_{12}mimCl concentration and that if average aggregation number changes with concentration, the change is too small to be detected by conductometry [64]. The aggregation number of the C_{12}mimCl turned out to be 41. This value is on average smaller than those quantities of the respective C_{12}TACl and C_{12}PyCl analogues found in literature (cp. Table V-6). Probably, a different packing efficiency of the planar imidazolium head groups within the formed aggregates could be responsible for this observation, which was also proposed by El Seoud [16]. In contrast to the conductance data of the C_{12}mimCl system, which could be described very well by the mixed electrolyte model over the whole concentration range studied (up to 0.1 mol L^{-1}), the complete modelling of the conductivity isotherms up to 0.1 mol L^{-1} failed for C_{14}mimCl and C_{16}mimCl, respectively. Additionally, the conductivity isotherm of the C_{16}mimCl differs noteworthy from that received during the former conductivity experiment. Again, the $\kappa - c$ –plot of C_{16}mimCl (Figure V-9, bottom, inset) exhibits a pronounced breakpoint indicating the *cac*, however a significant deviation from linearity appears immediately after the *cac*, which was visible in the first experiment not till higher concentrations. This observation mostly results from the higher resolution of the present conductivity measurements because of the increased number of data points and the higher accuracy of the dilution cell. The $\kappa - c$ –plot of C_{14}mimCl is similar to that obtained from the measurement performed previously in the small volume cells (Figure V-9, middle, inset). However, it has been found during the data modelling of the conductance data by the MEM that a slight deviation at higher SLIL concentration from "ideality" occurs, which can be hardly seen in the $\kappa - c$ –plot. Since the conductance reflects the nature of the present charge carriers, the observed deviation must be attributed to an evolution of the C_{14}mimCl and C_{16}mimCl aggregates, respectively. Consequently, a growth of the micelles, which is equal to a change in N_{agg}, and/or a change of β_{mic}, at higher SLIL concentration is supposable.

Surfactant	cac $mmol\ L^{-1}$	β_{mic}	α_{mic}	N_{agg}	Λ_I^0	λ_I^0	λ_{Cl^-/Br^-}^0	Λ_m^0	λ_m^0	r_I	r_{Cl^-}	r_m	A_1	A_m
					$cm^2\ S\ mol^{-1}$					nm	nm	nm		
C$_{12}$mimCl	14.54[a]	0.609[a], 0.596[a]	0.391[a], 0.404[a], 0.170[a]	41[a]	95.65[a]	19.33[a]	76.32*	81.93[a]	5.61[a]	0.477[a]	0.121[a]	1.64[a]	82.60[a]	584.36[a]
	13.47[b]	0.77[b]	0.23[b]	58[b]	-	-	-	-	-	-	-	-	-	-
C$_{14}$mimCl	3.55[a]	0.650[a], 0.635[a]	0.350[a], 0.365[a], 0.164[a]	61[a]	94.98[a]	18.66[a]	76.32*	82.45[a]	5.33[a]	0.494[a]	0.121[a]	1.94[a]	82.45[a]	758.34[a]
	3.68[b]	0.80[b]	0.20[b]	79[b]	-	-	-	-	-	-	-	-	-	-
C$_{16}$mimCl	0.89[a]	0.668[a], 0.648[a]	0.332[a], 0.352[a], 0.159[a]	95[a]	92.62[a]	16.30[a]	76.32*	80.37[a]	4.05[a]	0.565[a]	0.121[a]	2.21[a]	81.90[a]	752.45[a]
	0.86[b]	0.81[b]	0.19[b]	99[b]	-	-	-	-	-	-	-	-	-	-
C$_{12}$mimBr	9.53[c]	0.76[c]	0.24[c]	43[c]	95.3[c]	17.2[c]	78.1*	-	-	-	-	-	65.3	-
	9.80[d]	0.73[d]	0.27[d]	44[d] (0.055 M)	113.1[d]	35[d]	78.1*	-	-	-	-	-	-	-
C$_{14}$mimBr	2.61[c]	0.78[c]	0.22[c]	61[c]	97.0[c]	18.9	78.1*						82.3	
	2.50[d]	0.76[d]	0.24[d]	59[d] (0.025 M)	111.1[d]	33[d]	78.1*	-	-	-	-	-	-	-
C$_{16}$mimBr	0.65[c]	0.77[c]	0.23[c]	76[c]	93.0[c]	14.9[c]	78.1*	-	-	-	-	-	87.6	-
	0.61[d]	0.70[d]	0.30[d]	66[d] (0.01 M)	110.1[d]	32[d]	78.1*	-	-	-	-	-	-	-
C$_{12}$TACl	-	-	-	60-67[e]	-	-	-	-	-	-	-	-	-	-
C$_{14}$TACl	-	-	-	62[f]	-	-	-	-	-	-	-	-	-	-
C$_{16}$TACl	-	-	-	94-110[g], 90-120[e]	-	-	-	-	-	-	-	-	-	-
C$_{12}$PyCl	15.6[h]	0.62[h], 0.73[i]	0.38[h], 0.27[i]	25[h], 52[i]	103.97[h]	27.62[h]	76.35*	-	-	-	-	-	-	-
C$_{14}$PyCl	-	0.77[i]	0.23[i]	70[i]	-	-	-	-	-	-	-	-	-	-
C$_{16}$PyCl	-	0.80[i]	0.20[i]	87[i]	-	-	-	-	-	-	-	-	-	-

Table V-6 : Results of the mixed electrolyte model (MEM) for the investigated SLILs at 25°C. Presented are the *cac*, degree of counterion binding β_{mic}, degree of counterion dissociation α_{mic}, aggregation number N_{agg}, equivalent and limiting equivalent conductivities at infinite dilution of the present species (Λ_I^0, Λ_m^0, λ_I^0, $\lambda_{Cl^-}^0$, λ_m^0), and the constants A_1, A_m. Also, meaningful literature data of conventional surfactants and the recently published quantities for the C$_n$mimCl and C$_n$mimBr analogues are given. [a]This work, *cac* was obtained by the method of Carpena et al.; the first α_{mic} (or β_{mic}) value was estimated by the Frahms method, the second from MEM, and the third from Evans method; all remaining values were estimated from MEM. [b]Ref [16]; all values were estimated from fluorescence quenching at constant SLIL concentration. [c]Ref. [18] all values were estimated from MEM; Λ_I^0 and λ_I^0 were extracted from plots. [d]Ref. [12]; all values were obtained from conductivity; N_{agg} was estimated from fluorescence quenching at constant C$_n$mimBr concentrations, which are given in parenthesis. [e]Ref. [70]; from SANS in the concentration range 0.2-0.6 M (C$_{12}$TACl) and 0.03-0.6 M (C$_{16}$TACl), respectively. [f]Ref. [52]; value was obtained from static light scattering. [g]Ref. [71]; N_{agg} was estimated from fluorescence quenching in the concentration range 21-86 mM. [h]Ref [72]; values were estimated from MEM. Ref. [73]; values were calculated from osmotic pressure and calorimetric data. *Note: Literature value of the limiting equivalent conductivity of Cl⁻ and Br⁻; quantities were taken from Ref. [74].

This is quite pronounced for the C_{16}mimCl. The successful application of the mixed electrolyte model, however, presumes spherical micelles with constant N_{agg} and unchanging β_{mic} over the whole concentration range. For this reason, the MEM was applied only near the *cac* of each system, where the aggregate structure can be assumed to be more or less constant. The modelled curves are given in Figure V-9 (middle) and Figure V-9 (bottom) for the C_{14}mimCl and C_{16}mimCl, respectively. It is evident that the model curve of the C_{14}mimCl fits the data quite well nearly over the whole concentration range examined, whereas the model fits fail already just above the *cac* for the C_{16}mimCl. The deviations of the model curves from the experimental data occur at about 1.7×10^{-2} mol L^{-1} and 2.1×10^{-3} mol L^{-1} for C_{14}mimCl and C_{16}mimCl, respectively. Accordingly, these concentrations correspond to the upper limits where the MEM model is able to describe the conductivity effectually and thus, to the boundary above which the extracted micellization parameters became unreasonable. The determined quantities of β_{mic} are somewhat, but not significantly smaller than the previous values achieved from the ratio of the post- and pre-micellar slopes. Aggregation numbers of 61 and 95 were obtained from the data range where the MEM was supposed to be applicable for C_{14}mimCl and C_{16}mimCl, respectively. Compared to the aggregation numbers found in the literature for conventional surfactants (in a comparable concentration range), the values of C_{14}mimCl and C_{16}mimCl are slightly smaller, in agreement to the result already given for the C_{12}mimCl. In fact, this affirms the existence of a different packing efficiency of the 1-alkyl-3-methyl-imidazolium chlorides within their self-assembled aggregates compared to conventional chloride amphiphiles. Additionally, the micellar radii of the $C_n$mimCl aggregates under the assumption of spherical geometry were obtained from the MEM. Values of 1.64 nm, 1.94 nm, and 2.21 nm were derived for the formed aggregates of C_{12}mimCl, C_{14}mimCl, and C_{16}mimCl, respectively. All radii are reasonable and agree satisfactorily with theoretically calculated core radii using the Tanford formula [75]. All estimated MEM parameters for both SLILs are summarized in Table V-6.

The aggregation number of C_{12}mimBr published by Inoue et al. for the C_{12}mimBr agrees very well with that value determined here for C_{12}mimCl (cp. Table

V-6) [18]. This is in line with the conclusion got for conventional surfactants, no dramatic change of the aggregation number was reported by changing the counterion from bromide to chloride [5, 66]. Interestingly, Inoue et al. was also able to model the conductance data of C_{14}mimCl and the C_{16}mimCl completely indicating no aggregate evolution of these SLILs in the investigated concentration range. However, the authors measured concentrations only up to approximately 2.25×10^{-2} mol L^{-1}, 8.10×10^{-3} mol L^{-1}, 2.5×10^{-3} mol L^{-1} for C_{12}mimBr, C_{14}mimBr, and C_{16}mimBr, respectively. In contrast, the here presented conductance data ranges up to 1.14×10^{-1} mol L^{-1}, 7.55×10^{-2} mol L^{-1}, and 1.21×10^{-2} mol L^{-1} for C_{12}mimCl, C_{14}mimCl, and C_{16}mimCl, respectively. Considering the deviation concentrations already reported for C_{14}mimCl and C_{16}mimCl, it seems likely that Inoue et al. obtained perfect agreement between the MEM and their whole experimental data, since the aggregate evolutions may occur beyond their investigated concentration ranges. Further, this conclusion is based on the fact that aggregate growth happens at higher concentrations for bromide surfactants compared to their chloride analogues, which was shown by Gonzales-Perez et al for alkylpyridinium bromides and chlorides, for example [48]. The aggregation number of C_{14}mimBr shown by Inoue et al. is the same as that value derived in this work for C_{14}mimCl. Again, this is in good agreement to the former conclusion drawn for the C_{12}mimCl. For C_{16}mimCl an aggregation number of 95 was calculated, which is considerably higher than the quantity of 76 reported by Inoue et al. This difference can be attributed to the substantial aggregate evolution considering the fact that in the present case, N_{agg} must be seen rather as an average value. Principally, the same conclusions as discussed previously concerning N_{agg} can be drawn from the reported data of Vanýur et al. who also investigated the $C_n$mimBr SLILs in aqueous solution by a combination of conductivity and fluorescence measurements [12]. Finally, it is noteworthy that Vanýur et al. give limiting molar conductivities of the imidazolium cations, 35 cm^2 S mol^{-1}, 33 cm^2 S mol^{-1}, and 32 cm^2 S mol^{-1} for C_{12}mim$^+$, C_{14}mim$^+$, and C_{16}mim$^+$, respectively. These quantities are approximately two times higher than the corresponding limiting equivalent conductivities λ_I^0 calculated in this work. However, the here presented values agree very well with those extracted from the conductivity plots of Inoue et al. (cp. Table V-6).

Aggregation numbers of the $C_n$mimCl series (n = 12, 14, 16) obtained by fluorescence quenching were recently presented by El Seoud et al (cp. Table V-6). They achieved values of 58, 79, and 99 for C_{12}mimCl, C_{14}mimCl, and C_{16}mimCl, respectively. These N_{agg} are significantly higher than those quantities obtained in this work. This discrepancy may be the consequence the different estimation methods used for the determination of N_{agg} [51]. In order to enable the direct comparison of the degree of counterion dissociation reported by El Seoud et al. with data of this study, α_{mic} was recalculated by using the Evans equation (Eq. (IV-11)) and the aggregation numbers derived from the MEM. Values of 0.170, 0.164, and 0.159 were calculated for C_{12}mimCl, C_{14}mimCl, and C_{16}mimCl, respectively. Interestingly, these quantities are lower than those α_{mic} given by El Seoud et al. However, the change of the dissociation degree with increasing alkyl-chain described above is preserved (cp. Table V-6).

Recent X-Ray results of crystalline C_{14}mimCl, and theoretical calulations on the interactions in bmimCl have been discussed based on the formation of hydrogen-bonding between the counterion and the protons of the heterocyclic head group, particularly at the H(2) [76, 77]. Further, hydrogen bonding persists also in aqueous solution of imidazolium ionic liquids [78]. For this reason, one can attribute the higher aggregation tendency of SLILs compared to their conventional counterparts, to a better electrostatic attraction between the counterion and the (more acidic) hydrogens of the heteroatomic imidazolium ring leading to direct or water-mediated hydrogen bonds between the two ion types. Consequently, the surface charge of the micellar aggregates formed by imidazolium SLILs may be screened more effectively (lower α_{mic}) by such donor-acceptor interactions, which are not (or to a less extent) present in the case of common cationic surfactants (higher α_{mic}), resulting in more favourable aggregation tendencies. In order to proof this hypothesis, another issue of the present work was the application of the low concentration chemical model (lcCM) to the conductivity data of the $C_n$mimCl series below their *cac*s, where ionic surfactants behave as normal 1:1 electrolytes. The special interest was to estimate the equilibrium constant K_A, which is directly connected to the fraction of oppositely, charged ions acting as ion pairs [79].
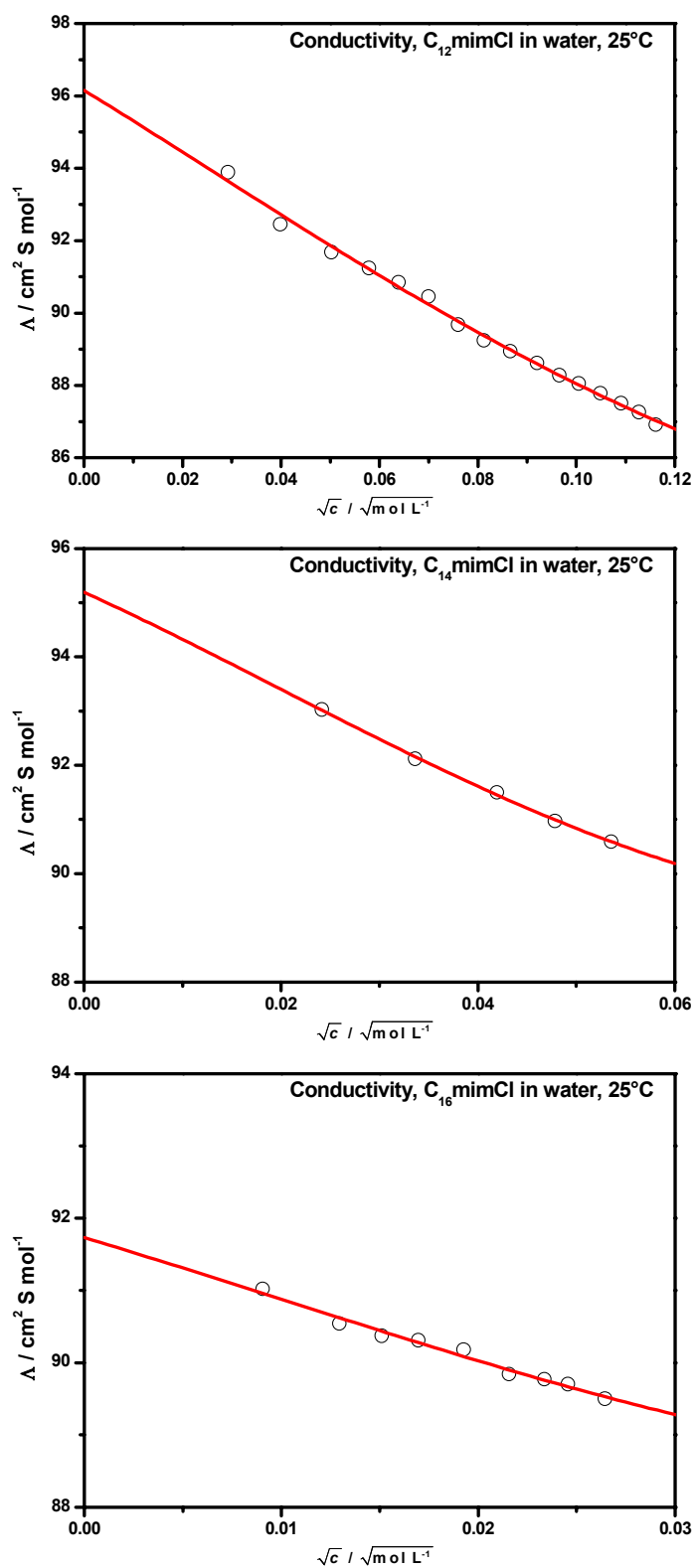
Figure V-10 : Molar conductivities of aqueous solutions of the C$_n$mimCl series below the *cac* at 25°C. Full red lines: lcCM calculations.

Surfactant	c mmol L^{-1}	Λ^{exp} cm^2 S mol^{-1}	Λ^{calc} cm^2 S mol^{-1}	$f_\pm$	α	K_A	Λ^0 cm^2 S mol^{-1}
C$_{12}$mimCl	0.86	93.89	93.65	0.995	0.970		
	1.59	92.45	92.73	0.992	0.960		
	2.53	91.68	91.84	0.987	0.952		
	3.35	91.24	91.21	0.983	0.946		
	4.08	90.85	90.72	0.979	0.942		
	4.90	90.46	90.24	0.976	0.938		
	5.77	89.68	89.78	0.972	0.934		
	6.60	89.24	89.38	0.968	0.930	5.93	96.15
	7.50	88.94	88.98	0.964	0.927		
	8.47	88.62	88.59	0.960	0.924		
	9.33	88.28	88.28	0.957	0.922		
	10.14	88.05	88.01	0.954	0.919		
	11.01	87.78	87.73	0.950	0.917		
	11.89	87.51	87.46	0.947	0.915		
	12.73	87.26	87.23	0.944	0.913		
	13.53	86.91	87.02	0.941	0.911		
C$_{14}$mimCl	0.58	93.03	93.02	0.995	0.974		
	1.13	92.12	92.16	0.990	0.966		
	1.76	91.50	91.45	0.985	0.959	9.91	95.19
	2.29	90.97	90.99	0.980	0.954		
	2.87	90.59	90.59	0.976	0.950		
C$_{16}$mimCl	0.08	91.02	90.96	0.999	0.990		
	0.17	90.54	90.62	0.998	0.986		
	0.23	90.37	90.44	0.998	0.983		
	0.29	90.31	90.28	0.997	0.982		
	0.37	90.18	90.09	0.996	0.980	10.59	91.73
	0.47	89.84	89.90	0.995	0.977		
	0.55	89.77	89.76	0.995	0.975		
	0.60	89.70	89.67	0.994	0.974		
	0.70	89.50	89.53	0.993	0.972		

Table V-7 : Experimental molar conductivities Λ^{exp}, calculated molar conductivities Λ^{calc}, limiting molar conductivities, and association constants K_A of the C$_n$mimCl series in water at 25°C calculated by the lcCM.

Normally, the presence of hydrogen bonds between the imidazolium hydrogens should result in higher values of K_A arising from donor acceptor interactions, which favour the formation of ion pairs compared to completely dissociated salts. For the conductivity evaluation based on the lcCM, the input data was set to the known solvent properties of water [68] and the distance parameter R was appreciated by the following assumptions (cp. also Chapter IV.3.2.3, Eq. (IV-34)): (i) The contact distance of cation and anion is given by the sum of their ionic radii and the length of an oriented solvent molecule. For chloride, an ionic radius of 0.121 nm was used that was obtained from the Stokes-Einstein expression and the equivalent conductivity at infinite solution at 25°C taken from the literature [74]. The length of an OH– group (0.280 nm) was used for the s parameter. Since no literature values were available, the ionic radii of the imidazolium cations were also assumed by the application of the Stokes-Einstein relation together with the corresponding limiting equivalent conductivities obtained previously leading to 0.477 nm, 0.494 nm, and 0.565 nm for C_{12}mimCl, C_{14}mimCl, and C_{16}mimCl, respectively (cp. Table V-6). Note that asymmetric imidazolium cations have a shape far from spherical, especially when the imidazolium is substituted with a long carbon chain. Therefore, these values are only rough presumptions, but should be accurate enough, since the distance parameter R influences the result of K_A only slightly as already reported in literature and verified from test evaluations using different values of R (from 0.5 up to 2 nm) [80]. Here for all the systems investigated, $n = 2$ was chosen in order to encompass three types of ion pairs: contact, solvent shared and solvent separated ion pairs. Figure V-10 presents the conductivity isotherms of the $C_n$mimCl series below the *cac* and the corresponding least-square fits based on the low concentration chemical model. The fits were carried out using a well-established in-house program already successfully used in earlier investigations [81]. All achieved equivalent conductivities at infinite dilution Λ^0, association constants K_A, cation/anion dissociation degrees α, and activity coefficients $f_\pm$ calculated by the lcCM for the three SLIL homologues are gathered in Table V-7. As can be seen, the determined limiting conductivities agree well with those given previously. The values of the association constants are relatively low, $K_A \approx 6–11$, for the investigated $C_n$mimCl homologues. Therefore, all the investigated

salts can be regarded as strong electrolytes completely dissociated in water below their *cac*. However, K_A increases slightly with increasing length of the hydrophobic alkyl-chain, which is in accordance to the change of association degree already reported for the $C_n$mimCl homologues in the self-assembled state.

1.4   Fluorescence quenching: *cac*, N_{agg}

Beside the mixed electrolyte model, another possibility to obtain the mean aggregation numbers of surfactant aggregates in solution is the static luminescence quenching technique originally proposed by Turro and Yeka [82]. This method was applied to the three $C_n$mimCl/water systems in order to confirm the results achieved from the conductivity measurements. All systems were investigated at 25°C by pyrene (probe) fluorescence quenching with 1-hexadecylpyridinium chloride (quencher). The *cac* was acquired by varying the SLIL concentration using constant pyrene amount and for the determination of the mean aggregation number, the SLIL concentration was varied keeping probe and quencher constant. Determination of the *cac* was carried out by investigating the ratio change of the first and third vibronic bands (I_1, at 373 nm and I_3, at 383 nm) of the pyrene emission spectrum with increasing $C_n$mimCl concentration. Figure V-11 gives the I_1/I_3 ratio as a function of the logarithm of SLIL concentration. The *cac*s were calculated by using second derivatives of sigmoid data fits indicating the inflection points associated to the critical aggregation concentrations. Aggregation numbers were derived from the fluorescence intensities of micelle-solubilised pyrene in presence (*I*) and absence (I_0) of pyridinium quencher. Plots of $ln(I_0/I)^{-1}$ versus $C_n$mimCl concentration (Figure V-12) lead to straight lines whose slopes are related to the mean aggregation numbers and the intersections with the x-axis represent rough estimations for the *cac*s (cp. Eq. (IV-55)). All derived results are summarized in Table V-8, which also includes meaningful literature data of conventional surfactant analogues and, in addition, the recently published fluorescence quenching data of El Seoud et al. and Vanýur et al. for the $C_n$mimCl and $C_n$mimBr series, respectively. The *cac*s derived from the pyrene solubilisation are all consistently less than those values obtained from surface tension and conductance measurements, but the trend is preserved.
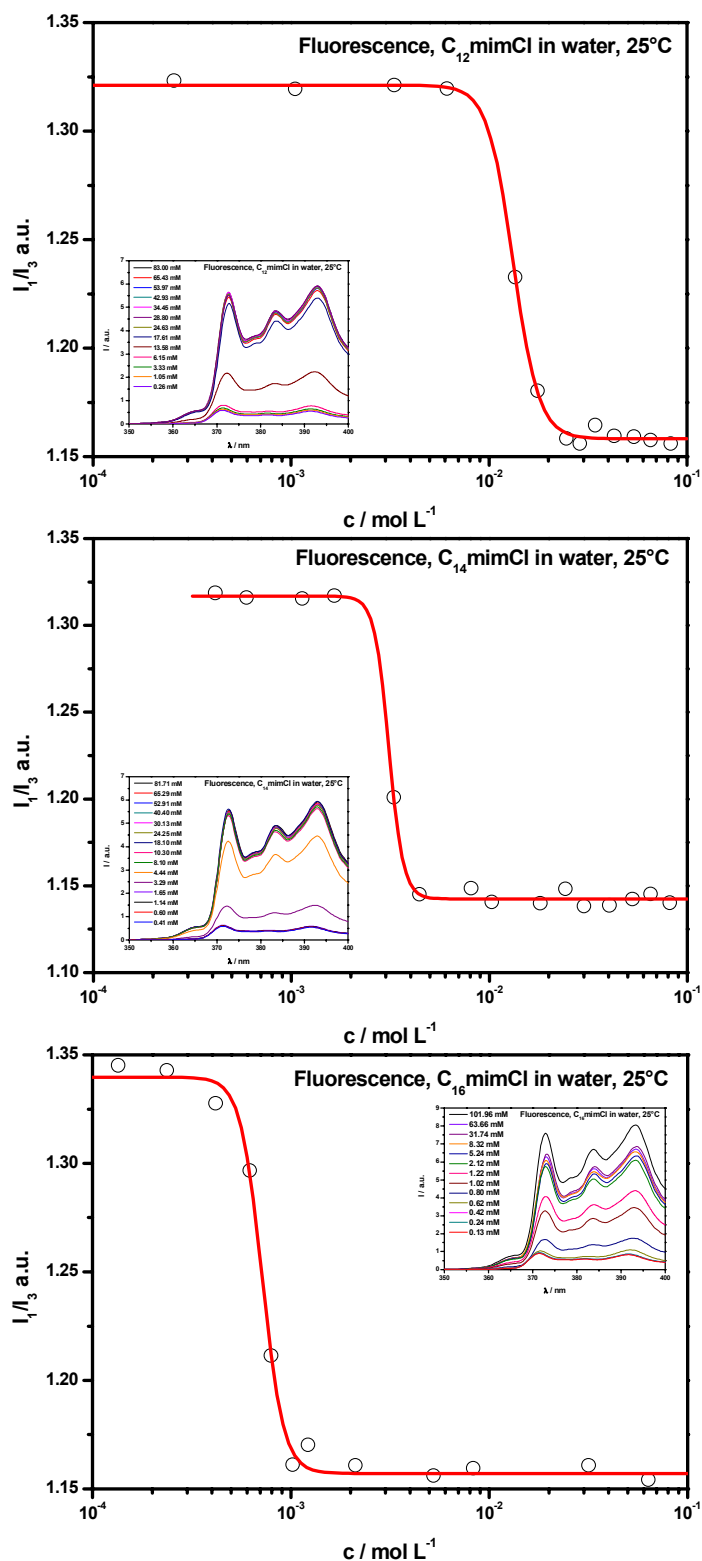
Figure V-11 : Intensity ratios of the I_1/I_3 vibronic bands of the $C_n$mimCl homologues solubilised pyrene at 25°C and the corresponding sigmoidal data fits (red line). The insets show the change of the emission intensity as a function of SLIL concentration. The pyrene amount was kept constant for each measurement.

Surfactant	*cac* / mmol L^{-1}	N_{agg}
C$_{12}$mimCl	13.25[a]	43[a]
	14.00[b]	58[b]
C$_{14}$mimCl	3.11[a]	57[a]
	3.65[b]	79[b]
C$_{16}$mimCl	0.72[a]	65[a]
	1.30[b]	99[b]
C$_{12}$mimBr	-	44[c]
C$_{14}$mimBr	-	59[c]
C$_{16}$mimBr	-	66[c]
C$_{12}$TAC	24.40[d]	57[e], 47[f]
C$_{14}$TAC	5.27[d]	66[f]
C$_{16}$TAC	1.31[d]	69-93[g], 66[e], 81[f]
C$_{12}$PyCl	17.50[d]	52[h]
C$_{14}$PyCl	3.88[d]	70[h]
C$_{16}$PyCl	0.98[d]	87[h]

Table V-8 : Steady-state fluorescence results of the investigated SLILs including *cac* and mean aggregation number *N*$_{agg}$ obtained at 25°C. For comparison, comparable fluorescence quenching data of conventional surfactants extracted from the literature are given. Additionally, the fluorescence data of El Seoud et al (C$_n$mimCl) and Vanyúr et al. (C$_n$mimBr) are presented. As far as possible, all fluorescence quantities presented from literature were obtained from steady-state fluorescence technique at 25°C. [a]This work. [b]Ref. [16]; values were determined at fixed SLIL concentrations (10 times the *cac*) using constant pyrene, and varying quencher (C153) concentrations. [c]Ref. [12]; *N*$_{agg}$ was obtained at constant C$_n$mimBr concentrations (0.055 M, 0.025 M and 0.010 M for C$_{12}$mimBr, C$_{14}$mimBr and C$_{16}$mimBr, respectively) using constant pyrene and varying quencher concentrations (C$_{12}$PyBr, C$_{14}$PyBr and C$_{16}$PyBr for C$_{12}$mimBr, C$_{14}$mimBr and C$_{16}$mimBr, respectively). [d]Ref. [83]; *cac* estimated by using MQAE fluorescence probe. [e]Ref. [84]; *N*$_{agg}$ was determined at constant surfactant concentration (0.109 M and 0.097 M for C$_{12}$TAC and C$_{16}$TAC, respectively) by using pyrene (probe) and varying C$_{16}$PyCl (quencher) concentrations. [f]Ref. [85]; Nagg was obtained by dynamic fluorescence method at constant Amphiphile concentration (near the *cac*) using the probe/quencher pair 1-methylpyrene and C$_{14}$PyCl. [g]Ref. [86]; *N*$_{agg}$ were determined by dynamic fluorescence quenching at constant surfactant concentrations (in the range 0.007–0.040 M) using 1-MePy and C$_{16}$PyCl as probe and quencher, respectively. [h]Ref. [73]; from osmotic pressure and calorimetric data; no fluorescence data available.

This discrepancy is due to the difference of the methods employed for the determination of the *cac* [51]. Figure V-12 shows good linear correlation of the *ln(I$_0$/I)$^{-1}$* versus SLIL concentration plots for all C$_n$mimCl salts in the concentration range examined. As ex-

pected, the *cac*s derived from the intercept with the abscissa, differ quite a lot from the values achieved from the I_1/I_3-ratio, for C_{16}mimCl even a negative *cac* was extracted. Such disagreements and, additionally, a negative *cac* was already reported by Gratzel et al., who determined N_{agg} of alkylsulfonic acids by steady-state fluorescence quenching and addressed the inconsistency of the obtained *cac*s to the fluorescence quenching method [87]. Therefore, the *cac* determination from fluorescence measurements should be carried out by pyrene solubilisation technique and not by fluorescence quenching. At this point, it must be noted that the *cac* problem has no bearing on the estimation of N_{agg}, as discussed by Gratzel et al. The aggregations numbers diminish from C_{16}mimCl to C_{12}mimCl and, additionally, they are in very good agreement with those quantities reported from the conductivity measurements. This observation is not surprising for the C_{12}mimCl and the C_{14}mimCl system, since the concentration regions, which were investigated by fluorescence quenching, are within the ranges examined previously by the MEM. However, this is not the case for C_{16}mimCl, for which the results of the fluorescence quenching method suppose a constant aggregation number (linearity of the $ln(I_0/I)^{-1}$-*c*-plot over the investigated concentration range) also at concentrations, where the MEM model already indicates aggregate evolution. One possible reason for this may be a higher sensitivity of the conductivity technique.

The comparison of the steady-state fluorescence quenching results with those reported for conventional alkyltrimethylammonium and alkylpyridinium analogues leads to the same conclusion as already drawn from the conductance experiments: The aggregation numbers of amphiphiles incorporating the imidazolium head group are generally lower which may be attributed to the difference in the head group size. Note that the head group packing ability is directly linked to the aggregation number of the formed aggregates as was already shown by Anacker et al. [88, 89]. This means, that by increasing the bulkiness of the surfactant head group N_{agg} is usually reduced due to the packing requirement specified from the molecules aggregating into a micelle with high curvature. With other words, the asymmetry of the 1-alkyl-3-methylimidazolium scaffold may favour the formation of micelles with low aggregation numbers (at low SLIL concentration).
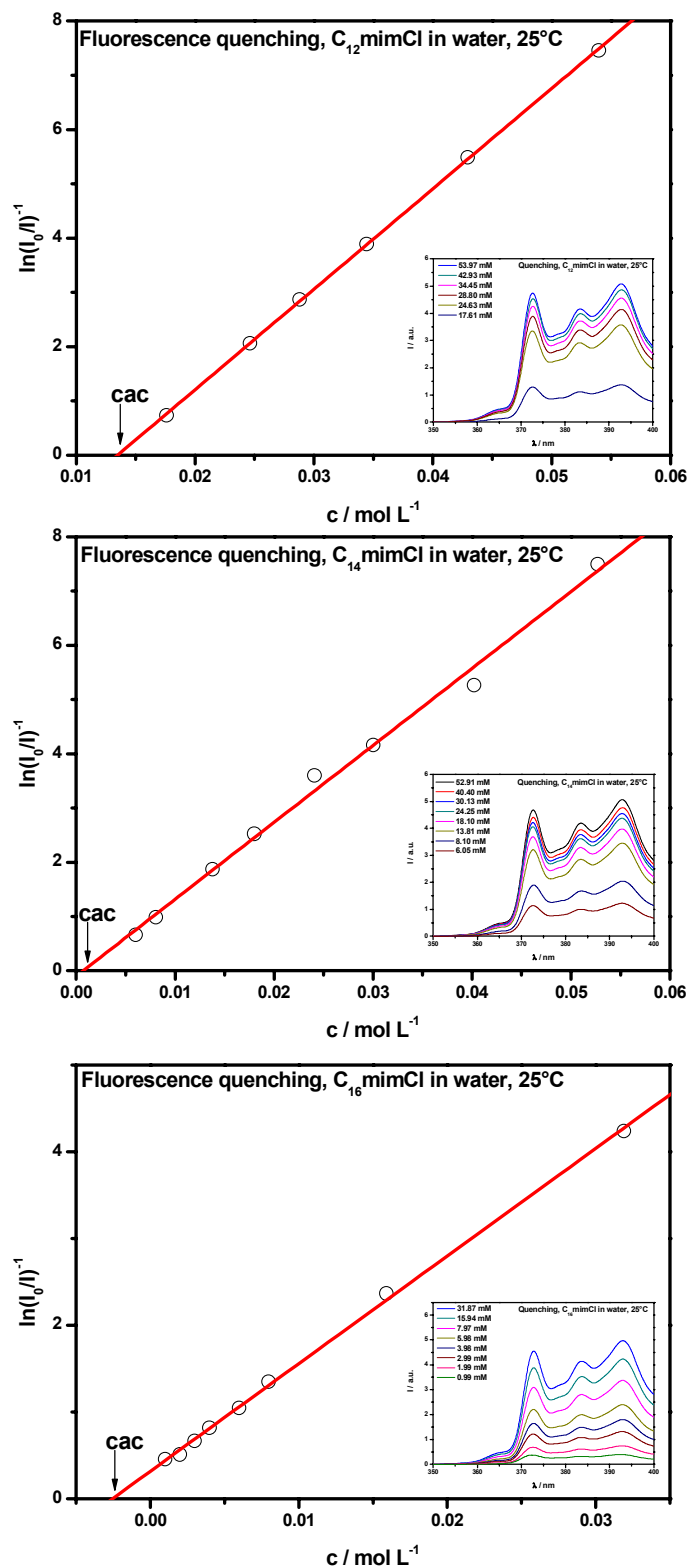
Figure V-12 : Pyrene fluorescence quenching by hexadecyl-pyridinium chloride at various SLIL concentrations (insets), with constant probe and quencher amount. For the calculation of the intensity data, the emission at 373 nm in presence and absence of quencher was used.

Furthermore, the bulkiness and the planarity of the imidazolium head (perhaps together with the hydrogen-bon ability) may be the reason for the high tendency to reduce the curvature of the self-assembled structures at higher SLIL concentrations, e.g. by growing or shape change, since a parallel packing of the planar asymmetric imidazolium within aggregates of low curvature seems more reasonable. This was already assumed by Kaper et al. during her investigations of the phase behaviour of the C_{16}mimCl/water-system [19].

The calculated mean aggregation numbers are nearly equal to those published by Vanyur et al. for the $C_n$mimBr analogues (Table V-8), who also established the fluorescence quenching technique. In contrast to the underlying investigations, they measured at constant SLIL and pyrene concentration by varying the quencher concentration, however. Thus, an absolute comparison of the aggregation numbers is difficult, since their values are only valid for the adjusted SLIL concentration, whereas the here presented values describe the aggregate structure over a concentration range, i.e. in the present case mean aggregation numbers are reported. For the same reason, no direct comparison between N_{agg} given by El Seoud et al. and those N_{agg} presented here is possible. In general, the values of El Seoud et al. are considerably higher, which was already noticed previously during the MEM evaluations of the conductance data (cp. Table V-8). Two possible explanations for this gap are meaningful: (i) As already pointed out, the aggregation numbers presented by El Seoud et al. were obtained for constant SLIL concentrations, whereas in this work averaged N_{agg}s, which were estimated for a concentration range, are presented. (ii) El Seoud et al., used another quencher molecule, which has an additional bearing on the achieved aggregation numbers due to different solubilisation states of each quencher molecule [90].

1.5   Density: Apparent molar volumes

Density measurements are an important tool for colloid chemists to obtain the apparent molar volumes of amphiphiles in the aggregation phase and the apparent molar volumes of a surfactant in the monomeric form. Additionally, the knowledge of the density enables the conversion between temperature dependent concentration quantities into

non-temperature dependent ones, e.g. molonity to molarity. Therefore, the density as a function of concentration was determined for all investigated $C_n$mimCl/water systems and analyzed according to the theory presented in Chapter IV.1.2.1.

As a general feature, the trends shown in Figure V-13 would exclude the occurrence of micellar aggregation at the experimental temperature and concentration range, since the classical discontinuity due to the different partial molar volumes of the surfactant in the dispersed and micellized forms is not displayed, perhaps because of too low resolution of the used density meter in these low concentration ranges. Nevertheless, above the *cac*s satisfactory correlations between concentrations and densities were obtained, which were used to extract the apparent molar volumes of the SLILs in the aggregation phase V_Φ^{mic}. The collection of the results is given in Table V-9 together with meaningful literature data.

From the theory of micellar aggregation it is clear that the intercept of the V_Φ-$\tilde{m}^{-1}$-plot with the y-axis at concentrations above the *cac* gives V_Φ^{mic}. It can be seen that the apparent molar volumes of SLILs in the aggregated phase increase with the growth of the alkyl-chain. This observation is to be expected because of the increasing size of the surfactant molecule and was already reported for a homologues series of conventional amphiphiles [91]. Wang et al. report a value of 304.9 cm^3 mol^{-1} for C_{12}mimBr in the aggregated form. This value is higher than hat V_Φ^{mic} achieved for C_{12}mimCl resulting from the exchange of the counterion from bromide to chloride. The difference between V_Φ^{mic} of the two imidazolium analogues is 9.3 cm^3 mol^{-1}, which fairly matches that between Br$^-$ and Cl$^-$ ions [92]. A literature value of V_Φ^{mic} = 288.5 cm^3 mol^{-1} is reported for C_{12}TACl by Yamanaker et al., which is lower than the corresponding value of 295.6 cm^3 mol^{-1} derived for C_{12}mimCl [93]. It seems reasonable to attribute this result to the difference in head group size of the two surfactant types. This thesis is in line with the investigations of other authors, who examined the influence of the head group size on V_Φ^{mic} of dodecylsurfactants [94].
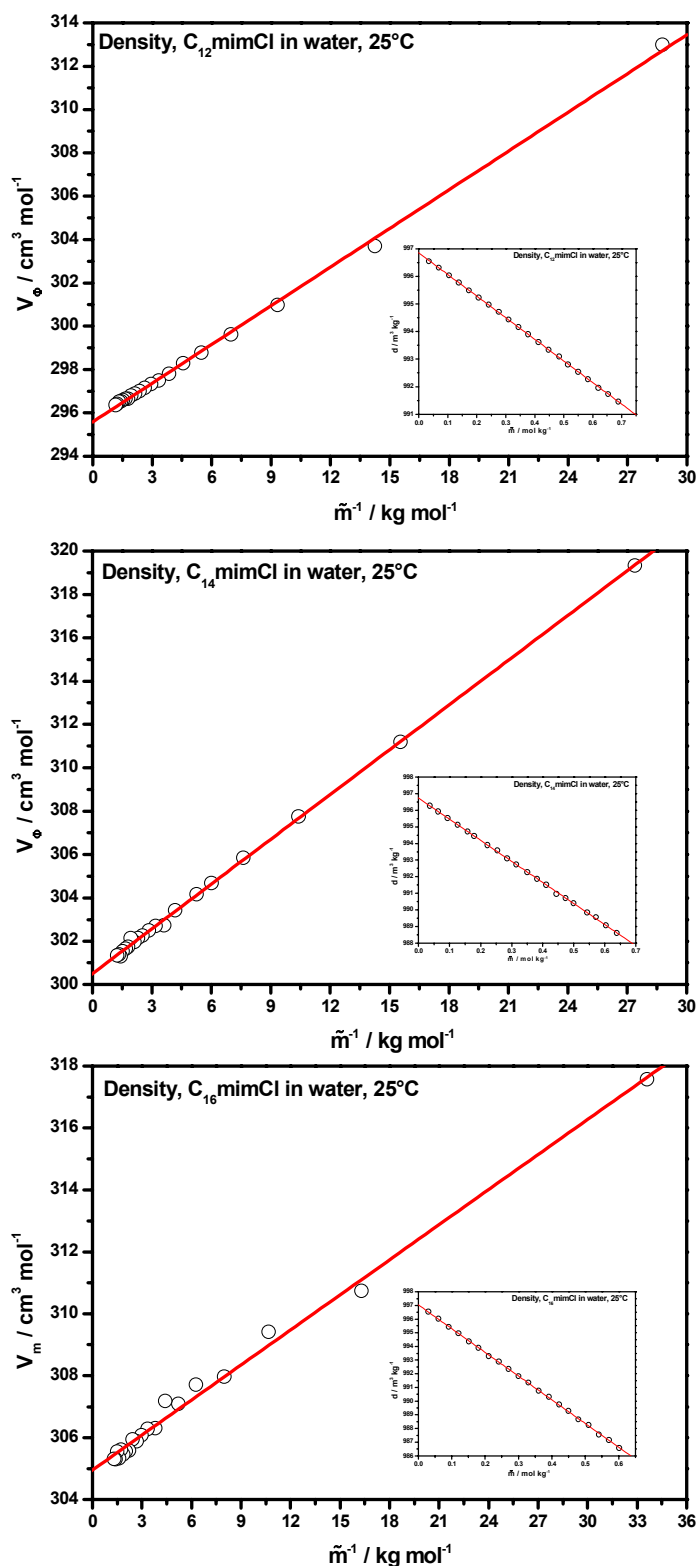
**Figure V-13 : Variation of the apparent molar volume with the re-
verse of the molality for the three C$_n$mimCl systems. The red lines
are linear fits used for the calculation of V_{Φ}^{mic}. The insets give the
density variations as a function of SLIL molonity and the linear fits
from which the density coefficients were obtained.**

Surfactant	V_{Φ}^{mic} / cm^3 mol^{-1}	D / kg^2 mol^{-1} m^{-3}
C$_{12}$mimCl	295.6	-7.8255
C$_{14}$mimCl	300.5	-12.6875
C$_{16}$mimCl	305.0	-17.3417
C$_{12}$mimBr	304.9[a]	-
C$_{12}$TAC	288.5[b]	-

Table V-9: Apparent molar volumes of the SLILs in the aggregated phase at 25°C obtained from density measurements using the pseudo-phase model of micellization. For comparison, the density of C$_{12}$mimBr and C$_{12}$TACl, which were available from literature, are given. Additionally, the density coefficients for each system are given. [a]Ref. [14]. [b]Ref. [93].

1.6   Small-angle neutron scattering: Micellar structure

In order to obtain information about the size and shape of the micellar structures formed by the C$_n$mimCl surfactants in water and to get insight about the present interactions between these aggregates in the micellar phase, small angle neutron scattering experiments were carried out at 25°C using the V4 spectrometer, at the Hahn-Meitner-Institute in Berlin. For the measurements, water was replaced by D$_2$O in order to match the contrast conditions, which apply for this scattering technique, accepting slight changes of the *cac*s that depend on the isotopic state of the water hydrogen atoms [95]. The C$_{12}$mimCl, C$_{14}$mimCl and C$_{16}$mimCl were investigated in a concentration range from a few weight percents up to nearly 5 wt.%.

1.6.1   Basic considerations used for the model fitting of the neutron scattering data

Because of strong interactions, normally present in charged micellar systems, the analysis of such SANS patterns needs a self-consistent treatment of the single particle form factor *P(q)* depending on the shape and the size of the particles, and the interparticle structure factor *S(q)*, which is decided by the spatial distribution of the particles [96, 97]. For a system of monodisperse interacting micelles, the coherent differential scattering cross section per unit volume ($d\Sigma/d\Omega$ or *I(q)*) is given by [97]

$$\frac{d\Sigma}{d\Omega} = n_p \left(\rho_m - \rho_s \right)^2 V_p^{\;2} \left\langle \left| F(q) \right|^2 \right\rangle S(q) + BG_{incoh} \qquad\qquad \text{(V-1)}$$

where n_p denotes the number density of the micelles, ρ_m and ρ_s are, respectively, the scattering length densities (*sld*) of micelle and solvent, and V_p is the volume of the scattering particle. BG_{incoh} is a constant background term that represents the remaining incoherent scattering, which is mainly due to hydrogen in the sample. For the analysis of the scattering spectra a core-shell ellipsoidal shape factor $<F(q)^2>$, where the brackets denote the average over all particle orientations, in combination with a *S(q)* of interacting hard-spheres was used. The latter was calculated using the rescaled mean spherical approximation (RMSA), which is a good approximation provided the axial ratio of the micelles is not significantly greater than unity [70, 98].

The description of the micelle shapes utilizing the ellipsoidal shape factor is widely used in the analysis of small-angle scattering data because it also includes other different possible shapes of micelles such as spherical and rod-like. In other words, by the usage of this model it is possible to describe several shapes by the ratio of the axial directions, *a* and *b* where *a* is the equatorial semi-axis (rotational axis) and *b* is the principle semi-axis of the spheroid, respectively. Thus, spheres are represented by $a = b$, prolate ellipsoids by $a > b$, oblate ellipsoids by $a < b$, and rods by $a \gg b$. For this reason, the growth of particles resulting from the change of solution conditions (e.g. concentration, ionic strength, temperature, ect.) can be analyzed by one form factor model. Usually, micelles grow along one of the axial directions of the aggregate, whereas the growths along the other axial directions are restricted by the length of the surfactant molecule to avoid the energetically unfavourable empty space or water penetration inside the micelle. In addition to the micellar dimensions, the scattering length densities of the different micellar regions, namely that of the hydrophobic hydrocarbon core and that of the head group region (interface region), have to be taken into account with respect to the *sld* of the solvent. Based on these considerations, the form factor of a spheroid micelle is described by the following main parameters

(i) The scattering length densities of the hydrophobic core, ρ_{core}, interface region (including head group, counterions, solvent), ρ_{shell}, and solvent, ρ_{solv}.

(ii) The geometrical parameters, which define the core-shell spheroid, are the core dimensions (a, b) and the thickness of the shell t (including head groups, counterions, and solvent).

Table V-10 shows the scattering length densities of the investigated $C_n$mimCl/D_2O systems that were used in the SANS analysis divided into the different scattering contributions of hydrocarbon core, shell components, and solvent, respectively. The *sld*s were calculated according to the already presented theory (cp. Chapter IV.7.2.2). The contrast model presented in the Table is based on the assumptions of Tanford, who proposed a hydrophobic micellar core consisting entirely of portions of the surfactant hydrocarbon chains. The $-CH_3$ groups are always contained in this core, but one or more methylene groups near the amphiphile head group may not be [75].

In the present investigation, it was assumed that ($m - 1$), where m is the total number of methylene groups of the SLIL alkyl-chains, $-CH_2-$ groups form the micellar core, which is in agreement with results of Wang et al., who performed simple geometrical calculations for self-assembled C_8mimBr, C_{10}mimBr, and C_{12}mimBr [14]. Consequently, values of ρ_{core} were calculated from the physical data of undecane, tridecane, and pentadecane for C_{12}mimCl, C_{14}mimCl, and C_{16}mimCl, respectively. The shell region of the imidazolium micelles is represented by the $-CH_2-[mim]^+$ fragment and defines, together with the fraction of condensed chloride counterions and a possible fraction of penetrated solvent, ρ_{shell}. Since the scattering length densities are 1.35×10^{10} cm^{-2}, 3.31×10^{10} cm^{-2}, and 6.37×10^{10} cm^{-2} for the $-CH_2-[mim]^+$ part, Cl$^-$, and D$_2$O, respectively, the following constraint must hold true for ρ_{shell}: 1.37×10^{10} cm$^{-2} \leq \rho_{shell} \leq 6.37 \times 10^{10}$ cm^{-2}.

Parameter	Hydrocarbon core			Shell components		Solvent
	$-[C_{11}H_{23}]$	$-[C_{13}H_{27}]$	$-[C_{15}H_{31}]$	$-CH_2[mim^+]$	$[Cl^-]$	D_2O
M / g mol^{-1}	155.31[a]	183.36[a]	211.41[a]	-	-	20.03[a]
d / g cm^{-3}	0.740[a]	0.756[a]	0.796[a]	-	-	1.107[a]
V_Φ / cm^3 mol^{-1}	209.88[b]	242.54[b]	274.92[b]	98.20[c]	17.40[d]	18.09[b]
V / cm^3	3.49×10^{-22}	4.03×10^{-22}	4.57×10^{-22}	1.63×10^{-22}	2.89×10^{-23}	3.00×10^{-23}
$\sum b_i$ / cm^{-1}	-1.29×10^{-12}	-1.46×10^{-12}	-1.63×10^{-12}	2.20×10^{-12}	9.58×10^{-13}	1.92×10^{-13}
sld / cm^{-2}	-3.71×10^9	-3.63×10^9	-3.57×10^9	1.35×10^{10}	3.31×10^{10}	6.37×10^{10}

Table V-10: The scattering length densities (*sld*) of the component blocks applied in the SANS evaluation together with the quantities used for their calculation. [a]Ref. [38]; molar mass and density (25°C) of the alkanes corresponding to the length of the hydrophobic block and of D$_2$O, respectively. [b]Calculated from the ratio of molar mass and density. [c]Ref. [58]. [d]Ref. [92].

As can be seen in by the negative *sld* of the different core materials (cp. Table V-10), there exists a very strong contrast for the micellar core in D_2O with respect to the head group and the counterions forming the particle's shell. For this reason, the neutrons mainly 'see' the core of the micelles and the scattering pattern of a micelle in solution of D_2O is dominated by the strong hydrocarbon scattering of the core. On the contrary, the shell materials show positive scattering length densities which results in low resolution with respect to the interface region of the micellar aggregate. Figure V-14 graphically illustrates the variation of the neutron scattering length densities typical for core-shell micellar aggregates applied for the modelling of the obtained SANS patterns [100].
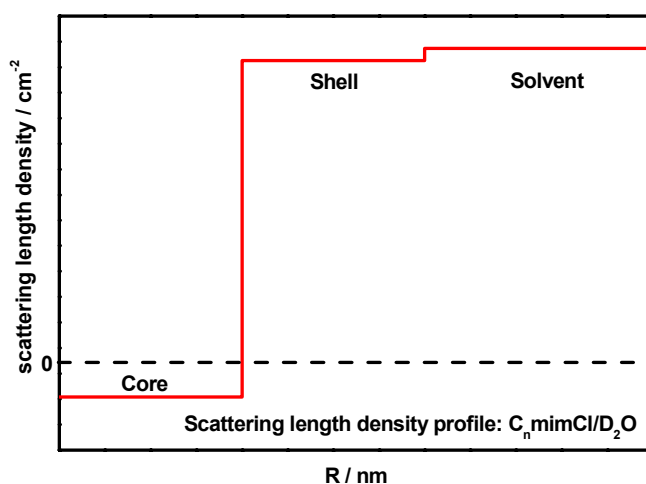
Figure V-14 : Scattering length density profile of a micellar core-shell particle. The two steps correspond to the scattering length densities of core and shell, respectively.

The RMSA structure factor used for the data interpretation describes the arrangement of interacting spherical macro-ions. This model bases on the repulsion of particles in succession of a screened Coulomb potential. For not too high concentrations and low axis ratios in the case of non-spherical aggregates, the RMSA approach is successfully applicable, since the potentials of long-ranged ellipsoids with axis ratios near unity are very similar to those of spheres. However, the limits will be reached at higher concentrations or increasing anisotropy of the micelles [70, 98]. The RMSA structure factor is defined by the following base parameters:

(i)   The temperature T.

(ii)   The hard-sphere volume fraction of the macro-ions Φ_{hs} in solution.

(iii)   The hard-sphere radius (interaction radius) of one macro-ion R_{hs} in solution.

(iv)   The number of elementary charges Z_{eff} per micelle, which assigns the strength of the electrostatic interactions (Coulombic repulsion) between the particles.

(v)   The ionic strength I, which is related to the Debye-Hückel inverse screening length λ_D that also influences the interactions between the micelles. With other words, λ_D describes the effective screening of the micellar charge by the present ions. λ_D is defined as

$$\lambda_D = \sqrt{\frac{8 \cdot \pi \cdot N_A \cdot e^2 \cdot I}{10^3 \cdot \varepsilon \cdot k_B \cdot T}} \qquad (V\text{-}2)$$

where N_A is the Avogadro number, e the elementary charge, ε the dielectric constant of the solvent, k_B the Boltzmann constant, and T the temperature at which the measurement is carried out. The ionic strength is given by the following sum:

$$I = \frac{1}{2} \sum_i c_i \cdot z_i^2 \qquad (V\text{-}3)$$

Here z_i is the charge and c_i the molar concentration of the different ion species present in the solution. For micellar solutions without additionally added salt, the ionic strength can be rewritten as

$$I = cac + \frac{1}{2} \alpha_{mic} c \qquad (V\text{-}4)$$

I is determined by the *cac* and dissociated counterions from the micelle. α_{mic} ($= Z_{eff} / N_{agg}$) is the charge per surfactant molecule in the micelle and is a meas-

ure of the dissociation of the counterions of the amphiphile in the micelle. c represents the concentration of the surfactant.

The volume fraction Φ_{hs} and the hard-sphere radius R_{hs} are primarily appointed by the average distance between the micelles in solution, which is represented by the location of the first order correlation maximum of the structure factor and consequently, by the correlation peak in the scattering curve. Z_{eff} and λ_D gives the height and the width of the maximum.

In order to obtain reliable fit results of the scattering patterns, the number of free parameters included in $P(q)$ and $S(q)$, respectively, were restricted as far as possible by conclusive assumptions. The scattering length densities of core and solvent were fixed to the values given in Table V-10. The fitting range of ρ_{shell} was limited to the interval given above. One axis of the assumed spheroid was set to the maximal length of a fully extended hydrocarbon chain of the imidazolium surfactant minus one carbon atom in accordance to Tanford. Additionally, polydispersity was considered during the data fitting using a log-normal distribution along one axis of the particle [101].

The aggregation numbers of the micellar aggregates were calculated from the ratio of the core volume V_{core}, which was estimated from the aggregate dimensions a and b, to the volume V_{chain} of one hydrocarbon tail, which is incorporated in the micellar core (Eq. (V-5)) [97, 100, 102].

$$N_{agg} = \frac{4\pi \cdot a \cdot b^2}{3V_{chain}} = \frac{V_{core}}{V_{chain}} \tag{V-5}$$

The restriction of the $S(q)$ key parameters has to be done carefully, because the RMSA model used in this study is only completely valid for spherical aggregate geometries. However, this structure factor is able to describe the arrangement of the aggregates approximately by the application of certain constraints. The hard-sphere interactions between anisotropic ellipsoids differ slightly from those of spheres with the equivalent volume. Therefore, R_{hs} has to be scaled down to a value, which corresponds to the

smallest reasonable radius of the micellar core. The chosen values of R_{hs} were calculated by $R_{hs} = \sqrt[3]{(a \cdot b^2)}$ [103-105]. The ionic strength of the investigated systems was calculated by the term presented previously using α_{mic} estimated from the conductivity. The temperature T was set to 298.15 K.

Beside the choice of an appropriate form factor and structure factor for the description of the system under investigation, the provision for the instrumental resolution is another crucial part in the analysis of scattering patterns. The finite divergence and the size of the direct beam, the wavelength resolution and the pixel size of the detector contribute to a smearing of the real intensity scattered by the particle can lead to inaccurate results [106, 107]. Therefore, all theoretical scattering curves, which were adjusted to the experimental data, were smeared during the calculations in order to achieve the best possible description of the experimental scattering pattern. The contributions of the smearing effects were calculated taking into account the apparatus geometry as well as the FWHM = 11 % of the V4 spectrometer (cp. Table IV-6).

The data analysis in this study was exclusively performed by using the small-angle analysis software package SASFit developed by Kohlbrecher [108]. This program met all requirements needed to fit the previous presented $P(q)$ and $S(q)$ combination to the measured scattering spectra. SASFit is also able to consider a resolution function to the theoretical model fit. The program minimizes the deviations of the theoretical scattering function to the experimental data by variation of the model parameters. The quality of a fit can be estimated by the sum of the quadratic deviations of the data points to the theoretical function, χ^2. The lower χ^2, the better the chosen model describes a measured dataset [69]. Beside the magnitude of χ^2, other important criteria were used to cross-check the fitting consistency during the data evaluation. First, the volume fraction Φ_{fit} obtained from the scale factor n_p (particle number density) and the particle dimension was compared to the expected volume fraction Φ_{exp} calculated from the molar volumes of the SLILs in the aggregated state and the known SLIL concentrations minus the corresponding cacs. Further, the hard-sphere volume fraction Φ_{hs} obtained from fitting the RMSA structure factor to the scattering pattern has to be in the order of magnitude as the values of Φ_{fit} and Φ_{exp}, respectively. If there was a significant departure between

Φ_{fit}, Φ_{exp}, and Φ_{hs}, the fitting function was discarded and the initial model parameters were changed for the next fit. This procedure was repeated until a satisfactory description with consistent model parameters was achieved.

1.6.2   Model fitting results

Figure V-15 gives the obtained small-angle neutron scattering spectra for various concentrations of the $C_{12}mimCl/D_2O$, $C_{16}mimCl/D_2O$, and $C_{16}mimCl/D_2O$ system, respectively. The insets show the same spectra, but as $log\,I$ vs. q plots for better resolution. For all investigated systems, the scattering intensity increases with growing SLIL concentration indicating a growing number of scatters and/or an increase of the particle size. Simultaneously, a correlation peak arises, which results from the scattering contribution of the interparticle structure factor $S(q)$. This peak usually occurs at the inner part of the scattering spectra at $Q_{max} \sim 2\pi/d$, where d is the average distance between the micelles and Q_{max} is the value of q at the peak position, and represents the higher degree of order as well as the lower isothermal compressibility of the system at high SLIL concentrations [104, 109]. The locations of scattering patterns of the three SLIL homologues compared to each other slightly shift towards smaller q-values as the hydrocarbon chain becomes longer. In accordance to the scattering theory, this is the direct consequence of the formation of bigger particles in the sequence: $C_{12}mimCl$, $C_{14}mimCl$, and $C_{16}mimCl$. The solid lines in Figure V-15 correspond to best model curves of the core-shell ellipsoid $P(q)$ in combination with a Hayter-Penfold $S(q)$ obtained by the fitting concept described in the previous chapter.

For the $C_{12}mimCl$ in D_2O, the aggregates are spherical at low concentrations and become more and more elongated upon increasing SLIL amount (cp. Table V-11). The most consistent data fits (minimized χ^2 and most consistent volume fractions) were obtained by setting the principle semi-axis b to a constant value of 1.55 nm, which corresponds to the length of a fully extended undecyl-hydrocarbon chain, and fitting the rotational axis a of the ellipsoid.
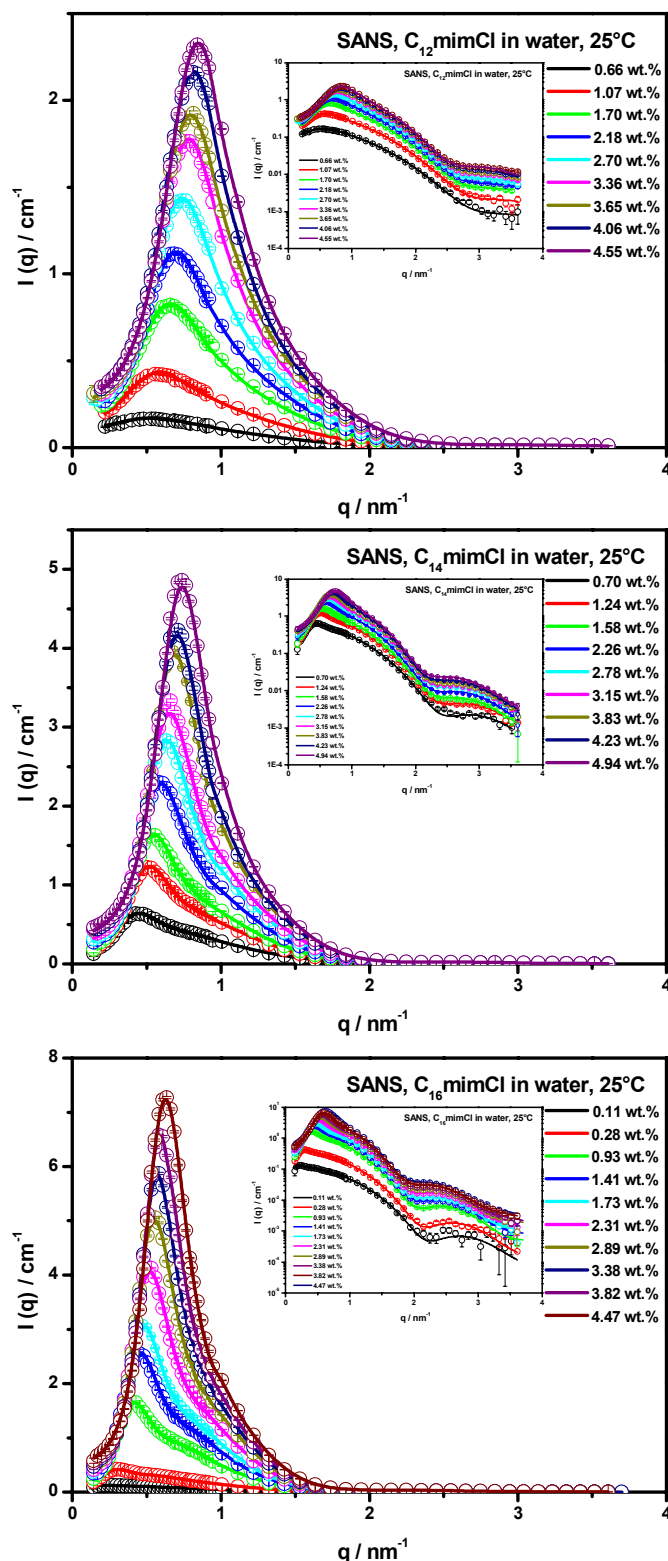
Figure V-15 : SANS data from aqueous micellar solutions of C$_{12}$mimCl, C$_{14}$mimCl, and C$_{16}$mimCl, respectively. The coloured lines represent the best fits to the datasets. Additionally, the corresponding *log I* vs. *q* plots are given as insets for better resolution.

This lead to axial ratios, $X = a/b$, of 1 (spheres) at low SLIL concentrations and to $X > 1$ (prolate ellipsoids) for higher concentrations studied. Goodchild et al. already found the same behaviour for $C_{10}mimBr$ at higher concentrations, whereas Bowers et al. reported the formation of oblate micelles for C_8mimCl with increasing ionic liquid content [8, 15]. The fits could be improved further by the introduction of a log-normal distribution along the semi-major axis of the prolate ellipsoid [101]. These results show that the morphologies of the micelles formed by $C_{12}mimCl$ are spherical at low concentrations and become prolate ellipsoids with a certain length polydispersity. However, the length polydispersity is relatively low for the $C_{12}mimCl$ system, as indicated by the small value of σ_x, which represents the distribution parameter of the assumed log-norm distribution and therefore denotes the standard deviation from the average size parameter, the rotational axis in the present case (cp. Table V-11). The aggregation numbers calculated from the micellar geometries were found to be 45 in the region just above the *cac*. This observation agrees very well with N_{agg} reported before from the other techniques, fluorescence quenching ($N_{agg} = 43$) and conductance experiment ($N_{agg} = 41$), respectively, which were performed in the same concentration range where N_{agg} was found to be constant by SANS. At higher $C_{12}mimCl$ content, N_{agg} increases up to 55 for the highest concentration investigated in this study. In addition to the core dimensions, the shell thicknesses t and the scattering length densities of the micellar shell ρ_{shell} were obtained from fitting $P(q)$. Averaged values of 0.42 nm and $6.08\text{-}\times\text{-}10^{10}$ cm^{-2} were extracted for t and ρ_{shell}, respectively. The shell thickness seems a little bit too low considering the geometry of the imidazolium head. Although the *sld* of the shell is within the previously defined interval, it seems that its value is a little bit too high taking into account the scattering length densities of the different shell materials. Since t and ρ_{shell} are highly connected within $P(q)$, the observed discrepancy may arise from the same reason. The most reasonable explanation for the difficulty to extract the shell thickness and the shell contrast with higher certainty is the disadvantageous scattering contrast of the shell with respect to D_2O.

wt.%	0.66	1.07	C$_{12}$mimCl/D$_2$O					4.06	4.55
			1.70	2.18	2.70	3.36	3.65		
c / mol L^{-1}	2.55×10^{-2}	4.10×10^{-2}	6.51×10^{-2}	8.33×10^{-2}	1.03×10^{-1}	1.29×10^{-1}	1.40×10^{-1}	1.55×10^{-1}	1.74×10^{-1}
Φ_{hs} / %	0.65	1.23	2.20	2.90	3.67	4.83	5.37	6.26	7.41
a / nm	1.55	1.55	1.55	1.55	1.55	1.55	1.55	1.55	1.55
b / nm	1.55	1.55	1.55	1.58	1.63	1.68	1.75	1.75	1.80
t / nm	0.41	0.40	0.40	0.41	0.42	0.43	0.42	0.43	0.44
ρ_{shell} / cm^{-2}	6.15×10^{10}	6.13×10^{10}	6.04×10^{10}	6.09×10^{10}	6.05×15^{10}	6.03×10^{10}	6.09×10^{10}	6.05×10^{10}	6.08×10^{10}
N_{agg}	45	45	45	47	50	52	54	57	60
α_{mic}	0.355	0.369	0.393	0.404	0.393	0.402	0.409	0.396	0.382
Z_{eff}	16	17	18	19	19	21	22	23	23
σ_x	0.21	0.24	0.20	0.19	0.21	0.20	0.22	0.23	0.19
χ^2	5.04	17.67	14.46	14.23	26.30	40.14	30.69	36.80	46.05

Table V-11 : Summary of indicative SANS data fitting parameters for aqueous solutions of C$_{12}$mimCl using a core-shell ellipsoid model with a Hayter-Penfold charged sphere structure factor.

The problem of low resolution between the head group and D_2O is also well known in the literature for common trimethylammonium surfactants, although the scattering length density of the trimethylammonium head group is negative (--4.25--$\times$-10^{10} cm^{-2}) compared to the positive value of the imidazolium cation [110]. The attempt to overcome this difficulty by fixing the head group thickness to higher values during the data fitting resulted in unreasonable values for the volume fraction and/or ρ_{shell}. Consequently, the results were chosen with respect to the physical correctness of the gained volume fractions, and also with respect to the quality of the fit of the data. Beside the ellipsoidal form factor, a structure factor, which mainly dominates the scattering curves at low q-values, was used to describe the repulsive interparticle interactions of the charged $C_{12}mimCl$ micelles. The obtained fitting parameters, Φ_{hs} and Z_{eff}, are given also summarized in Table V-11. The volume fractions of the scattering hard-sphere particles Φ_{hs} extracted from the $S(q)$-fits are in good agreement to the expected volume fractions of the micelles at low $C_{12}mimCl$ concentrations, but they start to deviate slightly at higher SLIL content, where also the data fits become somewhat poorer as indicated by the higher χ^2. The ratio of Z_{eff} and N_{agg} defines the fractional charge α_{mic} on the micellar aggregates. It is seen that α_{mic} of the $C_{12}mimCl$ micelles is nearly constant over the concentration range investigated and it agrees well with the values obtained from the conductivity measurements.

The proceeding of the data fitting of the $C_{14}mimCl/D_2O$ series was the same as for the $C_{12}mimCl/D_2O$ series. Only the base parameters, b and ρ_{core}, were updated to the new SLIL. For this purpose, b was fixed to 1.79 nm obtained from the Tanford equation and assuming a tridecyl-hydrocarbon chain that builds the micelle core. ρ_{core} was fixed to -3.63 $\times$ 10^9 cm^{-2} (cp. Table V-10). The key parameters extracted from the SANS analysis are given in Table V-12 for $C_{14}mimCl$. The trend of the fit parameters for the $C_{14}mimCl$ system is basically the same as for $C_{12}mimCl$. However, some differences between the two SLILs can be identified. First, the absolute scattering intensities for this system are significantly higher than the intensities of the $C_{12}mimCl$ series even at low SLIL concentrations.

wt.%			C$_{14}$mimCl/D$_2$O						
wt.%	0.70	1.24	1.58	2.26	2.78	3.15	3.83	4.23	4.94
c / mol L^{-1}	2.44×10^{-2}	4.31×10^{-2}	5.50×10^{-2}	7.87×10^{-2}	9.68×10^{-2}	1.10×10^{-1}	1.33×10^{-1}	1.47×10^{-1}	1.72×10^{-1}
Φ_{hs} / %	0.96	1.74	2.21	3.06	3.93	4.52	5.76	6.26	6.93
a / nm	1.79	1.85	1.91	1.92	1.95	1.95	2.07	2.07	2.09
b / nm	1.79	1.79	1.79	1.79	1.79	1.79	1.79	1.79	1.79
t / nm	0.44	0.47	0.48	0.47	0.45	0.48	0.45	0.46	0.44
ρ_{shell} / cm^{-2}	5.96×10^{10}	5.99×10^{10}	5.86×10^{10}	5.85×10^{10}	5.65×10^{10}	5.73×10^{10}	5.73×10^{10}	5.76×10^{10}	5.76×10^{10}
N_{agg}	60	64	68	68	71	71	80	80	81
α_{mic}	0.302	0.338	0.353	0.356	0.344	0.359	0.352	0.350	0.357
Z_{eff}	18	22	24	24	24	26	28	28	29
σ_x	0.24	0.24	0.21	0.21	0.23	0.22	0.20	0.19	0.18
χ^2	10.36	38.10	11.82	24.73	27.49	22.56	31.11	40.55	37.10

Table V-12 : Summary of the key parameters extracted from SANS data fitting for aqueous solutions of C$_{14}$mimCl using a core-shell ellipsoid model with a Hayter-Penfold charged sphere structure factor.

The more intensive scattering could be the consequence, of course, of a higher aggregate concentration, but it could be also due to the presence of bigger aggregates. The scattering pattern of the lowest measured $C_{14}mimCl$ concentration can be fitted by a spherical form factor with $a = b = 1.79$ nm and a low polydispersity ($\sigma_x = 0.24$). The corresponding aggregation number of the sphere is $N_{agg} = 60$. This value is in close agreement to the N_{agg} of 57 obtained from the steady-state fluorescence quenching measurement that was performed within the concentration range where the first $C_{14}mimCl$ SANS sample is located. Additionally, the N_{agg} equals the MEM fitting result ($N_{agg} = 61$) of the conductance data in the concentration range where the mixed electrolyte model still describes the conductivity. At higher concentrations ($c > 0.0244$ -mol-L^{-1}), the $C_{14}mimCl$ micelles grow rapidly along the rotational semi-axis and prolate ellipsoidal particles with small length polydispersities (σ_x around 0.20), as in the case of the $C_{12}mimCl$, are formed. a grows from 1.79 nm to 2.09 nm, which corresponds to an increase of the axial ration, a/b, from 1 to 1.17 over the concentration range studied. Additionally, N_{agg} becomes larger in accordance to the theory of micellar growth. These observations are in accordance to the failure of the MEM above concentrations of 1.70×10^{-2} mol L^{-1}. On average, the shell thicknesses were found to be slightly higher than the quantities obtained for $C_{12}mimCl$. The scattering length densities, however, are somewhat smaller for the $C_{14}mimCl$. Again, it must be noted that the parameters observed for shell region contain some uncertainties due to the contrast condition. The fit qualities are similar to those obtained for the $C_{12}mimCl$ series and become also slightly poorer at high particle volume fractions. The condition $\Phi_{exp} \approx \Phi_{fit}$ was fulfilled for all investigated samples, but Φ_{hs} was found somewhat too high at higher SLIL contents, where also χ^2 increases. This was already observed during the data analysis of the $C_{12}mimCl$ scattering patterns, and it seems likely that $S(q)$ is not able to fully describe the present interactions, perhaps because of the increasing anisotropy of the aggregates. Interestingly, this inconsistency of Φ_{hs} was already reported for other SLILs with shorter alkyl-chains in the literature [8, 15]. However, the hard-sphere radius required to fit the SANS data corresponds reassuringly with the overall particle radius. The counterion dissociations of the $C_{14}mimCl$ series are slightly lower

than those α_{mic} of the C_{12}mimCl series and nearly equal to the quantities calculated from the conductivity measurements.

The data evaluation of the C_{16}mimCl/D$_2$O series was performed in the same way as previously described for the C_{12}mimCl/D$_2$O and the C_{14}mimCl/D$_2$O datasets. b and ρ_{core} were set to 2.05 nm and -3.57 $\times$ 10^9 cm^{-2}, respectively. Principally, as can be seen from Table V-13, the C_{16}mimCl follows the same trend as other two imidazolium chlorides. The formed aggregates are spherical at the lowest concentration investigated and become more and more elongated upon increasing SLIL amount forming prolate objects. However, the growth is more pronounced for C_{16}mimCl. The values of a increase from 2.05 nm to 2.43 nm corresponding to $N_{agg} = 79$ and $N_{agg} = 111$, respectively. Contrarily to the previous investigated SLIL systems, the aggregation number calculated from the fluorescence data differs quite a lot from those of obtained from SANS. Since the fluorescence quenching technique only gives accurate N_{agg} for spheres, this discrepancy can be attributed to the significant deviation of the prolate shape of the C_{16}mimCl micelles from spherical geometry which already happens just above the cac. The evolution of the particles as a function of C_{16}mimCl concentration monitored by SANS is in very good agreement to the conclusions drawn from the conductivity data of this system from which a substantial aggregate growth was postulated. The aggregation number obtained by the MEM applied near the *cac* is in better agreement with the SANS data compared to the fluorescence quenching, but the deviation is still high. Again, the significant deviation from the spherical shape just above the *cac* may be responsible for the failure of the MEM, which is only able to describe spherical micelles in solution. The shell thickness is slightly higher compared to the other two C$_n$mimCl systems and equals 0.53 nm on average. The quantities of ρ_{shell} are slightly smaller to those of the C_{14}mimCl series. As for the other two systems, the shell parameters are quite uncertain due to the low scattering length density difference between shell components and D$_2$O. The quality of the SANS fits are very good for samples incorporating low SLIL amounts. At higher concentrations, the fits become increasingly poor, although $\Phi_{exp} \approx \Phi_{fit}$.

wt.%	0.11	0.28	C$_{16}$mimCl/D$_2$O						3.82	4.47
			0.93	1.41	1.73	2.31	2.89	3.38		
c / mol L^{-1}	3.85×10^{-3}	9.13×10^{-3}	2.99×10^{-2}	4.52×10^{-2}	5.52×10^{-2}	7.38×10^{-2}	9.23×10^{-2}	1.08×10^{-1}	1.22×10^{-1}	1.43×10^{-1}
Φ_{hs} / %	0.16	0.38	1.24	2.06	2.49	3.35	4.16	4.80	5.59	6.80
a / nm	2.05	2.08	2.15	2.23	2.27	2.30	2.34	2.37	2.40	2.43
b / nm	2.05	2.05	2.05	2.05	2.05	2.05	2.05	2.05	2.05	2.05
t / nm	0.53	0.53	0.52	0.53	0.52	0.54	0.52	0.54	0.52	0.54
ρ_{shell} / cm^{-2}	5.51×10^{10}	5.51×10^{10}	5.59×10^{10}	5.54×10^{10}	5.52×10^{10}	5.52×10^{10}	5.63×10^{10}	5.53×10^{10}	5.63×10^{10}	5.62×10^{10}
N_{agg}	79	81	87	94	97	100	103	106	108	111
α_{mic}	-	0.272	0.298	0.290	0.287	0.293	0.293	0.298	0.291	0.287
Z_{eff}	-	22	26	27	28	29	30	32	32	32
σ_x	0.18	0.18	0.17	0.18	0.18	0.19	0.18	0.19	0.19	0.20
χ^2	1.98	1.89	10.54	19.96	25.51	33.42	33.51	33.13	32.23	40.12

Table V-13 : Key parameters extracted from SANS data fitting for aqueous solutions of C$_{16}$mimCl using a core-shell ellipsoid model with a Hayter-Penfold charged sphere structure factor.

As for C_{12}mimCl and C_{14}mimCl, Φ_{hs} deviates slightly from the theoretical volume fraction, but R_{hs} seems to be reasonable, since it fully represents the correlation peak. Consequently, the RMSA $S(q)$ may be responsible for the lower quality, which is not able to completely handle the interactions, especially, at high concentrations where prolate ellipsoids are present instead of spheres. The fractions of micelle ionisation are lower than those values observed for C_{12}mimCl and C_{14}mimCl, respectively. In addition, they are slightly smaller than the values obtained from the conductance data of C_{16}mimCl.

The obtained $S(q)$ are given in Figure V-16, As can be seen, $S(0)$ decreases with increasing $C_n$mimCl concentration and simultaneously a maximum $S(q)$ value appears. The latter sharpens and shifts towards higher q-values as the amount of SLIL becomes higher. These observations are equal for each investigated series and they are the consequence of two effects: (i) the isothermal compressibility of the system, which is directly connected to the structure factor, changes and, additionally, (ii) the distance between the micelles diminishes at higher SLIL amounts. Also, pronounced minima and maxima occur at higher q-values, which reflect the higher degree of order present at high concentrations resulting from long-range interactions [95, 111].

A comparison of the SANS results obtained for the C_{12}mimCl and C_{16}mimCl salts with C_{12}TAC and C_{16}TAC can be accomplished using the work of Hayter & Penfold [70]. Some interesting disparities between the two surfactant types can be noted: Basically, the best fits of the scattering patterns of the two alkyltrimethylammonium chloride surfactants were obtained by Hayter et al. assuming spherical geometry in combination with a low polydispersity ($\leq 20\%$) and the RMSA structure factor. In contrast to the results of the $C_n$mimCl systems presented in this work, the spherical model held true (with a receivable polydispersity) even for very high concentrations, up to 0.6 mol L^{-1} for the two 1-alkyl-trimethylammonium chlorides.
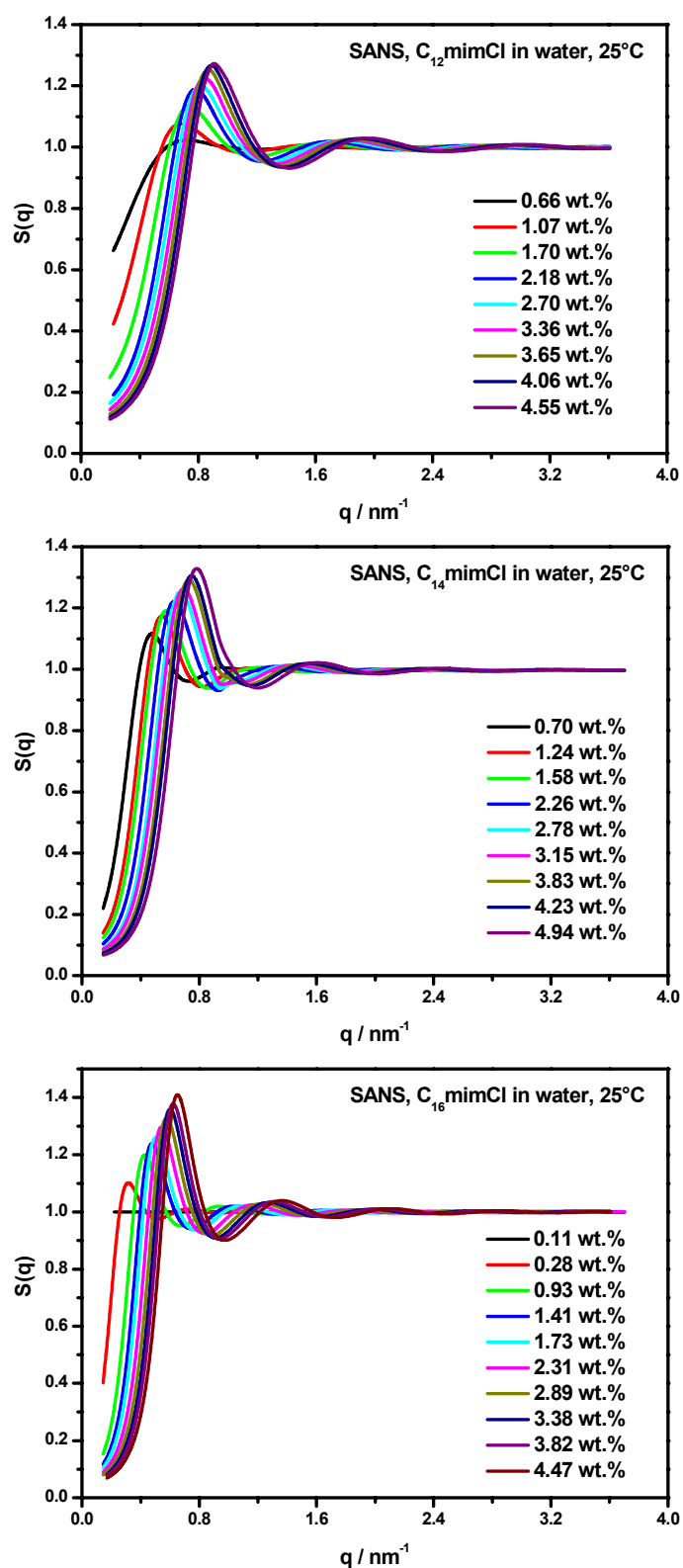
Figure V-16 : Structure factors of the C$_n$mimCl/D$_2$O systems obtained from the Hayter-Penfold structure factor.

While $C_{12}TAC$, as presented by Hayter et. al., showed no tendency to grow over the studied concentration range, a substantial growth of $C_{12}mimCl$ was found just above 0.1 mol L^{-1} in the present work. Indeed, Hayter et al. reported a slight growth of $C_{16}TAC$ spheres upon concentration, but this tendency is much smaller than the behaviour found in the case of $C_{16}mimCl$. The aggregation numbers of the two types of surfactant also differ quite significantly. Both ammonium surfactants, $C_{12}TAC$ and $C_{16}TAC$, have considerably higher N_{agg} than the corresponding SLILs indicating a different packing of the planar imidazolium head groups at the aggregate surface.

The results obtained from the SANS data, in particular, tend to confirm that particle growth (reducing curvature) is more favourable for the imidazolium surfactants than for the ammonium ones. The geometry and the charge delocalisation of the imidazolium head together with a good charge screening by the counterions may be the reason for these observations.

1.7   Bibliography

[1]   D. F. Evans; *The Colloidal Domain: Where Physics, Chemistry, Biology, and Technology Meet, 2nd Edition*. Wiley-VCH, (1998).

[2]   H. Mollet and A. Grubenmann; *Formulation Technology: Emulsions, Suspensions, Solid Forms, 1st Edition*. Wiley-VCH, (2001).

[3]   K. Holmberg; *Handbook of Applied Surface and Colloid Chemistry, Volume 1, 1st Edition*. John Wiley & Sons, (2002).

[4]   K. Holmberg, D. O. Shah and M. J. Schwuger; *Handbook of Applied Surface and Colloid Chemistry, Volume 2, 1st Edition*. John Wiley & Sons (2002).

[5]   M. J. Rosen; *Surfactants and Interfacial Phenomena, 3rd Edition*. Wiley & Sons, (2004).

[6]   D. Myers; *Surfactant Science and Technology, 3rd Edition*. Wiley & Sons, (2005).

[7]   K. O. Evans; Room-temperature ionic liquid cations act as short-chain surfactants and disintegrate a phospholipid bilayer. *Colloids and Surfaces, A: Physicochemical and Engineering Aspects* **274**, 1-3, 11-17 (2006).

[8]   J. Bowers, C. P. Butts, P. J. Martin, M. C. Vergara-Gutierrez and R. K. Heenan; Aggregation Behavior of Aqueous Solutions of Ionic Liquids. *Langmuir* **20**, 6, 2191-2198 (2004).

[9]   Z. Miskolczy, K. Sebok-Nagy, L. Biczok and S. Goektuerk; Aggregation and micelle formation of ionic liquids in aqueous solution. *Chemical Physics Letters* **400**, 4-6, 296-300 (2004).

[10]   J. Sirieix-Plenet, L. Gaillon and P. Letellier; Behaviour of a binary solvent mixture constituted by an amphiphilic ionic liquid, 1-decyl-3-methylimidazolium bromide and water. Potentiometric and conductimetric studies. *Talanta* **63**, 4, 979-986 (2004).

[11]   L. Gaillon, J. Sirieix-Plenet and P. Letellier; Volumetric Study of Binary Solvent Mixtures Constituted by Amphiphilic Ionic Liquids at Room Temperature (1-Alkyl-3-Methylimidazolium Bromide) and Water. *Journal of Solution Chemistry* **33**, 11, 1333-1347 (2004).

[12]   R. Vanyur, L. Biczok and Z. Miskolczy; Micelle formation of 1-alkyl-3-methylimidazolium bromide ionic liquids in aqueous solution. *Colloids and Surfaces, A: Physicochemical and Engineering Aspects* **299**, 1-3, 256-261 (2007).

[13]   B. Dong, N. A. Li, L. Zheng, L. I. Yu and T. Inoue; Surface Adsorption and Micelle Formation of Surface Active Ionic Liquids in Aqueous Solution. *Langmuir* **23**, 8, 4178-4182 (2007).

[14]   J. Wang, H. Wang, S. Zhang, H. Zhang and Y. Zhao; Conductivities, Volumes, Fluorescence, and Aggregation Behavior of Ionic Liquids [C$_4$mim][BF$_4$] and [C$_n$mim]Br (n = 4, 6, 8, 10, 12) in Aqueous Solutions. *Journal of Physical Chemistry B* **111**, 22, 6181-6188 (2007).

[15]   I. Goodchild, L. Collier, S. L. Millar, I. Prokes, J. C. D. Lord, C. P. Butts, J. Bowers, J. R. P. Webster and R. K. Heenan; Structural studies of the phase, aggregation and surface behaviour of 1-alkyl-3-methylimidazolium halide + water mixtures. *Journal of Colloid and Interface Science* **307**, 2, 455-468 (2007).

[16]   O. A. El Seoud, P. A. R. Pires, T. Abdel-Moghny and E. L. Bastos; Synthesis and micellar properties of surface-active ionic liquids: 1-Alkyl-3-methylimidazolium chlorides. *Journal of Colloid and Interface Science* **313**, 1, 296-304 (2007).

[17]   S. Thomaier and W. Kunz; Aggregates in mixtures of ionic liquids. *Journal of Molecular Liquids* **130**, 1-3, 104-107 (2007).

[18]   T. Inoue, H. Ebina, B. Dong and L. Zheng; Electrical conductivity study on micelle formation of long-chain imidazolium ionic liquids in aqueous solution. *Journal of Colloid and Interface Science* **314**, 1, 236-241 (2007).

[19]   H. Kaper and B. Smarsly; Templating and phase behavior of the long chain ionic liquid C_{16}mimCl. *Zeitschrift fuer Physikalische Chemie* **220**, 10-11, 1455-1471 (2006).

[20]   Y. Zhou and M. Antonietti; Preparation of highly ordered monolithic super-microporous lamellar silica with a room-temperature ionic liquid as template via the nanocasting technique. *Advanced Materials* **15**, 17, 1452-1455 (2003).

[21]   Y. Zhou and M. Antonietti; A novel tailored bimodal porous silica with well-defined inverse opal microstructure and super-microporous lamellar nanostructure. *Chemical Communications* **20**, 2564-2565 (2003).

[22]   M. Antonietti, D. Kuang, B. Smarsly and Y. Zhou; Ionic liquids for the convenient synthesis of functional nanoparticles and other inorganic nanostructures. *Angewandte Chemie (Int. Ed.)* **43**, 38, 4988-4992 (2004).

[23]   Y. Zhou and M. Antonietti; A Series of Highly Ordered, Super-Microporous, Lamellar Silicas Prepared by Nanocasting with Ionic Liquids. *Chemistry of Materials* **16**, 3, 544-550 (2004).

[24] B. Smarsly, D. Kuang and M. Antonietti; Making nanometer thick silica glass scaffolds: an experimental approach to learn about size effects in glasses. *Colloid and Polymer Science* **282**, 8, 892-900 (2004).

[25] T. Wang, H. Kaper, M. Antonietti and B. Smarsly; Templating Behavior of a Long-Chain Ionic Liquid in the Hydrothermal Synthesis of Mesoporous Silica. *Langmuir* **23**, 3, 1489-1495 (2007).

[26] H. Kaper, F. Endres, I. Djerdj, M. Antonietti, B. M. Smarsly, J. Maier and Y.-S. Hu; Direct low-temperature synthesis of rutile nanostructures in ionic liquids. *Small* **3**, 10, 1753-1763 (2007).

[27] K. Shinoda, M. Hato and T. Hayashi; Physicochemical properties of aqueous solutions of fluorinated surfactants. *Journal of Physical Chemistry* **76**, 6, 909-914 (1972).

[28] R. G. Laughlin; Aqueous phase science of cationic surfactant salts. *Surfactant Science Series* **37**, Cationic Surfactants, 1-40 (1991).

[29] C. Baar, R. Buchner and W. Kunz; Dielectric Relaxation of Cationic Surfactants in Aqueous Solution. 1. Solvent Relaxation. *Journal of Physical Chemistry B* **105**, 15, 2906-2913 (2001).

[30] K. Lunkenheimer, G. Wienskol and A. J. Prosser; Automated High-Performance Purification of Surfactant Solutions: Study of Convective-Enhanced Adsorption. *Langmuir* **20**, 14, 5738-5744 (2004).

[31] K. Holmberg, B. Jönsson, B. Kronberg and B. Lindman; *Surfactants and Polymers in Aqueous Solution, 2nd Edition*. Wiley & Sons, (2002).

[32] H. B. Klevens; Structure and aggregation in dilute solutions of surface-active agents. *Journal of the American Oil Chemists' Society* **30**, 74-80 (1953).

[33] J. Mata, D. Varade and P. Bahadur; Aggregation behavior of quaternary salt based cationic surfactants. *Thermochimica Acta* **428**, 1-2, 147-155 (2005).

[34] H. Lange; Effect of electrolytes on the micelle formation in colloidal-electrolyte solutions. *Kolloid-Zeitschrift* **121**, 66-71 (1951).

[35] G. Choux and R. L. Benoit; Solvation in dipolar aprotic solvents. Ionic enthalpies of transfer. *Journal of the American Chemical Society* **91**, 23, 6221-6224 (1969).

[36] M. J. Rosen; The relation of structure to properties in surfactants. IV. Effectiveness in surface or interfacial tension reduction. *Journal of Colloid and Interface Science* **56**, 2, 320-327 (1976).

[37] M. J. Rosen, M. Dahanayake and A. W. Cohen; Relationship of structure to properties in surfactants. 11. Surface and thermodynamic properties of N-dodecylpyridinium bromide and -chloride. *Colloids and Surfaces* **5**, 2, 159-172 (1982).

[38] M. I. Viseu, M. M. Velazquez, C. S. Campos, I. Garcia-Mateos and S. M. B. Costa; Structural Transitions in a Bicationic Amphiphile System Studied by Light-Scattering, Conductivity, and Surface Tension Measurements. *Langmuir* **16**, 11, 4882-4889 (2000).

[39] Y. Hayami, H. Ichikawa, A. Someya, M. Aratono and K. Motomura; Thermodynamic study on the adsorption and micelle formation of long chain alkyltrimethylammonium chlorides. *Colloid and Polymer Science* **276**, 7, 595-600 (1998).

[40] S. B. Johnson, C. J. Drummond, P. J. Scales and S. Nishimura; Electrical double layer properties of hexadecyltrimethylammonium chloride surfaces in aqueous solution. *Colloids and Surfaces, A: Physicochemical and Engineering Aspects* **103**, 3, 195-206 (1995).

[41] T. Mehrian, A. de Keizer, A. J. Korteweg and J. Lyklema; Thermodynamics of micellization of n-alkylpyridinium chlorides. *Colloids and Surfaces, A: Physicochemical and Engineering Aspects* **71**, 3, 255-267 (1993).

[42] A. Semmler and H.-H. Kohler; Surface Properties of Alkylpyridinium Chlorides and the Applicability of the Pendant Drop Technique. *Journal of Colloid and Interface Science* **218**, 1, 137-144 (1999).

[43] P. Carpena, J. Aguiar, P. Bernaola-Galvan and C. C. Ruiz; Problems Associated with the Treatment of Conductivity-Concentration Data in Surfactant Solutions: Simulations and Experiments. *Langmuir* **18**, 16, 6054-6058 (2002).

[44] T.-M. Perger and M. Bester-Rogac; Thermodynamics of micelle formation of alkyltrimethylammonium chlorides from high performance electric conductivity measurements. *Journal of Colloid and Interface Science* **313**, 1, 288-295 (2007).

[45] A. Rodriguez, M. Munoz, M. d. M. Graciani and M. L. Moya; Role of the counterion in the effects of added ethylene glycol to aqueous alkyltrimethylammonium micellar solutions. *Journal of Colloid and Interface Science* **298**, 2, 942-951 (2006).

[46] J. J. Galan, A. Gonzales-Perez, J. L. Del Cactillo and J. R. Rodriguez; Thermal parameters associated to micellization of dodecylpyridinium bromide and chloride in aqueous solution. *Journal of Thermal Analysis and Calorimetry* **70**, 1, 229-234 (2002).

[47] R. A. Thakur, A. A. Dar and G. M. Rather; Investigation of the micellar growth of 1-dodecylpyridinium chloride in aqueous solution of phenol. *Journal of Molecular Liquids* **136**, 1-2, 83-89 (2007).

[48] A. Gonzalez-Perez, L. M. Varela, M. Garcia and J. R. Rodriguez; Sphere to rod transitions in homologous alkylpyridinium salts: a Stauff-Klevens-type equation for the second critical micelle concentration. *Journal of colloid and interface science* **293**, 1, 213-221 (2006).

[49] J. J. Galan, A. Gonzalez-Perez, J. A. Seijas, E. Uriarte and J. R. Rodriguez; Effect of counterion on thermodynamic micellar properties of tetradecylpyridinium in aqueous solutions. *Colloid and Polymer Science* **283**, 4, 456-460 (2005).

[50] M. S. Bakshi and I. Kaur; Aggregates of cationic surfactants and anionic polyelectrolytes influenced by bulky head group modifications. *Colloids and Surfaces, A: Physicochemical and Engineering Aspects* **224**, 1-3, 185-197 (2003).

[51]   P. Mukerjee and K. J. Mysels; Critical Micelle Concentrations of Aqueous Surfactant Systems (**NSRDS-NBS 36**). 222 (1971).

[52]   T. Imae and S. Ikeda; Sphere-rod transition of micelles of tetradecyltrimethylammonium halides in aqueous sodium halide solutions and flexibility and entanglement of long rodlike micelles. *Journal of Physical Chemistry* **90**, 21, 5216-5223 (1986).

[53]   T. Imae and S. Ikeda; Characteristics of rodlike micelles of cetyltrimethylammonium chloride in aqueous sodium chloride solutions: their flexibility and the scaling laws in dilute and semidilute regimes. *Colloid and Polymer Science* **265**, 12, 1090-1098 (1987).

[54]   J. Frahm, S. Diekmann and A. Haase; Electrostatic properties of ionic micelles in aqueous solutions. *Berichte der Bunsen-Gesellschaft* **84**, 6, 566-571 (1980).

[55]   R. Zana; Ionization of cationic micelles: effect of the detergent structure. *Journal of Colloid and Interface Science* **78**, 2, 330-337 (1980).

[56]   R. Zielinski, S. Ikeda, H. Nomura and S. Kato; Effect of temperature on micelle formation in aqueous solutions of alkyltrimethylammonium bromides. *Journal of Colloid and Interface Science* **129**, 1, 175-184 (1989).

[57]   N. Muller; Temperature dependence of critical micelle concentrations and heat capacities of micellization for ionic surfactants. *Langmuir* **9**, 1, 96-100 (1993).

[58]   L.-J. Chen, S.-Y. Lin and C.-C. Huang; Effect of Hydrophobic Chain Length of Surfactants on Enthalpy-Entropy Compensation of Micellization. *Journal of Physical Chemistry B* **102**, 22, 4350-4356 (1998).

[59]   G. C. Kresheck and W. A. Hargraves; Thermometric titration studies of the effect of head group, chain length, solvent, and temperature on the thermodynamics of micelle formation. *Journal of Colloid and Interface Science* **48**, 3, 481-493 (1974).

[60]   G. Sugihara and M. Hisatomi; Enthalpy-Entropy Compensation Phenomenon Observed for Different Surfactants in Aqueous Solution. *Journal of Colloid and Interface Science* **219**, 1, 31-36 (1999).

[61]   J. J. Galan, A. Gonzalez-Perez and J. R. Rodriguez; Micellization of dodecyldimethylethylammonium bromide in aqueous solution. Thermal parameters. *Journal of Thermal Analysis and Calorimetry* **72**, 2, 465-470 (2003).

[62]   T. Inoue, B. Dong and L.-Q. Zheng; Phase behavior of binary mixture of 1-dodecyl-3-methylimidazolium bromide and water revealed by differential scanning calorimetry and polarized optical microscopy. *Journal of Colloid and Interface Science* **307**, 2, 578-581 (2007).

[63]   L. T. Okano, F. H. Quina and O. A. El Seoud; Fluorescence and Light-Scattering Studies of the Aggregation of Cationic Surfactants in Aqueous Solution: Effects of Headgroup Structure. *Langmuir* **16**, 7, 3119-3123 (2000).

[64]   P. C. Shanks and E. I. Franses; Estimation of micellization parameters of aqueous sodium dodecyl sulfate from conductivity data. *Journal of Physical Chemistry* **96**, 4, 1794-1805 (1992).

[65]   D. F. Evans; Self-organization of amphiphiles. *Langmuir* **4**, 1, 3-12 (1988).

[66]   B. L. Bales and R. Zana; Characterization of Micelles of Quaternary Ammonium Surfactants as Reaction Media I: Dodeclytrimethylammonium Bromide and Chloride. *Journal of Physical Chemistry B* **106**, 8, 1926-1939 (2002).

[67]   J. Barthel, F. Feuerlein, R. Neueder and R. Wachter; Calibration of conductance cells at various temperatures. *Journal of Solution Chemistry* **9**, 3, 209-219 (1980).

[68]   M. Bester-Rogac, R. Neueder and J. Barthel; Conductivity of sodium chloride in water + 1,4-dioxane mixtures at temperatures from 5 to 35°C. Part 1. Dilute solutions. *Journal of Solution Chemistry* **28**, 9, 1071-1086 (1999).

[69]   J. R. Taylor; *An Introdction to Error Analysis*. VCH, (1988).

[70]   J. B. Hayter and J. Penfold; Determination of micelle structure and charge by neutron small-angle scattering. *Colloid and Polymer Science* **261**, 12, 1022-1030 (1983).

[71]   R. Ranganathan, L. T. Okano, C. Yihwa and F. H. Quina; Growth of Cetyltrimethylammonium Chloride and Acetate Micelles with Counterion Concentration. *Journal of Colloid and Interface Science* **214**, 2, 238-242 (1999).

[72]   A. A. Dar, M. A. Bhat and G. M. Rather; Application of mixed electrolyte massaction model to the micellization of 1-dodecylpyridinium chloride in aqueous medium. *Colloids and Surfaces, A: Physicochemical and Engineering Aspects* **248**, 1-3, 67-74 (2004).

[73]   T. P. McGinnis and E. M. Woolley; Thermodynamic properties of aqueous 1-n-alkanepyridinium chlorides at temperatures from 283.15 K to 343.15 K. *Journal of Chemical Thermodynamics* **29**, 4, 401-422 (1997).

[74]   R. A. Robinson and R. H. Stokes; *Electrolytic Solutions*. Dover Pubn Inc, (1955).

[75]   C. Tanford; Micelle shape and size. *Journal of Physical Chemistry* **76**, 21, 3020-3024 (1972).

[76]   S. T. Handy and M. Okello; The 2-position of imidazolium ionic liquids: substitution and exchange. *The Journal of organic chemistry* **70**, 5, 1915-1918 (2005).

[77]   S. Kossmann, J. Thar, B. Kirchner, P. A. Hunt and T. Welton; Cooperativity in ionic liquids. *Journal of Chemical Physics* **124**, 17, 174506/1-174506/12 (2006).

[78]   J. Dupont; On the solid, liquid and solution structural organization of imidazolium ionic liquids. *Journal of the Brazilian Chemical Society* **15**, 3, 341-350 (2004).

[79]   J. M. G. Barthel, H. Krienke and W. Kunz; *Physical Chemistry of Electrolyte Solutions - Modern Aspects*. Springer, (1998).

[80] D. Rudan-Tasic, C. Klofutar and M. Bester-Rogac; The electric conductivities of aqueous solutions of rubidium and cesium cyclohexylsulfamates, potassium ace-sulfame and sodium saccharin. *Acta Chimica Slovenica* **53**, 3, 324-330 (2006).

[81] J. Barthel and R. Neueder; *DECHEMA Data Series, Volume XII: Electrolyte Data Collection: Conductivites, Transference Numbers, Limiting Ionic Conduc-tivities*. DECHEMA, 1997.

[82] N. J. Turro and A. Yekta; Luminescent probes for detergent solutions. A simple procedure for determination of the mean aggregation number of micelles. *Jour-nal of the American Chemical Society* **100**, 18, 5951-5952 (1978).

[83] T. Asakawa, H. Kitano, A. Ohta and S. Miyagishi; Convenient Estimation for Counterion Dissociation of Cationic Micelles Using Chloride-Sensitive Fluores-cence Probe. *Journal of Colloid and Interface Science* **242**, 2, 284-287 (2001).

[84] R. G. Alargova, I. I. Kochijashky, M. L. Sierra and R. Zana; Micelle Aggrega-tion Numbers of Surfactants in Aqueous Solutions: A Comparison between the Results from Steady-State and Time-Resolved Fluorescence Quenching. *Lang-muir* **14**, 19, 5412-5418 (1998).

[85] E. Roelants and F. C. De Schryver; Parameters affecting aqueous micelles of CTACL, TTAC, and DTAC probed by fluorescence quenching. *Langmuir* **3**, 2, 209-214 (1987).

[86] S. Reekmans, D. Bernik, M. Gehlen, J. van Stam, M. Van der Auweraer and F. C. De Schryver; Change in the micellar aggregation number or in the size distri-bution? A dynamic fluorescence quenching study of aqueous cetyltrimethylam-monium chloride. *Langmuir* **9**, 9, 2289-2296 (1993).

[87] Y. Moroi, R. Humphry-Baker and M. Gratzel; Determination of micellar aggre-gation number of alkylsulfonic acids by fluorescence quenching method. *Jour-nal of Colloid and Interface Science* **119**, 2, 588-591 (1987).

[88] E. W. Anacker, R. D. Geer and E. H. Eylar; Dependence of micelle aggregation number on polar head structure. I. Light scattering by aqueous solutions of de-

cylammonium salts and related surfactants. *Journal of Physical Chemistry* **75**, 3, 369-374 (1971).

[89]   E. W. Anacker and R. D. Geer; Dependence of micelle aggregation number on polar head structure. II. Light scattering by aqueous solutions of decyldiethyl-ammonium bromide and related heterocyclic surfactants. *Journal of Colloid and Interface Science* **35**, 3, 441-446 (1971).

[90]   M. Almgren, K. E. Wang and T. Asakawa; Fluorescence Quenching Studies of Micellization and Solubilization in Fluorocarbon-Hydrocarbon Surfactant Mixtures. *Langmuir* **13**, 17, 4535-4544 (1997).

[91]   S. Causi, R. De Lisi and S. Milioto; Thermodynamic properties of N-octyl-, N-decyl- and N-dodecylpyridinium chlorides in water. *Journal of Solution Chemistry* **20**, 11, 1031-1058 (1991).

[92]   F. J. Millero; Molal volumes of electrolytes. *Chemical Reviews* **71**, 2, 147-176 (1971).

[93]   M. Yamanaka and S. Kaneshina; Volume behavior of mixed micelles of dodecyltrimethylammonium chloride and bromide. *Journal of Solution Chemistry* **20**, 12, 1159-1167 (1991).

[94]   R. De Lisi, E. Fisicaro and S. Milioto; Thermodynamic properties and conductivities of some dodecylsurfactants in water. *Journal of Solution Chemistry* **17**, 11, 1015-1041 (1988).

[95]   P. Lindner and T. Zemb; *Neutron, X-Ray and Light Scattering: Introduction to an Investigative Tool for Colloidal and Polymeric Systems*. Elsevier Science Publishing, (1991).

[96]   P. Lindner and T. Zemb; *Neutrons, X-Rays and Light: Scattering Methods Applied to Soft Condensed Matter*. North-Holland Elsevier Science Publishers B.V., (1991).

[97] S. H. Chen; Small angle neutron scattering studies of the structure and interaction in micellar and microemulsion systems. *Annual Review of Physical Chemistry* **37**, 351-399 (1986).

[98] J. B. Hayter and J. Penfold; Self-consistent structural and dynamic study of concentrated micelle solutions. *Journal of the Chemical Society, Faraday Transactions 1: Physical Chemistry in Condensed Phases* **77**, 8, 1851-1863 (1981).

[99] D. R. Lide; *CRC Handbook of Chemistry and Physics, 83rd Edition*. CRC Press (2002).

[100] Y. Chevalier and T. Zemb; The structure of micelles and microemulsions. *Reports on Progress in Physics* **53**, 3, 279-371 (1990).

[101] K. L. Gawrys and P. K. Kilpatrick; Asphaltenic aggregates are polydisperse oblate cylinders. *Journal of colloid and interface science* **288**, 2, 325-334 (2005).

[102] S. Vass, J. Plestil, S. Borbely, T. Gilanyi and H. Pospisil; Aggregation number of ionic micelles from SANS. Problems and limits. *Journal of Molecular Liquids* **72**, 1/3, 69-83 (1997).

[103] V. K. Aswal and P. S. Goyal; Role of counterion distribution on the structure of micelles in aqueous salt solutions: small-angle neutron scattering study. *Chemical Physics Letters* **357**, 5,6, 491-497 (2002).

[104] V. K. Aswal and P. S. Goyal; Selective counterion condensation in ionic micellar solutions. *Physical Review E: Statistical, Nonlinear, and Soft Matter Physics* **67**, 5-1, (2003).

[105] D. Varade, T. Joshi, V. K. Aswal, P. S. Goyal, P. A. Hassan and P. Bahadur; Effect of salt on the micelles of cetylpyridinium chloride. *Colloids and Surfaces, A: Physicochemical and Engineering Aspects* **259**, 1-3, 95-101 (2005).

[106] J. S. Pedersen, D. Posselt and K. Mortensen; Analytical treatment of the resolution function for small-angle scattering. *J. Appl. Cryst.* **23**, 321-333 (1990).

[107] I. Grillo; Effect of instrumental resolution and polydispersity on ideal form factor in Small-angle Neutron Scattering. *ILL Technical Report* **ILL01GR08T**, 1-20 (2001).

[108] J. Kohlbrecher; Software package SASfit for fitting small-angle scattering curves. *Paul Scherrer Institute* (2008).

[109] V. K. Aswal and P. S. Goyal; Role of counterion distribution on the structure of micelles in aqueous salt solutions: small-angle neutron scattering study. *Chemical Physics Letters* **357**, 5,6, 491-497 (2002).

[110] S. S. Berr, E. Caponetti, J. S. Johnson, Jr., R. R. M. Jones and L. J. Magid; Small-angle neutron scattering from hexadecyltrimethylammonium bromide micelles in aqueous solutions. *Journal of Physical Chemistry* **90**, 22, 5766-5770 (1986).

[111] O. Glatter; *Lecture: Streumethoden; Department of Physical Chemistry, University of Graz, Austria*. (1993).

[112] P. D. T. Huibers; Quantum-Chemical Calculations of the Charge Distribution in Ionic Surfactants. *Langmuir* **15**, 22, 7546-7550 (1999).

[113] P. D. T. Huibers and P. T. Jacobs; The effect of polar head charge delocalization on micellar aggregation numbers of decylpyridinium salts, revisited. *Journal of Colloid and Interface Science* **206**, 1, 342-345 (1998).

[114] T. I. Morrow and E. J. Maginn; Molecular Dynamics Study of the Ionic Liquid 1-n-Butyl-3-methylimidazolium Hexafluorophosphate. *Journal Title:Journal of Physical Chemistry B* **106**, 49, 12807-12813 (2002).

[115] S. Shimizu and O. A. El Seoud; Synthesis and Aggregation of Benzyl(2-acylaminoethyl)dimethylammonium Chloride Surfactants. *Langmuir* **19**, 2, 238-243 (2003).

2   Aggregation of SLILs in solution of room temperature molten salts

Amphiphiles are well-known to self-assemble into a large variety of nano-, micro-, and macro-structures, which are held together by cooperative non-covalent interactions. Beside water that is clearly recognized to promote self-aggregation of surfactants, only a small number of alternative solvents were identified in which self-assembled structures can exist [1]. Generally, protic solvents including hydrazine [2, 3], low molecular weight amides (e.g. acetamide, formamide) [4-6], and glycols [6] were found (beside water) as amphiphile self-assembly media during the last decades. From these studies, the conclusion was drawn that the ability of a solvent to form multiple hydrogen-bonds – leading to solvent structure – may be an important feature for promoting self-assembly [1]. This thesis is based on the fact that aggregation of surfactants is always accompanied by a loss of freedom (translational and rotational) while amphiphile monomers transfer from the bulk solvent into the formed aggregates. Therefore, the entropic driving force is negative in part and makes an unfavourable contribution to the free energy of micellization as well as to other aggregation processes. In structured solvents, however, there is weak van-der-Waals bonding between the solvent molecules and the surfactant hydrocarbon chains and consequently, a layer of structured solvent surrounds the hydrocarbon chains. During the aggregation process, the solvent-hydrocarbon interactions are reduced and thus the entropy increases. Therefore, the driving force for interactions between surfactant molecules must result from the intrinsic form of the enthalpy in hydrogen-bonding solvents [1, 7-9]. On the other hand, a sufficient high cohesive energy was also postulated to be a further crucial factor for a solvent to promote self-aggregation of surfactants. The Gordon parameter, which can be understood as a measure of the cohesiveness of liquids, is defined by the surface tension and the molar volume of the solvent. It was supposed by Evans et al. that only solvents with a Gordon parameter G_p greater than 1.3 J m^{-3} are able to promote aggregation of surfactants [1, 9].

In addition to non-aqueous molecular solvents in which self-assembly of surfactants has been observed, aggregation of ionic amphiphiles in ethylammonium nitrate – a

room-temperature molten salt – was reported over twenty years ago by Evans et al. [7, 10]. Furthermore, Evans et al. showed the formation of lyotropic smectic phases by lipids in this low melting fused salt and the authors related these findings to the ability of EAN to form a three-dimensional hydrogen structure in the liquid state similar to that of water as well as to the sufficient high Gordon parameter in accordance to the concept previously described [11]. Although great attention has been paid to the investigation of ILs and RTMS by many scientists concerning the use of these substances as reaction media for chemical synthesis [12] or as compounds in electrochemical devices [13-21], only few studies have been emerged following the pioneering work of Evans et al. However, the number of publications in which RTMS act as solvent media for amphiphilic molecular self-assembly has increased rapidly during the last few years. Especially, protic ionic liquids (PILs), to which also EAN belongs, were identified as suitable non-aqueous media for the formation of lyotropic liquid crystalline phases by common ionic and non-ionic surfactants [22-26]. Beside, these studies, which focus the high concentration range of surfactant/PIL mixtures, also micellar systems formed in EAN were reported [27, 28]. In addition, self-assembly in aprotic imidazolium based RTMS was shown by several workgroups in the case of solubilised block copolymers [29] and common surfactants [28, 30-36], respectively. Although more and more investigations deal with surfactant aggregation in RTMS, this field is almost unexplored [36]. Therefore, the study of micelle formation in RTMS presents an upcoming research direction in ionic liquid science, which could open new applications in micellar catalysis, solvent enhancement for apolar entities and manufacturing of new nanomaterials. But also from a fundamental point of view, the investigation of surfactant aggregation in molten salts is a very important topic considering the fact that nearly all of the RTMS in which amphiphilic self-assembly was satisfactorily shown possess Gordon parameters significantly lower than the value of 1.3 J m^{-3} previously postulated by Evans et al. as the minimum value required for a solvent to have sufficient driving force to promote the aggregation of an amphiphile [1, 23]. It seems likely that the old claim of Evans et al. that a solvent must have a 3-D-structure similar to water in addition to a sufficient value of the Gordon parameter has to be updated to the recent situation.

Beside the work of Evans et al., the more recent investigations of Rico and Lattes also focused surfactant aggregation in non-aqueous media. Mainly, they used formamide and its analogues as water replacement. From their examinations, they postulated that a water substitute should have the following properties in order to support amphiphilic self-assembly in solution: (i) A high polarity (high static permittivities), (ii) a high solvating power, and (iii) highly structured [65]. In order to evaluate, whether a solvent is suitably structured, Rico and Lattes applied the concept of Dack et al., which is based on two main parameters, the cohesion energy density, *ced*, and the internal pressure, P_i [66]. By considering the physicochemical properties of ionic liquids, it becomes clear that these substances meet not all requirements given by Rico and Lattes for structure promoting solvents. Indeed, molten salts possess high solvating power for both inorganic and organic compounds [67], but they have only relatively low static permittivities, which normally range in the order of magnitude as those of linear alcolohls (between 6 and 30) with carbon numbers of 3 to 9 [40, 41, 68]. So, basically, the same problem arises as already for the theory of Evans: The basic prerequisites for self-assembly promoting solvents postulated by Rico and Lattes cannot be generalized to RTMS. It seems likely that the discrepancies of the two concepts in connection with ionic liquid featured colloidal systems may result from the fact that nearly all investigations, which were used to develop these two theories, are based on surfactant systems containing molecular solvents rather than RTMS.

For this reason, concerning both, the fundamental as well as the applicable aspects, the following chapter deals with the investigation of new formulated micellar RTMS solutions formed by the already presented SLILs (C_{12}mimCl, C_{14}mimCl, and C_{16}mimCl) and a RTMS as solvent. For the latter, two different salts were chosen: (i) the well-known protic ionic liquid, ethylammonium nitrate, and (ii) an aprotic imidazolium based ionic liquid, the 1-butyl-3-methyl-imidazolium tetrafluoroborate. As can be seen in Table V-14, the solvent properties of these two ionic liquids differ quite a lot from each other with regard to their polarities and cohesiveness.

Solvent	$E_{T(30)}$ kcal mol^{-1}	σ mN m^{-1}	V_m cm^{-3} mol	G_p J m^{-3}	ced J cm^{-3}	P_i J cm^{-3}	ced–P_i J cm^{-3}	n	ε_r
water	63.1[a]	71.99[c]	18.07[f]	2.74[g]	2303[h]	151[h]	2152	0.07	78.4[l]
EAN	61.6[a]	46.30[d]	89.30[f]	1.05[g]	980[i]	n.a.	n.a.	-	26.3[m]
bmimBF$_4$	42.3[b]	43.60[e]	186.72[f]	0.76[g]	673[j]	492[k]	181	0.73	11.7[n]

Table V-14: Solvent properties of the used RTMS at 25°C. The corresponding water values are also presented for comparison. [a]Ref. [25], determined by Reichardt's dye. [b]Ref. [37], determined by Reichardt's dye. [c]Ref. [38]. [d]Refs. [23-25]. [e]Ref. [39]. [f]calculated by $V_m = M / d$; for the used densities see Ref. [38] (water), and this work. [g]calculated by $G = \sigma / V_m^{1/3}$. [h]Ref. [66]. [i]Surface tension (obtained in this work) was used for the calulation of ΔH_{vap} following the concept of Ref. [69]; ΔH_{vap} was applied for the calulation of ced. [j]ΔH_{vap} was used for the calulation of ced; ΔH_{vap} from Ref. [69]. [k]Calculated from α_p and β_T; these parameters were obtained by fitting the experimental data of Ref. [70] with a second order polynomial and subsequent extrapolation to 0.1 MPa. [l]Ref. [38]. [m]Ref. [40]. [n]Ref. [41].

Concerning the $E_{T(30)}$ values, EAN has only a slightly lower polarity as water, but the polarity difference is much more pronounced if the relative static permittivities of the two compounds are compared. It is well known that polarity is not rigorously defined, and polarity scales depend on the experimental method used. In the case of the $E_{T(30)}$ polarity scale for example, the obtained polarities are considerably affected by the used solvatochromic Reichardt's betaine dye. Because of its structure (cp. Figure II-4), the solvatochromic shift of the betaine probe is strongly influenced by the hydrogen-bond donor ability of the solvent, which stabilizes the ground state more than the excited state. The $E_{T(30)}$ scale is therefore considerably, but not exclusively, a measure of hydrogen-bonding acidity of the solvent system. For this reason, the similar $E_{T(30)}$ values of water and EAN are in good agreement with the proposed ability of EAN to develop hydrogen-bonds and to form a 3-D-structure similar to that of water [42]. However, by comparison of ε_r, it is evident that EAN is less polar than water. Additionally, it possesses a quite lower cohesive energy than water reflected by the lower Gordon parameter, i.e. EAN is lower structured than water. Note that the value of G_p for EAN, which was calculated from the available literature data of the density and surface tension, is about 0.4 J m^{-3} smaller than the value originally published by Evans et al. [9], but it agrees very well with the quantity given by Greaves et al. [23, 24, 26]. An explanation for this discrepancy is not evident from the literature. By following the $E_T(30)$ parameter as well as

the ε_r of bmimBF$_4$ presented in Table V-14, it is seen that this RTMS possesses a considerably lower polarity compared to water as well as to EAN. In addition, bmimBF$_4$ has the lowest G_p parameter, which is about 4 times lower than that of water and 0.25 J m^{-3} lower than the corresponding value of EAN, respectively. Therefore, the cohesion within this liquid is very low and consequently it is sparsely structured.

The concept of Lattes and Rico involves the usage of the cohesion energy density *ced* and the internal pressure P_i for the classification of solvent structuring [65]. In principal, the same conclusion can be drawn from these two parameters as previously from the $E_{T(30)}$ value and G_p (cp. Table V-14). Since the *ced* parameter stands for the total strength of the intermolecular solvent structure, the high *ced* value of water represents its highly structured nature. In contrast, the *ced* of both RTMS are considerably lower and consequently, they are less structured. However, in comparison to conventional solvents , the *ced* of EAN is still quite high (cp. Table II-11). Contrary to the *ced*, an overall comparison between the P_i parameters of the RTMS and that of water is not possible due to lack of information in the public literature about the thermal expansion coefficients, α_p, and the isothermal compressibilities of EAN, β_T, which must be known for the estimation of P_i (cp. Chapter II.2.3.6). For bmimBF$_4$, however, it is evident that its P_i is about 3 times higher than the value of water. Because of the fact that P_i is mainly a reflection of dispersion and dipole-dipole interactions within a solvent, it is clear that the cohesion resulting from polar/non-polar interactions between the molecules are significantly higher for bmimBF$_4$ than for water, which is in agreement to the nature of RTMS [67]. If one compares the *ced* and P_i of bmimBF$_4$ with literature data of conventional solvents, one sees that they agree well with the corresponding values of DMF, which is also an aprotic polar solvent. For EAN, the *ced* is similar to that of ethane-1,2-diol, a protic polar solvent, which is also capable of hydrogen bonding due to the presence of two hydroxyl groups. The similarity of EAN and ethane-1,2-diol concerning their solvent parameters is further manifested, if one assumes that the P_i of EAN is similar to that of bmimBF$_4$, i.e. in the range 300-600 J cm^{-3} (cp. Table II-11). Note that Singh and Kumar just recently reported P_i values for several RTMS. It can be seen from these values that P_i ranges from around 350-600 J cm^{-3} for RTMS [68]. So, this as-

sumption seems quite rational. The contribution of specific solvent/solvent interactions, e.g. hydrogen bonding, to the cohesive energy density of a solvent can be calculated from the difference of *ced* and P_i. Taking the latter into account, it is quite obvious that bmimBF$_4$ exhibits only weak hydrogen bonding, whereas in the case of EAN, if its P_i value is assumed to be in the order of magnitude as that of bmimBF$_4$, hydrogen bonding significantly contributes to the *ced* of this protic molten salt. Again, this is in good agreement to the high $E_{T(30)}$ value of ethylammonium nitrate and further to the presumption of Evans et al.

Keeping in mind the solvent parameters, the two solvent RTMS were chosen particularly because of their significant different solvent properties, as this addresses the central issue of the role of hydrogen-bonding as well as the role of cohesiveness for the promotion of self-assembly. Furthermore, bmimBF$_4$ was chosen, since its combination with the long-chain imidazolium chlorides gives a new challenge in imidazolium-IL (im-IL) science, in which the investigation of im-IL/im-IL-mixtures is a very recent topic. Up to now, the study is only limited to electrochemical investigations, where different RTMS/1-propyl-3-methy-imidazolium iodine-mixtures were studied in consideration of their application in dye-sensitized solar cells. Here, two im-RTMS were mixed in order to reduce the viscosity and to increase the transport properties of the pure im-IL that way [43-45]. Contrarily to the latter study in which the physical property (the viscosity) of an imidazolium ionic liquid was adjusted, the main interest of the present work is the formulation of colloidal IL/RTMS-systems obtained by admixing a structuring imidazolium ionic liquid (the already presented SLILs) to a RTMS acting as solvent. With other words, this work is focused on the possibility to form micellar aggregates in two RTMS (ethylammonium nitrate and 1-butyl-3-methyimidazolium tetrafluoroborate) by admixing SLILs. The investigations included DSC, surface tension, density, SAXS, and SANS measurements. From these techniques, the solubility behaviour, the *cac*s, the partial molar volumes, and structural information of the formed SLIL aggregates in the two RTMS were obtained. Additionally, thermodynamic parameters including the surface excess concentrations, the minimum areas occupied per SLIL molecules at the RTMS/gas interface, the contributions of the SLIL discrete segments to

Gibbs free energies of adsorption, and the Gibbs free energies of micellization were calculated from the surface tension isotherms measured for the SLIL/EAN- and SLIL/bmimBF$_4$-systems, respectively, at 25°C and 40°C.

Beside the investigations at ambient and near ambient temperature, further studies of the SLIL/RTMS-mixtures were carried out at higher temperatures (up to 150°C) in order to verify the high-temperature stability of the formulated systems taking advantage of the wide temperature range, over which ionic liquids are liquid and stable. Since structures due to electrostatic interactions do not show pronounced temperature dependence, it can be expected that the micellar aggregates also persist at such high temperatures. Especially in nanoscale technology, where pure ionic liquids are already used as high-temperature templates for the synthesis of nano-and nano-structured materials [46], such high-temperature stable colloidal ionic liquid mixtures may be also very interesting as new matrix for nanomaterial design. For this reason, the possibility for the design of ionic liquid based micellar systems, which extend the limited temperature range of aqueous colloidal systems, was another central issue in the present work.

2.1   Solubility behaviour

In order to get an idea of the solubility of the different SLILs in EAN and bmimBF$_4$, respectively, various samples with varying SLIL contents (up to 25 wt.%) were prepared and homogenized under agitation at elevated temperature. Then, the fused salt-mixtures were cooled and slowly heated again. The temperature, at which the last amount of surfactant dissolved, was determined by visual inspection. The heating and cooling cycles were repeated several times. It was found that all SLIL/EAN-systems (SLIL = C$_{12}$mimCl, C$_{14}$mimCl, and C$_{16}$mimCl) form clear isotropic solutions within this temperature range indicating a very good miscibility between the imidazolium chlorides and ethylammonium nitrate. When bmimBF$_4$ was used as solvent, the same results were observed, except for C$_{16}$mimCl, which already phase separated at a concentration of about 0.3 wt.% at 25°C. By optical investigation, the solubility boundary of the C$_{16}$mimCl/bmimBF$_4$-system was roughly estimated to be between 36-38°C. Figure V-17 exemplarily shows the formulated SLIL/RTMS-mixtures with a SLIL con-

centration of 10 wt.%. As can be seen, the 10 wt.% C_{16}mimCl/bmimBF$_4$-mixture is turbid at 25°C and isotropic at 40°C.
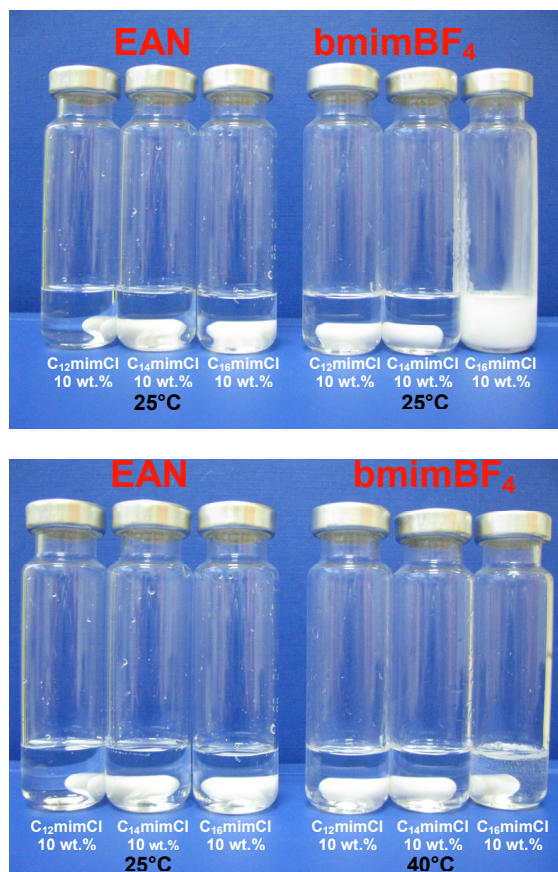
Figure V-17: Formulated SLIL/RTMS-mixtures with a SLIL concentration of 10 wt.%. As can be seen, the 10 wt.% C_{16}mimCl/bmimBF$_4$-mixture is turbid at 25°C and isotropic at 40°C.

For an accurate estimation of the C_{16}mimCl/bmimBF$_4$-solubility borderline, DSC measurements were carried out. Figure V-18 shows the heat flow/temperature plots of five C_{16}mimCl/bmimBF$_4$-mixtures with different SLIL concentrations. No solubility temperature for the C_{16}mimCl/bmimBF$_4$ could be determined by DSC below 5 wt.% of C_{16}mimCl because of a too small heat flow during solubilisation of the SLIL. Defined endothermic peaks indicating the solubilisation of C_{16}mimCl were obtained for samples consisting of at least 5 wt.% of SLIL. The respective temperatures T_{on}, where the SLIL began to solubilise, were calculated by onset analysis of each DSC up-scan.
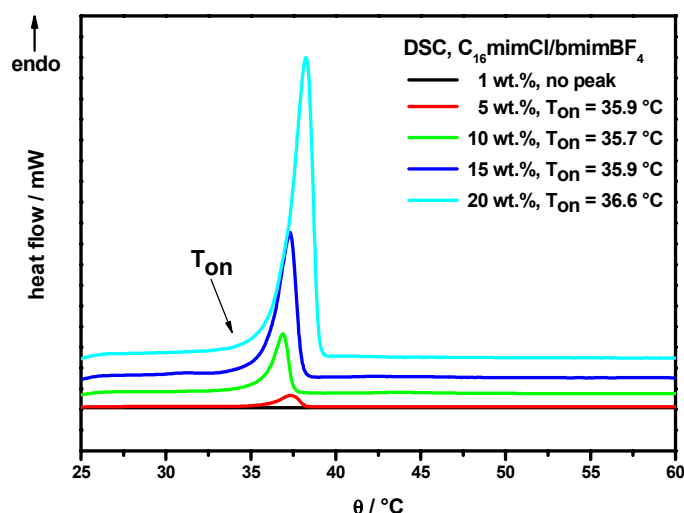
Figure V-18 : DSC scans of different C₁₆mimCl/bmimBF₄-solutions. The curves are shifted for better comparison. All calculated T_{on} are given in the legend.

The quantities of T_{on} were estimated to be 35.9°C, 35.7°C, 35.9°C, and 36.6°C for the concentrations of 5 wt.%, 10 wt.%, 15 wt.%, and 20 wt.%, respectively. The extracted temperatures of the samples with different $C_{16}mimCl$ content in $bmimBF_4$ differ only slightly from each other. This solubility behaviour is similar to that of amphiphiles in water which also exhibit certain lower solubility temperatures denoted as Krafft boundary [47-49].

Taking into account these results of the solubility investigations, all following low temperature measurements were carried out at 25°C and at 40°C for the SLIL/EAN- and the SLIL/bmimBF₄-systems, respectively.

2.2   Surface tension: *cac*, Γ_{max} , A_{min} , ΔG^{0}_{mic}

Surface tension measurements of the $C_n mimCl$ homologues in EAN and $bmimBF_4$ were carried out in order to get a picture of the aggregation behaviour of the SLILs in these media. The surface tension isotherms observed for the SLIL/RTMS-systems have a similar appearance to those obtained for the $C_n mimCl$ series in water. As can be seen in Figure V-20 and Figure V-21, σ decreases for all SLIL/RTMS-systems as the SLIL concentration increases indicating the SLIL adsorption at the gas/solution interface. Then, a final value is reached, which remains constant with further SLIL addi-

tion. No minima in the surface tension isotherm were observed which underlines the high purity of the SLILs and the solvent RTMS, respectively. Estimates for the *cac*s of all investigated SLIL/RTMS-systems are listed in Table V-15.

SLIL / solvent RTMS	cac / mmol L^{-1}	$\Gamma_{max} \times 10^{-6}$ / mol m^{-2}	A_{min} / nm	ΔG^0_{mic} / kJ mol^{-1}
C$_{12}$mimCl/EAN, 25°C	88.7	2.34	0.71	-11.97
C$_{14}$mimCl/EAN, 25°C	38.9	2.42	0.69	-14.02
C$_{16}$mimCl/EAN, 25°C	13.4	3.12	0.53	-16.66
C$_{12}$mimCl/bmimBF$_4$, 40°C	251.2	3.48	0.48	-7.94
C$_{14}$mimCl/bmimBF$_4$, 40°C	131.5	3.22	0.52	-9.62
C$_{16}$mimCl/bmimBF$_4$, 40°C	81.3	2.67	0.62	-10.87

Table V-15: Relationship between SLIL/RTMS-system and *cac*, surface excess concentration Γ_{max} **, area at the liquid/gas interface** A_{min} **, and Gibbs free energy of micellization** ΔG^0_{mic} **.**

The *cac*s of the SLILs in the two RTMS are considerably higher than the respective values observed in aqueous solution. This observation is in keeping with the results of Evans et al. and other workgroups, who found that *cac*s of classical surfactants in ionic liquids are generally higher than in water [7, 10, 27, 31-33, 35, 36, 50]. Of course, this is attributed to the less structured nature of the RTMS compared to water and to their lower polarities. As presented in Figure V-19, plots of *log(cac)* vs. carbon number *n* yield straight parallel lines for the two classes of solvent RTMS (R$_{EAN}$= 0.998, R$_{bmimBF4}$= 0.997). A fit of the data to the Klevens equation gives the constants 1.43 (*A*), 0.21 (*B*) and 0.85 (*A*), 0.12 (*B*) for the EAN-series and bmimBF$_4$-series, respectively. By comparison with the values of 1.49 (*A*) and 0.28 (*B*) obtained for the C$_n$mimCl homologues in water, it can be seen that the effect of increasing chain length is greater in water than in RTMS. The parameters of the EAN-series are in good agreement to those obtained by Evans et al. for common C$_n$TAB and C$_n$PyBr surfactants in EAN [7]. It seems likely that the only slight difference between the Klevens constants of the aqueous SLIL-system and the SLIL-EAN-system may be attributed to the similar structuring of the two solvents concerning the 3-D-hydrogen-bonded network [42]. Contrarily, the Klevens-parameters of the bmimBF$_4$-system are about 2 times lower, which could be referred to the lower cohesive density of this RTMS. It should be noted that the temperature employed in the

bmimBF$_4$ experiments was slightly higher (40°C) than that used for the corresponding studies in water and EAN (25°C), respectively. This may slightly influence the Klevens-constants, but by far to a lesser extent than observed.
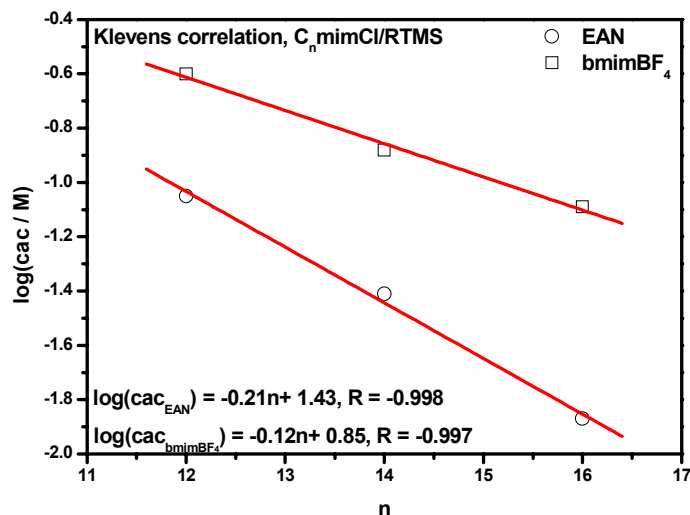
Figure V-19: Dependence of the *cac*s on the SLIL chain length *n* in the two different solvent RTMS and the Klevens fits.

Γ_{max} can be obtained from the surface tension isotherms by the usage of the Gibbs equation. However, the dissociation degree of the species, which is adsorbed at the interface, must be known in the case of an ionic surfactant. Contrary to the situation of an ionic surfactant solubilised in water, which is considered as completely dissociated into cations and anions below the *cac*, it seems more likely to describe the solubilization status of an ionic surfactant in a RTMS as completely associated due to the ionic nature of the fused salt [7]. Therefore, Γ_{max} of the present systems were calculated using the Gibbs equation for non-ionic surfactants solubilised in water, which assumes completely associated species. Γ_{max} and the corresponding A_{min} for all SLIL/RTMS-systems are presented in Table V-15. The values of A_{min} for the C$_n$mimCl/EAN series are slightly smaller than the respective values of the aqueous systems. As in water, they decrease with the alkyl chain length. Contrarily, A_{min} of the SLIL/bmimBF$_4$-series increases with SLIL chain length indicating a different packing mechanism at the surface. The areas at the liquid/gas interface obtained for the SLIL/bmimBF$_4$ series are in the same order of magnitude as in the case of the corresponding EAN-systems.
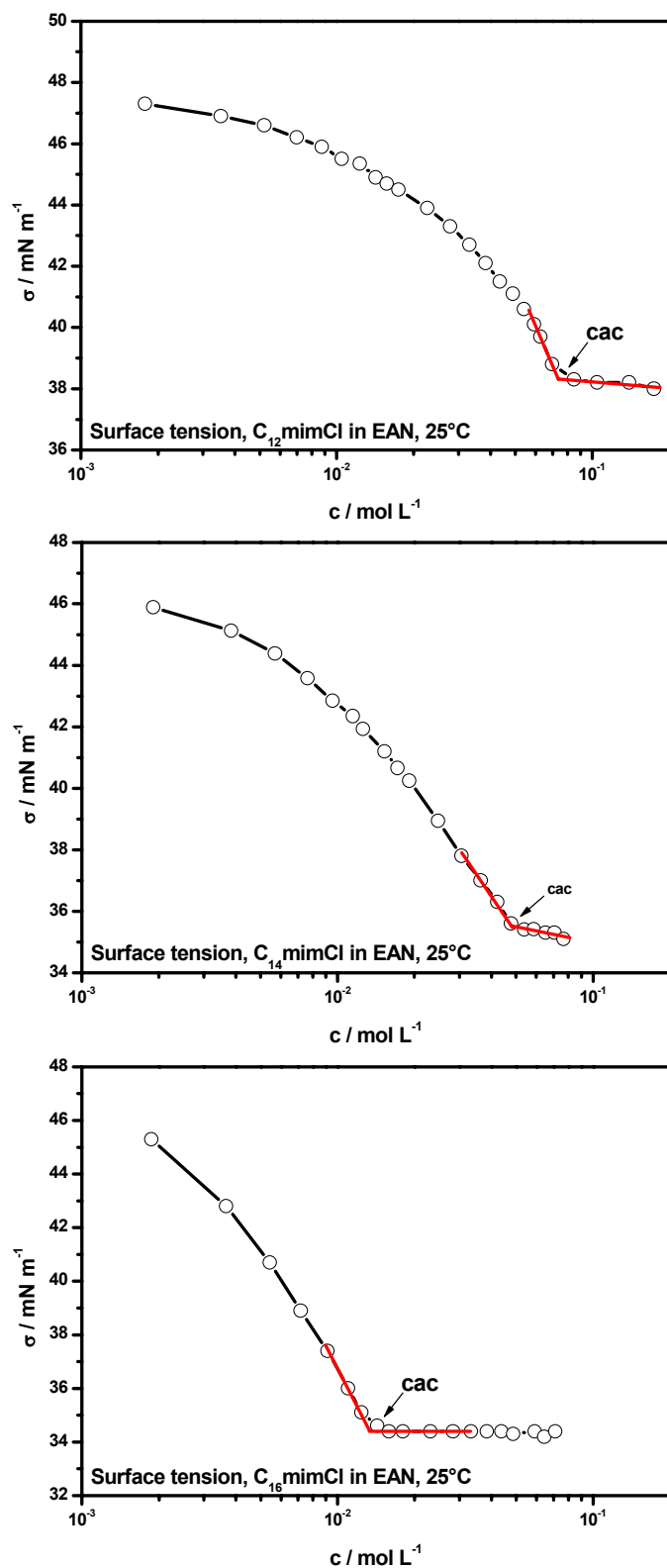
Figure V-20: Surface tensions isotherms measured for the SLIL/EAN-systems at 25°C. The *cac*s are indicated by red straight lines.
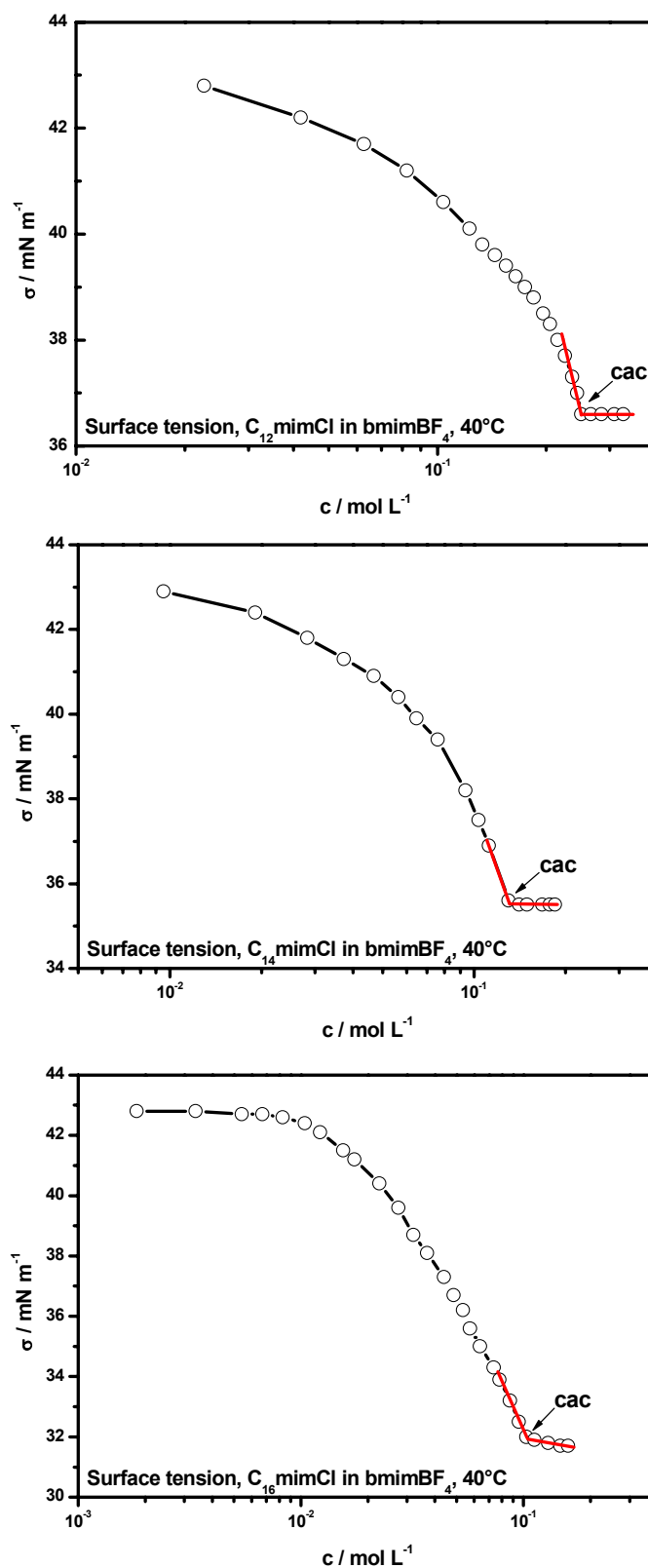
Figure V-21: Surface tensions isotherms measured for the SLIL/bmimBF₄-systems at 40°C. The *cac*s are indicated by red straight lines.

The influence of the solvent on micellization is also indicated from the contribution of additional methylene groups to micellization in the different solvents. In order to quantify how the different solvent RTMS affect the micellization process, the Gibbs energy of micellization, and additionally, the free energy of transfer of a methylene group from the solvent to the interior of the aggregate were calculated from the change of *cac* with chain length of the SLILs. However, this requires the use of a model such as the phase separation or the equilibrium model for micelle formation. For micellization in RTMS, it is not completely clear which model is appropriate, but it seems that the phase separation model, which takes no dissociation of the micellar aggregates into account, is the most suitable, since the very high ionic strength of the RTMS will result in a micellar aggregate completely surrounded by a shell of counterions [7]. The calculated values of ΔG^0_{mic} for the investigated systems are given in Table V-15. One can see that the free energies of micellization for both SLIL/RTMS series are considerably less negative than the respective quantities in water. For this reason, the micellization process of the SLILs is less spontaneous in the fused salts compared to water. Furthermore, all ΔG^0_{mic} observed for the SLIL/bmimBF$_4$ series are still higher than those for the EAN-systems. The calculated values of the free energy for the transfer of a methylene group from the bulk solution into the micelle, $\Delta G^0_{mic}(-CH_2-)$, are -1.17 kJ mol^{-1} and -0.73 kJ mol^{-1} for the EAN and bmimBF$_4$ series, respectively. In contrast, a value of -3.02 kJ mol^{-1} in water was obtained. The results of $\Delta G^0_{mic}(-CH_2-)$ for the SLILs in EAN and in water agree well with the values of -1.55 kJ mol^{-1} (EAN) and -2.85-kJ-mol^{-1} (water) reported by Evans et al. for the transfer of a –CH$_2$– from the solvent to the micelle at 25°C [7]. The solvophobic effect explains qualitatively the dependence of ΔG^0_{mic}, and therefore on $\Delta G^0_{mic}(-CH_2-)$, on the bulk phase composition. Figure V-22 correlates the G_p and the *ced* of the solvents in which the self-assembly of the SLILs were investigated with the calculated values of ΔG^0_{mic} for each system. It should be remarked that the *cac*s of the SLIL/bmimBF$_4$ series was estimated at 40°C, which may have led to a slight underestimate of ΔG^0_{mic} in comparison to the water and EAN-systems, respectively. It seems likely that the spontaneity of self-assembly for the SLILs (and therefore also very probably for a homologous series of common ionic surfactants)

in fused salts depends linearly on the Gordon parameter based on the cohesive energy density of water.
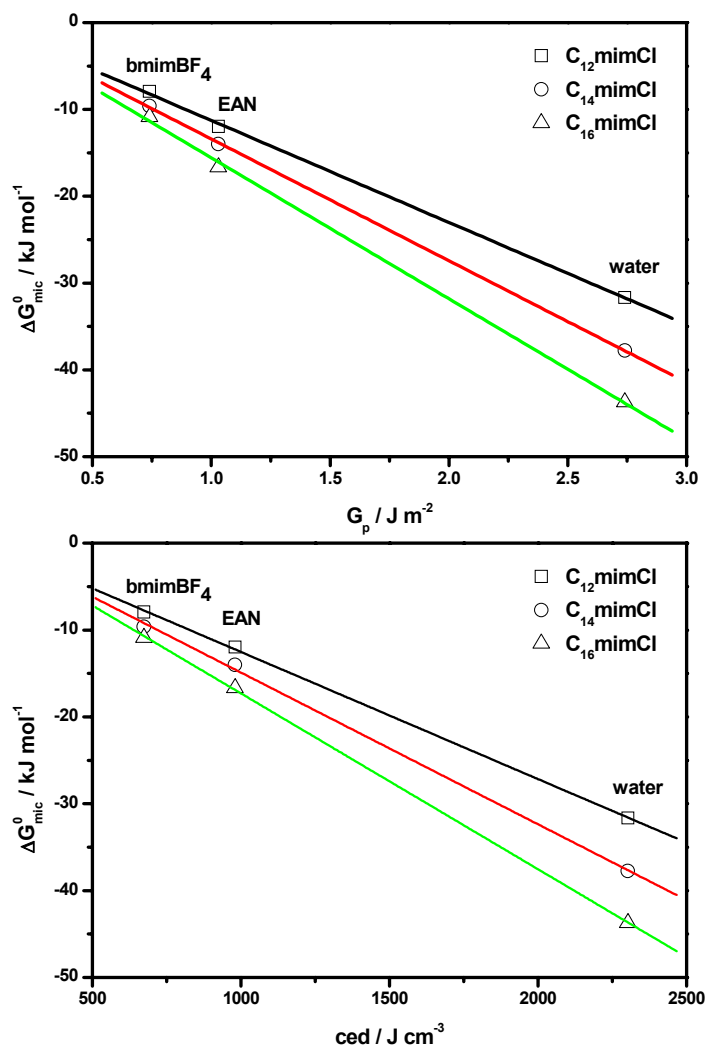
**Figure V-22: Relationship between the free energies of micelliza-
tion, G_p and the cohesive energy densities for the SLILs in water
(25°C), EAN (25°C), and bmimBF$_4$ (40°C), respectively.**

Such a linear correlation between ΔG^0_{mic} and G_p was already reported very recently for homologous series of common ionic and non-ionic surfactants in solvent/water mixtures covering a cohesive energy range between approximately 1.2 J m^{-2} and 2.8 J m^{-2} [51]. However, up to now this thesis is only a speculation since not enough data, especially in the range between 1.2 J m^{-2} and 2.5 J m^{-2}, is available in order to make general conclusions.

2.3   Density: Apparent molar volumes

For the conversion of wt.% into other required concentration units as well as for the appreciation of standard apparent molar volumes of the SLILs in the monomeric and aggregated form, density measurements of $C_{12}mimCl$, $C_{14}mimCl$, and $C_{16}mimCl$ solutions of varying SLIL concentration were carried out in media of the two different solvent RTMS. Figure V-23 and Figure V-24 show the relevant data plots for the EAN- and the $bmimBF_4$-systems. In all cases studied, two linear segments within the plots of the calculated apparent molar volumes vs. molality were found. Consequently, these plots are similar to those obtained for long-chain surfactants in aqueous solution [52-54]. However, one difference has to be noted, which concerns the concentration range below the *cac*. For conventional surfactants, the apparent molar volume does not change much below the cac, which is not the case for the present SLIL/RTMS systems. In this work, a significant linear change of the apparent molar volume was observed for all systems below the *cac*. Until now, it is not entirely clear, if these observations are due to uncertainties in the measurement or due to anomalous behaviour of the SLILs below their *cac*s. Consequently, the extracted molar volumes of the SLILs in the monomeric form have to be treated with caution. All other parameters obtained from the density isotherms should be reliable. Nevertheless, the presence of some kinds of aggregates in the solutions is indicated because of the appearance of breakpoints within the data plots. This confirms the results observed from the surface tension isotherms. The *cac*s were determined from the intercepts of both linear adjustments for every isotherm. The values of the *cac*s are presented in Table V-16 for every system studied. It is evident that the obtained *cac*s differ quite a lot from the quantities extracted from the surface tension isotherm. Only the value of the $C_{16}mimCl$/EAN-system is in good agreement with the data reported previously. The large discrepancies between the *cac*s calculated from the two techniques may be the result of the wide transition regime in which the SLILs self-assemble leading to unincisive breakpoints. Consequently, the exact estimation of the *cac* is quite difficult.
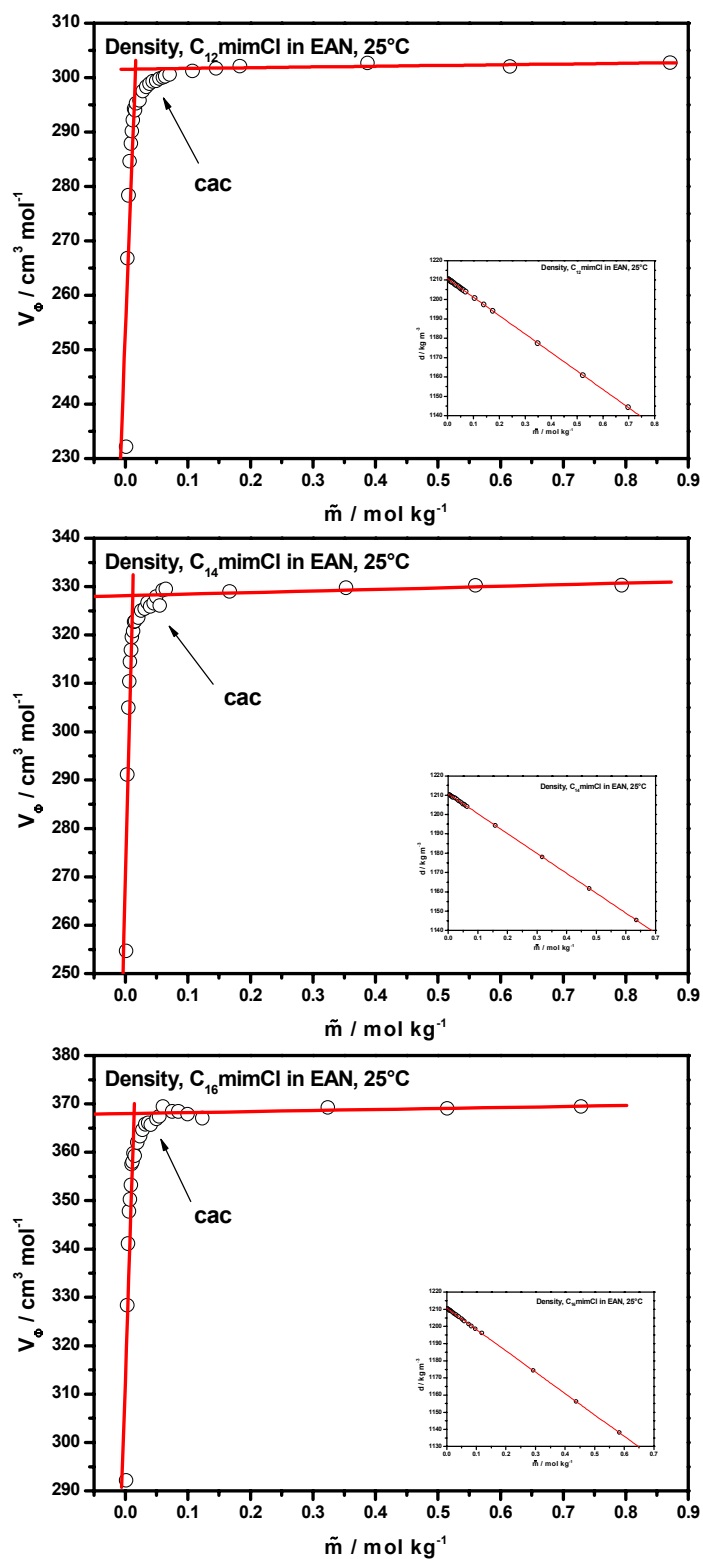
Figure V-23 : Variation of V_Φ with the molality for the three $C_n$mimCl/EAN-systems. The red line shows the linear fit used for the determination of V_Φ^0 and V_Φ^{mic}, respectively. The insets give the density variation as a function of SLIL molonity and the linear fit from which the density gradient was obtained.
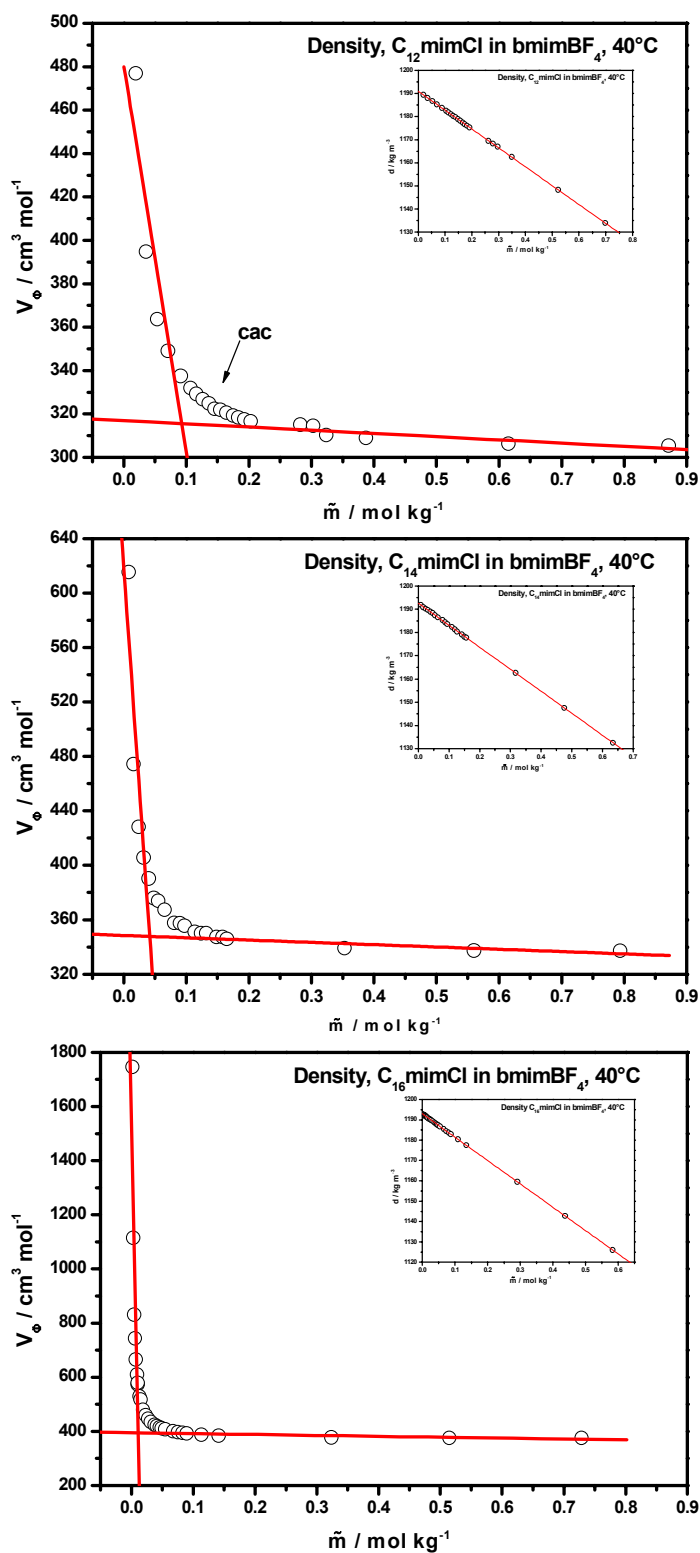
Figure V-24 : Variation of the apparent molar volume with the reverse of the molality for the three C$_n$mimCl/bmimBF$_4$-systems. The red line shows the linear fit used for the calculation of V_Φ^{mic}. The insets give the density variation as a function of SLIL molonity and the linear fit from which the density gradient was obtained.

Taking into account the extrapolation procedure for the determination of the standard apparent molar volume of the SLIL monomer and the wide transition intervals, it seems likely that the quantities obtained from the density measurements are somewhat underestimated and, in fact, all *cac*s are lower than the corresponding values from the surface tension isotherms. The good consistency in the case of the $C_{16}mimCl/EAN$-system is in agreement with the latter conclusion, since this system showed the sharpest breakpoint. Using the molality dependence of the density data, the apparent molar quantities for the studied SLIL/RTMS-systems in the pre-micellar and the post-micellar range were extracted by extrapolation of the two linear portions. The obtained data is summarized in Table V-16. Studying the extracted quantities for the apparent molar volume of the SLILs in the monomeric state, it is seen that all V_Φ^0 of the SLIL/bmimBF$_4$-systems are considerably higher than the corresponding apparent molar volumes of the aggregated state. In contrast, the differences between V_Φ^0 and V_Φ^{mic} of the SLIL/EAN-systems are much smaller and further, V_Φ^0 is always lower than V_Φ^{mic}.

SLIL / solvent RTMS	cac / mmol L^{-1}	V_Φ^0 / cm^3 mol^{-1}	V_Φ^{mic} / cm^3 mol^{-1}	D / kg^2 mol^{-1} m^{-3}
C$_{12}$mimCl / EAN, 25°C	20.3	252.87	301.56	-95.14
C$_{14}$mimCl / EAN, 25°C	14.4	269.14	328.14	-102.80
C$_{16}$mimCl / EAN, 25°C	13.2	312.97	368.00	-124.48
C$_{12}$mimCl / bmimBF$_4$, 40°C	105.3	480.83	317.00	-81.69
C$_{14}$mimCl / bmimBF$_4$, 40°C	46.5	619.18	348.49	-94.63
C$_{16}$mimCl / bmimBF$_4$, 40°C	12.8	1529.90	395.07	-114.87

Table V-16: Monomeric V_Φ^0 and aggregated apparent molar volumes V_Φ^{mic} of the SLILs in EAN and bmimBF$_4$, respectively. Additionally, the density gradients *D* obtained from *d* vs. molonity plots of each investigated system are given.

One possibility for the large values of the apparent molar volumes of the SLIL monomers in solution of bmimBF$_4$ may be an enlargement of the volumes due to solvent effects: It must be pointed out that the apparent molar volume is affected by solvent molecules (solvent cation and anion in the present case) with a significant interaction with the solute. In this context, two contributions, which can increase V_Φ^0, may be considered for the instant situation: (i) a significant counterion exchange between the

SLIL and the RTMS, and (ii) considerable interactions of the solvent RTMS cations, which exhibit the same imidazolium scaffold, with the imidazolium SLILs. The latter suggest that the SLILs are more solvated as free monomers than in the micellar state, when they are solubilised in bmimBF$_4$. This fact explains also the *cac* results obtained from surface tension and density isotherms: the *cac*s of the SLIL/bmimBF$_4$-systems are higher than the corresponding values for the SLIL/EAN-systems because of the good solvation of the SLIL monomers in solution of bmimBF$_4$, which makes an unfavourable contribution to the micellization tendency of the SLILs in bmimBF$_4$. Note, the latter is consistent with the lower values of ΔG^0_{mic} calculated for the SLIL/bmimBF$_4$-systems in comparison to the respective SLIL/EAN-systems. The higher ΔG^0_{mic} of the SLIL/EAN-systems agrees with their lower values of V^0_Φ, which may be the result of lower solvation of the SLILs within the ammonium RTMS. In contrast to the quite high difference of the V^0_Φ quantities, the values of V^{mic}_Φ observed for the SLIL/EAN-systems and the respective SLIL/bmimBF$_4$-systems differ only slightly from each other. In general, somewhat higher V^{mic}_Φ were found for the bmimBF$_4$-systems. Therefore, the solvation of the aggregated SLILs within the two types of RTMS may be similar. The small differences of V^{mic}_Φ may be also attributed to different solvent properties of EAN and bmimBF$_4$ affecting the SLILs in their micellized form as already discussed previously (e.g. different rates of anion exchange and/or different types of solvent-micelle interactions).

Compared to the V^{mic}_Φ of the aqueous SLIL-systems, the respective apparent molar volumes of the SLIL/RTMS series are higher. Again, solvent effects may be responsible for this observation.

Beside the *cac* and the apparent molar volumes of the SLILs in the two RTMS, the density gradients *D*, which were used to convert the different concentration scales into each other, are also given in Table V-16.

2.4   Small angle neutron scattering: Micellar structure

In order to confirm the presence of micellar structures formed by the C$_n$mimCl amphiphiles in EAN and bmimBF$_4$, respectively, SANS measurements of different

C$_{12}$mimCl/EAN-, C$_{14}$mimCl/EAN-, C$_{16}$mimCl/EAN-, and C$_{16}$mimCl /bmimBF$_4$-mixtures were performed at the V4 neutron scattering instrument of the Hahn-Meitner-Institute at 25°C. It is worth noting that neither the surfactant-like ionic liquids nor the solvent RTMSs were deuterated in order to improve the scattering contrast. For this reason, mixtures with a very high SLIL concentrations (up to about 20 wt.% for each series) were measured to obtain an adequate scattering intensity.

During the next chapters only the detailed analysis of the C$_{16}$mimCl/EAN and C$_{16}$mimCl/bmimBF$_4$ will be presented, since the C$_n$mimCl/RTMS SANS measurements were applied together with Dipl. Chem. Oliver Zech, who will present the results of the remaining SLIL/RTMS-systems in an upcoming work.

2.4.1   Primary data inspection: Dimensionality and Porod regime

$I(q)$ vs. q plots of the investigated SLIL/RTMS-mixtures and the pure RTMS are presented in Figure V-25 and Figure V-26 for the EAN solutions and bmimBF$_4$ solutions, respectively. Because of the low scattering contrast (remember no deuterated SLIL or RTMS was used for these experiments), the absolute scattering intensities are quite low (< 1 cm^{-1}) for all solutions under investigation, especially when the investigated solutions contain bmimBF$_4$ as solvent RTMS. This observation can be mainly attributed to the boron atom of the BF$_4^-$ anion, which is well known to absorb neutrons, leading to low scattering intensities. The curves of scattered intensity $I(q)$ for all solutions with added SLIL exhibit a peak whose intensity $I(q_{max})$ and position q_{max} depend on concentration for a given SLIL. The peak becomes quite pronounced at higher concentrations. It is evident that the presence of a peak in the scattering intensity is indicative for the formation of aggregates within the molten salt solutions, since the pure RTMS show no scattering. Only flat curves were observed for pure EAN and pure bmimBF$_4$, respectively.

Before specific models were applied to fit the SANS curves, a fundamental inspection of the scattering data was performed using scaling laws, which are model independent.
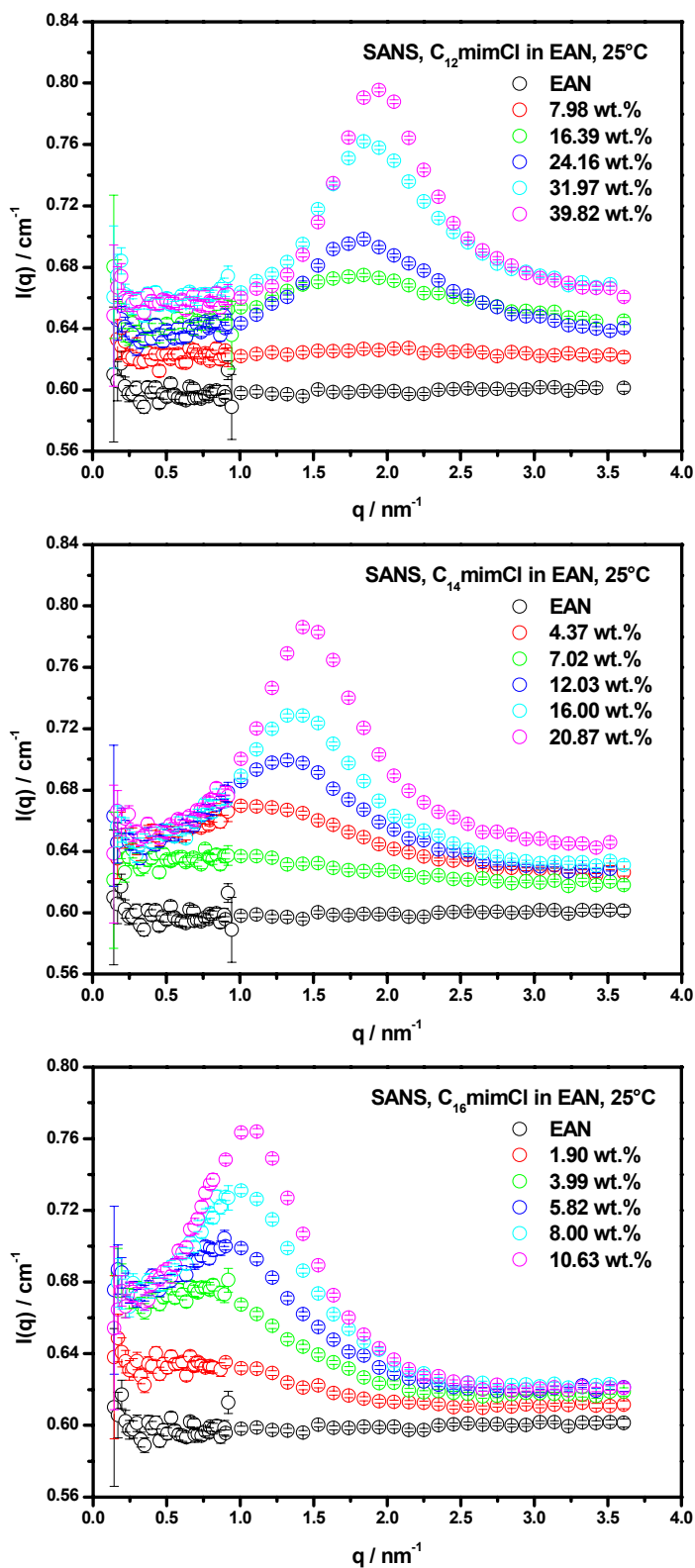
Figure V-25: Scattering patterns of the different C_nmimCl/EAN samples obtained by SANS at 25°C. Additionally, the scattering curve of pure EAN is shown.
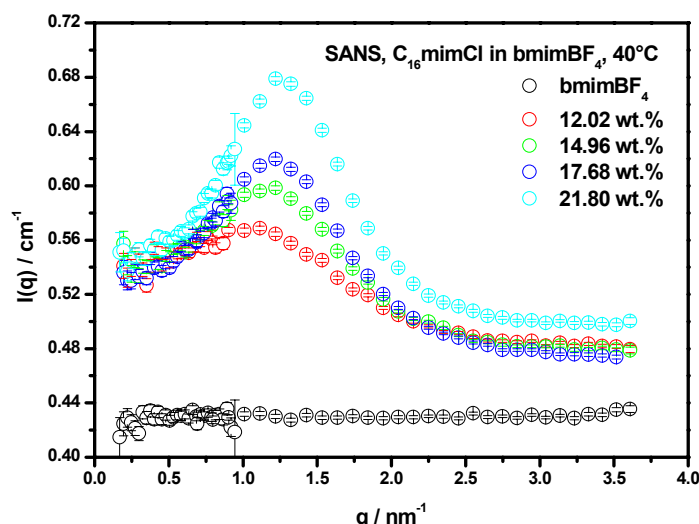
Figure V-26: Scattering pattern of the different $C_{16}mimCl/bmimBF_4$ samples obtained by SANS at 40°C. Additionally, scattering curve of pure $bmimBF_4$ is shown.

This procedure is quite important because of the complexity of the investigated salt mixtures compared to systems, where surfactants are solubilised in conventional solvents, which are not composed of two charged species and therefore cannot dissociate. When long-chain imidazolium chlorides are dissolved in a solvent RTMS, several additional factors that notably influence the aggregate formation have to be considered. These will include (i) the high ionic strength of the SLIL/RTMS-systems (the Debye length is approximately 0.1 nm) [23], (ii) a competitive counterion binding between the chloride of the C_nmimCl amphiphiles and solvent RTMS anion (in the present cases the nitrate or the tetrafluoroborate anion), and finally (iii) the distribution of the solvent-RTMS anion and cation between the bulk solvent phase and the self-assembled aggregates (e.g. some RTMS components may act also as co-surfactants).

In order to get an idea about the selection of an appropriate form factor model for the scattering patterns and its base parameters, the interpretation of scattering curves according to scaling laws are very useful. For this reason, the intermediate, and large q-range of all scattering patterns of the $C_{16}mimCl/EAN$ and $C_{16}mimCl/bmimBF_4$, respectively, were analyzed. From the intermediate q-range the dimensionality of the formed aggregates can be predicted, whereas the high q-range gives the surface areas of the particle/solvent interfaces per unit volume of solution S/V according to Porod et al. [55,]

[56]. By using S/V, it is also possible to obtain an estimate of the particle size by calculation of the Porod radius [57]. For the extraction of the particle dimensionality $log\,I(q)$ vs. $log\,q$ plots were applied to all measured concentrations of the C_{16}mimCl/RTMS series. Then, the decay of the intermediate q-portion of the scattering curve was determined. Figure V-27 exemplifies such a plot for the 1.90 wt.% and 12.02 wt.% of C_{16}mimCl in EAN and bmimBF$_4$, respectively.
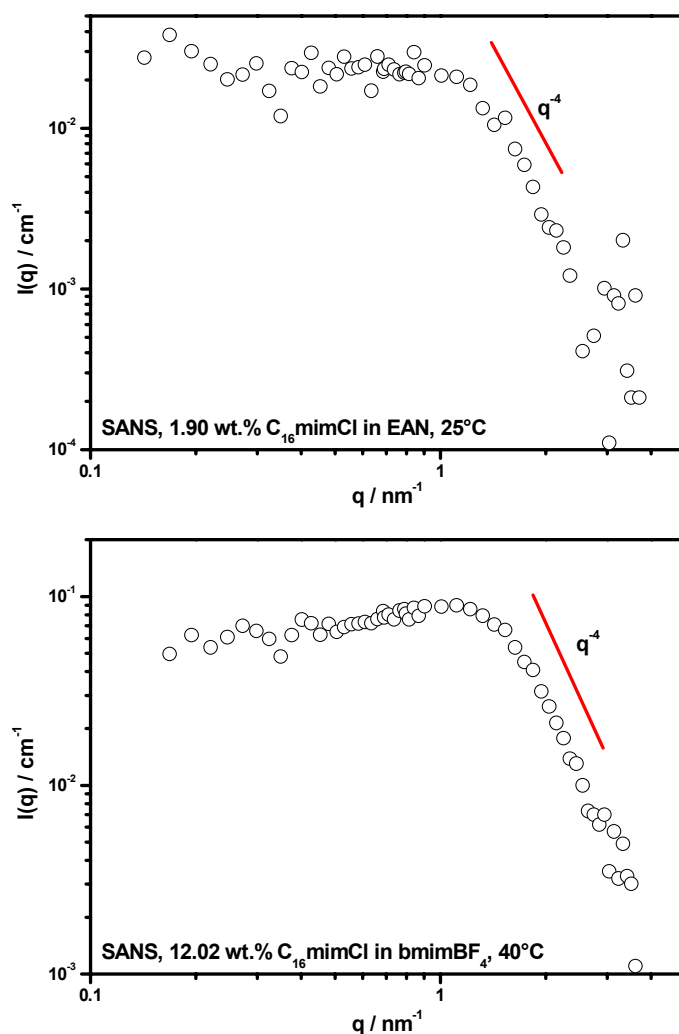
Figure V-27: $\log I(q)$ **vs.** q **plots of a 1.90 wt.% and 12.02 wt.% solution of C$_{16}$mimCl in EAN and bmimBF$_4$, respectively, used for the determination of the particle dimensionality. The scattering pattern was corrected by the background scattering. The red line shows the** q^{-4} **decay in the mediate** q**-range, which is indicative for spherical objects.**

As illustrated by the red lines, each of the two curves show defined q^{-4} decay in the mediate q-range which is indicative for spherical globular aggregates. In order to get an impression about the size of the aggregates in solution, Porod-plots, $I(q)q^4$ as a function of q, were established for all concentrations of the $C_{16}mimCl/EAN$ and $C_{16}mimCl/bmimBF_4$ series, respectively. In Figure V-28, representative plots are given for $C_{16}mimCl$ in EAN and in $bmimBF_4$, respectively.
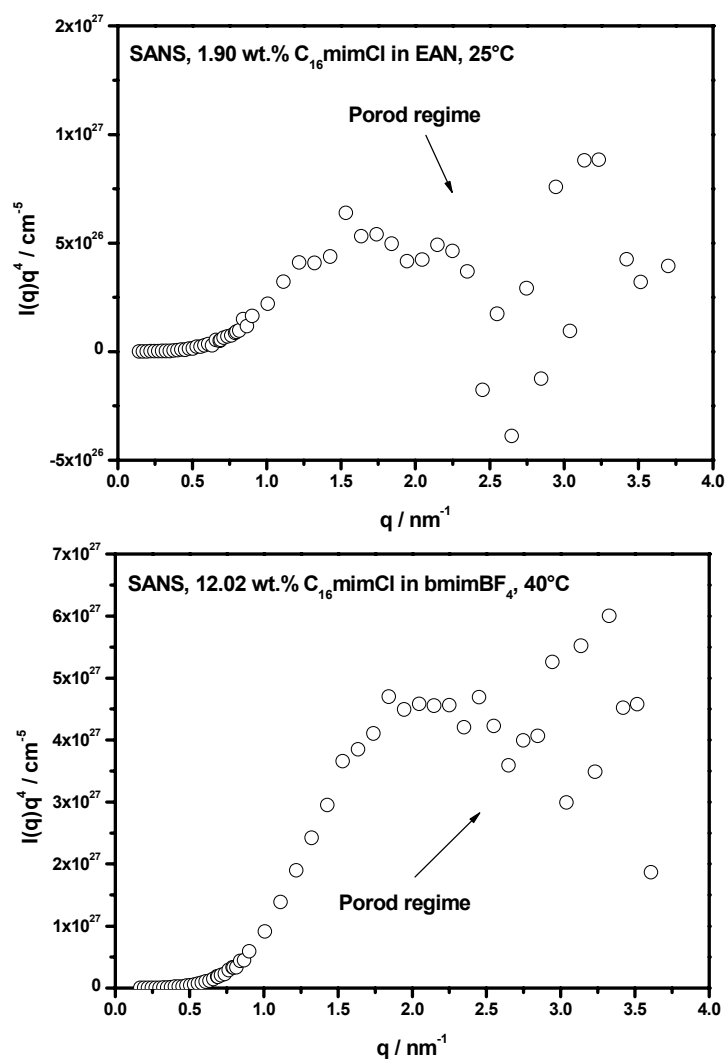
Figure V-28: Porod plots of a 1.90 wt.% and a 12.02 wt.% solution of C$_{16}$mimCl in EAN and bmimBF$_4$, respectively. The scattering pattern was corrected by the background scattering.

In the area where the asymptote is reached, the two curves strongly oscillate around an average value that represents the Porod constant. The oscillations arise from

the small difference between the scattering length densities of the aggregate and solvent leading to relatively high errors of the scattering intensity in the high q-regime. For this reason, it was impossible to extract the value of S/V with any certainty. However, qualitative information could be obtained from the appearance of the Porod-plot. Since the observation of a Porod limit is a precondition for the presence of particles with sharp and smooth interfaces in the sample solution, the presence of defined aggregates in the C_{16}mimCl/EAN- as well as in the C_{16}mimCl/bmimBF$_4$-system is proven[56].

2.4.2   Basic considerations used for the model fitting of the neutron scattering data

Based on the results achieved from the primary inspection of the scattering data using scaling laws, the following form factor model was developed to fit the scattering data. The scattering intensity of a number of aggregates in solution per unit volume is expressed by the already presented formula incorporating the products of the number density of particles n_p, the scattering contrast $\rho_m - \rho_{solv}$, the volume of the particle V_p, shape factor $F(q)$, structure factor $S(q)$, and a constant background term BG_{incoh}[55]:

$$\frac{d\Sigma}{d\Omega} = n_p \left(\rho_m - \rho_s \right)^2 V_p^{\,2} \left\langle \left| F(q) \right|^2 \right\rangle S(q) + BG_{incoh} \qquad \text{(V-6)}$$

As in the case of the aqueous C$_n$mimCl solutions, a core-shell model was assumed for the C$_{16}$mimCl/EAN as well as for the C$_{16}$mimCl/bmimBF$_4$-system. Further, a spherical geometry of the scatterers expressed by the radius of the aliphatic core R and a particle shell with the thickness t was applied in accordance to the information obtained from the dimensionality plots. Thus, the form factor is described by the following key parameters:

(i)   The scattering length densities of the hydrophobic core, ρ_{core}, interface region (including head group, counterions, solvent), ρ_{shell}, and solvent, ρ_{solv}.

(ii)   The geometrical parameters, which define the core-shell spheroid: the dimensions R and t that is the radius of the sphere and the thickness of the shell (including head group, counterions, solvent), respectively.

Table V-17 shows the scattering length densities of the investigated $C_{16}mimCl/RTMS$ systems that are of interest in the following analysis. The *sld*s are divided into the different scattering contributions of hydrocarbon core, possible shell components, and solvent RTMS. The *sld*s were calculated according to the already presented theory (cp. Chapter IV.7.2.2). A dry aggregate core consisting of the $-[C_{16}H_{33}]$ fragment of the $C_{16}mimCl$ was assumed with a $\rho_{core} = -3.53 \times 10^9$ cm^{-2}. The scattering length density of the shell is the consequence of the various *sld*s of the components possibly located at the aggregate surface. In the present case, ρ_{shell} results from the imidazolium cation (-mim$^+$) and the different types of anions (Cl$^-$, BF$_4^-$, NO$_3^-$) in the investigated systems. Consequently, the value of ρ_{shell} should range within 1.35×10^{10} cm$^{-2} \leq \rho_{shell} \leq 5.56 \times 10^{10}$ cm^{-2} and 1.35×10^{10} cm$^{-2} \leq \rho_{shell} \leq 3.81 \times 10^{10}$ cm^{-2} for the $C_{16}mimCl/EAN$- and $C_{16}mimCl/bmimBF_4$-systems, respectively. Considering these quantities, it may be clear that the exact determination of t and the corresponding ρ_{shell} is a very difficult task, because of the low scattering contrast between shell components and solvent resulting from the very similar *sld*s. Therefore, the question arises how far the neutrons are sensitive to the shell region. Figure V-29 schematically illustrates the scattering length density profile used for data fitting of the $C_{16}mimCl/RTMS$-systems.
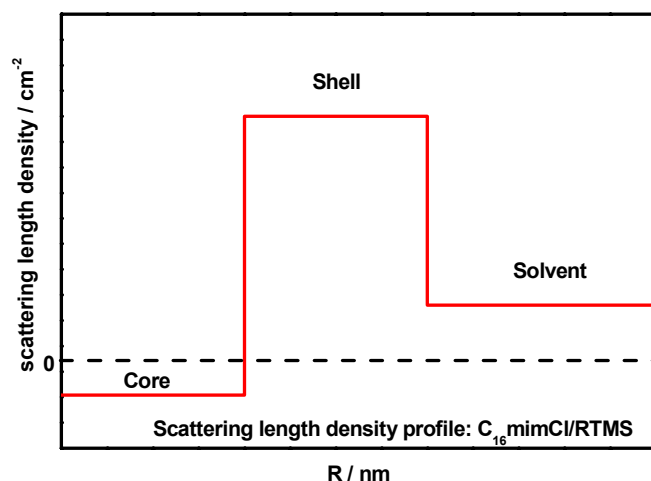
Figure V-29: Scattering length density profile of a micellar core-shell particle. The two steps correspond to the scattering length densities of core and shell, respectively.

For the consideration of the interparticle interactions present at high C_{16}mimCl concentrations, a structure factor of uncharged hard spheres was used following the work of Evans et al. who also supposed that the interactions between micelles formed by a cationic surfactant in a RTMS are well described by a hard-sphere potential [10]. Since all RTMS have high molarity in salt (equivalent to a high ionic strength), and are completely ionized, the positive charge associated with the imidazolium head groups at the surface of the micelle may be almost completely neutralized by counterions contained within the shell region. Consequently, there is no separation of charge and no double layer in the usual sense. Because of the diminished Coulombic interactions, a suitable choice of the hard-sphere $S(q)$ used for the data fitting is the Percus-Yevick (PY) structure factor. The PY structure factor is defined by the following three base parameters:

(i)   The temperature T.

(ii)   The hard-sphere volume fraction of the aggregates Φ_{hs}.

(iii)   The hard-sphere radius of the aggregates R_{hs}.

So far, the key parameters, which are necessary to fit the scattering patterns, are R, t, ρ_{core}, ρ_{shell}, ρ_{solv}, R_{hs}, Φ_{hs} and BG_{incoh}. Additionally, a polydispersity of the particle radius was considered using a log-norm distribution [60]. Therefore, an additional fitting parameter σ_x, which represents the distribution parameter of the assumed log-norm distribution, was introduced to the model. σ_x denotes the standard deviation from the average particle radius.

In order to obtain reliable fit results of the scattering patterns, the number of free parameters included in $P(q)$ and $S(q)$, respectively, were restricted as far as possible by conclusive assumptions: The scattering length densities of hydrocarbon core and solvent were fixed to the values given in Table V-17. ρ_{shell} was restricted to the intervals given previously and the value of R_{hs} was set to $R_{hs} = R + t$, since the latter expression represents the hard-sphere radius of the aggregate in solution.

Parameter	Hydrocarbon core		Shell components			Solvent RTMS	
	$-[C_{16}H_{33}]$	$-[mim^+]$	$[Cl^-]$	$[NO_3^-]$	$[BF_4^-]$	EAN	$bmimBF_4$
M / g mol^{-1}	225.44	-	-	-	-	108.10	226.02
d / g cm^{-3}	0.773[a]	-	-	-	-	1.210[e]	1.196[e]
V_Φ / cm^3 mol^{-1}	291.64[b]	82.10[c]	17.40[d]	29.00[d]	44.18[d]	89.30[b]	188.98[b]
V / cm^3	4.84×10^{-22}	1.63×10^{-22}		4.82×10^{-23}	7.34×10^{-23}	1.48×10^{-22}	3.14×10^{-22}
$\sum b_i$ / cm^{-1}	-1.71×10^{-12}	2.20×10^{-12}	9.58×10^{-13}	2.68×10^{-12}	2.79×10^{-12}	1.95×10^{-12}	4.37×10^{-12}
sld / cm^{-2}	-3.53×10^{9}	1.35×10^{10}	3.31×10^{10}	5.56×10^{10}	3.81×10^{10}	1.31×10^{10}	1.39×10^{10}

Table V-17: The scattering length densities (*sld*) of the component blocks applied in the SANS evaluation together with the quantities used for their calculation. [a]Ref. [38]; density (25°C) of hexadecane. [b]Calculated from the ratio of molar mass and density. [c]Ref. [58]. [d]Ref. [59]. [e]Estimated from density measurements at 25°C and 40°C for EAN and bmimBF$_4$, respectively.

On this basis, the remaining parameters were fitted to the experimental data using the SASFit program package, which minimizes the deviations of the theoretical scattering function to the experimental data by variation of the model parameters [61]. The consistency of the fitted model parameters obtained from SASFit were cross-checked by comparison of Φ_{fit} obtained from the scale factor n_p (particle number density) with the expected volume fraction Φ_{exp} appreciated from the molar volume of C_{16}mimCl in the aggregated state and the known SLIL concentrations minus the corresponding *cac*s. Further, the hard-sphere volume fraction Φ_{hs} obtained from fitting the PY structure factor to the scattering pattern has to be in the order of magnitude as the values of Φ_{fit} and Φ_{exp}, respectively. If there was a significant departure between Φ_{fit}, Φ_{exp}, and Φ_{hs}, the fitting function was discarded and the initial model parameters were changed for the next fitting attempt. This procedure was repeated until a satisfactory description with consistent model parameters was achieved.

During the fitting procedure, all theoretical scattering curves, which were adjusted to the experimental data, were smeared in order to achieve the best possible description of the experimental scattering pattern. SASfit takes into account the apparatus geometry as well as the FWHM calculated the contribution of the smearing effects = 11 % of the V4 spectrometer (cp. Table IV-6).

From the core radius R of the micelle, the aggregation number N_{agg} was estimated by the ratio of the core volume to the volume V_{chain} of the hexadecane tail, which was assumed to build up the micellar core:

$$N_{agg} = \frac{4\pi \cdot R_{core}{}^3}{3V_{chain}} = \frac{V_{core}}{V_{hexadecane}} \qquad \text{(V-7)}$$

2.4.3   Model fitting results

The best fits to the data of the two investigated systems are shown in Figure V-30. The obtained fitting values are given in Table V-18 and Table V-19, respectively. Good fits were obtained for all scattering patterns (low χ^2). The core radii of the model fits are constant over the concentration range covered for the two C_{16}mimCl/RTMS-

systems. In this context, values of approximately 2.54 nm and 2.05 nm were obtained for the C_{16}mimCl/EAN and C_{16}mimCl/bmimBF$_4$ series, respectively. The corresponding aggregation numbers are also nearly constant for the investigated concentration range. Average values of 87 and 37 were estimated for N_{agg} of the two C_{16}mimCl/RTMS-systems.
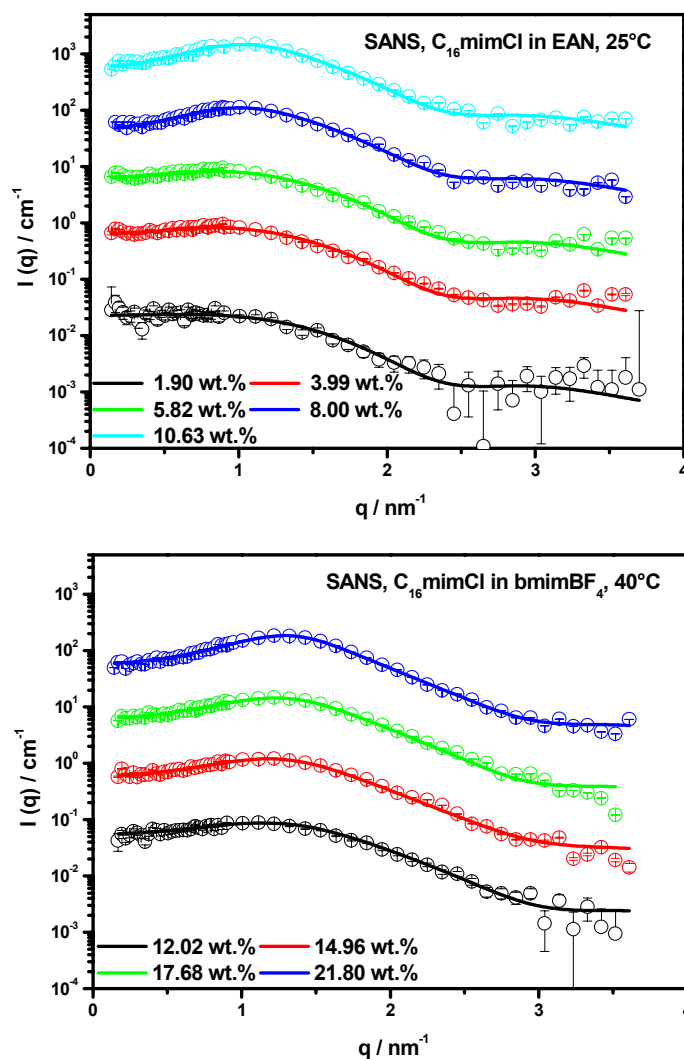
Figure V-30: SANS data of the investigated C_{16}mimCl/RTMS-systems with the best fits to the datasets. The scattering curves were multiplied by factors of 10^0, 10^1, 10^2, 10^3, and 10^4 for clarity.

Considering the Tanford formula for the appreciation of chain-length of a hydrocarbon chain, which predicts a value of 2.17 nm for a fully extended hexadecane chain,

it is clear that the obtained core radii for the investigated systems are significantly lower than that value. This requires that many of the hydrophobic surfactant chains be crumbled so that their terminal methyl groups are located close to or at the surface of the micellar core. Interestingly, the folding appears to be more dominant for the C_{16}mimCl/bmimBF$_4$-system reflected by the lower core radii of the aggregates. From this observations, it can be assumed, that the choice of the solvent-RTMS tunes the size and therefore the aggregation number of a given surfactant. Interestingly, Evans et al., who performed light scattering measurements of common pyridinium surfactants in EAN, already reported that micelles of ionic surfactants are considerably smaller in the RTMS than in water. Further, the authors supposed a chain folding of the pyridinium surfactants [10]. Patrascu et al. investigated the self-assembly of various C_iE_j-based surfactants by means of DLS and SANS in bmimBF$_4$ and in bmimPF$_6$, respectively [36]. The extracted quantities of the micellar radii and of the aggregation numbers for the non-ionic surfactants were found to be significantly smaller than the corresponding values in aqueous solution. Additionally, a considerable size variation of the micelles depending on the solvent-RTMS was reported. For example, radii of 2.5 nm and 1.4 nm were reported for $C_{14}E_8$ dissolved in bmimBF$_4$ and in bmimPF$_6$, respectively. The corresponding N_{agg} were reported as 75 and 15. The observations of Patrascu et al., and also those of Evans et al., agree very well with the SANS findings for the C_{16}mimCl micelles obtained in the underlying work.

The shell thicknesses of the micelles are similar for the two C_{16}mimCl/RTMS-series and no change was observed, regardless of the SLIL concentration. A value of around 0.4 nm was achieved for the C_{16}mimCl/EAN- and C_{16}mimCl/bmimBF$_4$-system, respectively. Keeping in mind that the imidazolium ring is a planar pentagon, and the N1–C1 and C1–N2 bond lengths are 0.132 nm and the C2–C3 bond length is 0.134 nm, indicating the conjugated double-bond nature. The N1–C3 and N2–C2 bond lengths are 1.370 nm, which are shorter than that of a pure C–N single bond (typically 0.147 nm) [62]. Considering these distances combined with a assumed circular geometry of the imidazolium cation, the diameter of the imidazolium ring can be estimated to be approximately 0.214 nm.

	C$_{16}$mimCl/EAN				
wt.%	**1.90**	**3.99**	**5.82**	**8.00**	**10.63**
c / mol L^{-1}	6.08×10^{-2}	1.27×10^{-1}	1.86×10^{-1}	2.55×10^{-1}	3.39×10^{-2}
Φ_{hs} / %	1.91[a]	4.61[a]	6.02	9.00	11.96
R / nm	2.54	2.54	2.54	2.54	2.54
t / nm	0.38	0.38	0.38	0.38	0.38
ρ_{shell} / cm^{-2}	5.09×10^{10}	5.09×10^{10}	5.09×10^{10}	5.09×10^{10}	5.09×10^{10}
N_{agg}	87	87	87	87	87
σ_x	0.12	0.12	0.12	0.12	0.12
χ^2	0.92	2.42	2.08	1.88	2.61

Table V-18: Overview of the SANS results extracted from model fitting of the investigated C$_{16}$mimCl/EAN series at 25°C. [a]No structure factor was used for the data fitting. Consequently, the presented aggregate volume fraction was calculated from the scaling parameter.

	C$_{16}$mimCl/bmimBF$_4$			
wt.%	**12.02**	**14.96**	**17.68**	**21.80**
c / mol L^{-1}	4.59×10^{-1}	5.72×10^{-1}	6.76×10^{-1}	8.33×10^{-1}
Φ_{hs} / %	12.13[a]	15.59	17.07	20.93
R / nm	2.01	2.03	2.05	2.05
t / nm	0.40	0.40	0.40	0.40
ρ_{shell} / cm^{-2}	3.05×10^{10}	3.05×10^{10}	3.05×10^{10}	3.05×10^{10}
N_{agg}	36	37	38	38
σ_x	0.12	0.13	0.12	0.12
χ^2	2.01	1.73	2.15	2.06

Table V-19: Overview of the SANS results extracted from model fitting of the investigated C$_{16}$mimCl/bmimBF$_4$ series at 40°C. [a]No structure factor was used for the data fitting. Consequently, the presented aggregate volume fraction was calculated from the scaling parameter.

Using the latter together with two times the 0.147 nm for the length of the N–CH$_3$ group and the N–CH$_2$ group, the shell thicknesses of about 0.40 nm for both

C_{16}mimCl/RTMS-systems seem quite reasonable. Since it is known from structural studies of imidazolium-based ionic liquids that the anions are away from the methyl group, which is substituted at the nitrogen atom, and rather close to the hydrophobic region produced by the n-alkyl-group at N1, the counterions may not significantly increase the shell. Consequently, the length of the imidazolium head group may mainly define the shell thicknesses, which is in accordance to the previous calculation. The scattering length densities of the shell were evaluated as constant for the both C_{16}mimCl/RTMS-systems indicating a constant shell region over the concentration range studied. Values of 5.09×10^{10} cm^{-2} and 3.05×10^{10} cm^{-2} were obtained for C_{16}mimCl/EAN- and C_{16}mimCl/bmimBF$_4$-series, respectively. These ρ_{shell} are slightly higher than the value of 1.35×10^{10} cm^{-2} calculated for the [$-$mim$^+$] group of C_{16}mimCl and the value of 3.31×10^{10} cm^{-2} calculated for the chloride anion. Since EAN and bmimBF$_4$ are 11.1 M and 5.3 M in nitrate ion and tetrafluoroborate ion, respectively, these ions may be the dominant counterions of the aggregates in the respective system. Hence, it seems likely that the quantities of ρ_{shell} extracted for the two C_{16}mimCl/RTMS-series are the results of the scattering contributions of the imidazolium/nitrate and the imidazolium/tetrafluoroborate combination, respectively. Taking into account the scattering length densities of nitrate and tetrafluoroborate, which are higher than the scattering length density of the imidazolium headgroup, the observed values of ρ_{shell} are reasonable.

For both analyzed C_{16}mimCl/RTMS-sytems, the particle volume fractions calculated from the scaling factor were always consistent with the respective values extracted from the structure factor and further with the expected volume fractions appreciated from the molar volume of C_{16}mimCl. Figure V-31 illustrates the hard-sphere structure factors obtained by fitting the scattering spectra of C_{16}mimCl in EAN and bmimBF$_4$, respectively. No structure factors for the 1.90 wt.% and the 3.99 wt.% samples of the C_{16}mimCl/EAN-system were used to describe the scattering patterns as indicated by $S(q) = 1$ in Figure V-31 (top).
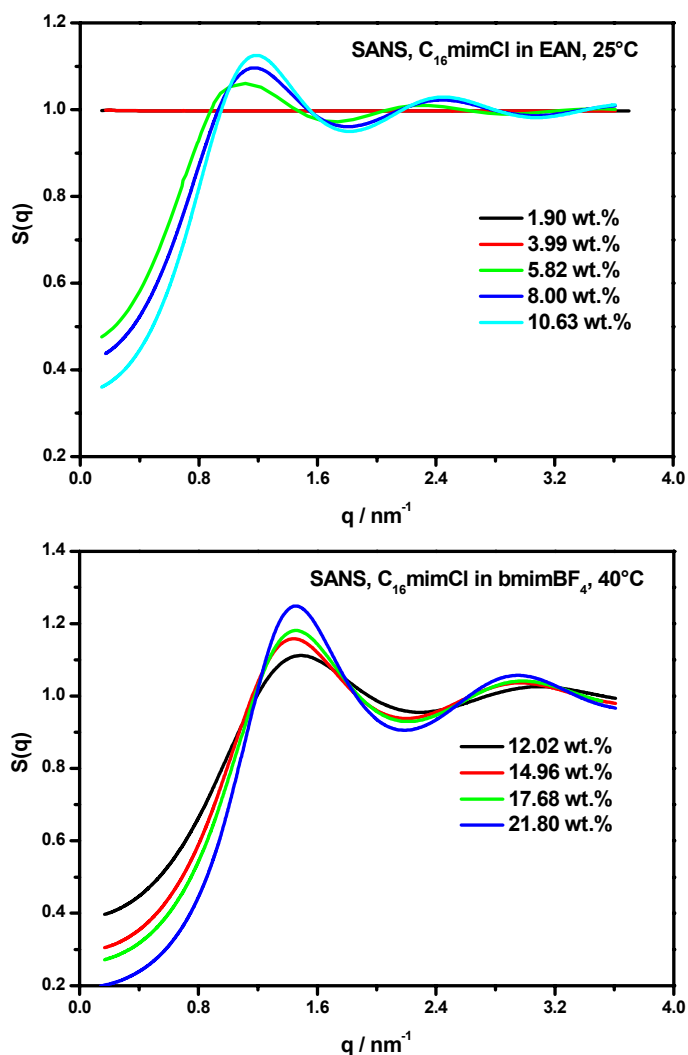
Figure V-31: Structure factors obtained from the data fitting for C$_{16}$mimCl aggregates in EAN and bmimBF$_4$, respectively.

The structure factors for the higher concentrations of all examined C$_{16}$mimCl/EAN samples show an increase concerning the height of the maximum of $S(q)$ and simultaneously oscillations at higher q-values become more and more pronounced indicating interparticle interactions of higher long-range order. Additionally, $S(q=0)$ decreases because of the reduced isothermal compressibility for an increased number of aggregates as the SLIL concentration rises. Contrarily, all scattering patterns of the C$_{16}$mimCl/bmimBF$_4$ had to be fitted by using a $S(q)$ contribution, because of the high particle number density of the very concentrated C$_{16}$mimCl/bmimBF$_4$-samples. As Figure V-31 illustrates, the $S(q)$ evolution of the C$_{16}$mimCl/bmimBF$_4$-system is the same as for the series where EAN acted as solvent-RTMS, the height of the $S(q)$-

maxima increases and the oscillations become more pronounced with increasing C_{16}mimCl content.

2.5   High-temperature measurements

In addition to the investigations of $C_n$mimCl/EAN and $C_n$mimCl/bmimBF$_4$ mixtures at low temperatures, the thermal stability of the binary SLIL/RTMS mixtures and the existence of self-assembled micellar structures at high temperatures ($\gg$ 100°C), was a central part of the present work taking advantage of the wide temperature range over which IL-systems are liquid and stable. In order to define the maximum stability temperature of the $C_n$mimCl/RTMS systems substantial thermal gravimetric analyses of the pure substances as well as of different SLIL/RTMS mixtures were performed. The phase behaviour as a function of temperature (within the estimated temperature stability range) was investigated visually for SLIL/RTMS solutions with concentrations up to 25 wt.%. Further on, the presence of micellar aggregates within the C_{16}mimCl/EAN- and C_{16}mimCl/bmimBF$_4$-solutions, respectively, was verified using high-temperature scattering techniques (HT-SAXS and HT-SANS).

2.5.1   Thermal gravimetric analysis: T_{dec}

In order to proof the high-temperature stability of the $C_n$mimCl/RTMS-mixtures, thermal gravimetric measurements were carried out. Figure V-32 and Figure V-33 shows the TGA results obtained for the pure SLILs and RTMS, respectively. Decomposition temperatures T_{dec}^{SLIL} of 273°C, 280°C, and 274°C were achieved for C_{12}mimCl, C_{14}mimCl, and C_{16}mimCl (cp. also Table V-20). These values are about 20°C higher than $T_{dec}^{C_nTAC}$ of the corresponding common C_nTAC surfactant analogues, which were found to be $T_{dec}^{C_{12}TAC}$ = 256°C, $T_{dec}^{C_{14}TAC}$ = 262°C, and $T_{dec}^{C_{16}TAC}$ = 258°C, respectively (cp. insets of Figure V-32). The higher decomposition temperature of the $C_n$mimCl series in comparison to the common trimethylammonium chloride surfactants results from the aromatic imidazolium head group, which makes decomposition via an elimination reaction at the N1-position less favourable than an elimination of the long alkyl-chain at the nitrogen in the case of the C_nTAC analogues [63].
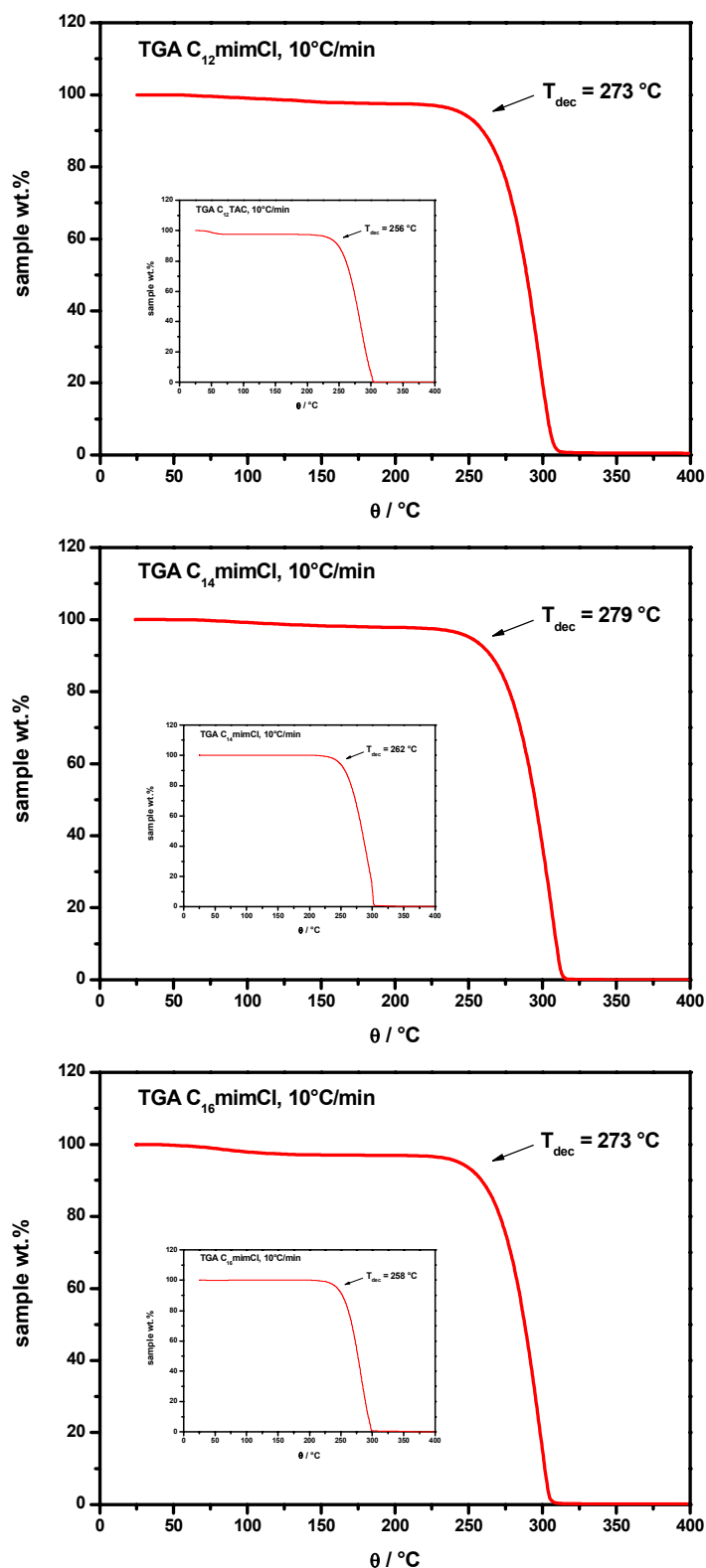
Figure V-32: TGA curves of the three SLILs under investigation. The decomposition temperature, T_{dec}^{SLIL} of each SLIL is indicated by an arrow. Additionally, the TGA graphs of the corresponding C_nTAC analogues are given as insets.
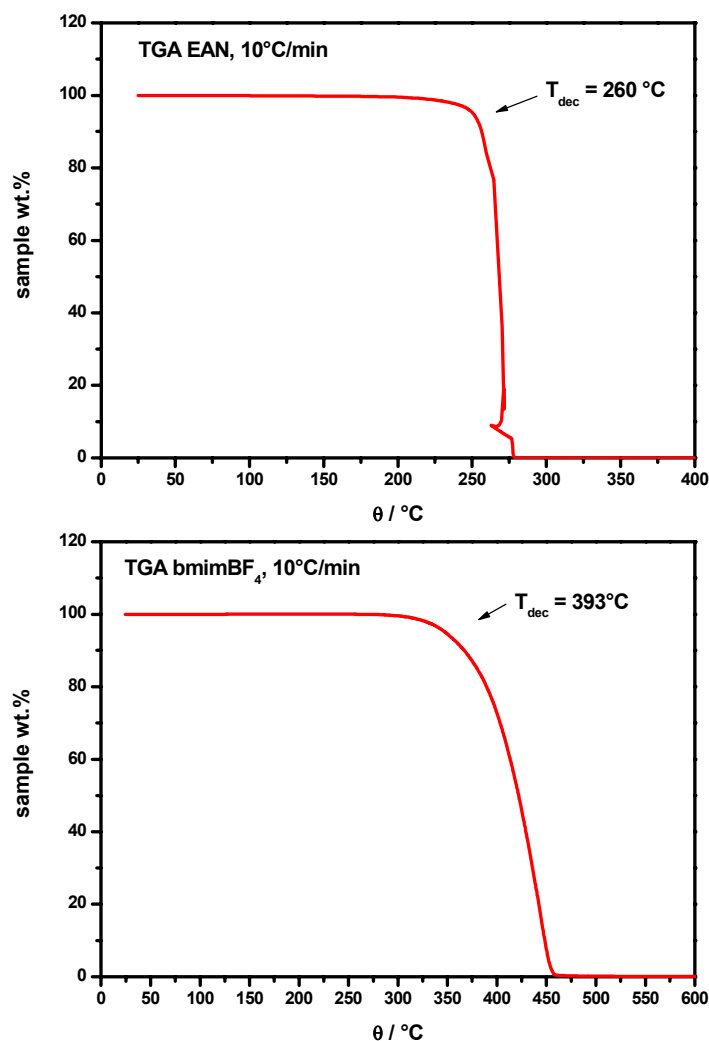
Figure V-33: TGA curves of the two solvent-RTMS under investigation. The decomposition temperature, T_{dec}^{RTMS} of each RTMS is indicated by an arrow.

For this reason, the imidazolium surfactants may be more suitable for high-temperature applications than the conventional amphiphiles incorporating the trimethyl-ammonium head group.

Values of 260°C and 393°C were obtained for EAN and bmimBF$_4$, respectively, in agreement to the literature values [25, 64]. This huge stability difference of about 130°C is in line with the already presented fundamentals concerning ionic liquids in which PILs were denoted as less stable compared to APILs, since the decomposition takes place by reversion of the acid/base reaction (cp. Chapter II.1.4.2). The latter is energetically more favourable than dealkylation of the imidazolium head group reflected by the lower T_{dec}^{RTMS} .
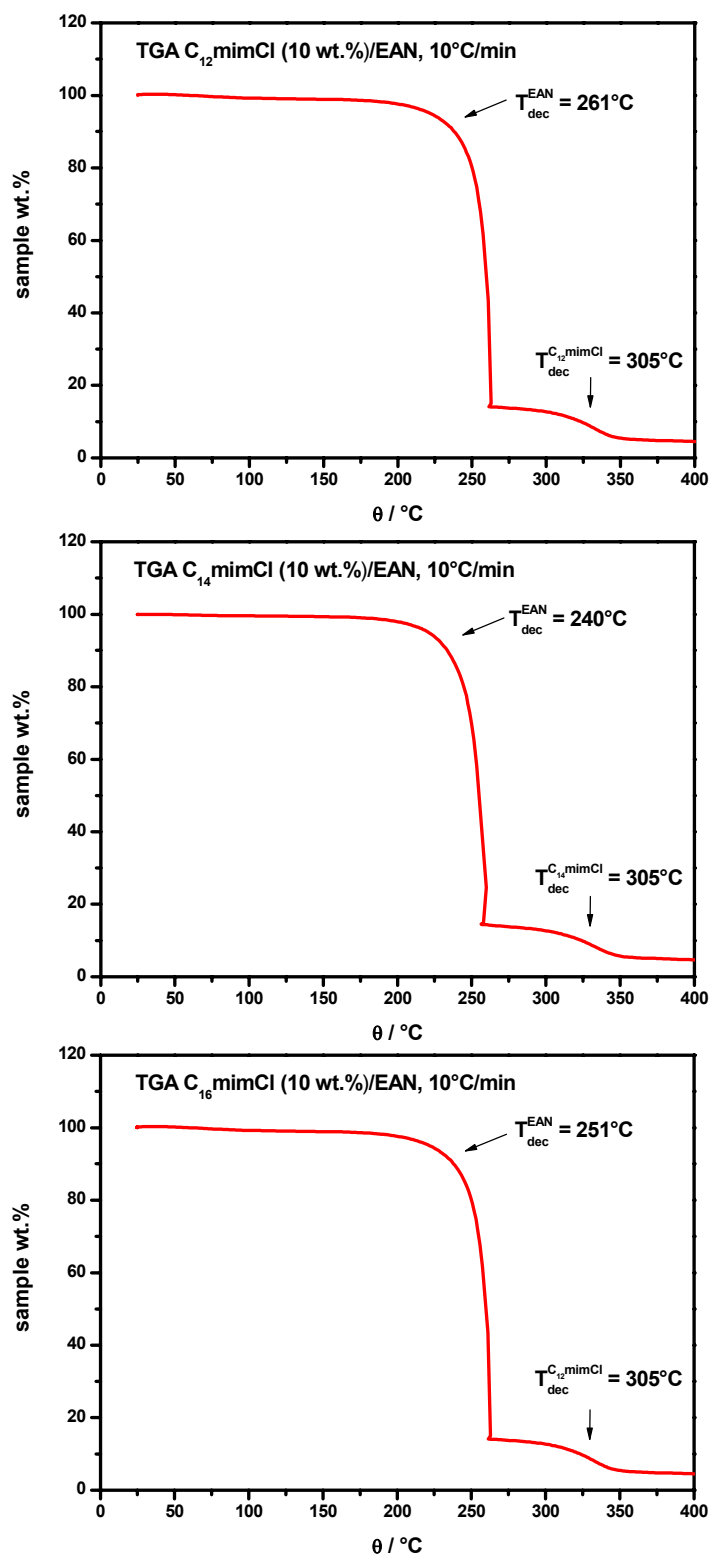
Figure V-34: TGA curves for the $C_n$mimCl/EAN mixtures (10 wt.% SLIL). Two decomposition temperatures, T_{dec}^{SLIL} as well as T_{dec}^{EAN}, found for each mixture are indicated by an arrow.
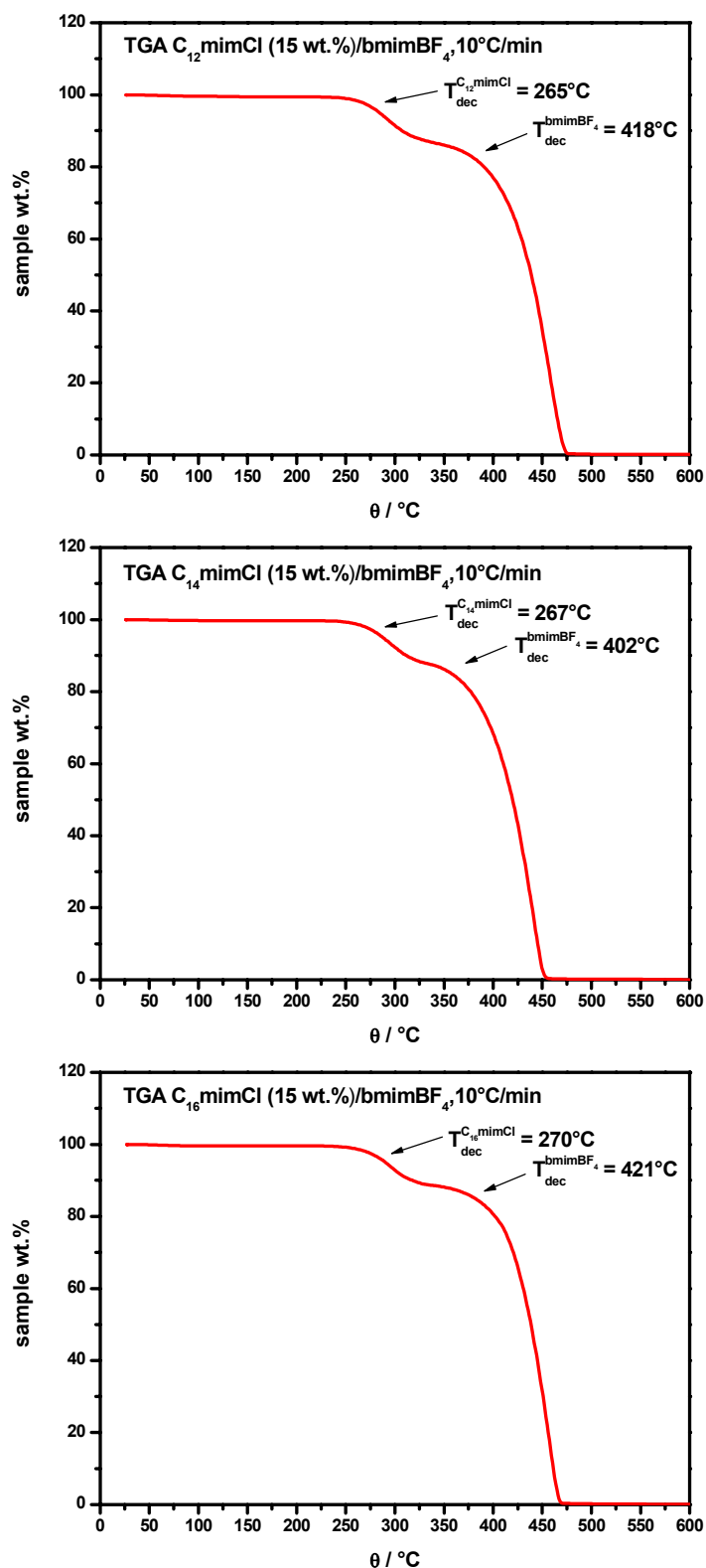
Figure V-35: TGA curves for the $C_n$mimCl/bmimBF$_4$ mixtures (10 wt.% SLIL). Two decomposition temperatures, T_{dec}^{SLIL} as well as $T_{dec}^{bmimBF_4}$, of each mixture are indicated by an arrow.

Figure V-34 and Figure V-35 give the TGA curves obtained for the $C_n$mimCl/EAN (10 wt.% SLIL) and the $C_n$mimCl/bmimBF$_4$ (15 wt.% SLIL) mixtures. Contrary to the results presented for the pure ILs, two decomposition temperatures could be identified for the SLIL/RTMS mixtures, which are linked to the two steps visible in the sample wt.% vs. temperature plot. This two-step degradation is obviously due to the decomposition of the SLILs and the RTMS, respectively. An overview of the observed results including the decomposition temperature of the SLIL T_{dec}^{SLIL}, the decomposition temperature of the RTMS T_{dec}^{RTMS}, and the connected weight percentage differences, $\Delta wt.\%^{SLIL}$ and $\Delta wt.\%^{RTMS}$, are shown in Table V-20. In the case of the SLIL/EAN mixtures the first huge substance loss ($\approx$ 90 wt.%) can be assigned to the decomposition of EAN, whereas the second one ($\approx$ 10 wt.%) represents the degradation of the present SLIL.

Samples	T_{dec}^{SLIL} / °C	T_{dec}^{RTMS} / °C	$\Delta wt.\%^{SLIL}$	$\Delta wt.\%^{RTMS}$
C$_{12}$mimCl	273	-	-	-
C$_{14}$mimCl	280	-	-	-
C$_{16}$mimCl	274	-	-	-
EAN	-	260	-	-
bmimBF$_4$	-	393	-	-
C$_{12}$mimCl/EAN, 10 wt.%	305	261	8	92
C$_{14}$mimCl/EAN, 10 wt.%	305	241	9	91
C$_{16}$mimCl/EAN, 10 wt.%	305	251	9	91
C$_{12}$mimCl/bmimBF$_4$,15 wt.%	266	418	14	86
C$_{14}$mimCl/bmimBF$_4$,15 wt.%	267	402	12	88
C$_{16}$mimCl/bmimBF$_4$,15 wt.%	270	421	11	89

Table V-20: Results of the TGA measurements for SLILs (C$_{12}$mimCl, C$_{14}$mimCl, C$_{16}$mimCl), RTMS (EAN, bmimBF$_4$), and their mixtures.

The EAN decomposition occurs at around 250°C which is approximately the same value as that of the pure RTMS. Compared to the pure SLILs slightly higher de-

composition temperatures (305°C) were extracted for the $C_n$mimCl salts dissolved in EAN.

A reversed situation was found for the $C_n$mimCl/bmimBF$_4$ mixtures. Here, the first decomposition is due to the degradation of the SLIL and the second one represents the decomposition of the RTMS. The values of T_{dec}^{SLIL} and T_{dec}^{RTMS} agree very well with those quantities obtained for the pure salts.Since the high-temperature stability of each SLIL/RTMS-system is limited by the first occurring degradation, the upper stability temperature of the two investigated systems is very similar, approximately 260-270°C. However, the limiting compound is different, RTMS in the case of the EAN mixtures and the SLILs in the case of the bmimBF$_4$ mixtures. It is noteworthy that no variation of the decomposition temperatures with SLIL content (up to 25 wt.%) was observed. Therefore, the presented TGA results are also representative for SLIL/RTMS mixtures incorporating less quantities of amphiphilic ionic liquid.

2.5.2   Visual observations

In order to get information about the phase behaviour as function of temperature and especially about potentially appearing demixing temperatures, SLIL/RTMS solutions with different $C_n$mimCl concentrations above the *cac*s (up to 25 wt.%) were characterized visually in the wide temperature range of 25-150°C. No phase separation was observed for each system. For this reason, micellar structures can be supposed for each investigated SLIL/RTMS system also up to 150°C. Figure V-36 shows representative examples of SLIL/RTMS mixtures illustrating the isotropic appearance of the solutions between 25°C temperature (or 40°C in the case of the bmimBF$_4$-systems) and 150°C. The SLIL content was 10 percent of weigth for each sample shown.
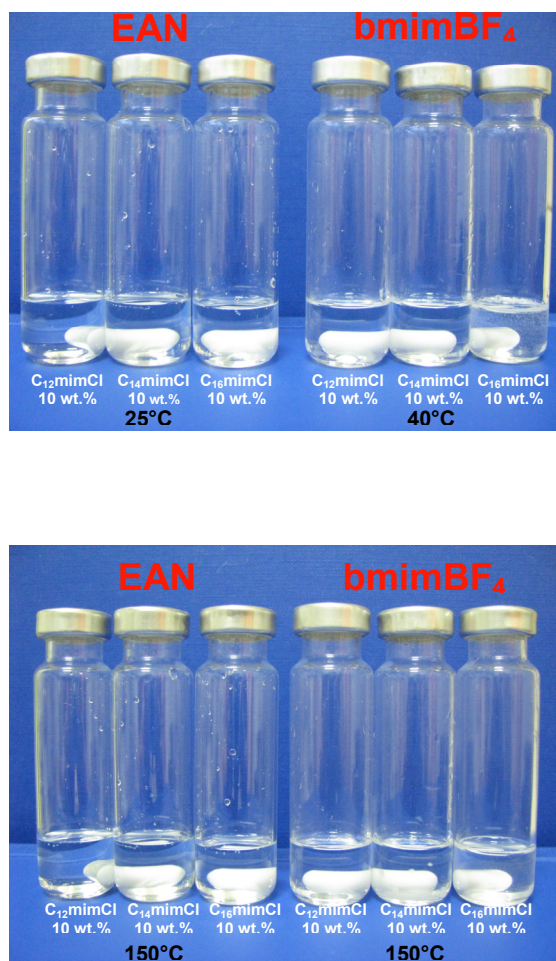
Figure V-36: Representative examples of SLIL/RTMS mixtures illustrating the isotropic appearance of the solutions between 25°C (40°C in the case of the bmimBF$_4$-systems) and 150°C.

2.5.3   High-temperature small-angle scattering

In order to establish the proof of self-assembled aggregates within the examined SLIL/RTMS-mixtures also at elevated temperatures (>> 100°C), high-temperature (HT) SAXS- and SANS-measurements were carried out using a traditional Kratky apparatus at the MPI Golm and the D22 instrument at the LLB Grenoble, respectively. Because of the limited beam time at the two institutes, especially in the case of the SANS measurements, which were performed in parallel to another main project, only C$_{16}$mimCl/EAN as well as C$_{16}$mimCl/bmimBF$_4$ solutions were investigated. Based on the visual observations and the TGA measurements, the following high-temperature

scattering investigations were performed up to a maximal temperature of 150°C at which definitely no decomposition of the SLIL/RTMS-systems occurs. Figure V-37 presents the obtained SAXS patterns of a constant C_{16}mimCl amount dissolved in EAN (10.03 wt.% SLIL) and bmimBF$_4$ (24.94 wt.% SLIL), respectively.

The C_{16}mimCl/EAN solution was measured at five different temperatures between 25°C and 150°C. Additionally, the spectra of pure EAN at 25°C is given, which is also representative for the higher temperatures, since no scattering differences of EAN between room-temperature and the higher temperatures were observed. Due to the low statistics of the used traditional Kratky camera employing a 1D-detector, the given scattering patterns show significant fluctuations of the data points. In order to demonstrate that these fluctuations are exclusively due to the instrument setup and not due to unfavourable X-ray scattering of the micelles, the inset of Figure V-37 (top) additionally shows the SAXS spectrum of the same C_{16}mimCl/EAN sample measured on a rotating anode instrument with a 2D-detector system. As can be seen, a smooth spectrum was achieved resulting from the better statistics of this instrument setup. However, all HT-SAXS measurements had to be performed at the Kratky instrument, since it allowed measurements also at temperatures greater than 50°C. Nevertheless, the resolution of the Kratky instrument is enough in order to draw the following general conclusions: Contrary to the pure EAN sample the scattering curve of the 10.03 wt.% C_{16}mimCl/RTMS solution measured at 25°C shows a peak at $q_{max} \approx 0.8$ nm^{-1}, which is indicative for the presence of self-assembled aggregates within the sample. From the shape of the peak, substantial intermicellar interactions can be assumed. As the temperature increases, the peak shape changes and becomes more diffuse and shifts slightly towards lower q-values. These observations are the consequence of two effects: (i) the isothermal compressibility of the system changes, which is directly connected to the appearance of the interaction peak, and, additionally, (ii) the distance between the micelles increases. The latter may be the direct result of the presence of a lower number of micelles caused by the temperature dependence of the *cac*, which increases as the temperature becomes higher. Thus, the number of micelles diminishes, since a lower amount of SLIL is available for aggregate formation. The central part of the SAXS pat-

tern decays identically for all temperatures indicating no significant change of micellar shape and size for this sample also at higher temperatures.
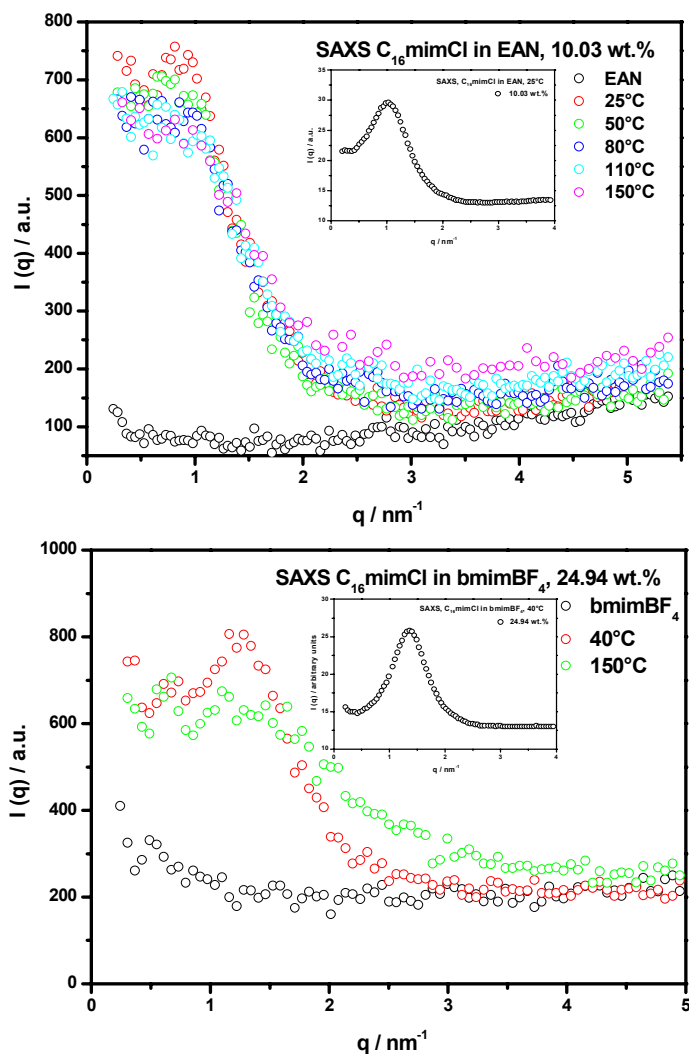
Figure V-37: HT-SAXS spectra of the investigated C_{16}mimCl/EAN and C_{16}mimCl/BF$_4$ systems, respectively, obtained by the Kratky instrument at various temperatures. Additionally, the spectra of pure EAN and bmimBF$_4$ are given for comparison. The insets show the SAXS data of the respective C_{16}mimCl/RTMS solutions obtained by the rotating anode instrument at 25°C and 40°C, respectively.

A similar conclusion can be drawn from the scattering curves of the 25 wt.% C_{16}mimCl/bmimBF$_4$ sample, although only two temperatures were measured. Again, the scattering curve of the SLIL containing sample shows a pronounced peak at 25°C

and 150°C, respectively. The peak is not found in the scattering pattern of the pure bmimBF$_4$. However, the peak location is shifted towards higher q-values ($q_{max} \approx 1.2$ nm^{-1}) compared to the EAN system. Further, the location and the appearance of the scattering decay in the central part of the curve obtained at 40°C differs significantly from that obtained at 150°C. Therefore, a progressive change of the aggregate shape as a function of temperature and/or a polydispersity increase is presumable at higher temperatures. As for the C$_{16}$mimCl/EAN-sample, the inset in Figure V-37 (bottom) shows the SAXS curve obtained from the rotating anode instrument for comparison.

Figure V-38 shows the HT-SANS patterns of C$_{16}$mimCl/EAN- and C$_{16}$mimCl/bmimBF$_4$-samples with varying SLIL concentrations measured at a temperature of 150°C. In opposition to the HT-SAXS measurements, where the change of the scattering pattern as a function of temperature was monitored, the HT-SANS experiments focus the scattering evolution as a function of SLIL concentration in the two solvent-RTMS. For these investigations, the same concentrations were used as for the SANS measurements performed at room-temperature at the Hahn-Meitner-Institute (cp. Chapter V.2.4).

As can be seen for the C$_{16}$mimCl/EAN- and the C$_{16}$mimCl/bmimBF$_4$-series, respectively, the samples with high SLIL content (≥ 5.99 wt.% of SLIL in EAN and ≥ 18 wt.% of SLIL in bmimBF$_4$) show a peak in the scattering pattern indicating the presence of particles also at 150°C. Contrary to the scattering experiments at 25°C, where micellar scattering was observed for all investigated concentrations, the samples with lower SLIL concentrations measured at 150°C show no scattering behaviour, which characterizes micellar scattering. Again, this finding supports the speculation that a significantly higher amount of C$_{16}$mimCl may be necessary for the formation of self-assembled aggregates in the RTMS at 150°C.

Unfortunately, it was not possible to perform a complete model analysis of the HT-SAXS data as well as of the HT-SANS data beside the qualitative interpretations, because of the following reasons: In the case of the HT-SAXS measurements, it was not

possible to obtain absolute scattering intensities, as indicated by the denotation of the y-axis of the SAXS graphs in Figure V-37.
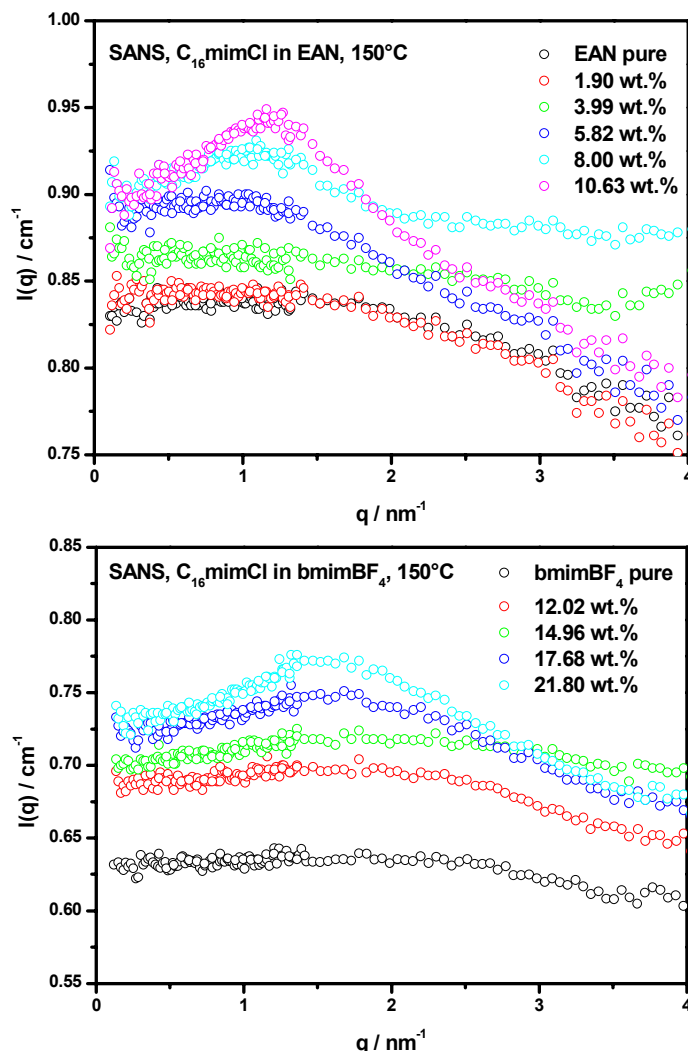
Figure V-38: HT-SANS spectra of the investigated C$_{16}$mimCl/EAN and C$_{16}$mimCl/BF$_4$ systems, respectively, obtained at 150°C. Also, the spectra of pure EAN and bmimBF$_4$ are given for comparison.

This was due to the fact that the workgroup, which was responsible for the used Kratky-SAXS-apparatus at the MPI, was not properly equipped for measurements on absolute scale. No quartz cuvettes and no possibility to perform transmission measurements, which are crucial for the calculation of absolute intensities, were available during the research visits at the MPI. On the other hand, (ii) the HT-SANS were obtained on absolute scale, but the curves are unusable for model fitting for some other reason.

As can be seen in Figure V-38, the scattering curves of both investigated systems show exceptional decay behaviour in the high q-region for some concentrations, perhaps caused by the sample holder or a problem concerning the detector itself during the measurement. Until now, the responsible problem is unclear. Again, a model dependent analysis is impossible.

Although this situation is not satisfactory, the qualitative interpretation of the scattering patterns, however, establishes the proof that C_{16}mimCl forms aggregates in both solvent-RTMS also at high temperatures (up to 150°C, perhaps more). Therefore, it could be demonstrated that it is possible to extend the limited temperature range of aqueous surfactant systems by the present C_{16}mimCl/RTMS-systems.

It seems noteworthy that a further SANS proposal was submitted to the HMI Berlin in order to perform extensive scattering investigations of the SLIL/RTMS mixtures over a wide temperature and concentration range. The proposal was accepted by the scientific committee, which classified this investigation as high priority due to its highly innovative character. The results of the upcoming SANS measurements will be presented by Dipl.-Chem. Oliver Zech in an upcoming work.

2.6   Bibliography

[1]   D. F. Evans; Self-organization of amphiphiles. *Langmuir* **4**, 1, 3-12 (1988).

[2]   M. S. Ramadan, D. F. Evans and R. Lumry; Why micelles form in water and hydrazine. A reexamination of the origins of hydrophobicity. *Journal of Physical Chemistry* **87**, 22, 4538-4543 (1983).

[3]   M. S. Ramadan, D. F. Evans, R. Lumry and S. Philson; Micelle formation in hydrazine-water mixtures. *Journal of Physical Chemistry* **89**, 15, 3405-3408 (1985).

[4]   S. Dev, K. Gunaseelan and K. Ismail; Micellization of Surfactants in Acetamide Melt. *Langmuir* **16**, 15, 6110-6113 (2000).

[5]   C. McDonald; Effect of change of solvent on the critical micelle concentration of a non-ionic surfactant. *Journal of Pharmacy and Pharmacology* **22**, 2, 148-150 (1970).

[6]   A. Ray; Solvophobic interactions and micelle formation in structure forming nonaqueous solvents. *Nature* **231**, 5301, 313-315 (1971).

[7]   D. F. Evans, A. Yamauchi, R. Roman and E. Z. Casassa; Micelle formation in ethylammonium nitrate, a low-melting fused salt. *Journal of Colloid and Interface Science* **88**, 1, 89-96 (1982).

[8]   A. H. Beesley, D. F. Evans and R. G. Laughlin; Evidence for the essential role of hydrogen bonding in promoting amphiphilic self-assembly: measurements in 3-methylsydnone. *Journal of Physical Chemistry* **92**, 3, 791-793 (1988).

[9]   D. F. Evans; *The Colloidal Domain: Where Physics, Chemistry, Biology, and Technology Meet, 2nd Edition.* Wiley-VCH, (1998).

[10]   D. F. Evans, A. Yamauchi, G. J. Wei and V. A. Bloomfield; Micelle size in ethylammonium nitrate as determined by classical and quasi-elastic light scattering. *Journal of Physical Chemistry* **87**, 18, 3537-3541 (1983).

[11]   D. F. Evans, E. W. Kaler and W. J. Benton; Liquid crystals in a fused salt: b,g-distearoylphosphatidylcholine in N-ethylammonium nitrate. *Journal of Physical Chemistry* **87**, 4, 533-535 (1983).

[12]   T. Welton; Room-Temperature Ionic Liquids. Solvents for Synthesis and Catalysis. *Chemical Reviews* **99**, 8, 2071-2083 (1999).

[13]   N. Byrne, P. C. Howlett, D. R. MacFarlane and M. Forsyth; The zwitterion effect in ionic liquids: Towards practical rechargeable lithium-metal batteries. *Advanced Materials* **17**, 20, 2497-2501 (2005).

[14]   H. Matsumoto and Z.-B. Zhou; Ionic liquid, its manufacture, and secondary lithium battery and double layer capacitor comprising the liquid. National Institute

of Advanced Industrial Science and Technology, Japan. **WO 2005063773** (2005).

[15]   S. Seki, Y. o. Kobayashi, H. Miyashiro, Y. Ohno, A. Usami, Y. Mita, M. Watanabe and N. Terada; Highly reversible lithium metal secondary battery using a room temperature ionic liquid/lithium salt mixture and a surface-coated cathode active material. *Chemical Communications* **5**, 544-545 (2006).

[16]   H. Sakaebe, H. Matsumoto and K. Tatsumi; Application of room temperature ionic liquids to Li batteries. *Electrochimica Acta* **53**, 3, 1048-1054 (2007).

[17]   D. Kuang, C. Klein, Z. Zhang, S. Ito, J. E. Moser, S. M. Zakeeruddin and M. Gratzel; Stable, high-efficiency ionic-liquid-based mesoscopic dye-sensitized solar cells. *Small* **3**, 12, 2094-2102 (2007).

[18]   M. Berginc, U. Opara Krasovec, M. Hocevar and M. Topic; Performance of dye-sensitized solar cells based on Ionic liquids: Effect of temperature and iodine concentration. *Thin Solid Films* **516**, 20, 7155-7159 (2008).

[19]   Y. Cao, J. Zhang, Y. u. Bai, R. Li, S. M. Zakeeruddin, M. Gratzel and P. Wang; Dye-Sensitized Solar Cells with Solvent-Free Ionic Liquid Electrolytes. *Journal of Physical Chemistry C* **112**, 35, 13775-13781 (2008).

[20]   M. Gorlov and L. Kloo; Ionic liquid electrolytes for dye-sensitized solar cells. *Dalton Transactions* **20**, 2655-2666 (2008).

[21]   D. Kuang, S. Uchida, R. Humphry-Baker, S. M. Zakeeruddin and M. Graetzel; Organic dye-sensitized ionic liquid based solar cells: remarkable enhancement in performance through molecular design of indoline sensitizers. *Angewandte Chemie (Int. Ed.)* **47**, 10, 1923-1927 (2008).

[22]   M. U. Araos and G. G. Warr; Self-Assembly of Nonionic Surfactants into Lyotropic Liquid Crystals in Ethylammonium Nitrate, a Room-Temperature Ionic Liquid. *Journal of Physical Chemistry B* **109**, 30, 14275-14277 (2005).

[23]   T. L. Greaves, A. Weerawardena, C. Fong and C. J. Drummond; Many Protic Ionic Liquids Mediate Hydrocarbon-Solvent Interactions and Promote Amphiphile Self-Assembly. *Langmuir* **23**, 2, 402-404 (2007).

[24]   T. L. Greaves, A. Weerawardena, C. Fong and C. J. Drummond; Formation of Amphiphile Self-Assembly Phases in Protic Ionic Liquids. *Journal of Physical Chemistry B* **111**, 16, 4082-4088 (2007).

[25]   T. L. Greaves and C. J. Drummond; Protic Ionic Liquids: Properties and Applications. *Chemical Reviews* **108**, 1, 206-237 (2008).

[26]   T. L. Greaves, A. Weerawardena, I. Krodkiewska and C. J. Drummond; Protic Ionic Liquids: Physicochemical Properties and Behavior as Amphiphile Self-Assembly Solvents. *Journal of Physical Chemistry B* **112**, 3, 896-905 (2008).

[27]   S. Bordel Velasco, M. Turmine, D. Di Caprio and P. Letellier; Micelle formation in ethyl-ammonium nitrate (an ionic liquid). *Colloids and Surfaces, A: Physicochemical and Engineering Aspects* **275**, 1-3, 50-54 (2006).

[28]   S. Thomaier and W. Kunz; Aggregates in mixtures of ionic liquids. *Journal of Molecular Liquids* **130**, 1-3, 104-107 (2007).

[29]   A. Triolo, O. Russina, U. Keiderling and J. Kohlbrecher; Morphology of Poly(ethylene oxide) Dissolved in a Room Temperature Ionic Liquid: A Small Angle Neutron Scattering Study. *Journal of Physical Chemistry B* **110**, 4, 1513-1515 (2006).

[30]   T. L. Merrigan, E. D. Bates, S. C. Dorman and J. H. Davis, Jr; New fluoroalkyl-containing imidazolium compounds as surfactants in conventional room-temperature ionic liquids. *Chemical Communications* **20**, 2051-2052 (2000).

[31]   J. L. Anderson, V. Pino, E. C. Hagberg, V. V. Sheares and D. W. Armstrong; Surfactant solvation effects and micelle formation in ionic liquids. *Chemical Communications* **19**, 2444-2445 (2003).

[32] K. A. Fletcher and S. Pandey; Surfactant Aggregation within Room-Temperature Ionic Liquid 1-Ethyl-3-methylimidazolium Bis(trifluoromethyl-sulfonyl)imide. *Langmuir* **20**, 1, 33-36 (2004).

[33] C. D. Tran and S. Yu; Near-infrared spectroscopic method for the sensitive and direct determination of aggregations of surfactants in various media. *Journal of Colloid and Interface Science* **283**, 2, 613-618 (2005).

[34] H. Jingcheng, S. Aixin, W. Jingzheng, C. Xiao, Z. Wenchang, S. Feng, Z. Feng and L. Weimin; Self-assembled structure in room-temperature ionic liquids. *Chemistry* **11**, 13, 3936-3940 (2005).

[35] J. Tang, D. i. Li, C. Sun, L. Zheng and J. Li; Temperature dependent self-assembly of surfactant Brij 76 in room temperature ionic liquid. *Colloids and Surfaces, A: Physicochemical and Engineering Aspects* **273**, 1-3, 24-28 (2006).

[36] C. Patrascu, F. Gauffre, F. Nallet, R. Bordes, J. Oberdisse, N. de Lauth-Viguerie and C. Mingotaud; Micelles in ionic liquids: Aggregation behavior of alkyl poly(ethyleneglycol)-ethers in 1-butyl-3-methyl-imidazolium type ionic liquids. *ChemPhysChem* **7**, 1, 99-101 (2006).

[37] C. Chiappe and D. Pieraccini; Ionic liquids: solvent properties and organic reactivity. *Journal of Physical Organic Chemistry* **18**, 4, 275-297 (2005).

[38] D. R. Lide; *CRC Handbook of Chemistry and Physics, 83rd Edition.* CRC Press, (2002).

[39] M. H. Ghatee and A. R. Zolghadr; Surface tension measurements of imidazolium-based ionic liquids at liquid-vapor equilibrium. *Fluid Phase Equilibria* **263**, 2, 168-175 (2008).

[40] H. Weingaertner, A. Knocks, W. Schrader and U. Kaatze; Dielectric Spectroscopy of the Room Temperature Molten Salt Ethylammonium Nitrate. *Journal of Physical Chemistry A* **105**, 38, 8646-8650 (2001).

[41] C. Wakai, A. Oleinikova, M. Ott and H. Weingaertner; How Polar Are Ionic Liquids? Determination of the Static Dielectric Constant of an Imidazolium-based Ionic Liquid by Microwave Dielectric Spectroscopy. *Journal of Physical Chemistry B* **109**, 36, 17028-17030 (2005).

[42] D. F. Evans, S.-H. Chen, G. W. Schriver and E. M. Arnett; Thermodynamics of solution of nonpolar gases in a fused salt. Hydrophobic bonding behavior in a nonaqueous system. *Journal of the American Chemical Society* **103**, 2, 481-482 (1981).

[43] M. Zistler, P. Wachter, C. Schreiner, M. Fleischmann, D. Gerhard, P. Wasser-scheid, A. Hinsch and H. J. Gores; Temperature Dependent Impedance Analysis of Binary Ionic Liquid Electrolytes for Dye-Sensitized Solar Cells. *Journal of the Electrochemical Society* **154**, 9, B925-B930 (2007).

[44] P. Wachter, M. Zistler, C. Schreiner, M. Fleischmann, D. Gerhard, P. Wasser-scheid, J. Barthel and H. J. Gores; Temperature Dependence of the Non-Stokesian Charge Transport in Binary Blends of Ionic Liquids. *Journal of Chemical & Engineering Data (in press)* (2008).

[45] P. Wachter, C. Schreiner, M. Zistler, D. Gerhard, P. Wasserscheid and H. J. Gores; A microelectrode study of triiodide diffusion coefficients in mixtures of room temperature ionic liquids, useful for dye-sensitized solar cells. *Micro-chimica Acta* **160**, 1-2, 125-133 (2008).

[46] M. Antonietti, D. Kuang, B. Smarsly and Y. Zhou; Ionic liquids for the conven-ient synthesis of functional nanoparticles and other inorganic nanostructures. *Angewandte Chemie (Int. Ed.)* **43**, 38, 4988-4992 (2004).

[47] F. K. Broome, C. W. Hoerr and H. J. Harwood; The binary systems of water with dodecylammonium chloride and its N-methyl derivatives. *Journal of the American Chemical Society* **73**, 3350-3352 (1951).

[48]   K. Shinoda, M. Hato and T. Hayashi; Physicochemical properties of aqueous solutions of fluorinated surfactants. *Journal of Physical Chemistry* **76**, 6, 909-914 (1972).

[49]   K. Shinoda, Y. Minegishi and H. Arai; Correlation between melting points of alkanoic acids and Krafft points of their sodium salts. *Journal of Physical Chemistry* **80**, 18, 1987-1988 (1976).

[50]   T. Alessandro, R. Olga, K. Uwe and K. Joachim; Morphology of poly(ethylene oxide) dissolved in a room temperature ionic liquid: a small angle neutron scattering study. *The Journal of Physical Chemistry B* **110**, 4, 1513-1515 (2006).

[51]   M. L. Moya, A. Rodriguez, M. d. M. Graciani and G. Fernandez; Role of the solvophobic effect on micellization. *Journal of Colloid and Interface Science* **316**, 2, 787-795 (2007).

[52]   K. Ballerat-Busserolles, C. Bizzo, L. Pezzine, K. Sullivan and E. M. Woolley; Apparent molar volumes and heat capacities of aqueous n-dodecylpyridinium chloride at molalities from 0.003 mol kg-1 to 0.15 mol kg-1, at temperatures from 283.15 K to 393.15 K, and at the pressure 0.35 MPa. *Journal of Chemical Thermodynamics* **30**, 8, 971-983 (1998).

[53]   M. Yamanaka and S. Kaneshina; Volume behavior of mixed micelles of dodecyltrimethylammonium chloride and bromide. *Journal of Solution Chemistry* **20**, 12, 1159-1167 (1991).

[54]   J. L. del Castillo, J. Czapkiewicz, A. Gonzalez Perez and J. R. Rodriguez; Micellization of decyldimethylbenzylammonium chloride at various temperatures studied by densitometry and conductivity. *Colloids and Surfaces, A: Physicochemical and Engineering Aspects* **166**, 1-3, 161-169 (2000).

[55]   P. Lindner and T. Zemb; *Neutron, X-Ray and Light Scattering: Introduction to an Investigative Tool for Colloidal and Polymeric Systems. 1st Edition.* Elsevier Science Publishing, (1991).

[56]   R. Kirste and G. Porod; Small-angle scattering of x-rays by colloidal systems. Asymptotic behavior of the scattering curves. *Kolloid-Zeitschrift* **184**, No. 1, 1-7 (1962).

[57]   T. Perche, X. Auvray, C. Petipas, R. Anthore, E. Perez, I. Rico-Lattes and A. Lattes; Micellization of N-Alkylpyridinium Halides in Formamide Tensiometric and Small Angle Neutron Scattering Study. *Langmuir* **12**, 4, 863-871 (1996).

[58]   J. Wang, H. Wang, S. Zhang, H. Zhang and Y. Zhao; Conductivities, Volumes, Fluorescence, and Aggregation Behavior of Ionic Liquids [C_4mim][BF_4] and [$C_n$mim]Br (n = 4, 6, 8, 10, 12) in Aqueous Solutions. *Journal of Physical Chemistry B* **111**, 22, 6181-6188 (2007).

[59]   F. J. Millero; Molal volumes of electrolytes. *Chemical Reviews* **71**, 2, 147-176 (1971).

[60]   K. L. Gawrys and P. K. Kilpatrick; Asphaltenic aggregates are polydisperse oblate cylinders. *Journal of colloid and interface science* **288**, 2, 325-334 (2005).

[61]   J. Kohlbrecher; Software package SASfit for fitting small-angle scattering curves. *Paul Scherrer Institute* (2008).

[62]   S. Saha, S. Hayashi, A. Kobayashi and H. O. Hamaguchi; Crystal structure of 1-butyl-3-methylimidazolium chloride. A clue to the elucidation of the ionic liquid structure. *Chemistry Letters* **32**, 8, 740-741 (2003).

[63]   J. Sun, D. R. MacFarlane and M. Forsyth; A new family of ionic liquids based on the 1-alkyl-2-methyl pyrrolinium cation. *Electrochimica Acta* **48**, 12, 1707-1711 (2003).

[64]   C. P. Fredlake, J. M. Crosthwaite, D. G. Hert, S. N. V. K. Aki and J. F. Brennecke; Thermophysical properties of imidazolium-based ionic liquids. *Journal of Chemical and Engineering Data* **49**, 4, 954-964 (2004).

[65]   A. Lattes and I. Rico; Aggregation in formamide solution: Reactivity and structure of non-aqueous microemulsions. *Colloids and Surfaces* **35**, 2-4, 221-235 (1989).

[66]   M. R. J. Dack; Importance of solvent internal pressure and cohesion to solution phenomena. *Chemical Society Reviews* **4**, 2, 211-229 (1975).

[67]   P. Wasserscheid and T. Welton; *Ionic Liquids in Synthesis, 2nd Edition.* Wiley-VCH, (2003)**.**

[68]   T. Singh and A. Kumar; Static dielectric constant of room temperature ionic liquids: internal pressure and cohesive energy density approach. *The journal of physical chemistry. B* **112**, 41, 12968-12972 (2008).

[69]   D. H. Zaitsau, G. J. Kabo, A. A. Strechan, Y. U. Paulechka, A. Tschersich, S. P. Verevkin and A. Heintz; Experimental Vapor Pressures of 1-Alkyl-3-methyl-imidazolium Bis(trifluoromethylsulfonyl)imides and a Correlation Scheme for Estimation of Vaporization Enthalpies of Ionic Liquids. *Journal of Physical Chemistry A* **110**, 22, 7303-7306 (2006).

[70]   A. Tekin, J. Safarov, A. Shahverdiyev and E. Hassel; (p, ρ, T) Properties of 1-butyl-3-methylimidazolium tetrafluoroborate and 1-butyl-3-methylimidazolium hexafluorophosphate at T=(298.15 to 398.15) K and pressures up to p=40 MPa. *Journal of Molecular Liquids* **136**, 1-2, 177-182 (2007).

3 Formulation and characterisation of surfactant-like ionic liquid/room temperature molten salt-based microemulsions

In addition to binary colloidal systems constituted by an amphiphilic molecule and a solvent, multi-component self-assembled systems, well known as microemulsions, are of great interest for colloid chemists from the perspective of fundamental investigations as well as from an applicable point of view. Especially, reverse microemulsions in which a polar compound is solubilised by a surfactant, sometimes with the help of a co-surfactant, in an apolar medium (oil) have attracted considerable attention due to their ability to host hydrophilic components in organic solvents. These systems are suitable media for processes, which involve hydrophobic and hydrophilic reactants. Especially as "micro-reactors", microemulsions have gained great attention for a variety of chemical and biological reactions. Until now, the majority of the microemulsion investigations use water as the polar component [1-6].

Over the past years, attempts have been made to formulate and study waterless microemulsions. In this effort, water has been replaced by polar solvents with relatively high dielectric constants and which are immiscible with hydrocarbons [7, 8]. These nonaqueous microemulsions are essentially oil continuous and have attracted much recent interest from both, theoretical (thermodynamics, particle interactions) and practical (potential use as novel reaction media) viewpoints [9, 10]. Several distinct advantages of nonaqueous microemulsions over the aqueous ones are reported in the literature: (i) Nonaqueous systems often show much larger stability regions of isotropic solutions as compared to the analogous aqueous systems [11, 12]. (ii) A larger variety of different surfactants can be used to give nonaqueous microemulsions. For example, a long-chain phosphonium halide could be incorporated in nonaqueous microemulsions, while the corresponding attempts to prepare aqueous microemulsions with this surfactant were unsuccessful [13]. (iii) Waterless microemulsions can be used as good reaction media [14]. They are, of course, particularly attractive for those reactants, which react with water. The most common polar solvents used as water substitutes include formamide (FA),

dimethylformamide (DMF) dimethylacetamide (DMA), ethylene glycol (EG), pro-poylene glycol (PG), and glycerol (GY) [9, 10, 15-18].

More recent studies focus the possibility to design nonaqueous microemulsions using RTMS as water substitutes [19-27]. For this purpose, an apolar solvent such as cyclo-hexane [19], and toluene [20, 23], p-xylene [22], triethylamine [28], and ethylene glycol [26] were used as continuous phase in combination with bmimBF$_4$ and bmimPF$_6$ as the polar mi-cro-environment, respectively. In all cases, the solubilization of the RTMS was estab-lished by the non-ionic Triton X-100 surfactant. The first phase diagram with all sub-regions including (O/RTMS), bicontinuous, and (RTMS/O) of such microemulsions containing an RTMS as polar compound were presented by Han and co-workers in 2004. They clearly demonstrated by freeze-fracture electron microscopy the presence of reverse (RTMS/O) microemulsions build-up by defined bmimBF$_4$ droplet structures similar to those already known from classical (W/O) systems [19]. Their subsequent re-ports also show the usage of bmimPF$_6$ as polar component to enable solubility in tolu-ene [20]. These pioneering studies were followed by investigations concerning the struc-tural details on (RTMS/O) microemulsions. Herein, RTMS microemulsions of TX-100 in p-xylene using polar bmimBF$_4$ as water substitute were investigated by various ex-perimental techniques, e.g. DLS, Fourier transform infrared spectroscopy (FTIR), nu-clear magnetic resonance (NMR) spectroscopy, and UV-Vis spectroscopy. The results showed that the sizes of the RTMS droplets are in the order of magnitude as in classical water containing microemulsions, and that the diameters of the aggregates increase with increasing the bmimBF$_4$ content. Further, the interaction of TX-100 with bmimBF$_4$ was studied. It was found that the electronegative oxygen atoms of EO units are bonded to the electropositive imidazolium ring. The micropolarity of the formed reverse microe-mulsion droplets were monitored by absorption spectroscopy as a function of added bmimBF$_4$ amount using methyl orange (MO) as probe [22]. The same conclusions were drawn for bmimBF$_4$/TX-100/toluene microemulsions, which were also investigated via UV-Vis spectroscopy in combination with a suitable dye probe (methyl orange (MO) and methylene blue (MB), respectively) [24]. Eastoe et al. investigated bmimBF$_4$/TX-100/cylohexane by SANS. The authors found a regular increase in droplet volume with

added bmimBF$_4$ which is common to many droplet microemulsions [29]. The same system was characterized by Seth et al. who studied the effects of confinement in bmimBF$_4$ on solvation dynamics and rotational relaxation of Courmarin-153 using steady-state and picosecond time-resolved emission spectroscopy [21]. Another workgroup investigated the reverse microemulsion droplet interaction forces of the latter system by means of iso-thermal titration calorimetry and the second virial coefficient b_2 was derived from the heat of dilution based on a hard-sphere interaction potential assumption. Much stronger interaction forces between the bmimBF$_4$ microemulsion droplets than in aqueous sys-tems were found as indicated by a much greater b_2 [30]. Furthermore, an ethylene gly-col/TX-100/bmimPF$_6$ containing microemulsion system is described in the literature with characteristics very similar to the already introduced RTMS/TX-100/hydrocarbon microemulsions [26].

Recently, Atkin et al. published a very interesting work about RTMS containing microemulsions featuring several non-ionic alkyl oligoethyleneoxide surfactants (C_iE_j), alkanes (octane, decane, dodecane, and tetradecane) and a protic RTMS (EAN), as polar phase [25]. They investigated different compositions with SAXS and observed a single broad scattering peak like in aqueous systems. The Teubner-Strey model (TS-model) for microemulsions was used to describe the scattering patterns. From this work, two main conclusions were drawn: (i) Generally, the phase behaviour and microstructure of ternary mixtures of the non-ionic surfactants, alkanes, and EAN closely parallels obser-vations in water. However, the surfactant chain-length must be about 4 to 6 –CH$_2$– segments longer in EAN microemulsions to obtain similar effects (e.g. a strongly struc-tured microemulsion) to those observed in the corresponding aqueous systems. (ii) From the SAXS analyses, Atkin et al. supposed that the EAN microemulsions are more structured than their aqueous counterparts are.

Interestingly, all these investigations deal with microemulsions in which a RTMS acts as polar microenvironment and non-ionic surfactant as amphiphile. Until now, no microemulsion systems composed of oil, ionic surfactant, co-surfactant, and a RTMS as water substitute have been reported in the open literature. Based on this fact

as well as on the previous studies directed to the application of SLILs in structured colloidal systems, the third part of the present work was attributed to the formulation of RTMS microemulsions featuring a SLIL in combination with a co-surfactant and oil. For this purpose, C_{16}mimCl was chosen as amphiphile, since this salt exhibited the strongest aggregation ability under the investigated SLILs. Additionally, 1-decanol as co-surfactant, dodecane as oil together with EAN and bmimBF$_4$, respectively, were used. It may be assumed that such RTMS microemulsions comprising ionic liquid amphiphile may show considerable different phase behaviour compared to the corresponding systems with non-ionic surfactants. This could provide new information for the fundamental understanding of RTMS based microemulsions. Further, all compounds used for the formulation of the C_{16}mimCl/1-decanol/dodecane/RTMS microemulsions exhibit no or high boiling points (bp. 1-decanol: 232.9°C; bp. dodecane: 215-217°C)[h] as well as good thermal stabilities. The latter as well as the fact that ionic surfactant based microemulsions are less vulnerable to temperature induced demixing (or significant phase change) than RTMS-microemulsions formed by non-ionic surfactants [26] may predestine these systems also for high-temperature applications, e.g. as high-temperature stable micro-reactors (cp. also Chapter I).

The following studies focus on reverse RTMS/dodecane microemulsions. In this context, the realms of existence of clear and monophasic areas of two pseudo-ternary systems only differing by the RTMS (EAN or bmimBF$_4$) used as water substitute will be presented. The phase behaviour of the two systems along defined experimental paths, which are located in the region of the phase diagrams where reverse RTMS nanodroplets may be assumed, was characterized by means of conductivity, viscosity, dynamic light scattering, UV-Vis spectroscopy, steady-state fluorescence spectroscopy, and SAXS. Furthermore, preliminary investigations concerning the high-temperature stability of the microemulsions were carried out by means of visual observations, DSC, and HT-SANS.

---

[h] *The Merck Index on CD-Rom, Version 12:1.*

3.1   Phase diagrams & experimental paths

Phase diagrams the phase behaviour of microemulsions as a function of the containing substances. Even though four species (C_{16}mimCl, RTMS (EAN or bmimBF$_4$), dodecane and 1-decanol) were used, the phase behaviour at a constant temperature can be described as a pseudo-ternary phase diagram by displaying SLIL and co-surfactant together (at a constant molar ratio). The following phase diagrams were obtained by ascertaining the intersection between 1-phase (1-Φ) and multiphase regions. The determinations were carried out under nitrogen atmosphere in an air-conditioned room, working at 30.0°C.

Phase determinations were performed according to the dynamic and static procedure described by Clausse et al. [31]. Therefore, the surfactant was primarily dissolved in the co-surfactant (1-decanol), to get a stock solution in the molar ratio of 1:4 (C_{16}mimCl:1-decanol), which was transparent and homogeneous. After that, a concentration series of C_{16}mimCl/1-decanol in dodecane was prepared in 5 wt.% steps by adding different amounts of dodecane to a certain amount of stock solution. Thus obtained 21 samples covering a range of surfactant-to-oil mass ratio from $w_{s/o} = 0$ to $w_{s/o} = 1$, were precisely weighted into closable tubes. A schematic phase diagram is given in Figure V-39 where the sample series is located on the surfactants axis (the one on the right), which represents the binary mixtures of C_{16}mimCl/1-decanol (1:4) and dodecane in the ternary diagram. Along the red lines given in Figure V-39, the RTMS was progressively added drop by drop, while a magnetic stirrer assured gentle agitation. Each titration experiment was stopped, once a clouding appeared. To improve the clearness of the transparency-to-turbidity transition, the samples were observed through crossed polarized filters. If the clouding did not disappear after some minutes, the sample tubes were weighed and the amount of RTMS initiating the phase separation was calculated. The actual intention was to identify 1-phase isotropic regions, which have to be not only kinetically, but also thermodynamically stable. This was proofed by static investigations in which different samples located within the isotropic 1-phase region estimated from the previous dynamic procedure were prepared and further stored for several weeks at

30°C. If no phase separation occurred during these period, the samples were supposed to be also thermodynamically stable.
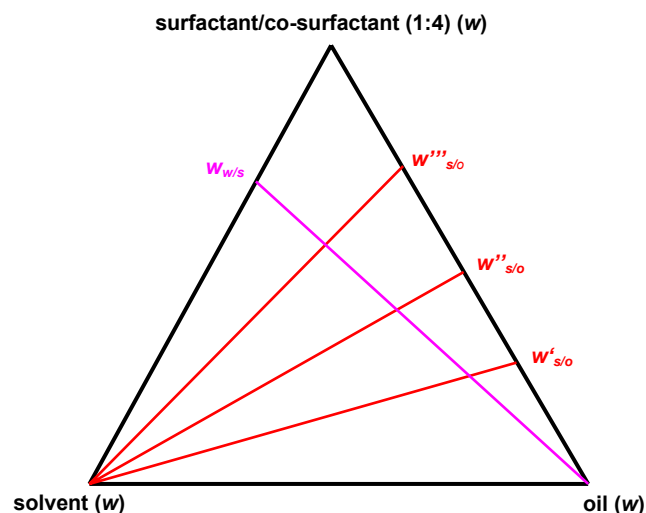
Figure V-39: Schematic pseudo-ternary phase diagram. The red lines represent the continuous titration with RTMS in terms of the proceeding of the phase diagram determination. $w''_{s/o} > w'_{s/o} > w_{s/o}$.

Figure V-40 shows the achieved pseudo-ternary phase diagrams of the two investigated $C_{16}mimCl$/1-decanol/RTMS/dodecane systems. The multi-phase regions are displayed grey and dashed, whereas the transparent 1-phase regions (*L*) left clear. The entire phase diagrams were randomly cross-checked by continuous adding of oil to several solutions of different solvent-to-surfactant mass ratios $w_{w/s}$ representatively highlighted by the purple line in Figure V-39. It was estimated that the accuracy of the measurements for the transparency-to-turbidity transition was always better than ± 2%.

For the EAN containing system, a large monophasic region extending from oil-rich to EAN-rich regions was observed. The boundary between the microemulsion area *L* and the multi-phase region is irregular and exhibits an appendage towards 100% EAN. The demixing limit of EAN and the pseudo-constituent is 72% (w/w) of EAN. In contrast, the *L*-phase in the bmimBF4 system is significantly smaller compared to the EAN system. The amount of bmimBF$_4$ that can be solubilised increases nearly linearly with the SLIL/1-decanol concentration until around 60% (w/w). Further, the phase diagram

is regular and no appendage could be observed. The demixing limit of bmimBF$_4$ and the pseudo-constituent is 41% (w/w) of bmimBF$_4$,which is one reason for the reduced single-phase area compared to the EAN phase diagram.
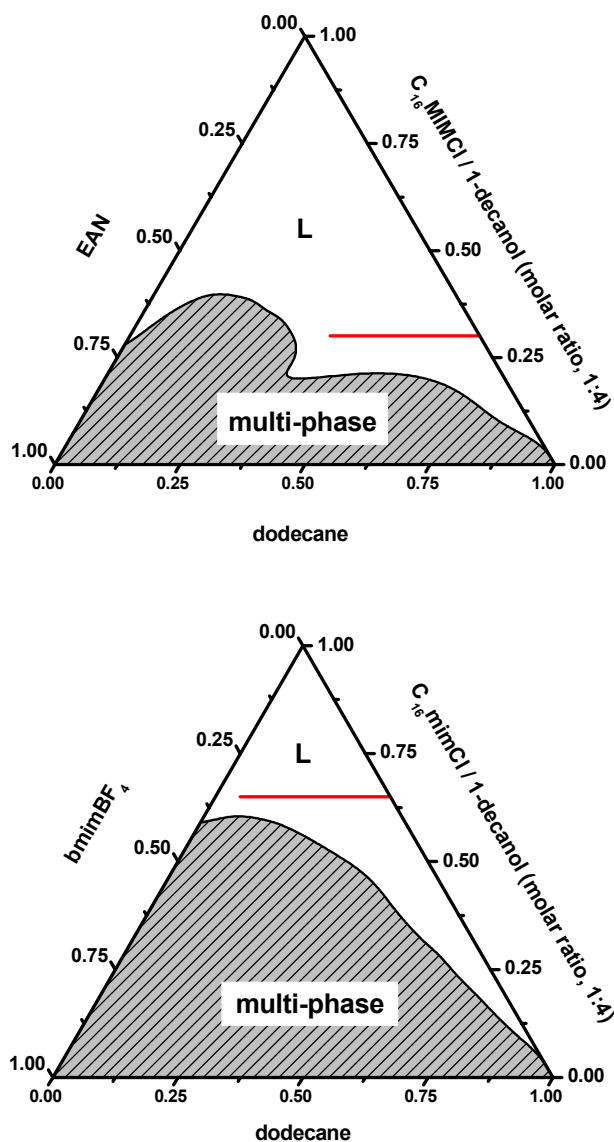
Figure V-40: Pseudo-ternary phase diagrams of C$_{16}$mimCl/1-decanol/RTMS (EAN or bmimBF$_4$)/ do-decane obtained at 30°C. A C$_{16}$mimCl to 1-decanol molar ratio of 1:4 was applied. Additionally, red broken lines indicate the experimental paths used for the upcoming investigations.

It is noteworthy that the shaded regions not necessarily have to be denoted as instable demixing regions. Indeed the intersection between the two regions satisfies the real characteristics of the compositions, but those characteristics were not studied towards higher amounts of RTMS. Especially for the determination of eventually present Windsor phases, which are normally located in the bottom part of the phase diagrams within the multi-phase region, more RTMS should be added to the turbid solutions to see if they become clear again [32-34]. However, this was not the scope of the present studies.

At this point, a reason has to be given for choosing a molar ratio of C_{16}mimCl to 1–decanol of 1:4, which is approximately related to a mass ratio of 1:2. An explanation will be given schematically for the bmimBF$_4$–system, but the same trend was found for the EAN–system. Regarding the bmimBF$_4$–system the solubility power of the formulations containing SLIL/co-surfactant mass ratios of 1:1 , 1:2, and 1:3, respectively, with respect to bmimBF$_4$ were compared. For this purpose, three samples were prepared comprising the particular amounts of SLIL and co-surfactant. Then, each sample tube was loaded with dodecane in order to maintain a mass ratio of SLIL/1-decanol to dodecane of $w_{s/o} = 0.65$. Following the red line within Figure V-40 (bottom), bmimBF$_4$ was continuously added until clouding appeared. The corresponding amount of up-taken bmimBF$_4$ is highlighted by the cyan bottom areas in Figure V-41, whereas the areas on top of it sequentially stand for the amount of oil (purple area), SLIL (yellow area) and 1-decanol (olive area). The mass ratio of SLIL/1-decanol to oil does not change concerning all of the three systems. By contrast, the different surfactant/co-surfactant ratios labelling the x–axis can be identified by comparing the yellow areas with the olive ones on the top. The sample containing the same mass of C_{16}mimCl and 1-decanol seems to be most promising, since it takes the highest amount of bmimBF$_4$ by remaining a 1-phase region. The lowest solubility performance showed the sample comprising a mass ratio of 1:3. The 1:2 sample lies between. Although the system, containing a mass ratio of 1:1, took the highest amount of RTIL until demixing was observed, a mass ratio of 1:2 (molar ratio 1:4) was used for all further investigations. This decision bases upon the fact that C_{16}MIMCl was not completely dissolvable in 1-decanol at a mass ratio of

1:1 at 30°C. Additionally, the temperature of the sample solution addition had to be kept above 50°C during bmimBF$_4$ in order to obtain an isotropic solution which would make an handling of the RTMS-based microemulsions near room-temperature impossible. For this reason, the choice of the 1:2 mass ratio is a reasonable trade-off in consideration of solubilization efficiency and application.
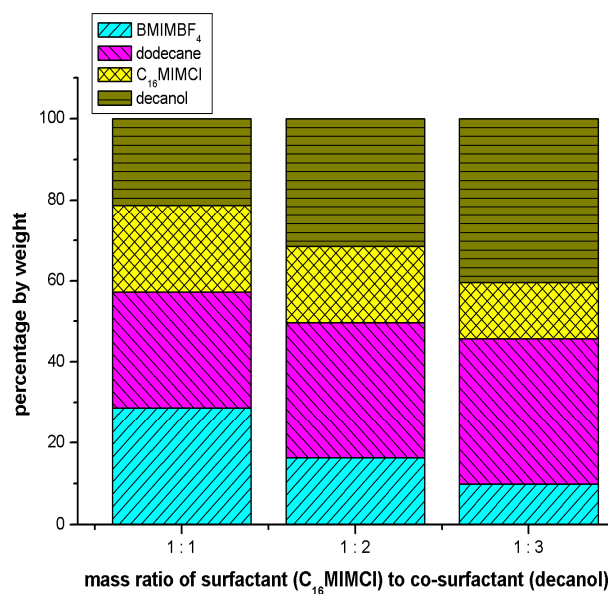
Figure V-41: Comparison of the solubility power of different SLIL/1-decanol mass ratios with respect to bmimBF$_4$. The mass ratio of SLIL/1-decanol to dodecane was kept constant at $w_{s/o}$ = 0.65.

The broken red lines within the phase diagrams of Figure V-40 represent the experimental paths used for all upcoming investigations. Consequently, the C$_{16}$mimCl/1-decanol amount was kept constant (mass ratio of 0.30 for the EAN-system and 0.65 for the bmimBF$_4$-system) during the further studies, whereas the mass ratio of RTMS/dodecane was varied.

3.2   Conductivity: Percolation & charge fluctuation model

The single-phase region of microemulsions can be divided into different sub-regions, such as polar solvent in oil microemulsion region, oil in polar solvent microe-

mulsion region, and bicontinuous region. Following the work of Clausse et al., the different sub-regions can be conveniently evaluated by electrical conductivity measurements [35]. In this work, the phase evolution along the experimental pathways presented within the EAN phase diagram and the bmimBF$_4$ phase diagram, respectively, was determined by this method.

The estimation of a microstructure using conductivity measurements is based on the percolation theory. The static percolation model, which attributes percolation to the appearance of a bicontinuous polar solvent structure, has been proposed to describe the mechanism of percolation in polar solvent containing microemulsions. In this description it is assumed that the open polar solvent channels are responsible for electrical conduction [31, 36]. The polar solvent in oil microemulsion can be regarded as a two-component system in which conducting spherical droplets of polar solvent covered by a surfactant film are embedded in a continuous, insulative oil medium. Connected polar solvent paths consequently explain the sharp increase in the electrical conductivity in such a microemulsion system. In addition, a dynamic percolation model has also been used based on the attractive interactions between the solvent droplets or micelles in order to describe microemulsions [37, 38]. In this picture, the approach considers that the attractive interactions between polar solvent globules are responsible for the formation of percolation clusters, and that charge transport is assured by hopping of ions on globule clusters, which rearrange in time.

Figure V-42 (top) shows the specific conductivity κ along the experimental paths defined previously for the EAN and bmimBF$_4$ containing microemulsions, respectively. In the case of the EAN-system, the phase evolution could be clearly monitored by electrical conduction. At low volume fraction of EAN ($\Phi_{EAN} < 0.04$) the conductivity does not change significantly and stays around 10^{-6}-10^{-5} S m^{-1}. Then, at a defined EAN concentration, it suddenly increases linearly and deviates again at higher EAN content ($\Phi_{EAN} < 0.20$) from linear behaviour. Following the theory of percolation in microemulsion systems, these observations can be interpreted as follows (cp. Chapter II.2.5.3) [36, 37, 39-44].
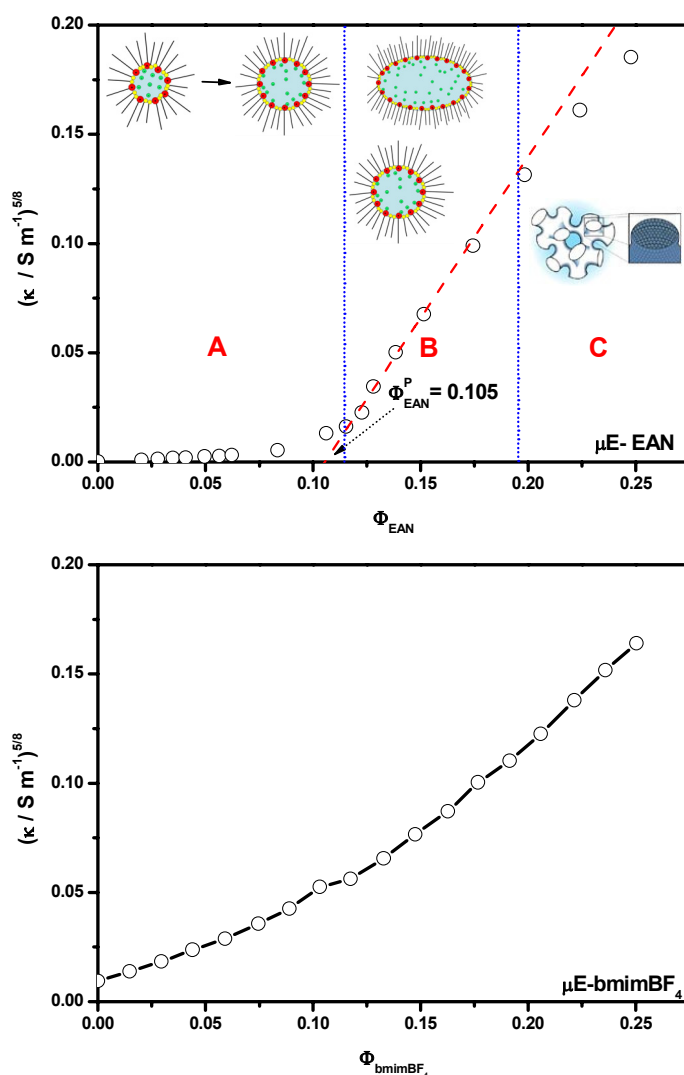
Figure V-42: $\kappa^{5/8}$ **vs. volume fraction RTMS. For the two C$_{16}$mimCl/1-decanol/dodecane/RTMS experimental paths, the amount of SLIL/1-decanol was constant, 0.30 and 0.65 for the EAN-microemulsions and bmimBF$_4$-microemulsions, respectively. In the case of the EAN-system, the conductivity clearly shows the phase evolution along the experimental path: A-C are EAN in dodecane micro-droplets, micro-droplet agglomeration, build-up of the bicontinuous structure. The percolation threshold of EAN Φ_{EAN}^{P} was found as 0.105.**

In the volume fraction range of EAN, where the conductivity remains nearly constant, defined reverse micro droplets are formed consisting of EAN surrounded by a SLIL/co-surfactant film, which is embedded in a continuous dodecane medium with very low conductivity (Figure V-42, top, A). At $\Phi_{EAN}^{P} = 0.105$, the concentration induced percola-

tion threshold of EAN, a percolation phenomenon occurs that is ascribed to reverse micro-droplet aggregation/clustering, which enables ion transfer or transport through the formed interconnections leading to an abrupt increase in conductance (charge transfer). The percolation threshold expressed by the overall droplet volume fraction of core material (EAN) and surface-active compounds (C_{16}mimCl/1-decanol) Φ^P is 0.330 and equals the theoretically calculated value at which the effective medium theory of conductor-insulator mixtures begins to hold true [36]. The following linear increase of κ is the consequence of the formation of further EAN/dodecane micro-domains resulting from the partial fusion of associated/clustered reverse micro droplets (Figure V-42, top, B). The deviation of the conductivity from linearity at higher EAN concentrations ($\Phi_{EAN} \approx 0.20$) reveals that the system begins to undergo a structural transition and becomes more bicontinuous due to the progressive growth and interconnection of the EAN/dodecane micro-domains (Figure V-42, top, C).

The conductivity below and above the percolation threshold can be described by appropriate asymptotic power laws defined by the two characteristic exponents μ and s. From computer simulations it is known that the exponents μ and s vary depending on the present percolation type, dynamic and static, respectively [36]. Consequently, it is possible to distinguish between dynamic or static percolation in microemulsion systems. Additionally, it is possible to obtain the width of the percolation transition Δ. For this purpose, $ln(\kappa)$ was plotted as a function of $ln\left(\left|\Phi - \Phi_P\right|\right)$. μ and s could be determined from the linear fits of the two linear compartments, whereas Δ is the intersection point of the latter fits (Figure V-43). The values found for the parameters μ, s, and Δ are 1.65, 1.28, and 0.015, respectively. These quantities are inline with values already presented for dynamic percolation happened in conventional W/O microemulsions [45, 46]. Note that one of the conditions to observe percolative behaviour is that the interfacial film formed by the surface-active components has to be flexible enough. Additionally, considerable attractive interactions together with a subsequent material exchange between the reverse EAN nanodroplets are a precondition. In the region where κ is very small (10^{-6}–10^{-5} S m^{-1}) and increases linearly with the volume fraction of the droplet forming ingredients Φ, the charge fluctuation range model of Eicke et al. is applicable.
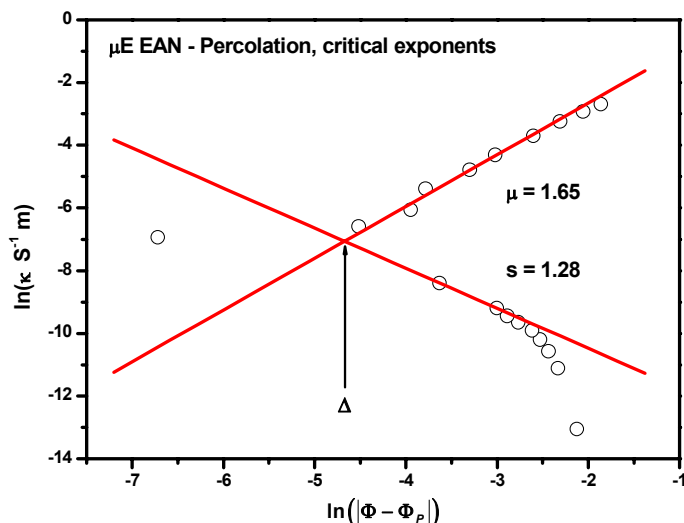
Figure V-43: Plot for the determination of the critical exponents
μ , s , and Δ **based on the theory of percolation**
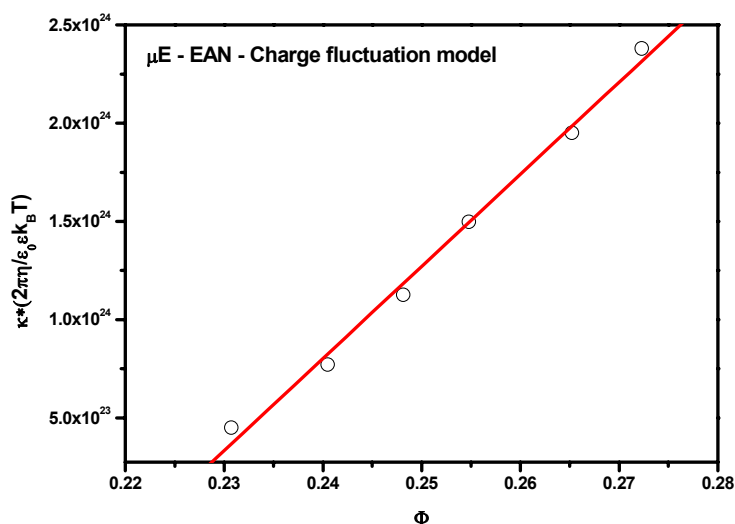
Figure V-44: Plot according to the charge fluctuation model for
the estimate of the droplet radius from the dilute microemulsion
regime.

It allows the estimate of the average radius r_d of the reverse EAN droplets, if they are diluted enough and thus, the conductivity only corresponds to "Stokes transport" of charged nanodroplets [47]. To ensure that the charge fluctuation model is valid, Φ in the range of 0.24 to 0.28 were used together with the physical parameters of the continuous phase, dodecane in this case. For the calculation a viscosity $\eta = 0.00123$ Pas, a dielectric constant $\varepsilon_r = 2.2$, and a temperature of $T = 303.15$ K were applied [48, 49]. Thus, the averaged droplet radius was determined by the slope of the linear fit of the

data presented in Figure V-44. A value of 1.91 nm was extracted. However, it is evident that the model of Eicke et al. gives only a rough impression about the size of the present droplets, since it was found that the radii obtained from this model sometimes deviate about some percents from the real radii [37, 50, 51].

Contrary to the conductivity of the EAN-system from which a lot of information could be obtained concerning the phase behaviour and the present interactions, the conductivity of the bmimBF$_4$-system shows no well-defined bend along the experimental path with a constant SLIL/1-decanol mass ratio of 0.65 (Figure V-42, bottom). An increase of the electrical conductance with bmimBF$_4$ content is evident and maybe a "smeared" percolation transition is indicated between Φ_{bmimBF_4} = 0.075 and Φ_{bmimBF_4} = 0.125. Since, a small and well-defined transition interval Δ is of fundamental importance to use the power laws of the percolation theory, a quantitative interpretation of the $\kappa^{5/8}$-Φ_{bmimBF_4}-plot was not reasonably possible [52]. The sharpness of the transition interval is normally connected to the conductivity ratio of the continuous medium (dodecane) and the solubilised polar solvent, bmimBF$_4$ in this case. If the ratio is large, Δ becomes wide leading to a low resolution around the percolation threshold. For the present situation, this explanation cannot be true, because of the high bmimBF$_4$ conductivity (0.58 S m^{-1}) and the very low dodecane conductivity ($< 10^{-13}$ S m^{-1}) [53, 54]. But another thesis seems to be more probable: Compared to the conductivity of the EAN-system at low Φ_{EAN}, the base conductivity of the bmimBF$_4$-system at low Φ_{bmimBF_4} is about 20 times higher resulting from the higher amount of present ionic C$_{16}$mimCl. This drastically alters the resolution and smears the transition break eventually occurring from the percolation phenomenon and the phase transition, respectively. A further speculation, which seems somewhat rational, is that the experimental path chosen for the conductivity experiment could be located within the same sub-region (along the path where conductivity was measured). Consequently, neither a phase change and nor a percolation occurs which can be seen in the electrical conduction measurement.

3.3   Viscosity

The dynamic viscosity η of the two systems was measured along the same experimental paths as the conductivity. Within the range of the used shear rates, 10 s^{-1} to 400 s^{-1}, Newtonian behaviour of all measured samples was found for both systems (cp. Figure V-45, insets), which is in accordance to findings already reported for aqueous and waterless microemulsions [15, 55]. As can be seen from Figure V-45, η increases for the two investigated C$_{16}$mimCl/1-decanol/RTMS microemulsions as a function of RTMS content. Complementary to the conductivity data, a significant change of the slope within the EAN-system is observed at about $\Phi_{EAN} = 0.080$ (in good agreement to $\Phi_{EAN} = 0.105$ extracted from conductivity), which again can be contributed to the percolation phenomenon. However, it was not possible to confirm the dynamic percolation behaviour of the EAN-system quantitatively by the application of the appropriate power laws, which finally give the critical exponents. Of course, this is because the ratio $\eta_{dodecane} / \eta_{EAN}$ at 30°C (1.23 cP / 23.10 cP $\approx$ 0.05) [49, 56] is too large and therefore, the transition interval Δ is wide making a quantitative analysis impossible. Such a problem is already well-known for common aqueous as well as for non-aqueous microemulsion systems. It has been reported for non-aqueous microemulsions that the ratio of $\eta_{oil} / \eta_{polar\,solvent}$ should be in the range of 10^{-4} to 10^{-5} [52] in order to enable a quantitative analysis, which is not the case here. Contrary to the viscosity ratio, the conductivity ratio $\kappa_{dodecane} / \kappa_{EAN}$ at 30°C is very low (considering $\kappa_{dodecane} < 10^{-13}$ S m^{-1} and $\kappa_{EAN} = 2.14$ S m^{-1}) [53, 57] leading to a very small (sharp) transition regime. Therefore, an exact estimation of the percolation threshold as well as of the critical exponents was only possible from the conductivity data and not from the viscosity measurements. Nevertheless, qualitatively, the sudden increase of the viscosity in the neighbourhood of the threshold determined by the study of conductivity is a satisfactory result and basically confirms the conclusions drawn from the κ data. As the conductivity, the viscosity data of the bmimBF$_4$ path shows no evaluable features. Only a monotonic raise of η as a function of added RTMS was found, no considerable change in slope was observed. Again, a

wide transition interval as well as the location of the experimental path within an un-changing sub-region may be the reason for this observation.
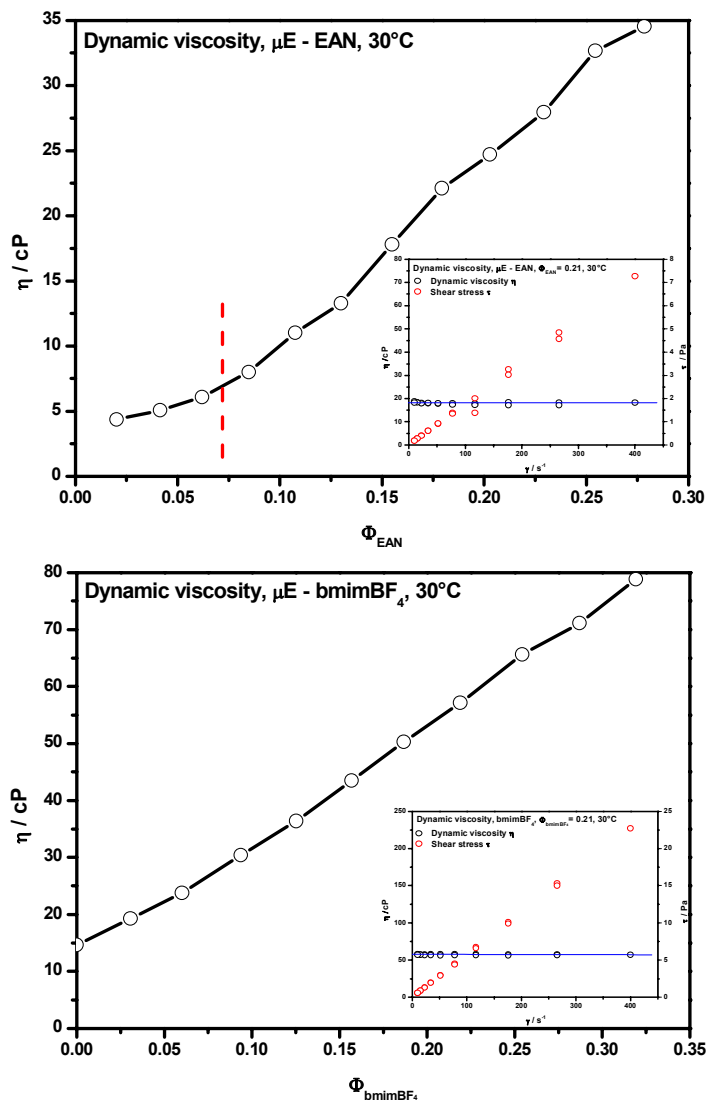
Figure V-45: Dynamic viscosity η in dependence of the volume fraction of RTIL, Φ_{EAN} and Φ_{bmimBF_4}, respectively. For both C$_{16}$mimCl/1-decanol/RTMS microemulsion systems, representative examples of the Newtonian behaviour are given as insets for an EAN-sample (Φ_{EAN} = 0.21) and a bmimBF$_4$-sample (Φ_{bmimBF_4} = 0.21). The red broken line within the EAN-graph represents the appreciated percolation threshold.

3.4   Fluorescence-Spectroscopy: Microenvironment

In order to get more insight to the phase behaviour of the EAN- and bmimBF4-based microemulsion systems, respectively, fluorometric investigations were additionally performed using the cationic dye Auramine-O (Au.O) as fluorescence probe (cp. Figure IV-22). This dye, follows the microviscosity of its environment, and consequently, its fluorescence spectra show changes in intensity and position depending on the viscosity of the surrounding solvent [58, 59]. For the present case, it is noteworthy that the cationic dye Au.O is not soluble in hydrocarbons like dodecane, but it can be readily solubilised in polar RTMS such as EAN and bmimBF$_4$, respectively. However, this dye can be dissolved in apolar solvents by the help of surfactants (or surfactant/co-surfactant mixtures) forming reverse micelles or reverse microemulsion droplets, if the surfactant is used together with an appropriate polar solvent. Thus, when a C$_{16}$mimCl/1-decanol mixture is added to dodecane (and the concentration of the C$_{16}$mimCl/1-decanol mixture is above its *cac*), reverse micelles begin to form. Consequently, Au.O can be considered as completely solubilised in the polar cores of reverse micelles, which consist of imidazolium head groups, chloride counterions, and OH-groups of the co-surfactant. If EAN or bmimBF$_4$ is added to the C$_{16}$mimCl/1-decanol reverse micelles along the experimental path, the RTMS/C$_{16}$mimCl/1-decanol/dodecane microemulsion can form, since the RTMS is accommodated into the core of the reverse micelles. When RTMS is added to a certain extent, free polar pools may appear and Au.O molecules may move gradually from the interfacial layer of the reverse micellar core to the free polar RTMS pools due to the electrostatic repulsion with the imidazolium head group of the C$_{16}$mimCl surfactant [59]. Therefore, the strong emission bands are expected to report on the properties of the microenvironment inside the aggregates, and additionally on the first formation of a free polar RTMS phase within the reverse micelles leading to real microemulsion droplets.

The effect of successive addition of EAN on the microenvironment in the reverse micelles of C$_{16}$mimCl/1-decanol/dodecane is demonstrated in Figure V-46 (inset) by the fluorescence spectra (open circles; note that only every fifth point is shown for

clarity). With an increase of the EAN volume fraction, λ_{max} of Au.O increases and simultaneously the intensity decreases because of the changing microenvironment. In order to quantify this observation and to determine the transition from reverse micelles to real reverse microemulsion droplets a plot of λ_{max} as a function of EAN content has to be established. However, the estimation of λ_{max} evaluation was difficult, since the fluorescence around the intensity maximum of each sample showed strong fluctuations which made an exact determination of the intensity maxima (and therefore of the according wavelength) impossible from the raw spectra. For this reason, the raw data were fitted to a polynomial of higher degree of order and then the maxima were obtained from the second derivative (cp. Figure V-46, inset, lines).
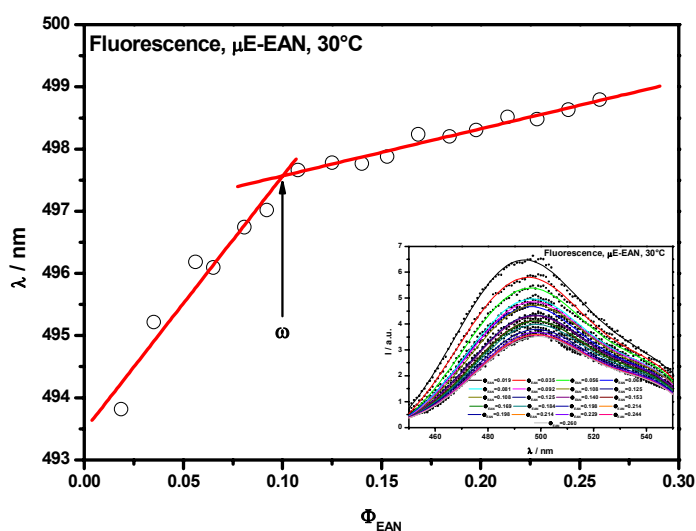
Figure V-46: Plot of wavelengths of maximum fluorescence vs. the amount of added EAN. The inset shows the fluorescence spectra (open circles) with the corresponding polynomial fit (lines). Note that only every fifth point of the raw data is shown for clarity.

Figure V-46 shows the obtained plot of the wavelengths of the maximum fluorescence intensities vs. added EAN amount Φ_{EAN} along the previously defined experimental path. λ_{max} raises, until a sharp breakpoint, $\omega = 0.10$, appears, which corresponds to the completion of the solvation of the polar groups of the surfactant, and is indicative for the first appearance of a free polar EAN pool in the reverse micelle [59]. Above $\omega = 0.10$, λ_{max} only slightly increases. Interestingly, the value of ω is very similar to the already

presented percolation thresholds which could be extracted from the conductivity and viscosity, respectively.

The measured fluorometric data of the bmimBF$_4$ microemulsions are given in Figure V-47. As can be seen, contrary to the EAN-system, the fluorescence maxima do not change significantly with bmimBF$_4$ content indicating no change in microviscosity. This suggests, together with the previous results for the bmimBF$_4$-system that the chosen experimental path could be located within the same sub-region of the system, and therefore no change of the Au.O fluorescence is observed. However, an additional question arises: Are the microemulsions formulated with bmimBF$_4$ along the experimental path isotropic and stable due to the formation of a structured microemulsion, or are they only "molecular" (unstructured) solutions of the components?
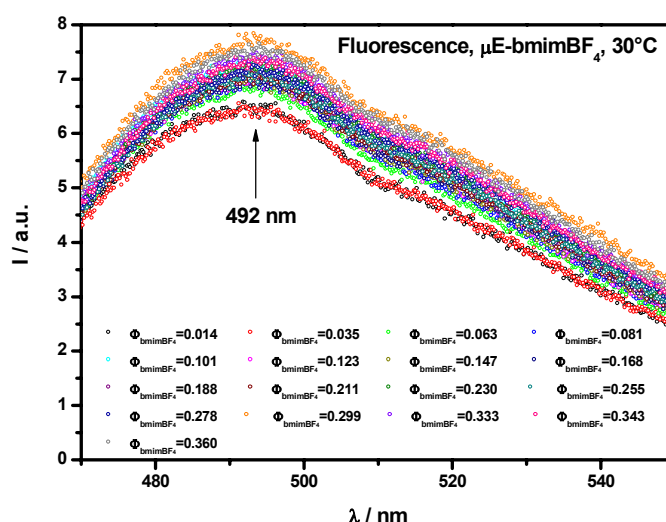
Figure V-47: Fluorescence spectra of samples along the experimental path of the bmimBF$_4$-microemulsion system. The arrow illustrates the invariance of the wavelength (≈ 492 nm).

3.5   Dynamic light scattering: Diffusion & Size

In order to clearly supply the proof that the present systems are structured, dynamic light scattering measurements were carried out at 30°C. It is clear that only if particles are present in the isotropic C$_{16}$mimCl/1-decanol/dodecane/RTMS-solutions a considerable amount of scattering intensity should be observed preconditioned that the scattering contrast between the aggregates and the continuous medium is high enough.

The compositions selected are the same as those previously used for the already presented measurements.

High scattering intensities were obtained for all EAN based microemulsions. This observation strongly suggests the presence of well-defined self-assembled structures formed within this system. In the case of the bmimBF$_4$-microemulsions, also scattering could be observed, but with a much lower intensity, which is, in fact, the first direct confirmation of structuring of this system. However, it was impossible to accomplish a reliable quantitative interpretation of the DLS data due to the lack of intensity, which was at most 0.25 in the best case. Therefore, the following section deals only with DLS studies carried out on the reverse EAN-microemulsions.

Figure V-48 shows the normalized autocorrelation function obtained from the DLS measurements at an angle of 90° for various samples with different EAN volume fractions and the corresponding mono-exponential data fits.
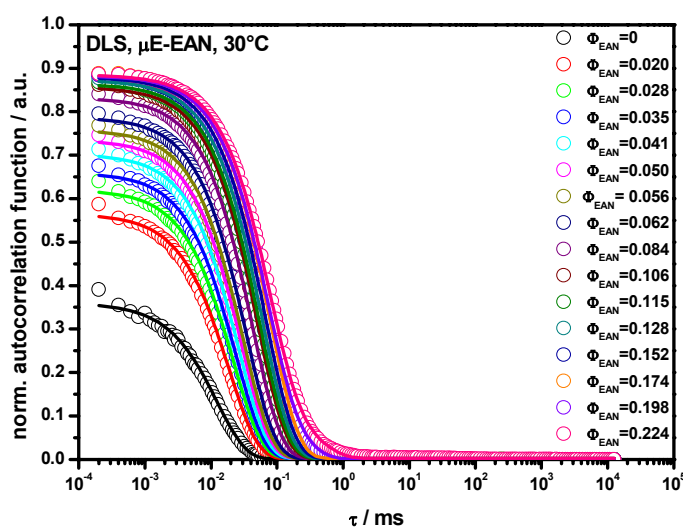
Figure V-48: Normalized autocorrelation functions obtained by DLS (at 90°) for all investigated EAN-microemulsions differing by the solubilised EAN volume fraction (Φ_{EAN}). The solid lines represent the calculated data fits.

Note that the DLS curve of $\Phi_{EAN} = 0$ (Figure V-48, black open circles) represents the scattering behaviour of the reverse C$_{16}$mimCl/1-decanol micelles formed in

dodecane at the fixed surfactant/co-surfactant weight fraction of 0.30 (defined by the chosen experimental path). Figure V-48 clearly demonstrates that the intensity of the autocorrelation function increases as the amount of EAN raises. The low scattering intensity observed for the reverse C_{16}mimCl/1-decanol micelles is the consequence of two basic contributions: (i) The optical contrast between dissolved particles and solvent, and (ii) the size of the particles (correlated with the volume fraction of the particles within the scattering volume). Since the refractive index difference between particles and solvent defines the resolution of a light scattering experiment, it seems most likely that the reverse C_{16}mimCl/1-decanol micelles are near the refractive index matching condition, i.e. the refractive index of the dispersed micelles is nearly equal to that of dodecane. The latter could be also the reason for the very low scattering intensities of the bmimBF$_4$-microemulsions. Furthermore, the scattering intensity is directly proportional to the sixth exponent of the particle radius and therefore on the quality of the autocorrelation function. Thus, the reverse C_{16}mimCl/1-decanol micelles seem to be low in size. With increasing EAN content, both, the optical contrast as well as the size, may be advantageously tuned, because of the gradual accommodation of the EAN within the core of the reverse micelles leading to the formation of microemulsion droplets with bigger size and good optical contrast leading to higher scattering intensities.

The fitting of the DLS data allows the determination of the apparent diffusion coefficient (D^{app}) of the particles in solution, the respective hydrodynamic radii (R_h^{app}), and the size distributions characterized by the polydispersity ($PDI.$) of the reverse micelles and nanodroplets, respectively. For clarity, it should be pointed out that D^{app} as well as R_h^{app} denote apparent (app) magnitudes, since they, in general, can contain contributions from interparticle interactions and therefore, they can deviate from the mean quantities [60-65].

The autocorrelation functions of microemulsions with EAN volume fractions Φ_{EAN} below 0.128 (including also the reverse C_{16}mimCl/1-decanol micelles) could be described very well by a single exponential fitting function, whereas above $\Phi_{EAN} =$ 0.128, near the percolation threshold of EAN, a significant departure from single expo-

nential decay was observed for all correlation functions. In order to quantify the deviation from mono-exponential decay, the correlation functions were additionally analyzed by the method of cumulants. It is noteworthy that D^{app} obtained from the first cumulant was always consistent to the quantity obtained from fitting the single exponential function to the DLS data. The second cumulant achieved from this method is a measure of the polydispersity in the system, or with other words, a measure of the departure of the correlation function from a single exponential behaviour. The higher the polydispersity index, the higher the deviation from a single exponential function. Figure V-49 shows the evolution of the *PDI.* as a function of EAN volume fraction (the broken red line is a guide for the eyes).
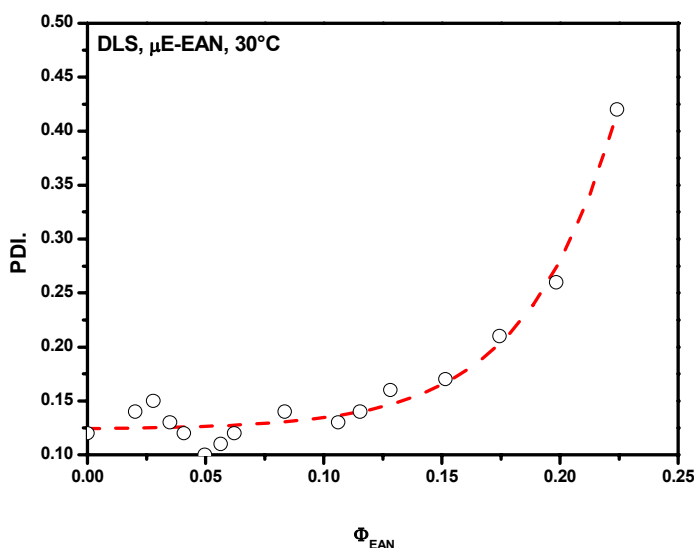
Figure V-49: Evolution of the PDI. as a function of EAN volume fraction. The broken red line is a guide for the eyes.

It can be seen that the deviation from single exponential decay as indicated by the sudden increase of the *PDI.* becomes significant when the EAN volume fraction raises above about 0.128. Nevertheless, below this value of Φ_{EAN} the PDI. stays approximately constant around 0.12 demonstrating the suitability of the mono-exponential fit in the EAN volume fraction range of $0 < \Phi_{EAN} < 0.128$. Consequently, one may expect that in this EAN content range the obtained apparent diffusion coefficients D^{app} may be close to the mean diffusion coefficients, the free-particle values, and hence the mean

hydrodynamic particle radii R_h can be calculated from the Stokes-Einstein relation. For the calculation of R_h, the viscosity ($\eta = 0.00123$) Pas and the refractive index ($n_D = 1.4135$) of the continuous phase, dodecane in this case, for 30°C were used. The viscosity of dodecane at 30°C was obtained from an exponential fit (Vogel-Fulcher-Tamman) of the data in Ref. [49], whereas the refractive index of dodecane at 30°C was directly taken from Ref. [66]. The evolution of R_h calculated form the extracted D^{app} in the range $0 < \Phi_{EAN} < 0.128$ is given in Figure V-50.
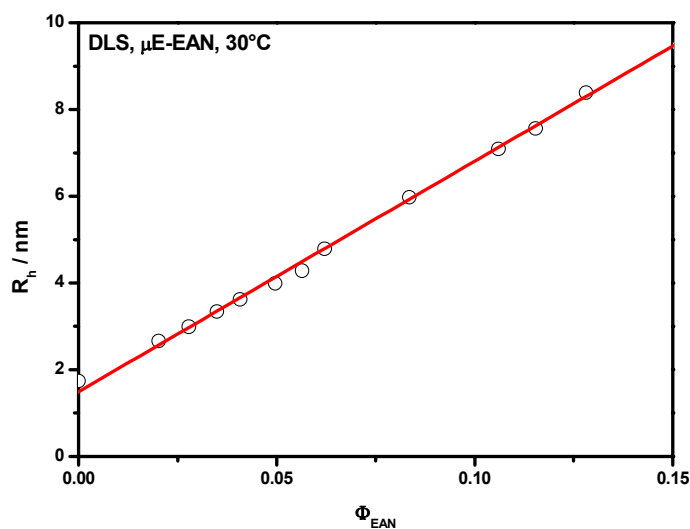
Figure V-50: Change of the hydrodynamic radius obtained from the apparent diffusion coefficient as a function of EAN volume fraction in the range 0 < Φ_{EAN}< 0.128. The red line is a linear fit to the data (R=0.999).

R_h of the aggregates increases linearly with dispersed EAN content. It is known from the swelling law for microemulsions that the size of the droplets should be a linear function of the polar phase (at fixed surfactant/co-surfactant concentration) if the droplets are spherical [67]. Figure V-50 clearly shows that the EAN-microemulsions obey this swelling law, indicating a spherical structure of the EAN-droplets in this Φ_{EAN}-range. The radius of the reverse C_{16}mimCl/1-decanol micelles was found to be 1.74 nm and the extracted radius of the microemulsion droplets increases from about 2.66 nm to about 8.39 nm as Φ_{EAN} raises from 0.020 to 0.128. Thus, the measured radii are in the same order of magnitude as already reported for aqueous and non-aqueous reverse microe-

mulsion droplets [68-74]. Additionally, the radii obtained from DLS for very low EAN volume fractions ($0 < \Phi_{EAN} < 0.05$), where the Eicke model was found to be valid are in the order of magnitude as the value of 1.91 nm calculated by the charge fluctuation model (cp. Chapter V.3.2).

The hydrodynamic radius of the EAN-microemulsion droplets can only be determined from DLS measurements, with any degree of confidence, for samples with correlation functions mono-exponentially decaying, i.e. in the present work for $\Phi_{EAN} <$ 0.128. In this region, the effects of interparticle interactions seem to be negligible. For this reason, no hydrodynamic radii for the measured EAN-microemulsions with $\Phi_{EAN} >$ 0.128 will be presented here. For some colloidal systems, the DLS spectra are found to be the sum of two exponentials described theoretically in terms of the collective and self diffusions, respectively [75-77]. These two diffusion processes have been observed in concentrated colloidal suspensions [78, 79], in charged dispersions [80, 81], and in reverse aqueous droplet microemulsions [71, 74, 77]. In addition, two relaxation modes have been reported in bicontinuous microemulsions. However, in the latter, the two diffusion processes have a different origin related to the local fluctuations of the topology of the bicontinuous network [82]. In order to pay attention to these reports, the relaxation behaviour of the EAN-microemulsions was checked using the CONTIN program package originally developed by Provencher [83]. There is a fundamental difference between describing the correlation function with multi-exponentials or with CONTIN. In effect, while in the first case multi-relaxation processes are assumed, in the second one, distributions of relaxation rates are taken into account. If one is sure that the distribution of the relaxation rates $G(\Gamma)$ extracted from the CONTIN-analysis is due to particle polydispersity, $G(\Gamma)$ can be converted into the corresponding distribution of the particle radii. As expected, the CONTIN analysis gave always one distribution of the relaxation rates at low EAN volume fractions in agreement to the previous findings. Consequently, the size distributions shown in Figure V-51 could be calculated from $G(\Gamma)$ for the samples with $\Phi_{EAN} < 0.128$. Here, the plot of $\Phi_{EAN} = 0$ corresponds to the size distribution of the reverse C_{16}mimCl/1-decanol micelles, whereas the remaining graphs present the size distributions of the suspended EAN-droplets.
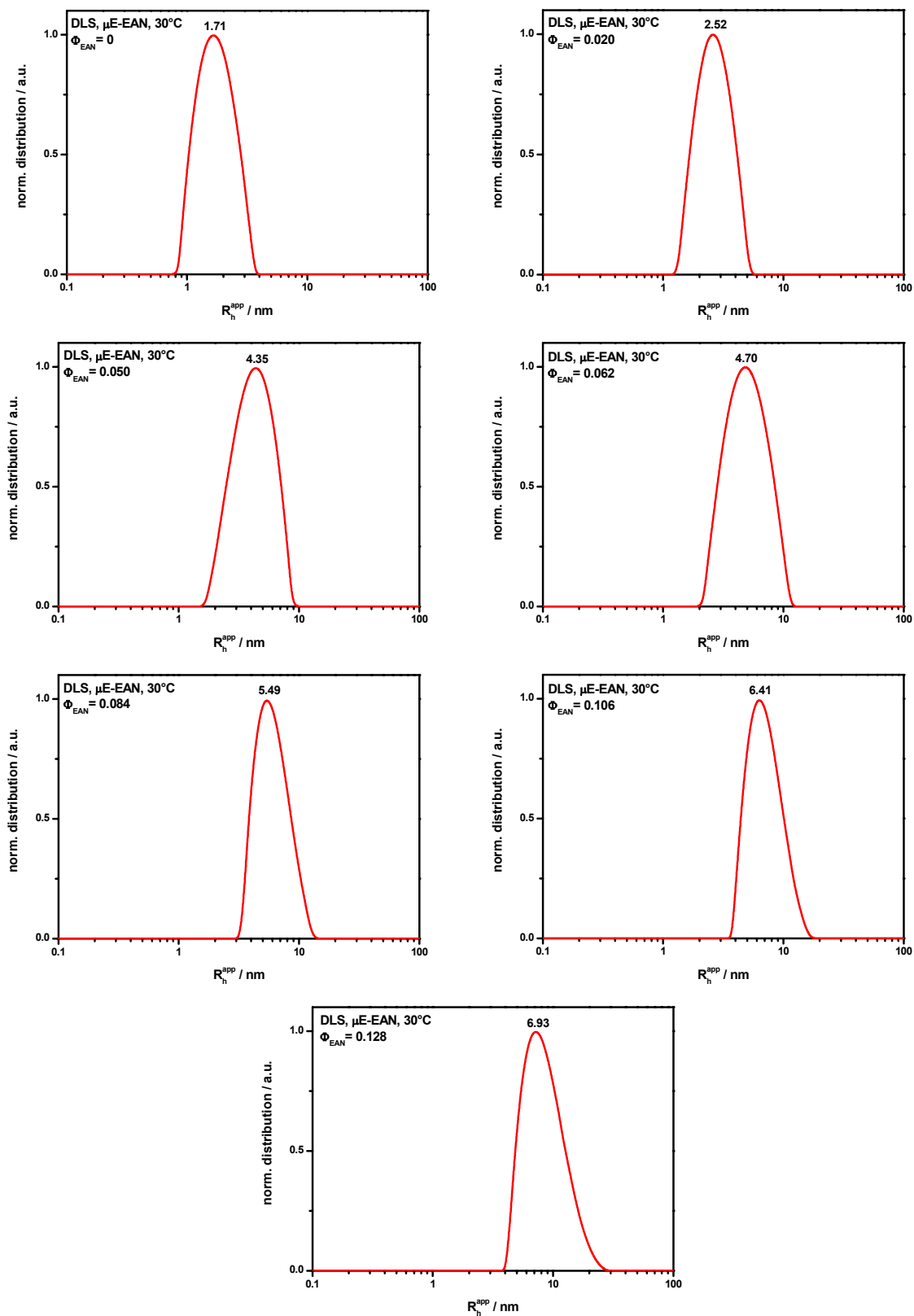
Figure V-51: Size distributions estimated from the distribution of the relaxation rates obtained by CONTIN for C$_{16}$mimCl/1-decanol/dodecane/EAN-microemulsions with EAN volume fractions 0 < Φ$_{EAN}$ < 0.128.

Rather low polydispersities were found for all measured samples as indicated by the width of the distributions. However, the polydispersity seems to increase slightly when the EAN volume fraction becomes higher and it is most pronounced for the sample with $\Phi_{EAN} = 0.128$ denoted by the overhanging decline of the size distribution to bigger particle radii. This observation is in agreement with the percolation phenomenon happening around $\Phi_{EAN}^{p} = 0.105$. As already explained previously, the reverse microemulsion droplets begin to aggregate into clusters at the percolation threshold. For this reason, the polydispersity increases as indicated also by DLS. The peak maxima of the size distributions, which mark the main droplet sizes, correspond quite well to those calculated from the mono-exponential fits. Figure V-52 shows the distributions of the decay times calculated by CONTIN for EAN-microemulsions incorporating EAN volume fractions greater than 0.128.
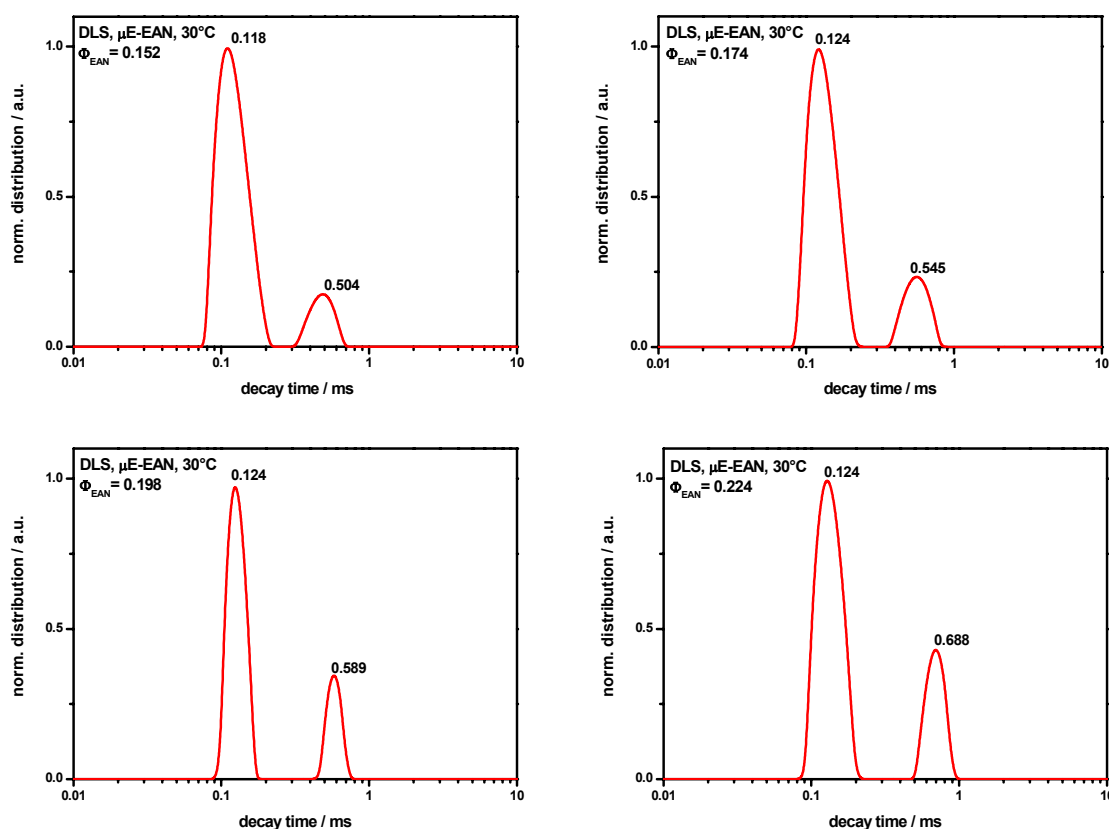
Figure V-52: Distribution of decay times obtained from the CONTIN analysis of the EAN-microemulsions with EAN volume fractions greater than 0.128.

CONTIN clearly detects two modes resulting from a fast diffusion process (small decay time) and a slow diffusion process (big decay time), respectively. Thus, the CONTIN evaluation confirms the results already obtained from the data analysis performed previously. As can be seen, the decay time of the fast diffusion process stays nearly constant independently of the EAN volume fraction, whereas the decay time of the slow diffusion process simultaneously increases as Φ_{EAN} raises. Further, the amplitude of the slow diffusion process increases as the EAN content becomes higher. In Figure V-53, the fast and the slow diffusion coefficients, D_f and D_s, respectively, are presented as a function of EAN volume fraction. Further, the diffusion constants associated to the EAN droplets, D_{app}, are given for comparison.
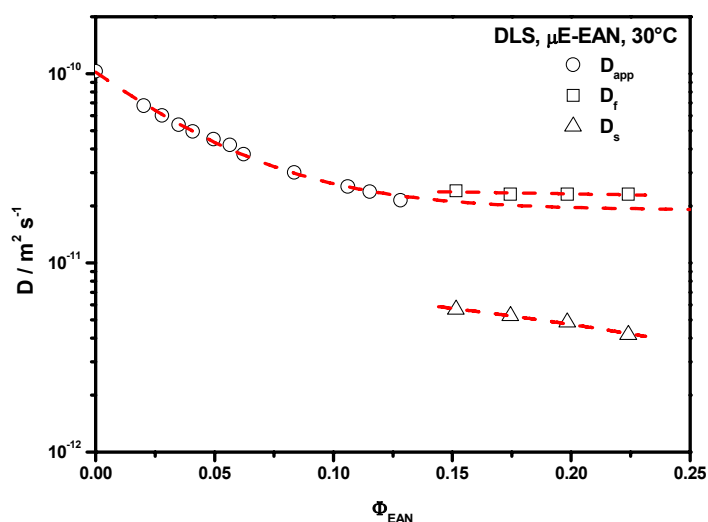
Figure V-53: Diffusion coefficients of the two relaxation processes observed for the reverse EAN-microemulsions as a function of EAN volume fraction. For comparison, the diffusion constants denoted to the EAN droplets are given. The red broken lines are guides for the eyes.

D_f stays nearly constant and is in the order of magnitude as D_{app}, whereas D_s varies with Φ_{EAN} and follows an exponential decay, instead of a power law as expected from D_{app}. Milner et al. and Peter et al., who investigated very swollen concentrated water in oil microemulsions by means of DLS, made very similar observations [82, 84]. These authors also achieved two relaxation modes for their systems and related their origin to an en-

ergy-activated process. They suggested that a topological relaxation mode in the microemulsions by membrane fusion, allowing oil to flow from one region of the space to the other, involving fusion of the droplets/domains, might be the reason for the appearance of the slow relaxation mode. For the present case, this theory would be in good agreement to the dynamic percolation phenomenon, which also involves partial fusion of associated/clustered reverse micro droplets and exchange of droplet material, found for the EAN-system.

3.6   Small angle X-ray scattering: Microemulsion microstructure

In order to clarify the structuring of the EAN-based microemulsions further, and to check the existence of structure within the bmimBF$_4$-microemulsions for which DLS was unsuccessful, small angle X-ray scattering measurements were performed on both formulated systems along the defined experimental tie-lines with constant amphiphile concentration at a temperature of 30°C[i]. Figure V-54 shows the SAXS results on absolute scale for the investigated samples of the EAN- and bmimBF$_4$-microemulsions, respectively. As can be seen, all scattering curves, even the compositions without added RTMS, show a single broad correlation peak with a characteristic q^{-4}-decay at large q. It is evident that the C$_{16}$mimCl/1-decanol/dodecane forms reverse micelles considering the fact that even without RTMS addition X-ray scattering was observed for the two binary compositions of C$_{16}$mimCl/1-decanol (molar ratio of 1:4) and dodecane incorporating either 0.30 or 0.65 weight fraction of surface active compound. For the C$_{16}$mimCl–1-decanol (0.30 weight fraction)/dodecane (0.70 weight fraction) composition, this agrees with the DLS result observed for this sample (cp. Chapter V.3.5). The peak location shifts towards lower q-values as the volume fraction of RTMS increases and simultaneously the peak becomes more pronounced. This behaviour equals the findings achieved for conventional aqueous microemulsions [85-111] and further, the results of Atkin & Warr, who also observed such a peak evolution during their SAXS-investigations of microemulsions consisting of EAN, non-ionic surfactant, and oil [25].

---

[i] The SAXS measurements were performed by Dr. P. Bauduin (CEA, Saclay).
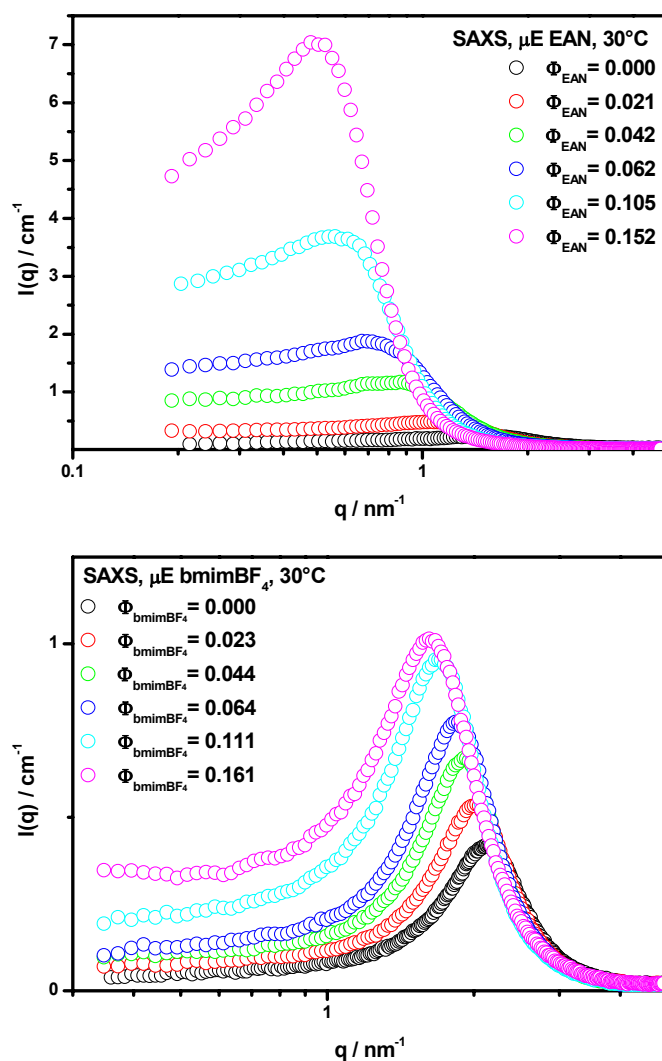
Figure V-54: SAXS spectra of EAN- and bmimBF₄-microemulsions as a function of RTMS volume fractions at 30°C.

3.6.1   Teubner-Strey model: Length scales

The obtained SAXS curves were fitted according to the TS-model that has been widely used to describe scattering from aqueous and non-aqueous microemulsions (cp. Chapter IV.7.2.10). It uses three fitting parameters to describe the observed peak and q^{-4}-decay in terms of two lengths; the periodicity d_{TS} of the oil and polar phase (RTMS) domains, and a correlation length ξ_{TS}, which can be understood as the length scale with which the periodic order decays Eq. (IV-103).
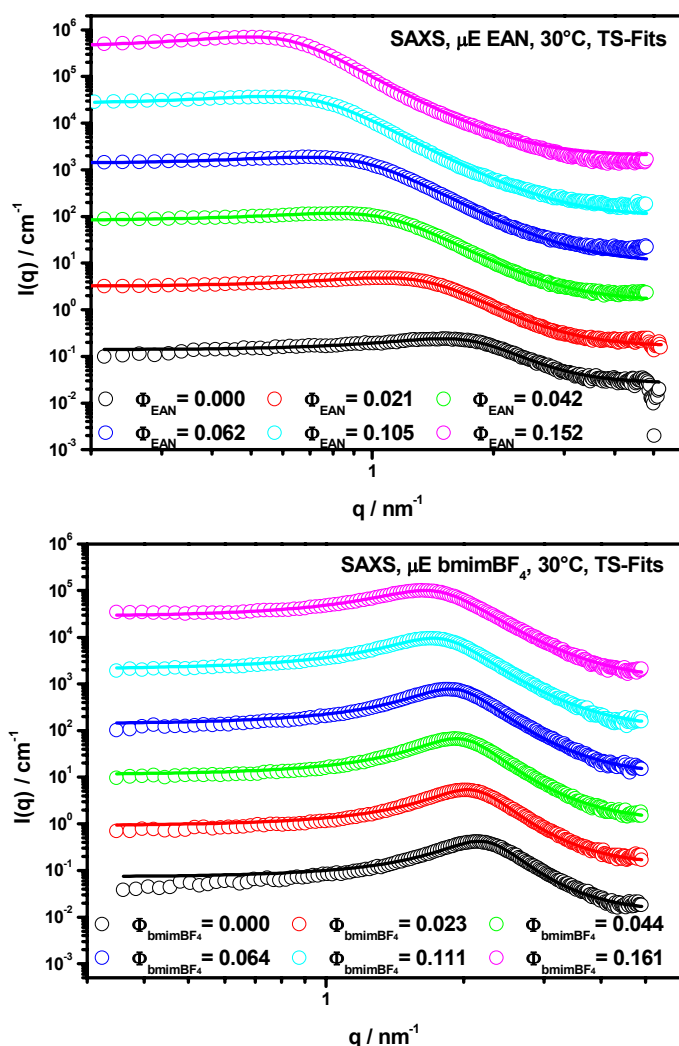
Figure V-55: The SAXS patterns of the investigated EAN- and bmimBF$_4$-microemulsions, respectively. The solid lines represent the TS-fit functions. For clarity, $I(q)$ of the scattering spectra were multiplied by factors of 10^0, 10^1, 10^2, 10^3, and 10^4 (in the order of increasing RTMS volume fractions).

The fitting results are shown in Figure V-55. For better clarity, all spectra are presented on double-log scale and are displaced from each other by multiplication of the scattering intensities by an integer number. The TS-model yield quantitative fits to all EAN- and bmimBF$_4$-based microemulsions, slight deviations from the experimental data are observed at high q for the EAN-system with $\Phi_{EAN} \geq 0.042$. Whether these deviations are due to experimental limitations or an inadequacy of Eq. (IV-103) is unclear. Looking very closely to the bmimBF$_4$-samples, the TS-fits show also some slight deviations at

intermediate q. The extracted TS-fit parameters a_1, c_1, and c_2 are summarized in Table V-21. Further, the calculated values of the two length scales, the periodicity d_{TS} (Eq. (IV-104)) and the correlation length ξ_{TS} (Eq. (IV-104)), are given together with the dimensionless quantities describing the degree of order present in the RTMS-SLIL-microemulsions, the ratio d_{TS}/ξ_{TS}, the amphilicity f_a (Eq. (IV-108)), and the C_3-parameter (Eq. (IV-109)). The peak positions q_{max} and the corresponding scattering intensities $I(q_{max})$ were determined by fitting Eq. (IV-107) to the experimental data. Additionally, the values of q_{max} were crosschecked via Eq. (IV-106), which finally lead to the same q_{max} obtained previously from the data fitting.

Figure V-56 shows the changes of q_{max} and $I(q_{max})$ for the EAN- and bmimBF$_4$-microemulsions, respectively, as a function of RTMS volume fraction solubilised in the microemulsion. In general, two fundamental conclusions can be drawn: (i) All extracted $I(q_{max})$ are much lower for the bmimBF$_4$-microemulsions compared to those of the EAN-microemulsions, and (ii) the peak locations, q_{max}, are located at higher q for the bmimBF$_4$-based microemulsions than the respective quantities determined for the investigated EAN-systems. This finding is indicative for smaller Bragg spacings present within the bmimBF$_4$-systems in comparison to the EAN-systems [88]. The change in $I(q_{max})$ with increasing RTMS content is quite different for the two systems. While there is an increase of $I(q_{max})$ over the whole tie-line of the EAN-system, the scattering intensities at q_{max} of the bmimBF$_4$-microemulsions increase nearly linearly up to a bmimBF$_4$ volume fraction of about 0.064 and then, they stay approximately constant (about 1 cm^{-1}). It should be noted that Lichterfeld et al. have been published the change in the intensities at q_{max} for the system H$_2$0/tetradecane/C$_{12}$E$_5$ as a function of added water volume fraction for constant surfactant volume fraction of 0.15 [88]. They observed a "negative parabolic" dependence of $I(q_{max})$ as the amount of water was increased in the system (cp. Figure V-57). The magnitude of $I(q_{max})$ reached a maximum for the composition where equal amounts of oil and water were incorporated (often connected to the formation of bicontinuous structures) [88-90, 105, 112].

	C$_{16}$mimCl/1-decanol/EAN/dodecane										
Φ_{EAN}	a_2 / cm	c_1 / cm nm^2	c_2 / cm nm^4	BG / cm^{-1}	d_{TS} / nm	ξ_{TS} / nm	q_{max} / nm^{-1}	$I(q_{max})$ / cm^{-1}	d_{TS}/ξ_{TS}	f_a	C_3
0.000	8.96	-3.81	0.85	0.027	3.79	1.41	1.50	0.22	2.69	-0.69	10.82
0.021	3.33	-2.11	0.93	0.016	5.11	1.62	1.06	0.47	3.15	-0.60	8.13
0.042	1.24	-1.13	0.87	0.015	6.54	1.92	0.81	1.16	3.40	-0.55	6.92
0.062	0.74	-0.87	0.93	0.010	7.60	2.17	0.69	1.86	3.50	-0.53	6.47
0.105	0.39	-0.80	1.31	0.010	9.64	2.89	0.55	3.75	3.34	-0.56	7.18
0.152	0.24	-0.77	1.56	0.020	11.15	3.74	0.50	7.08	2.98	-0.63	9.05

	C$_{16}$mimCl/1-decanol/bmimBF$_4$/dodecane										
Φ_{bmimBF_4}	a_2 / cm	c_1 / cm nm^2	c_2 / cm nm^4	BG / cm^{-1}	d_{TS} / nm	ξ_{TS} / nm	q_{max} / nm^{-1}	$I(q_{max})$ / cm^{-1}	d_{TS}/ξ_{TS}	f_a	C_3
0.000	16.91	-6.19	0.66	0.013	2.85	2.30	2.16	0.41	1.24	-0.93	30.07
0.023	12.81	-5.24	0.63	0.013	3.02	2.40	2.04	0.53	1.26	-0.92	29.50
0.044	9.87	-4.49	0.60	0.012	3.19	2.49	1.93	0.66	1.28	-0.92	28.93
0.064	7.86	-3.75	0.54	0.011	3.28	2.46	1.87	0.77	1.33	-0.91	27.62
0.111	5.06	-2.71	046	0.011	3.55	2.34	1.72	0.95	1.52	-0.89	23.76
0.161	3.73	-2.01	0.37	0.012	3.66	2.08	1.65	0.99	1.76	-0.85	19.87

Table V-21: Fit parameters a_2, c_1, and c_2 obtained by applying the TS-model to the experimental SAXS data of the EAN- and bmimBF$_4$-microemulsions, respectively. Further, the characteristic length scales, d_{TS} and ξ_{TS} are given together with the calculated dimensionless quantities standing for the order of the systems, d_{TS}/ξ_{TS}, f_a, and C_3.
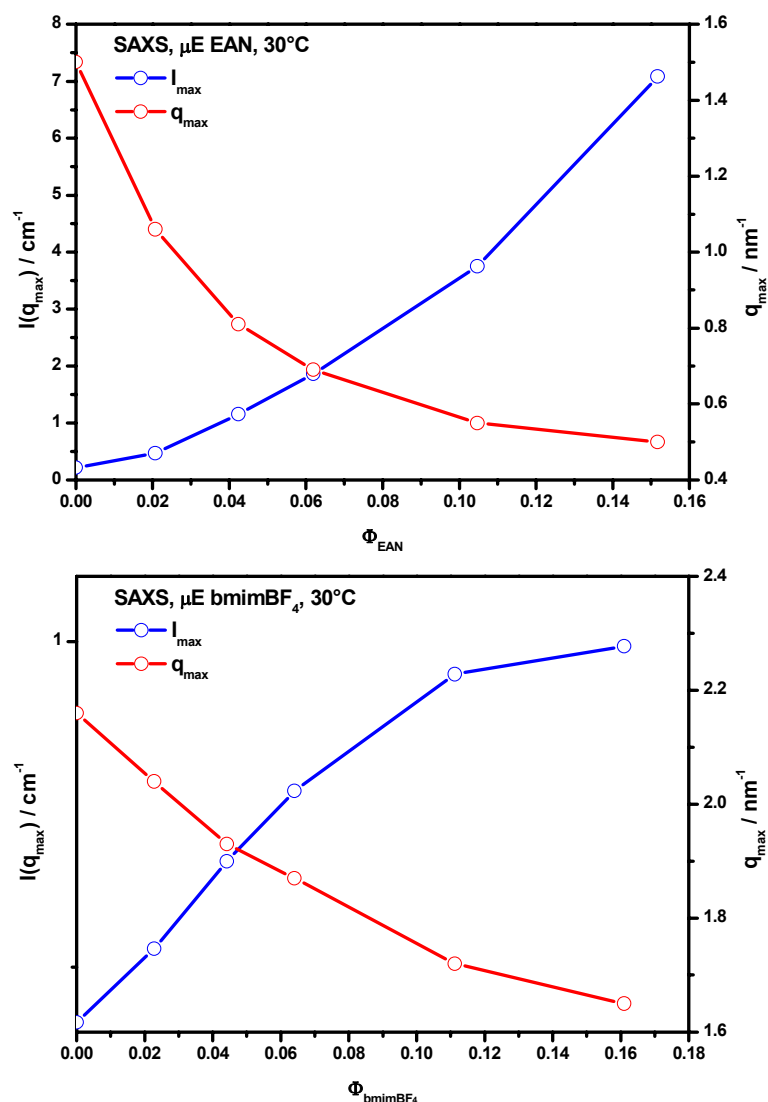
Figure V-56: Scattering intensity at the peak position $I(q_{max})$ from the investigated microemulsions as a function of the volume fraction of EAN and bmimBF$_4$, respectively. Additionally, the corresponding locations of q_{max} are given.

Atkin & Warr also achieved the latter observation for non-ionic surfactant/oil/EAN microemulsions. The comparison of the finding of Lichterfeld et al. and Atkin & Warr, respectively, concerning the $I(q_{max})$ evolution found for the present RTMS-microemulsion systems, lead to the following assumptions: For both RTMS-systems, $I(q_{max})$ changes in a similar way to the "negative parabolic" behaviour shown by Lichterfeld et al. However, it is clear that the experimental $I(q_{max})$ represent different sections of the "negative parabola". Whereas, the $I(q_{max})$ evolution of the EAN-

microemulsions qualitatively reproduce only the rise, the $I(q_{max})$ evolution of the bmimBF$_4$-microemulsions contrarily render the rise as well as the plateau region where the bicontinuous structure with equivalent amounts of polar phase and oil is normally located. Indeed, the bmimBF$_4$-microemulsion sample, which shows the highest $I(q_{max})$ and forms the plateau, consists of nearly equal amounts of bmimBF$_4$ and dodecane ($\Phi_{bmimBF_4} = 0.161$, $\Phi_{dodecane} = 0.169$). Figure V-57 schematically represents the findings of Lichterfeld et al. and the allocated sections of the $I(q_{max})$ behaviour of the two investigated RTMS-SLIL-microemulsions (cp. also Figure V-56).
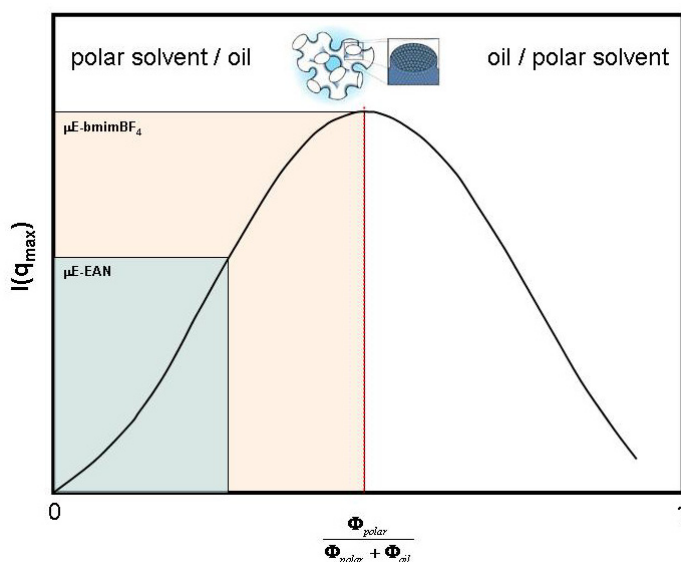
Figure V-57: Schematic representation of the $I(q_{max})$ change (black curve) shown by Lichterfeld et al. (the surfactant concentration was kept constant) [88]. Further, the assumed locations of the experimental $I(q_{max})$ of both investigated RTMS-microemulsions are given.

It is remarked that the assumed location of the EAN-microemulsion intensity behaviour correlates also well with the information previously obtained by the conductivity measurement from which a reverse droplet microemulsion at low EAN volume fraction ($\Phi_{EAN}^{p} < 0.105$) was presumed followed by droplet agglomeration/clustering above the percolation threshold ($\Phi_{EAN}^{p} = 0.105$) and finally by a smooth transition to the bicontinuous structure ($\Phi_{EAN} > 0.200$) (cp. Chapter V.3.2). The highest EAN volume fraction investigated with SAXS is 0.152, which corresponds to an oil volume fraction of 0.559.

Therefore, it is evident that this composition must be allocated to the steep rising section of the "negative parabola", where droplet agglomeration takes place, but no bicontinuous phase is formed. The change of q_{max} with increasing RTMS volume fraction is very similar for both systems. q_{max} decreases significantly as the amount of solubilised RTMS is increased. This observation is also inline with findings for aqueous microemulsions as well as for EAN-microemulsions [25, 88]. The fitted characteristic length scales, d_{TS} and ξ_{TS}, achieved for the two microemulsion systems are somewhat smaller that those on average found for aqueous microemulsions [89]. Atkin & Warr, who observed the same results for their non-ionic surfactant/EAN-microemulsions, attributed this to the lower surfactant efficiency in EAN-systems (higher interfacial area necessitates smaller domains) [25]. It seems very likely that the same explanation holds also true for the present SLIL/RTMS-microemulsions, since the $C_{16}mimCl$ efficiency is significantly less in EAN and bmimBF$_4$, respectively, than in water (cp. Chapter V.1 and Chapter V.1.6). Figure V-58 illustrates the evolution of the two length scales graphically as a function of volume fraction of EAN and bmimBF$_4$, respectively. As can be seen, the TS length scales of the EAN-microemulsions are considerably larger than the corresponding values obtained for the bmimBF$_4$-system. In addition, the change of the two quantities with RTMS-amount solubilised within the investigated SLIL/RTMS-systems differs quite a lot. In the case of the EAN-microemulsions, d_{TS} as well as ξ_{TS} increase steadily as the EAN content rises, whereas for the bmimBF$_4$-microemulsions another trend was observed. First, d_{TS} increases quite linearly as the bmimBF$_4$-content becomes higher (up to $\Phi_{bmimBF_4} = 0.044$), then a slight deviation from the linear behaviour takes place, but d_{TS} still increases. Interestingly, ξ_{TS} obtained for the bmimBF$_4$-system increases also quite linearly up to a bmimBF$_4$ volume fraction of 0.044, then it suddenly decreases as the bmimBF$_4$ amount further rises. Perhaps, this contains a reference to the occurrence of a structural rearrangement within the system. For aqueous microemulsions, many workgroups reported that $d_{TS} \approx 2\xi_{TS}$ [89, 105, 106]. This is not true for the current case, where the EAN- as well as the bmimBF$_4$-microemulsions show considerable deviation from this general result determined for aqueous microemulsions.

In the EAN-microemulsions d_{TS} is about $3\xi_{TS}$ for all examined compositions and for the bmimBF$_4$-system d_{TS} approximately equals ξ_{TS}.
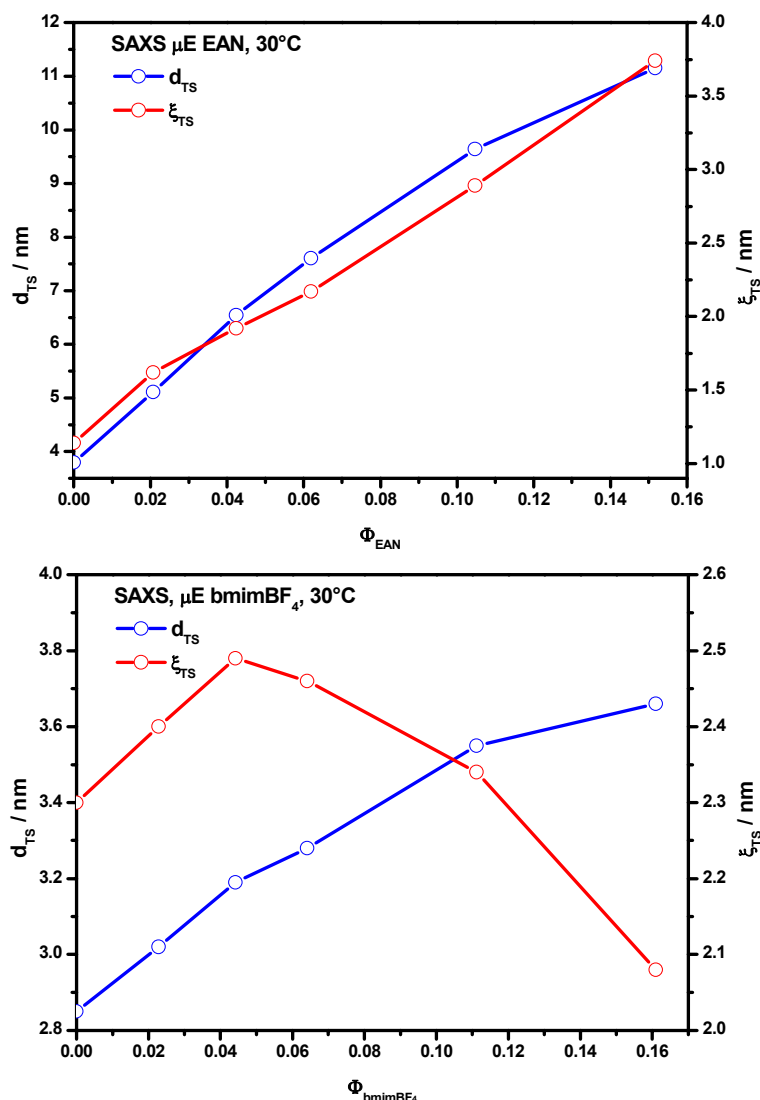
Figure V-58: TS length scales, d_{TS} and ξ_{TS}, are plotted against the volume fraction of EAN and bmimBF$_4$, respectively.

The latter is in good agreement with the results of Atkin & Warr, who also reported that the correlation length of their microemulsions is about the same size as the size of the oil or water domains [25]. This assumes for the bmimBF$_4$-system that the polar and apolar domains remain correlated across further internal interface, and that the microemulsions incorporating bmimBF$_4$ are more highly structured than the investigated EAN-systems. However, it must be noted that until now, it is not completely clear

whether the distinctive structure in the bmimBF$_4$-system is due to the different nature of the solvent-like RTMS or due to the higher amount of surfactant/co-surfactant weight fraction incorporated in the investigated C$_{16}$mimCl/1-decanol/dodecane/bmimBF$_4$-samples. In aqueous microemulsions, and also in C$_{14}$E$_{14}$/EAN/dodecane-microemulsions examined by Atkin & Warr, the d_{TS}/ξ_{TS} ratio decreases as the surfactant concentration increases [25, 105]. But from the data of Atkin & Warr, the change of d_{TS}/ξ_{TS} with increasing surfactant amount (from 45 wt.% to 55 wt.%) at a constant temperature of 50°C was found to be very small (1.23 to 0.98). Therefore, the presumption that different types of solubilised molten-salts in microemulsions may lead to varying interactions between the RTMS and the SLIL is very reasonable. Putting this into the present situation, the achieved results would give an indication that the solubilisation of an imidazolium based solvent-RTMS by an imidazolium based SLIL analogue seems more favourable than the solubilization of a "hetero-RTMS", EAN in the underlying case. Although, this thesis appears to be supposable, it has to be verified by additional scattering experiments, i.e. SAXS measurements along an experimental tie-line with a constant C$_{16}$mimCl/1-decanol weight fraction of 0.65 (as in the case of the bmimBF$_4$-system) and varying amounts of EAN and dodecane, respectively.

Beside the d_{TS}/ξ_{TS} ratio, two additional dimensionless quantities, the amphiphilicity factor f_a and the so-called C_3-parameter, describe the structuring of microemulsions (cp. Chapter IV.7.2.10.1) [91, 98, 106]. A graphical overview of f_a and C_3 for the two RTMS-microemulsion systems is given in Figure V-59. As can be seen, f_a as well as C_3 are self-consistent, i.e. the two parameters show the same trend for the two respective SLIL/RTMS-microemulsions. The amphilicity factors of the EAN-microemulsion series are found to be in the range -0.53 ≤ f_a ≤ -0.69. The lowest f_a (and therefore the highest surfactant strength of C$_{16}$mimCl/1-decanol) was observed for the sample with no added EAN. As the EAN amount is increased, f_a increases slightly until it reaches a maximum at an EAN volume fraction of 0.062. Above, f_a increases again. This observation suggests a lowering of the C$_{16}$mimCl/1-decanol surfactant strength as the EAN content is rising (inline with a decreased surfactant efficiency in molten-salts).
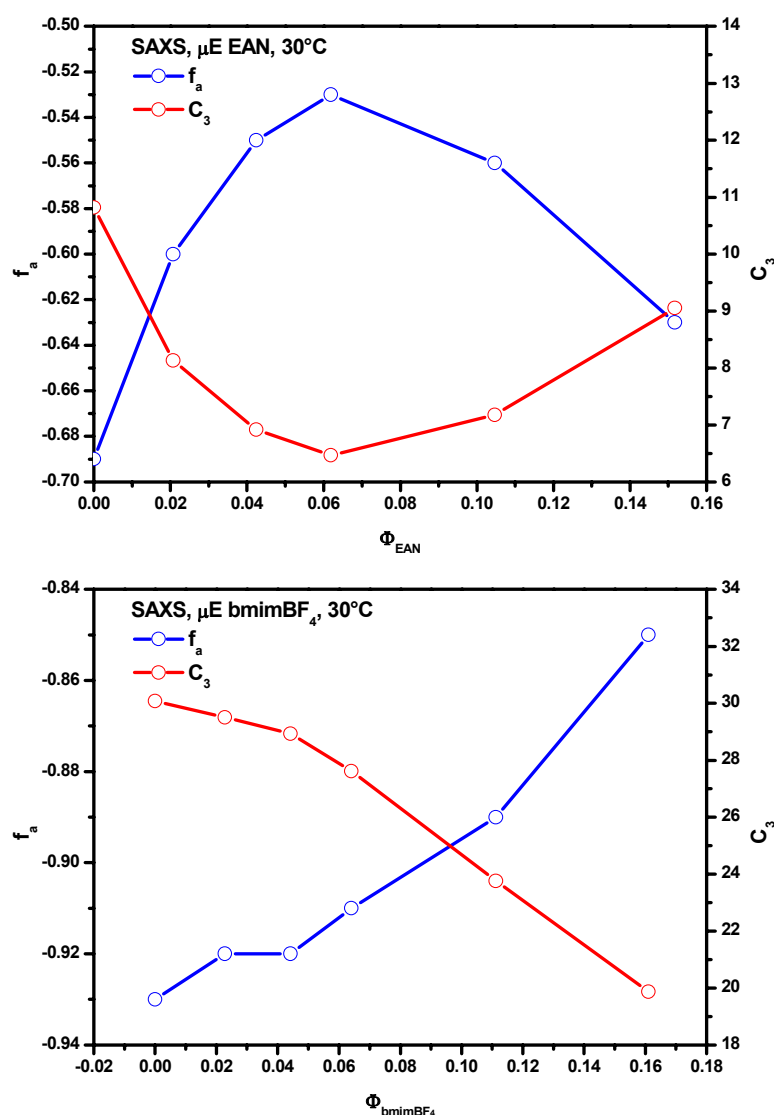
Figure V-59: Amphiphilic factors f_a and C_3-parameters calculated for the EAN- and bmimBF$_4$-microemulsions, respectively.

In the open literature the magnitude of f_a for aqueous systems was related to the presence of droplet microemulsions and bicontinuous structures, respectively (cp. Chapter IV.7.2.10.1). Following this examinations, a low value of the amphiphilic factor ($-0.90 \leq f_a \leq -0.70$) denotes well-structured bicontinuous microemulsions, whereas a higher f_a makes the occurrence of a droplet microemulsion supposable [110]. From the obtained f_a-values ranging between -0.069 and -0.053, a reverse EAN droplet microemulsion at low Φ_{EAN} (≤ 0.062) may be assumed which is in accordance to the conductivity and DLS measurements. At higher EAN volume fractions ($\Phi_{EAN} \geq 0.105$), f_a

begins to decrease which may be the consequence of droplet agglomeration and the stepwise transition towards a bicontinuous structure. Again, this observation is inline with the previous conclusion drawn from conductivity and DLS that at $\Phi_{EAN} \approx 0.10$ appreciable droplet agglomeration, also denoted as percolation, starts involving a transition towards the bicontinuous phase at higher EAN volume fractions (cp. also Chapter V.3.2. and Chapter V.3.5). Therefore, the f_a-value appears to feasibly reproduce the phase evolution within the EAN-microemulsions, because it matches very well the results achieved from the other techniques.

In agreement to f_a, the most distinctive structure denoted by the highest value of the C_3-parameter was found for the sample without solubilised EAN. With increasing EAN amount, C_3 indicate the same trend as previously presented for the amphiphilicity factor. Again, the microemulsions seem to become less structured as the EAN content increases up to $\Phi_{EAN} = 0.062$, as indicated by the lowering of the C_3-value. Above this volume fraction, the C_3-parameter, as f_a did, indicates the development of higher structured microemulsions. Chen et al. used the C_3-parameter in order to judge whether an aqueous microemulsion is bicontinuous or not. From their phenomenological observations, they suppose a disordered bicontinuous structure, if C_3-values much lower than 10 would be obtained for a given microemulsion system ("rule of ten") [91]. In the present work, the determined bicontinuity parameters, C_3, of the EAN-microemulsions range between 10.82 and 6.47. Hence, considering the work of Chen et al., disordered bicontinuous microstructures have to be supposed for the investigated EAN-samples except for the mixture in which no EAN was solubilised (cp. Table V-21 and Figure V-59). This conclusion does not agree with the results already presented for the EAN-microemulsions considering conductivity, DLS, and the amphiphilic factor from which the existence of separated reverse droplet EAN microemulsions followed by a droplet percolation was deduced. Therefore, it must be concluded that the C_3-criterion is not valid for the investigated tie-line of the EAN-system. It is noteworthy that Zemb et al. already reported such a discrepancy between the value of the "bicontinuity" parameter and the existence of the bicontinuous phase [113]. Hence, the concept involving

the amphiphilic factor appears to be the better choice in order to get an idea about the microstructure present within the RTMS-microemulsions.

As already discussed previously by using the d_{TS}/ξ_{TS} ratio, the bmimBF$_4$-microemulsions seem to be stronger structured than the investigated EAN-microemulsions. This assumption is confirmed well by f_a, which ranges between -0.93 and -0.85. The amphiphilicity factors of the bmimBF$_4$-microemulsions are by far more negative than the f_as of the EAN-microemulsions indicating the existence of well ordered phases (very likely bicontinuous) and also a very good surfactant efficiency of the C$_{16}$mimCl. The lowest f_a value (-0.93) was observed for the SLIL/1-decanol reverse micelles, as no bmimBF$_4$ was added. As the volume fraction of bmimBF$_4$ increases up to 0.064, f_a stays nearly constant (below -0.90). However, as Φ_{bmimBF_4} is increased further, f_a also increases. This raise was already reported for the EAN-system and is perhaps due to lowering of the C$_{16}$mimCl surfactant strength when RTMS is added. Further, an intercalation of the bmimBF$_4$ molecules into the surfactant film as a form of a co-surfactant could be possible. The latter assumption is not unusual, because of the molecular structure of bmimBF$_4$ composed of a butyl-chain and an imidazolium head group, which equals the general structure of alcohols classically used as co-surfactants in microemulsions. Another aspect, which affirms this thesis, is the fact that the polarity of bmimBF$_4$ reported in the literature matches those of conventional alcohols with intermediate chain lengths (C$_5$– to C$_8$–) [114, 115]. Note that for EAN a polarity nearly equal to that of water is reported [116], which makes a co-solubilisation of EAN more unfavourable. However, the increase of f_a is not as pronounced as the increase observed for the EAN-micromulsions supporting the consideration that the interactions between the surface-active components (C$_{16}$mimCl/1-decanol) and bmimBF$_4$ are more favourable in respect of microemulsion formation than in the case of the EAN-microemulsions. The evolution of C_3 shows the same trend as the amphiphilicity factor. At low Φ_{bmimBF_4}, C_3 remains nearly constant up to Φ_{bmimBF_4} = 0.064. Above this value, it drops down indicating a loss of structure within the system. While the observed C_3-parameters vary from 30.07 to 19.87 indicating the presence of highly ordered droplet microemulsions, the previous results of the conductivity and further the values of f_a favour bicontinuous

structures. Again, there is a doubt about the coherence of the "bicontinuity" parameter as already discussed previously for the EAN-system. Therefore, it must be concluded that the absolute values of C_3 are meaningless for both examined RTMS/SLIL-microemulsion systems. Only, the changes of C_3 denoting the structuring change within the systems are inline with the evolution obtained for f_a.

3.6.2 GIFT-evaluation: Percus-Yevick effective structure factor

For the investigated EAN-system, the results obtained by conductivity, DLS, fluorescence, and the TS-model analysis of the SAXS data, it was concluded that along the experimental path reverse micelles ($\Phi_{EAN} = 0.000$) and reverse EAN microemulsion droplets ($0.000 < \Phi_{EAN} \leq 0.105$), respectively, are present. In addition, a percolation phenomenon was reported for this system when Φ_{EAN} exceeds 0.105 (cp. Chapters V.3.2, V.3.4, V.3.5, and V.3.6.1). On this basis, the SAXS patterns of the EAN-microemulsions were analyzed further by using the model-free GIFT-technique. In contrast to the TS-model, which incorporates features of droplet microemulsions as well as of bicontinuous structures, the GIFT evaluation is solely based on the particulate picture of microemulsions, no bicontinuity is considered in this analysis [89, 111].

Figure V-60 shows the SAXS data and the corresponding GIFT-fits. Note that the background was subtracted before the data analysis. As can be seen, the fit quality is very good for all SAXS patterns (the mean deviation is given in Table V-22). First, the extracted $p(r)$-functions, which are given in Figure V-61, will be discussed. As reverse micelles and reverse EAN microemulsion droplets are supposed for the EAN-system, the $p(r)$-function can be interpreted in the classical way, as a 'histogram' of all the possible distances inside the micelle and droplet, respectively, summing over all aggregate sizes. Therefore, the maxima of the $p(r)$-functions denoted as r_{max} are representative for the particle dimensions present within the samples. It can be easily recognized that r_{max} increases nearly linearly as function of added EAN from 1.22 nm up to 4.46 (cp. also Figure V-63 and Table V-22). This systematic increase of the particle radius is the direct result of the droplet swelling according to the swelling law of microemulsions. Such a linear swelling is generally observed for systems in which the microemul-

sion droplets are spherical [67]. The presence of spherical EAN droplets is also well confirmed by the bell-shaped appearance of the $p(r)$-function that is characteristic for spherical homogeneous aggregates [117].
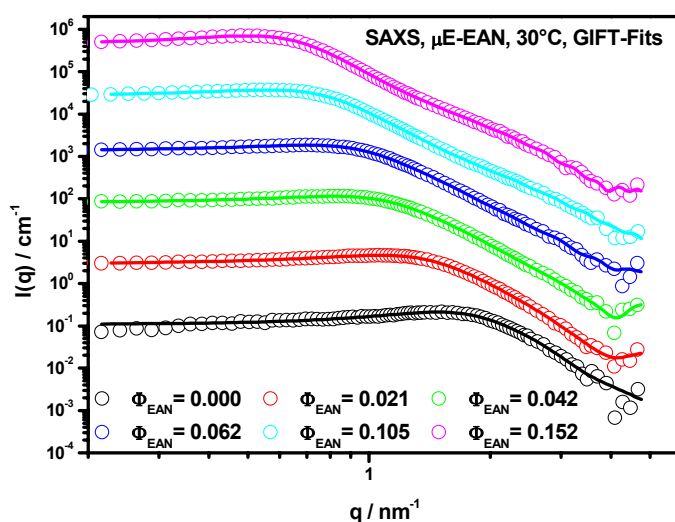
Figure V-60: Fits obtained from the GIFT technique of the EAN-microemulsions investigated by means of SAXS. For clarity, $I(q)$ of the scattering spectra were multiplied by factors of 10^0, 10^1, 10^2, 10^3, and 10^4 (in the order of increasing RTMS volume fractions).

Additionally, a polydispersity can be assumed for the droplets incorporating higher amounts of EAN. The polydispersity is indicated by the overhanging decline of the PDDFs at high r values leading to a significant asymmetry of the $p(r)$-functions (for homogeneous monodisperse spheres the PDDF is a highly symmetric bell-shaped function) [111]. From the literature, it is known that in microemulsions the polydispersity is often ≈ 25%, and from the GIFT evaluation the mean $p(r)$-function of all of the particle sizes in the solution is obtained. This leads to the general problem that it is not possible in a unique way to determine the shape of the aggregates in the systems from such averaged $p(r)$-functions, especially in polydisperse systems, since it was already shown by Mittelbach and Porod that the scattering pattern of an ellipsoid is identical with the scattering pattern of a system of polydisperse spheres [118].
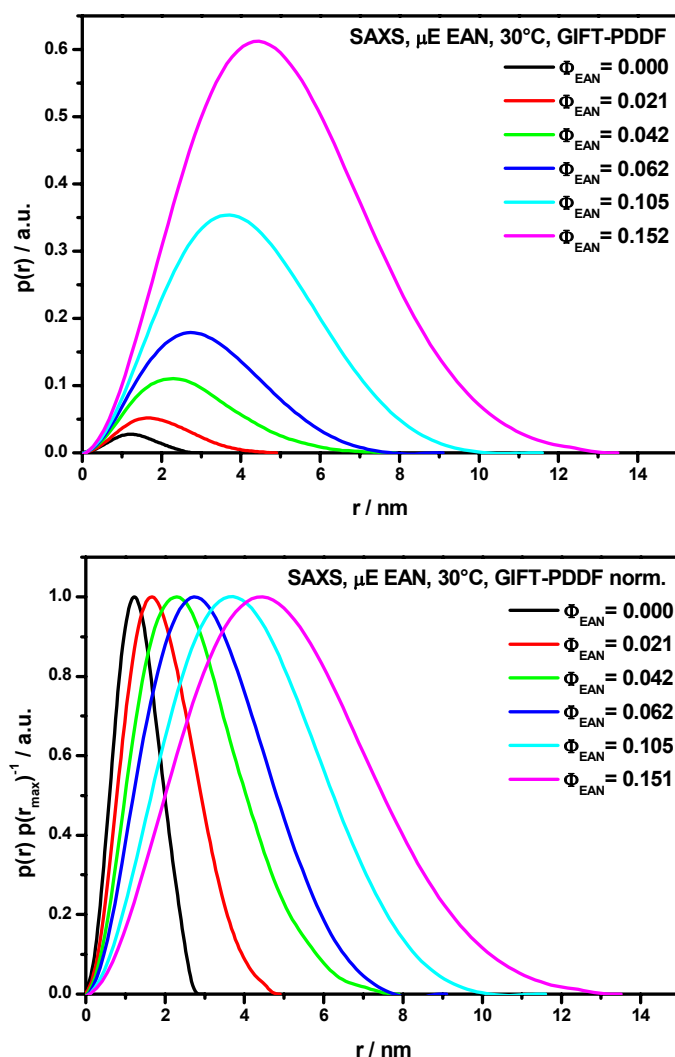
Figure V-61: Pair distribution functions of the EAN-system obtained from the GIFT-analysis (top) and the corresponding normalized pair distribution functions (bottom).

This means that the exact form of the particles remains unknown from the scattering pattern, but together with the DLS results (swelling law), the conclusion that polydisperse spherical EAN droplets are formed holds true. Further, one realises that there is no significant change in the form of the $p(r)$-functions, a fact that is completely independent of the aggregate shape. This leads to the logical reasoning that there is no essential structural variation throughout the experimental path under the given assumptions (whatever the shape of the particles is); only the typical sizes and scattering powers vary. The extracted radii are somewhat smaller than those quantities obtained from DLS. However, this is to be expected, because of the different detection principles of

SAXS compared to DLS. For the first technique, it is clear that mainly the droplet core of the aggregates is detected due to the contrast conditions of the reverse RTMS-microemulsions (high electron density of the core forming components and nearly equal electron density of the alkyl-chains of surfactant and co-surfactant, respectively, in comparison to the continuous dodecane phase). In contrast, the movement of the overall droplet is measured in a DLS experiment leading to radii that describe more or less the complete particle dimension.
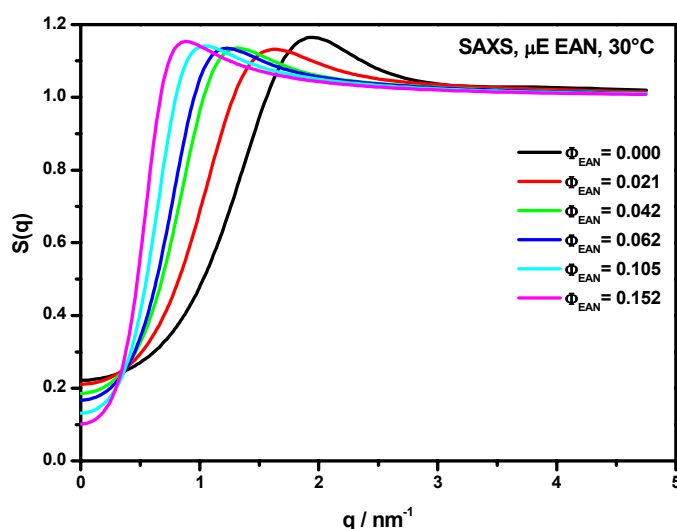
Figure V-62: Structure factors $S_{eff}(q)$ **extracted from the GIFT-evaluation for the measured samples along the experimental path of the EAN-system.**

In addition to the $p(r)$-functions, the effective structure factors $S_{eff}(q)$ (Table V-22) and the correlated parameters, the effective interaction radius R_{eff}, the volume fraction Φ_{eff} and the polydispersity $PDI.$, were obtained from the GIFT evaluation for each data set. Here, Φ_{eff} denotes the overall effective volume fraction of the components (EAN plus $C_{16}mimCl$ plus 1-decanol), which are participating in the aggregate formation. With other words, Φ_{eff} can be understood as the effective hard-sphere volume fraction of droplets in the microemulsion. One problem arises during the evaluation of $S_{eff}(q)$ and consequently of its parameters. There is a direct coupling between two parameters of $S_{eff}(q)$, namely polydispersity and volume fraction. Allowing a free variation of these quasi-linear dependent parameters during evaluation leads to unphysical

oscillations in the $S_{eff}(q)$ parameters. At the same time, a too low polydispersity would result in a too low volume fraction and vice versa [111]. Therefore, two different evaluation procedures are feasible. On the one hand, the polydispersity in the structure factor model can be fixed during the evaluation and the volume fraction can be varied or, on the other hand, the latter can be fixed and the polydispersity can be varied. Neglecting co-solubility of the droplet forming components in the continuous medium (dodecane), Φ_{eff} can be calculated from the sample composition. However, it is clear that up to now nothing about the partition coefficient p of EAN, C_{16}mimCl, and 1-decanol between the droplets and the surrounding dodecane is known. This may lead to a significant uncertainty in the calculation of Φ_{eff} from the known microemulsion composition. Nevertheless, $S_{eff}(q)$ were obtained from the GIFT-evaluation by fixing Φ_{eff} at the values of the theoretically calculated volume fractions assuming that all EAN, C_{16}mimCl, and 1-decanol, respectively, are involved within the reverse microemulsion droplets. To test the influence of the fixed Φ_{eff} on the results, especially on the polydispersity, all calculations were repeated with lower values of Φ_{eff}, which should simulate possible co-solubilisation effects. For this purpose, the theoretic volume fractions were reduced by a constant value supposing a constant co-solubility. As expected, the resulting polydispersities were systematically lower, but the trend was preserved. Nearly no influence on the absolute value of R_{eff} was observed. It should be noted that by applying the theoretical volume fractions in order to determine $S_{eff}(q)$ (and its parameters), no entirely exact values of the polydispersity can be expected; however, it is possible to follow trends in the distinct sample line. Figure V-62 summarizes the obtained effective structure factors for the investigated samples. The black curve corresponds to $S_{eff}(q)$ of the reverse micelles, whereas the coloured ones belong to $S_{eff}(q)$ of the reverse microemulsion droplets formed upon EAN addition. The peak of the structure factor shifts towards smaller q-values, as the EAN amount increases. Interestingly, the intensity of $S_{eff}(q)$ is highest for the reverse micelles formed by C_{16}mimCl and 1-decanol, it drops down for the first EAN-microemulsion and increases again in a continuous way as the EAN content rises. Simultaneously, the peak of the structure factor becomes more pronounced. Considering hard sphere interactions, the position of the structure factor peak is in a complex way

connected to the effective interaction radius R_{eff} and to the effective volume fraction Φ_{eff} and is a rough measure for the mean distance between neighbouring particles. In a monodisperse system of hard spheres, R_{eff} is, independent of Φ_{eff}, equal to the half distance between two spheres in contact, this means the radius of the spherical particles, and in the polydisperse case R_{eff} is related to the mean value of all of the radii [111, 119, 120]. For the interpretation of R_{eff}, basically, two possibilities can be considered: (i) In terms of the Teubner-Strey model $2R_{eff}$ is related to the typical repeat distance of the EAN domains (d_{TS}), and (ii) R_{eff} is the mean distance of the corresponding hard-sphere system [111]. The obtained values of R_{eff}, PDI. as well as the underlying Φ_{eff} calculated from the sample compositions are given in Table V-22.

		C$_{16}$mimCl/1-decanol/EAN/dodecane			
Φ_{EAN}	r_{max} / nm	Φ_{eff}	R_{eff} / nm	PDI.	MD
0.000	1.22	0.209	1.46	0.21	1.08
0.021	1.68	0.231	1.67	0.31	0.44
0.042	2.30	0.255	2.06	0.34	1.38
0.062	2.70	0.278	2.21	0.37	1.52
0.105	3.64	0.327	2.65	0.42	1.99
0.152	4.46	0.377	3.24	0.44	2.83

Table V-22: Fitting results of the EAN-microemulsions using the GIFT technique.

Further, R_{eff} is presented graphically in Figure V-63 together with the related r_{max} and $d_{TS}/2$, respectively. A systematic increase of the R_{eff} values was achieved. This finding is in good agreement with the trend already observed for r_{max}. Further, the extracted R_{eff} values are in a plausible range as can be seen by the comparison with r_{max} of the corresponding $p(r)$-functions and consequently, the results arising independently from the form factor and the effective structure factor are in good agreement to each other. A slight deviation between the half of the domain size d_{TS} and both R_{eff} and r_{max} can be recognized, however the systematic trend is preserved. The extracted polydispersities are somewhat higher than the quantities reported from the DLS, but the absolute

values range within the correct order of magnitude as expected for microemulsion systems [121-123]. Of course, this discrepancy can result from the already discussed coupling between the $PDI.$ and Φ_{eff}, and therefore from the uncertainty of the applied assumption concerning the calculation of Φ_{eff} from the sample composition. The lowest polydispersity was found for the reverse micelles (0.21). As EAN was added, the $PDI.$ increases and stays constant at about 0.35 for the samples with $\Phi_{EAN} = 0.021$, $\Phi_{EAN} = 0.042$, and $\Phi_{EAN} = 0.062$. When Φ_{EAN} becomes higher, the polydispersity further increases as already seen in the PDDFs. Once again, this observation qualitatively confirms the droplet agglomeration supposed for an EAN volume fraction of about 0.105. The agglomeration/clustering phenomenon at higher Φ_{EAN} is also evident by the comparison of the particle radii r_{max} and the corresponding interaction radii R_{hs}. For microemulsions with $\Phi_{EAN} \geq 0.105$, R_{hs} was found to be considerably lower than the corresponding droplet radius r_{max}. In accordance to the percolation phenomenon, this indicates that the long alkyl chains of neighbouring inverse droplets can overlap to a certain degree without excluded volume effects . This overlapping must cause a steric hindrance and increasing friction [125]. The latter is in good agreement to the viscosity measurements which show that the viscosity suddenly increases at the percolation concentration resulting from increasing friction within the microemulsion.

To summarize, the GIFT-evaluation can be very useful for the interpretation of scattering data of complex multi-component systems with a minimum of *a priori* information, since the *p(r)*-functions are completely model free. Keeping in mind the restrictions, which results from the scattering theory, together with the principle of the GIFT-evaluation, it was possible to follow qualitative trends along the experimental path. However, one has to remark that, although all obtained parameters are in very good agreement, both from an absolute point of view and from the evolutional point of view, to previous conclusions, all values extracted from the GIFT-evaluation have to be understood as preliminary results, because of the presented problematic concerning Φ_{eff} as well as the polydispersity.
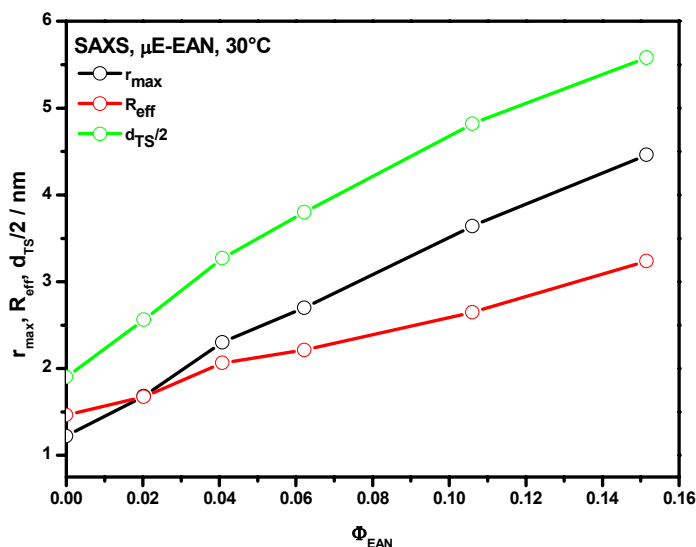
Figure V-63: Comparison between the length scale calculated from the data fit via the TS model (d_{TS}) and those quantities obtained via the GIFT evaluation (r_{max}, R_{eff}).

3.7 UV/Vis-Spectroscopy: Solubilization of metal salts

Today, the application of aqueous W/O reverse microemulsions as micro-reactors is well established. Especially, the synthesis of metallic or semiconductor nanomaterials using reverse microemulsions as reaction medium is a very important objective in current colloid science. In order to pre-evaluate the suitability of the C_{16}mimCl/RTMS-based microemulsions to host metallic salts, which often act as precursors in nano-material synthesis, one interests of the present work was to proof the possibility to solubilise ionic metal compounds in the newly formulated microemulsion systems. As reference compounds, $Ni(NO_3)_2$ as well as $CoCl_2$ were chosen mainly due to the fact that these two salts are suitable as molecular spectroscopic probes because of their deep colours in solution, green and blue, respectively. They do not dissolve in dodecane but will be soluble in the C_{16}mimCl/1-decanol/RTMS/dodecane microemulsions. Consequently, the solubility behaviour of these metal salts in the non-aqueous systems can be easily monitored by UV/Vis-spectroscopy. Instead of the pure RTMS, saturated RTMS solutions of $Ni(NO_3)_2$ and $CoCl_2$ were used to prepare the C_{16}mimCl/RTMS-microemulsions for the spectroscopic experiments. Figure V-64 (in-

sets) shows the results from the UV/Vis measurements of Ni(NO$_3$)$_2$ dissolved in the two RTMS microemulsion systems.
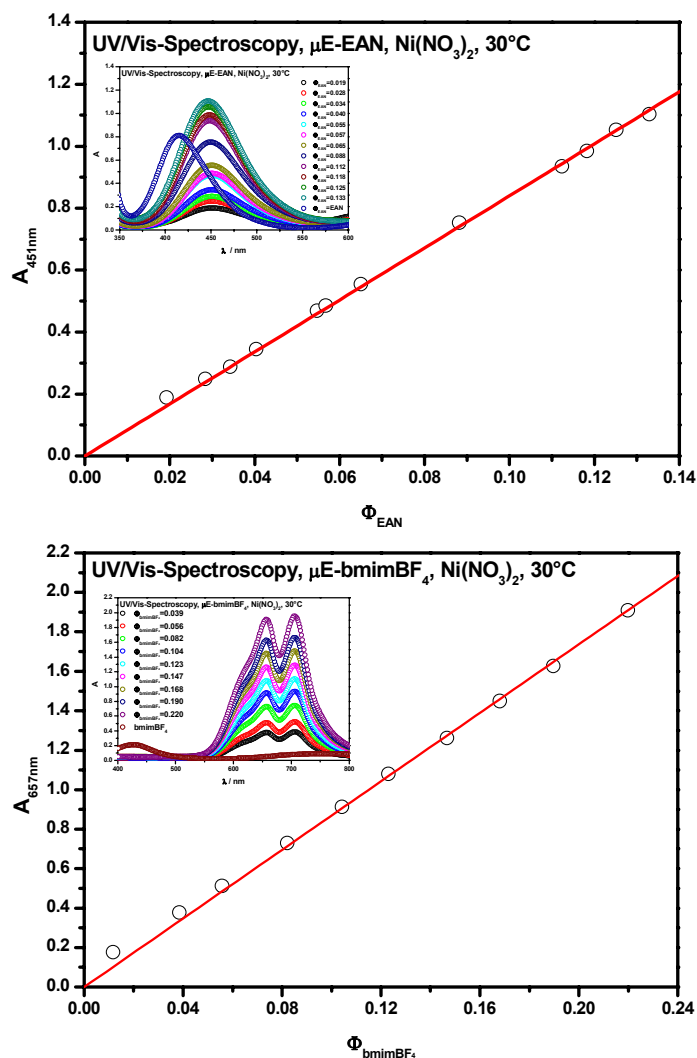
Figure V-64: Maximum absorbance intensities A_{max} of Ni(NO$_3$)$_2$ in the RTMS/SLIL-microemulsions as a function of RTMS content. For the determination of A_{max} wavelengths of 451 nm and 657 nm were used for the EAN- and bmimBF$_4$-system, respectively. The insets show the corresponding adsorption spectra.

The maximum absorbance A_{max} appears at about 415 nm for Ni(NO$_3$)$_2$ in pure EAN, whereas A_{max} is significantly red-shifted for the corresponding reverse EAN-microemulsions. Here, A_{max} can be found at about 451 nm. The maximum absorbance intensity increases with increasing EAN amount, because of the gradually increased

concentration of Ni(NO$_3$)$_2$ in the microemulsion system indicating that Ni(NO$_3$)$_2$ is solubilised in the RTMS micro-droplets. Figure V-64 (top) shows the maximum absorbance of Ni(NO$_3$)$_2$ as a function of EAN volume fraction. As can be seen, the maximum absorbance increases linearly with solubilised EAN amount and is in agreement with the Lambert-Beer law (R=0.999). In the case of bmimBF$_4$-microemulsions, nearly the same observations concerning A_{max} could be made (Figure V-64, bottom, inset). Ni(NO$_3$)$_2$ dissolved in pure bmimBF$_4$ shows a single A_{max} at 426 nm. In the bmimBF$_4$-microemulsions, the spectra of Ni(NO$_3$)$_2$ are red-shifted and two absorbance peaks appear at 657 and 706 nm, respectively. The maximum absorbencies at the two wavelengths increase linearly with solubilised bmimBF$_4$ (R=0.9997). Figure V-64 (bottom) represents the Lambert-Beer plot of the Ni(NO$_3$)$_2$ dissolved in bmimBF$_4$-microemulsions for λ_{max} = 657 nm. Thus, the UV/Vis spectroscopy clearly confirms that the metal salt Ni(NO$_3$)$_2$ could be solubilised in the new RTMS-microemulsions.

CoCl$_2$ was also used to investigate the solubilization of metal salts in the RTMS microemulsions. In addition to the obvious colour and absorption characteristics of the Co^{2+}-ion, CoCl$_2$ is chosen as a probe, since the Co element has attracted much attention in the preparation and processing of materials, especially nano-scale semiconductors and metal materials. Therefore, it is interesting to check the solubilization of this metal salt in the RTMS microemulsions and thus explore the feasibility of using the RTMS-microemulsions as templates for the preparation of nano-scale semiconductor or metal materials. Figure V-65 shows the UV/Vis absorption spectra of CoCl$_2$ in the two RTMS microemulsions with different amounts of the polar salt component. In pure EAN (Figure V-65, top, inset), there is only one absorbance peak appearing at 544 nm. However, when CoCl$_2$ is solubilised in the EAN-microemulsions, the absorbance spectra are red-shifted and three absorbance peaks appear at 629, 667, and 696 nm, respectively. The absorption spectra of CoCl$_2$ in pure bmimBF$_4$ as well as of the bmimBF$_4$-microemulsions are shown in Figure V-65 (bottom, inset). The A_{max} of the characteristic band of CoCl$_2$ in the pure bmimBF$_4$ was found at 544 nm, which accords with that reported for the pure EAN. As shown previously for the EAN-microemulsions, the absorption spectra of CoCl$_2$ in the bmimBF$_4$-microemulsions also show three bands at

632, 669, and 696 nm. Thus, the solubilization states of $CoCl_2$ in the EAN- as well as in the bmimBF$_4$-microemulsions may be quite similar. Again, the solubilization of the Co-salt in the two types of RTMS-microemulsions can be well described by a Lambert-Beer-plot (R=0.9998 and R=0.9506 for the EAN-system and bmimBF4-system, respectively) (Figure V-65).
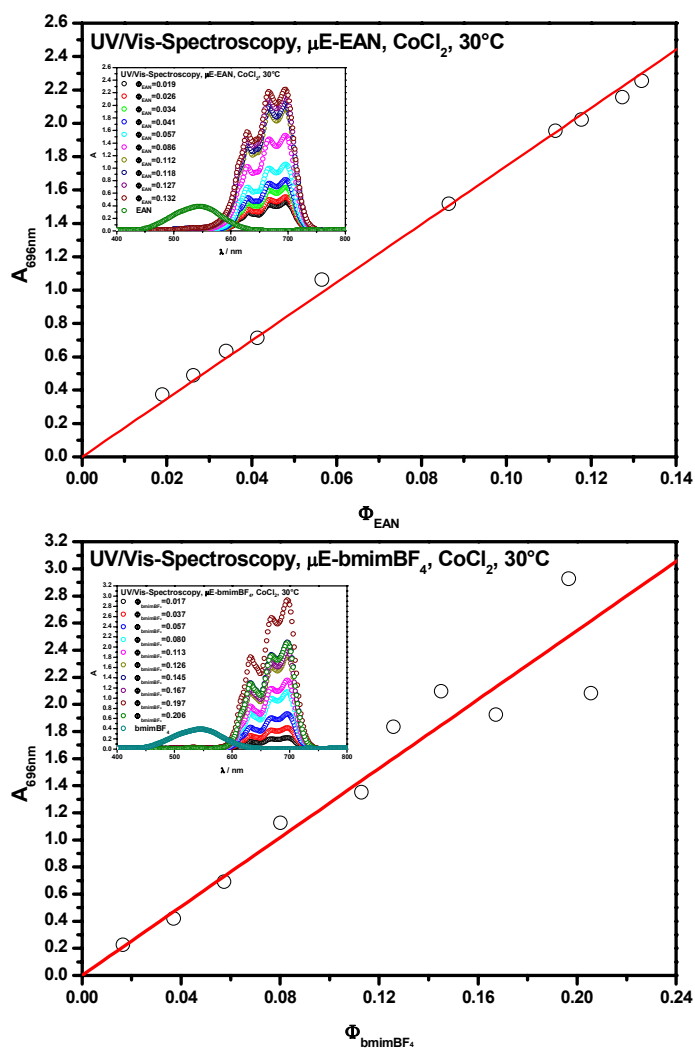
Figure V-65: Maximum absorbance intensities A_{max} of CoCl$_2$ in the RTMS/SLIL-microemulsions as a function of RTMS content. For the determination of A_{max} wavelengths of 696 nm were used for the EAN- as well as for the bmimBF$_4$-system, respectively. The insets show the corresponding adsorption spectra.

The possibility to dissolve metal salts in the RTMS/C_{16}mimCl/1-decanol/dodecane microemulsions is clearly confirmed from these results, and therefore, it can be supposed that the reverse RTMS-microemulsions could have potential application in the production of metallic or semiconductor nanomaterials.

The discrepancy between the spectra obtained for $Ni(NO_3)_2$ and $CoCl_2$ dissolved in the pure RTMS compared to the corresponding microemulsions can be attributed to the different properties of the free/pure RTMS molecules surrounding the metal ions compared to those of the microemulsion pool.

3.8   High-temperature measurements

As for the binary SLIL/RTMS-mixtures, the aim of the present study was to establish the proof that the reverse C_{16}mimCl/RTMS-microemulsios will be also stable at elevated temperatures. If one is able to show that the reverse SLIL/RTMS-based microemulsions are also structured and stable at temperatures far beyond 100°C, the general conclusion can be drawn that such SLIL/RTMS-based systems can significantly extend the very limited application temperature of aqueous microemulsions. In order to define the maximum stability temperature of the C_{16}mimCl/RTMS-microemulsions, the latter were investigated visually up to 150°C. Additionally, DSC measurements were carried out to check the thermal stability quantitatively. Further on, the structuring and high-temperature stability of the two SLIL/RTMS-systems, was verified using high-temperature small-angle neutron scattering (HT-SANS).

3.8.1   Differential scanning calorimetry: Upper stability limit

In order to get an idea about the upper application limit of the high-temperature stable microemulsions, the decomposition temperatures of two microemulsion mixtures incorporating EAN (Φ_{EAN} = 0.042) and bmimBF$_4$ (Φ_{bmimBF_4} = 0.044), respectively, were determined via DSC measurements. These experiments were carried out using a special high-pressure DSC. The measurements were performed by Dr. Didier Dalmazzone at the Ecole Nationale Supérieure de Techniques Avancées, France. The thermograms obtained with both samples are presented in Figure V-66. The heat flow signals are ex-

pressed on a watt (W) per gram basis and plotted on the same scale so that the results may be easily compared. An exothermic peak is observed for the EAN-microemulsion, beginning at approximately 150 °C and sharply accelerating over 220°C. The maximum heat flow evolution is 0.35 W/g at 250 °C. Integrating the peaks between 150 and 285°C gives an enthalpy change of -196.5 J/g (Al seal) and 199.5 J/g (Ni seal). At higher temperature, especially between 370 and 460°C, a mildly exothermic flow proceeds evolving. Above 460°C, a second peak seems to be forming but could not be recorded integrally since it is not finished at 500°C. No significant heat evolution can be observed below 270°C for the bmimBF$_4$-sample. Above this temperature, an exothermic flow is evidenced, which slightly increases with temperature up to 440°C.

$$\Phi_{EAN} = 0.042$$

$$\Phi_{bmimBF_4} = 0.044$$
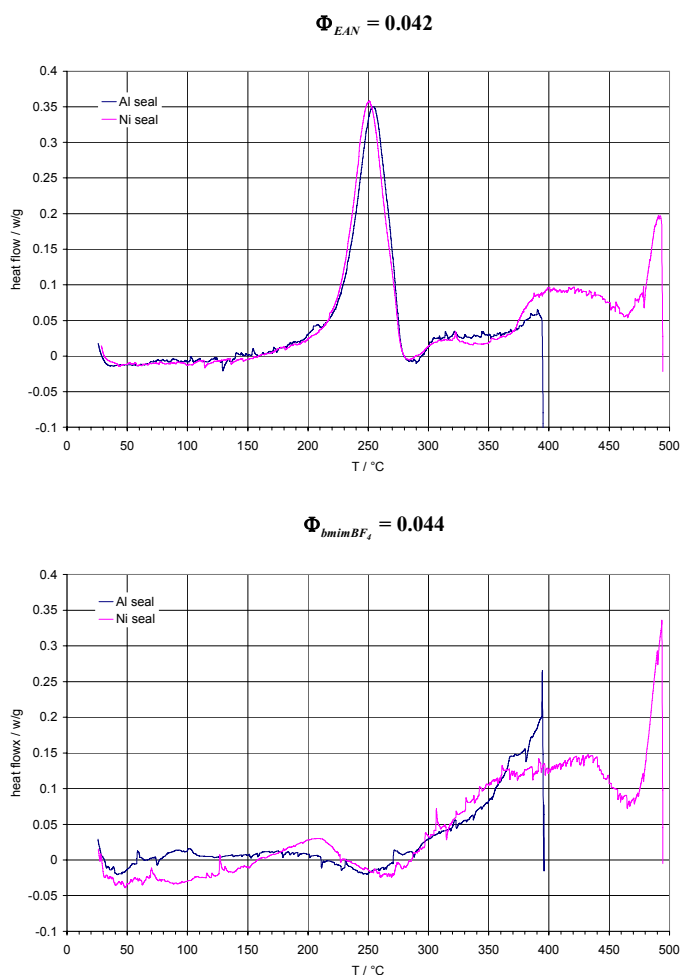
Figure V-66: DSC-thermograms obtained for the two RTMS-microemulsions.

A stronger exothermic peak begins to form from 470°C to the limit of the experiment. At high temperature, both compositions have a very similar behaviour, which can be interpreted as a slow thermal degradation above 270°C, followed by a sharper and stronger decomposition above 470°C. The main difference is the ≈ 200 J/g exothermic peak that takes place between 150 and 280°C. It can be attributed to the decomposition of ethyl ammonium nitrate in the microemulsion that contains this compound. On a 6 weight percent basis, this represents 3.3 kJ per gram of EAN. Therefore, the microemulsion composition incorporating bmimBF$_4$ provides a higher thermal stability as the EAN-sample does, as expected from the fact that PILs are less stable than AILs (cp. Chapter II.1.4.2). Nevertheless, both types of microemulsions are stable up to 200°C and further, no demixture temperatures were monitored for the two compositions via DSC leading to the assumption that these SLIL/RTMS-microemulsion systems provide very good temperature stabilities. Thus, they will be very interesting for high-temperature applications, if they are still structured and not only "molecular mixed" solutions at such high temperatures.

3.8.2   Visual characterisation: Demixing behaviour

The first impression about the high-temperature stability of the formulated RTMS-microemulsions was achieved by visual inspection of several samples along the previously defined experimental tie-lines at various temperatures from 30°C up to 150°C. This procedure was performed for the EAN-system and the bmimBF$_4$-system, respectively. During this experiment, the limit of thermal stability was defined as the temperature at which phase separation occurred for the first time denoted by a demixing of the microemulsion solution. Up to an EAN volume fraction of about 0.060 no demixing was observed for the EAN-system, however for $\Phi_{EAN} > 0.060$ phase separation occurred between 120 and 130°C, possibly due to an destabilization of the RTMS/dodecane-interface caused by higher solubility of the surfactant/co-surfactant-mixture in the oil and RTMS, respectively. However, additional experiments showed that the thermal stability of the EAN-microemulsions could be significantly improved further by increasing the mass fraction of the surface-active compound (C$_{16}$mimCl/1-

decanol) from 0.3 to 0.4. By this modification, reverse microemulsions could be formulated which were isotropic and monophasic at 150°C, even when they carried EAN volume fractions greater than 0.060. Due to this fact, the assumption that the C_{16}mimCl/1-decanol content in the reverse EAN-microemulsions defines the upper thermal application limit of the system seems reasonable. In contrast, all investigated bmimBF$_4$-samples along the experimental path defined previously remained clear up to 150°C, no modification had to be made in order to increase the thermal stability. The solubility increase of the C_{16}mimCl/1-decanol-mixture in dodecane and in bmimBF$_4$ with increasing temperature may be of less consequence for the thermal stability of this system due to the very high surfactant/co-surfactant mass fraction (0.65) incorporated in the composition.
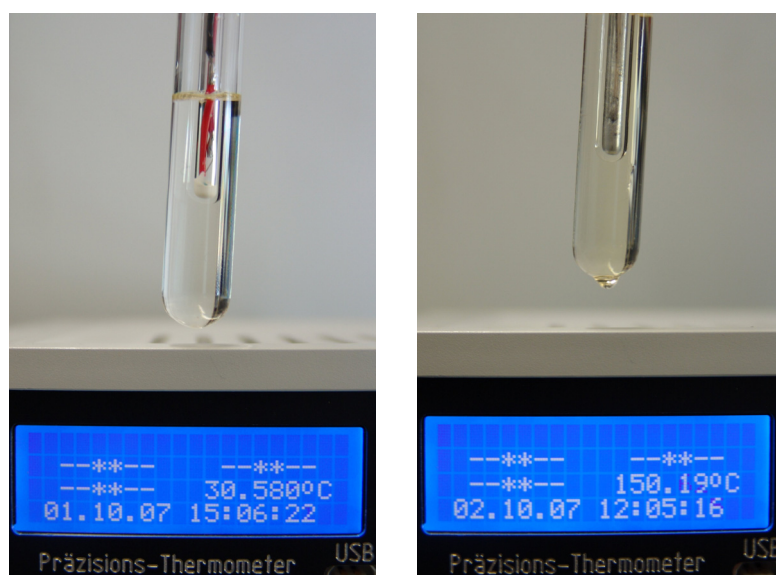
Figure V-67: Representative illustration of the high-temperature stabilities of the RTMS-microemulsions by means of the EAN-microemulsion incorporating an EAN volume fraction of 0.042. The two pictures clearly indicate the isotropic appearance of the microemulsion at 30°C (left) and at 150°C (right).

Figure V-67, which is also representative for reverse EAN-microemulsions with a higher amount of surface-active component (0.4) and for the bmimBF$_4$-microemulsions, respectively, exemplifies the high temperature stability of the microemulsions on the basis of a reverse EAN-microemulsion (Φ_{EAN} = 0.042) with a surface-

active component content of 0.30 mass fraction. The two pictures clearly indicate the isotropic appearance of the microemulsion at low (30°C) and high (150°C) temperature. Already from this easy experiment, very good high-temperature stabilities can be supposed for both formulated SLIL/RTMS-systems. However, this experiment does not confirm the existence of a self-assembled structure within the samples at 150°C.

3.8.3   High-temperature small-angle scattering

In order to establish the proof clearly that the newly formulated reverse C_{16}mimCl/RTMS-microemulsions are also structured at temperatures beyond 100°C, HT-SANS, measurements of various C_{16}mimCl/1-decanol/dodecane/RTMS-microemulsions were carried out using the D22 small-angle neutron scattering spectrometer at the LLB Grenoble. In the case of the C_{16}mimCl/bmimBF$_4$-system, samples along the experimental path defined previously were used for the experiments. For the C_{16}mimCl/EAN-system, samples with constant C_{16}mimCl/1-decanol (molar ratio of 1:4) mass fraction of 0.4 and varying EAN volume fractions were investigated due to their higher thermal stability compared to the EAN-microemulsions incorporating lower mass fraction of surface-active component (0.3).

At this point, it must be noted that in the following only a small part of the HT-SANS results will be shown and interpreted just qualitatively. Dipl.-Chem. Oliver Zech will give a detailed analysis of the whole HT-SANS data in an upcoming work. Further, he will present results of the EAN-microemulsions along the newly defined experimental path where the HT-SANS measurements of C_{16}mimCl/EAN-system were obtained.

Figure V-68 shows the temperature dependent neutron scattering behaviour of the C_{16}mimCl/1-decanol/dodecane/EAN-sample and the C_{16}mimCl/1-decanol/dode-cane/bmimBF$_4$-sample incorporating RTMS weight fractions of 0.06. Both graphs clearly show a scattering peak arising from the presence of structure within the scattering volume in the temperature range between 30°C and 150°C.
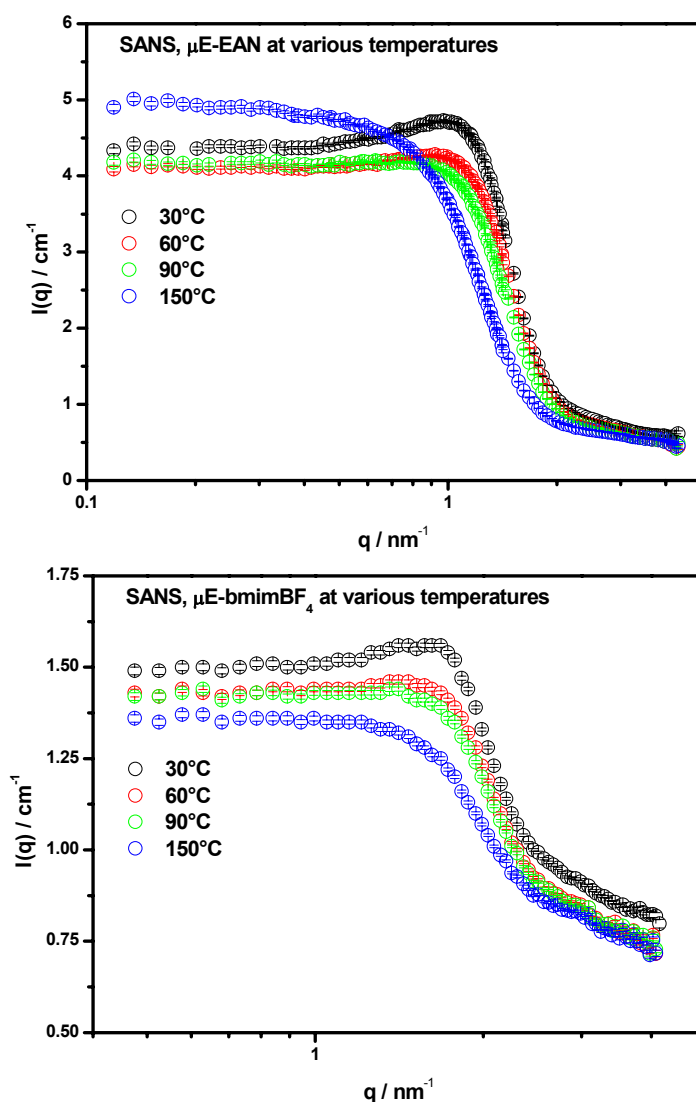
Figure V-68: Scattering pattern of RTMS-microemulsions (RTMS weight fraction is 0.06) measured at various temperatures. The C16mimCl/1-decanol-weight fraction was 0.40 and 0.65 for the EAN- and the bmimBF$_4$-system, respectively. The structure peak of the two microemulsions still persists at higher temperatures.

The widths of the microemulsion peaks of both systems increase as the temperature became higher indicating a lower correlation of the internal structures and therefore, a decreasing order. The peak position in both microemulsions decreases monotonically with increasing temperature indicating an increase in the characteristic length scale of the system and a decrease in the internal surface area [124]. This may arise from simple effects such as higher solubility of the surface-active components in dodecane and/or

RTMS at higher temperatures, or to an increase of the molar volumes of dodecane and RTMS, respectively. Both effects would reduce the amount of surfactant available to stabilize internal interfaces. The assumption that the higher solubility of the C_{16}mimCl/1-decanol-mixture in the oil and RTMS at higher temperatures may be the reason for the loss of structuring within the microemulsions would be in good agreement with the visual observations for the C_{16}mimCl/EAN-system from which also a solubility increase of the surfactant/co-surfactant component with raising temperature was assumed. Interestingly, the value of $I(q_{max})$ obtained for the EAN-sample at 150°C is considerably higher than the corresponding quantities at lower temperatures. Until now, it is not clear, what is the reason for this observation. Nevertheless, the HT-SANS results confirm that the upper application limit (demixing temperature) of SLIL/1-decanol/dodecane/RTMS-microemulsions is defined by the solubility behaviour of the surface-active compounds in the polar and apolar phases. These results clearly demonstrate that the structures of the newly formulated SLIL/RTMS-based systems still persist at very high temperatures and furthermore, that these formulations can extend the thermal stability range of conventional aqueous microemulsions. This was not possible by using the already known RTMS-microemulsions formed with nonionic surfactants due to the occurrence of the cloud point phenomenon at higher temperatures [29, 126].

3.9　Bibliography

[1]　M. P. Pileni; Reverse micelles as microreactors. *Journal of Physical Chemistry* **97**, 27, 6961-6973 (1993).

[2]　M. P. Pileni; Water in oil colloidal droplets used as microreactors. *Advances in Colloid and Interface Science* **46**, 139-163 (1993).

[3]　J. Casado, C. Izquierdo, S. Fuentes and M. L. Moya; Microemulsions as a new working medium in physical chemistry: an integrated practical approach. *Journal of Chemical Education* **71**, 5, 446-450 (1994).

[4]　N. Garti and K. Holmberg; Reactions in microheterogeneous media. *Current Opinion in Colloid & Interface Science* **8**, 2, 135-136 (2003).

[5] K. Holmberg; Organic reactions in microemulsions. *Current Opinion in Colloid & Interface Science* **8**, 2, 187-196 (2003).

[6] P. Bauduin, D. Touraud, W. Kunz, M.-P. Savelli, S. Pulvin and B. W. Ninham; The influence of structure and composition of a reverse SDS microemulsion on enzymatic activities and electrical conductivities. *Journal of Colloid and Interface Science* **292**, 1, 244-254 (2005).

[7] A. Martino and E. W. Kaler; Phase behavior and microstructure of nonaqueous microemulsions. *Journal of Physical Chemistry* **94**, 4, 1627-1631 (1990).

[8] A. Martino and E. W. Kaler; Phase Behavior and Microstructure of Nonaqueous Microemulsions. 2. *Langmuir* **11**, 3, 779-784 (1995).

[9] P. D. I. Fletcher, M. F. Galal and B. H. Robinson; Structural study of aerosol-OT-stabilized microemulsions of glycerol dispersed in n-heptane. *Journal of the Chemical Society, Faraday Transactions 1: Physical Chemistry in Condensed Phases* **80**, 12, 3307-3314 (1984).

[10] S. Ray and S. P. Moulik; Dynamics and Thermodynamics of Aerosol OT-Aided Nonaqueous Microemulsions. *Langmuir* **10**, 8, 2511-2515 (1994).

[11] E. Oliveros, M. T. Maurette and A. M. Braun; The formulation of four-components practically perfluorinated microemulsions. *Helvetica Chimica Acta* **66**, 4, 1183-1188 (1983).

[12] I. Rico and A. Lattes; Waterless microemulsions. 2. Use of formamide in place of water in the preparation of large monophasic areas of perfluorinated microemulsions. *Journal of Colloid and Interface Science* **102**, 1, 285-287 (1984).

[13] I. Rico and A. Lattes; Waterless microemulsions. *Nouveau Journal de Chimie* **8**, 7, 429-431 (1984).

[14] A. A. Z. Samii, A. De Savignac, I. Rico and A. Lattes; Waterless microemulsions. IV. Diels-Alder reaction of cyclopentadiene and methylacrylate as a probe of formamide microemulsions. *Tetrahedron* **41**, 18, 3683-3688 (1985).

[15]   C. Mathew, Z. Saidi, J. Peyrelasse and C. Boned; Viscosity, conductivity, and dielectric relaxation of waterless glycerol-sodium bis(2-ethylhexyl)sulfosuccinate-isooctane microemulsions: the percolation effect. *Physical Review A: Atomic, Molecular, and Optical Physics* **43**, 2, 873-882 (1991).

[16]   V. Arcoleo, F. Aliotta, M. Goffredi, G. La Manna and V. Turco Liveri; Study of AOT-stabilized microemulsions of formamide and n-methylformamide dispersed in n-heptane. *Materials Science & Engineering, C: Biomimetic Materials, Sensors and Systems* **C5**, 1, 47-53 (1997).

[17]   R. E. Riter, J. R. Kimmel, E. P. Undiks and N. E. Levinger; Novel Reverse Micelles Partitioning Nonaqueous Polar Solvents in a Hydrocarbon Continuous Phase. *Journal of Physical Chemistry B* **101**, 41, 8292-8297 (1997).

[18]   C. A. T. Laia, P. Lopez-Cornejo, S. M. B. Costa, J. d'Oliveira and J. M. G. Martinho; Dynamic Light Scattering Study of AOT Microemulsions with Nonaqueous Polar Additives in an Oil Continuous Phase. *Langmuir* **14**, 13, 3531-3537 (1998).

[19]   H. Gao, J. Li, B. Han, W. Chen, J. Zhang, R. Zhang and D. Yan; Microemulsions with ionic liquid polar domains. *Physical Chemistry Chemical Physics* **6**, 11, 2914-2916 (2004).

[20]   J. Li, J. Zhang, H. Gao, B. Han and L. Gao; Nonaqueous microemulsion-containing ionic liquid [bmim][PF$_6$] as polar microenvironment. *Colloid and Polymer Science* **283**, 12, 1371-1375 (2005).

[21]   D. Chakrabarty, D. Seth, A. Chakraborty and N. Sarkar; Dynamics of Solvation and Rotational Relaxation of Coumarin 153 in Ionic Liquid Confined Nanometer-Sized Microemulsions. *Journal of Physical Chemistry B* **109**, 12, 5753-5758 (2005).

[22]   Y. Gao, J. Zhang, H. Xu, X. Zhao, L. Zheng, X. Li and L. i. Yu; Structural studies of 1-butyl-3-methylimidazolium tetrafluoroborate/TX-100/p-xylene ionic liquid microemulsions. *ChemPhysChem* **7**, 7, 1554-1561 (2006).

[23] G. Yanan, W. Suqing, Z. Liqiang, H. Shuaibing, Z. Xuan, L. u. Deming, L. i. Yu, J. i. Yongqiang and Z. Gaoyong; Microregion detection of ionic liquid microemulsions. *Journal of Colloid and Interface Science* **301**, 2, 612-616 (2006).

[24] N. a. Li, G. Yan'an, Z. Liqiang, Z. Jin, L. i. Yu and L. i. Xinwei; Studies on the micropolarities of bmimBF$_4$/TX-100/toluene ionic liquid microemulsions and their behaviors characterized by UV-visible spectroscopy. *Langmuir* **23**, 3, 1091-1097 (2007).

[25] R. Atkin and G. G. Warr; Phase Behavior and Microstructure of Microemulsions with a Room-Temperature Ionic Liquid as the Polar Phase. *Journal of Physical Chemistry B* **111**, 31, 9309-9316 (2007).

[26] S. Cheng, X. Fu, J. Liu, J. Zhang, Z. Zhang, Y. Wei and B. Han; Study of ethylene glycol/TX-100/ionic liquid microemulsions. *Colloids and Surfaces, A: Physicochemical and Engineering Aspects* **302**, 1-3, 211-215 (2007).

[27] Z. Qiu and J. Texter; Ionic liquids in microemulsions. *Current Opinion in Colloid & Interface Science* (2007).

[28] N. A. Li, C. Quan, G. Yanan, Z. Jin, Z. Liqiang, B. Xiangtao, D. Bin, L. i. Zhen, Z. Mingwei and L. i. Yu; States of water located in the continuous organic phase of 1-butyl-3-methylimidazolium tetrafluoroborate/Triton X-100/triethylamine reverse microemulsions. *Chemphyschem : a European journal of chemical physics and physical chemistry* **8**, 15, 2211-2217 (2007).

[29] E. Julian, G. Sarah, R. S. E, P. Alison, W. Tom, H. R. K and G. Isabelle; Ionic liquid-in-oil microemulsions. *Journal of the American Chemical Society* **127**, 20, 7302-7303 (2005).

[30] N. A. Li, S. Zhang, L. Zheng, Y. Gao and L. I. Yu; Second Virial Coefficient of bmimBF4/Triton X-100/ Cyclohexane Ionic Liquid Microemulsion as Investigated by Microcalorimetry. *Langmuir* **24**, 7, 2973-2976 (2008).

[31] M. Clausse, A. Zradba and L. Nicolas-Morgantini; *Microemulsion Systems*, Marcell Dekker (**1987**) .

[32]   W. F. C. Sager; Microemulsion templating. *Schriften des Forschungszentrums Juelich, Materie und Material* **10**, Soft Matter: Complex, A6/1-A6/37 (2002).

[33]   D. F. Evans; *The Colloidal Domain: Where Physics, Chemistry, Biology, and Technology Meet, 2nd Edition*. Wiley-VCH, (1998).

[34]   M. J. Rosen; *Surfactants and Interfacial Phenomena, 3rd Edition*. (2004).

[35]   M. Clausse, J. Heil, C. Boned and B. Lagourette; Bicontinuous structure zones in microemulsions. *Nature* **293**, 5834, 636-638 (1981).

[36]   B. Lagourette, J. Peyrelasse, C. Boned and M. Clausse; Percolative conduction in microemulsion type systems. *Nature* **281**, 60-62 (1979).

[37]   C. Blattner, J. Bittner, G. Schmeer and W. Kunz; Electrical conductivity of reverse micelles in supercritical carbon dioxide. *Physical Chemistry Chemical Physics* **4**, 10, 1921-1927 (2002).

[38]   S. Schroedle, R. Buchner and W. Kunz; Percolating microemulsions of nonionic surfactants probed by dielectric spectroscopy. *ChemPhysChem* **6**, 6, 1051-1055 (2005).

[39]   G. S. Grest, I. Webman, S. A. Safran and A. L. P. Bug; Dynamic percolation in microemulsions. *Physical Review A: Atomic, Molecular, and Optical Physics* **33**, 4, 2842-2845 (1986).

[40]   J. Peyrelasse, C. Boned and Z. Saidi; Quantitative determination of the percolation threshold in waterless microemulsions. *Physical Review E: Statistical Physics, Plasmas, Fluids, and Related Interdisciplinary Topics* **47**, 5, 3412-3417 (1993).

[41]   W. Meier; On nanodroplet and bicontinuous states in percolated water-in-oil microemulsions. *Colloids and Surfaces, A: Physicochemical and Engineering Aspects* **94**, 1, 111-114 (1995).

[42]   C. M. Gambi, M. Grazia Giri, M. Carla, D. Senatra and A. Chittofrati; Dynamic percolation in fluorinated water-in-oil microemulsions. *Physical Review E: Sta-*

tistical Physics, Plasmas, Fluids, and Related Interdisciplinary Topics **56**, 4, 4356-4363 (1997).

[43] Z. A. Schelly; Dynamics in water-in-oil microemulsions. *Current Opinion in Colloid & Interface Science* **2**, 1, 37-41 (1997).

[44] S. K. Mehta and K. Bala; Tween-based microemulsions: a percolation view. *Fluid Phase Equilibria* **172**, 2, 197-209 (2000).

[45] S. P. Moulik, G. C. De, B. B. Bhowmik and A. K. Panda; Physicochemical Studies on Microemulsions: 6. Phase Behavior, Dynamics of Percolation, and Energetics of Droplet Clustering in Water/AOT/n-Heptane System Influenced by Additives (Sodium Cholate and Sodium Salicylate). *Journal of Physical Chemistry B* **103**, 34, 7122-7129 (1999).

[46] S. K. Hait, S. P. Moulik, M. P. Rodgers, S. E. Burke and R. Palepu; Physico-chemical Studies on Microemulsions: 7. Dynamics of Percolation and Energetics of Clustering in Water/AOT/Isooctane and Water/AOT/Decane w/o Microemulsions in Presence of Hydrotopes (Sodium Salicylate, a-Naphthol, b-Naphthol, Resorcinol, Catech. *Journal of Physical Chemistry B* **105**, 29, 7145-7154 (2001).

[47] H. F. Eicke, M. Borkovec and B. Das-Gupta; Conductivity of water-in-oil microemulsions: a quantitative charge fluctuation model. *Journal of Physical Chemistry* **93**, 1, 314-317 (1989).

[48] D. R. Lide; *CRC Handbook of Chemistry and Physics, 83rd Edition*. CRC Press, (2002).

[49] D. R. Caudwell, J. P. M. Trusler, V. Vesovic and W. A. Wakeham; The viscosity and density of n-dodecane and n-octadecane at pressures up to 200 MPa and temperatures up to 473 K. *International Journal of Thermophysics* **25**, 5, 1339-1352 (2004).

[50] N. Kallay and A. Chittofrati; Conductivity of microemulsions: refinement of charge fluctuation model. *Journal of Physical Chemistry* **94**, 11, 4755-4756 (1990).

[51] N. Kallay, M. Tomic and A. Chittofrati; Conductivity of water-in-oil microemulsions: comparison of the Boltzmann statistics and the charge fluctuation model. *Colloid and Polymer Science* **270**, 2, 194-196 (1992).

[52] C. Boned, J. Peyrelasse and Z. Saidi; Dynamic percolation of spheres in a continuum: the case of microemulsions. *Physical Review E: Statistical Physics, Plasmas, Fluids, and Related Interdisciplinary Topics* **47**, 1, 468-478 (1993).

[53] M. F. Hsu, E. R. Dufresne and D. A. Weitz; Charge Stabilization in Nonpolar Solvents. *Langmuir* **21**, 11, 4881-4887 (2005).

[54] J. Leys, M. Wuebbenhorst, C. P. Menon, R. Rajesh, J. Thoen, C. Glorieux, P. Nockemann, B. Thijs, K. Binnemans and S. Longuemart; Temperature dependence of the electrical conductivity of imidazolium ionic liquids. *Journal of Chemical Physics* **128**, 6, 064509/1-064509/7 (2008).

[55] J. Peyrelasse, M. Moha-Ouchane and C. Boned; Viscosity and the phenomenon of percolation in microemulsions. *Physical Review A: Atomic, Molecular, and Optical Physics* **38**, 8, 4155-4161 (1988).

[56] D. F. Evans, A. Yamauchi, G. J. Wei and V. A. Bloomfield; Micelle size in ethylammonium nitrate as determined by classical and quasi-elastic light scattering. *Journal of Physical Chemistry* **87**, 18, 3537-3541 (1983).

[57] C. A. Angell, N. Byrne and J.-P. Belieres; Parallel Developments in Aprotic and Protic Ionic Liquids: Physical Chemistry and Applications. *Accounts of Chemical Research* **40**, 11, 1228-1236 (2007).

[58] S. Miyagishi, T. Asakawa and M. Nishida; Influence of external environment on microviscosity in micelles. *Journal of Colloid and Interface Science* **115**, 1, 199-205 (1987).

[59] S. A. Moore and R. M. Palepu; Fluorometric investigations on the transition from reverse micelles to microemulsions in non-aqueous microemulsions. *Journal of Molecular Liquids* **135**, 1-3, 123-127 (2007).

[60] B. Chu; *Laser Light Scattering: Basic Principles and Practice*. Academic Press, (1974).

[61] B. J. Berne and R. Pecora; Dynamic Light Scattering: with Applications to Chemistry, Biology, and Physics. Dover Pubn, (2000).

[62] C. S. Johnson, Jr. and D. A. Gabriel; *Laser light scattering*. CRC Press, (1981).

[63] R. B. Jones and P. N. Pusey; Dynamics of suspended colloidal spheres. *Annual Review of Physical Chemistry* **42**, 137-169 (1991).

[64] W. Brown; Dynamic Light Scattering: The Method and Some Applications. 735 (1993).

[65] W. Brown; *Light Scattering: Principles and Development.* Oxford University Press, (1996).

[66] A. S. Al-Jimaz, J. A. Al-Kandary, A. M. Abdul-latif and A. M. Al-Zanki; Physical properties of anisole+ n-alkanes at temperatures between (293.15 and 303.15) K. *Journal of Chemical Thermodynamics* **37**, 7, 631-642 (2005).

[67] S. Hyde; *Handbook of Applied Surface and Colloid Chemistry*. John Wiley & Sons, (2001).

[68] P. D. I. Fletcher, M. F. Galal and B. H. Robinson; Structural study of aerosol-OT-stabilized microemulsions of glycerol dispersed in n-heptane. *Journal of the Chemical Society, Faraday Transactions 1: Physical Chemistry in Condensed Phases* **80**, 12, 3307-3314 (1984).

[69] P. D. I. Fletcher, M. F. Galal and B. H. Robinson; Structural study of microemulsions of glycerol stabilized by cetyltrimethylammonium bromide dispersed in heptane + chloroform mixtures. *Journal of the Chemical Society, Faraday Transactions 1: Physical Chemistry in Condensed Phases* **81**, 9, 2053-2065 (1985).

[70]   F. Caboi, G. Capuzzi, P. Baglioni and M. Monduzzi; Microstructure of Ca-AOT/Water/Decane w/o Microemulsions. *Journal of Physical Chemistry B* **101**, 49, 10205-10212 (1997).

[71]   C. A. T. Laia, P. Lopez-Cornejo, S. M. B. Costa, J. d'Oliveira and J. M. G. Martinho; Dynamic Light Scattering Study of AOT Microemulsions with Nonaqueous Polar Additives in an Oil Continuous Phase. *Langmuir* **14**, 13, 3531-3537 (1998).

[72]   H. Mays, M. Almgren, W. Brown and P. Alexandridis; Cluster and Network Formation toward Percolation in the Microemulsion L2 Phase Formed by an Amphiphilic Triblock Copolymer and Water in p-Xylene. *Langmuir* **14**, 4, 723-725 (1998).

[73]   M. M. Velazquez, M. Valero and F. Ortega; Light Scattering and Electrical Conductivity Studies of the Aerosol OT Toluene Water-In-Oil Microemulsions. *Journal of Physical Chemistry B* **105**, 42, 10163-10168 (2001).

[74]   A. Shukla, H. Graener and R. H. H. Neubert; Observation of Two Diffusive Relaxation Modes in Microemulsions by Dynamic Light Scattering. *Langmuir* **20**, 20, 8526-8530 (2004).

[75]   P. N. Pusey, H. M. Fijnaut and A. Vrij; Mode amplitudes in dynamic light scattering by concentrated liquid suspensions of polydisperse hard spheres. *Journal of Chemical Physics* **77**, 9, 4270-4281 (1982).

[76]   P. N. Pusey and R. J. A. Tough; Dynamic light scattering, a probe of Brownian particle dynamics. *Advances in Colloid and Interface Science* **16**, 143-159 (1982).

[77]   Y. D. Yan and J. H. R. Clarke; Dynamic light scattering from concentrated water-in-oil microemulsions: the coupling of optical and size polydispersity. *Journal of Chemical Physics* **93**, 7, 4501-4509 (1990).

[78] P. N. Pusey, P. N. Segre, O. P. Behrend, S. P. Meeker and W. C. K. Poon; Dynamics of concentrated colloidal suspensions. *Physica A: Statistical and Theoretical Physics* **235**, 1-2, 1-8 (1997).

[79] P. N. Segre and P. N. Pusey; Dynamics and scaling in hard-sphere colloidal suspensions. *Physica A: Statistical and Theoretical Physics (Amsterdam)* **235**, 1-2, 9-18 (1997).

[80] J. C. Brown, P. N. Pusey, J. W. Goodwin and R. H. Ottewill; Light scattering study of dynamic and time-averaged correlations in dispersions of charged particles. *Journal of Physics A: Mathematical and General* **8**, 5, 664-682 (1975).

[81] P. S. Dalberg, A. Boe, K. A. Strand and T. Sikkeland; Quasielastic light scattering study of charged polystyrene particles in water. *Journal of Chemical Physics* **69**, 12, 5473-5478 (1978).

[82] U. Peter, D. Roux and A. K. Sood; Observation of a Topological Relaxation Mode in Microemulsions. *Physical Review Letters* **86**, 15, 3340-3343 (2001).

[83] S. W. Provencher and V. G. Dovi; Direct analysis of continuous relaxation spectra. *Journal of Biochemical and Biophysical Methods* **1**, 6, 313-318 (1979).

[84] S. T. Milner, M. E. Cates and D. Roux; Hydrodynamic modes and topology in microemulsions and L3 phases. *Journal de Physique (Paris)* **51**, 22, 2629-2639 (1990).

[85] P. Debye and A. M. Bueche; Scattering by an inhomogeneous solid. *Journal of Applied Physics* **20**, 518-525 (1949).

[86] P. Debye, H. R. Anderson, Jr. and H. Brumberger; Scattering by an inhomogeneous solid. II. The correlation function and its application. *J. Appl. Phys.* **28**, 679-683 (1957).

[87] E. Caponetti, .. L. J. Magid, J. B. Hayter and J. S. Johnson, Jr; Small-angle neutron scattering from water-in-oil microemulsions. *Langmuir* **2**, 6, 722-731 (1986).

[88]   F. Lichterfeld, T. Schmeling and R. Strey; Microstructure of microemulsions of the system water-n-tetradecane-alkyl polyglycol ether (C12E5). *Journal of Physical Chemistry* **90**, 22, 5762-5766 (1986).

[89]   M. Teubner and R. Strey; Origin of the scattering peak in microemulsions. *Journal of Chemical Physics* **87**, 5, 3195-3200 (1987).

[90]   S. H. Chen, S. L. Chang and R. Strey; Structural evolution within the one-phase region of a three-component microemulsion system: water-n-decane-sodium bi-sethylhexylsulfosuccinate (AOT). *Journal of Chemical Physics* **93**, 3, 1907-1918 (1990).

[91]   S. H. Chen, S. L. Chang and R. Strey; On the interpretation of scattering peaks from bicontinuous microemulsions. *Progress in Colloid & Polymer Science* **81**, Trends Colloid Inter, 30-35 (1990).

[92]   S. H. Chen, S. L. Chang, R. Strey, J. Samseth and K. Mortensen; Structural evolution of bicontinuous microemulsions. *Journal of Physical Chemistry* **95**, 19, 7427-7432 (1991).

[93]   S. H. Chen, S. L. Chang and R. Strey; Simulation of bicontinuous microemulsions: comparison of simulated real-space microstructures with scattering experiments. *Journal of Applied Crystallography* **24**, 5, 721-731 (1991).

[94]   S. H. Shen, S. L. Chang, R. Strey and P. Thiyagarajan; Small angle neutron scattering investigation of structural inversion in a three-component ionic microemulsion. *Journal of Physics: Condensed Matter* **3**, 42, 91-107 (1991).

[95]   R. Strey, J. Winkler and L. Magid; Small-angle neutron scattering from diffuse interfaces. 1. Mono- and bilayers in the water-octane-pentaoxyethylene monododecyl ether (C12Es) system. *Journal of Physical Chemistry* **95**, 19, 7502-7507 (1991).

[96]   I. Ben Azouz, R. Ober, E. Nakache and C. E. Williams; A small angle x-ray scattering investigation of the structure of a ternary water-in-oil microemulsion. *Colloids and Surfaces* **69**, 2-3, 87-97 (1992).

[97] M. Gradzielski and H. Hoffmann; Influence of Charges on Structure and Dynamics of an O/W Microemulsion. Effect of Admixing Ionic Surfactants. *Journal of Physical Chemistry* **98**, 10, 2613-2623 (1994).

[98] K. V. Schubert, R. Strey, S. R. Kline and E. W. Kaler; Small angle neutron scattering near Lifshitz lines: transition from weakly structured mixtures to microemulsions. *Journal of Chemical Physics* **101**, 6, 5343-5355 (1994).

[99] M. Gradzielski, H. Hoffmann and D. Langevin; Solubilization of Decane into the Ternary System TDMAO/1-Hexanol/Water. *Journal of Physical Chemistry* **99**, 33, 12612-12623 (1995).

[100] M. Gradzielski, D. Langevin, L. Magid and R. Strey; Small-Angle Neutron Scattering from Diffuse Interfaces. 2. Polydisperse Shells in Water-n-Alkane-C10E4 Microemulsions. *Journal of Physical Chemistry* **99**, 35, 13232-13238 (1995).

[101] M. Gradzielski, D. Langevin and B. Farago; Experimental investigation of the structure of nonionic microemulsions and their relation to the bending elasticity of the amphiphilic film. *Physical Review E: Statistical Physics, Plasmas, Fluids, and Related Interdisciplinary Topics* **53**, 4-B, 3900-3919 (1996).

[102] M. Gradzielski, D. Langevin, T. Sottmann and R. Strey; Small angle neutron scattering near the wetting transition: discrimination of microemulsions from weakly structured mixtures. *Journal of Chemical Physics* **104**, 10, 3782-3787 (1996).

[103] M. Gradzielski and D. Langevin; Small-angle neutron scattering experiments on microemulsion droplets: relation to the bending elasticity of the amphiphilic film. *Journal of Molecular Structure* **383**, 1-3, 145-156 (1996).

[104] M. Gradzielski, D. Langevin, T. Sottmann and R. Strey; Droplet microemulsions at the emulsification boundary: The influence of the surfactant structure on the elastic constants of the amphiphilic film. *Journal of Chemical Physics* **106**, 19, 8232-8238 (1997).

[105] T. Sottmann, R. Strey and S. H. Chen; A small-angle neutron scattering study of nonionic surfactant molecules at the water-oil interface: area per molecule, microemulsion domain size, and rigidity. *Journal of Chemical Physics* **106**, 15, 6483-6491 (1997).

[106] H. Leitao, M. M. Telo da Gama and R. Strey; Scaling of the interfacial tension of microemulsions: A Landau theory approach. *Journal of Chemical Physics* **108**, 10, 4189-4198 (1998).

[107] d. C. Liliana, Y. Anan, G. Nissim, L. M. E, F. Britta and G. Otto; Five-component food-grade microemulsions: structural characterization by SANS. *Journal of colloid and interface science* **274**, 1, 251-67. FIELD Reference (2004).

[108] A. Yaghmur, L. de Campo, A. Aserin, N. Garti and O. Glatter; Structural characterization of five-component food grade oil-in-water nonionic microemulsions. *Physical Chemistry Chemical Physics* **6**, 7, 1524-1533 (2004).

[109] M. Tomsic, F. Podlogar, M. Gasperlin, M. Bester-Rogac and A. Jamnik; Water-Tween 40/Imwitor 308-isopropyl myristate microemulsions as delivery systems for ketoprofen: Small-angle X-ray scattering study. *International Journal of Pharmaceutics* **327**, 1-2, 170-177 (2006).

[110] S. Engelskirchen, N. Elsner, T. Sottmann and R. Strey; Triacylglycerol microemulsions stabilized by alkyl ethoxylate surfactants-A basic study; Phase behavior, interfacial tension and microstructure. *Journal of Colloid and Interface Science* **312**, 1, 114-121 (2007).

[111] N. Freiberger, C. Moitzi, L. de Campo and O. Glatter; An attempt to detect bicontinuity from SANS data. *Journal of Colloid and Interface Science* **312**, 1, 59-67 (2007).

[112] S. M. Choi, S. H. Chen, T. Sottmann and R. Strey; The existence of three length scales and their relation to the interfacial curvatures in bicontinuous microemul-

sions. *Physica A: Statistical Mechanics and Its Applications (Amsterdam, Netherlands)* **304**, 1-2, 85-92 (2002).

[113] I. S. Barnes, P. J. Derian, S. T. Hyde, B. W. Ninham and T. N. Zemb; A disordered lamellar structure in the isotropic phase of a ternary double-chain surfactant system. *Journal de Physique* **51**, 22, 2605-2628 (1990).

[114] A. J. Carmichael and K. R. Seddon; Polarity study of some 1-alkyl-3-methylimidazolium ambient-temperature ionic liquids with the solvatochromic dye, Nile Red. *Journal of Physical Organic Chemistry* **13**, 10, 591-595 (2000).

[115] C. Wakai, A. Oleinikova, M. Ott and H. Weingaertner; How Polar Are Ionic Liquids? Determination of the Static Dielectric Constant of an Imidazolium-based Ionic Liquid by Microwave Dielectric Spectroscopy. *Journal of Physical Chemistry B* **109**, 36, 17028-17030 (2005).

[116] C. Reichardt; Polarity of ionic liquids determined empirically by means of solvatochromic pyridinium N-phenolate betaine dyes. *Green Chemistry* **7**, 5, 339-351 (2005).

[117] O. Glatter; *Lecture: Streumethoden; Department of Physical Chemistry, University of Graz, Austria.* (1993).

[118] P. Mittelbach and G. Porod; Small-angle x-ray scattering by dilute colloid systems. The calculation of scattering-curves for parallelepipeds. *Acta Physica Austriaca* **14**, 185-211 (1961).

[119] R. Strey, O. Glatter, K. V. Schubert and E. W. Kaler; Small-angle neutron scattering of D2O-C12E5 mixtures and microemulsions with n-octane: direct analysis by Fourier transformation. *Journal of Chemical Physics* **105**, 3, 1175-1188 (1996).

[120] J. Brunner-Popela, R. Mittelbach, R. Strey, K. V. Schubert, E. W. Kaler and O. Glatter; Small-angle scattering of interacting particles. III. D_2O-$C_{12}E_5$ mixtures and microemulsions with n-octane. *Journal of Chemical Physics* **110**, 21, 10623-10632 (1999).

[121] M. Kotlarchyk, S. H. Chen and J. S. Huang; Temperature dependence of size and polydispersity in a three-component microemulsion by small-angle neutron scattering. *Journal of Physical Chemistry* **86**, 17, 3273-3276 (1982).

[122] W. M. Gelbart, A. Ben-Shaul and D. Roux; *Micelles, Membranes, Microemulsions, and Monolayers*. Springer, (1994).

[123] L. Arleth and J. S. Pedersen; Droplet polydispersity and shape fluctuations in AOT [bis(2-ethylhexyl)sulfosuccinate sodium salt] microemulsions studied by contrast variation small-angle neutron scattering. *Physical Review E: Statistical, Nonlinear, and Soft Matter Physics* **63**, 6-1, 061406/1-061406/18 (2001).

[124] P. Lindner and T. Zemb; *Neutrons, X-Rays and Light: Scattering Methods Applied to Soft Condensed Matter*. North-Holland Elsevier Science Publishers B.V., (1991).

[125] O. Glatter, D. Orthaber, A. Stradner, G. Scherf, M. Fanun, N. Garti, V. Clément and M. E. Leser; Sugar-Ester Nonionic Microemulsion: Structural Characterization. *Journal of Colloid and Interface Science* **241**, 215-225 (2001).

[126] R. Atkin and G. G. Warr; Self-Assembly of a Nonionic Surfactant at the Graphite/Ionic Liquid Interface. *Journal of the American Chemical Society* **127**, 34, 11940-11941 (2005).

VI.   Summary

In this thesis the formation of colloidal systems involving long-chain ionic liquids of the imidazolium type, which exhibit surfactant properties (surfactant-like ionic liquids, SLIL), was studied. The investigations included the characterisation of 1-dodecyl-3-methylimidazolium chloride (C_{12}mimCl), 1-tetradecyl-3-methylimidazolium chloride (C_{14}mimCl), and 1-hexadecyl-3-methylimidazolium chloride (C_{16}mimCl) in aqueous solution (Chapter V.1) and non-aqueous solution (Chapter V.2). In this context, non-aqueous means another ionic liquid, which was already liquid at room temperature and acted as water substitute. For this purpose, ethylammonium nitrate (EAN) and 1-butyl-3-methylimidazolium tetrafluoroborate (bmimBF$_4$) were chosen, because these room-temperature molten salts (RTMS) differ quite significantly from each other in consideration of their physico-chemical solvent properties, such as polaritiy and cohesive energy density. Due to this disparity, a substantial difference of the out-coming aggregation/phase behaviour was supposed leading to a fundamental understanding of the influence of the RTMS type on SLIL aggregation. Further, the comparison of the non-aqueous data with the aqueous results was a central part in the underlying work, since it adresses the old question which fundamental requirements of the solvent have to be considered to promote surfactant self-assembly in solution. As the investigation of new amphiphiles concerning their properties in solution is always a very important topic in colloid science, both scientifically, and from the application point of view, another aim of this work was to differentiate the imidazolium SLILs with respect to the well investigated alkyl trimethylammonium and alkyl pyridinium analogues in aqueous solution. For this purpose, the results obtained for the three aqueous SLILs systems were related to literature data of the common cationic surfactant. The third segment of the examinations was attributed to the formulation and characterization of non-aqueous SLIL/RTMS-based microemulsions using C_{16}mimCl as surfactant, 1-decanol as co-surfactant, RTMS (EAN or bmimBF$_4$) as polar phase, and dodecane as the oil phase. Such pseudo-ternary systems formed with the help of a cationic surfactant and a co-

surfactant are not reported in the open literature until now. Only RTMS-microemulsions incorporating non-ionic surfactants are reported. In this context, the special interest was the investigation of regions in the phase digram of the two systems where reverse droplet microemulsions may be located, since these type of microemulsions are very interesting from the application point of view as micro-reactors for chemical recations, e.g. nano-particle synthesis. Beside the studies of the SLIL/RTMS-systems and C_{16}mimCl/RTMS-microemulsions at low temperatures (room temperature and near room temperature), the applicability of the latter systems at temperatures beyond 100°C was evaluated. Ionic liquids, the SLILs as well as the RTMS, show excellent temperature resistances and negligible vapour pressures, and they are consequently very suitable substances for the application at high temperatures. The possibility to formulate colloidal systems, which are stable also at temperatures far beyond 100°C, would extend the limited thermal stability range of aqueous micellar and microemulsion systems without applying pressure.

1 Aggregation of surfactant-like ionic liquids in aqueous solution

Many different techniques were used to characterize the binary SLIL/water systems including (i) solubility measurements of the SLILs, (ii) surface tension, (iii) conductivity, (iv) fluorescence quenching, and finally (v) small-angle neutron scattering experiments. The data thus obtained were employed in order to obtain the Krafft temperature, maximal areas/surfactants at the liquid/gas interface, the critical aggregation concentrations, the degrees of counterion dissociation (and therefore the degree of counterion binding), aggregation numbers, and finally micellar properties, e.g. aggregate size and shape. In addition, thermodynamic parameters including the Gibbs free energies of adsorption and micellization, were calculated for C_{12}mimCl, C_{14}mimCl, and C_{16}mimCl, respectively. From Gibbs free energies of micellization, the contributions of enthalpies and entropies of micellization were extracted. The obtained values were related to literature data of conventional surfactant analogues, i.e. alkyl trimethylammonium chlorides (C_nTACl) and alkyl pyridinium chlorides (C_nPyCl), respectively.

Considerable differences of the $C_n$mimCl surfactants in aqueous media compared to their conventional counterparts were found in terms of all estimated surfactant parameters. In general, the SLILs show lower critical aggregation concentrations and lower free energies of adsorption and micellization, respectively, than the corresponding C_nTACl and C_nPyCl salts. This observation clearly indicates that the adsorption/aggregation tendency of the $C_n$mimCls is more favourable than that of the respective common surfactant chlorides. In addition, different packing behaviour of the SLIL monomers at the water surface as well as in the self-assembled aggregates was supposed for the imidazolium surfactants compared to C_nTACl and C_nPyCl, respectively. This conclusions are based on the disparities of the required areas per SLIL molecule at the (l/g) interface as well as of the achieved aggregation numbers of the SLIL aggregates reffered to the quantities reported for conventional amphiphiles. Furthermore, a significat higher tendency of aggregate growth was found for the SLILs which gives reason to assume a high tendency of the $C_n$mimCl surfactants to reduce the curvature of the formed aggregates at higher concentrations (in water). All observations made for the SLILs reflect a smaller repulsion of the head groups compared to the analogues with ammonium and pyridinium ones, which makes self-aggregation more favourable for the $C_n$mimCl salts. There may be two effects, which both reduce unfavourable head group repulsion in the case of the $C_n$mimCl surfactants leading to higher aggregation tendencies. One effect is the delocalized charge of the imidazolium head group and the other a lower counter-ion dissociation of the SLILs as indicated by conductivity measurements compared to other cationic surfactant types without or different charge delocalized head groups. Theoretical calculations taken from the literature concerning the charge localization within ammonium, pyridinium and 1-methylimidazolium head groups suggest that the high aggregation tendency of the SLILs is mainly due to the highly acidic H-atom at C(2) of the imidazolium ring, which coordinates the chloride counter ion by hydrogen bonding. Therefore, the head group charge is more effectively screened compared to the other two surfactant heads leading to lower repulsion forces. However, an attempt to relate the lower counterion dissociation of the SLILs to hydrogen bonds between the H(2) of the imidazolium head and the chloride ion, as proposed in the litera-

ture, was not successful by application of the low concentration chemical model to the conductivity data below the *cac* of the SLILs. Finally, it could be shown that all conclusions drawn from surface tension measurements, conductivity measurements, and fluorescence quenching are inline with the results obtained from small-angle neutron scattering experiments, which have been analyzed in terms of a ellipsoid form factor model in combination with a Hayter-Penfold structure factor of interacting charged hardspheres. Using the latter model, it was possible to extract the evolution of the particle shapes and dimensions for all three aqueous SLIL-systems.

2 Aggregation of SLILs in solution of room-temperature molten salts

The second part of this work was focused on the possibility to form micellar aggregates in two RTMS (ethylammonium nitrate and 1-butyl-3-methyimidazolium tetrafluoroborate) by admixing SLILs. The investigations included DSC, surface tension, density, SAXS, and SANS measurements. From these techniques, the solubility behaviour, the critical aggregate concentrations, the partial molar volumes, and structural information of the formed SLIL aggregates in the two RTMS were obtained. Additionally, thermodynamic parameters including the surface excess concentrations, the minimum areas occupied per SLIL molecules at the RTMS/gas interface, the contributions of the SLIL discrete segments to Gibbs free energies of adsorption, and the Gibbs free energies of micellization were calculated from the surface tension isotherms measured for the SLIL/EAN- and SLIL/bmimBF$_4$-systems at 25°C and 40°C, respectively. Beside the investigations at ambient and near ambient temperature, further studies of the SLIL/RTMS-mixtures were carried out at higher temperatures (up to 150°C) in order to verify the high-temperature stability of the formulated systems taking advantage of the wide temperature range, over which ionic liquids are liquid and stable.

It could be shown by surface tension as well as by small ange neutron scattering that SLILs form self-assembled aggregates in both types of RTMS. Compared to the results obtained in aqueous solution, the SLILs show higher *cac*s and also higher free

energies of micellization. Consequently, aggregate formation seems to be less favoured bmimBF$_4$. Interestingly, the finding of aggregates in bmimBF$_4$ are not in agreement to the postulation of Evans et al. who postulated a minimum cohesive energy density of 1.3 J/m^3 required to promote self-aggregation of amphiphiles in a solvent. Since bmimBF$_4$ possesses a considerably lower cohesive energy density of 0.75 J/m^3, it is clear, as already proposed in the literature, that the old claim of Evans et al. must be updated to the recent situation. The results obtained for the C$_{16}$mimCl/EAN- and C$_{16}$mimCl/bmimBF$_4$- system from small-angle scattering experiments, which were analyszed in consideration of a spherical form factor and a Percus-Yevick hard-sphere structure factor, also permit some interesting information: The aggregate evolution of C$_{16}$mimCl in RTMS is quite different to that in water, i.e. only spherical aggregates were formed and no aggregate growth was observed over the concentration range studied, and further, the size of the formed spherical micelles depends on the RTMS employed as solvent.

Unfortunatly, no quantitative analysis of the scattering data achieved at 150°C could be performed, because no absolute intensities in the case of the SAXS patterns were obtained. Further, problems concerning the neutron detector during the SANS experiments made an fitting of the scattering curves impossible. Although this situation is not satisfactory, the qualitative interpretation of the scattering patterns, however, established clearly the proof that C$_{16}$mimCl forms aggregates in both solvent-RTMS also at high temperatures (up to 150°C, perhaps more). Consequently, it could be demonstrated that it is possible to extend the limited temperature range of aqueous surfactant systems by the present C$_{16}$mimCl/RTMS-systems.

3 Formulation and characterisation of surfactant-like ionic liquid/room temperature molten salt -based microemulsions

The third part of this thesis dealt with the examination of reverse C$_{16}$mimCl/1-decanol/RTMS/dodecane microemulsions. In this context, the realms of existence of clear and monophasic areas of two pseudo-ternary systems only differing by the RTMS

(EAN or bmimBF$_4$) used as water substitute will be presented. The phase behaviour of the two systems along defined experimental paths, which are located in the region of the phase diagrams where reverse RTMS nanodroplets may be assumed, was characterized at 30°C by means of conductivity, viscosity, dynamic light scattering, UV-Vis spectroscopy, steady-state fluorescence spectroscopy, and SAXS. Furthermore, preliminary investigations concerning the high-temperature stability of the microemulsions were carried out by means of visual observations, DSC, and high-temperature SANS.

Both microemulsion systems show huge isotropic monophasic regions denoted as microemulsion areas (*L*-phase), when the molar ratio of the pseudo-constitute, surfactant and co-surfactant, was 1:4. This molar ratio was chosen, because it provided the best trade-off in consideration of solubilization efficiency and application. The experiments were caried out along two defined experimental paths incorporating constant surfactant/co-surfactant weight fraction, 0.30 and 0.65 for the EAN-microemulsions and bmimBF$_4$-microemulsions, respectively, and varying RTMS/dodecane ratios. The measurements carried out for the EAN-system showed very interesting features concerning the phase evolution along the experimental path. It could be demonstrated that at low EAN volme fractions separated reverse droplets are formed within the system followed by an dynamic percolation phenomenon at an EAN volume fraction of about 0.10. When higher amounts of EAN (volume fractions greater than 0.22) are solubilised, the system undergoes a steep transition towards a more bicontinuous-like phase. Below the percolation threshold determined for the EAN-system, DLS measurements gave monoeponentially decaying autocorrelation functions (only one relaxation process) from which the hydrodymamic radii of the reverse EAN micro-droplets were obtained. The radii increase and follow the linear swelling law of reverse microemulsions. The dimensions were found to be in the range of normal reverse aqueous microemulsion systems, i.e. between 2 and 10 nm. Further, DLS was able to monitor the occurance of an second relaxation process above the EAN percolation concentration. This observation was attributed to a topological relaxation mode in the microemulsions by membrane fusion, allowing oil to flow from one region of the space to the other, involving fusion of the droplets/domains. The latter is in good agreement to the dynamic percola-

tion theory. The buil-up of defined microemulsion droplets were further analyzed by determination of the microviscosity of the droplet cores using fluorescence technique and a suitable dye. A defined transition of reverse micelles to real reverse EAN hosting microemulsion droplets was observed. Contary to the EAN-system for which a lot of information could be achieved from conductivity and viscosity measurements, the bmimBF$_4$-system showed no special features in the data plots, only a monotonical raise of conductance and viscosity could be observed. Also the fluorescence measurements on microemulsions of the bmimBF$_4$ type did not show any characteristics. The obtained maximum fluorescence intensity as well as the corresponding wavelength showed no variance. Also DLS failed for this system, perhaps due to refractive index matching of solubilised and continuous phase. However, it was possible to establish the proof of structure within the bmimBF$_4$-microemulsions by SAXS, which gave characteristic scattering for both microemulsion types, EAN and bmimBF$_4$, respectively. The scattering curves were anylazed according to the Teubner-Strey-model from which two characteristic length scales, the periodicity and the correlation length, were attained. From this two quantities, the amphilicity factor, which can be related to the structure present within the system, was calculated. The values of the amphilicity factor showed that reverse droplet structures are formed within the EAN-system, whereas a bicontinuous structure is present in the case of the bmimBF$_4$-system. Additionally, it is supposable from the SAXS results that the investigated bmimBF$_4$ microemulsions seem to be more highly structured than the EAN microemulsions. However, it must be noted that until now, it is not completely clear whether the distinctive structure in the bmimBF$_4$-system is due to the different nature of the solvent-like RTMS or due to the higher amount of surfactant/co-surfactant weight fraction incorporated in the investigated C$_{16}$mimCl/1-decanol/dodecane/bmimBF$_4$-samples compared to the EAN microemulsions. Due to the fact that along the experimental path of the EAN-system reverse droplets were formed, the SAXS curves of this system were additionally evaluated in terms of the model-free GIFT-method using a Percus-Yevick structure factor. Contrary to the TS-model, which incorporates features of droplet microemulsions as well as of bicontinuous structures, this evaluation is solely based on the particulate picture of microemulsions, no biconti-

nuity is considered in this analysis. It was possible to extract the shape and the dimension of the particles present within the measured samples from the GIFT evaluation. The results confirm the presence of spherical objects as well as the swelling law already observed from DLS. For the estimation of the structure factor parameters, the hard-sphere volume fraction was restricted to the theoretically calculated values using the assumption that EAN, C_{16}mimCl, and 1-decanol are completely involved in the formation of the reverse microemulsion droplets. The latter directly affects the polydispersity value extracted from the structure factor, but not the quantity of the hard-sphere interaction radius of the reverse EAN droplets. Keeping in mind this restriction, which results from the scattering theory, together with the principle of the GIFT-evaluation, it was possible to follow qualitative trends of aggregate evolution along the experimental path. Although all obtained parameters are in very good agreement to previous conclusions, one has to remark, however, that all values extracted from the GIFT-evaluation have to be understood as preliminary results, because of the exclusion of cosolubility of the droplet components in the continuous phase during the GIFT evaluation. In order to pre-evaluate the suitability of the C_{16}mimCl/RTMS-based microemulsions to host metallic salts, which often act as precursors in nano-material synthesis, one interests of the present work was to proof the possibility to solubilise ionic metal compounds in the newly formulated microemulsion systems. For this purpose, UV/Vis-spectroscopy was applied. It was found that $Ni(NO_3)_2$ and $CoCl_2$, both acting as reference metal salts due their deep colours, can be easily solubilised within the two C_{16}mimCl/RTMS-systems. Therefore, it can be supposed that the reverse RTMS-microemulsions could have potential application in the production of metallic or semiconductor nanomaterials.

Beside the characterisation of the RTMS-microemulsions at 30°C, another major task was to show that these systems are also suitable for the application at temperatures far beyond 100°C. This was accomplished via high-temperature small angle-neutron scattering measurements, performed at 30°C, 60°C, 90°C, and 150°C. The obtained scattering curves show that the features, which are characteristic for structure in microemulsions, still persist at 150°C. Consequently, the C_{16}mimCl/1-decanol/

RTMS/dodecane microemulsions will be also very interesting for high-temperature applications for which common aqueous microemulsions are unsuitable.

VII. Appendix

1   Index of Figures

2   Index of Tables

(C_{16}TACl), respectively. [f]Ref. [52]; value was obtained from static light scattering. [g]Ref. [71]; N_{agg} was estimated from fluorescence quenching in the concentration range 21-86 mM. [h]Ref [72]; values were estimated from MEM. Ref. [73]; values were calculated from osmotic pressure and calorimetric data. *Note: Literature value of the limiting equivalent conductivity of Cl^{-} and Br^{-}; quantities were taken from Ref. [74].262

3 Scientific Contributions

3.1 Publications

1. S. Thomaier and W. Kunz; Aggregates in mixtures of ionic liquids. *Journal of Molecular Liquids* **130**, 1-3, 104-107 (2007).

2. O. Zech, M. Kellermeier, S. Thomaier, E. Maurer, R. Klein, C. Schreiner and W. Kunz; Alkali metal oligoether carboxylates - a new class of ionic liquids. *Chemistry-A European Journal* **15**, 6, 1341-1345 (2009).

3. O. Zech, S. Thomaier, P. Bauduin, T. Rueck, D. Touraud and W. Kunz; Microemulsions with an Ionic Liquid Surfactant and Room Temperature Ionic Liquids As Polar Pseudo-Phase. *Journal of Physical Chemistry B* **113**, 2, 465-473 (2009).

4. O. Zech, S. Thomaier, A. Kolodziejski, D. Touraud, I. Grillo and W. Kunz; Ionic Liquids in Microemulsions - a Concept to Extend the Conventional Thermal Stability Range of Microemulsions. *Chemistry-A European Journal* (2009). Submitted.

5. S. Thomaier, O.Zech, U. Keiderling and W. Kunz; Aggregation of surfactant-like ionic liquids (SLIL) in aqueous solution. *Langmuir* (2009). To be submitted.

6. S. Thomaier, O.Zech, U. Keiderling and W. Kunz; Aggregation of SLILs in solution of room temperature molten salts. *Journal of Physical Chemistry B* (2009). To be submitted.

3.2 Patent

1. W. Kunz, S. Thomaier, E. Maurer, O. Zech, M. Kellermeier and R. Klein; Onium salts of carboxyalkyl-terminated polyoxyalkylenes for use as high-polar solvents and electrolytes. BASF SE, Germany. **WO 2008135482** (2008).

3.3   Talks & Poster Presentations

1. <u>S. Thomaier</u> and W. Kunz; Aggregates in mixtures of Ionic Liquids – A new Class of Colloidal Systems. *3ʳᵈ Zsigmondy Colloquium of the Deutsche Kolloidgesellschaft*, 6ᵗʰ - 7ᵗʰ April 2006, Berlin, Germany. (Talk)

2. S. Thomaier, O. Zech, D. Touraud and W. Kunz; Ionic liquids in high temperature stable microemulsions. *43rd Meeting of the German Colloid Society*, 8ᵗʰ - 10ᵗʰ October 2007, Mainz, Germany. (Poster)

3. E. Maurer, M. Kellermeier, R. Klein, S. Thomaier, O. Zech and W. Kunz; Low melting ion pair amphiphiles (LIPA). *43rd Meeting of the German Colloid Society*, 8ᵗʰ - 10ᵗʰ October 2007, Mainz, Germany. (Poster)

4. S. Thomaier, O. Zech, D. Touraud and W. Kunz; Ionic liquids in high temperature stable microemulsions. *Formula V*, 19ᵗʰ - 22ⁿᵈ November 2007, Potsdam, Germany. (Poster)

5. Matthias Kellermeier, Stefan Thomaier, Oliver Zech, Eva Maurer, Regina Klein and Werner Kunz; Cryptoanionic Liquids - a New Type of Ionic Liquids. *7ᵗʰ Liquid Matter Conference*, 27ᵗʰ June - 1ˢᵗ July 2008, Lund, Sweden. (Poster)

6. Eva Maurer, Matthias Kellermeier, Regina Klein, Stefan Thomaier, Oliver Zech, Werner Kunz; Simple ionic liquid ion pair amphiphiles (LIPA): A new class of surfactants. *21ˢᵗ Conference of the European Colloid and Interface Society ECIS*, 10ᵗʰ - 14ᵗʰ September 2008, Geneva, Switzerland. (Poster)

7. O. Zech, S. Thomaier, A. Kolodziejski, D. Touraud and W. Kunz; Ionic liquids in microemulsions - a concept to extend the conventional thermal stability range of microemulsions. *4ᵗʰ European Detergents Conference EDC*, 15ᵗʰ - 17ᵗʰ October 2008, Würzburg, Germany. (Poster)

8. <u>O. Zech</u>, S. Thomaier, A. Kolodziejski, D. Touraud and W. Kunz; Ionic liquids in microemulsions - a concept to extend the conventional thermal stability range of microemulsions. *5ᵗʰ Zsigmondy Colloquium of the Deutsche Kolloidgesellschaft*, 16ᵗʰ - 17ᵗʰ March 2009, Bayreuth, Germany. (Talk)

3.4 Experimental Reports

1. S. Thomaier, O. Zech and U. Keiderling; SANS study of aqueous long-chain ionic liquid systems (Proposal N° CHE-04-1462, Instrument V4). *BENSC Experimental Reports 2007*, Hahn-Meitner-Institute, Berlin, Germany.

2. O. Zech, S. Thomaier and I. Grillo; High temperature stable IL-microemulsions (Proposal N° 9-10-899, Instrument D22). *ILL Experimental Reports 2007*, Institute Max von Laue - Paul Langevin, Grenoble, France.

Declaration

I hereby declare that this thesis, apart from the help recognized, is my own work and effort, and it has not been formerly submitted to another university for any award.

Stefan Thomaier

Regensburg, April 2009